

2-D(max)

NTIS Ac \$23.00

NASA CR-130164

AED R-3318F
April 23, 1970

ITOS Meteorological Satellite System

TIROS M Spacecraft (ITOS 1) Final Engineering Report

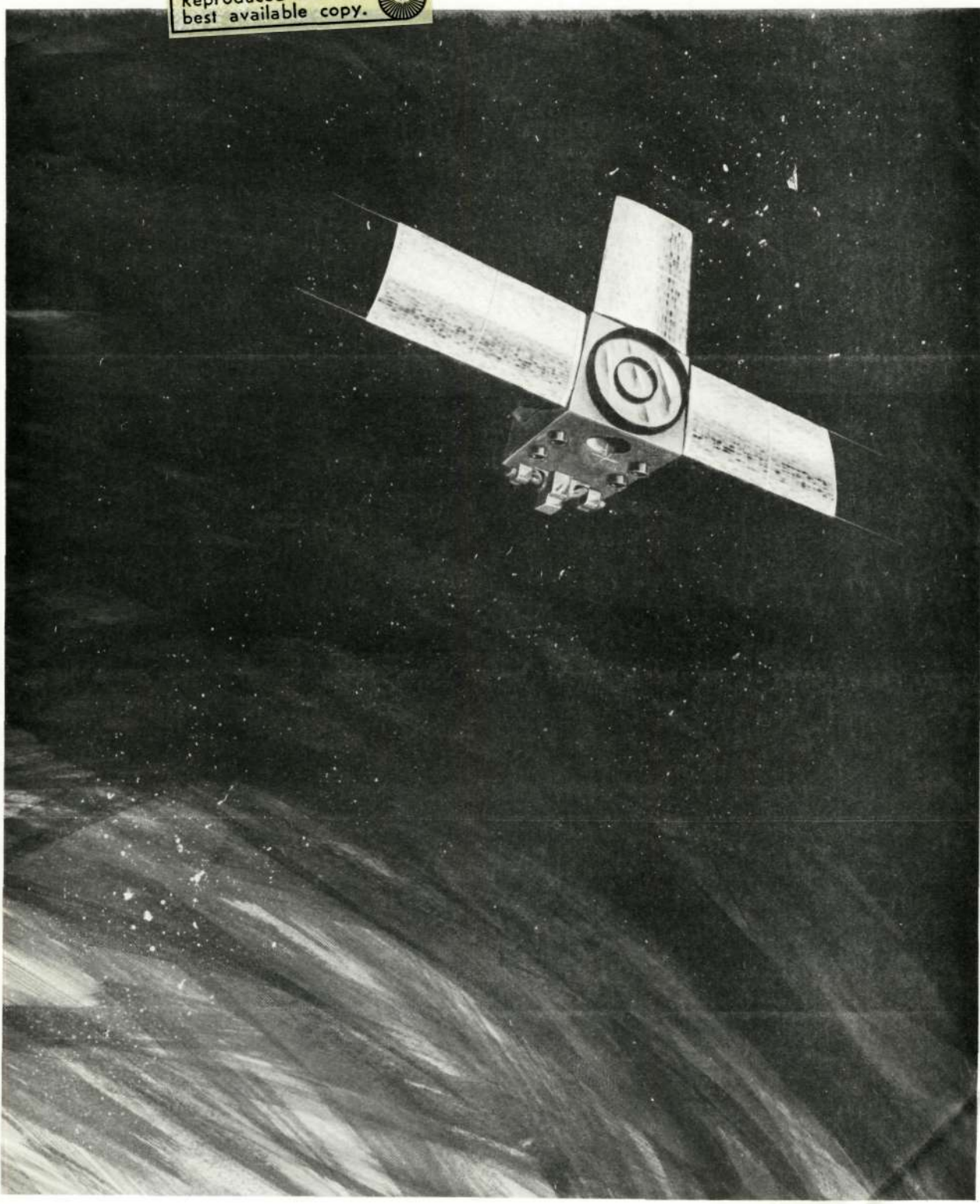
Volume II

(NASA-CR-130164)	ITOS METEOROLOGICAL	N73-16881
SATELLITE SYSTEM:	TIROS M SPACECRAFT	
(ITOS 1), VOLUME 2	Final Engineering	
Report (Radio Corp. of America)	419 p	Unclas
HC \$23.00	CSSL 22B G3/31	54429

Prepared for
Goddard Space Flight Center
National Aeronautics and Space Administration
Washington, D.C.
Contract No. NAS5-10306



Reproduced from
best available copy.



Artist's Concept of the ITOS Spacecraft

PREFACE

The TIROS M (ITOS 1) spacecraft was developed and built by the Astro-Electronics Division of RCA Corporation for the Goddard Space Flight Center of the National Aeronautics and Space Administration, under NASA Contract NAS5-10306. The TIROS M (ITOS 1) spacecraft was developed to meet the requirements of an Improved TIROS Operational System (ITOS) mission, and became, upon attaining successful operation in orbit, the first of the second-generation operational meteorological satellites.

This document provides system, subsystem, and component descriptions for the spacecraft and ground support equipment, and documents the design, development, testing, and integration phases of the program. It also describes the prelaunch and launch activities in which RCA personnel participated.

TABLE OF CONTENTS

Section		Page
VOLUME 1		
PART 1. INTRODUCTION		
I	THE ITOS SYSTEM AND MISSION	1-I-1
II	PROGRAM SUMMARY	1-II-1
III	ITOS MISSION PROFILE	1-III-1
IV	DESIGN PHILOSOPHY AND CONSTRAINTS	1-IV-1
V	THE TIROS M SPACECRAFT	1-V-1
	A. System Design	1-V-1
	B. Subsystem Description	1-V-2
	1. General	1-V-2
	2. Command Reception and Processing	1-V-2
	3. Dynamics Control	1-V-2
	4. Primary Sensors	1-V-3
	a. Real-Time Data	1-V-3
	b. Stored Data	1-V-4
	5. Secondary Sensors	1-V-4
	6. Communications	1-V-5
	a. S-Band Link	1-V-5
	b. Real-Time Link	1-V-5
	c. Beacon and Command Link	1-V-6
	7. Power Supply	1-V-6
	8. Subsystem Redundancy	1-V-7
	a. Operating Goals	1-V-7
	b. Alternate Modes of System Operation	1-V-7
VI	ITOS GROUND COMPLEX	1-VI-1
	A. General	1-VI-1
	B. Command, Programming, and Analysis Centers ...	1-VI-1
	C. Command and Data Acquisition (CDA) Stations	1-VI-2
	D. Spacecraft Checkout Facilities	1-VI-2
	E. Scope of Ground Equipment Coverage	1-VI-3

PRECEDING PAGE NUMBER NOT FILMED

TABLE OF CONTENTS (Continued)

Section	Page
VII	SYSTEM PERFORMANCE 1-VII-1
A.	General 1-VII-1
B.	Launch and Orbit Injection Conditions 1-VII-1
C.	Mission Life and Attitude 1-VII-3
1.	Mission Life 1-VII-3
2.	Mission Attitude 1-VII-4
D.	Data Coverage 1-VII-4
1.	System Operation 1-VII-4
2.	Visible Spectrum 1-VII-5
a.	Picture Coverage 1-VII-5
b.	Picture Sequence 1-VII-5
3.	Scanning Radiometer Subsystem 1-VII-6
a.	Data Coverage 1-VII-6
b.	Data Sequence 1-VII-6
4.	Data Time Codes 1-VII-6
5.	Data Acquisition 1-VII-7
VIII	ORBIT CHARACTERISTICS 1-VIII-1
A.	The ITOS Orbit 1-VIII-1
B.	Operational Effects of Orbit Characteristics 1-VIII-4
1.	Ground Illumination 1-VIII-5
2.	Spacecraft Sun Angle and Eclipse Time 1-VIII-5
3.	Ground Station Contact Time 1-VIII-9
C.	Effect of Date and Time of Launch 1-VIII-9
D.	Effects of Injection Errors 1-VIII-13
E.	Sensors and Sensor Coverage 1-VIII-13
1.	Primary Sensor Subsystems 1-VIII-13
2.	Secondary Sensors Subsystem 1-VIII-19

PART 2. SPACECRAFT DESIGN

I	INTRODUCTION 2-I-1
II	SPACECRAFT STRUCTURE 2-II-1
A.	General 2-II-1
B.	Design Approach 2-II-1
1.	Requirements and Constraints 2-II-1
2.	Design Synthesis 2-II-4
3.	Spacecraft Structure 2-II-5
4.	Mechanisms 2-II-6
5.	Stress Analysis 2-II-7
C.	Design Philosophy 2-II-9
1.	General 2-II-9
2.	Mechanical Alignment 2-II-10

TABLE OF CONTENTS (Continued)

Section	Page
3. Component Accessibility	2-II-10
4. Weight	2-II-11
5. Fabrication and Assembly	2-II-11
6. Integration of Electronic Equipment	2-II-13
7. Interchangeability	2-II-13
D. Structural Components	2-II-14
1. Separation Ring	2-II-14
2. Baseplate	2-II-17
3. Equipment Mounting Panels	2-II-18
4. Access Panels	2-II-21
a. Earth-Oriented Panel	2-II-21
b. Anti-Earth Side Panel	2-II-22
5. Scanning Radiometer Mounting Plate	2-II-27
6. Crossbrace Assembly	2-II-27
7. Thermal Fence	2-II-27
8. Solar Array Structure and Deployment Mechanism	2-II-29
9. Momentum and Attitude Control Coils	2-II-34
10. Nutation Dampers	2-II-38
11. Active Thermal Controller (ATC)	2-II-38
a. Actuator Sensor Unit	2-II-38
b. Louver and Hinge Assenbly	2-II-41
12. Accelerometer Assembly	2-II-43
E. Interior Electronics Arrangement	2-II-44
1. General	2-II-44
2. Interior Electronics Arrangement of the Mechanical Test Model (MTM)	2-II-45
3. Interior Electronics Arrangement of the Fight Model Spacecraft	2-II-45
F. Design History Timetable	2-II-45
II THERMAL DESIGN	2-III-1
A. General	2-III-1
B. Functional Description	2-III-4
1. Thermal Fence	2-III-4
2. Active Thermal Controller (ATC)	2-III-8
3. Thermal Insulation	2-III-8
4. Thermal Painting	2-III-9
5. Temperature Sensors	2-III-9
C. Design History	2-III-10
1. Final Design Requirements	2-III-10
2. Definition of Preliminary Design	2-III-12

TABLE OF CONTENTS (Continued)

Section	Page
a. Acquisition Mode	2-III-12
b. Operational Mode	2-III-14
c. Critical Parameter Variation	2-III-14
3. Modifications of Thermal Design Due to Detailed Analysis and Fabrication	2-III-15
a. Relocation of the ATC Flaps	2-III-15
b. Insulation Change	2-III-15
c. Redistribution of Baseplate Radiator	2-III-16
d. Reduction of Total Radiator Area	2-III-16
4. Transient Thermal Analysis	2-III-16
a. Acquisition Mode	2-III-16
b. Operational Mode	2-III-17
5. Modification of Thermal Design Due to Analytical Evaluation, TTM Testing and Launch Vehicle Reconfiguration	2-III-18
a. Redistribution of the Radiator Area	2-III-18
b. Alteration of Baseplate Radiator Surface Finish	2-III-18
c. Redesign of Insulation	2-III-18
6. Predicted Flight Temperatures for Small-to- Large Sun Angles at an Orbit Altitude of 775 Nautical Miles	2-III-19
7. Predicted Flight Temperatures for Normal Operating Sun Angles at Orbiting Altitudes of 600 and 900 Nautical Miles	2-III-19
8. Modifications of Thermal Design Due to Thermal and Electrical Testing of the Fully Integrated Flight Spacecraft	2-III-19
9. Predicted Flight Temperatures for Mission Mode Sun Angles at an Orbit Altitude of 790 Nautical Miles	2-III-20
10. Acquisition Mode Flight Temperature Predictions	2-III-38
11. Solar Panel Flight Temperature Predictions ...	2-III-38
IV COMMAND SUBSYSTEM	2-IV-1
A. General	2-IV-1
B. Functional Description	2-IV-2
1. Command Data Format	2-IV-4
2. Command Data Reception and Verification	2-IV-4
3. Command and Control Functions	2-IV-4

TABLE OF CONTENTS (Continued)

Section	Page
C. Dual Command Decoder	2-IV-11
1. General Description	2-IV-11
a. Power and Signal Interfaces	2-IV-13
b. Decoder Data Format	2-IV-17
2. Functional Operation	2-IV-18
a. General Decoding Processes	2-IV-18
b. Detailed Circuit Description	2-IV-22
(1) Analog Circuits	2-IV-22
(2) Digital (Integrated) Circuits	2-IV-27
(3) Buffer Circuits	2-IV-30
D. Command Distribution Units (CDU'S) A and B	2-IV-30
1. General Description	2-IV-30
2. Functional Operation	2-IV-31
a. General	2-IV-31
b. Command Decoding	2-IV-33
c. Decoded Commands and Their Functions ..	2-IV-33
(1) Scanning Radiometer (SR) Subsystem	
Motor Controls	2-IV-37
(2) SR Electronics	2-IV-37
(3) SR Recorder	2-IV-38
(4) Real-Time Transmitter Subsystem	
Controls	2-IV-39
(5) APT Camera Subsystem Control	2-IV-39
(6) Beacon Transmitter Control	2-IV-39
(7) Housekeeping Telemetry Subsystem	
Control	2-IV-40
(8) 3.9-kHz Telemetry Subsystem	2-IV-40
(9) 2.3-kHz Telemetry Subsystem	2-IV-42
(10) Digital Telemetry Subsystem Control	2-IV-43
(11) Data Format Converter and Associated	
Sensors	2-IV-43
(12) Time Base Unit	2-IV-44
(13) Programmer	2-IV-44
(14) AVCS Cameras	2-IV-44
(15) AVCS Tape Recorders	2-IV-44
(16) S-Band Transmitter and MUX	2-IV-45
(17) Power Supply Electronics Control	2-IV-46
(18) Pitch Control Subsystem	2-IV-46
(19) Attitude Control Coils	2-IV-47
(a) QOMAC and Magnetic Bias Coils	2-IV-47
(b) Momentum Coils	2-IV-47
(20) Solar Panel Squib Firing	2-IV-48
(21) Nutation Dampers and Yo-Yo's	2-IV-48

TABLE OF CONTENTS (Continued)

Section	Page
d. Command Sequencing	2-IV-48
e. Interlocked Commands and Functions	2-IV-49
f. Special Operational Features	2-IV-50
(1) Push-to-Talk Operation	2-IV-50
(2) Emergency Tone Telemetry Request	2-IV-50
(3) TBU Overflow	2-IV-51
(4) QOMAC High Torque Mode	2-IV-51
(5) AVCS Direct Picture Mode	2-IV-51
(6) Telemetry Commutator Outputs	2-IV-51
E. Dual Command Programmer	2-IV-51
1. General Description	2-IV-51
a. Physical Description	2-IV-53
b. Functional Description	2-IV-53
(1) Programmer Input and Output Interfaces ..	2-IV-53
(2) Program Data Loading	2-IV-56
2. Operating Modes	2-IV-64
a. AVCS, APT, and SR Control	2-IV-64
(1) Mode 1	2-IV-65
(2) Mode 2	2-IV-70
(3) Modes 1 or 2 with Altered Timing	2-IV-70
(4) Mode 3	2-IV-71
(5) Mode 4	2-IV-71
b. QOMAC Control	2-IV-73
c. Proportional QOMAC Control	2-IV-74
F. Dual Time Base Unit (TBU)	2-IV-74
1. General Description	2-IV-74
a. TBU Circuits	2-IV-76
b. Counting Technique	2-IV-76
c. Redundancy	2-IV-77
d. Special Requirements	2-IV-77
2. Functional Operation	2-IV-78
a. Input Signals	2-IV-78
b. Output Signals	2-IV-78
c. Power Control and Conversion	2-IV-79
d. Time Base Generator (TBG)	2-IV-82
e. Time Code Generator (TCG)	2-IV-82
V PRIMARY ENVIRONMENTAL SENSOR SUBSYSTEMS ...	2-V-1
A. Introduction	2-V-1
B. Advanced Vidicon Camera Subsystem (AVCS)	2-V-2
1. General Description	2-V-2
2. Functional Description	2-V-5

TABLE OF CONTENTS (Continued)

Section	Page
a. Record Mode	2-V-5
b. Playback Mode	2-V-10
c. Direct Mode	2-V-11
3. AVCS Components	2-V-11
a. Camera Sensor and Camera Electronics...	2-V-11
(1) General Description	2-V-11
(a) AVCS Camera Sensor	2-V-15
<u>1.</u> AVCS Hybrid Vidicon	2-V-15
<u>2.</u> Gray Scale Calibrator Assembly	2-V-19
<u>3.</u> Deflection Yoke	2-V-19
<u>4.</u> Shutter Assembly	2-V-21
<u>5.</u> Lens	2-V-21
<u>6.</u> Preamplifier	2-V-21
<u>7.</u> Vidicon Electrode Decoupler	2-V-21
(b) Camera Electronics	2-V-21
(2) Functional Operation	2-V-23
(a) AVCS Camera Sensor	2-V-23
(b) Camera Electronics	2-V-27
<u>1.</u> AC Video Amplifier	2-V-28
<u>2.</u> Video Clamp Dark Current Sampling	2-V-28
<u>3.</u> Shading Correction	2-V-34
<u>4.</u> DC Amplifier	2-V-43
<u>5.</u> Black and White Clippers, Video Blanking and Porch, and Time Code Insertion	2-V-44
<u>6.</u> Output Emitter Follower and Sync Insertion	2-V-46
<u>7.</u> Horizontal Deflection	2-V-47
<u>8.</u> Vertical Deflection	2-V-49
<u>9.</u> Yoke Skew Corrector	2-V-49
<u>10.</u> Main Converter	2-V-49
<u>11.</u> Filament DC-to-DC Converter	2-V-52
<u>12.</u> +13-Volt Regulator	2-V-52
<u>13.</u> Beam Current Regulator	2-V-53
<u>14.</u> Main Power Switch	2-V-54
<u>15.</u> Standby Power Switch	2-V-56
<u>16.</u> Shutter Drive	2-V-56
<u>17.</u> Command Buffers	2-V-58
<u>18.</u> Gray Scale Calibrator Regulator	2-V-59
<u>19.</u> Telemetry	2-V-59
b. AVCS Tape Recorder	2-V-59
(1) General Description	2-V-59
(a) Interface Signals	2-V-60
(b) Tape Transport Assembly	2-V-65

TABLE OF CONTENTS (Continued)

Section	Page
(c) Motor Drive Circuit	2-V-70
(d) Video Signal Record and Playback Circuits	2-V-70
(e) Flutter-and-Wow Record and Playback Circuit	2-V-71
(2) Functional Operation	2-V-71
(a) Electronics	2-V-71
<u>1.</u> Record Power Switch	2-V-71
<u>2.</u> Playback Power Switch.....	2-V-71
<u>3.</u> Playback End-of-Tape Circuit	2-V-72
<u>4.</u> Operating Status Telemetry.....	2-V-72
<u>5.</u> One-Shot and Differentiating Circuit	2-V-72
<u>6.</u> Motor Drive Circuit	2-V-73
<u>7.</u> Start Mode	2-V-74
<u>8.</u> Record Mode	2-V-76
<u>9.</u> Playback Signal	2-V-77
<u>10.</u> Telemetry Circuits	2-V-78
(b) Mechanical	2-V-79
<u>1.</u> Motor and Drive	2-V-79
<u>2.</u> Chassis and Container Mounting	2-V-79
<u>3.</u> Negator Springs	2-V-79
C. APT Camera Subsystem	2-V-79
1. General Description	2-V-79
2. Functional Description	2-V-83
3. APT Components	2-V-86
a. APT Camera Sensor and Camera Electronics	2-V-86
(1) General Description	2-V-86
(a) APT Camera Sensor	2-V-89
<u>1.</u> Introduction and Design Changes	2-V-89
<u>2.</u> Camera Lens	2-V-92
<u>3.</u> Vidicon Tube	2-V-93
<u>4.</u> Focus and Deflection Yokes	2-V-94
<u>5.</u> Shutter Mechanism	2-V-94
<u>6.</u> Video Preamplifier and Amplifier	2-V-95
(b) Camera Electronics Unit	2-V-96
<u>1.</u> Introduction.....	2-V-96
<u>2.</u> Design Changes	2-V-96
a. Shutter Drive Circuit	2-V-96
(1) Initial Design Considerations and Constraints	2-V-96
(2) Design Approach	2-V-98

TABLE OF CONTENTS (Continued)

Section	Page
(3) ETM Shutter Tests	2-V-99
(4) Breadboard Evaluation	2-V-100
(5) Circuit Description	2-V-105
b. Sequence Timer	2-V-107
(1) General	2-V-107
(2) Signal Inputs to Sequence	2-V-108
(3) Output Timing Signals Generated by the Sequence Timer	2-V-109
(4) Sequence Timer Versus APT Camera Cycle Timing	2-V-110
(5) Sequence Timer/APT Camera Interface Circuits	2-V-113
c. Power Switch and Overvoltage Protection Circuit	2-V-113
(1) General	2-V-113
(2) Circuit Description	2-V-123
(3) Transient Responses	2-V-125
d. Digital-to-Analog Converter and Ladder ..	2-V-127
(1) General	2-V-127
(2) Circuit Description	2-V-127
(3) Breadboard and ETM Test	2-V-129
e. Telemetry Circuits	2-V-129
(1) General	2-V-129
(2) Telemetry Circuit Design Constraints	2-V-130
(3) Deflection Circuits	2-V-131
(4) Focus Current Regulator	2-V-131
(5) Electrode Switching and Beam Current Regulator	2-V-131
(6) Target Lamp Control	2-V-132
(7) Sampling Pulse Generator	2-V-132
(8) Video Chain	2-V-133
(9) Power Supply	2-V-134
D. Scanning Radiometer Subsystem	2-V-134
1. General Description	2-V-134
2. Functional Description	2-V-137
3. Scanning Radiometer Subsystem Components...	2-V-138
a. Scanning Radiometer and Scanning Radiometer Electronics	2-V-138
(1) General Description	2-V-138
(2) Electrical Description	2-V-139
(3) Optical Design	2-V-145
(4) Mechanical Design	2-V-152

TABLE OF CONTENTS (Continued)

Section	Page
b. Dual SR Processor	2-V-158
(1) General Description	2-V-158
(2) Functional Operation	2-V-160
(a) Real-Time Channel	2-V-160
<u>1.</u> Signal Conditioner and Selector	2-V-161
<u>2.</u> Limiter and Signal Injector	2-V-161
<u>3.</u> Double-Balanced Modulator	2-V-162
<u>4.</u> Output Buffer Circuit	2-V-162
<u>5.</u> Output Disable Circuit	2-V-163
<u>6.</u> Modulator Chopper Signals	2-V-163
<u>7.</u> Mode Selection Circuit	2-V-163
(b) 7-Pulse Sync Generator	2-V-163
<u>1.</u> Sequencer	2-V-164
<u>2.</u> Buffer	2-V-165
<u>3.</u> Signal Conditioners	2-V-165
(c) Commutator	2-V-165
<u>1.</u> Address Register Decode Gates	2-V-167
<u>2.</u> MOS Drivers	2-V-169
<u>3.</u> FET Switching Matrix	2-V-170
<u>4.</u> Limiter Network	2-V-170
<u>5.</u> Power Reset Circuit	2-V-170
<u>6.</u> Full-Scale Calibrate Voltage	2-V-171
<u>7.</u> Marker Generator	2-V-171
<u>8.</u> Power Monitor Telemetry Circuit	2-V-171
c. Scanning Radiometer Recorder (SRR)	2-V-172
(1) General Description	2-V-172
(2) Design History	2-V-176
(a) Basic Source of Design	2-V-176
<u>1.</u> Electrical Design	2-V-176
<u>2.</u> Mechanical Design	2-V-179
(b) New Design	2-V-179
<u>1.</u> Command and Control Circuitry	2-V-179
<u>2.</u> Power Switching Circuits	2-V-180
<u>3.</u> Tape Drive and Circuits	2-V-180
(c) Major Tradeoffs	2-V-181
1. Capstan Drive System Parametric Evaluation	2-V-181
2. Optimization and Analysis of DC Servo Drive System	2-V-184
(3) Functional Description	2-V-188
(a) General	2-V-188
(b) Record Mode	2-V-189

TABLE OF CONTENTS (Continued)

Section	Page
(c) Playback Mode	2-V-190
(d) Erase Head	2-V-191
(e) Tape Transport	2-V-191
<u>1.</u> Motor Design Life	2-V-194
<u>2.</u> Negator Springs Design Life	2-V-194
<u>3.</u> Magnetic Tape	2-V-195
<u>4.</u> Bearing Lubrication	2-V-195
(f) Telemetry Circuits	2-V-195
<u>1.</u> SR Recorder Operational Status	2-V-195
<u>2.</u> Motor Current Telemetry	2-V-195
<u>3.</u> Temperature and Pressure Telemetry Circuits	2-V-196

VOLUME II

PART 2 (contd)

VI SECONDARY SENSORS SUBSYSTEM	2-VI-1
A. General	2-VI-1
B. Secondary Sensor Devices	2-VI-1
1. Solar Proton Monitor	2-VI-1
a. Purpose and Use	2-VI-1
b. Sensor Assembly	2-VI-6
c. Data Processing Electronics	2-VI-7
d. Functional Operation	2-VI-13
(1) Sensor Assembly	2-VI-13
(a) Proton Sensors 1 and 2 ($E_p > 60$ MeV and $E_p > 30$ MeV)	2-VI-13
(b) Proton Sensor 3 ($E_p > 10$ MeV)	2-VI-13
(c) Electron Sensor ($100 < E_e < 750$ keV)	2-VI-13
(d) Dual Channel Proton Sensors (5 and 6)	2-VI-15
(2) Data Processing Electronics	2-VI-15
(a) Amplifier-Discriminator Chains	2-VI-15
(b) Pulse Handling Logic	2-VI-16
(c) Data Commutator and Accumulator Control	2-VI-16
(d) Data Accumulator	2-VI-16
(e) Floating Point Compressor	2-VI-17
(f) Processor Control	2-VI-17
(g) Output Circuits	2-VI-17
(h) Power and Telemetry	2-VI-17
2. Flat Plate Radiometer	2-VI-18
a. General	2-VI-18
(1) Sensors	2-VI-19
(2) Calibration in Orbit	2-VI-21
(3) Telemetry Data	2-VI-22

TABLE OF CONTENTS (Continued)

Section	Page
b. Functional Operation	2-VI-24
(1) Radiative Equilibrium Sensor and Thermistor Data Handling	2-VI-28
(2) Thermal Feedback Data Handling	2-VI-28
(3) Output Shift Register	2-VI-28
(a) Seven-Bit Data	2-VI-30
(b) Ten-Bit Data	2-VI-30
(4) TF Calibration	2-VI-30
(5) Other Functions	2-VI-31
C. Data Format Converter	2-VI-31
1. General Description	2-VI-31
2. Design History	2-VI-32
3. Functional Description	2-VI-33
a. Operating Modes	2-VI-33
(1) Record Mode	2-VI-33
(2) Standby Mode	2-VI-33
(3) Playback Mode	2-VI-33
(4) Off Mode	2-VI-34
b. Signal Interfaces	2-VI-34
(1) Logic Interfaces	2-VI-34
(a) TBU Interfaces	2-VI-34
(b) Solar Proton Monitor Interface	2-VI-35
(c) Flat Plate Radiometer Interfaces	2-VI-35
(d) ITR Interfaces	2-VI-35
(2) Analog Signal Interfaces	2-VI-37
(3) Signal Inputs	2-VI-37
c. Circuit Description	2-VI-38
(1) Commutator	2-VI-38
(2) Analog-to-Digital Converter	2-VI-39
(3) Time Code Sequencer	2-VI-41
(4) ITR Controller	2-VI-42
D. Incremental Tape Recorder (ITR)	2-VI-44
1. General Description	2-VI-44
a. Tape Transport Assembly	2-VI-45
b. Electronics Assembly	2-VI-46
c. Characteristics	2-VI-47
2. ITR Design	2-VI-47
a. Basic Source and Improvement	2-VI-47
b. Life Limiting Parts and Lubrication	2-VI-51
(1) Motor Stepper	2-VI-51
(2) Motor Playback	2-VI-52
(3) Magnetic Clutch	2-VI-52

TABLE OF CONTENTS (Continued)

Section	Page
(4) Negator Springs	2-VI-52
(5) Magnetic Tape	2-VI-52
(6) Bearing Lubrication	2-VI-52
3. Detailed Physical Description	2-VI-52
a. Tape Transport Assembly	2-VI-52
(1) Tape Drive	2-VI-53
(2) Tape Reel Subassembly	2-VI-54
(3) Record/Playback and Erase Head Subassembly	2-VI-54
b. Electronics Assembly	2-VI-55
4. Functional Description	2-VI-55
a. General	2-VI-55
b. Record Mode	2-VI-56
(1) Stepper Drive Circuitry	2-VI-56
(2) Record Amplifiers	2-VI-56
c. Playback Mode	2-VI-59
(1) General	2-VI-59
(2) Playback Amplifiers	2-VI-60
d. Telemetry Circuits	2-VI-61
(1) Combined Telemetry	2-VI-61
(2) Pressure Telemetry	2-VI-61
VI COMMUNICATIONS SUBSYSTEM	2-VII-1
A. General	2-VII-1
B. Command Receiving Link	2-VII-1
1. General	2-VII-1
2. Signal Characteristics	2-VII-5
3. Components	2-VII-6
a. Antenna Group	2-VII-6
b. Dual Command Receiver	2-VII-6
(1) General Description	2-VII-6
(2) Functional Operation	2-VII-7
C. Beacon and Telemetry Link	2-VII-7
1. General Description	2-VII-7
2. Signal Characteristics	2-VII-11
a. Housekeeping	2-VII-11
b. Command Data Verification	2-VII-11
c. Digital Solar Aspect Sensor	2-VII-12
d. Roll Sensors	2-VII-12
e. Pitch Sensors	2-VII-12
f. Solar Proton Monitor	2-VII-12
g. Time Code	2-VII-12

TABLE OF CONTENTS (Continued)

Section	Page
3. Components	2-VII-13
a. Digital Solar Aspect Sensor	2-VII-13
(1) Aspect Sensor (Sensing Element)	2-VII-13
(2) Electronics Package	2-VII-14
b. Accelerometer Control Unit (ACU)	2-VII-15
c. Signal Conditioner and Telemetry	
Commutator Unit	2-VII-20
(1) General Description	2-VII-20
(2) Design History	2-VII-21
(3) Functional Operation	2-VII-22
(a) Initial Delay and Initial Gate	2-VII-38
(b) Sequential Operational Gates	2-VII-38
(c) Sequential Operation of Gate Groups	2-VII-42
(d) Common Output Buffer	2-VII-42
(e) Frame Pulse Output	2-VII-42
d. Dual SCO	2-VII-42
(1) General Description	2-VII-42
(2) Functional Description	2-VII-43
e. Beacon Transmitter.....	2-VII-46
f. Beacon and Command Antenna Group	2-VII-47
(1) Introduction	2-VII-47
(2) Design Considerations	2-VII-48
(3) Diplexing, Isolation, and Insertion Loss...	2-VII-48
(4) 136-MHz Notch Filter	2-VII-50
(5) 148-MHz Notch Filter.....	2-VII-51
(6) 148-MHz Bandpass Filter and Hybrid	
Coupler	2-VII-52
(7) RF Switch	2-VII-52
(8) Antenna Assembly	2-VII-53
(9) Performance of the Electrical Test	
Model (ETM)	2-VII-53
(a) Measurement and Presentation	2-VII-53
(b) Solar Panels Stowed	2-VII-55
(c) Beacon Pattern, Solar Panels Deployed ...	2-VII-60
(d) Command Pattern, Solar Panels Stowed ...	2-VII-61
(e) Command Pattern, Solar Panels	
Deployed	2-VII-61
D. Real-Time Video Link	2-VII-62
1. General Description	2-VII-62
2. Video Signal Characteristics	2-VII-62
a. APT Signals	2-VII-62
b. SR Signals	2-VII-64

TABLE OF CONTENTS (Continued)

Section	Page
3. Component Description	2-VII-66
a. Real-Time Transmitter	2-VII-66
(1) General Description	2-VII-66
(2) Functional Description	2-VII-66
(a) Modulation Amplifier and Voltage Regulator	2-VII-67
(b) Voltage Controlled Crystal Oscillator	2-VII-68
(c) Frequency Doublers	2-VII-68
(d) Driver and Power Amplifier	2-VII-69
(e) Telemetry Circuits	2-VII-69
b. Antenna Group	2-VII-69
(1) Introduction	2-VII-69
(a) Configuration Tests	2-VII-70
(2) Design Considerations.....	2-VII-71
(a) Reliability Enhancement	2-VII-71
(b) Deployment Design	2-VII-72
(3) Antenna Drive and Matching Insertion Loss	2-VII-77
(4) 148-MHz Notch Filter	2-VII-78
(5) Hybrid Coupler and Termination	2-VII-78
(6) Antenna Assembly	2-VII-78
(7) Performance of the Electrical Test Model (ETM)	2-VII-79
(a) Nonradiation Tests	2-VII-79
(b) Radiation Characteristics	2-VII-79
E. S-Band Playback Video Link	2-VII-81
1. General	2-VII-81
2. Signal Characteristics	2-VII-82
a. AVCS Signals.....	2-VII-82
b. Scanning Radiometer Signals	2-VII-84
c. Secondary Sensors	2-VII-86
3. Component Description	2-VII-87
a. Dual Multiplexer	2-VII-87
(1) Design History	2-VII-89
(a) Input Buffering Pads	2-VII-90
(b) Filters	2-VII-91
(c) Double-Balanced Modulators	2-VII-92
(d) Frequency Doublers.....	2-VII-92
(e) Frequency-Divider Chain	2-VII-93
(f) Output Variable Pads	2-VII-93
(g) Summing Amplifier	2-VII-94
(h) Output Gating Amplifier and Cross- Coupling Arrangement	2-VII-95

TABLE OF CONTENTS (Continued)

Section	Page
(i) Power Turn-On Transient Suppressor.....	2-VII-96
(j) Harness Board	2-VII-96
(k) Mechanical and Thermal Design.....	2-VII-97
(2) Detailed Functional Description	2-VII-98
(a) AVCS Video Channel	2-VII-98
(b) SR Recorder No. 1 Flutter-and-Wow Channel.....	2-VII-101
(c) SRR A Channel	2-VII-102
(d) SRR B Channel	2-VII-103
(e) DFC Channel	2-VII-104
(f) TBU Channel	2-VII-104
(g) Summing Amplifier	2-VII-105
(h) Gating Amplifier	2-VII-105
b. S-Band Transmitter	2-VII-106
c. Antenna Group	2-VII-109
(1) Introduction	2-VII-109
(2) Design Considerations	2-VII-110
(a) Reliability	2-VII-110
(b) Spacecraft Effects	2-VII-110
(3) Insertion Loss, Isolation, and Matching...	2-VII-112
(4) Termination	2-VII-114
(5) S-Band Coupler	2-VII-114
(6) S-Band Antenna Assembly	2-VII-114
(7) Performance of the Electrical Test Model (ETM).....	2-VII-116
 VIII VEHICLE DYNAMICS SUBSYSTEM	 2-VIII-1
A. Subsystem Description	2-VIII-1
B. Initial Orientation Maneuver	2-VIII-4
1. Sequence	2-VIII-4
2. Biased Flywheel Operation	2-VIII-6
C. Nutation Damping	2-VIII-9
1. General	2-VIII-9
2. Basic Design	2-VIII-9
a. Mathematical Analysis	2-VIII-9
b. Mechanical Configuration	2-VIII-10
c. Pressurization	2-VIII-10
3. Time Constant	2-VIII-10
4. Weight Tradeoff	2-VIII-10
D. Attitude Sensing	2-VIII-13
1. General	2-VIII-13
2. Digital Solar Aspect Sensor	2-VIII-14

TABLE OF CONTENTS (Continued)

Section	Page
3. Infrared Sensors	2-VIII-14
a. General	2-VIII-14
b. Electronics	2-VIII-18
4. Pitch and Roll Sensing	2-VIII-20
a. General	2-VIII-20
b. Pitch Sensing	2-VIII-22
c. Roll Sensing	2-VIII-24
E. Magnetic Attitude Control and Momentum Control ..	2-VIII-25
1. General	2-VIII-25
2. Coordinate System	2-VIII-25
3. Geomagnetic Field Equations	2-VIII-27
4. Quarter-Orbit Magnetic Attitude Control (QOMAC)	2-VIII-28
5. Unipolar Torque	2-VIII-29
6. Magnetic Bias Control (MBC)	2-VIII-33
7. Magnetic Bias Switch	2-VIII-36
8. Momentum Control After Pitch Lock	2-VIII-36
a. Momentum Magnitude	2-VIII-36
b. Spin Momentum Change (T_{SPIN})	2-VIII-38
c. Precession Due to Momentum Correction (TPREC)	2-VIII-39
9. Momentum Control Prior to Pitch Lock	2-VIII-41
F. Pitch Control	2-VIII-48
1. General	2-VIII-48
2. Pitch Sensing	2-VIII-50
3. Servo Design	2-VIII-50
4. Three-Axis Considerations	2-VIII-55
5. Capture Verification	2-VIII-65
6. Component Description	2-VIII-68
a. General	2-VIII-68
b. Pulse Width Modulator (PWM) Error Detector	2-VIII-68
c. Compensation Amplifier	2-VIII-71
d. Gain Switching Circuit	2-VIII-72
e. Summing Amplifier	2-VIII-72
f. Power Amplifier	2-VIII-73
g. Torque Motor	2-VIII-73
h. Encoder	2-VIII-75
i. Encoder Electronics	2-VIII-76
j. DC-to-DC Converter	2-VIII-76
k. Pitch Sensor Threshold Amplifiers	2-VIII-76

TABLE OF CONTENTS (Continued)

Section	Page
1. Earth Blanking	2-VIII-76
m. Electronics Box	2-VIII-77
7. Pitch Control Mechanical Design	2-VIII-77
8. Applicable Test Results	2-VIII-81
a. General	2-VIII-81
b. Test Descriptions	2-VIII-82
c. Brush Wear Data	2-VIII-84
d. Special Tests	2-VIII-86
(1) Wheel Tilt Test	2-VIII-86
(2) Motor Survival Test	2-VIII-86
e. Oil Loss	2-VIII-88
f. Bearing Wear	2-VIII-88
G. Accuracy Analysis	2-VIII-90
1. General	2-VIII-90
2. Pointing	2-VIII-90
3. Jitter	2-VIII-97
H. System Interfaces	2-VIII-101
1. Power	2-VIII-101
2. Command and Control	2-VIII-101
3. Telemetry	2-VIII-101
I. Disturbance Analysis	2-VIII-102
1. Residual Magnetic Dipoles	2-VIII-102
2. Solar Torques	2-VIII-107
3. Magnetic Losses	2-VIII-109
a. Hysteresis	2-VIII-109
b. Eddy Current	2-VIII-109
4. Gravity Gradient	2-VIII-110
5. Internal Rotating Components	2-VIII-110
IX POWER SUPPLY SUBSYSTEM	2-IX-1
A. General	2-IX-1
B. Functional Description	2-IX-7
1. General	2-IX-7
2. Solar Array	2-IX-11
3. Batteries	2-IX-14
4. Series Voltage Regulators	2-IX-15
5. Charge Controllers	2-IX-15
6. Shunt Limiter	2-IX-16
7. System Protection	2-IX-16
C. Components	2-IX-17
1. Solar Cell Array	2-IX-17

TABLE OF CONTENTS (Continued)

Section	Page
a. Design History	2-IX-17
b. Characteristics	2-IX-18
c. Functional Description	2-IX-19
2. Batteries	2-IX-23
a. General Description	2-IX-23
b. Design History	2-IX-25
c. Detailed Functional Description	2-IX-25
3. Power Supply Electronics	2-IX-28
a. General Description	2-IX-28
b. Functional Operation	2-IX-30
(1) Voltage Regulator	2-IX-30
(a) General Description	2-IX-30
(b) Functional Operation	2-IX-31
(2) Shunt Limiter	2-IX-31
(a) General Description	2-IX-31
(b) Functional Operation	2-IX-35
<u>1</u> . Control Amplifier	2-IX-35
<u>2</u> . Signal Distribution Board	2-IX-36
<u>3</u> . Shunt Dissipator	2-IX-41
<u>4</u> . Failure Detection Control	2-IX-42
(3) Battery Charge Controller	2-IX-42
(a) General Description	2-IX-42
(b) Functional Operation	2-IX-47
(4) Telemetry	2-IX-51
(a) General Description	2-IX-51
(b) Voltage Telemetry	2-IX-51
(c) On-Off Telemetry Functional Operation ...	2-IX-54
(d) Temperature Telemetry Functional Operation	2-IX-55
(e) Current Telemetry	2-IX-58

VOLUME III

PART 3. TEST HISTORIES

I	DESCRIPTION OF TEST PROGRAM.....	3-I-1
II	MECHANICAL TEST MODEL TESTING	3-II-1
	A. Introduction	3-II-1
	B. MTM Tests	3-II-5
	1. Summary	3-II-5
	2. Mechanical Test Model Configuration	3-II-6

TABLE OF CONTENTS (Continued)

Section	Page
3.	Condition of Structure Before and After
	Vibration Test 3-II-6
	a. General..... 3-II-6
	b. Alignment 3-II-8
	c. Solar Panel Preload 3-II-9
	d. Solar Panel Deployment 3-II-9
	e. Real-Time Antenna Deployment 3-II-10
	f. Active Thermal Controller 3-II-10
4.	List of Components With Responses
	Over 10 G 3-II-10
5.	Other MTM Test Results 3-II-12
	a. General..... 3-II-12
	b. Moment of Inertia 3-II-12
	c. Dynamic Balance 3-II-14
	d. Dynamic Deflections 3-II-14
III	THERMAL TEST MODEL TESTING 3-III-1
A.	Thermal Test Model 3-III-1
B.	Test Simulation..... 3-III-3
	1. Solar Input 3-III-3
	2. Power Dissipation 3-III-4
	3. Instrumentation..... 3-III-4
	4. Control 3-III-4
C.	The TTM Testing (Initial)..... 3-III-4
	1. Test Objectives..... 3-III-4
	a. Injection Mode Simulation 3-III-4
	b. Operational Mode Simulation 3-III-5
	2. Test Procedure..... 3-III-5
	3. Initial Test Results 3-III-5
	4. Test Results for Reconfigured Model..... 3-III-6
D.	Insulation Evaluation Test 3-III-6
E.	Emittance Test 3-III-7
	1. Test Program 3-III-7
	2. IR Simulation of the Thermal Fence 3-III-7
	a. Test Objectives 3-III-7
	b. Test Theory 3-III-8
	c. Test Results 3-III-9
	3. Active Thermal Controller (ATC) Effective
	Emissivity Evaluation 3-III-9
	a. General 3-III-9
	b. Test Objective 3-III-10
	c. Test Results 3-III-10

TABLE OF CONTENTS (Continued)

Section	Page
4. Baseplate Effective Emissivity Test	3-III-10
a. General	3-III-10
b. Test Objective	3-III-10
c. Test Theory	3-III-10
F. Momentum Wheel Assembly Tests	3-III-11
1. Baseplate Emissivity Testing	3-III-11
a. Test Plan	3-III-11
2. Initial TTM Testing	3-III-12
a. Test Plan	3-III-12
b. Test Results	3-III-13
3. TTM Retesting	3-III-13
a. Test Simulation	3-III-14
b. Test Procedure	3-III-15
c. Test Results	3-III-15
4. Conclusions	3-III-17
G. Thermal Fence Test	3-III-17
1. Test Program	3-III-17
2. Test Results	3-III-17
H. Conclusions	3-III-20
IV ANTENNA TEST MODEL TESTING	3-IV-1
A. General	3-IV-1
B. Equipment Tested	3-IV-1
C. Test Objectives	3-IV-4
D. Summary of ATM Test Results	3-IV-5
E. Phase I Test Results	3-IV-5
1. S-Band Antenna System	3-IV-5
a. S-Band VSWR	3-IV-5
b. S-Band Isolation	3-IV-6
c. S-Band Insertion Loss	3-IV-6
2. Real-Time Antenna System	3-IV-6
a. Real-Time VSWR	3-IV-6
b. Real Time Antenna Insertion Loss	3-IV-7
c. Real-Time Antenna Phase Measurement	3-IV-7
3. Beacon and Command Antenna System	3-IV-8
a. Beacon and Command VSWR	3-IV-8
b. Beacon and Command Isolation	3-IV-8
c. Beacon and Command Insertion Loss	3-IV-8
4. Isolation Between Input Ports	3-IV-9
5. Range Calibration	3-IV-9
a. Real-Time Link Calibration	3-IV-9
b. Beacon Link Calibration	3-IV-9

TABLE OF CONTENTS (Continued)

Section	Page
c. Command Link Calibration	3-IV-10
d. S-Band Link Calibration	3-IV-11
6. Antenna Pattern Checks	3-IV-11
a. Beacon Antenna Pattern	3-IV-11
b. Real-Time Antenna Pattern	3-IV-12
c. S-Band Antenna Pattern	3-IV-12
F. Phase II Test Results - RF Equipment	3-IV-12
1. Bench Tests	3-IV-12
a. S-Band Link	3-IV-12
b. Real-Time Staircase Test	3-IV-17
2. RF Subsystem Test	3-IV-18
a. Command Sensitivity	3-IV-18
b. Command Signal Spurious Observations	3-IV-18
c. Spurious Outputs	3-IV-18
 V ETM SPACECRAFT TEST PROGRAM	 3-V-1
A. ETM Test Philosophy	3-V-1
B. ETM Spacecraft Test Chronology	3-V-1
1. Harness Ringout	3-V-1
2. Initial Power and Functional Checkout (IPFC)	 3-V-1
3. Detailed Electrical Test	3-V-4
a. General	3-V-4
b. RF Data Link Test	3-V-4
c. APT Camera Subsystem Test	3-V-4
d. Dynamics Subsystem Test	3-V-7
e. SR, AVCS, and Secondary Sensor (SS) Subsystem Tests	 3-V-8
f. Pitch Control System Test	3-V-9
4. Go/No-Go- Electrical Test	3-V-10
5. Measurement of Magnetic-Dipole Moments (Partial)	 3-V-10
6. Dynamic Suspension Test (Test No. 1)	3-V-10
7. Standard Electrical Performance Evaluation Test (SEPET)	 3-V-11
8. Special Scanning Radiometer Test	3-V-12
9. RFI Test (Test No. 1)	3-V-13
10. Special Power System Test	3-V-14
11. Solar Proton Monitor Test	3-V-14
12. Transient Test	3-V-14
13. Balance and Moment-of-Inertia Measurements	 3-V-14

TABLE OF CONTENTS (Continued)

Section	Page
14. Spacecraft Console No. 2 Operational Check	3-V-15
15. Dynamic Suspension Test (Test No. 2)	3-V-16
16. Spacecraft Optical Alignment	3-V-17
17. Secondary Sensor Subsystem Data Reduction Debugging	3-V-17
18. Abbreviated SEPET	3-V-17
19. Thermal-Vacuum Facility Check	3-V-17
20. Training Tape Test	3-V-18
21. RFI Test (Test No. 2)	3-V-19
22. Indoor Solar Array/PSE Test	3-V-19
23. Launch Checkout	3-V-19
24. Dynamic Suspension Test (Test No. 3).....	3-V-19
25. Thermal-Vacuum Check and Thermal Cycle	3-V-20
26. Outdoor Solar Array Check	3-V-20
27. RF Tests	3-V-20
 VI COMPONENT TEST HISTORIES	 3-VI-1
A. Introduction	3-VI-1
B. Subsystem Testing	3-VI-7
1. AVCS Subsystem	3-VI-7
2. Pitch Control Subsystem	3-VI-11
C. Component Testing	3-VI-12
1. Dual Command Decoder	3-VI-12
a. Prototype	3-VI-12
2. Dual Command Programmer	3-VI-13
a. Prototype	3-VI-13
b. Flight Model.....	3-VI-14
3. Dual Time Base Unit	3-VI-14
a. Electrical Test Model	3-VI-14
b. Prototype	3-VI-14
c. Flight Model.....	3-VI-15
4. Command Distribution Units (CDU) A and B ..	3-VI-15
a. Prototype	3-VI-15
b. Flight Model.....	3-VI-16
5. AVCS Camera Subsystem	3-VI-16
a. Electrical Test Model	3-VI-16
b. Prototype	3-VI-17
c. Flight Model	3-VI-25
(1) AVCS Camera Subsystem No. 1	3-VI-25
(2) AVCS Camera Subsystem No. 2	3-VI-26
6. AVCS Tape Recorder	3-VI-27

TABLE OF CONTENTS (Continued)

Section	Page
a. Electrical Test Model	3-VI-27
b. Prototype	3-VI-27
c. Flight Model.....	3-VI-28
(1) AVCS Tape Recorder Subsystem	
No. 1.....	3-VI-31
(2) AVCS Tape Recorder Subsystem	
No. 2.....	3-VI-32
7. APT Camera Subsystem	3-VI-32
a. Electrical Test Model	3-VI-32
b. Prototype	3-VI-33
c. Flight Model.....	3-VI-33
(1) APT Camera Subsystem No. 1	3-VI-34
(2) APT Camera Subsystem No. 2	3-VI-35
8. Scanning Radiometer Assembly	3-VI-36
a. Electrical Test Model	3-VI-36
b. Prototype	3-VI-36
c. Flight Model.....	3-VI-40
9. Dual Scanning Radiometer Processor	3-VI-41
a. Electrical Test Model	3-VI-41
(1) Real-Time Channel.....	3-VI-41
(2) Commutator	3-VI-47
b. Prototype	3-VI-47
c. Flight Model.....	3-VI-47
10. Scanning Radiometer Recorder and	
Recorder Electronics	3-VI-51
a. Electrical Test Model	3-VI-51
b. Prototype	3-VI-59
c. Flight Model.....	3-VI-62
(1) Scanning Radiometer Recorder	
Assembly Ser. No. 02	3-VI-62
(2) Scanning Radiometer Recorder	
Assembly Ser. No. 05	3-VI-63
11. Data Format Converter	3-VI-64
a. Electrical Test Model	3-VI-64
b. Prototype	3-VI-65
c. Flight Model	3-VI-65
12. Incremental Tape Recorder	3-VI-66
a. Electrical Test Model	3-VI-66
b. Prototype	3-VI-66
c. Flight Model	3-VI-66

TABLE OF CONTENTS (Continued)

Section	Page
13. Beacon and Command Antenna Group.....	3-VI-67
a. Bandpass Filter	3-VI-68
b. 148-MHz Notch Filter	3-VI-68
c. 136-MHz Notch Filters	3-VI-68
d. Command Hybrid Coupler	3-VI-68
e. RF Switch Assembly	3-VI-69
(1) Prototype	3-VI-69
(2) Flight Model	3-VI-70
14. Dual Command Receiver	3-VI-70
a. Prototype	3-VI-70
b. Flight Model	3-VI-70
15. Beacon Transmitter	3-VI-70
a. Prototype	3-VI-70
b. Flight Model	3-VI-71
16. Dual Subcarrier Oscillators (SCO's)	3-VI-72
a. Electrical Test Model	3-VI-72
b. Prototype	3-VI-72
17. Signal Condition	3-VI-72
a. Prototype	3-VI-72
b. Flight Model	3-VI-73
c. Prototype	3-VI-73
18. Telemetry Commutators	3-VI-74
19. Real-Time Transmitter	3-VI-74
a. Prototype	3-VI-74
b. Flight Model	3-VI-74
(1) Real-Time Transmitter Ser. No. 03	3-VI-74
(2) Real-Time Transmitter Ser. No. 05	3-VI-75
20. Real-Time Antenna Group	3-VI-76
a. Real-Time Antenna	3-VI-76
(1) Electrical Test Model	3-VI-76
(2) Prototype	3-VI-76
(3) Flight Model	3-VI-76
b. 148-MHz Notch Filters	3-VI-76
c. Antenna Hybrid Couplers	3-VI-76
21. Dual Multiplexer	3-VI-77
a. Electrical Test Model	3-VI-77
b. Prototype	3-VI-78
c. Flight Model	3-VI-78

TABLE OF CONTENTS (Continued)

Section	Page
22. S-Band Transmitter	3-VI-79
a. Electrical Test Model	3-VI-79
b. Prototype	3-VI-79
c. Flight Model	3-VI-79
23. S-Band Antenna and Couplers	3-VI-80
a. Electrical Test Model	3-VI-80
b. Prototype	3-VI-80
c. Flight Model	3-VI-81
24. Digital Solar Aspect Sensor (DSAS) and Electronics	3-VI-81
a. Prototype	3-VI-81
b. Flight Model	3-VI-82
25. Nutation Dampers	3-VI-82
26. Attitude Control Coil Unit	3-VI-82
27. Magnetic Bias Coil (MBC) Switch	3-VI-82
a. Prototype	3-VI-82
b. Flight Model	3-VI-83
28. Dual Momentum Coil	3-VI-83
29. Pitch Control Electronics	3-VI-83
a. Electrical Test Model	3-VI-83
b. Prototype	3-VI-83
c. Flight Model	3-VI-84
30. Momentum Wheel Assembly	3-VI-85
a. Electrical Test Model	3-VI-85
b. Prototype	3-VI-86
c. Flight Model	3-VI-87
31. Strain Gage Amplifier	3-VI-87
a. Electrical Test Model	3-VI-87
b. Prototype	3-VI-90
c. Flight Model	3-VI-90
32. Solar Array Panels	3-VI-90
a. Prototype	3-VI-90
(1) Initial Illumination Test	3-VI-91
(2) Electrical Component Tests	3-VI-92
(3) Vibration	3-VI-93
(4) Post-Vibration Illumination and Electrical Test	3-VI-93
(5) Pre-Thermal-Vacuum Test	3-VI-94
(6) Thermal-Vacuum Testing	3-VI-94
(7) Post-Thermal-Vacuum Test	3-VI-94
(8) Thermal Cycling Test	3-VI-94

TABLE OF CONTENTS (Continued)

Section	Page
(9) Post-Thermal Cycling Illumination and Electrical Parameters	3-VI-95
(10) Antenna Cable Tests (Thermal Cycling)	3-VI-95
(11) Thermal-Vacuum Retest	3-VI-95
(12) Electrical Retest	3-VI-96
(13) Thermal-Vacuum Retest	3-VI-96
(14) Prototype Test Results	3-VI-96
b. Flight Model	3-VI-96
(1) Solar Array Panel Ser. No. 002	3-VI-96
(2) Solar Array Panel Ser. No. 003	3-VI-97
(3) Solar Array Panel Ser. No. 005	3-VI-99
33. Solar Array Panel Actuators	3-VI-100
34. Battery Pack Assembly	3-VI-100
a. Electrical Test Model	3-VI-100
b. Prototype	3-VI-108
c. Flight Model	3-VI-109
35. Power Supply Electronics	3-VI-109
a. Electrical Test Model	3-VI-109
b. Prototype	3-VI-110
c. Flight Model	3-VI-115
36. Active Thermal Controller	3-VI-119
a. Actuator/Sensors	3-VI-119
(1) Electrical Test Model	3-VI-119
(2) Prototype	3-VI-121
(3) Flight Model	3-VI-121
b. Louver and Hinge Assemblies, Flight Model	3-VI-122
37. Accelerometer Assembly and Acceleration Control Unit, Flight Model	3-VI-122
38. Separation Switches, Flight Model	3-VI-123
VII TIROS M SPACECRAFT FLIGHT ACCEPTANCE	
TESTING	3-VII-1
A. Assembly, Debugging and Interface Verification ...	3-VII-1
1. Power Interface	3-VII-1
2. Power Application	3-VII-1
3. Bus Functional Checkout	3-VII-3
4. Sensor Mounting, Functional Checkout and DET	3-VII-4
5. Operational Mode Tests	3-VII-4
6. Thermal Tests	3-VII-5
7. Final Mechanical Assembly	3-VII-7

TABLE OF CONTENTS (Continued)

Section	Page
B. System Evaluation and Prequalification	
Calibration Cycle	3-VII-7
C. Environmental Qualification	3-VII-10
1. Vibration	3-VII-13
2. Thermal-Vacuum Tests	3-VII-14
a. Thermal Survey	3-VII-15
b. Flight Acceptance Tests	3-VII-16
c. Resumption of Thermal-Vacuum Tests ..	3-VII-19
d. Special Blanket Thermal Tests	3-VII-20
D. Final Calibration	3-VII-20
1. Magnetic Dipole Check	3-VII-21
2. Standard Electrical Performance	
Evaluation Test (SEPET)	3-VII-22
3. Battery Capacity Test	3-VII-22
4. Camera Calibration	3-VII-22
a. AVCS Calibration	3-VII-22
b. APT Calibration	3-VII-30
5. Scanning Radiometer Calibration	3-VII-30
6. Solar Proton Monitor and Flat Plate	
Radiometer Calibration	3-VII-42
a. SPM Electronics Test	3-VII-42
b. SPM Sensor Test	3-VII-42
c. FPR Tests	3-VII-42
7. Sensor Alignment Check	3-VII-43
a. Camera Alignment	3-VII-44
b. Scanning Radiometer Optical Alignment..	3-VII-44
c. Digital Solar Aspect Sensor Alignment...	3-VII-44
8. RF Testing	3-VII-49
9. Fine Balancing	3-VII-49
10. Moment-of-Inertia and Center-of-Gravity	
Measurements and Final Weighing	3-VII-50
E. Conclusion of Testing	3-VII-51

VOLUME III

PART 4. TIROS M LAUNCH-SUPPORT OPERATIONS

I	PRELAUNCH ACTIVITIES	4-I-1
	A. Introduction	4-I-1
	B. ETM Spacecraft Operations	4-I-1
	C. TIROS M Spacecraft Operations	4-I-2

TABLE OF CONTENTS (Continued)

Section	Page
II	POST-LAUNCH ACTIVITIES 4-II-1
	A. Beginning of Operation 4-II-1
	B. Initial Performance Evaluation 4-II-2
PART 5. GROUND STATION EQUIPMENT	
I	INTRODUCTION 5-I-1
	A. General 5-I-1
	B. System Description 5-I-1
	C. Command and Data Acquisition (CDA) Stations 5-I-5
	D. Automatic Picture Transmission (APT) Ground Stations 5-I-5
	E. The TOS Operations Center (TOC) and TOS Evaluation and Checkout Center (TEC/TCC) 5-I-6
	F. Microwave Link Data Transmission Equipment 5-I-7
	G. Other Participating Facilities 5-I-7
	1. The Data Acquisition Facility (DAF) 5-I-7
	2. The NESC Data Processing and Analysis Facility (DAPAF) 5-I-8
	3. The GSFC Tracking and Data Systems Directorate 5-I-8
II	COMMAND AND DATA ACQUISITION STATIONS 5-II-1
	A. General 5-II-1
	B. Design Approach 5-II-9
	1. General 5-II-9
	2. AVCS Video Processing and Display Equipment 5-II-14
	3. APT Video Processing Equipment 5-II-15
	4. Recorded Scanning Radiometer Data Processing Equipment 5-II-15
	5. Secondary Sensor Data Processing Equipment 5-II-15
	6. Tape Recorders 5-II-16
	7. Beacon and Telemetry Data Processing Equipment 5-II-17
	a. General 5-II-17
	b. Beacon Processing 5-II-18
	c. Beacon Display 5-II-18
	d. Telemetry 5-II-19
	8. Microwave Link Transmission Equipment 5-II-20
	9. Programming Equipment 5-II-20

TABLE OF CONTENTS (Continued)

Section	Page
C. Functional Description	5-II-21
1. General	5-II-21
2. Video Data Processing and Display Equipment	5-II-22
3. Programming Equipment	5-II-24
4. Master Timing Equipment	5-II-27
5. Beacon Data Processing Equipment	5-II-28
6. Microwave Link Transmission Equipment ...	5-II-33
7. CDA Station Recorders	5-II-41
a. Tape Recorders	5-II-41
b. Events Recorder	5-II-44
c. Beacon Data Recorder	5-II-50
d. Attitude Data Recorder	5-II-51
e. Visicorder	5-II-51
8. Station Control Circuits	5-II-52
III TOS OPERATIONS CENTER (TOC)	5-III-1
A. General	5-III-1
B. RCA-Supplied Equipment	5-III-2
C. Major TOC Subsystems	5-III-5
D. Overall Functional Description	5-III-6
E. Station Switching Control Equipment	5-III-10
F. Beacon Data Processing Equipment	5-III-10
G. Events Processing Equipment	5-III-17
H. Recording Equipment	5-III-17
1. Events Recorder	5-III-17
2. Beacon Data Recorder	5-III-18
3. Attitude Recorders	5-III-22
I. AC Distribution and Blower Fault Protection Circuitry	5-III-24
IV TOS EVALUATION CENTER AND TOS CHECKOUT CENTER	5-IV-1
A. General	5-IV-1
B. RCA-Supplied Equipment	5-IV-2
C. Major TEC/TCC Subsystems	5-IV-6
D. Overall Functional Description	5-IV-7
E. Station Switching Control Equipment	5-IV-13
F. Beacon Data Processing Equipment	5-IV-14
G. Events Processing Equipment	5-IV-19
H. Recording Equipment	5-IV-19
1. Events Recorder	5-IV-19
2. Beacon Data Recorder	5-IV-20
3. Attitude Recorder	5-IV-22

TABLE OF CONTENTS (Continued)

Section	Page
I. Secondary Sensor Subsystem Data Display Equipment	5-IV-23
J. AC Distribution and Blower Fault Protection Circuitry	5-IV-25
V SPACECRAFT CHECKOUT EQUIPMENT.....	5-V-1
A. General	5-V-1
1. AED Checkout Equipment	5-V-1
2. Go/No-Go Launch Support Van	5-V-2
B. Functional Description of GSE Equipment.....	5-V-2
1. Patching Equipment	5-V-2
2. APT Receiving and Processing Equipment	5-V-7
3. AVCS Receiving and Processing Equipment ...	5-V-7
4. SR Receiving and Processing Equipment	5-V-7
5. Secondary Sensor Receiving and Processing Equipment	5-V-7
6. Beacon Receiving and Processing Equipment ..	5-V-8
7. Command Support Console	5-V-8
8. Spacecraft Support Console	5-V-8
9. Varian 620i Computer	5-V-8
VI DESIGN DEVELOPMENTS.....	5-VI-1
A. General	5-VI-1
B. S-Band Communications Link	5-VI-1
C. Demultiplexer	5-VI-3
D. ITOS Beacon Display	5-VI-4
E. Microwave Link Interface	5-VI-5
F. Station Control	5-VI-7
G. Subcarrier Signal Monitoring	5-VI-10
H. Command Transmission Rate and Address Shift	5-VI-12
I. TOC and TEC/TCC Equipment	5-VI-14
J. Spacecraft Checkout Facilities	5-VI-17
VII PROGRAM MILESTONES	5-VII-1

TABLE OF CONTENTS (Continued)

Section	Page
APPENDICES	
A	THE ITOS RADIATION HARDENING PROGRAM A-1
B	BATTERY LIFE CYCLING TEST B-1
C	ITOS MAGNETIC TAPE EVALUATION C-1
D	COMPONENT BOX SERIAL NUMBERS D-1

LIST OF ILLUSTRATIONS

Figure		Page
VOLUME I		
PART 1. INTRODUCTION		
1-III-1	Launch to Mission Mode Events	1-III-1
1-VIII-1	ITOS Mission Mode, Showing Primary Sensor Coverage	1-VIII-2
1-VIII-2	Geometry of the Sun-Synchronous Orbit	1-VIII-4
1-VIII-3	Seasonal Variations in Illumination for an Afternoon Sun-Synchronous Orbit.....	1-VIII-6
1-VIII-4	Picture Illumination Angle vs Geographic Latitude; 1500 Hour AN Orbit, 1968 Sun Data	1-VIII-7
1-VIII-5	Seasonal Variation of Spacecraft Sun Angle for Afternoon AN Orbits	1-VIII-8
1-VIII-6	Satellite Time in Sunlight	1-VIII-10
1-VIII-7	Typical Ground-Contact Boundaries for Wallops Island and Alaska CDA Stations	1-VIII-11
1-VIII-8	Typical CDA Station Contact Time	1-VIII-12
1-VIII-9	Nodal Drift Rate Error vs Inclination Error	1-VIII-14
1-VIII-10	Nodal Drift Rate Error vs Mean Height Error	1-VIII-14
1-VIII-11	Spacecraft Pitch Attitude Offset vs Altitude	1-VIII-15
1-VIII-12	Effect of Launch Window and Injection Error on Mission Mode Sun Angle (Worst Case)	1-VIII-16
1-VIII-13	Camera Field of View for Orbit at 790-Nautical- Mile Altitude	1-VIII-18
1-VIII-14	Orbit Coverage of Primary Sensors	1-VIII-20

PART 2 - SPACECRAFT DESIGN

2-I-1	The ITOS Spacecraft, Functional Block Diagram	2-I-3
2-II-1	ITOS Spacecraft Orientation	2-II-2
2-II-2	Spacecraft Component Integration Configuration	2-II-3
2-II-3	ITOS Basic Structure, Showing Panel Access Ports (Cutouts) and Hinged AVCS Equipment Panel Opened...	2-II-5
2-II-4	AVCS Equipment Panel	2-II-15
2-II-5	Baseplate Assembly	2-II-19

LIST OF ILLUSTRATIONS (Continued)

Figure		Page
2-II-6	Earth-Oriented Access Panel	2-II-23
2-II-7	Anti-Earth Access Panel	2-II-25
2-II-8	Top Assembly (Panel 5)	2-II-28
2-II-9	Thermal Fence Assembly Configuration	2-II-30
2-II-10	Solar Panel, Mechanical Configuration	2-II-31
2-II-11	Solar Panel Hydraulic Actuator	2-II-33
2-II-12	Solar Panel Retention and Release Mechanism	2-II-35
2-II-13	Deployment of Solar Panel	2-II-37
2-II-14	ATC Actuator Sensor Unit	2-II-39
2-II-15	ATC Louver and Hinge Assembly	2-II-42
2-II-16	Spacecraft Alignment Reference Axes	2-II-46
2-III-1	Thermal Control Components	2-III-2
2-III-2	Thermal Radiators	2-III-3
2-III-3	Thermal Control Fence	2-III-4
2-III-4	Spacecraft Configuration	2-III-5
2-III-5	Net Heat Exchange Between Thermal Fence Plate and 20°C Spacecraft	2-III-7
2-III-6	Active Thermal Control, Functional Characteristics ..	2-III-13
2-III-7	Structure Thermal Model for 131-Body Analysis	2-III-21
2-III-8	Component Thermal Model for 131-Body Analysis	2-III-22
2-III-9	Flight Predictions Temperatures Versus Sun Angles for Scanning Radiometer	2-III-23
2-III-10	Flight Predictions Temperatures Versus Sun Angles for Momentum Wheel Assembly	2-III-24
2-III-11	Flight Predictions Temperatures Versus Sun Angles for APT Camera	2-III-25
2-III-12	Flight Predictions Temperatures Versus Sun Angles for AVCS Camera	2-III-26
2-III-13	Flight Predictions Temperatures Versus Sun Angles for SR Recorder	2-III-27
2-III-14	Flight Predictions Temperatures Versus Sun Angles for AVCS Recorder	2-III-28
2-III-15	Flight Predictions Temperatures Versus Sun Angles for Battery	2-III-29
2-III-16	Flight Predictions Temperatures Versus Sun Angles for Power Supply Electronics	2-III-30
2-III-17	Flight Predictions Temperatures Versus Sun Angles for Pitch Control Electronics	2-III-31
2-III-18	Solar Panel Thermal Analysis Model	2-III-39
2-III-19	Solar Panel Temperatures, Launch to Separation	2-III-40
2-III-20	Solar Cell Temperature Prior to Solar Panel Deployment	2-III-41

LIST OF ILLUSTRATIONS (Continued)

Figure		Page
2-III-21	Power Transistor Case Temperature Prior to Solar Panel Deployment	2-III-42
2-III-22	Resistor Mounting Temperature Prior to Solar Panel Deployment	2-III-43
2-III-23	Solar Panel Temperature Worst-Case-Hot Operational Mode (30-Degree Orbit BOL)	2-III-44
2-III-24	Solar Panel Temperatures Worst-Case-Cold Operational Mode (60-Degree Orbit EOL)	2-III-45
2-IV-1	Command Subsystem, Functional Block Diagram	2-IV-3
2-IV-2	Command Subsystem Components	2-IV-12
2-IV-3	Decoder Input and Output Interfaces	2-IV-14
2-IV-4	Decoder Simplified Logic Flow Diagram	2-IV-19
2-IV-5	ITOS Decoders, Block Diagram	2-IV-23
2-IV-6	Decoder Timing Diagram	2-IV-25
2-IV-7	Direct Command Matrix, Set I - Digital and Octal Codes	2-IV-34
2-IV-8	Direct Command Matrix, Set II - Digital and Octal Codes	2-IV-35
2-IV-9	Typical CDU Decoding Gate, Schematic Diagram	2-IV-36
2-IV-10	Decoder and CDU Interconnections, Simplified Block Diagram	2-IV-36
2-IV-11	Dual Command Programmer, Block Diagram	2-IV-57
2-IV-12	T ₀ Word Sequencer Flow Diagram	2-IV-61
2-IV-13	Orbit Counter Clock Rephasing, Flow Diagram	2-IV-62
2-IV-14	Load Picture Program Command Tag Sequencer and Data Verification Extender, Flow Diagram	2-IV-63
2-IV-15	Sensor Sequencing, Typical Gross Orbital Timing	2-IV-66
2-IV-16	AVCS and APT Camera Control, Timing Diagram	2-IV-67
2-IV-17	APT Picture/SR Modulator Day Enable Signal Delections Via Bits 16 through 26 of Picture Program Rephasing Word, Timing Diagram	2-IV-72
2-IV-18	Unipolar Torquing Cycle	2-IV-75
2-IV-19	Time Base Unit Signal Interface Diagram	2-IV-79
2-IV-20	TBU Output Signals Timing Diagram	2-IV-80
2-IV-21	TBU Block Diagram.....	2-IV-83
2-IV-22	TCG Signal Characteristics	2-IV-85
2-V-1	AVCS Subsystem, Block Diagram	2-V-3
2-V-2	AVCS Components	2-V-4
2-V-3	AVCS Subsystem, Timing Diagram	2-V-7
2-V-4	Operation of the Double-Bladed Focal Plane Shutter....	2-V-9
2-V-5	Composite Video Signal	2-V-10
2-V-6	AVCS Camera Sensor and Electronics, Block Diagram	2-V-12

LIST OF ILLUSTRATIONS (Continued)

Figure		Page
2-V-7	Vidicon Reticle Pattern	2-V-13
2-V-8	Gray Scale Calibrator, Schematic Diagram	2-V-20
2-V-9	Hybrid Vidicon Tube	2-V-23
2-V-10	Equivalent Circuit of Vidicon Target, Simplified Schematic	2-V-24
2-V-11	Vidicon Signal Sequence Diagram	2-V-25
2-V-12	Preamplifier, Schematic Diagram	2-V-27
2-V-13	AC Video Amplifier, Schematic Diagram	2-V-29
2-V-14	Dark Current Sampling Circuit, Schematic Diagram ..	2-V-31
2-V-15	Video Signal with No Incident Light	2-V-32
2-V-16	Dark Current Pedestal	2-V-32
2-V-17	Clamp Circuit, Schematic Diagram	2-V-33
2-V-18	Dark Current Sampling, Timing and Sequencing Diagram	2-V-34
2-V-19	Shading Correction Circuit, Block Diagram	2-V-35
2-V-20	Vertical Shading Components	2-V-36
2-V-21	Video Modulator Operation, Simplified Schematic Diagram	2-V-38
2-V-22	Differential Amplifier, Video Modulator Bias, Differential Amplifier Balance and Emitter Followers, Schematic Diagram	2-V-39
2-V-23	Horizontal Parabola Generator and Size Controls	2-V-41
2-V-24	Vertical Sawtooth Amplitude and Clipper Controls for Sensitivity and Background Corrections	2-V-42
2-V-25	Amplifier, Schematic Diagram	2-V-43
2-V-26	Black and White Clippers, Video Blanking and Porch, and Time Code Insertion, Schematic Diagram	2-V-45
2-V-27	Output Emitter Follower and Sync Insertion, Schematic Diagram	2-V-46
2-V-28	Horizontal Deflection Circuit, Simplified, Schematic Diagram	2-V-47
2-V-29	Horizontal Deflection Generator, Simplified, Schematic Diagram	2-V-48
2-V-30	Constant Current Generator, Schematic Diagram	2-V-49
2-V-31	Yoke Skew Corrector, Schematic Diagram	2-V-50
2-V-32	Main Converter, Simplified Schematic	2-V-51
2-V-52	Filament DC-to-DC Converter, Schematic Diagram	2-V-52
2-V-34	+13-Volt Regulator, Schematic Diagram	2-V-53
2-V-35	Beam Current Regulator, Schematic Diagram	2-V-54
2-V-36	Main and Standby Power Switches, Schematic Diagram	2-V-55

LIST OF ILLUSTRATIONS (Continued)

Figure		Page
2-V-37	Shutter Drive, Schematic Diagram	2-V-57
2-V-38	Command Buffers, Schematic Diagram	2-V-61
2-V-40	Standby Telemetry, Schematic Diagram	2-V-63
2-V-41	AVCS Tape Recorder/Playback Electronics, Block Diagram	2-V-64
2-V-42	AVCS Tape Recorder Drive and Control, Block Diagram	2-V-65
2-V-43	Waveforms, Power Drive Circuitry	2-V-75
2-V-44	AVCS Recorder Transport, Negator Side	2-V-80
2-V-45	AVCS Recorder Transport, Reel Side	2-V-80
2-V-46	APT Camera Subsystem Block Diagram (One of Two Redundant Cameras)	2-V-81
2-V-47	APT Camera Subsystem	2-V-82
2-V-48	APT Camera Subsystem, Timing and Sequencing Diagram	
2-V-49	Camera Sensor Assembly, Block Diagram	2-V-90
2-V-50	Shutter Blade Sequence of Operation	2-V-92
2-V-51	Vidicon Construction	2-V-93
2-V-52	Vidicon Reticle Pattern	2-V-95
2-V-53	APT Camera Electronics Assembly, Block Diagram	2-V-97
2-V-54	Shutter Command Pulses	2-V-98
2-V-55	Evolution of Shutter Drive Circuit, Block Diagram	2-V-101
2-V-56	ITOS APT Shutter Drive Circuit, Block Diagram	2-V-103
2-V-57	
2-V-58	Sequence Timer Versus APT Camera Cycle, Timing Diagram	2-V-111
2-V-59	Cathode Sampling Switch Circuit	2-V-115
2-V-60	Target Lamp Switch Circuit	2-V-115
2-V-61	Prepare Command Input Circuit	2-V-116
2-V-62	Horizontal Blanking to Horizontal Deflection Circuit	2-V-116
2-V-63	Power Supply Sync Circuit	2-V-117
2-V-64	Clock Buffer Circuit	2-V-117
2-V-65	Target or Mesh Relay Driver Circuit	2-V-118
2-V-66	Subcarrier Generator Buffer Circuit	2-V-118
2-V-67	T1A-T3, T4-T5B to G1 Regulator Circuit	2-V-119
2-V-68	T1-T6 to G1 Regulator Circuit	2-V-119
2-V-69	T1-T6 to 4.2-kHz Inhibit Input Circuit	2-V-120
2-V-70	T1-T6 to Vertical Deflection Circuit	2-V-120
2-V-71	T1-T6 to Hold and PED Telemetry Circuit	2-V-121
2-V-72	Start Tone, Phasing, and White Clamp Circuit	2-V-121

LIST OF ILLUSTRATIONS (Continued)

Figure		Page
2-V-73	Power Reset Circuit	2-V-73
2-V-74	Gated 4800-Hz to 50-Microsecond One-Shot Trigger Circuit	2-V-122
2-V-75	Power Switch and Overvoltage Protection Circuit, Block Diagram	2-V-124
2-V-76	Power Switch and Overvoltage Protection Circuit, Schematic Diagram	2-V-124
2-V-77	Digital-to-Analog Converter and Ladder Circuit, Simplified Schematic Diagram	2-V-128
2-V-78	Scanning Radiometer Subsystem	2-V-135
2-V-79	Scanning Radiometer Subsystem, Block Diagram	2-V-136
2-V-80	SR Scan Projection	2-V-137
2-V-81	Scanning Radiometer, Block Diagram	2-V-143
2-V-82	Scanning Radiometer, Signal Phase Relationships	2-V-146
2-V-84	Scanning Radiometer, Detailed Optical Schematic	2-V-148
2-V-85	Aft Optics Assembly	2-V-150
2-V-86	IR Response versus Displacement Angle	2-V-152
2-V-87	Visible Channel, Relative Spectral Response	2-V-153
2-V-88	IR Channel, Relative Spectral Response	2-V-153
2-V-89	Scanner Housing Module, Outline Dimensions	2-V-155
2-V-90	SR Electronics Module, Outline Dimensions	2-V-159
2-V-91	SR Processor Real-Time Channel, Block Diagram	2-V-161
2-V-92	SR Processor Commutators, Block Diagram	2-V-166
2-V-93	Commutator FET Connection Diagram	2-V-168
2-V-94	Timing Diagram for Commutator FET's Showing One Complete Frame of 32 States	2-V-168
2-V-95	SR Recorder, Simplified Block Diagram	2-V-177
2-V-96	Flutter-to-Torque Ratio versus Frequency	2-V-185
2-V-97	Simplified Servo Drive, Block Diagram	2-V-186
2-V-98	SR Tape Transport Top View, Dome Removed	2-V-192
2-V-99	SR Tape Transport Removed from Enclosure, Top View	2-V-192
2-V-100	SR Tape Transport Removed from Enclosure, Bottom View	2-V-193

VOLUME II

PART 2 (Cont'd)

2-VI-1	Secondary Sensors Subsystem, Block Diagram	2-VI-2
2-VI-2	SPM Sensor Bracket	2-VI-7
2-VI-3	Detector Response to Protons, Electrons, and Alpha Particles	2-VI-9

LIST OF ILLUSTRATIONS (Continued)

Figure		Page
2-VI-4	SPM Data Processing Electronics Unit	2-VI-9
2-VI-5	Conversion of 800 Counts to a 9-Bit FPB Code	2-VI-11
2-VI-6	Conversion of 127,413 Counts to a 9-Bit FPB Code ...	2-VI-12
2-VI-7	SPM Sensor Units	2-VI-14
2-VI-8	SPM Data Format	2-VI-18
2-VI-9	Flat Plate Radiometer (Shown Without Thermal Blanket)	2-VI-19
2-VI-10	Flat Plate Radiometer, FPR, Exploded View (Showing Flight and Test Heads)	2-VI-20
2-VI-11	Flat Plate Radiometer Sensor Assembly, Exploded View	2-VI-22
2-VI-12	FPR Orientation	2-VI-23
2-VI-13	Spectral Regions Used by the FPR	2-VI-24
2-VI-14	FPR Calibrator (TF)	2-VI-25
2-VI-15	Flat Plate Radiometer, Solar Illumination (3 PM Orbit)	2-VI-26
2-VI-16	FPR Timing Diagram	2-VI-29
2-VI-17	Time Code Sequencer State Diagram	2-VI-43
2-VI-18	ITR Controller State Diagram	3-VI-44
2-VI-19	Incremental Tape Recorder	2-VI-45
2-VI-20	Tape Transport Assembly, Bottom Mounting Base Section Removed	2-VI-46
2-VI-21	Tape Transport Mechanism, Simplified Diagram	2-VI-53
2-VI-22	Incremental Tape Recorder, Simplified Block Diagram	2-VI-57
2-VI-23	Stepper Drive Signal Phasing	2-VI-59
2-VII-1	Communications Subsystem Components	2-VII-4
2-VII-2	Command Receiving Link	2-VII-5
2-VII-3	Command Receiver, Block Diagram	2-VII-8
2-VII-4	Beacon and Telemetry Link, Block Diagram	2-VII-9
2-VII-5	Digital Solar Aspect Sensor and Associated Electronics Unit	2-VII-13
2-VII-6	Accelerometer Control Unit, Block Diagram	2-VII-18
2-VII-7	Accelerometer Control Unit, Schematic Diagram ...	2-VII-19
2-VII-8	120 Channel Commutator, Block Diagram	2-VII-39
2-VII-9	Telemetry Commutator, Timing Diagram	2-VII-41
2-VII-10	Dual SCO, Block Diagram	2-VII-45
2-VII-11	Beacon Transmitter, Block Diagram	2-VII-46
2-VII-12	Beacon and Command Antenna Group, Simplified Block Diagram	2-VII-47

LIST OF ILLUSTRATIONS (Continued)

Figure		Page
2-VII-13	Spherical Coordinate System Used for Beacon and Command and Real-Time Antenna Group Measurements	2-VII-54
2-VII-14	Beacon and Command Antenna Contour Plots for Stowed Mode at Beacon Transmitter Frequency	2-VII-56
2-VII-15	Beacon and Command Antenna Contour Plots for Deployed Mode at Beacon Transmitter Frequency	2-VII-57
2-VII-16	Beacon and Command Antenna Contour Plots for Stowed Mode at Command Receiver Frequency	2-VII-58
2-VII-17	Beacon and Command Antenna Contour Plots for Deployed Mode at Command Receiver Frequency	2-VII-59
2-VII-18	Real-Time Transmission Link, Block Diagram	2-VII-63
2-VII-19	Real-Time IR and Visible Channel Subcarrier Modulating Signals in the SR Processor	2-VII-65
2-VII-20	Real-Time Transmitter, Block Diagram	2-VII-67
2-VII-21	Gain Requirements, Deployed Panels	2-VII-70
2-VII-22	Real-Time Antenna Group, Simplified Block Diagram...	2-VII-72
2-VII-23	Antenna Deployment	2-VII-73
2-VII-24	Antenna Deployment	2-VII-75
2-VII-25	Real-Time Antenna, Left Panel	2-VII-80
2-VII-26	Playback Video Link, Block Diagram	2-VII-83
2-VII-27	Dual Multiplexer Output Spectrum	2-VII-88
2-VII-28	Multiplexer Unit, Block Diagram	2-VII-99
2-VII-29	Dual Multiplexer, Simplified Block Diagram	2-VII-101
2-VII-30	S-Band Transmitter, Block Diagram	2-VII-107
2-VII-31	S-Band Antenna Subsystem	2-VII-110
2-VII-32	Relation of ITOS Spacecraft to the Coordinate System as Used in Pattern Measurements for S-Band Antenna	2-VII-111
2-VII-33	Transmitter Isolation	2-VII-113
2-VII-34	Coaxial Termination	2-VII-113
2-VII-35	Dipole Antenna	2-VII-115
2-VII-36	S-Band Antenna VSWR, ETM	2-VII-117
2-VII-37	S-Band Patterns, ETM	2-VII-119
2-VII-38	S-Band Ellipticity, ETM	2-VII-120
2-VIII-1	Vehicle Dynamics Subsystem, Block Diagram	2-VIII-3
2-VIII-2	Typical Signals Telemetered on 2.3-kHz Subcarrier ...	2-VIII-5
2-VIII-3	Equipment Module Momentum Versus Spin Rate	2-VIII-7
2-VIII-4	Gyroscopic Stability Prior to Solar Panel Deployment ..	2-VIII-8
2-VIII-5	Liquid-Filled Nutation Damper	2-VIII-11
2-VIII-6	Optimization Curve for Dynamic Mass	2-VIII-13

LIST OF ILLUSTRATIONS (Continued)

Figure		Page
2-VIII-7	Digital Solar Aspect Sensor Alignment Angles Relative to Spacecraft Reference Axis	2-VIII-15
2-VIII-8	Digital Solar Aspect Sensor, Functional Diagram	2-VIII-16
2-VIII-9	Scan Lines of Attitude Sensors	2-VIII-17
2-VIII-10	Infrared Bolometer	2-VIII-18
2-VIII-11	Pitch and Roll Sensor Electronics, Block Diagram	2-VIII-19
2-VIII-12	Attitude Sensor Configuration	2-VIII-20
2-VIII-13	Pitch Sensor Scan Geometry	2-VIII-21
2-VIII-14	Sensor Electronics Measured Signal Response	2-VIII-23
2-VIII-15	Pitch Offset Versus Orbit Altitude	2-VIII-23
2-VIII-16	Orbital Coordinates	2-VIII-26
2-VIII-17	Spacecraft Coordinates and Attitude Angles	2-VIII-26
2-VIII-18	Unipolar Pulse Mode	2-VIII-30
2-VIII-19	Unipolar Torque Correction for Solar Pressure Disturbance	2-VIII-31
2-VIII-20	Momentum Vector Attitude Drift	2-VIII-34
2-VIII-21	Magnetic Momentum Vector Control, Simplified Block Diagram	2-VIII-37
2-VIII-22	Momentum Change Versus Torquing Period (Single Coil)	2-VIII-40
2-VIII-23	Attitude Change Versus Torquing Period (Single Coil)	2-VIII-42
2-VIII-24	Geometry for Momentum Control Prior to Pitch Lock..	2-VIII-43
2-VIII-25	Dipole and Phase Definition for Momentum Control Prior to Pitch Lock	2-VIII-43
2-VIII-26	Ground-Commanded Momentum Coil Commutation Utilizing Roll Sensor and Pitch Index	2-VIII-45
2-VIII-27	Time Between Required Momentum Coil Dipole Reversals Prior to Pitch Lock	2-VIII-46
2-VIII-28	Commutation Error Effect on Torquing Efficiency	2-VIII-46
2-VIII-29	Pitch Axis Control Loop, Operational Block Diagram ..	2-VIII-49
2-VIII-30	Momentum Wheel Assembly, Cross Section	2-VIII-51
2-VIII-31	Geometry of Horizon Pulse and Reference Index Pulse	2-VIII-52
2-VIII-32	Open Loop Frequency Response of Pitch Control Loop (Without Cross-Coupling, Fine Gain)	2-VIII-56
2-VIII-33	Open Loop Frequency Response of Pitch Control Loop (Without Cross-Coupling, Coarse Gain)	2-VIII-57
2-VIII-34	Open Loop Frequency Response of Tachometer Loop ..	2-VIII-58
2-VIII-35	Digital Computer Simulation of Pitch Loop System	2-VIII-59
2-VIII-36	Pitch Capture Phase-Plane Plot (Dynamic Suspension Rig)	2-VIII-67

LIST OF ILLUSTRATIONS (Continued)

Figure		Page
2-VIII-37	Error Detection	2-VIII-71
2-VIII-38	Operational Amplifier, Simplified Schematic Diagram	2-VIII-72
2-VIII-39	Gain Switching Circuit, Block Diagram	2-VIII-72
2-VIII-40	Summing Amplifier, Simplified Schematic Diagram ...	2-VIII-73
2-VIII-41	Torque and Speed Characteristics at Power Amplifier Voltage for Inland Torque Motor of -24 Volts	2-VIII-74
2-VIII-42	Brush Reserve Amplifier Assembly	2-VIII-75
2-VIII-43	Molecular Flow Loss of MWA Lubricant P-10	2-VIII-80
2-VIII-44	MWA Long-Term Test Profiles	2-VIII-84
2-VIII-45	No. 1 Motor Brush Wear at Completion of 6 Month Life Test (MWA 05)	2-VIII-87
2-VIII-46	Motor Survival Test (MWA 01PP, Motor No. 1)	2-VIII-89
2-VIII-47	Spacecraft Reference Coordinates	2-VIII-91
2-VIII-48	Nutation Cone Angles Due to Transverse Momentum	2-VIII-111
2-IX-1	Orbit Load Profile	2-IX-8
2-IX-2	Power Supply Subsystem, Block Diagram	2-IX-10
2-IX-3	Maximum and Minimum Current Array Solar Cell Characteristics	2-IX-21
2-IX-4	Power Dissipation Versus Shunt Current	2-IX-22
2-IX-5	Drawn-Case, 4-Ampere-Hour, Battery Cell	2-IX-24
2-IX-6	Battery, Top Cover Removed	2-IX-24
2-IX-7	Battery Charging Voltage Limit Versus Temperature ..	2-IX-26
2-IX-8	Battery Electrical Diagram	2-IX-27
2-IX-9	Power Supply Electronics	2-IX-29
2-IX-10	-24.5 Volt Regulator, Block Diagram	2-IX-30
2-IX-11	Voltage Regulator, TIROS M	2-IX-32
2-IX-12	Shunt Limiter, Functional Block Diagram	2-IX-34
2-IX-13	Control Amplifier Detection Control, Block Diagram ..	2-IX-35
2-IX-14	Control Amplifier, Schematic Diagram	2-IX-37
2-IX-15	Signal Distribution Board, Schematic Diagram	2-IX-39
2-IX-16	Shunt Dissipator Leg (Part of Shunt Dissipator), Schematic Diagram	2-IX-41
2-IX-17	Battery Charge Controller, Functional Block Diagram	2-IX-44
2-IX-18	Regions of Charge Controller Operation	2-IX-45
2-IX-19	Current Regulator, Block Diagram	2-IX-45
2-IX-20	Charge Controller Operation in Region II, Simplified Schematic	2-IX-46
2-IX-21	Charge Controller, Schematic Diagram	2-IX-49
2-IX-22	Regulated Bus Voltage Telemetry, Schematic Diagram	2-IX-53

LIST OF ILLUSTRATIONS (Continued)

Figure		Page
2-IX-23	Solar Array, Battery, and Unregulated Bus Voltage Telemetry, Schematic Diagram	2-IX-53
2-IX-24	Shunt Limiter Control Amplifier Selector Telemetry, Schematic Diagram	2-IX-54
2-IX-25	Regulator and Charge Current Mode Selector Telemetry, Schematic Diagram	2-IX-55
2-IX-26	Battery Temperature Telemetry, Schematic Diagram ...	2-IX-56
2-IX-27	PSE Temperature Telemetry, Schematic Diagram	2-IX-56
2-IX-28	Shunt Limiter Temperature Telemetry, Schematic Diagram	2-IX-57
2-IX-29	Solar Array Temperature Telemetry, Schematic Diagram	2-IX-57
2-IX-30	Battery Charge Current Telemetry, Schematic Diagram	2-IX-59
2-IX-31	Solar Panel Current Telemetry, Schematic Diagram	2-IX-60
2-IX-32	Shunt Dissipator Current Telemetry, Schematic Diagram	2-IX-61

VOLUME III

PART 3. TEST HISTORIES

3-II-1	Mechanical Test Model with DAC Attach Fitting on the Vibration Test Fixture	3-II-2
3-II-2	MTM on Dynamic Balance Machine	3-II-3
3-II-3	MTM Suspended in Bifilar Pendulum for Moments of Inertia Measurement	3-II-4
3-II-4	Moments of Inertia Axes	3-II-13
3-III-1	ITOS Thermal Test Model	3-III-2
3-III-2	Thermal Blanket Test Configuration	3-III-6
3-III-3	Baseplate Test Assembly	3-III-11
3-III-4	Thermal Control Fence Design	3-III-19
3-IV-1	Antenna Test Model in RF Test Building	3-IV-2
3-IV-2	ATM Spacecraft, Block Diagram	3-IV-3
3-IV-3	RF Test Tower at RCA Premises (ATM is being hoisted into building)	3-IV-4
3-IV-4	Real-Time Antenna 1 Pattern, Panels Deployed	3-IV-13
3-IV-5	Real-Time Antenna 1 Pattern, Panels Stowed	3-IV-14
3-IV-6	Real-Time Antenna 2 Pattern, Panels Deployed	3-IV-15
3-IV-7	S-Band Antenna Pattern	3-IV-16

LIST OF ILLUSTRATIONS (Continued)

Figure		Page
3-V-1	Beacon and Command Link (RF Data Link Test)	3-V-5
3-V-2	Real-Time RF Link (RF Data Link Test).....	3-V-6
3-V-3	S-Band Link (RF Data Link Test)	3-V-6
3-V-4	ETM Spacecraft Suspended from Dynamic Suspension Rig	3-V-12
3-V-5	ETM Spacecraft on SEPET Fixture	3-V-13
3-V-6	RFI Test of ETM Spacecraft	3-V-15
3-V-7	ETM Spacecraft Suspended from Bifilar Pendulum	3-V-16
3-V-8	Optical Alignment Setup for ETM Spacecraft	3-V-18
3-V-9	ETM Spacecraft in the AED RF Tower	3-V-21
3-VI-1	Flight-Model and Prototype Thermal-Vacuum Test Profile for Components (Except Recorders and Sensors)	3-VI-8
3-VI-2a	Thermal-Vacuum Test Profiles for the Prototype Scanning Radiometer	3-VI-9
3-VI-2b	Thermal-Vacuum Test Profiles for the Prototype Scanning Radiometer	3-VI-9
3-VI-3	Thermal-Vacuum Test Profile for the Flight Scanning Radiometer	3-VI-9
3-VI-4	Thermal-Vacuum Test Profile for the Scanning Radiometer Recorder and Incremental Tape Recorder (Prototype and Flight Units)	3-VI-10
3-VI-5	Thermal-Vacuum Test Profile for the APT Subsystem .	3-VI-10
3-VI-6	Thermal-Vacuum Test Profile for the AVCS Subsystem (Prototype and Flight Units)	3-VI-10
3-VI-7	Real-Time Channel Response for Visual Data Inputs ...	3-VI-43
3-VI-8	Real-Time Channel Response for IR Data Inputs	3-VI-44
3-VI-9	Real-Time Channel Frequency Spectrum for 50 Percent Duty Cycle Carrier	3-VI-45
3-VI-10	Real-Time Channel Frequency Spectrum for 25 Percent Duty Cycle Carrier	3-VI-46
3-VI-11	Commutator Offset at Ground Input for all Channels Versus Temperature	3-VI-48
3-VI-12	Commutator Source Impedance Sensitivity for One Channel at Full-Scale Input	3-VI-49
3-VI-13	SRR ETM Servo Inverse Plot, Record Mode	3-VI-53
3-VI-14	SRR ETM Servo Inverse Plot, Playback Mode	3-VI-54
3-VI-15	SRR ETM Flutter Characteristics at 25° C	3-VI-56
3-VI-16	SRR ETM Flutter Characteristic at 51° C	3-VI-57
3-VI-17	SRR ETM Flutter Characteristics at -10° C	3-VI-58
3-VI-18	Strain Gage Amplifier and Power Supply, Functional Block Diagram	3-VI-88

LIST OF ILLUSTRATIONS (Continued)

Figure		Page
3-VI-19	Solar Panel Mounted in Clamshell Chamber	3-VI-104
3-VI-20	Nickel Cadmium Battery Life Cycling Test	3-VI-105
3-VI-21	Nickel Cadmium Battery Life Cycling Test, Battery End-of-Discharge Voltage Versus Cycle	3-VI-106
3-VI-22	Nickel-Cadmium Battery Life Cycling Test, Percent Recharge Versus Cycle	3-VI-107
3-VI-23	Actuator Sensor Life Test Assembly	3-VI-120
3-VII-1	TIROS M Spacecraft in Dynamic Suspension Test Fixture	3-VII-9
3-VII-2	TIROS M in Separation Shock Test	3-VII-11
3-VII-3	TIROS M on Vibration Table	3-VII-13
3-VII-4	Flight Model Solar Panels in Thermal-Vacuum Chamber	3-VII-14
3-VII-5	Thermal-Vacuum Test Profile	3-VII-15
3-VII-6	TIROS M Being Removed from the 8-Foot Thermal- Vacuum Chamber	3-VII-17
3-VII-7	AVCS Camera 1 Scan Format	3-VII-23
3-VII-8	AVCS Camera 2 Scan Format	3-VII-24
3-VII-9.	Orientation of AVCS Cameras for Distortion Photographs	3-VII-25
3-VII-10	AVCS Camera 1 Distortion Calibration Photograph	3-VII-26
3-VII-11	AVCS Camera 2 Distortion Calibration Photograph	3-VII-27
3-VII-12	AVCS Camera 1 Sensitivity Calibration Curve	3-VII-28
3-VII-13	AVCS Camera 2 Sensitivity Calibration Curve	3-VII-29
3-VII-14	APT Camera 1 Scan Format	3-VII-31
3-VII-15	APT Camera 2 Scan Format	3-VII-32
3-VII-16	Orientation of APT Cameras for Distortion Photograph	3-VII-33
3-VII-17	APT Camera 1 Distortion Calibration Photograph	3-VII-34
3-VII-18	APT Camera 2 Distortion Calibration Photograph	3-VII-35
3-VII-19	APT Camera 1 Sensitivity Calibration Curve	3-VII-36
3-VII-20	APT Camera 2 Sensitivity Calibration Curve	3-VII-37
3-VII-21	Scanning Radiometer 1, IR Channel Radiance Calibration Curves	3-VII-38
3-VII-22	Scanning Radiometer 2, IR Channel Radiance Calibration Curves	3-VII-39
3-VII-23	Scanning Radiometer 1 Visible Channel Radiance Calibration Curve	3-VII-40
3-VII-24	Scanning Radiometer 2 Visible Channel Radiance Calibration Curve	3-VII-41
3-VII-25	Spacecraft Alignment Reference Axes	3-VII-43
3-VII-26	AVCS and APT Picture Orientation for 3 PM Ascending Node Orbit	3-VII-45

LIST OF ILLUSTRATIONS (Continued)

Figure		Page
3-VII-27	Alignment AVCS and APT TV Cameras Optical Axes ...	3-VII-46
3-VII-28	SR Readout Orientation for 3 PM Ascending Node Orbit	3-VII-47
3-VII-29	Scanning Radiometer Scan Orientation	3-VII-48
3-VII-30	TIROS M in RCA RF Test Tower	3-VII-49
3-VII-31	TIROS M Moment-of-Inertia Measurement	3-VII-50

PART 4. TIROS M LAUNCH-SUPPORT OPERATIONS

4-II-1	SR Infrared Picture of Saudi Arabia Taken by ITOS 1 Orbit 241, February 11, 1970	4-II-4
4-II-2	SR Visible Channel Picture of Saudi Arabia Taken by ITOS 1 Orbit 241, February 11, 1970	4-II-4

PART 5. GROUND STATION EQUIPMENT

5-I-1	ITOS/TOS Ground Complex, Functional Block Diagram	5-I-3
5-II-1	CDA Station, Functional Block Diagram	5-II-2
5-II-2	CDA Station Equipment Arrangements	5-II-10
5-II-3	Beacon Data Handling, Block Diagram	5-II-17
5-II-4	Video Data Processing Equipment, Simplified Block Diagram	5-II-25
5-II-5	Beacon Data Processing	5-II-31
5-II-6	Microwave Link Transmission Equipment, Functional Block Diagram	5-II-35
5-II-7	Microwave Link Transmission Equipment Video and Flutter-and-Wow Select Matrix	5-II-37
5-II-8	Secondary Sensor Signal Conditioner, Functional Block Diagram	5-II-39
5-II-9	Events Recorder Circuitry, Logic Diagram	5-II-47
5-II-10	Beacon and Attitude Recorders, Block Diagram	5-II-50
5-II-11	AC Power Control, Simplified Schematic Diagram	5-II-53
5-II-12	CDA Station Equipment Control Circuits, Simplified Schematic Diagram	5-II-55
5-II-13	CDA Station Acquisition Mode Control Circuits, Schematic Diagram	5-II-57
5-II-14	VERT SYNC NOR/ALT Switch-Indicator Circuit	5-II-60
5-II-15	PTR Manual/Alarm Timer Switch Indicator	5-II-61
5-II-16	Events Recorder AUTO/MAN Control Circuit, Schematic Diagram	5-II-62
5-II-17	Beacon OPR/CAL Switch Indicator	5-II-63

LIST OF ILLUSTRATIONS (Continued)

Figure		Page
5-III-1	TOC Equipment Racks, Front Panel Elevation	5-III-3
5-III-2	TOS Operations Center (TOC), Block Diagram	5-III-7
5-III-3	Jack Panel Front Elevation (Rack 37)	5-III-9
5-III-4	TOC Station Switching Control Equipment, Simplified Schematic Diagram	5-III-11
5-III-5	Events Processing Equipment, Functional Block Diagram	5-III-19
5-III-6	Beacon and Attitude Recorders, Block Diagram	5-III-23
5-III-7	AC Distribution and Blower Fault Protection Circuits, Simplified Schematic Diagram	5-III-24
5-IV-1	TEC/TCC Station Equipment Racks, Front Panel Elevations	5-IV-2
5-IV-2	TEC/TCC Station Equipment Arrangement Diagram	5-IV-3
5-IV-3	TEC/TCC Station Overall System, Functional Block Diagram	5-IV-9
5-IV-4	TEC/TCC Real-time Beacon and Events Data Recorders, Functional Block Diagram	5-IV-11
5-IV-5	Secondary Sensor Subsystem Data Display Signal Flow, Simplified Block Diagram	5-IV-26
5-V-1	Spacecraft Test Console	5-V-10
A-1	Comparison of ITOS Ionization Damage Profiles	A-4
A-2	Worst-Case Beta Values for Transistor 2N930	A-6
A-3	Comparison of MOS Six-Channel Switches from Four Different Manufacturers	A-8
B-1	Battery Test Parameters Versus Life Cycling	B-4
B-2	Battery End-of-Discharge Voltage Versus Life Cycling	B-5
B-3	Cell Current and Average Cell Voltage Versus Time (New Cells Tested-Orbit Cycles 2476 and 2661)	B-6
B-4	Cell Current and Average Cell Voltage Versus Time (Old Cells Tested-Orbit Cycles 2476 and 2661)	B-7
B-5	Cell Current and Average Cell Voltage Versus Time (New Cells Tested-Orbit Cycles 2473 and 2663)	B-8
B-6	Cell Current and Average Cell Voltage Versus Time (Old Cells Tested-Orbit Cycles 2473 and 2663)	B-9
B-7	Percent Recharge Versus Sample Cycling at Lower and Upper Voltage Limits	B-10
B-8	Cell Current and Average Cell Voltage Versus Time (New Cells Tested-Orbit Cycles 15, 219, and 381)	B-11
B-9	Cell Current and Average Cell Voltage Versus Time (Old Cells Tested-Orbit Cycles 15, 219, and 381).	B-12

LIST OF ILLUSTRATIONS (Continued)

Figure		Page
B-10	Cell Current and Average Cell Voltage Versus Time (New Cells Tested-Orbit Cycles 28 and 383)	B-13
B-11	Cell Current and Average Cell Voltage Versus Time (Old Cells Tested-Orbit Cycles 28 and 383)	B-14
B-12	Cell Current and Average Cell Voltage Versus Time (New Cells Tested-Orbit Cycles 394, 622, and 738) ...	B-15
B-13	Cell Current and Average Cell Voltage Versus Time (Old Cells Tested-Orbit Cycles 394, 622, and 738)	B-16
B-14	Cell Current and Average Cell Voltage Versus Time (New Cells Tested-Orbit Cycles 396, 624, and 750) ...	B-17
B-15	Cell Current and Average Cell Voltage Versus Time (Old Cells Tested-Orbit Cycles 396, 624, and 750)	B-18
B-16	Cell Current and Average Cell Voltage Versus Time (New Cells Tested-Orbit Cycles 788, 966, and 1145) ..	B-19
B-17	Cell Current and Average Cell Voltage Versus Time (Old Cells Tested-Orbit Cycles 788, 966, and 1145) ...	B-20
B-18	Cell Current and Average Cell Voltage Versus Time (New Cells Tested-Orbit Cycles 801, 978, and 1156) ..	B-21
B-19	Cell Current and Average Cell Voltage Versus Time (Old Cells Tested-Orbit Cycles 801, 978, and 1156) ...	B-22
B-20	Cell Current and Average Cell Voltage Versus Time (New Cells Tested-Orbit Cycles 1169, 1322, and 1524)	B-23
B-21	Cell Current and Average Cell Voltage Versus Time (Old Cells Tested-Orbit Cycles 1169, 1322, and 1524)	B-24
B-22	Cell Current and Average Cell Voltage Versus Time (New Cells Tested-Orbit Cycles 1183, 1335, and 1526)	B-25
B-23	Cell Current and Average Cell Voltage Versus Time (Old Cells Tested-Orbit Cycles 1183, 1335, and 1526)	B-26
B-24	Cell Current and Average Cell Voltage Versus Time (New Cells Tested-Orbit Cycles 1536, 1701, and 1894)	B-27
B-25	Cell Current and Average Cell Voltage Versus Time (Old Cells Tested-Orbit Cycles 1536, 1701, and 1894)	B-28
B-26	Cell Current and Average Cell Voltage Versus Time (New Cells Tested-Orbit Cycles 1538, 1703, and 1904)	B-29

LIST OF ILLUSTRATIONS (Continued)

Figure		Page
B-27	Cell Current and Average Cell Voltage Versus Time (Old Cells Tested-Orbit Cycles 1538, 1703, and 1904)	B-30
B-28	Cell Current and Average Cell Voltage Versus Time (New Cells Tested-Orbit Cycles 2023, 2149, and 2290)	B-31
B-29	Cell Current and Average Cell Voltage Versus Time (Old Cells Tested-Orbit Cycles 2023, 2149, and 2290)	B-32
B-30	Cell Current and Average Cell Voltage Versus Time (New Cells Tested-Orbit Cycles 2034, 2161, and 2303)	B-33
B-31	Cell Current and Average Cell Voltage Versus Time (Old Cells Tested-Orbit Cycles 2034, 2161, and 2303)	B-34
C-1	Magnetic Tape Test Setup for ITOS Recorders, Block Diagram	C-3
C-2	SR Tape Recorder Breadboard Model, Top View	C-4
C-3	Dropout Detector Circuit, Block Diagram	C-5
C-4	3M-551 Magnetic Tape Condition After +55° C Test Run, Showing Severe Oxide Binder Pullouts	C-8
C-5	Record Head, After +55° C Test Run of 3M-551 Tape	C-8
C-6	3M-551 Magnetic Tape Condition After +50° C Test Run, Showing Damage at End-of-Tape Record	C-11
C-7	Record Head with Accumulated Deposits After +50° C Test Run of 3M-551 Tape	C-11
C-8	3M-551 Magnetic Tape Condition After 100 Cycles of Operation at +45° C	C-13
C-9	Record Head, Showing Debris on Head After 57-Cycle Test Run of 3M-551 Tape at +45° C	C-13
C-10	Record Head, Showing Debris on Head After Completing 100-Cycle Test Run of 3M-551 Tape at +45° C	C-14
C-11	Flutter Variation in 3M-551 Tape at +55° C (10 Cycles)	C-16
C-12	Flutter Variation in 3M-551 Tape at +50° C (100 Cycles)	C-16
C-13	Flutter Variation in 3M-551 Tape at +45° C (100 Cycles)	C-17
C-14	Memorex 161 Magnetic Tape Condition After 117th Record-Playback Cycle at +45° C	C-18
C-15	Record (Left) and Playback Heads, Shown After Completion of Memorex 161 Magnetic Tape Test at +45° C	C-18

LIST OF TABLES

Table		Page
VOLUME I		
PART 1. INTRODUCTION		
1-VIII-1	Particulars of the ITOS Nominal Orbit	1-VIII-3
1-VIII-2	Effect of Sun Angle on Picture-Taking Capability	1-VIII-8
PART 2. SPACECRAFT DESIGN		
2-II-1	Actuator Sensor Characteristics	2-II-40
2-II-2	Balance Weight and Inertia Data For MTM	2-II-47
2-II-3	Mechanical and Physical Parameters	2-II-48
2-III-1	Thermal Paint Specification	2-III-9
2-III-2	Spacecraft Thermal Control System Final Design Requirements	2-III-11
2-III-3	Operational and Acquisition Mode Flight Temperature Predictions	2-III-32
2-IV-1	ITOS Commands	2-IV-6
2-IV-2	Decoder Output Interface Signals	2-IV-15
2-IV-3	Decoder Data Format	2-IV-17
2-IV-4	Telemetry Priorities	2-IV-41
2-IV-5	Format of T ₀ Word	2-IV-59
2-IV-6	Format of Rephasing Word	2-IV-60
2-IV-7	Format of QOMAC Program Word	2-IV-64
2-V-1	AVCS Camera and Electronics Characteristics	2-V-16
2-V-2	AVCS Camera Electronics and Spacecraft Interface Signals	2-V-17
2-V-3	AVCS Tape Recorder Characteristics	2-V-66
2-V-4	AVCS Tape Recorder Signal Data	2-V-67
2-V-5	AVCS Tape Recorder and Spacecraft Interface Signals	2-V-68
2-V-6	APT Camera Subsystem Characteristics	2-V-87
2-V-7	APT Camera Subsystem and Spacecraft Interface	2-V-89
2-V-8	Power Supply and Tolerances	2-V-90

LIST OF TABLES (Continued)

Table		Page
2-V-9	Interface Circuits	2-V-114
2-V-10	Breadboard Test Results	2-V-129
2-V-11	Telemetry Circuit Design Constraints	2-V-130
2-V-12	Subsystem Characteristics	2-V-140
2-V-13	Scanning Radiometer Characteristics	2-V-141
2-V-14	IR Commutator Input Points	2-V-160
2-V-15	Visible Commutator Input Points	2-V-169
2-V-16	SRR Component Board Assemblies	2-V-172
2-V-17	SRR Circuit Boards	2-V-173
2-V-18	SRR Input Control Signals	2-V-174
2-V-19	SRR Characteristics	2-V-174
2-V-20	SRR Drive System Tradeoff Characteristics	2-V-182
2-V-21	Record Mode Required Torque	2-V-187
2-V-22	Playback Mode Maximum Required Torque	2-V-188
2-V-23	SRR Operational Status Telemetry	2-V-195

VOLUME II

PART 2 (Cont'd)

2-VI-1	Summary of Secondary Sensors Subsystems Characteristics	2-VI-3
2-VI-2	SPM Detector Characteristics	2-VI-8
2-VI-3	FPR Word Content	2-VI-27
2-VI-4	ITR Input and Output Signals	2-VI-48
2-VI-5	ITR Characteristics	2-VI-49
2-VII-1	Summary of Communications Links	2-VII-2
2-VII-2	Gray Code Outputs of Digital Solar Aspect Sensor (DSAS) and Corresponding Sun Angles	2-VII-16
2-VII-3	External and Internal Telemetry Signals	2-VII-23
2-VII-4	Housekeeping Telemetry Data Point Characteristics ...	2-VII-24
2-VII-5	Comparison of Single-Element and Four-Element Beacon and Command Antenna Designs	2-VII-49
2-VII-6	Isolation of Beacon and Command Antenna Group Components	2-VII-51
2-VII-7	Insertion Losses of Components of Beacon and Command Antenna Group	2-VII-52
2-VII-8	Circuit Characteristics of Beacon and Command Antenna Group	2-VII-55
2-VII-9	Insertion Loss	2-VII-78
2-VII-10	Margin Calculation for Real-Time Antenna	2-VII-81
2-VII-11	Dual Multiplexer Signal Inputs	2-VII-87

LIST OF TABLES (Continued)

Table		Page
2-VII-12	Insertion Losses, S-Band Antenna	2-VII-112
2-VII-13	Nonradiation Characteristics, S-Band Antenna ETM Frequency = 1697.5 MHz	2-VII-116
2-VII-14	Measured and Specified Antenna Pattern Data	2-VII-118
2-VIII-1	Damper Time Constants During Various Modes	2-VIII-12
2-VIII-2	QOMAC Coil Parameters	2-VIII-29
2-VIII-3	MBC Coil Operating Parameters	2-VIII-35
2-VIII-4	MBC Coil Physical Parameters	2-VIII-36
2-VIII-5	Momentum Coil Parameters	2-VIII-39
2-VIII-6	Computed Inertial Ranges for Pitch Control Loop	2-VIII-60
2-VIII-7	Summary of Three-Axis Pitch Loop Computer Simulation	2-VIII-63
2-VIII-8	Inertia Values Used in Computer Study	2-VIII-65
2-VIII-9	Single-Axis Capture Data Obtained in Suspension Rig Testing	2-VIII-66
2-VIII-10	Pitch Axis Control Loop Electronic Specifications	2-VIII-69
2-VIII-11	Life Test Brush Wear Summary	2-VIII-85
2-VIII-12	Life Test Brush Wear Summary	2-VIII-85
2-VIII-13	Random Roll Error Contributions	2-VIII-94
2-VIII-14	Bias Roll Error Contributions	2-VIII-94
2-VIII-15	Maximum Principal-Point Roll-Error Contributions ...	2-VIII-95
2-VIII-16	Pitch-Error Contributions	2-VIII-96
2-VIII-17	Operational Power Requirements	2-VIII-102
2-VIII-18	Summary of Disturbances and Effects	2-VIII-103
2-VIII-19	Transverse Momentum Disturbances	2-VIII-113
2-VIII-20	Three Orbit Computer Simulation of Uncompensated Momentum Effects	2-VIII-114
2-IX-1	ITOS Load Requirements	2-IX-2
2-IX-2	Energy Balance Analysis Results	2-IX-6
2-IX-3	Power Supply Subsystem Losses (Orbit Average Values).....	2-IX-9
2-IX-4	Power Supply Subsystem Loads During Pre- operational Mode	2-IX-9
2-IX-5	Summary of ITOS Power Supply Subsystem Parameters	2-IX-12
2-IX-6	Summary of Telemetry Characteristics	2-IX-52

VOLUME III

PART 3. TEST HISTORIES

3-II-1	MTM Component Test Versions	3-II-7
3-II-2	Preloading of Panels	3-II-9

LIST OF TABLES (Continued)

Table		Page
3-II-3	Panel Deployment Times	3-II-10
3-II-4	Components with Responses Over 10 G	3-II-11
3-II-5	MTM Moment of Inertia Tests Data	3-II-13
3-II-6	Dynamic Deflection	3-II-14
3-III-1	Temperature and Power Levels for TTM Retest	3-III-16
3-III-2	Correlation of Test Data, First and Second TTM Tests	3-III-18
3-IV-1	S-Band Insertion Loss	3-IV-6
3-IV-2	Real-Time Antenna Insertion Loss	3-IV-7
3-IV-3	Beacon and Command VSWR	3-IV-8
3-IV-4	Beacon and Command Isolation	3-IV-8
3-IV-5	Beacon and Command Insertion Loss	3-IV-9
3-IV-6	Isolation Between Input Ports	3-IV-10
3-IV-7	S-Band Link Amplitude Response	3-IV-17
3-IV-8	S-Band Signal and Noise-to-Noise Ratios	3-IV-17
3-VI-1	History of Component Testing	3-VI-3
3-VI-2	Component Vibration and Acceleration Test Requirements	3-VI-6
3-VI-3	Summary of ETM AVCS Camera Test Results	3-VI-18
3-VI-4	Summary of ETM AVCS Recorder Specification Limits and Test Results	3-VI-28
3-VI-5	Prototype Scanning Radiometer Assembly Test History	3-VI-37
3-VI-6	Output of Signal Conditioner and Limiter Versus Temperature for Visual Input	3-VI-41
3-VI-7	Output of Signal Conditioner and Limiter Versus Temperature for IR Input	3-VI-42
3-VI-8	Real-Time Channel Harmonic Distortion Components (Attenuation)	3-VI-42
3-VI-9	Scanning Radiometer Recorder Summary of Specification Limits and ETM Test Results	3-VI-60
3-VI-10	Summary of Initial Performance Testing (ETM) on Strain Gage Amplifier Circuitry	3-VI-89
3-VI-11	Identification of Battery Storage Cells	3-VI-102
3-VI-12	Battery Cycling Schedule	3-VI-103
3-VI-13	Summary of ETM Performance Testing on Power Supply Electronics	3-VI-111
3-VI-14	Test Results of Significant Parameters, Power Supply Electronics	3-VI-116
3-VII-1	Chronology of TIROS M Flight Acceptance Tests	3-VII-2
3-VII-2	Spacecraft Vibration Test Requirements	3-VII-12

LIST OF TABLES (Continued)

Table		Page
3-VII-3	Measured Magnetic Dipole Moments, Uncompensated . . .	3-VII-21
3-VII-4	Measured Magnetic Dipole Moments, Compensated	3-VII-21
3-VII-5	TV Cameras Optical Alignment Summary	3-VII-44
3-VII-6	Mechanical and Physical Parameters of TIROS M	3-VII-52

PART 4. TIROS M LAUNCH-SUPPORT OPERATIONS

PART 5. GROUND STATION EQUIPMENT

5-II-1	Major CDA Station Operating Parameters	5-II-3
5-II-2	CDA Station Equipment	5-II-11
5-II-3	Beacon Subcarrier Utilization, ITOS	5-II-28
5-II-4	Tape Recorder Channel Assignments	5-II-42
5-II-5	Equalized Playback Speeds	5-II-44
5-II-6	Events Recorder Channel Assignments	5-II-45
5-III-1	Beacon Subcarrier Utilization, TOS/APT	5-III-13
5-III-2	Beacon Subcarrier Utilization, TOS/AVCS	5-III-14
5-III-3	Beacon Subcarrier Utilization, ITOS	5-III-15
5-III-4	Events Recorder Channel Assignments	5-III-21
5-IV-1	Beacon Subcarrier Utilization, TOS/APT	5-IV-15
5-IV-2	Beacon Subcarrier Utilization, TOS/AVCS	5-IV-16
5-IV-3	Beacon Subcarrier Utilization, ITOS	5-IV-17
5-IV-4	Events Recorder Channel Assignments	5-IV-21
5-IV-5	ITR Track 3 Data Frame Content	5-IV-24
5-V-1	Backup CDA Station (GSE-3) Equipment	5-V-3
5-V-2	Factory Test Set (GSE-6) Equipment	5-V-4
5-V-3	Launch Support Van (GSE-5) Equipment	5-V-5
5-VI-1	Composite Subcarrier Signals	5-VI-2
5-VII-1	Program Milestones	5-VII-1
A-1	ITOS Radiation Environment	A-3
B-1	Storage Cells Tested for Overcharge	B-2
B-2	Seven-Month Battery Life Cycling Test Summary	B-3
C-1	Test Equipment for ITOS Magnetic Tape Test	C-4
C-2	3M-551 Tape Test Results at +25°C and +55°C	C-7
C-3	3M-551 Tape Test Results at +50°C for First 50 Cycles	C-9
C-4	3M-551 Tape Test Results at +50°C for Second 50 Cycles	C-9
C-5	3M-551 Tape Test Results at +45°C for 57 Cycles (First Test Run)	C-12

LIST OF TABLES (Continued)

Table		Page
C-6	3M-551 Tape Test Results at +45°C for 43 Cycles (Second Test Run)	C-12
C-7	Memorex 161 Tape Test Results at +45°C	C-17
D-1	TIROS M Component Serial Numbers	D-1

PART 2. SPACECRAFT DESIGN

SECTION VI

SECONDARY SENSORS SUBSYSTEM

A. GENERAL

The secondary sensors subsystem is designed to gather earth heat balance data and to measure proton flux levels at the spacecraft altitude. It comprises two sensory devices, a flat plate radiometer (FPR) as well as solar proton monitor (SPM) and a data format converter (DFC), and an incremental tape recorder (ITR). The data collected by the solar proton monitor and the flat plate radiometer during orbit is converted and is stored on the incremental tape recorder. The data format converter controls the SPM, the FPR, and the ITR; it provides the desired data format and the interfaces for the sensor units with the spacecraft. Data from the sensors, time code data, in-orbit telemetry, and a clock signal are recorded on three channels of the recorder. On playback, the three channels modulate three subcarrier oscillators in the data format converter. These signals are combined, up converted in the multiplexer, and transmitted to the ground station on the playback (S-band) link. The interrelation of the units within the secondary sensors subsystem is shown in Figure 2-VI-1. The secondary sensors are supplied to the spacecraft as GFE. Table 2-VI-1 summarizes the signal characteristics of the secondary sensor subsystem.

When the beacon transmitter is on and is not commanded to transmit other data, the solar proton monitor output frequency-modulates the IRIG channel 9 subcarrier oscillator to give direct readout capability for the SPM data.

B. SECONDARY SENSOR DEVICES

1. Solar Proton Monitor

a. PURPOSE AND USE

The solar proton monitor (SPM) is designed to measure the proton fluxes encountered in the ITOS orbit and to convert these measurements to a floating point binary code for recording and subsequent playback and transmission to ground stations. Alternatively, the SPM data can be transmitted directly, in real time, over one of the spacecraft telemetry channels. The SPM equipment on the spacecraft consists of a sensor assembly, an electronics assembly, and an electrical harness, all of which are supplied as GFE to RCA. (The Applied Physics Laboratory of the Johns Hopkins University is the supplier to ESSA.)

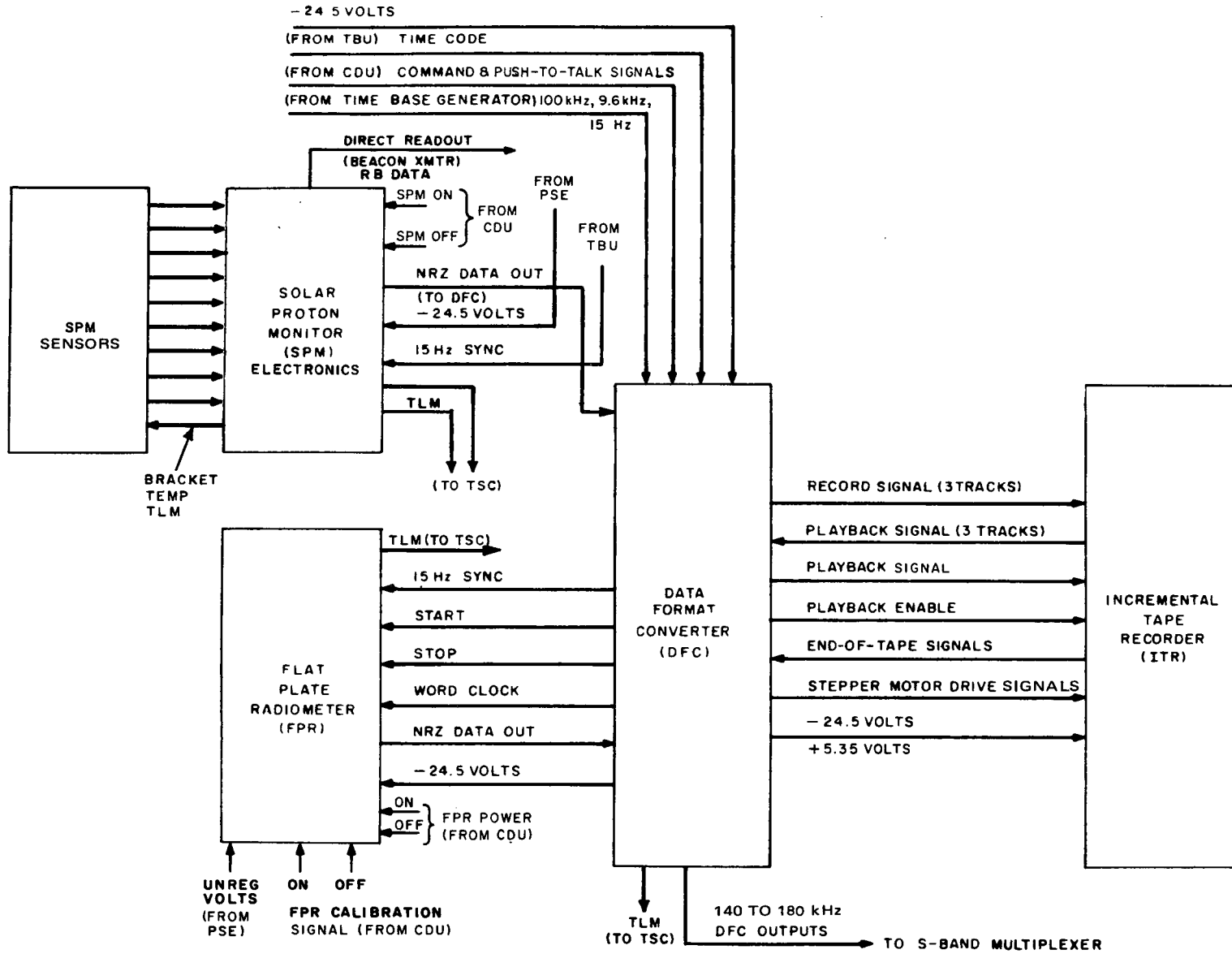


Figure 2-VI-1. Secondary Sensors Subsystem, Block Diagram

TABLE 2-VI-1. SUMMARY OF SECONDARY SENSORS SUBSYSTEMS CHARACTERISTICS

Parameter	Solar Proton Monitor		FPR	Digital Telemetry	Clock	Time Code
	Real Time	Recorded				
1. <u>Sensor Characteristics</u>						
Sensor Type	Silicon radiation detector		Thermocouples & Thermopiles	Various	-	-
Spectral Response (μ M)	-	-	Black -0.3-30 White 7-30	-	-	-
Dynamic Range	$\left\{ \begin{array}{l} \text{Protons } 0.1 > E_p > 60 \text{ MeV} \\ \text{Electrons } E_e > 0.25 \text{ MeV} \\ \text{Alpha } E_\alpha > 12.4 \text{ MeV} \end{array} \right\}$		-	-	-	0 to 2^{22} s in 1/4-s steps
Sensors Orientation (with respect to local vertical)	90 and 180 degrees		0 degree	-	-	-
Resolution	Varies with count		see below	± 1 percent	-	+1/8 s
Item Measured	Solar protons and electrons		-	-	-	-
Accumulation Time (s)	1, 2, 3, 0 or 12		8/15	8/15	-	-
Full Scale	~ 1 million counts/channel		(2^8-1) or $(2^{11}-1)$	2^8-1	-	$2^{25}-1$ count
2. <u>Signal Characteristics</u>						
Spectrum (kHz)	-	476 \pm 4.0	444 \pm 4	444 \pm 4	460 \pm 4	444 \pm 4
Data "1" $\left\{ \begin{array}{l} \text{- voltage} \\ \text{- frequency (kHz)} \end{array} \right.$	-0.5 \pm 0.25 3.666	+3.8 \pm 0.5 -	0 -	0 -	0 -	0 -
Bias $\left\{ \begin{array}{l} \text{- voltage} \\ \text{- frequency (kHz)} \end{array} \right.$	-2.5 \pm 0.25 3.900	na na	na na	na na	na na	na na
Data "0" $\left\{ \begin{array}{l} \text{- voltage} \\ \text{- frequency (kHz)} \end{array} \right.$	-4.5 \pm 0.25 4.134	0.25 \pm 0.25 -	4.2 \pm 0.5 -	-5.0 -	+4.7 -	-5.0 -
Frame Period $\left\{ \begin{array}{l} \text{- record (s)} \\ \text{- playback (ms)} \end{array} \right.$	12.0 -	12.0 90	32 416	32 416	- -	32 416
Frame Rate - Record (frames per minute)	5	5	1.875	1.875	-	1.875
Frames per Orbit	570	570	213.75	213.75	-	213.75
Frame Sync	Barker word	Barker word	16 "1's"	16 "1's"	-	16 "1's"

TABLE 2-VI-1. SUMMARY OF SECONDARY SENSORS SUBSYSTEM CHARACTERISTICS (Continued)

Parameter	Solar Proton Monitor		FPR	Digital Telemetry	Clock	Time Code
	Real Time	Recorded				
2. Signal Characteristics (Continued)						
Day	Yes	Yes	Yes	Yes	Yes	Yes
Night	Yes	Yes	Yes	Yes	Yes	Yes
Words per Frame	20	20	15	39	-	4
Bits per Word - Data	Characteristic 4 + Mantissa 5		7	7	-	28
- Marker	None	None	1	1	-	4
Marker Level	-	-	Frame: 16 "1's" Channel: "0"	Frame: 16 "1's" Channel: "0"	-	Frame: 16 "1's" Channel: "0"
Bit Rate, Real Time or Recorded (Hz)	15	15	15	15	7.5	15
Playback (Hz)	-	~2000	~2000	~2000	~1000	~2000
Clock Signal Location	Self	ITR track 2	ITR track 2	ITR track 2	-	ITR track 2
LSB Location (bit no.)	Last	Last (when recorded)	← First (when recorded in satellite) →			
Bits per Measurement	9 (floating point binary)		7 or 10	7	-	24
Test or Cal. Signals	None	-	Yes	3 levels	-	None
Associated Data	Sensor temperature telemetry		Flags	Ch 6 on hkp tlm	-	None
Data Word Capacity	$2^{20} - 1$	$2^{20} - 1$	2^7 to 2^{10}	2^7	-	2^{24}
Data Word Accuracy	Approx 3 percent		Varies	Approx 1 percent	-	$\pm 1/8$ s
3. Recording Characteristics						
Name of Recorder	-	ITR	ITR	ITR	ITR	ITR
Playback Direction (with respect to record)	-	Reversed	Reversed	Reversed	Reversed	Reversed

TABLE 2-VI-1. SUMMARY OF SECONDARY SENSORS SUBSYSTEM CHARACTERISTICS (Continued)

Parameter	Solar Proton Monitor		FPR	Digital Telemetry	Clock	Time Code
	Real Time	Recorded				
3. <u>Recording Characteristics</u> (Continued)						
Speed Ratio	-	~1:133	~1:133	~1:133	~1:133	~1:133
Record Operation	-	Continuous	Continuous	Continuous	Continuous	Continuous
Capacity	-	3 orbits	← 320,000 bits (3 orbits) →			
Maximum Playback Time (min)	-	2.7	2.7	2.7	2.7	2.7
Track	-	1	3	3	2	3
4. <u>Data Modulation</u>						
RF Link (MHz)	136.77	S-band	S-band (1697.5)	S-band (1697.5)	S-band (1697.5)	S-band (1697.5)
Subcarrier (kHz)	3.900	476 ±4	444 + 4	444 + 4	460 ±4	444 + 4
Carrier	PM	FM	FM	FM	FM	FM
Subcarrier	FSK	FSK	FSK	FSK	FSK	FSK
Data "1" (kHz)	3.666	479.2	440.4	440.4	456.4	440.4
Data "0" (kHz)	4.134	472.4	447.2	447.2	463.2	447.2
5. <u>Data Demodulation</u>						
Demux Output (kHz)	-	176 ±4	144 ±4	144 ±4	160 ±4	144 ±4
Display Equipment	Printer	Computer printout	Computer output device	Computer output device	-	Computer output device
Freq. into Long Lines (kHz)	-	22 ±0.5	18 ±0.5	18 ±0.5	20 ±0.5	18 ±0.5
Long Line Channel	-	A	A	A	A	A

The solar proton monitor will be used, in conjunction with other satellite-borne and ground-based sensors, to provide warnings of solar proton storms. These warnings are currently used in several ways. High altitude users, such as supersonic transports and manned spacecraft, make provisions for the protection of personnel on the basis of this data. Solar proton storms affect radio frequency links (VLF through HF), and since satellite warnings often precede ionospheric disturbances, alternate radio paths or frequencies are often selected in advance. Several nuclear detection methods may be falsely triggered by proton events (Vela and VLF phase shifts are two examples), and advance warning of proton events can be advantageous to these programs.

The ITOS SPM data will be correlated with data from other satellites (such as IMP, Vela, and Pioneer), rocket probes, and with ground based optical/radio sightings. The long term goal of this data-gathering and correlation activity is the better understanding of the interaction between solar radiation and the earth's environment by providing a systematic monitoring of the proton fluxes over an extended period of time, especially during the current solar cycle.

b. SENSOR ASSEMBLY

The sensor assembly of the SPM is shown in Figure 2-VI-2. One surface of the L-shaped sensor bracket contains four sensors (1, 2, 3 and 6), which point away from the earth at all times (anti-earth sensors), in the normal ITOS orbit. The other surface contains two additional sensors (4 and 5) which are oriented to point along the orbit normal. Table 2-VI-2 lists the sensors and their characteristics. Two of the sensors (5 and 6) contain two detector elements which are used to detect particles at several different energy levels. The other four sensors contain the equivalent of single element detectors with fixed threshold levels. Three of the single-element sensors are proton sensors while the fourth is used to monitor electron flux levels. High-energy electrons contained within the Van Allen belts will contaminate the data from the proton detectors while the electron detector output count is due to electrons alone. In the polar regions,* however, there are few electrons in the response range of any detector and, thus, good proton data may be obtained. The cutoff in data from the electron detector will be used to define the edges of the trapping regions.

The sensor elements are essentially reverse-biased large-area silicon diodes analogous to an ionization chamber wherein the usual gas has been replaced with

*In general, the regions from about 65 degrees North to 90 degrees North and 65 degrees South to 90 degrees South; however, strictly speaking, these are geomagnetic poles (which are inclined about 11 degrees from geographic poles).

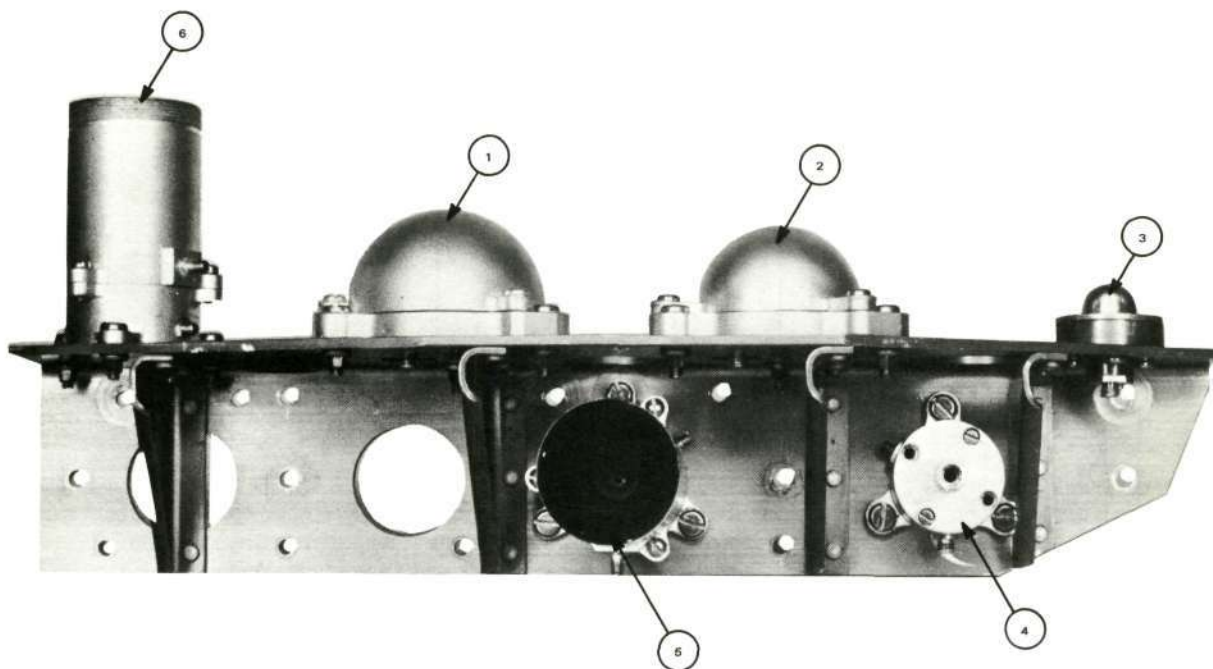


Figure 2-VI-2. SPM Sensor Bracket

a semiconducting solid. The applied reverse-bias develops a depletion region in which charges (electron-hole pairs) are produced by ionizing charged particles. The charge carrier formation is proportional to the particle energy if the particle is completely stopped within the detector. The signal versus incident energy relationship is shown in Figure 2-VI-3 for electrons, protons and α -particles. It can be seen from this representative figure that particle-type identification can be made by selective use of pulse height discrimination levels. It is also apparent that channels may contain signals due to more than one type of particle. The expected population over the polar regions following solar-flare events is given in Table 2-VI-1 for each readout channel.

The charge output from the sensors is collected on a capacitor in charge-sensitive preamplifier to produce a voltage-step proportional to the incident particle energy. This signal is amplified and used to feed pulse-height discriminators for detection. Combinations of electronic discriminator levels and detector shielding thicknesses are employed to define the energy response of each detector.

c. DATA PROCESSING ELECTRONICS

The data processing electronics is contained in a 5.5-pound unit 6.23 inches high, 6.2 inches wide, and 6.0 inches deep (see Figure 2-VI-4). This unit contains

TABLE 2-VI-2. SPM DETECTOR CHARACTERISTICS

Detector and Word Designation	Energy Range (MeV) (a)			Absorber	Field of View	Look Direction	Geometric Factor (cm ² ster)	Accumulation Time (sec)	Duty Cycle (percent)	Word Number (h)	Logic (i)	Discrimination Levels (MeV)
	Protons	Alphas	Electrons									
1	<u>≧ 60</u>	≧ 240	> 8	4.98g/cm ² Cu (dome) (c)	2π ster	Zenith	6.28	12	100	6	---	0.15
2	<u>≧ 30</u>	≧ 120	> 2.15	1.42g/cm ² Cu (dome) (c)	2π ster	Zenith	6.28	12	100	11	---	0.15
3	<u>≧ 10</u>	≧ 40	> 60	0.17g/cm ² Al (dome) (c)	2π ster	Zenith	0.791	12	100	16	---	0.30
41	2.09- 2.37		<u>≧ 0.140</u>	16.7 mg/cm ² Ni (d)	Cone 6.5 degrees half angle 0.040 ster	Perpendicular to orbit plane	2.74 × 10 ⁻³	3	50 (g)	2, 12	D ₁ D ₂	D ₁ = 0.10 D ₂ = 0.75
42	<u>> 2.37</u>		<u>≧ 0.770</u> [low eff]					3	50 (g)	7, 17	D ₂	
51 (61)	<u>0.27-0.56</u>	0.48-0.78	<u>> 200</u> [low eff]	0.222 mg/cm ² Ni (e)	Cone 20 degrees half angle 0.38 ster	Detector 5, perpendicular to orbit plane; detector 6, zenith	0.38	1.2 (1.2) (f)	10 (10)	3 (13)	A ₁ A ₂ B	A ₁ = 0.20
52 (62)	<u>0.56-1.05</u>	0.78-1.28	---					1.2 (1.2)	10 (10)	4 (14)	A ₂ A ₃ B	A ₂ = 0.50
53 (63)	<u>1.05-3.2</u>	1.28-4.1	---					1.2 (1.2)	10 (10)	5 (15)	A ₃ A ₄ B	A ₃ = 1.0
54 (64)	<u>3.2-60</u>	> 12.5	---					1.2 (1.2)	10 (10)	8 (18)	A ₁ B	A ₄ = 4.0
55 (65)	---	<u>12.5-32</u>	---					1.2 (1.2)	10 (10)	9 (19)	A ₁ B	B = 0.30 (same for detectors 5 and 6)
56 (66)	<u>60-86</u> +bkgd (b)	bkgd (b)	---					1.2 (1.2)	10 (10)	10 (20)	A ₁ B	

NOTES: (a) Primary contributor over polar caps during solar proton event is underlined.
(b) Background (bkgd) is count from particles penetrating shielding (present to some extent in all channels).
(c) Shielding (except for dome) is ≧ 60 MeV proton equivalent of Cu.
(d) Shielding (except for aperture) is ≧ 50 MeV proton equivalent of Cu.
(e) Shielding (except for aperture) is ≧ 30 MeV proton equivalent of Cu.
(f) 6 channels of detector 5 accumulated simultaneously during words 1 and 2.
6 channels of detector 6 accumulated simultaneously during words 11 and 12.
(g) 41 and 42 each sampled twice per 12-second frame.
(h) Word order is for real-time (and record) modes; on playback, it is reversed. Word 1 is the Barker code.
(i) Refer to RCA logic diagram 1976102.

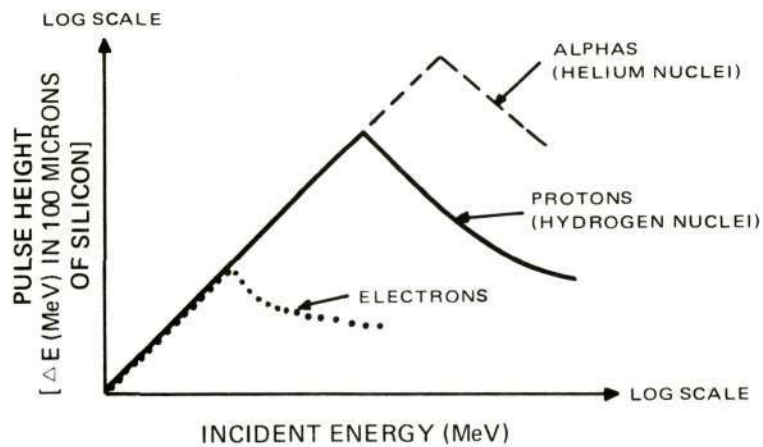


Figure 2-VI-3. Detector Response to Protons, Electrons, and Alpha Particles

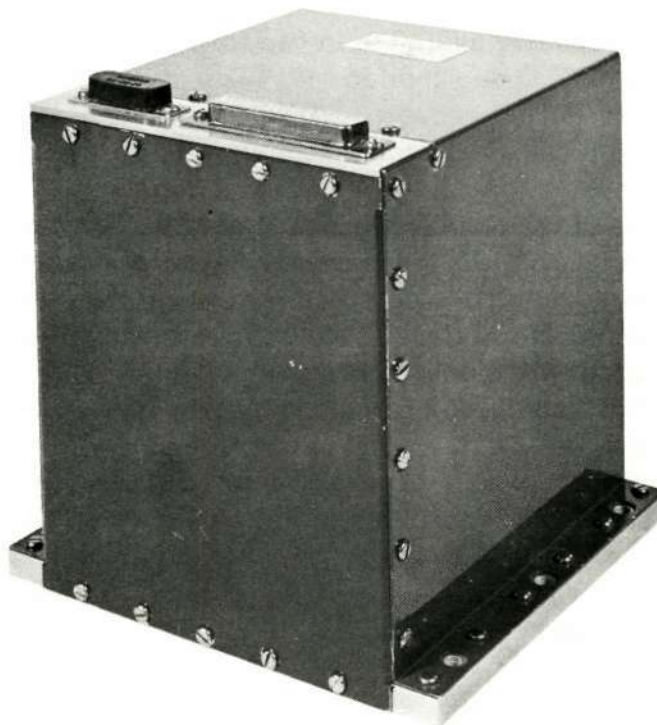


Figure 2-VI-4. SPM Data Processing Electronics Unit

all circuitry for processing the SPM sensor outputs consisting basically of the amplifier-discriminator chains for each data channel, the data encoder which compresses and formats the SPM information, and the power supply which generates the several DC voltages required by the electronics and the bias voltages for detectors.

Each SPM output is accumulated in a 20-stage counter with a capacity of $(2^{20} - 1)$ or 1,048,575 bits. At the end of each accumulation, the 20-bit data word is converted to a 9-bit floating point binary format by breaking the number into a characteristic (N) and mantissa (M) so that the data has the form $M2^N$. In the SPM subsystem, N is limited to 4 bits, and M to 5 bits which yields a resultant accuracy of 1 part in 2^5 (or approximately 3 percent), and a count capacity of $(2^{20} - 1) - (2^{15} - 1)$ or 1,015,809.

Examples of two number conversions into the floating point binary (FPB) code are given in Figures 2-VI-5 and 2-VI-6. In the first example, the code produces a perfect answer. In the second, the answer (11001111) is an imperfect approximation, which is typical of this type of coding. The floating point permits the 9 bits to convey a wide range of counts with the same overall accuracy. There are 20 words in a data frame, of which 19 are data words of 9-bit floating point binary codes each. The data words are preceded by a frame synchronization word. A unique (Barker) code is used which can be recognized even under highly adverse signal-to-noise conditions, thus maintaining frame sync even under such conditions.

The SPM data is simultaneously available in two forms (see Table 2-VI-1). The primary data form is a NRZ code supplied to track 1 of the incremental tape recorder (ITR) via the data format converter (DFC). This data is recorded throughout the orbit and is played back upon command over a CDA station.

As an alternative means of transmitting the SPM data to the ground, the 3.9-kHz SCO of the 136.77-MHz beacon will transmit the RB code supplied by the SPM unless a higher priority function has been commanded. The required interconnection is accomplished by latching relays. When this alternative is in use, real-time SPM data is radiated by the beacon continuously except for brief interruptions for command verification and (when commanded) housekeeping telemetry. In this manner, it is possible to use STADAN and other receiving sites to acquire SPM data. This arrangement is valuable because on many orbits the data being stored on the ITR cannot be played back until the satellite is in range of the next CDA site. The beacon transmission of the data avoids a prolonged delay between acquiring the data at the spacecraft and acquiring it on the ground. Timely warnings of a solar proton storm can thus be assured.

GIVEN: 800 COUNTS

FIND: FLOATING POINT BINARY: $M2^N$ (N = 4 BITS, M = 5 BITS)

1. BINARY NUMBER FOR 800 COUNTS IS:

2^0	2^1	2^2	2^3	2^4	2^5	2^6	2^7	2^8	2^9	2^{10}	2^{11}	2^{12}	2^{13}	2^{14}	2^{15}	2^{16}	2^{17}	2^{18}	2^{19}	
0	0	0	0	0	1	0	0	1	1	0	0	0	0	0	0	0	0	0	0	0

2. SHIFT RIGHT → UNTIL A "1" APPEARS IN 2^{19}

(1)	X	0	0	0	0	0	1	0	0	1	1	0	0	0	0	0	0	0	0	0
(2)	X	X	0	0	0	0	0	1	0	0	1	1	0	0	0	0	0	0	0	0
(3)	X	X	X	0	0	0	0	0	0	0	0	1	1	0	0	0	0	0	0	0

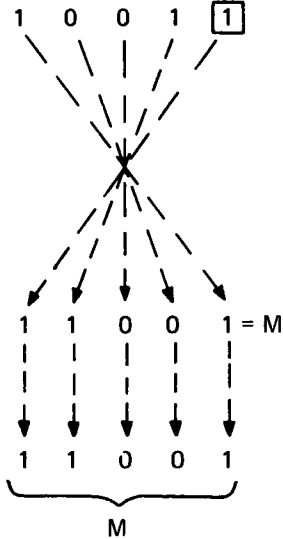


(8)	X	X	X	X	X	X	X	X	0	0	0	0	0	1	0	0	1	1	0	0
(9)	X	X	X	X	X	X	X	X	X	0	0	0	0	0	1	0	0	1	1	0
(10)	X	X	X	X	X	X	X	X	X	0	0	0	0	0	1	0	0	1	1	

3. SUBTRACT NUMBER OF SHIFTS (10) FROM 15, THE RESULT IS N

DECIMAL
15
-10
5

BINARY CODE
1 1 1 1
(-)1 0 1 0
0 1 0 1



4. THE BITS IN THE 2^{15} THROUGH 2^{19} ARE M

5. THE COMPLETE WORD IS N, M OR:

ANSWER

0	1	0	1	1	1	0	0	1
N				M				

6. CHECK $M2^N$

	2^3	2^2	2^1	2^0	2^4	2^3	2^2	2^1	2^0
	← N →				← M →				
BINARY	0	1	0	1	1	1	0	0	1
DECIMAL	5 = N				25 = M				

$$M2^N = 25 \cdot 2^5 = 25 \cdot 32 = 800$$

Figure 2-VI-5. Conversion of 800 Counts to a 9-Bit FPB Code

GIVEN: 127,413 COUNTS

FIND: FLOATING POINT BINARY: $M2^N$ (N = 4 BITS, M = 5 BITS)

1. BINARY NUMBER FOR 127,413 COUNTS IS:

2^0	2^1	2^2	2^3	2^4	2^5	2^6	2^7	2^8	2^9	2^{10}	2^{11}	2^{12}	2^{13}	2^{14}	2^{15}	2^{16}	2^{17}	2^{18}	2^{19}
1	0	1	0	1	1	0	1	1	0	0	0	1	1	1	1	1	0	0	0

2. SHIFT RIGHT → UNTIL A "1" APPEARS IN 2^{19}

(1)	X	1	0	1	0	1	1	0	1	1	0	0	0	1	1	1	1	1	0	0
(2)	X	X	1	0	1	0	1	1	0	1	1	0	0	0	1	1	1	1	1	0
(3)	X	X	X	1	0	1	0	1	1	0	1	1	0	0	0	1	1	1	1	1

3. SUBTRACT NUMBER OF SHIFTS (3) FROM 15, THE RESULT IS N

DECIMAL	BINARY CODE
15	1 1 1 1
- 3	(-) 0 0 1 1
-----	-----
12	1 1 0 0

4. THE BITS IN THE 2^{15} THROUGH 2^{19}

5. THE COMPLETE WORD IS N, M OR:

ANSWER	1	1	0	0	1	1	1	1	1	1	1	1	1
	└──────────┘				└──────────┘								
	N				M								

6. CHECK $M2^N$

	2^3	2^2	2^1	2^0	2^4	2^3	2^2	2^1	2^0	
BINARY	1	1	0	0	1	1	1	1	1	
DECIMAL	12 = N				31 = M					$M2^N = 31 \cdot 2^{12} = 31 \cdot 4096$
	$M2^N = 126,976$ (WHICH IS AN APPROXIMATION OF 127,413)									

Figure 2-VI-6. Conversion of 127,413 Counts to a 9-Bit FPB Code

d. FUNCTIONAL OPERATION

The six detector units and the bracket temperature sensor are connected to the SPM electronics unit by a harness assembly made up of 9 shielded leads. The detailed logic diagram is RCA 1976102, which can be found in a separate manual.*

(1) SENSOR ASSEMBLY

(a) Proton Sensors 1 and 2 ($E_p > 60 \text{ MeV}$ and $E_p > 30 \text{ MeV}$)

Each of these two higher energy channels consists of three 700-micron-thick silicon surface barrier detectors mounted on orthogonal axes and surrounded by a hemispherical shield as shown in Figure 2-VI-7(a). The three outputs are wired in parallel to provide a fairly uniform cross section over a complete hemisphere.

The only difference between these two units is the thickness of the shielding dome, its thickness being by far the most important factor in determining the energy threshold of the detectors. Sensor 1 detects proton particles with energy 60 MeV or greater and sensor 2 detects protons at 30 MeV or greater.

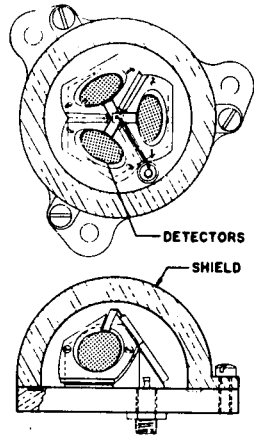
(b) Proton Sensor 3 ($E_p > 10 \text{ MeV}$)

This detector consists of a lithium-drifted silicon detector in the shape of a 3-millimeter cube and surrounded by a thin aluminum shield. Figure 2-VI-7(b) is a cross section diagram of this unit. The dimensions of this detector are small due to the large proton flux in the energy range $E_p > 10 \text{ MeV}$ that is possible following solar-flare events. At lower latitudes, electron contribution will be a major portion of this detector's data.

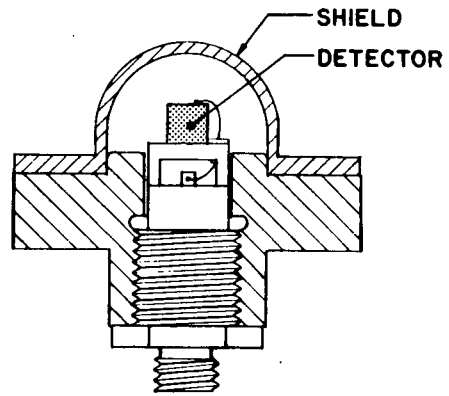
(c) Electron Sensor ($100 < E_e < 750 \text{ keV}$)

The electron sensor (4) consists of a single detector wafer inside a shielding mount with an aperture that defines the sensor look-angle. A thin light-shield prevents extraneous signals should the detector look toward the sun. A cross section of this detector is given in Figure 2-VI-7(c). The thermistor located in the base of sensor 4 is used to determine the temperature of the assembly. The difference in temperature between detectors should be small. The operation for

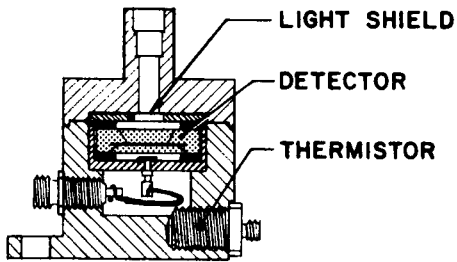
*RCA Corporation, Astro-Electronics Division, TIROS M/ITOS Spacecraft Logic Diagrams, AED M-2175, Contract NAS 5-10306, Princeton, N. J., June 15, 1969.



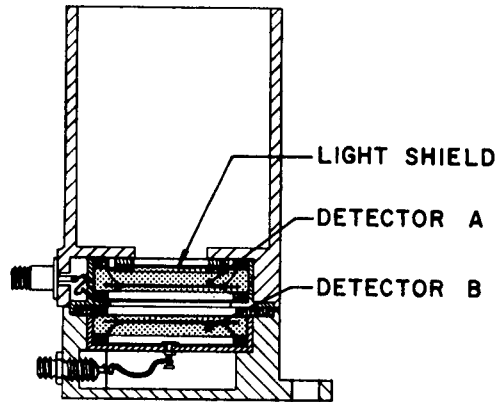
(a) Proton Sensors 1 and 2



(b) Proton Sensor 3



(c) Electron Sensor 4



(d) Dual Channel Proton Sensors 5 and 6

Figure 2-VI-7. SPM Sensor Units

the electron detector is different from the other sensors in that the last amplifier output has two pulse-height discriminators, designated upper-level and lower-level, which feed an anticoincidence circuit. The function of the anticoincidence is to give a pulse out if only the lower level discriminator is triggered and not if both the upper and lower-level discriminators fire. The anticoincidence circuit output and upper-level discriminator output are subcommutated into one data accumulator which is read out four times each frame.

(d) *Dual Channel Proton Sensors (5 and 6)*

Sensors 5 and 6 are identical except for orientation on the sensor bracket. This unit, shown in Figure 2-VI-7(d), is a telescopic arrangement of two surface barrier devices, a 100-micron thick detector (A) backed up by a 200-micron thick detector (B). Discriminator levels and the logic applied are given in Table 2-VI-2 yielding the energy ranges shown. These sensors will provide data on lower energy proton fluxes beginning at 270 keV and extending up to 60 MeV as well as α -particles from 12.5 to 32 MeV.

The data from these detectors is subcommutated into two amplifier channels, one for both front-detector elements and the other for both rear detectors. The outputs from the five discriminator units for these chains are fed to the low energy channel pulse handling logic. The front and rear detector arrangement is used to determine direction and energy level of incident particles. For example, a particle detected in both the front and rear detector by coincidence methods is defined as coming through the opening aperture with an energy level within a given range, whereas a particle detected only in the rear detector probably came in through the shielding due to the geometric properties of the sensor and the detectors and is used in determining background rates. The response from the front detector follows the relationship shown in Figure 2-VI-3.

(2) *DATA PROCESSING ELECTRONICS*

(a) *Amplifier-Discriminator Chains*

The charge output from each solid-state detector is transferred to a voltage output by the charge-sensitive preamplifier, amplified twice, and then detected in a discriminator unit. The preamplifier (P) design in SPM yields approximately 4.5 millivolts per MeV incident particle energy deposited. Each amplifier (A) stage has a voltage gain of about 30 or a total output at the discriminator of approximately 0.7 volt per MeV. RC double differentiation is used between amplifier stages to allow for fast counting rates with minimum offset. The pulse output from the last amplifier is detected by a discriminator (which is adjustable to allow trim of the entire system) that produces a standard pulse for counting.

(b) Pulse Handling Logic

The pulse handling logic is used to separate the signals from sensors 5 and 6 into the energy ranges given in Table 2-VI-2 by sampling the discriminator outputs for pulse height information and by performing coincidence measurements between them. The discriminators that feed the pulse handling logic cause flip-flops FF-1 through FF-5 to be set according to the input pulse height. An output from the coincidence gate sets FF-6. These flip-flops serve as 1-bit buffer registers.

In operation, a set input at FF-4 and/or FF-5 initiates a chain of events which causes the information in FF-2 to FF-5 to be transferred (via G2 to G5) to the channel selector inputs. All flip-flops are reset 0.15 microsecond after the output pulse, and the equipment awaits the next particle.

In the event that both the front and rear wafers detect a signal, within 100 nanoseconds of each other, the coincidence gate is triggered to set FF-6. When this occurs, gates G1 and G6 are enabled to transfer the contents of FF-1 and FF-6 into the channel selector. Again, all flip-flops are reset 0.15 microsecond later.

(c) Data Commutator and Accumulator Control

This unit determines the input data source and the readout sequence for the seven data accumulators. Sensors 1, 2, and 3 are read out once per frame. The two data words from sensor 4 and the six output lines from the pulse handling logic are each read out twice per frame. The data from the pulse handling logic is from detector 5 for the first set of readings each frame and from detector 5 for the second set.

The data commutator and accumulator control is driven by the 15-Hz clock via a countdown chain made up of a divide-by-9 shift register and a divide-by-20 counter. The divide-by-9 shift register is wired to generate a Barker code that is shifted into the data stream once each 20 words and used as the synchronization pattern. The output from the divide-by-9 register also triggers the processor control into operation once each output word. The divide-by-20 counter provides the address for controlling the frame of 20 words.

(d) Data Accumulator

Data accumulator 1 is typical of the other six accumulators. The 20-bit scaler is free to count input pulses continuously. When the register is to be read out, the input data is first inhibited in the accumulator control, a transfer

pulse is applied to the output gates B1 to B20, and the register is then reset to zero. All B gate outputs from the 7 accumulators are wired "OR" into the 20 parallel output lines.

(e) *Floating Point Compressor*

The floating point compressor is made up of the 20-bit shift register and the divide-by-16 counter. The 20-bit register is transfer loaded from one of the seven 20-bit accumulators for each readout. After transfer, the data in the register is shifted until a "1" is in the most significant digit or until 15 shifts have occurred. As explained in Paragraph 2.VI.B.1.c, the number of shifts denotes the value of the characteristic. The 5 most significant bits in the 20-bit shift register are the mantissa of the count. (See Figure 2-VI-8.)

(f) *Processor Control*

The processor control generates the shift pulse train and the input inhibit, data transfer, and accumulator reset pulses for each word. A 1-MHz generator is used to produce the processor control pulse rate. This control unit is triggered into operation by the word clock from the divide-by-9 register and triggered "off" by the data in the word being processed.

(g) *Output Circuits*

The 4 characteristic and 5 mantissa bits are parallel-transferred into the 10-bit shift register. This register serves as a parallel-to-serial converter and allows one word to be clocked out while another is being processed. The output is provided in both a NRZ and RB format. A data encoder is used to generate the return-to-bias (RB) output to be used for real-time transmission.

As shown in Figure 2-VI-8, during the first word interval of each frame, the Barker word is transmitted in place of data. For the SPM, the Barker code is 111000101.

(h) *Power and Telemetry*

The SPM electronics unit contains an SPM ON/OFF latching relay (operated from the CDU) which controls SPM power application in accordance with ground commands. The -24.5-volt input is converted into eight other DC voltages (varying between -6 and +300 volts) by an internal DC-to-DC converter. Fusing for the SPM is provided in the power supply electronics.

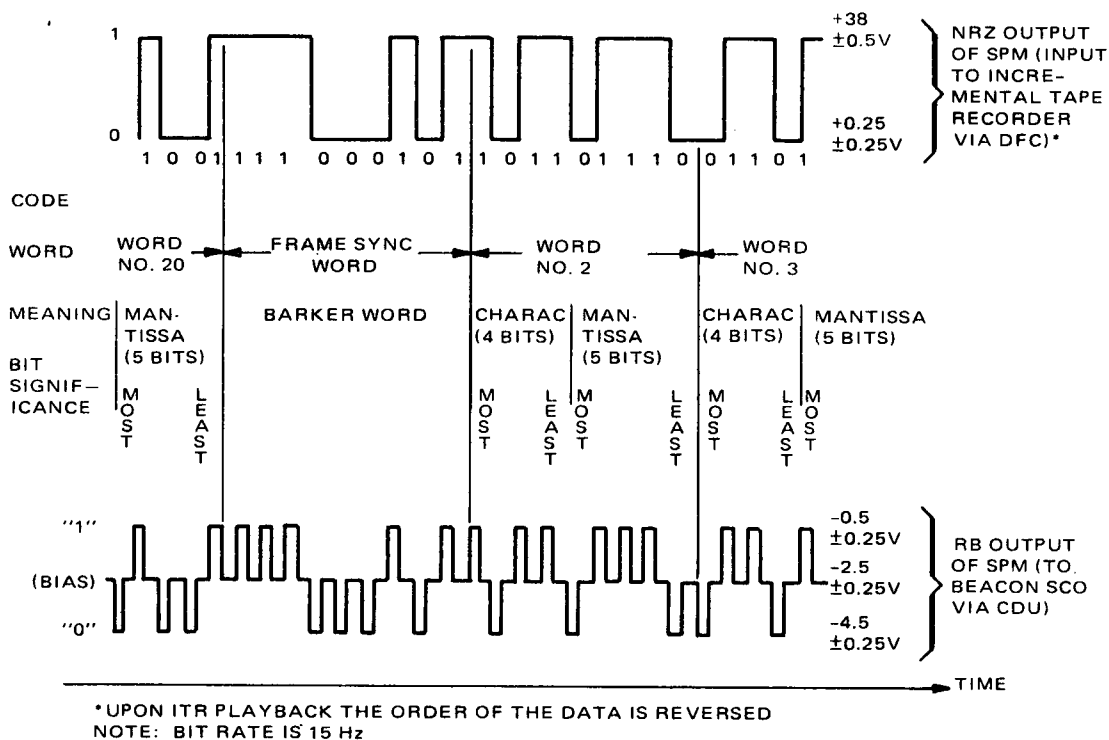


Figure 2-VI-8. SPM Data Format

Two telemetry points are available. One is derived from the converter and its presence denotes that the relay is in the "SPM ON" state and the DC-to-DC converter is producing an output. Absence of telemetry indicates that the relay is in the "SPM OFF" state, that the fuse has blown, or that the converter is inoperative. A thermistor is attached to the sensor bracket to provide sensor bracket temperature telemetry.

2. Flat Plate Radiometer

a. GENERAL

The flat plate radiometer (FPR) measures the amount of heat being radiated by the earth and is employed to continue the program of mensuration of the earth's heat balance initiated on the TOS AVCS spacecraft program. By knowing the solar input (believed to be a constant) to the earth, the amount of heat absorbed by the earth may be determined. One of the FPR program objectives is to determine the long term heat changes, thus determining whether the earth is getting warmer or cooler.

The FPR is being designed and built for ESSA by the University of Wisconsin, and the device is being supplied GFE to RCA for integration into the spacecraft.

The FPR is housed in a single enclosure of honeycomb material which includes the four sensors, electronics, and means for calibration of one pair of sensors (see Figure 2-VI-9). The unit is mounted on the earth-facing surface of the satellite and is partially covered with a thermal blanket.

The FPR consists of two portions, the electronics package (see (a) of Figure 2-VI-10) and the sensor head. In orbit, the head shown at (b) is used. The head consists of the four radiometers, a portion of the radiative equilibrium (RE) cooling mirror, the motor which drives the thermal feedback (TF) sensors, the TF hemispheres, and the sensors to telemeter the mount and hemisphere temperatures. The dummy head, shown at (c), is used for test purposes. This head consists of fixed resistors that exercise the electronics and provide fixed format words from the FPR.

(1) SENSORS

The RE sensors are mounted to a honeycomb plate which, in turn, is thermally isolated from the rest of the FPR structure. The sensors (one black

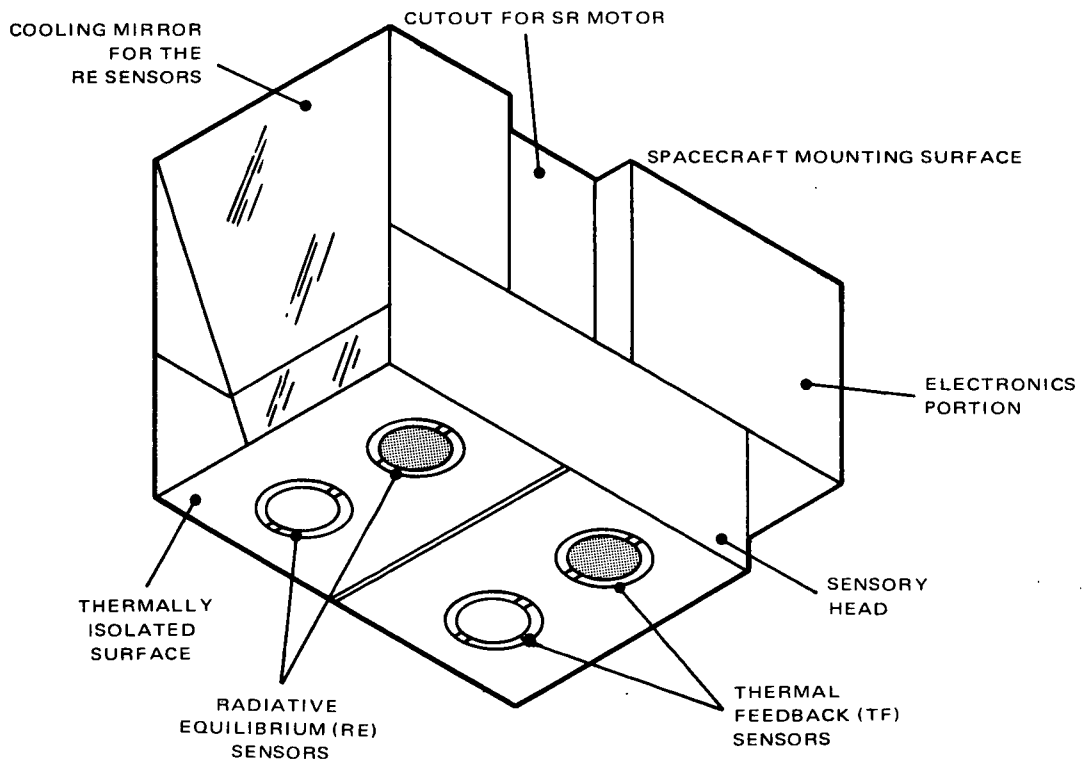


Figure 2-VI-9. Flat Plate Radiometer (Shown Without Thermal Blanket)

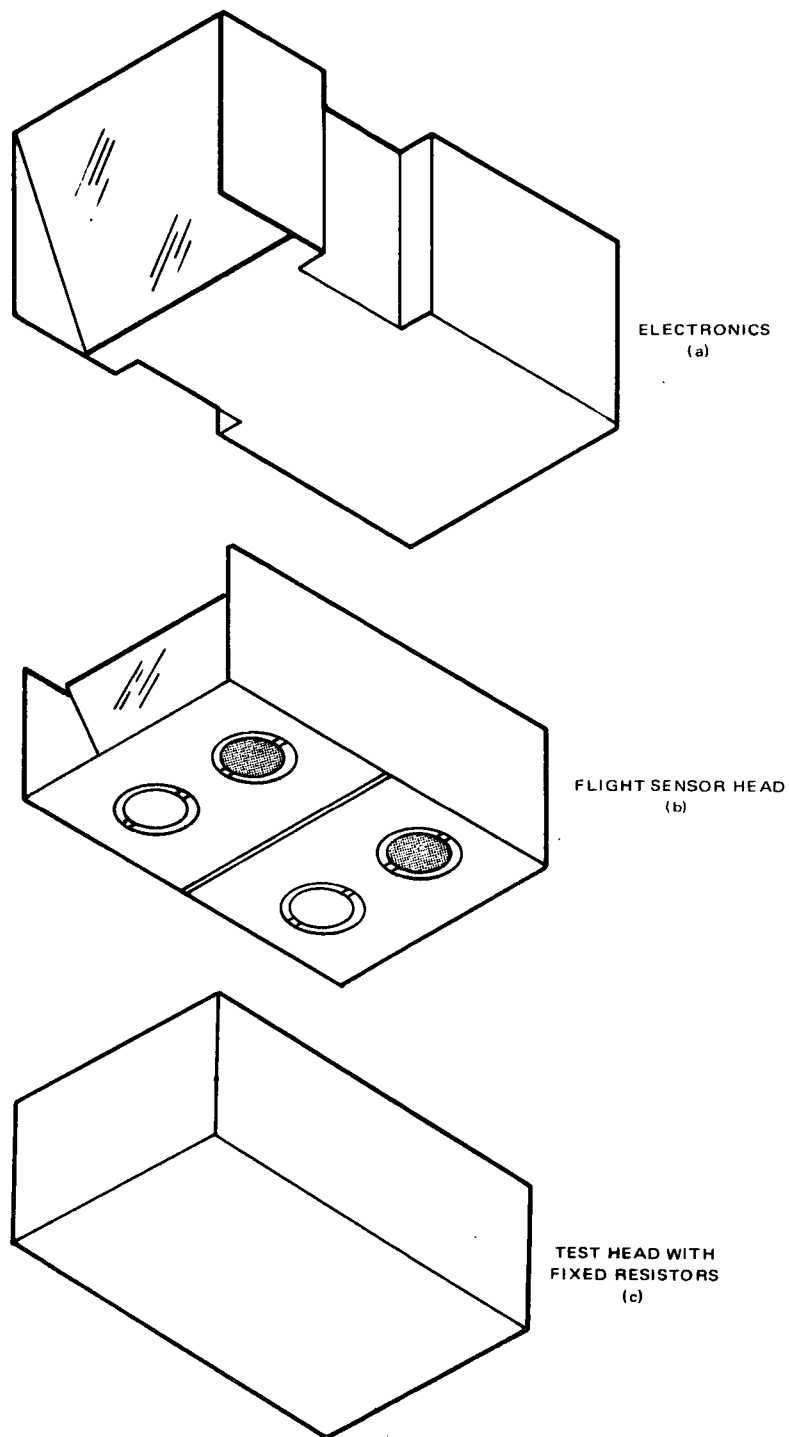


Figure 2-VI-10. Flat Plate Radiometer, FPR, Exploded View (Showing Flight and Test Heads)

and one white) are the same as those used on the TOS AVCS satellites; each one consists of a thermistor that is carefully isolated from its mount (see Figure 2-VI-11). These detectors are cooled (with the use of a mirror) by radiation from the rear (see Figure 2-VI-12). In normal operation the sun does not fall into the field of view of the mirror.

The second set of sensors is a pair of TF black and white detectors, mounted on a common shaft which is coupled to a bidirectional motor. The black detector is sensitive over the range of approximately 0.3 to 30 microns, and the white detector is limited to about 7 to 30 microns. These are the same ranges as the corresponding RE sensors. Figure 2-VI-13 shows the sources of energy in these spectral ranges. Each TF sensor has its own thermal hemisphere, the temperature of which is telemetered.

The TF sensors are a new design. The advantage of the TF sensor is that the incident power on the sensor thermistor provides a simple readout that is linear and more readily interpreted. The output of the RE sensors is proportional to the fourth power of the absolute temperature, and interpretation involves several assumptions which have been difficult to justify.

(2) CALIBRATION IN ORBIT

Since surface degradation of the white sensor can cause a shift in the response spectrum and consequently in the radiative power input, a means of recalibration in orbit is required. This can be accomplished by the following methods:

- Isothermal hemispheres are mounted within the radiometer housing. The radiometers are rotated 180 degrees to view the isothermal hemispheres, as shown in Figure 2-VI-14. Heating surges of known amounts are applied to the TF sensors during alternate frames while the sensors are viewing the hemispheres, and hemisphere temperatures are telemetered along with the sensor data.
- Readings from the RE and TF sensors will be compared and used for data correlation.
- One means of recalibration is inherently available. During orbital sunrise and sunset, the sun illuminates the front of the sensors (see Figure 2-VI-15). The angle of incidence is low (to 34 degrees independent of the orbit plane alignment with respect to the sun) but the thermal input is high. By knowing the thermal input from sun and earth, the sensor may be coarsely calibrated. Note, therefore, that during the orbital sunrise and sunset, the FPR data is contaminated by the sun.

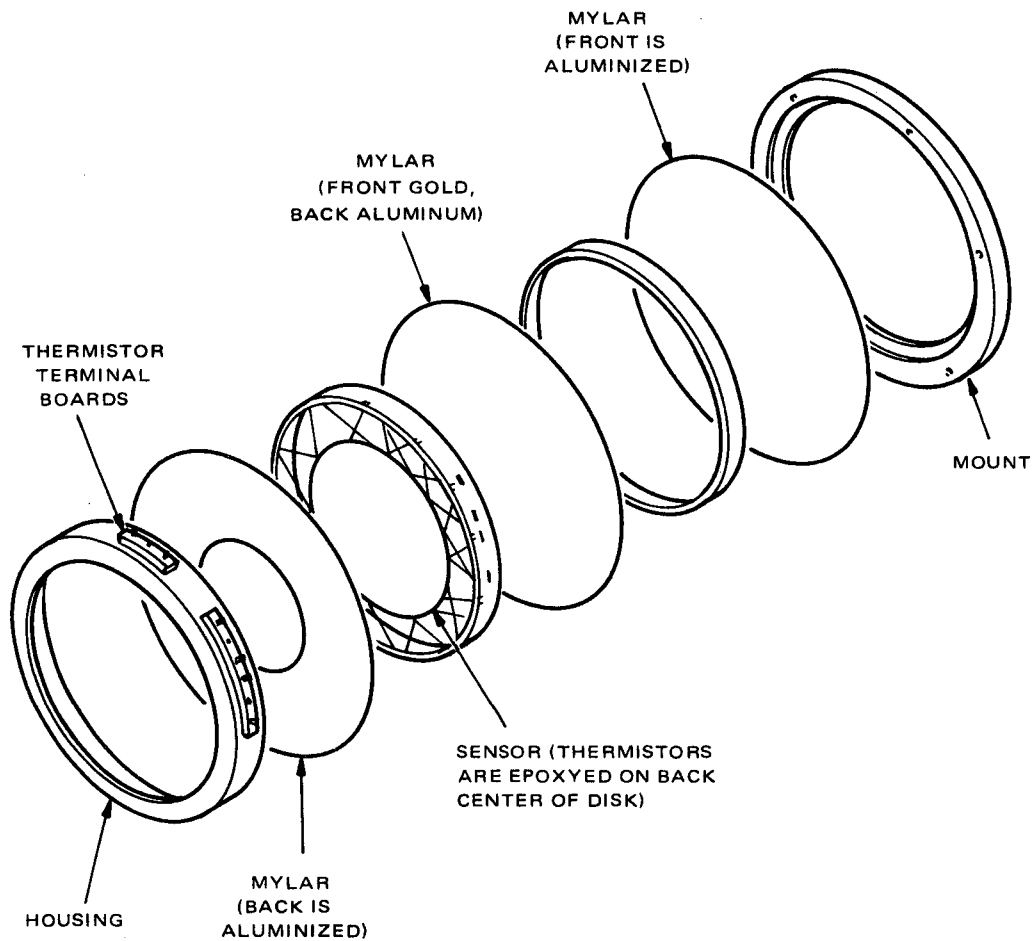


Figure 2-VI-11. Flat Plate Radiometer Sensor Assembly, Exploded View

(3) *TELEMETRY DATA*

The data from the RE sensors is telemetered as 10-bit words. The TF sensors, mounts, and several other temperatures are telemetered as 7-bit words.

Certain "flag" indicators are also included in the words to denote the calibrate mode. The electronics portion takes these data inputs and sequentially forms them into a standardized word which consists of 7 data bits and a marker bit.

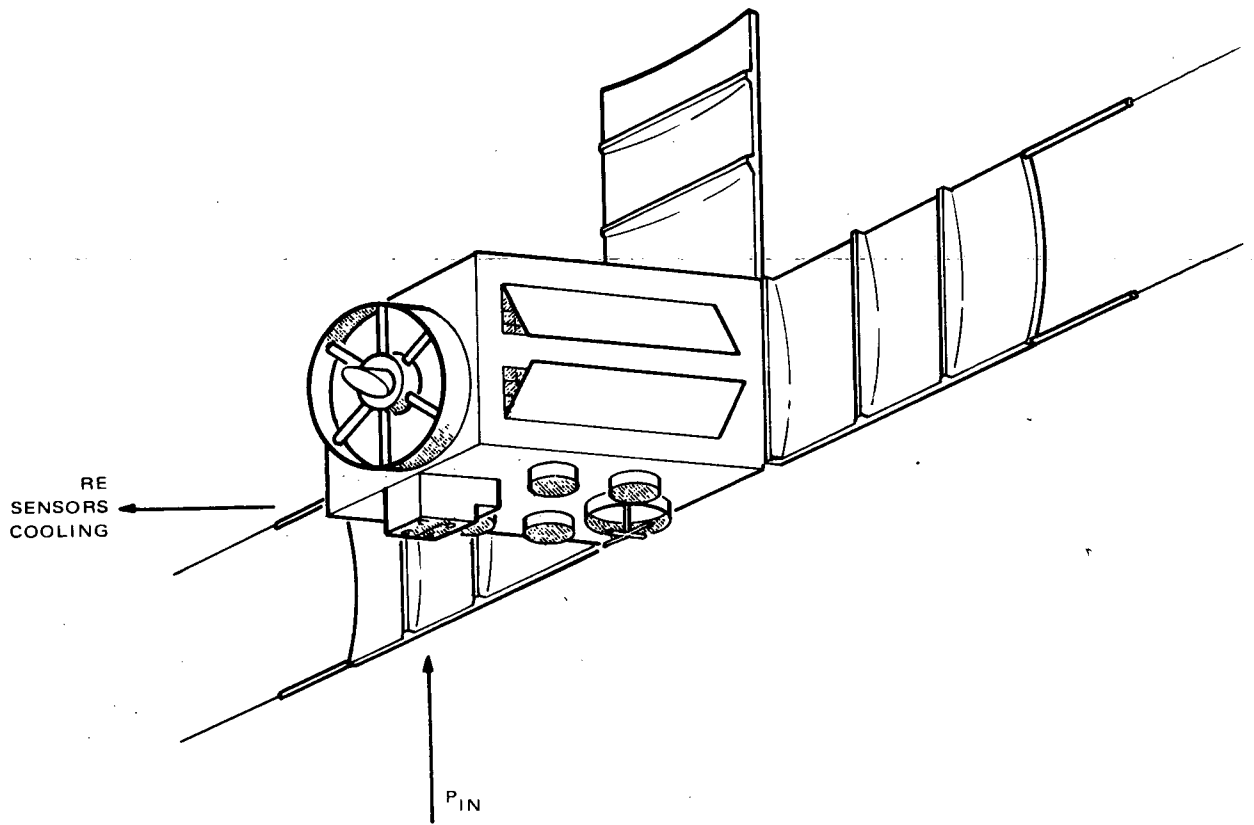


Figure 2-VI-12. FPR Orientation

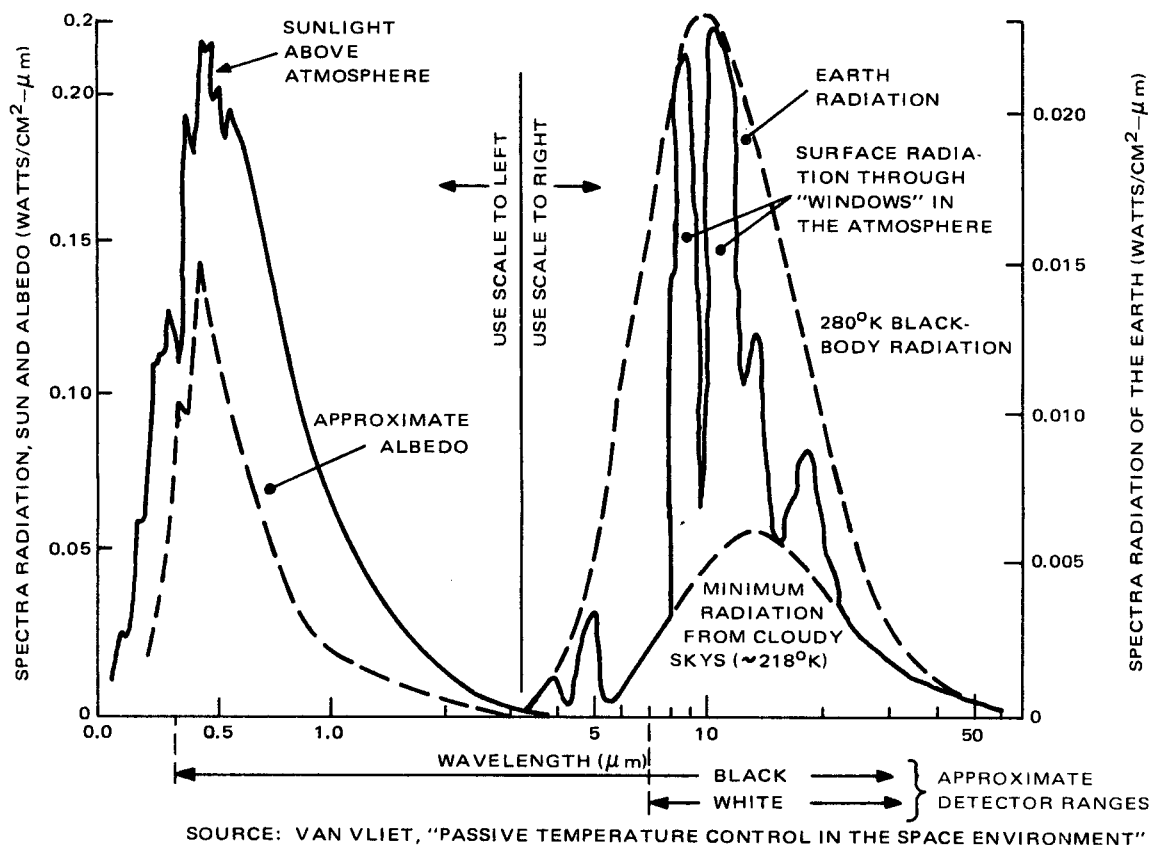


Figure 2-VI-13. Spectral Regions Used by the FPR

These words are inserted into the DFC bit stream at the proper times and are recorded on the incremental tape recorder (ITR) on track 3. There is no real-time readout directly from the FPR (there is a path for real-time data via the DFC and a telemetry commutator, but it is intended primarily as a diagnostic tool rather than an operational mode).

The sample rate of the FPR is one frame per 32 seconds. The track 3 ITR data also includes frame sync and time code information.

Table 2-VI-3 lists the FPR word content. Each word consists of 7 data bits and a marker bit. In the case of FPR words 1 and 3, the 3 most significant bits of the 10-bit data words are placed in the next word. The 4 remaining bits are reserved for "flags" or other data.

b. FUNCTIONAL OPERATION

The circuits contained in the electronics package (see RCA logic diagram 1976101) provide a resistance-to-frequency conversion for the RE sensors and

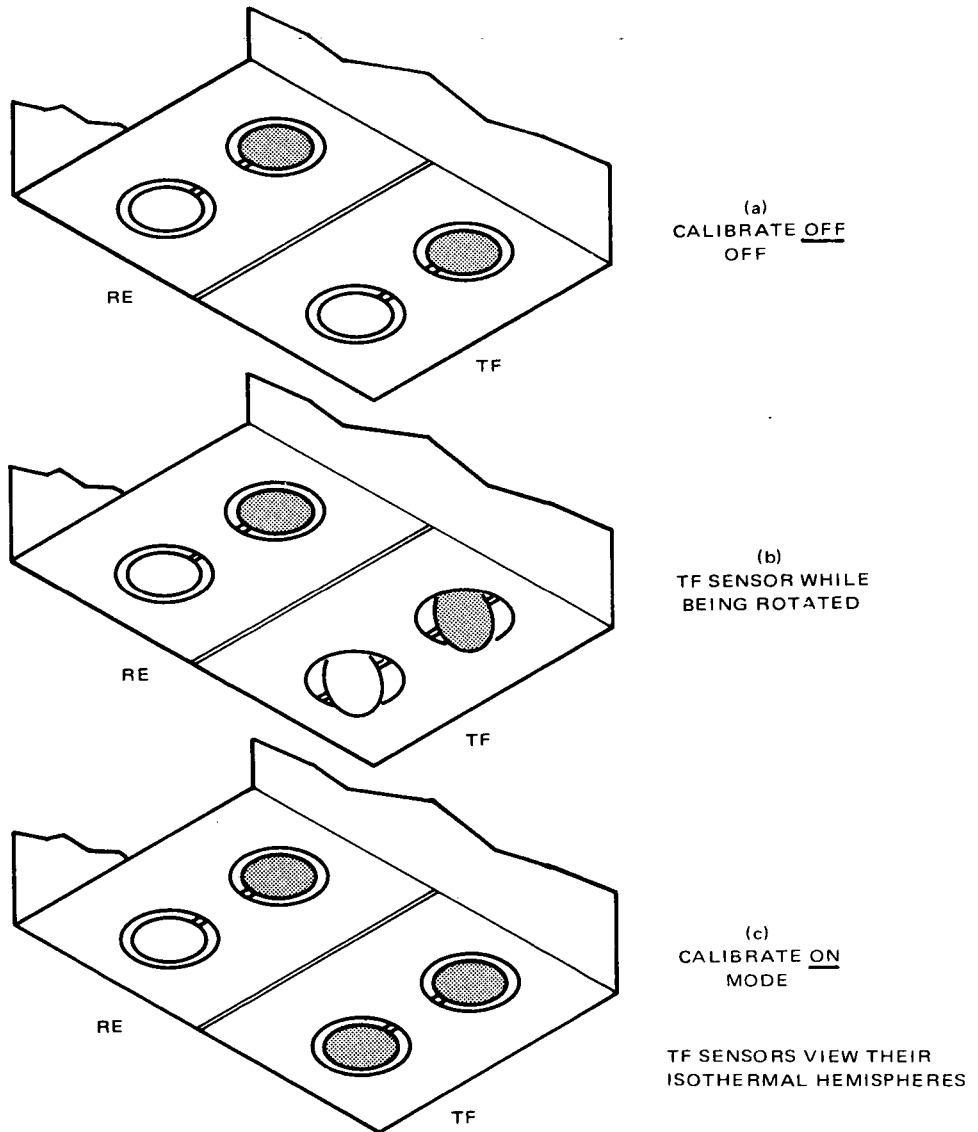


Figure 2-VI-14. FPR Calibrator (TF)

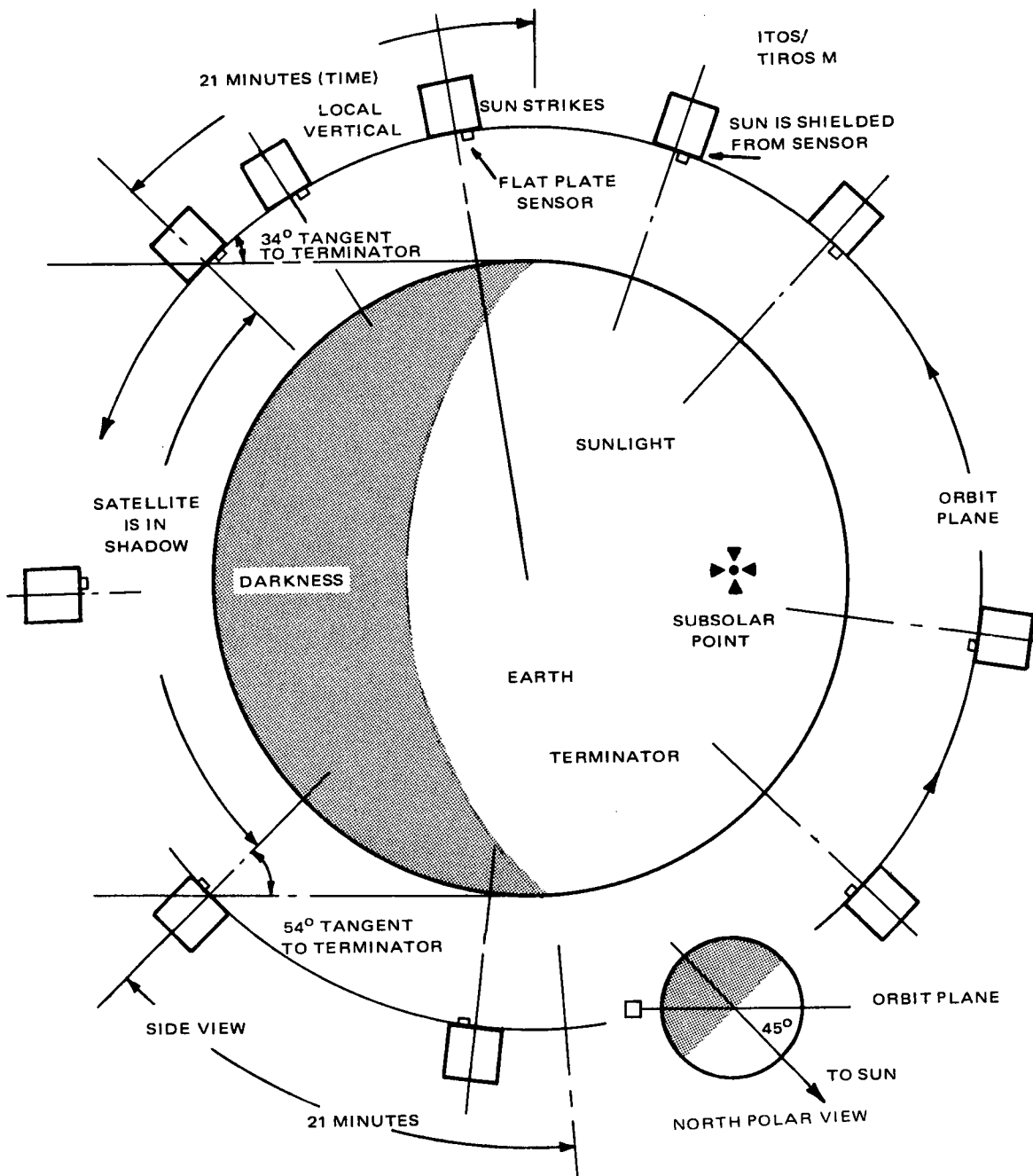


Figure 2-VI-15. Flat Plate Radiometer, Solar Illumination (3 PM Orbit)

TABLE 2-VI-3. FPR WORD CONTENT

FPR Channel No.	Secondary Sensor Subsystem Channel No.	Function	Bit Weight									
			Bit Position in Word									
			1	2	3	4	5	6	7	8		
(As recorded in satellite)												
1	7	RE White Data	M	1	2	4	8	16	32	64		
2	8	RE White Data and Flag	M	128	256	512	*	*	*	F		
3	9	RE Black Data	M	1	2	4	8	16	32	64		
4	10	RE Black Data and Flag	M	128	256	512	*	*	*	F		
5	11	RE Calibrate†	M	1	2	4	8	16	32	64		
6	12	RE Mount Temp White	M	1	2	4	8	16	32	64		
7	13	RE Mount Temp Black	M	1	2	4	8	16	32	64		
8	14	TF White Data	M	1	2	4	8	16	32	64		
9	15	TF Black Data	M	1	2	4	8	16	32	64		
10	16	TF Mount Temp	M	1	2	4	8	16	32	64		
11	17	TF White Cal Source	M	1	2	4	8	16	32	64		
12	18	TF Black Cal Source	M	1	2	4	8	16	32	64		
13	19	TF White Surface Temp	M	1	2	4	8	16	32	64		
14	20	TF Black Surface Temp	M	1	2	4	8	16	32	64		
15	21	Electronics Temp	M	1	2	4	8	16	32	64		

NOTES: M Denotes a marker bit (always a logic "0" level).
 F Denotes a flag hit to designate the state of the TF calibration rotator (a "0" denotes the sensor is in the earth-view or data-state; a "1" denotes it is in the internal hemisphere or calibrate state).
 * Denotes a not used bit (should always be at a "0").
 † Only the seven LSB bits are telemetered; 128, 256, 512 are not telemetered.

thermistors, count the energy pulses required to maintain the TF sensors at a constant temperature (heat loss to frequency conversion), and provide control of the TF calibrate mechanical drive, power switching, DC-to-DC voltage conversion, and data word commutation-formatting.

(1) *RADIATIVE EQUILIBRIUM SENSOR AND THERMISTOR DATA HANDLING*

The RE sensors are identical to those used in the ESSA satellite series. The associated data handling is also similar. The variable resistance of the sensors is used to control the frequency of a blocking oscillator. The resulting frequency is counted in a 10-stage counter (C1 through C10). The RE sensor data is read out as a 10-bit word. (Due to the FPR-DFC word structure, two words are actually required, each consisting of 7 bits plus a marker bit.)

The thermistors are handled in exactly the same manner. The RE sensors and thermistors are both applied to the blocking oscillator by a commutator which permits time-sharing. This commutator is controlled by the word shift register (WSR1 through WSR15). The blocking oscillator output is applied to a 9041 NAND gate. This gate, at the input to the 10-stage counter, is enabled at all times, except when flip-flops WSR8 and WSR9 are in the Q8 and Q9 stage.

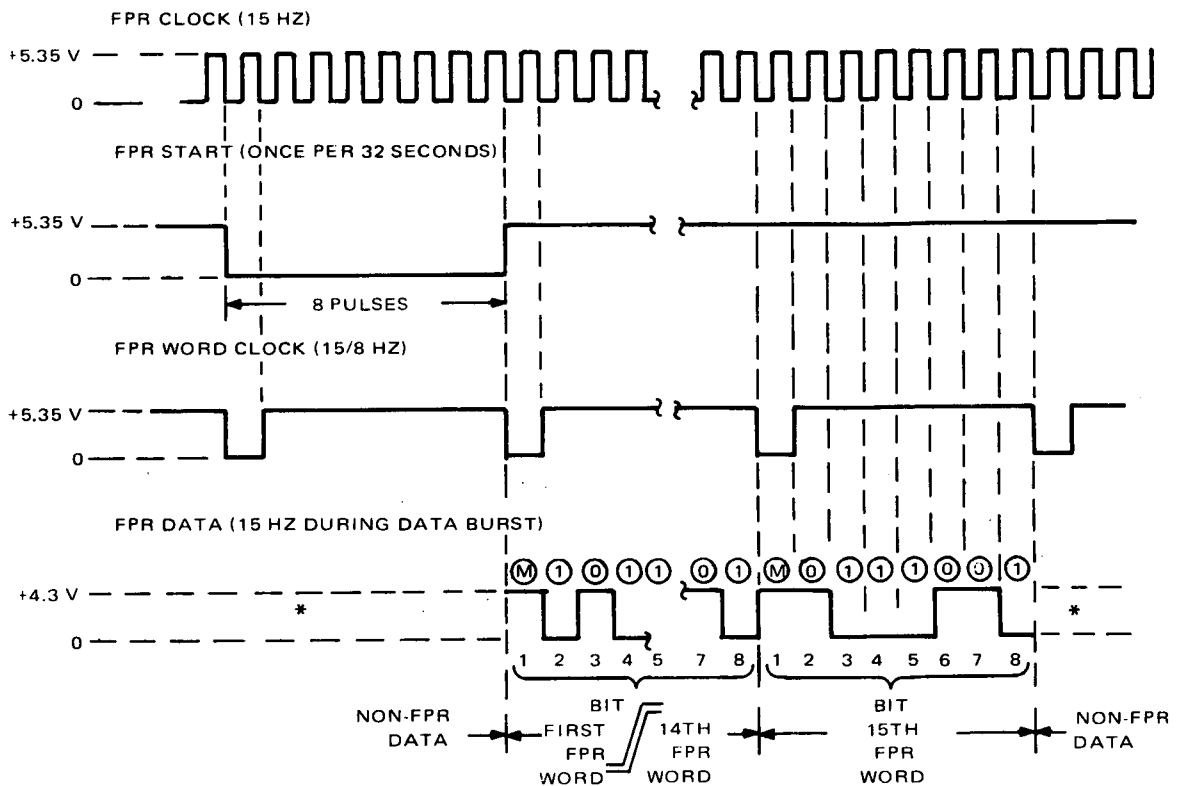
(2) *THERMAL FEEDBACK DATA HANDLING*

When the TF sensors are viewing the earth, the TF electronics attempts to maintain the sensors at a constant temperature by supplying the required number of constant energy pulses to a heater which is part of the sensor; these pulses are counted in the 10-stage counter. One 9041 NAND gate is used for each of the TF sensors. The TF black pulses are counted when WSR8 is in the Q8 state and the TF white pulses when WSR9 is in the Q9 state.

(3) *OUTPUT SHIFT REGISTER*

The format of the FPR output (Table 2-VI-1 and Figure 2-VI-16) consists of a burst of 15 eight-bit words. Each 8-bit word is composed of a single word marker pulse followed (in real time) by 7 data bits.

The actual data consists of a mixture of 1-bit (marker), 7-bit (TP sensor temperature and data), and 10-bit (RE mount temperature and data) words. These varying requirements are met by the parallel transfer gates and between the 10-stage counter (C1 through C10) and the 7-stage output shift register (OSR).



NOTES:

- * DURING THIS PERIOD EITHER LEVEL MAY BE USED
- (M) MARKER BIT (ALWAYS AT +4.3 V)
- (1) LOGIC LEVEL "1" ($\pm 0V$)
- (0) LOGIC LEVEL "0" (+4.3 V)
- BIT 2 IS THE LEAST SIGNIFICANT BIT (LSB)
- BIT 8 IS THE MOST SIGNIFICANT BIT (MSB)
- THE DATA SHOWN IS FOR THE OUTPUT OF THE FPR,
UPON PLAYBACK THE ORDER IS REVERSED.

Figure 2-VI-16. FPR Timing Diagram

(a) *Seven-Bit Data*

For the TF sensor data, TF calibration hemisphere temperatures, TF sensor temperatures, and the electronics compartment temperature, the operation is straight-forward. Counters C1 through C7 are loaded with data, with the most significant bit (MSB) being in C7 and the least significant bit (LSB) in C1 (counters C8 through C10 are not in use). After the individual count has been accumulated, the contents of C1 through C7 are parallel-transferred to OSR7 through OSR1, respectively. The data in OSR1 through OSR7 is shifted out serially at a 15-Hz rate with the first bit being the LSB.

Eight shifts are made (the final shift is always a "0" and is the word marker pulse).

(b) *Ten-Bit Data*

For the RE sensors and the associated calibration thermocouple, 10-bit accuracy is required. This is achieved by dividing each 10-bit word into 2 segments; the first segment contains the 7 least significant bits, and the second segment contains the 3 most significant bits. In the case of the RE calibrate function, only the 7 least significant bits are telemetered. The states of the 3 most significant bits are inferred from the other data.

Counter stages C1 through C10 may be loaded. In this condition, the least significant bit (LSB) is in C1. The contents of C1 through C7 are parallel-transferred into OSR6 through OSR1, respectively. After the 6 data bits and the word marker have been shifted out of the OSR, it is ready to receive the remaining 3 bits of the 10-bit word. The contents of C8 through C10 are parallel-transferred into OSR7 through OSR5. "Flags" denoting the state of the TF heater calibration power are inserted into OSR1. The 10-stage counter is reset and refilled with new data in preparation for the next word.

(4) *TF CALIBRATION*

Calibration is performed with and without heat being supplied to the TF sensor. The calibration sequence is initiated by the Calibrate FPR command from the CDA station, and the following sequence of events occurs:

- a. The sensor revolves 180 degrees to view the hemisphere, the temperature of which is telemetered.
- b. During the first frame period (32 seconds) a known amount of heat is supplied to the TF sensor by means of direct current

through a resistance heater. A calibration reading is received by counting the number of heat-producing pulses required to bring the sensor to the proper temperature.

- c. On the next frame, the DC heater power is removed and another calibration reading is received. Since the DC component is removed, additional pulses will be required.
- d. The heater cycling continues (32 seconds on, 32 seconds off) until an FPR ON command is received from the CDA station, at which point the sensor is rotated back to view earth, and all DC heater power is removed. The thermal time constant of the TF sensors is fast enough to permit this type of cycling without appreciable residual heat being left during the heater-off reading.

(5) OTHER FUNCTIONS

The FPR has its own DC-to-DC converter. All power (-24.5 and unregulated voltage) is switched by relays (within the FPR) controlled from the CDU.

If, while in the FPR ON state, a "calibrate FPR" signal is received, a second relay is energized (also from the CDU) to permit unregulated power to be applied to the calibrate motor. End-of-travel switches are used to turn off the motor. If the switches fail to turn the motor off, a mechanical end-of-travel stop or a built-in timer will turn off motor power within 30 seconds regardless of the angle (if any) to which the motor has turned the sensors.

FPR status telemetry indicates the presence (or absence) of -24.5 volts on the output of the power relay in the FPR.

For a flight, a two-wire jumper is required on plug P2 between pins 14 and 15 and 16 and 17.

C. DATA FORMAT CONVERTER

1. General Description

The data format converter (DFC) receives data from the flat plate radio-meter (FPR), solar proton monitor (SPM), housekeeping telemetry, and time code for storage on the incremental tape recorder (ITR).

The DFC performs the following functions:

- Accepts digital time code information from the time base unit (TBU),
- Accepts digital solar proton measurement data from the SPM,
- Accepts digital radiometer data from the FPR,
- Controls the operation of the ITR,
- During ITR playback, provides a frequency multiplexed output of three VCO's, each FM modulated with the ITR data,
- Commutates and digitizes spacecraft telemetry data,
- Provides a return-to-bias output to the housekeeping commutator which is a replica of the time code, FPR, and telemetry data, and
- Provides indication of its status to the housekeeping telemetry commutator.

The DFC is housed in the standard electronics package used for the command boxes, with the exception that the three VCO's are mounted so that they protrude from the top of the box to provide access for adjustments.

2. Design History

The DFC is a new design developed especially for the ITOS program. The new design areas are, specifically, the solid-state commutator, the analog-to-digital converter and associated circuits, and the control logic for operation of the ITR. The DFC has been optimized to make full use of the storage capacity of the ITR, taking into account its speed limitations and the minimum sampling time of the FPR and SPM. The long time allowable between samples of FPR data makes it possible for additional data to be recorded on the ITR, and with the addition of the commutator and analog-to-digital converter, spacecraft telemetry data can be recorded in the compatible digital format.

The commutator design was chosen because it is completely solid-state, reliable, and radiation resistant; it has low offset and gain error, is very stable in the presence of temperature variations, and all its building blocks are compatible with the manufacturing and assembly techniques used in the ITOS electronics boxes. The successive approximation technique used in the analog-to-digital converter was chosen because it is optimum for the type of random varying data normally generated by a commutator.

3. Functional Description

a. OPERATING MODES

The DFC has four modes of operation which control data handling and the functions performed by the ITR. The four modes are as follows:

- Record mode,
- Standby mode,
- Playback mode, and
- Off mode.

(1) RECORD MODE

The record mode, the normal mode of operation, is entered upon receipt of the "DFC ON" signal as long as the "end-of-tape record" signal is not present. It is automatically returned to at "end-of-tape playback".

In this mode, the DFC processes all data for the three ITR tracks and provides stepping pulses to the ITR. The DFC will accept "DFC OFF", "DFC ON", and "playback ITR" signals when in this mode.

(2) STANDBY MODE

The standby mode is entered upon receipt of the "end-of-tape record" level from the ITR. In this mode, all data processing continues as in the record mode, but the ITR stepper pulses are inhibited. The DFC will come out of this mode only upon receipt of the "playback ITR" signal, even though it will accept "DFC ON" and "DFC OFF" signals.

(3) PLAYBACK MODE

The playback mode is entered upon receipt of the "playback ITR" signal while the "S-band switched ground" signal is present and the "end-of-tape playback" signal is not present. When this mode is entered, the following events take place:

- Power is applied to the VCO's and mixer amplifier to receive ITR playback data,

- A "playback enable" signal is sent to the ITR to turn on the playback motor, and
- A playback signal is sent to the ITR 1.067 seconds after "playback enable", to start the playback of data.

The playback mode is terminated and the record mode reentered when any of the following occurs:

- "End-of-tape playback" signal,
- "DFC ON" signal, or
- Removal of "S-band switched ground" signal.

(4) *OFF MODE*

This mode is entered upon receipt of the "DFC OFF" signal. Power is removed from the DFC and ITR in this mode. When in this mode, the DFC will accept only a "DFC ON" signal.

b. SIGNAL INTERFACES

(1) *LOGIC INTERFACES*

The DFC receives clocking signals for internal operation and ITR timing from the TBU; in addition, the DFC receives time code data from the TBU and a switched ground from the section of the TBU that is turned off. The DFC receives NRZ logic data from the SPM and FPR and provides NRZ data to the ITR for recording. See RCA logic diagram 1976088 (sheet 4).

(a) *TBU Interfaces*

The inputs from the TBU can come from either of two redundant units, but only those from the selected unit are enabled, since the standby unit provides a ground level used to inhibit its own inputs to prevent noise coupling into the DFC.

The TBU inputs are

- 9.6 kHz used to synchronize all switching in the DFC;
- 15 Hz used as the basic data rate from the DFC to the ITR;
- 100 kHz used as the clock for the analog-to-digital converter;

- Time code clock signal used to shift the time code NRZ data into the DFC;
- Time code NRZ data, to be inserted with each frame of data on ITR track 3; and
- Time code rest, to indicate the time at which a complete burst of time code NRZ data occurs (to facilitate correct time code acquisition).

(b) *Solar Proton Monitor Interface*

The SPM NRZ data is present at flip-flop 1MF, synchronized by timing gate CG11, and stored on track 1 of the ITR. No control or modification of this data is performed by the DFC.

(c) *Flat Plate Radiometer Interfaces*

The DFC provides the following three signals to the FPR:

- "FPR clock", a 15-Hz signal used for data shifting;
- "FPR word clock", a 1/15th second pulse occurring every 8/15 second; and
- "FPR start", an 8/15th second pulse occurring during word 6 of the ITR track 3 data frame. This pulse signals the FPR to start loading data into the DFC.

The FPR provides the DFC with the "FPR data in" signal, a group of fifteen 7-bit words of NRZ data multiplexed by the DFC with time code and telemetry information prior to recording on ITR track 3.

(d) *ITR Interfaces*

The DFC provides the following signals to the ITR:

- "ITR track 1 data", the SPM NRZ signal synchronized by the DFC to be coherent with the data on tracks 2 and 3;
- "ITR track 2 data", a 7.5-Hz square wave derived from the CG11 gate and used as a clock in ITR playback to locate data bits on tracks 1 and 3; and

- "ITR track 3 data", the time-multiplexed composite of the time code, FPR, and spacecraft telemetry inputs. Each frame in the data train is made up of 60 words of 7 bits each preceded by a word marker, which is always at logical "0" (+5-volt level).

The frame breakdown is as follows:

Words 1 and 2, frame marker. Each word contains 8 logical "1" bits (ground level). The frame marker is 16 logical "1's" with no word marker.

Words 3 to 6, time code information. Since the time code is 24 bits, 4 words of the frame are needed, with the last 4 bits of the sixth word not being used. The processing of the time code information is discussed subsequently in Paragraph 2.VI.C.3.c.

Words 7 to 21, FPR data. The "FPR data in" input is enabled by setting the XG19 input to gate MG2 high during this period. The data is thus allowed to reach the ITR track 3 input. The word marker is introduced for all the data words in the frame when the BG4 input to gates MG2 and MG3 goes to ground for 1 bit period out of every 8.

Words 22 to 60, spacecraft telemetry. The 39 inputs from various spacecraft sensors are time-multiplexed by the commutator, converted from analog levels to a 7-bit digital code, and shifted out to the ITR by the OVF input of gate MG3. The commutator and the analog-to-digital converter are discussed subsequently in Paragraph 2.VI.C.3.c.

- "Playback enable to ITR", a signal normally at a 5.35-volt level. Upon receipt of a valid "playback ITR" signal, the "playback enable" signal goes to ground. It returns to +5.35 when playback terminates. The ITR uses this signal to turn on the playback motor.
- "Playback command to ITR", a signal normally at +5.35 volts which goes to ground 16/15 seconds after the "playback enable" signal goes to ground. It returns to +5.35 volts when playback terminates. The ITR uses this signal to start the actual playback.
- "ITR clock", a 15-Hz square wave used by the ITR to control the stepper motor during recording. During standby and playback modes, this signal is at a 5.35-volt level.

The ITR provides the DFC with the following signals:

- "ITR tracks 1, 2, 3 playback data", a signal obtained during playback at a nominal rate of 2 kilobits per second. It is used in the DFC to frequency-modulate three VCO's whose outputs are mixed and sent to the S-band transmitter via the multiplexer.
- "End-of-tape record", a ground level generated by the ITR at the end of the tape while recording. The DFC enters the standby mode in response to this signal.
- "End-of-tape playback", a ground level generated by the ITR at the end-of-tape while in playback. This level causes the DFC to leave the playback mode and enter the record mode.

(2) ANALOG SIGNAL INTERFACES

The DFC receives from the spacecraft 36 analog DC levels from various environmental sensors which are commutated, converted to digital form, and stored in the ITR.

The DFC also generates four internal calibration voltages from one stable reference source which can be connected to the commutator and analog-to-digital converter to monitor their accuracy and stability.

(3) SIGNAL INPUTS

The following signal inputs are needed to operate the DFC and ITR (see RCA logic diagram 1976088, sheet 4, A7J1):

- "DFC ON" signal is a -24.5-volt pulse which picks up a latching relay (K1) in the DFC to apply -24.5-volt power to the DC-to-DC converter and other circuitry in the DFC that operates on -24.5 volts. It also applies -24.5-volt power to the ITR for its operation. The DFC supplies the ITR with +5.35-volt power to operate its internal logic. The "DFC ON" pulse is used in the DFC to generate a reset pulse used to reset all the logic in the DFC to the starting state. It is finally delivered to the ITR to be used as a reset pulse in that unit.
- "DFC OFF" signal is a -24.5-volt pulse used to remove power from the DFC and ITR. It resets relay K1.

- "Playback signal from CDU" initiates the playback of ITR when the logical conditions are proper as described under DFC modes of operation.
- "Manual disable" is a signal used for test purposes only. It will stop the word counter at any word in the frame and is used mostly for checking the characteristics of the commutator and the analog-to-digital converter. This function is not available in flight.

c. CIRCUIT DESCRIPTION

This section covers in detail the circuit areas which are significant either because they are new or because they are especially important and necessary for a clear understanding of the operation of the DFC.

(1) COMMUTATOR

The commutator (see RCA logic diagram 1976088, sheet 1) in the DFC is a new design developed specifically for ITOS and used in the DFC and the dual SR processor. It is mounted on one printed circuit board. As used in the DFC, the commutator has 42 inputs, but the board has provisions for expansion to 60 inputs by adding three additional MEM-2009 multiple FET chips.

The inputs are switched by a three-level tree of FET switches with the logic designed to make maximum use of the six FET's per chip in the MEM-2009. The switching of the FET's is controlled by a 60-state Johnson counter arranged in a 6 x 5 x 2 array. The 6-state counter is made up of flip-flops 1F, 2F, and 3F. At G6 time, G16 is enabled to allow the 5-state counter made up of 4F, 5F, and 6F to cycle. At G11 time, after the 5-state counter has received 5 input pulses, G18 is enabled to change flip-flop 7F. The 60 states of this counter are used to control the words in the frame of track 3 data besides controlling the switching of the commutator FET's.

Since the spacecraft telemetry data is multiplexed in the track 3 data starting with word 22, the first three FET chips in the first level are not assembled on the board (Z1, Z2, and Z3 are spares) and only the second half of Z4 is used, so that channels 1, 2, and 3 are not used; the first useful commutator channel is No. 4. If any signals were connected to channels 1, 2, and 3, they could not be processed since power is removed from the commutator during this time. The switched voltages (-24.5, +12, and -12) are turned on during the word marker for words 22 to 60, inclusive; thus the commutator is only on for 66 milliseconds every word.

The FET gates are powered from a -24.5-volt source to allow enough margin for proper operation in the expected space radiation environment. While the normal threshold voltage required to turn on the FET's is about -7 volts, radiation tests showed that this voltage can decrease to about -12 volts, so that a voltage of -24.5 offers a wide margin of safety to the expected radiation damage and input voltage swings.

The operational amplifier Z33 is used to provide a high input impedance to each commutator input signal to minimize errors caused by FET impedance variations and also to provide a low impedance source to drive the analog-to-digital converter.

The one transistor buffer inverter used to convert the logic outputs to the levels required for FET operation is normally on, applying +5 volts to the gates to bias the FET's off, and is turned off at the proper time by the control gate so that its -24.5-volt output biases the FET's on. The body connection of the FET's is tied to +5 volts, thus protecting the devices from damage when voltages up to +5 volts are applied to the commutator inputs. Protection for the operational amplifier is provided by diodes CR1 and CR2, and resistor R23 protects the diodes and the FET's from damage due to overvoltage application at the commutator inputs. Diodes CR3 and CR4 are used to protect the input circuits of the operational amplifier from damage due to excessive voltage swings occurring during power switching transients.

A stable reference voltage is generated by VR1 and divided by a resistor network to generate full scale, three-quarter scale, half scale, and one-quarter scale analog voltages to be used to calibrate the commutator and analog-to-digital converter. These voltages are brought out of the DFC and reconnected to commutator inputs as dictated by systems requirements.

(2) ANALOG-TO-DIGITAL CONVERTER

The analog-to-digital converter and the associated control logic are housed on two printed circuit boards. The analog-to-digital converter board contains the reference supply (Z5, Q1, and Q2), the analog-to-digital ladder network (A9), the digital-to-analog switches (A1 to A7), the sample-and-hold capacitor (C5) and associated switch (Q3 of A12), the comparator buffers (Q1A and Q1B of A11), and the μ A 710 comparator (Z6). These are shown on RCA logic diagram 1976088, sheet 2.

The analog-to-digital logic board contains the Johnson counter and associated decoding gates, the analog-to-digital register, and the transfer gates that transfer the digital code into the data register from which it is shifted to the ITR track 3 input. See RCA logic diagram 1976088, sheet 2.

The analog-to-digital converter in the DFC employs the successive approximation technique. This method is most useful when there is a large difference between two consecutive inputs, as is the case for the output of a commutator. The analog-to-digital converter operates at a rate of 100 kHz and completes one conversion in a total time span of 104 microseconds. Its output, however, is shifted out at the rate of 15 bits per second and is always preceded by a marker pulse at logical "0". The total time to complete a code readout is thus approximately 530 milliseconds.

In order to conserve power, the analog-to-digital converter and commutator are switched on during the occurrence of the marker pulse and are off while the actual code is read out. This is accomplished by gates XG20 and XG21 located on the interface logic board. When the power comes on, the commutator input corresponding to the word in the frame is connected to the analog-to-digital sample-and-hold capacitor through FET Q3, which is held on by gate G12A. This is the rest-and-sample time. At the same time, the F64 (Z25) flip-flop in the analog-to-digital register is set, causing the ladder output to be at half-scale. This remains so for nearly 66 milliseconds until, toward the end of the marker pulse, the GO pulse, generated by XG9 and CG11 and lasting 104 microseconds, starts operation of the analog-to-digital converter by allowing the analog-to-digital Johnson counter to cycle through the states identified by gate numbers G11A (preset) to G10A (rest-and-sample). See RCA logic diagram 1976088, sheet 2.

G10A is the rest-and-sample state described previously. At the first clock pulse after the GO pulse, the counter moves to state G11A, FET Q3 is turned off to prevent further changing of the analog voltage at the sample-and-hold capacitor, and the last 7 bits (1WRF to 7WRF) of the 24-bit storage register are cleared to zero. During this period, the comparator compares the unknown voltage input with the half-scale ladder output. The next clock pulse, which sets F32 and resets F64 if the inverse of the comparator output is +5 volts, enables G1A, indicating that the analog input is more positive than -2.5 volts. If the inverse of the comparator output (710)' is 0 volt, indicating that the analog input is more negative than -2.5 volts, flip-flop F64 is left in the set state. This process is repeated up to state G6A with all the other flip-flops in the register. At G7A time, flip-flop F1 is reset, if necessary, and the complete digital word is stored in flip-flops F64 to F1.

In the next state (G8A) the data is transferred into the last 7 bits (1WRF to 7WRF) of the 24-bit storage register by enabling the transfer gates MO1 to MO7. The counter now remains in this state until the end of the GO pulse, at which time 4ADF is allowed to reset, and the counter enters the rest-and-sample state to be ready for the next conversion, which will occur during the marker pulse for the next word.

The -5-volt reference supply is made up of a temperature-stable zener diode biased at 5 milliamperes by selecting resistor R19. The zener output is then divided down by a resistive network, with coarse adjustment given by R10 and fine variable adjustment provided by potentiometer R20. The divider network feeds the noninverting input of an operational amplifier to minimize loading effects. The output of the amplifier is connected to a Middlebrook buffer stage which is part of the amplifier feedback loop. This stage provides the high current, low impedance drive necessary for the ladder network. To avoid oscillations in the output, capacitor C12 and resistor F15 are used to control the gain and phase response of the stage so that the phase shift will never exceed 135 degrees at unity gain for the stage.

The comparator buffer (A11) is used to provide matched voltage drops between the ladder output and pin 2 of the comparator and between the sample-and-hold capacitor and pin 3 of the comparator. It also provides a low impedance source for the μ A710 input current. The matching is accomplished by using in the input and output circuits dual transistors made up of two adjacent chips in the wafer, selected for closeness of parameters and aged together.

The two resistors R6 and R7 in the emitter circuits of the MD 1130 buffer are used to provide a fine adjustment to compensate for the initial system offset and to set the switching point from code 63 (0111111) to code 64 (1000000) at exactly -2.500 volts. Notice that either R6 or R7 is used, depending on the direction of the offset.

The function of the digital-to-analog switches is to supply the arms of the ladder network with either 0 volt or -5 volts. They must therefore provide a low impedance, low offset path to either voltage. Two types of switches are used. Type 1 (group 501) is used for positions A6 and A7 where a lower offset from the switch is desirable to reduce total system offset; this type uses the inverted connection for the transistor and reduces offset at the expense of a larger base current. Type 2 (group 502) is used in positions A1 through A5; this type uses the normal transistor connection to reduce base current, but its offset is larger, a factor which is not detrimental because the offset is divided down by the ladder and contributes much less to the total system offset. The design and selection of these switches is such that the maximum error at end of life is expected to be +5 millivolts at full scale ladder output and -7.3 millivolts at zero scale output.

(3) TIME CODE SEQUENCER

The purpose of this sequencer is to load the time code from the TBU into the DFC so that it can be included in the track 3 data frame. The time code from the TBU is read out at 120 pps and is updated every 1/4 second. This rate

is faster than the DFC data rate; therefore, the time code data is stored in the DFC in a 24-bit storage register and is then read out at the DFC rate.

The sequencer state diagram is shown in Figure 2-VI-17.

As can be seen, the sequencer is reset to state 1 by "DFC ON" which causes the general reset. When the "TC rest" pulse is high, during "words 1 and 2", the sequencer advances to state 2. At this time, TG14 is generated and used to pre-set the 24-bit register to all "0's" except for bit 24 (24WRF) which is set to "1". The next clock pulse advances the sequencer to state 3 and ends the TG14 signal. After the expiration of the "TC rest" pulse, at the first "TC shift" pulse which coincides with 5CF being a "1", the sequencer enters state 4 and proceeds to state 5 on the next clock pulse.

State 5 is decoded by TG15, inverted by TG16, gated with "words 1 and 2" by TG18 and used as a shift pulse to advance the TC NRZ data into the 24-bit register. If register overflow is still low, the sequencer is advanced to state 6, from which it proceeds to state 8 and back to state 3 if 5CF is reset, if there is a "TC shift" pulse, and if there are two clock pulses.

This process is repeated 23 times until overflow occurs, at which time the sequencer advances from state 5 to state 7. The sequencer is also returned to state 7 from state 5 by the termination of the "words 1 and 2" gate (XG12A). The sequencer will remain in state 7 until the end of "words 1 and 2" at which time it returns to state 1. This feature prevents the loading of more than one time code data burst, since up to four complete readouts can occur during "words 1 and 2".

Note also the two exit paths from state 4 to state 3 and from state 8 to state 6 if the wrong signal is present from 5CF, indicating lack of synchronization.

(4) ITR CONTROLLER

The ITR controller state diagram is shown in Figure 2-VI-18.

The "DFC ON" signal sets the controller to state 1 which is the record mode. In this mode, stepper pulses are provided to the ITR by gate G111. To initiate playback, the controller must advance to state 5. If a playback signal is received from the CDU while an "S-band switched ground" is present, indicating that the transmitter is turned on and the "end-of-tape playback" (EOTP) is not present, the controller advances to state 2. From state 2 it will advance to state 3 upon receiving the 8/15-Hz clock signal from BG7. At this time, the "playback enable" and the "VCO's switched power" signals are generated by 2AF through gates G131 and G135, respectively, located on the interface logic board.

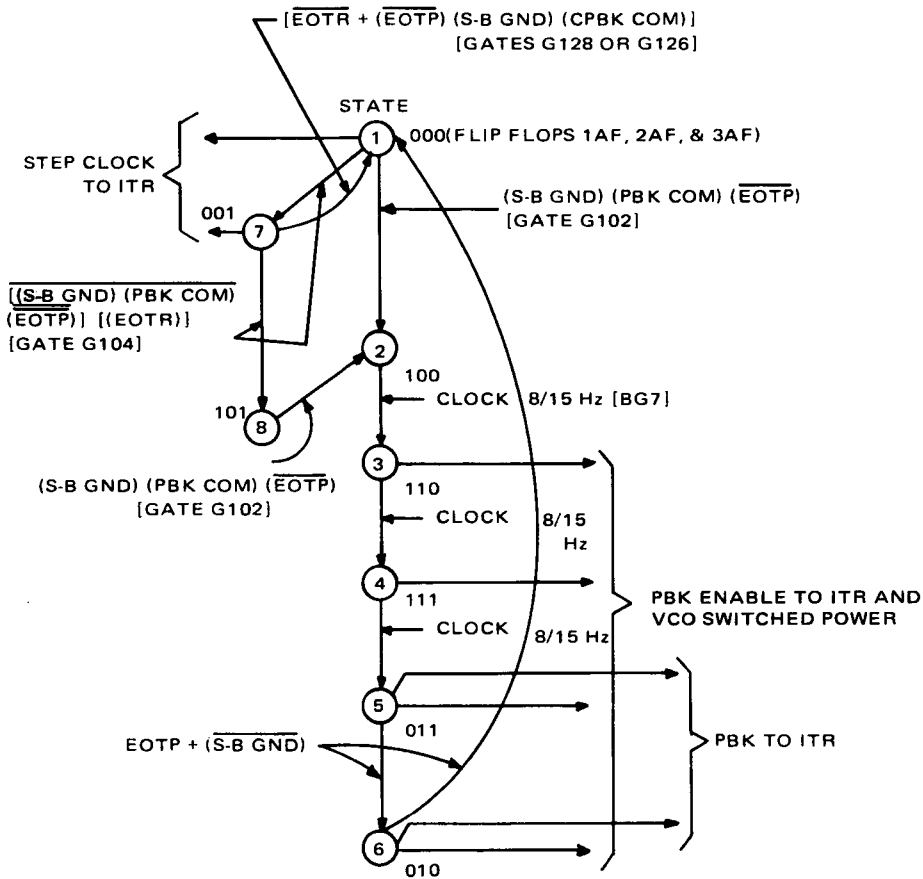


Figure 2-VI-18. ITR Controller State Diagram

D. INCREMENTAL TAPE RECORDER (ITR)

1. General Description

The incremental tape recorder (ITR) is a digital, three-track tape recorder used as a data storage and readout facility for the secondary sensors subsystem in the ITOS spacecraft. The functions of the ITR are to record, playback, and erase data signals from the solar proton monitor (SPM) and the flat plate radiometer (FPR) telemetry signals and a clock pulse. All input signals to the ITR are processed by or through the data format converter (DFC).

Data is recorded at a rate of 15 pulses per second and stored at a density of 300 bits per inch. The tape reels hold 90 feet of tape which can store 324,000 bits per track, or a total of 972,000 bits for the three tracks, which is sufficient to record all the data for three orbits. Total record time is 350 minutes minimum.

The playback rate is approximately 2,000 bits per second, and playback of the entire tape requires 2.7 minutes. A permanent magnet automatically erases the tape after playback. Conductive strips, 7.73 inches long, are bonded to each end of the magnetic tape to provide end-of-tape (EOT) signals when shorting the EOT sensors. Mechanical locks prevent the tape from coming off the reels in case the electrical EOT sensing fails or is disabled.

The ITR, as shown in Figure 2-VI-19, is composed of two assemblies, (1) the tape transport assembly and (2) the electronics assembly.

a. TAPE TRANSPORT ASSEMBLY

The tape transport assembly is mounted atop the electronics assembly and the two assemblies are bolted together at their flange mounting ends. The tape transport assembly is housed in a two-section, machined-magnesium enclosure that is sealed by an O-ring and pressurized with 90-percent air and 10-percent helium at 16.3 lbf/in² absolute. This assembly contains two tape reels, two motors (a two-phase stepper motor used for record and a DC motor for playback), an electromagnetic clutch, capstan, an erase head, two end-of-tape sensors, a pressure transducer, and two multipin connectors (J1 and J2) which provide for

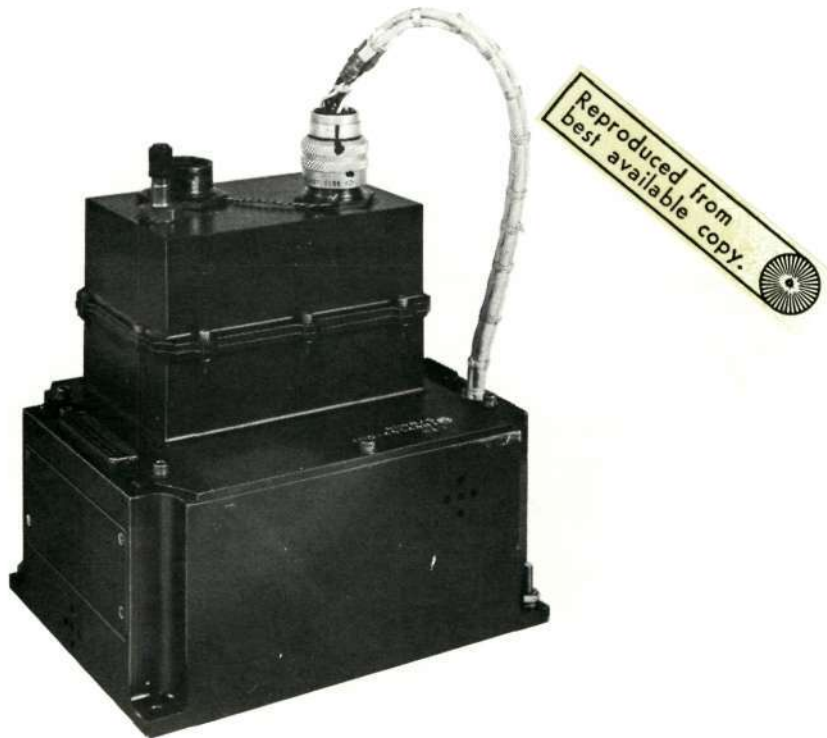


Figure 2-VI-19. Incremental Tape Recorder

electrical connections to the electronics assembly. A view of the tape transport assembly, with its bottom mounting base section removed, is shown in Figure 2-VI-20.

b. ELECTRONICS ASSEMBLY

The electronics assembly is housed in a separate, machined-magnesium enclosure which provides maximum electrostatic shielding. The top of this assembly is covered by the bottom mounting base section of the tape transport assembly, and the bottom is mounted to the spacecraft. The tape recorder electronics assembly consists entirely of solid-state circuitry, mounted and encapsulated on four printed circuit boards as indicated below:

<u>Printed Circuit Board</u>	<u>Circuit</u>
A1	Playback amplifier
A2	Playback amplifier
A3	Record amplifiers and flip-flops
A4	Steppers and clamps

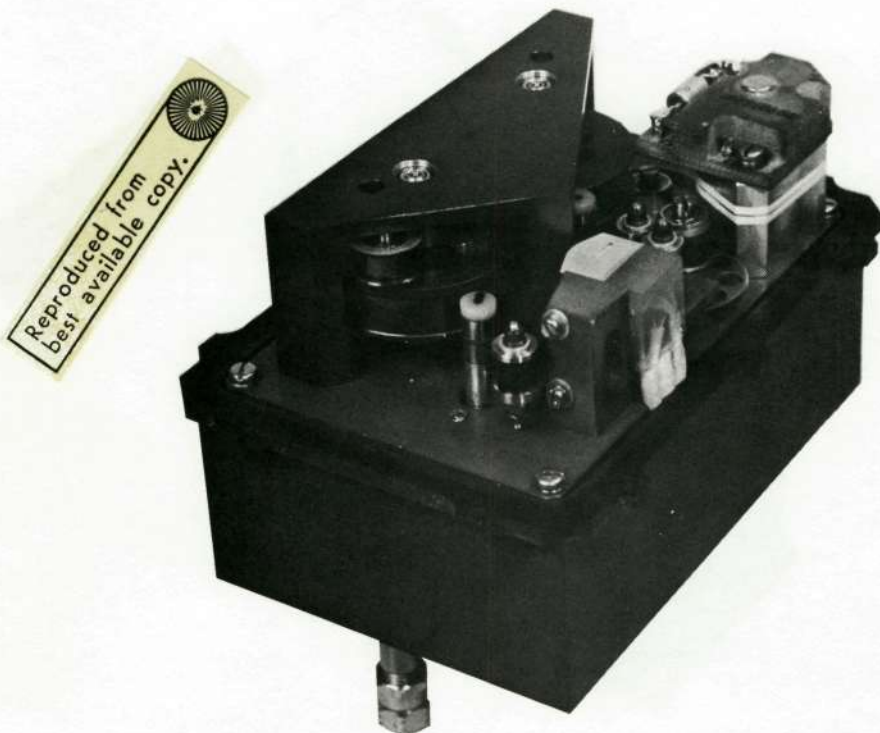


Figure 2-VI-20. Tape Transport Assembly, Bottom Mounting Base Section Removed

Input and output electrical connectors (J3 and J4), which are mounted at opposite sides of the electronics assembly to minimize cross-coupling between signal and power leads, provide connections to the tape transport assembly, the DFC, and the command distribution unit (CDU).

c. CHARACTERISTICS

The ITR uses two sources of DC power, +5.35 volts and -24.5 volts, supplied by the DFC. Power consumption of the ITR in the record mode is 2.4 watts, and in the playback mode, 5.15 watts. The ITR measures 7.44 inches high and 5.75 inches wide overall and the maximum total weight is approximately 5.5 pounds.

The ITR input and output signals and their functions are listed in Table 2-VI-4. The ITR's primary characteristics are summarized in Table 2-VI-5.

2. ITR Design

a. BASIC SOURCE AND IMPROVEMENT

The design of the incremental tape recorder is basically the same as the design for the QRD-6 tape recorder. Mechanical and electrical improvements were incorporated to meet the requirements for ITOS.

The mechanical improvements include the following:

- Increased capstan wrap angle for better tape traction and
- Lubrication of gears and bearings by Barden G-6 (Esso "ANDOK" C) grease.

The electrical improvements include:

- Integral stepper motor pulse generation logic from a single spacecraft clock input,
- Reduction of integrated circuit and logic power supply level to 5.35 volts nominal to ensure maximum life of the Fairchild integrated circuits,
- Reevaluation of circuits for radiation hardening,
- Addition of combined telemetry and DFC reset circuitry, and
- Improved layout of the playback amplifier boards to increase the stability margin by reduction in undesired stray feedback paths or crosstalk.

TABLE 2-VI-4. ITR INPUT AND OUTPUT SIGNALS

Type Signal	Function
Input:	
Data Track No. 1	Records digital NRZ data ("1" and "0") from SPM in a format of twenty 9-bit words, one of which is a frame marker.
Data Track No. 2	Records 7.5-Hz square wave clock pulses used for data synchronization in playback.
Data Track No. 3	Records digital NRZ data from FPR together with telemetry signal and time code data in a format of 8-bit words; 1 bit of each word is a word marker.
Playback Enable Command	Turns on power to playback electronics and to the playback DC motor.
Playback Command	Turns on power to the clutch which initiates playback.
ITR Step Clock	A 15-Hz square wave which drives the stepper motor drive logic circuitry for generating four pulse train signals to step-drive the motor during the record mode.
DFC Reset Pulse	Inhibits the stepper motor drive circuits during power turn-on for a period of 100 milliseconds.
Output:	
Data Track No. 1	Digital NRZ waveforms (0 volt for input data "1"; -4.5 volts for input data "0") present only during playback.
Data Track No. 2	
Data Track No. 3	
End-of-Tape Record	Generated when tape has reached its end during record operation. This signal is a backup to the internally generated EOTR signal which disables the stepper motor drive circuitry.
End-of-Tape Playback	Generated when tape has reached its end during playback operation. This signal is a backup to the internally generated EOTP signal which switches power off from the playback electronics, playback motor, and clutch. The signal resets the playback circuitry in the DFC.

TABLE 2-VI-5. ITR CHARACTERISTICS

Parameter	Characteristics
Input Data Signals:	
Data Tracks Nos. 1, 2, and 3	Data "1" and data "0" are 0 to 0.5 volt and 5.35 ± 0.4 volts, respectively.
Output Data Signals:	
Data Tracks Nos. 1, 2, and 3	Data "1" and data "0" are 0 to -0.5 volt -4.5 ± 0.5 volts, respectively.
Command Signals:	
Playback Enable	Data "1" and data "0" are 0 to 0.5 volt and $+5.35 \pm 0.4$ volts, respectively. Data "1" turns on power to playback electronics and to playback motor. Data "0" turns off power to same and to the clutch.
Playback	Signal characteristics same as for playback enable. Data "1" turns on power to the clutch to initiate playback. Data "0" turns off power to the clutch.
ITR Step Clock Signal	Data "1" and data "0" are 0.0 ± 0.5 volt and 5.35 ± 0.4 volts, respectively; present as a 15-Hz square wave during record. During playback, a constant level of 5.35 ± 0.4 volts is present.
DFC Reset Pulse	"On" input voltage level: -21 ± 3 volts DC; "Off" input voltage level: 0 ± 0.5 volt DC; (Current: 1.53 mA minimum; 2.03 mA maximum)
Track Signal Allocation:	
Data Track No. 1	(See Table 2-VI-4.)
Data Track No. 2	(See Table 2-VI-4.)
Data Track No. 3	(See Table 2-VI-4.)
Tape Speed:	
Record Mode	15 bits per second per track; tape advances in 0.0033-inch increments 15 times per second.

TABLE 2-VI-5. ITR CHARACTERISTICS (Continued)

Parameter	Characteristic
Playback Mode	2000 bits per second \pm 15 percent; 6.67 inches per second \pm 15 percent.
Playback/Record Speed Ratio	133:1 (approximately)
Tape Time (Capacity):	
Record	350 (minimum) minutes (for 90 feet of usable tape)
Playback	162 seconds \pm 15 percent (for 90 feet of usable tape)
Tape Dimensions:	
Length	90 feet of usable mylar base, magnetic tape (plus 7.73-inch lengths of metalized, electrically conductive strips bonded at both ends to provide EOT signals and two 3.18-inch chrome oxide polishing strips to clean the magnetic head and the EOT sensors).
Width	0.25 inch
Thickness	0.0008 inch
End-of-Tape Sensors	Static precision metal contacts.
Heads	One three-track magnetic head used for both record and playback. One permanent magnet erase head.
Telemetry Signals:	
(1) Combined Telemetry	
-24.5 volts DC Power Off	0.0 volt nominal
Stepper Motor (Phase 1 and 2) On	-1.8 volts \pm 10 percent
Stepper Motor (Phase 1 and 2) Off (Standby)	-2.7 volts \pm 10 percent
Playback in Process	-3.6 volts \pm 10 percent
Playback Enabled, Clutch Disengaged	-4.5 volts \pm 10 percent

TABLE 2-VI-5. ITR CHARACTERISTICS (Continued)

Parameter	Characteristic
(2) Pressure Telemetry	0 volt at 0 lbf/in ² absolute, and -5.0 volts at 25 lbf/in ² absolute
Power Sources	-24.5 volts DC (primary power) 5.35 volts DC
Power Drain:	
Record Mode	2.4 watts
Playback Mode	5.15 watts
Record Motor	Two-phase, incremental drive stepper motor
Playback Motor	Continuous drive DC motor (10,000 r/min nominal speed)
Tape Transport Assembly:	
Pressurization	16.3 ± 0.5 lbf/in ² absolute (90-percent dry air and 10-percent helium)
Seal	O-ring, flange, and pressure fitting
Mission Life	1 year minimum (in orbit)
Storage Life	2 years maximum (30- to 50-percent relative humidity and 72 ± 5° F)
Operating Temperatures	-10° to + 45° C
Size	7.44 inches high by 5.75 inches wide overall
Weight	5.5 pounds (maximum)

b. LIFE LIMITING PARTS AND LUBRICATION

(1) MOTOR STEPPER

The design operational life for the motor stepper is for a minimum period of 2 years of continuous operation at a rate of 15 steps per second.

(2) *MOTOR PLAYBACK*

The design operational life is for a minimum period of 400 hours. Since orbit requirements are for 32 minutes of operation per day, life of the motor is approximately 2 years.

(3) *MAGNETIC CLUTCH*

The design life for the magnetic clutch is for a minimum period of 2 years at a rate of 10,000 energizing pulses each with a period of 15 seconds.

(4) *NEGATOR SPRINGS*

The minimum life of the negator springs on the incremental tape transport assembly is 2500 cycles. Worst-case orbital conditions (record and playback every orbit) result in negator spring cycling of 4600 cycles per year. The present spring design has a minimum life of 6.5 months and an average life of 9.7 months under worst-case conditions.

(5) *MAGNETIC TAPE*

The 3M 590 magnetic tape used in the incremental tape recorder is the same as that used in the tape transport for a classified program. An operational life of 12 months or more is indicated from the results obtained on the classified program.

(6) *BEARING LUBRICATION*

Bearings used in the incremental tape recorder are Barden precision bearings, lubricated with Esso "ANDOK" C grease (the same as that used for the AVCS and scanning radiometer recorders).

3. Detailed Physical Description

a. TAPE TRANSPORT ASSEMBLY

The tape transport assembly comprises two motors, a precision gear train with electromagnetic clutch, a capstan, a record/playback and erase head sub-assembly, and a tape reel subassembly. The tape transport assembly is mounted

between two plates that are doweled and bolted together to form a chassis. The tape reel subassembly is held in place by shoulder-type ball bearings set in the two plates. All the other components of the tape transport are attached to the larger of the two plates.

The gear train comprises precision aluminum gears and stainless steel pinions which minimize noise and ensure long life. The ball bearings are prelubricated, and the gears are greased during assembly with a military-specification lubricant. A simplified diagram of the transport mechanism is shown in Figure 2-VI-21.

(1) TAPE DRIVE

The tape is driven during both record and playback by the capstan which, in turn, is powered through the gear train and the clutch. The clutch serves as a mechanical switch between the recording and playback motors. During the recording mode, a two-phase stepper motor drives the record input gear, which is frictionally coupled to the clutch output pinion that drives the capstan. While the clutch is deenergized in the record mode, the clutch output pinion remains engaged with the capstan gear. The stepper motor is powered by a pulse train from the record/playback control circuit in the recorder electronics. This

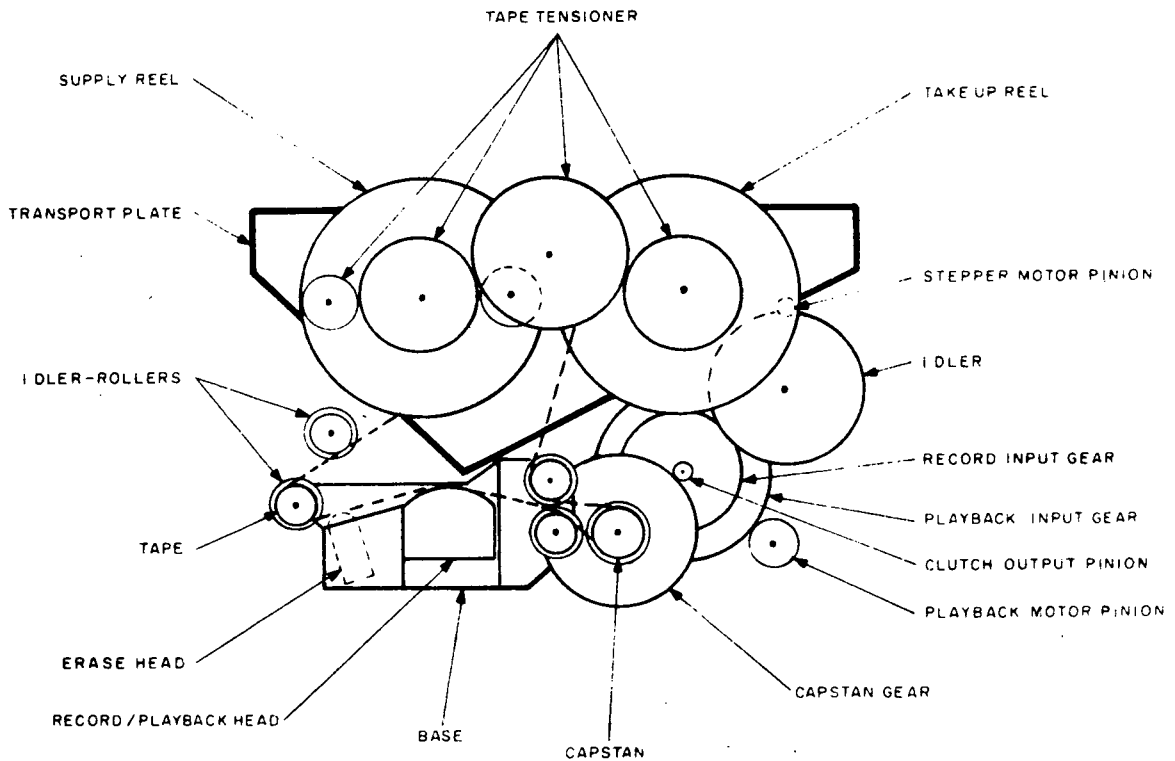


Figure 2-VI-21. Tape Transport Mechanism, Simplified Diagram

pulse train causes the rotor of the stepper motor to rotate in 45-degree steps. The precision gear train reduces this to a 1-degree rotation of the capstan, which is translated into a 1/300-inch motion of the tape.

During playback, the clutch is energized, which frees the record input gear and engages the playback motor pinion. A DC motor drives the playback motor gear. A zener diode in series with the motor input gives it a nominal speed of 10,000 r/min. The gear ratio between the playback motor pinion and playback input gear produces a playback rate of 2000 pulses per second. The motor is totally enclosed and its input filtered to minimize noise pickup by the record/playback heads during the playback mode.

(2) TAPE REEL SUBASSEMBLY

The tape reel subassembly consists of the tape, tape reels, tape tensioning devices, and end-of-tape sensors. The entire tape is approximately 112 feet long. During loading, each tape end is threaded into a slotted keeper mounted on the reel hub, and the keeper is rotated so that the tape end wraps around it. When the tape is adequately anchored, a locking screw is inserted to prevent the keeper from loosening. The end-of-tape sensors are static, precious-metal contacts. To provide end-of-tape signals, 7.73-inch metallized strips are bonded to the ends of the tape. As the tape approaches either end, the metallized strip touches the sensor, causing the input of a switching circuit to be grounded and thereby stopping the drive. In the unlikely event that both the external stop and the end-of-tape signals fail, the capstan slips against the tape until a ground command is received to reverse the recorder operation. The correct tape tension is provided by a negator, constant-rate spring system mounted on the supply reel.

(3) RECORD/PLAYBACK AND ERASE HEAD SUBASSEMBLY

This subassembly employs two heads for three functions. Both record and playback functions are performed by a simple, magnetic, four-track head of conventional design; however, only three of its tracks are used in this application. The head is rigidly attached to a precision-machined base which also supports three idler rollers and the erase head. The idler rollers guide the tape to and from the capstan. The base and head are preassembled, and the head is aligned with the idler rollers to establish a tape track of the required accuracy. The permanent-magnet erase head is a simple bar magnet, mounted so that the tape passes within 0.003 inch of its face without touching.

b. **ELECTRONICS ASSEMBLY**

The electronics assembly comprises three record amplifiers, three playback amplifiers, stepper drive circuitry, and control circuitry, all mounted on four printed circuit boards. The four boards, and two input/output connectors (J3 and J4), are housed in a magnesium enclosure which mates with and provides a base for the tape transport; the transport housing covers the electronics assembly. The tape electronics enclosure provides tight joints and good ground paths to the baseplate.

The input and output connectors are mounted at opposite sides of the enclosure to minimize coupling between signal and power leads. Feedthrough filters are provided for the internal connection of critical electronic circuits requiring shielding. Eleven test points permit the following parameters to be monitored during a test: three record amplifier outputs, three playback amplifier outputs, three NRZ data inputs, and two end-of-tape outputs. During tape recorder operation, two telemetry points allow (1) tape transport pressure, and (2) record and playback power to be monitored (combined telemetry).

The layout of the printed circuits minimizes the effects of crosstalk and noise on the differential amplifiers. Minimum lead lengths and shield planes provide additional protection. Components are located so as to minimize stress due to board flexing. The boards are stiffened by sandwiched polyurethane spacers bonded to the two board combinations.

4. Functional Description

a. **GENERAL**

A simplified block diagram of the incremental tape recorder is shown in Figure 2-VI-22. The detailed logic diagram is RCA 1976091. Three channels of data storage (record) and playback are provided. Two channels (data tracks Nos. 1 and 3) store digital NRZ data from the SPM and the FPR, respectively, via the data format converter. The 15-Hz ITR clock signal and combined telemetry are also recorded on track No. 3. On channel 2 (track No. 2), 7.5-Hz square wave clock pulses in digital form are recorded and are used as a reference for playback. Initially, during power turn-on, +5.35 volts DC power from the DFC is applied to the ITR system record circuits which include the record control circuits, the record amplifiers, and the record stepper motor drive circuits. At the same time, a -21-volt DC reset pulse from the DFC is applied to the stepper motor drive circuitry, inhibiting operation of the record stepper motor for 100 milliseconds. This, in effect, is a standby condition. After this initial delay, the ITR system commences its record mode of operation.

b. RECORD MODE

(1) STEPPER DRIVE CIRCUITRY

The input to the stepper motor drive circuitry is a 15-Hz ITR step clock signal from the DFC. This signal is sequenced by the record stepper motor drive circuits, comprising four integrated circuits, which generate four pulse trains, as depicted in Figure 2-VI-23. Stepper drive waveforms Nos. 1, 2, 3, and 4 show the time relationship between the pulse applied to the stepper motor. Each time one of two pulses overlaps, the stepper motor will advance the tape one step (0.0033 inch). Two of the pulse trains drive one transistor bridge, while the other two drive a second bridge. Only one of the two bridges is "on" at a time. The output from each bridge is a series of voltages having an "on" period and an "off" period of 33.3 milliseconds. The "off" period occurs after one half of the bridge is shut off and before the other half is turned on. This "off" period conserves power and ensures that both halves are not on simultaneously, which would cause a failure. The output of each bridge drives one phase of the two-phase stepper motor. The rotor of the stepper motor rotates 45 degrees each step; this is reduced by the precision gear train ratio of 45:1 to 1 degree at the capstan.

Recording is performed at a rate of 15 bits per second per track; i. e., 15 times per second the stepper motor advances the tape by 0.0033 inch. While the tape is stopped, 1 bit is recorded per track; the tape is again moved and, thus, 300 bits are recorded per inch. When the tape has reached its end (90 feet of tape), the stepper motor is automatically cut off by an "end-of-tape record" (EOTR) signal. This signal also generates an external signal which is sent to the programmer in the DFC and its level changes from +5.35 volts (data "0") to 0.0 volt (data "1"). The ITR system is now in standby and will remain so until a "playback enable" signal initiates the playback mode.

(2) RECORD AMPLIFIERS

Each of the three record amplifiers comprises three switching transistors (a buffer amplifier and two emitter followers) that amplify the NRZ data from the DFC. The switching transistors alternately drive the center-tapped record/playback head coil, with a 2.7-milliampere output current, sufficient to saturate the tape in either direction. Recording is accomplished by reversing the direction of the current in the head coil. A reversal occurs after the tape has completed its advance and is at rest. In the clock track (track No. 2), the head current reverses every 66.7 milliseconds, 3 milliseconds before the start of a stepping pulse.

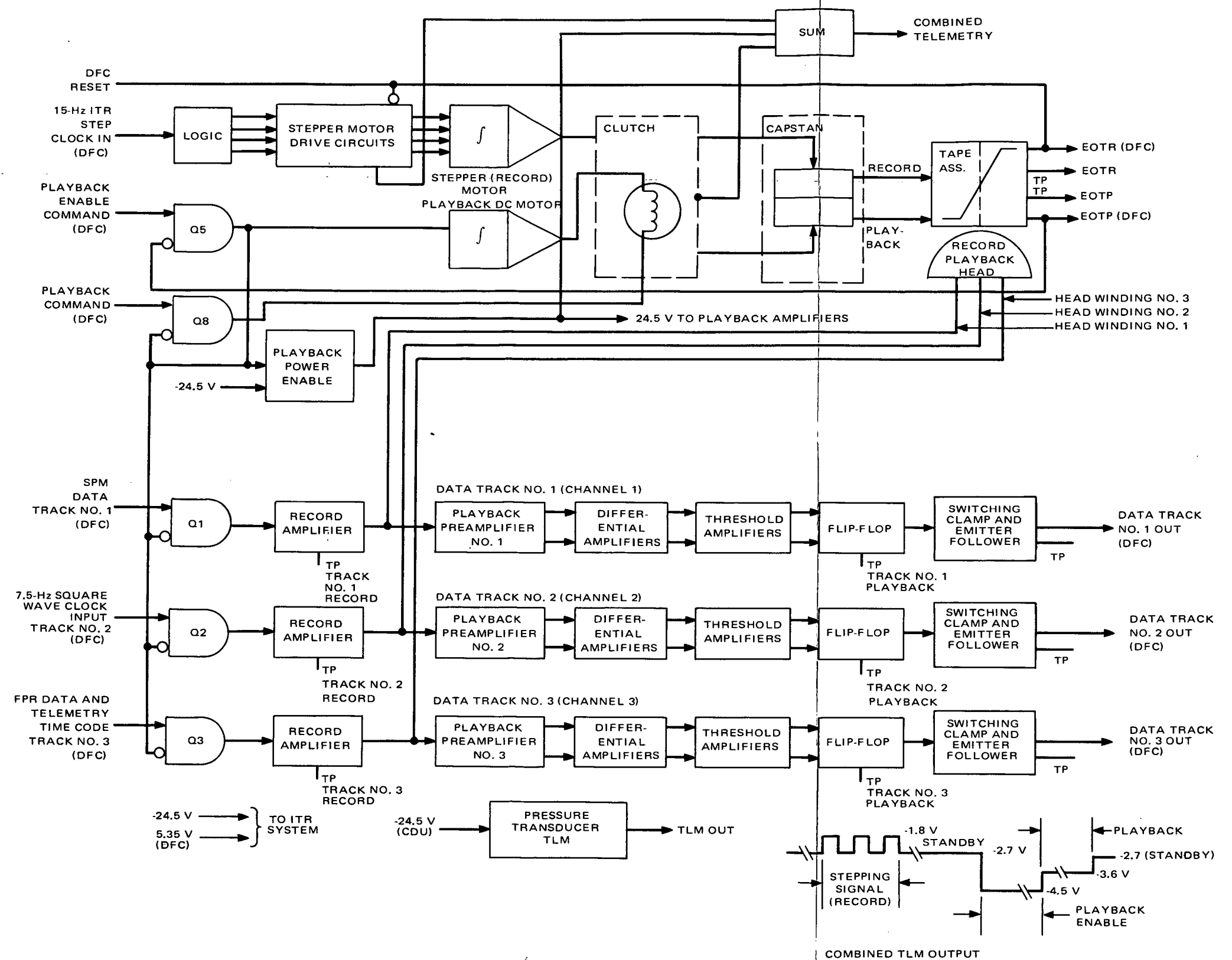


Figure 2-VI-22. Incremental Tape Recorder, Simplified Block Diagram

FOLDOUT FRAME 1

FOLDOUT FRAME 2

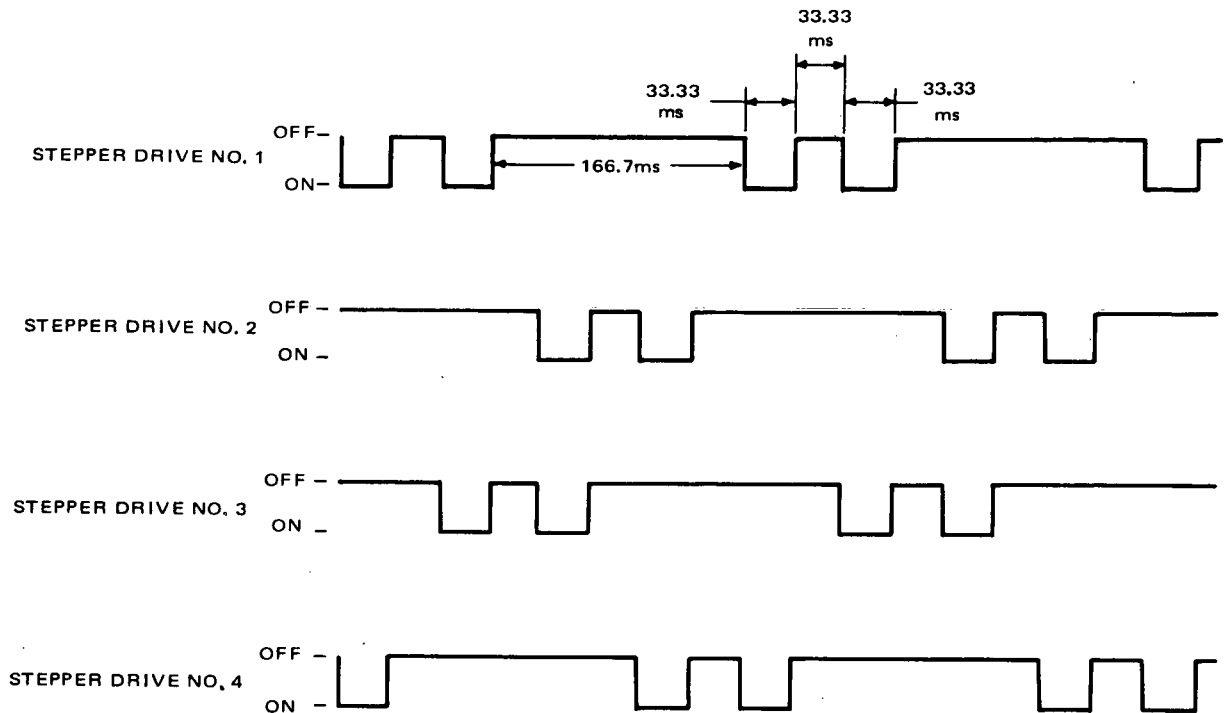


Figure 2-VI-23. Stepper Drive Signal Phasing

The current reversal in the other two data tracks (tracks Nos. 1 and 3) is dependent upon the input data. During playback, the record amplifiers are disabled by a constant voltage so that there is no input to the head windings.

The two levels of NRZ data recorded are 0.0 volt for data "1" and +5.35 volts for data "0". The transition from "0" to "1" or "1" to "0" occurs 29.5 to 33.0 milliseconds after the ITR step clock input transition from data "1" to data "0".

c. PLAYBACK MODE

(1) GENERAL

Two separate commands from the DFC are necessary to play back the data recorded on the tape; the playback enable command and the playback command (both data "1's" at the 0.0-volt level). During this mode of operation, the 15-Hz ITR step clock input is present at a level of $+5.35 \pm 0.4$ volts.

The playback control circuits comprise transistor switching circuits that accept command signals from, and provide end-of-tape signals to, the programmer in the DFC. When the playback enable input to the control circuit is grounded, the

-24.5-volt DC input is applied to the three playback amplifiers and to the DC playback amplifiers and to the DC playback motor, while the record amplifiers are inhibited by this same DC voltage supply. When the playback command input is grounded, there is a minimum 1-second delay, after which a transistor turns on and applies power to the clutch. The 1-second delay allows the DC playback motor to attain full running speed before the clutch is engaged.

(2) *PLAYBACK AMPLIFIERS*

Each of the three playback amplifiers processes data from one of the three record/playback head windings. The signals coming from the head are of the order of several millivolts. The preamplifier is linear and has a closed-loop gain of 1300. The input is capacitively coupled to a differential amplifier stage with a high, common mode rejection for noise occurring in both windings of the head coils. This stage is directly coupled to another differential amplifier which drives two single-ended threshold amplifiers (one from each output of the differential amplifier). Each threshold amplifier drives one side of a flip-flop that is biased to a given threshold level. The output of the flip-flop drives a switching clamp that feeds an emitter follower to produce a low impedance square wave output.

The outputs from the three tracks are NRZ waveforms whose levels are 0.0 volt for data "1" and -4.5 volts for data "0".

The DC motor has a nominal speed of 10,000 r/min and its input is filtered to minimize noise pickup by the magnetic head during playback. The playback tape speed is 6.67 inches per second, corresponding to a bit playback rate of 2000 bits per second per track. The total playback time for 90 feet of tape is 162 seconds.

After the tape has passed the magnetic head, all the data is erased by a permanent bar magnet erase head which is 0.003-inch distance from and parallel to the tape. At the end of playback, power to the DC motor and clutch and to the playback electronic circuitry is automatically cut off by an end-of-tape playback (EOTP) signal. This signal, in a similar manner as for the record mode, generates an external signal which is sent to the programmer in the DFC; this signal level changes from +5.35 volts (data "0") to 0.0 volt (data "1"). The ITR system is now in standby condition.

d. TELEMETRY CIRCUITS

(1) COMBINED TELEMETRY

The combined telemetry circuit provides information concerning the operational status of the ITR system. It sums information from five sources and presents to the output load five possible voltages as described below.

When the -24.5-volt power supply voltage is off, the combined telemetry output voltage is 0 volt. In the record mode, when the stepper motor is energized, the combined telemetry output voltage is a 15-Hz square wave measuring -1.8 volts when the stepper motor phase 1 and phase 2 are on. When the stepper motor phase 1 and phase 2 are off, the combined telemetry voltage measures -2.7 volts. (This is an equivalent standby condition.)

When the playback enable command signal is applied to the ITR system, power is applied to the playback electronics and to the DC motor; the combined telemetry output voltage is -4.5 volts. When the playback command signal is applied, the clutch is engaged; the combined telemetry output voltage is now -3.6 volts. For all ITR system standby conditions, the combined telemetry output voltage is -2.6 volts.

(2) PRESSURE TELEMETRY

A pressure transducer, located inside the tape transport assembly, provides information concerning the pressure inside the sealed transport assembly. The telemetry output voltage is 0 volt at 0 lbf/in² absolute and -5.0 volts at 25 lbf/in² absolute.

SECTION VII

COMMUNICATIONS SUBSYSTEM

A. GENERAL

The communications subsystem provides four separate RF links for handling the communications traffic between the spacecraft and the ground stations. These four links are:

- Command link for transmitting command messages from the CDA stations to the spacecraft.
- Beacon and telemetry link for transmitting tracking signals, telemetry data, attitude data, solar proton monitor data, and command verification data from the spacecraft to the CDA stations.
- Real-time video link for transmitting APT camera and scanning radiometer data from the spacecraft to APT stations.
- Playback video link for transmitting the recorded AVCS picture, radiometer and secondary sensors data to CDA stations.

The total requirements and the essential characteristics of the four communications links are summarized in Table 2-VII-1. The communications subsystem is designed to permit operation of all four links concurrently and to be compatible with the CDA and APT ground stations. The components of the communications subsystem are shown in Figure 2-VII-1.

B. COMMAND RECEIVING LINK

1. General

A block diagram of the spacecraft portion of the command receiving link is shown in Figure 2-VII-2. The relationship of the command receiving link to the beacon and telemetry link with which it shares a common, single-element antenna is also indicated. Commands are transmitted to the spacecraft from the CDA ground stations as amplitude modulations of a 148-MHz carrier wave, and are received via the command and beacon antenna, the 136-MHz notch filters, the 148-MHz bandpass filter, the hybrid coupler, and the command receivers. The commands are in the form of two tone pairs, each consisting of an enable tone and a frequency-shift keyed (FSK) subcarrier, both of which amplitude-modulate the 148-MHz RF carrier. Each pair of command tones is associated with one of the two sections of the dual spacecraft decoder. The tone pair is transmitted sequentially (only one tone is present at any given time).

TABLE 2-VII-1. SUMMARY OF COMMUNICATIONS LINKS

Link Carrier Frequency	Information Signal	Baseband Bandwidth	Type Signal	Subcarrier Frequency	Modulation Subcarrier/ RF Carrier	Signal Bandwidth in RF Spectrum
Command 148.56 MHz	Enable tones and digital commands; bipolar RZ train	10 bits per second	CW tone digital data	Enable: F1* Data: F2*	AM/AM FSK/AM	22.6 kHz
Beacon and Telemetry 136.77 MHz	Housekeeping telemetry and command verification; attitude data	59 Hz 160 Hz	Analog data	3.9 kHz 2.3 kHz	FM/PM FM/PM	8.5 kHz (total)
Real Time 137.5 MHz	Analog APT video and SR data	1600 Hz	AM sub-carrier	2.4 kHz	AM/FM	
Playback 1697.5 MHz	Recorded analog video (AVCS)	60 kHz	FM sub-carrier	90 kHz	FM/FM	2.1 MHz (total)
	Flutter correction	500 Hz	FM sub-carriers (3)	12.5 kHz 200 kHz 400 kHz	FM/FM	
	Radiometer data	7.2 kHz	FM sub-carriers (2)	250 kHz 350 kHz	FM/FM	

* Command subcarrier frequencies are specified in supplement 1 to the TIROS M Programming and Control Handbook (AED R-3365F Supplement 1)

TABLE 2-VII-1. SUMMARY OF TIROS M COMMUNICATIONS LINKS (Continued)

Link Carrier Frequency	Information Signal	Baseband Bandwidth	Type Signal	Subcarrier Frequency	Modulation Subcarrier/ RF Carrier	Signal Bandwidth in RF Spectrum
	Secondary sensors data	2.0 kilobits per second	FSK sub-carriers	17B, 19B, 21B*	FSK/FM	2.1 MHz (total)
	Pilot tone	-	CW	300 kHz	CW	
*IRIG standard subcarrier frequencies 144, 160, and 176 kHz, respectively.						

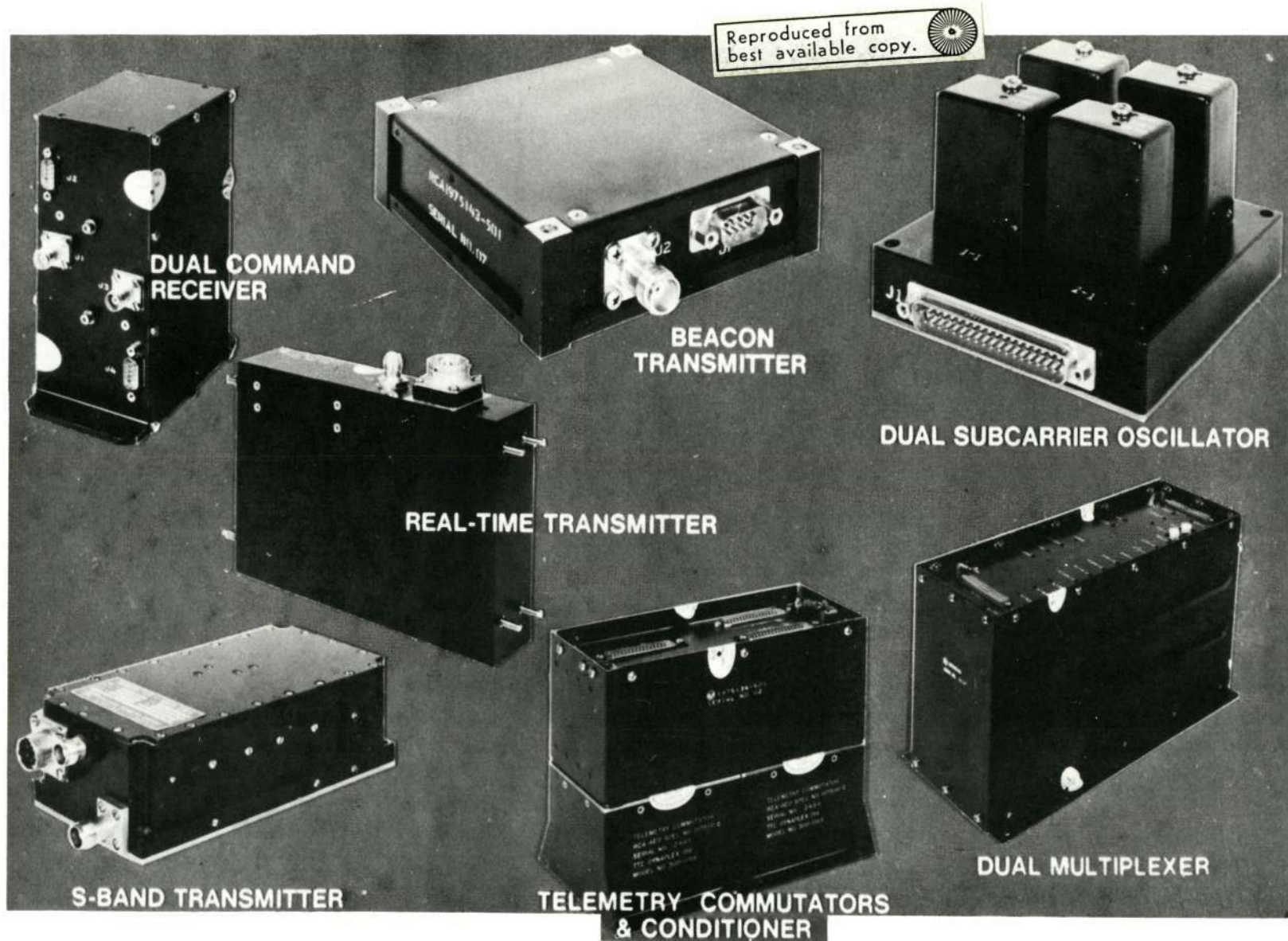


Figure 2-VII-1. Communications Subsystem Components

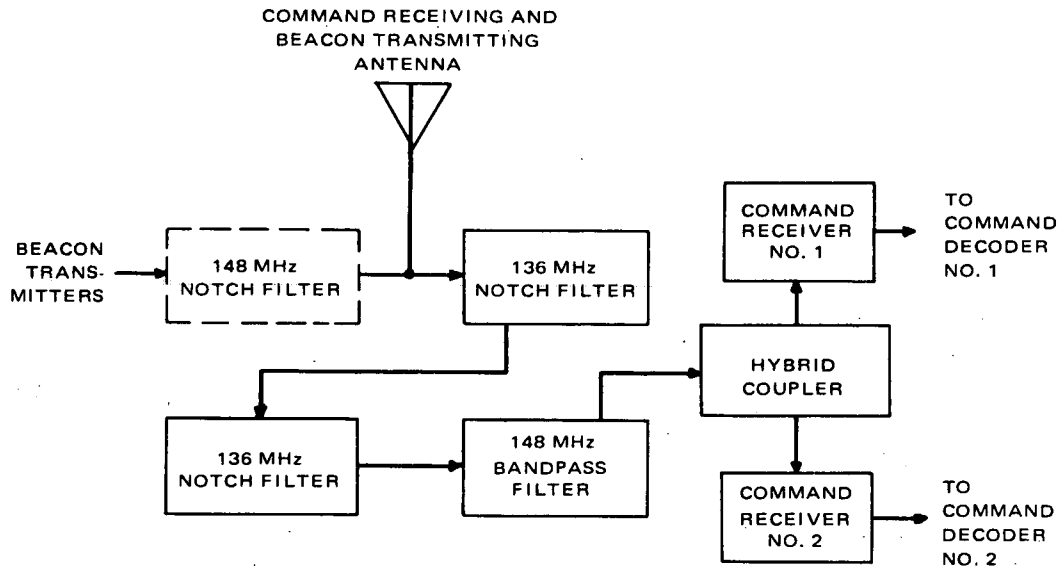


Figure 2-VII-2. Command Receiving Link

The antenna is linearly polarized while the transmitted electromagnetic wave is circularly polarized, which results in a 3-dB polarization loss. Another loss of 3-dB is incurred due to the splitting of the RF power, which is then applied to the two identical command receiver channels. Command receiver No. 1 is connected to decoder No. 1, while receiver No. 2 is connected to decoder No. 2. The outputs of the receivers are identical and consist of either the enable tone or the FSK subcarrier.

2. Signal Characteristics

The requirements of the RF command system are similar to those of the present TOS system. The first signal of the command tone pair is an unmodulated sinusoidal enable tone. The second tone is FSK modulated with the 10-bits-per-second, return-to-zero, bipolar command data. Each tone amplitude-modulates the 148-MHz RF carrier with a modulation index of 90 percent. Only one tone is transmitted at a time. Two unique pairs of tones are used, a pair to address each of the redundant decoder channels.

Each command decoder is tuned to a given enable tone and a given FSK subcarrier. The 3-dB bandwidths are ± 7.5 percent of the center frequency for the enable tones. The FSK subcarriers are modulated by a bipolar, return-to-zero waveform at a rate of 10 bits per second. A bit "1" is represented by a frequency shift of +7.75 percent of the FSK subcarrier; "0" is represented by a frequency shift of -7.75 percent from the center frequency. A rest period, during which the center frequency is transmitted, always follows a "1" or a "0". The bit information is extracted by two bandpass filters centered at the binary "1" and "0" subcarrier frequencies followed by envelope detectors. The

3-dB bandwidths of these filters are ± 2 percent of the FSK subcarrier center frequency.

3. Components

a. ANTENNA GROUP

A single quarter wave stub serves as both the receiving antenna for the 148.56-MHz command carrier and the transmitting antenna for the 136.77-MHz beacon and telemetry signals. The pattern is essentially a dipole pattern with the nulls along the pitch axis. In addition to the antenna, the antenna group includes matching stubs and filters, a hybrid coupler, and the interconnecting cables. Because the design considerations for the command receiving components also involve design considerations of the beacon and telemetry components, these two antenna groups are discussed together under Paragraph 2.VII.C.3.f.

b. DUAL COMMAND RECEIVER

(1) GENERAL DESCRIPTION

The ITOS dual command receiver is similar to the command receivers previously used on TIROS and TOS. The redundant receivers are in one assembly.

Each receiver demodulates the RF command signal that is transmitted to the spacecraft from the CDA station. The RF command signal is amplitude-modulated by enable tones and frequency shift keying (FSK) tones. One enable and one FSK tone is associated with each receiver-decoder combination. The carrier is modulated by a single tone at any given time.

For ITOS, the receiver bandwidth (controlled by the crystal filter) is at least 48 kHz at 6 dB down, while in TOS, it was 40 kHz minimum at 6 dB down. The wider bandwidth crystal filter is mechanically interchangeable with the previously supplied narrower bandwidth crystal filters.

The receiver has a mounting surface of 5.86 by 2.90 inches and is 6.50 inches high. Each receiver has its own TNC connector for the RF input and a 9-pin connector for input supply voltage, audio output, and AGC telemetry. The dual receiver weighs 2.6 pounds.

(2) FUNCTIONAL OPERATION

Two identical command receivers (both contained in the single unit) are aboard the spacecraft. As shown on Figure 2-VII-3, each is a single-conversion, crystal-controlled superheterodyne receiver. The incoming RF signal, on a 148.56-MHz carrier, is amplified and mixed with the output of a 128.56-MHz local oscillator to produce an intermediate frequency (IF) of 20 MHz. This IF signal is amplified and applied to a bandpass filter that provides selectivity.

After three more stages of IF amplification, the signal is applied to an AGC detector and an audio tone detector. AGC is applied to the RF amplifier stage, mixer and the first three IF stages. The audio output is amplified and applied to the associated decoder.

C. BEACON AND TELEMETRY LINK

1. General Description

The beacon and telemetry link of the spacecraft provides for the continuous transmission of the beacon signal and for the telemetering of spacecraft operating parameters. The telemetry system has three modes of operation: launch, acquisition, and mission.

The launch mode is only available over set No. 1 of the beacon system and terminates upon separation of the spacecraft from the launch vehicle. It provides a communication link for accelerometer data during the actual launch. The acquisition mode provides DSAS data over both sets on the 3.9-kHz subcarrier; roll sensor, time code, or roll sensor and selected pitch index pulse data is available on the 2.3-kHz subcarrier during this mode. Following acquisition, the beacon system is normally switched to mission mode by ground command. The telemetered operating parameters in this mode include housekeeping telemetry, attitude (roll and pitch) data, command verification data, and solar proton monitor data.

The beacon and telemetry link, shown in Figure 2-VII-4, includes a signal conditioner with redundant commutators, a dual subcarrier oscillator assembly, and redundant transmitters. The beacon antenna group components are non-redundant. The antenna is shared with the command receiving link.

The two subcarrier oscillators associated with beacon transmitter No. 1 (SCO 1-1 and SCO 1-2) have the same respective frequencies as the subcarrier oscillators associated with beacon transmitter No. 2 (SCO 2-1 and SCO 2-2). Each subcarrier set is turned on simultaneously with the associated beacon transmitter. During the normal mission mode, the highest frequency SCO (3.9 kHz, IRIG channel No. 9) carries housekeeping telemetry, command verification data, or SPM data. In the acquisition mode, this channel carries DSAS data. The lowest frequency SCO (2.3 kHz, non-IRIG standard deviation channel)

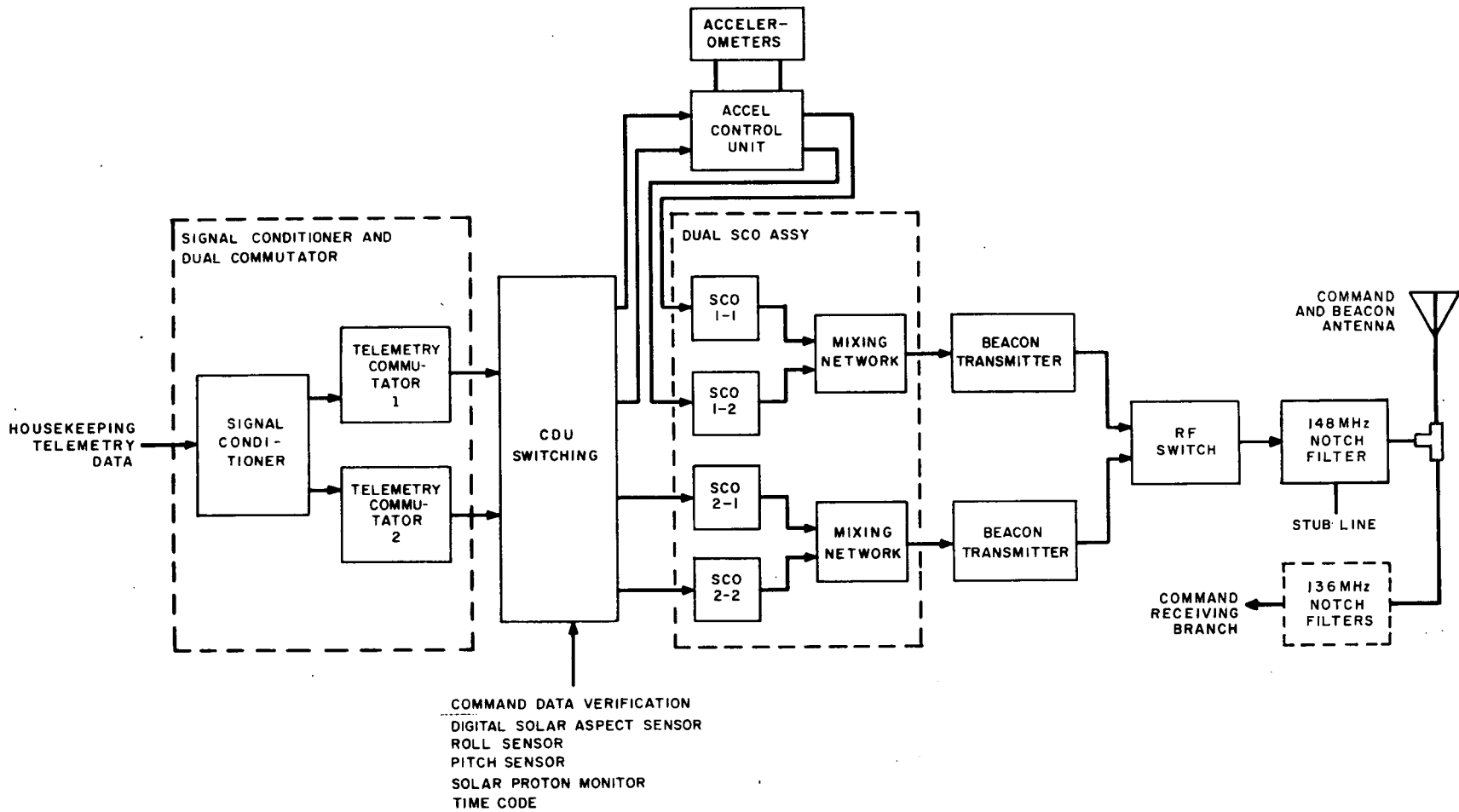


Figure 2-VII-4. Beacon and Telemetry Link, Block Diagram

during the normal mission mode carries one of the following signals: roll sensor No. 1 data, roll sensor No. 2 data, pitch sensor No. 1 data, pitch sensor No. 2 data, or time code. Pitch sensor data is not available during the acquisition mode. The CDU relay chain performs the functions of cross-strapping the various signals to the selected SCO unit and selecting the various signals in accordance with the following priority list:

3.9-kHz Subcarrier

Set No. 1

Mission Mode:

1. TLM Commutator No. 1
2. TLM Commutator No. 2
3. Decoder Channel No. 1
(command data verification)
4. Decoder Channel No. 2
(command data verification)
5. SPM Data

Acquisition Mode:
DSAS

Launch Mode:
Lateral Axis Accelerometer Data

Set No. 2

Mission Mode:

1. TLM Commutator No. 2
2. TLM Commutator No. 1
3. Decoder Channel No. 2
4. Decoder Channel No. 1
5. SPM Data

Acquisition Mode:
DSAS

Launch Mode:
Not Available

2.3-kHz Subcarrier

Set No. 1

Mission and Acquisition Modes:

1. Roll Sensor Data
2. Time Code Data
3. Roll Sensor and Selected
Pitch Index
4. Pitch Sensor Data
(Not present in Acquisition
Mode)

Launch Mode:
Thrust Axis Accelerometer Data

Set No. 2

Mission and Acquisition Modes:

1. Roll Sensor Data
2. Time Code Data
3. Roll Sensor and Selected
Pitch Index
4. Pitch Sensor Data
(Not present in Acquisition
Mode)

Launch Mode:
Not Available

2. Signal Characteristics

a. HOUSEKEEPING

The telemetry commutator samples 120 channels at a rate of either 15 channels per second or at a rate controlled by the command system. The commutator can be stopped at any desired point for continuous examination of data. When power is first applied to the commutator, a 1.2-second delay ensues before commutation begins. Telemetry may be requested by a standard digital command or by the transmission of a longer-than-normal enable tone. This added command capability is provided to permit the commanding of telemetry from a facility that does not possess the equipment required to generate the normal digital commands. However, if the beacons have been turned off, this emergency telemetry command has no facility to turn a beacon back on.

b. COMMAND DATA VERIFICATION

If housekeeping telemetry is not requested, command data verification from the two decoder channels has priority. In this case, the decoded data bits will be transmitted back to the ground station.

Each CDU has a data verification relay. On beacon system No. 1, only housekeeping telemetry has priority over decoder channel No. 1 data verification, which in turn has priority over decoder channel No. 2 data verification. On beacon system No. 2, the relative priorities of decoder channel No. 1 and decoder channel No. 2 data verification are reversed. The reason for interchanging priorities is to provide for data verification from the programmed decoder channels even if the other decoder generates an erroneous signal and energizes its data verification relay.

The data verification relays are nonlatching devices that are energized by the associated decoder channel when sync is detected and remain energized until the last bit of the 13-bit word is received. In addition, at the command "load programmer", the associated relay, now controlled by the programmer, remains energized until the programmer indicates that it has received a full complement of bits. Hence, should there be any spurious bits generated in the equipment between their detection and entry into the programmer, the register loads too quickly and the data verification relay is deenergized prematurely. Conversely, if a bit is lost between its generation and programmer acceptance, the programmer fails to deenergize the data verification relay, thereby indicating that erroneous data is stored in the programmer register.

c. DIGITAL SOLAR ASPECT SENSOR

The digital solar aspect sensor (DSAS) is a separate telemetry device that can modulate either one of the two 3.9-kHz subcarriers. The purpose of this device is to measure the angle between the pitch axis and the sun vector. The DSAS provides a digital readout.

d. ROLL SENSORS

The selection of either sensor No. 1 or No. 2 is performed in the vehicle dynamics subsystem. The beacon and telemetry subsystem receives either signal on the same input line. The required 3-dB bandwidth is 160 Hz. This is the largest bandwidth required by any of the attitude data signals.

e. PITCH SENSORS

There are two pitch sensors in the vehicle dynamics subsystem which require a 3-dB bandwidth of 160 Hz. This data is time-shared by ground command with the roll sensor data.

f. SOLAR PROTON MONITOR

The real-time transmission of solar proton monitor data over the beacon and telemetry link is a backup for the primary mode of transmission over the S-band playback link. In the real-time mode, the modulating signal is derived directly from the solar proton monitor electronics and not from the data format converter, as in the playback mode.

The SPM output consists of 15-pps, RB digital data. Each data frame comprises 20 words, the first word of each frame being a synchronization word with a 111000101 pattern. A data word consists of 9 bits of which the first 4 bits are the characteristic and the next 5 are the mantissa. This data modulates the 3.9 kHz VCO subcarrier of the dual SCO assembly and is transmitted to earth over the beacon and telemetry transmitter.

g. TIME CODE

The time code is a 120-bit-per-second RB digital waveform from the TBU.

3. Components

a. DIGITAL SOLAR ASPECT SENSOR

The digital solar aspect sensor comprises two separate subassemblies: the sensing unit, containing the aspect sensor, and the electronics package, as shown in Figure 2-VII-5.

(1) ASPECT SENSOR (SENSING ELEMENT)

The sensing element consists of an 8-bit Gray-coded reticle, equipped with a small solar cell under each bit, and a double-slitted "command" reticle which also includes a solar cell. The reticle is a small oblong block of fused quartz with a slit centered along the top surface, and a light mask, arranged in a Gray-coded pattern photographically applied to the bottom surface. Fused quartz is used since it does not fluoresce, discolor, or otherwise deteriorate when irradiated with ultraviolet or other forms of radiation encountered in space; its index of refraction varies less with temperature than other materials, and it has a lower linear-dimension temperature coefficient.

Sunlight enters the sensor through the slit, casting a narrow band of illumination across the light mask. The light passing through the pattern generates an 8-bit binary word, coded to indicate the angle of incidence of the light on the mask. The coding of the angle is actually contained in the first 7 bits; the eighth bit is an end-of-word bit and is always coded as a binary "1". Gray code was chosen for the light-mask pattern to reduce the effect of any errors in the synchronization of the data bits. The spacing of the Gray-coded pattern is adjusted to correct for the nonlinear relationship between sun angle and distance from the center of the pattern, and is arranged to compensate for reduction in output due to cosine-law and reflection losses at extreme angles.

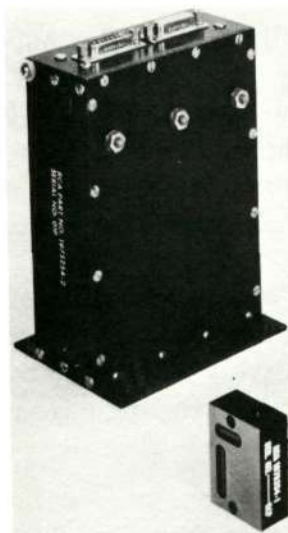


Figure 2-VII-5. Digital Solar Aspect Sensor and Associated Electronics Unit

Each of the first 7 bits on the Gray-coded reticle is superimposed on a photocell which detects the light (or notes the absence of light) in the aperture and produces a corresponding electrical output signal. N-on-P silicon solar cells are used as the photosensitive units. Although the output signal of this type of cell is relatively small (46 to 50 microamperes) and, therefore, requires amplification, the cells can readily withstand the space environment and possess uniform outputs having a linear relationship to the incidence of light. The effects of ultraviolet and Van Allen radiation are minimized since the cells are substantially shielded by the fuse-quartz block.

The command reticle with its associated photocell is used as a trigger for the aspect sensor. The unit permits the sun angle to be read out only when the sun is contained in a plane at a right angle to the slit over the Gray-coded reticle. The device consists of a reticle slitted on the top and bottom surfaces and mounted over a photocell. The slits are oriented 90 degrees to the slit in the Gray-coded reticle.

(2) ELECTRONICS PACKAGE

The electronics package contains amplifiers for each bit, an amplifier and set pulse generator for the command bit, an 8-stage shift register, a -10-volt regulator, a power turn-on generator, an oscillator, and an output buffer for generating the return-to-bias pulse train. (See RCA drawing 1976096, which can be found in a separate manual.)*

Application of the -24.5-volt power to the unit causes a ground level pulse to appear on the power on the reset line. This forces all 8 stages of the shift register, S1 through S8, to come up in the reset state. This, in turn, inhibits the 5.3-pps oscillator.

The output of each of the solar cells in the solar aspect sensor, provides a maximum signal of approximately 50 microamperes into a low impedance load. The outputs of the cells are direct-coupled into a differential amplifier for each bit. The bias network for the input requires a minimum solar cell current of 10 microamperes, prior to switching. The output of the amplifier is 0 volt for cell currents greater than 10 microamperes.

The command bit amplifier has a similar input bias network, requiring a 10-microampere cell current for state change. The command bit amplifier is a 4-stage amplifier which is capacitively coupled to the set pulse generator. A -10-volt set pulse is generated on the trailing edge of the command bit. The

*RCA Corporation, Astro Electronics Division, TIROS M/ITOS Spacecraft Logic Diagrams, AED M-2175, Contract NAS5-10306, Princeton, N.J., June 15, 1969.

set pulse simultaneously sets the S8 flip-flop and sets the remaining flip-flops where the corresponding bit amplifier is at -9 volts. The setting of the S8 flip-flop releases the inhibit of the oscillators.

The first shift pulse then resets S8 and starts the readout of the register at a 375-millisecond pulse rate. The output of the shift register and the oscillator are summed in the output buffer to produce the return-to-bias pulse train. After eight pulses have been shifted through the register, all flip-flops are again in the reset state and the oscillator is inhibited. The logic elements remain in this state until the trailing edge of the next command bit.

The Gray-coded binary outputs of the DSAS, for the complete range of measurable sun angles from 26.5 degrees to 153.5 degrees, with a 1-degree resolution, is shown in Table 2-VII-2.

b. ACCELEROMETER CONTROL UNIT (ACU)

The accelerometer control unit comprises the accelerometer bias circuits which includes three RC filters, three voltage dividers, and one armature relay. It is designed to filter and bias the outputs of two accelerometers so that the levels of the signal outputs are within the nominal range of the telemetry signals supplied to the subcarrier oscillators (SCO's) of beacon transmitter No. 1. Figure 2-VII-6 is a block diagram and Figure 2-VII-7 is a schematic diagram of the ACU.

The bias and filter circuits of the ACU are designed to provide the following volts per G accelerometer outputs.

- Lateral accelerometer output: bias is -2.5 volts; -5 volts for +4 G and 0 volt for -4 G along either the Y-Y axis or the X-X axis.
- Thrust accelerometer output: bias is -4.0 volts; 0 volt for +16 G and -5 volts for -4 G along the thrust axis.

Only two accelerometers are used, although there are three mounting positions on the accelerometer mount, because there are only two SCO's in the existing system for handling the incoming signals from the CDU. Once a particular mission is defined, the two accelerometers can be mounted in two of the three possible positions to provide the desired lateral-lateral or lateral-thrust acceleration information to the SCO's. By proper arrangement, any one of the following four possible combinations of lateral-lateral and lateral-thrust acceleration information for the SCO's can be effected:

- Lateral-Lateral (Y-Y axis and X-X axis). One of the two accelerometers provides Y-Y axis acceleration data to modulate the 3.9-kHz SCO 1-2 which has a bandwidth of 59 Hz. The

TABLE 2-VII-2. GRAY CODE OUTPUTS OF DIGITAL SOLAR ASPECT SENSOR (DSAS) AND CORRESPONDING SUN ANGLES

Gray Code								Sun Angle (degrees)	
Angle							E-O-W		
LSB	1	2	3	4	5	6			7
1	2	3	4	5	6	7	8		
0	0	0	0	0	0	0	0	1	26.5
1	0	0	0	0	0	0	0	1	27.5
1	1	0	0	0	0	0	0	1	28.5
0	1	0	0	0	0	0	0	1	29.5
0	1	1	0	0	0	0	0	1	30.5
1	1	1	0	0	0	0	0	1	31.5
1	0	1	0	0	0	0	0	1	32.5
0	0	1	0	0	0	0	0	1	33.5
0	0	1	1	0	0	0	0	1	34.5
1	0	1	1	0	0	0	0	1	35.5
1	1	1	1	0	0	0	0	1	36.5
0	1	1	1	0	0	0	0	1	37.5
0	1	0	1	0	0	0	0	1	38.5
1	1	0	1	0	0	0	0	1	39.5
1	0	0	1	0	0	0	0	1	40.5
0	0	0	1	0	0	0	0	1	41.5
0	0	0	1	1	0	0	0	1	42.5
1	0	0	1	1	0	0	0	1	43.5
1	1	0	1	1	0	0	0	1	44.5
0	1	0	1	1	0	0	0	1	45.5
0	1	1	1	1	0	0	0	1	46.5
1	1	1	1	1	0	0	0	1	47.5
1	0	1	1	1	0	0	0	1	48.5
0	0	1	1	1	0	0	0	1	49.5
0	0	1	0	1	0	0	0	1	50.5
1	0	1	0	1	0	0	0	1	51.5
1	1	1	0	1	0	0	0	1	52.5
0	1	1	0	1	0	0	0	1	53.5
0	1	0	0	1	0	0	0	1	54.5
1	1	0	0	1	0	0	0	1	55.5
1	0	0	0	1	0	0	0	1	56.5
0	0	0	0	1	0	0	0	1	57.5
0	0	0	0	1	1	0	0	1	58.5
1	0	0	0	1	1	0	0	1	59.5

Gray Code								Sun Angle (degrees)	
Angle							E-O-W		
LSB	1	2	3	4	5	6			7
1	2	3	4	5	6	7	8		
1	1	0	0	1	1	0	1	1	60.5
0	1	0	0	1	1	0	1	1	61.5
0	1	1	0	1	1	0	1	1	62.5
1	1	1	0	1	1	0	1	1	63.5
1	0	1	0	1	1	0	1	1	64.5
0	0	1	0	1	1	0	1	1	65.5
0	0	1	1	1	1	0	1	1	66.5
1	0	1	1	1	1	0	1	1	67.5
1	1	1	1	1	1	0	1	1	68.5
0	1	1	1	1	1	0	1	1	69.5
0	1	0	1	1	1	0	1	1	70.5
1	1	0	1	1	1	0	1	1	71.5
1	0	0	1	1	1	0	1	1	72.5
0	0	0	1	1	1	0	1	1	73.5
0	0	0	1	0	1	0	1	1	74.5
1	0	0	1	0	1	0	1	1	75.5
1	1	0	1	0	1	0	1	1	76.5
0	1	0	1	0	1	0	1	1	77.5
0	1	1	1	0	1	0	1	1	78.5
1	1	1	1	0	1	0	1	1	79.5
1	0	1	1	0	1	0	1	1	80.5
0	0	1	1	0	1	0	1	1	81.5
0	0	1	0	0	1	0	1	1	82.5
1	0	1	0	0	1	0	1	1	83.5
1	1	1	0	0	1	0	1	1	84.5
0	1	1	0	0	1	0	1	1	85.5
0	1	0	0	0	1	0	1	1	86.5
1	1	0	0	0	1	0	1	1	87.5
1	0	0	0	0	1	0	1	1	88.5
0	0	0	0	0	1	0	1	1	89.5
0	0	0	0	0	1	1	1	1	90.5
1	0	0	0	0	1	1	1	1	91.5
1	1	0	0	0	1	1	1	1	92.5
0	1	0	0	0	1	1	1	1	93.5

TABLE 2-VII-2. GRAY CODE OUTPUTS OF DIGITAL SOLAR ASPECT SENSOR (DSAS) AND CORRESPONDING SUN ANGLES (Continued)

Gray Code								Sun Angle (degrees)
Angle							E-O-W 8	
LSB 1	2	3	4	5	6	7		
0	1	1	0	0	1	1	1	94.5
1	1	1	0	0	1	1	1	95.5
1	0	1	0	0	1	1	1	96.5
0	0	1	0	0	1	1	1	97.5
0	0	1	1	0	1	1	1	98.5
1	0	1	1	0	1	1	1	99.5
1	1	1	1	0	1	1	1	100.5
0	1	1	1	0	1	1	1	101.5
0	1	0	1	0	1	1	1	102.5
1	1	0	1	0	1	1	1	103.5
1	0	0	1	0	1	1	1	104.5
0	0	0	1	0	1	1	1	105.5
0	0	0	1	1	1	1	1	106.5
1	0	0	1	1	1	1	1	107.5
1	1	0	1	1	1	1	1	108.5
0	1	0	1	1	1	1	1	109.5
0	1	1	1	1	1	1	1	110.5
1	1	1	1	1	1	1	1	111.5
1	0	1	1	1	1	1	1	112.5
0	0	1	1	1	1	1	1	113.5
0	0	1	0	1	1	1	1	114.5
1	0	1	0	1	1	1	1	115.5
1	1	1	0	1	1	1	1	116.5
0	1	1	0	1	1	1	1	117.5
0	1	0	0	1	1	1	1	118.5
1	1	0	0	1	1	1	1	119.5
1	0	0	0	1	1	1	1	120.5
0	0	0	0	1	1	1	1	121.5
0	0	0	0	1	0	1	1	122.5
1	0	0	0	1	0	1	1	123.5

Gray Code								Sun Angle (degrees)
Angle							E-O-W 8	
LSB 1	2	3	4	5	6	7		
1	1	0	0	1	0	1	1	124.5
0	1	0	0	1	0	1	1	125.5
0	1	1	0	1	0	1	1	126.5
1	1	1	0	1	0	1	1	127.5
1	0	1	0	1	0	1	1	128.5
0	0	1	0	1	0	1	1	129.5
0	0	1	1	1	0	1	1	130.5
1	0	1	1	1	0	1	1	131.5
1	1	1	1	1	0	1	1	132.5
0	1	1	1	1	0	1	1	133.5
0	1	0	1	1	0	1	1	134.5
1	1	0	1	1	0	1	1	135.5
1	0	0	1	1	0	1	1	136.5
0	0	0	1	1	0	1	1	137.5
0	0	0	1	0	0	1	1	138.5
1	0	0	1	0	0	1	1	139.5
1	1	0	1	0	0	1	1	140.5
0	1	0	1	0	0	1	1	141.5
0	1	1	1	0	0	1	1	142.5
1	1	1	1	0	0	1	1	143.5
1	0	1	1	0	0	1	1	144.5
0	0	1	1	0	0	1	1	145.5
0	0	1	0	0	0	1	1	146.5
1	0	1	0	0	0	1	1	147.5
1	1	1	0	0	0	1	1	148.5
0	1	1	0	0	0	1	1	149.5
0	1	0	0	0	0	1	1	150.5
1	1	0	0	0	0	1	1	151.5
1	0	0	0	0	0	1	1	152.5
0	0	0	0	0	0	1	1	153.5

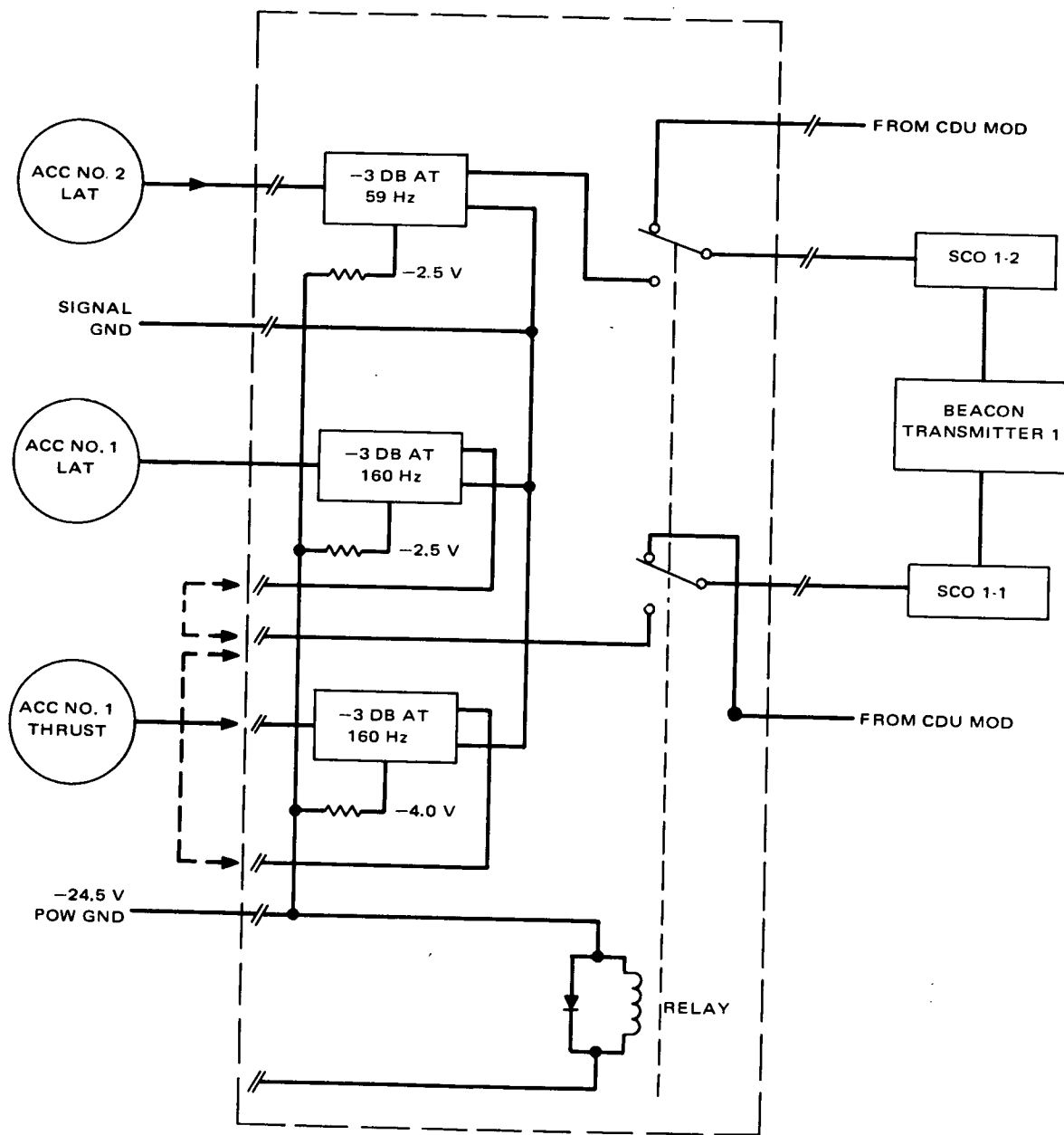


Figure 2-VII-6. Accelerometer Control Unit, Block Diagram

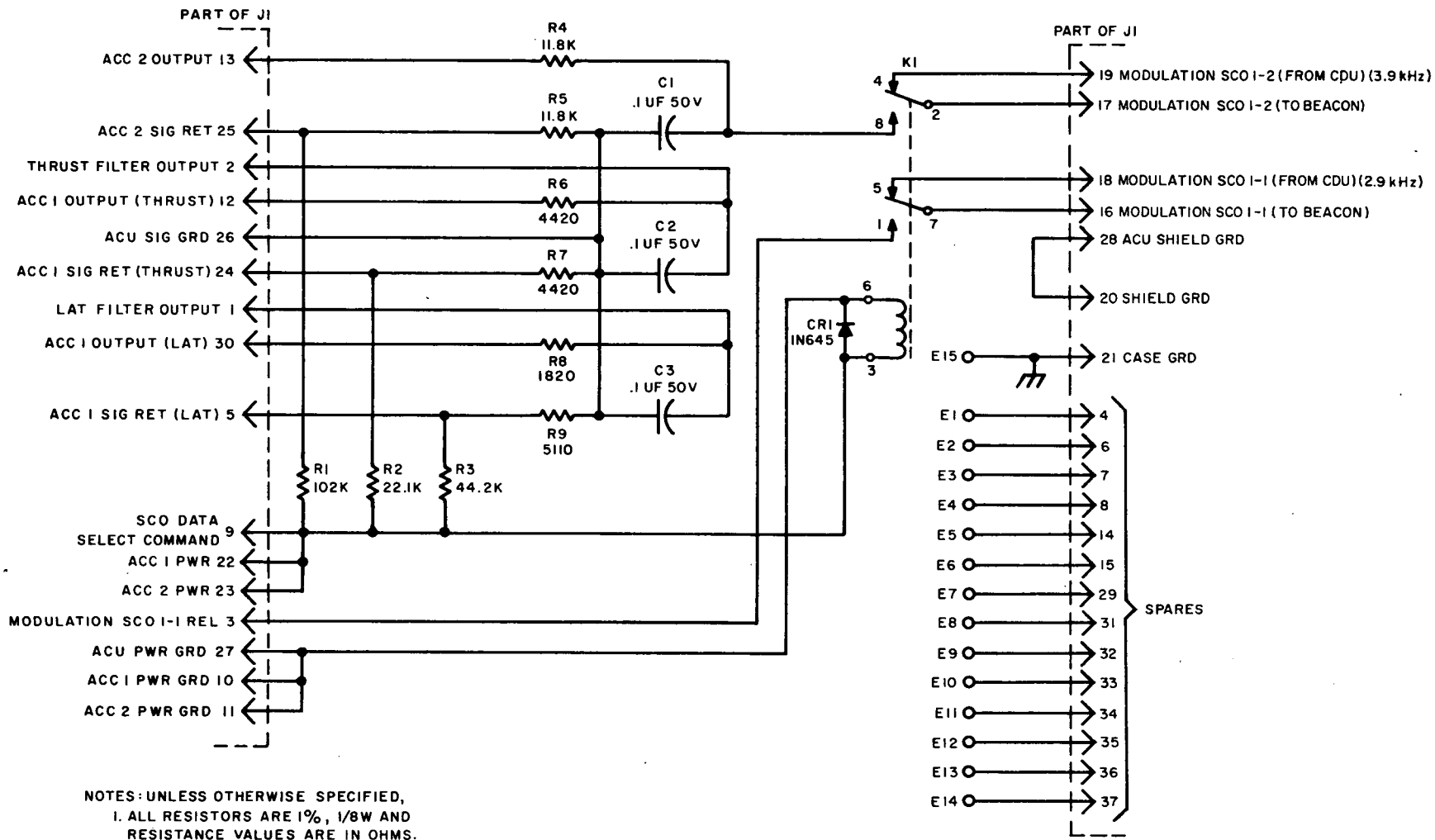


Figure 2-VII-7. Accelerometer Control Unit, Schematic Diagram

other accelerometer provides X-X axis acceleration data to modulate the 2.3-kHz SCO 1-1 which has a bandwidth of 160 Hz by external strapping of the correspondent output filter pin to the relay contact on the harness as shown in Figure 2-VII-6.

- Lateral-Lateral (X-X axis and Y-Y axis). Same arrangement as above except the Y-Y axis acceleration data modulates the wider bandwidth SCO 1-1.
- Lateral-Thrust (Y-Y axis and Z-Z axis). One accelerometer provides Y-Y axis acceleration data to SCO 1-2 and external strapping will provide thrust (or Z-Z axis) information to modulate SCO 1-1.
- Lateral-Thrust (X-X axis and Z-Z axis). Same arrangement as above except one accelerometer provides X-X axis acceleration data to modulate SCO 1-2 and Z-Z axis data still modulates SCO 1-1.

After separation from the 2nd stage the armature relay of the ACU is released allowing the signals from the command distribution unit to bypass the bias and filter circuits and go directly to the respective SCO's.

c. SIGNAL CONDITIONER AND TELEMETRY COMMUTATOR UNIT

(1) GENERAL DESCRIPTION

The signal conditioner and telemetry commutator unit accepts information signals from the telemetry points in the spacecraft, conditions them to satisfy commutator input requirements, samples them in a fixed sequence at a uniform rate, and delivers the resulting PAM time-multiplexed signal to the spacecraft command distribution unit. It also provides required calibration signals.

The conditioner and commutator circuit housing is 4.50 by 8.12 by 6.50 inches and has a nominal weight of 7.6 pounds.

The signal conditioning unit receives control and telemetry inputs; inputs which deviate from the standard levels are processed as necessary for use by the commutator. Selected inputs from redundant sources are combined to provide a single input to the commutators. The conditioning unit provides buffered test-point outputs for selected telemetry signals and generates (1) calibration voltages, from the commutator -4.5-volt reference output, and (2) -5.0-volt markers, from the -24.5-volt power supply input. These signals are delivered to appropriate channels of each commutator.

The commutators are provided with separate control power inputs; telemetry inputs are commutated synchronously with the clock inputs. Upon application of power, the selected commutator resets to its initial start position for 1.2 seconds, then steps to telemetry channel No. 1 and remains there until clock signals are present.

Sequential sampling of the 120 channels is done in the selected solid-state commutator. The input to the commutator is accomplished through input gating circuits, consisting of 8 groups of gate buffer circuits which include an initial start gate. The first group is composed of 16 input signal gates and the initial gate. The next 6 groups consist of 16 signal input gates. The eighth group consists of 8 signal input gates plus 1 gate which is returned to signal ground; this latter gate establishes zero output during the frame period. Each of the above groups is served by individual constant current source and buffer circuit which contain positive and negative overvoltage signal limiting features.

There are three output circuits in each commutator:

- The output of the individual input buffers are fed to a common output buffer which provides a low impedance PAM output.
- A frame pulse generating circuit provides an output pulse of approximately -18 volts which occurs during channel 121 time slot. The pulse enables a relay driver in the CDU to remove power from the telemetry commutator.
- A regulated -4.5-volt output is provided for use as a reference for establishing the four calibration voltages.

(2) DESIGN HISTORY

The basic design of the signal conditioner and telemetry commutators has been taken from those used on TIROS 9, ESSA 1, and all TOS (ESSA) spacecraft. The former units utilized 90-channel solid-state commutators, and the conditioners incorporated calibration voltages, marker voltages, AGC amplifiers, and various buffer circuits. Similar circuitry is utilized in the 120-channel device designed for ITOS. Packaging of the 120-channel signal conditioner and telemetry commutators differs considerably from that used on TOS. The signal conditioner makes use of four wired circuit boards, allowing for circuit changes if required. There is no interconnecting wiring between these boards.

Each commutator is equipped with four 37-pin connectors. The commutators are mounted on the baseplate and each conditioner board mates with one of the four connectors in both commutators.

(3) *FUNCTIONAL OPERATION*

The conditioning signals applied to the signal conditioner are listed in Table 2-VII-3. The inputs for channels 1, 2, 3, and 4 for commutators I and II originate from a -4.5-volt regulated output from the respective commutator power supplies. Voltage dividers on board A1 of the signal conditioner produce the appropriate output voltages listed in Table 2-VII-4. The 5.0-volt marker pulse output is derived from the voltage dividers on each board (see RCA 1976096, sheets 2, 3, 4, and 5, for boards A1, A2, A3, and A4, respectively) and originate from the regulated supply. These occur every 10 channels, from channel 10 to channel 120 for both commutators.

Regulated power (-24.5 volts) is applied simultaneously to command receiver No. 1 and No. 2 AGC processing circuit, on board A1, and the appropriate commutator power supply.

The conditioner provides buffering, as required, to each of the 120 channels of commutated data as follows:

- Externally conditioned signals. Eighty-nine external telemetry signals do not require conditioning and are wired directly to their respective commutator gates.
- Unconditioned signals. Two command receiver AGC signals are amplified in the conditioner.
- Diode OR'ed signals. There are seven groups of diode OR'ed signals developed from fourteen signals.
- Resistively OR'ed signals. One group of two external three-level signals resistively OR'ed to provide an output signal of half the input signal.
- Twelve external two-level signals are formed into six groups (two signals each), each group being resistively combined to produce a single four-level signal.

In addition the conditioner generates four calibration signals and 11 marker signals. The four calibration signals are generated from the -4.5-volt signal present in the powered commutator. The nominal calibration voltages are -0.5, -1.5, -3.5, and -4.5 volts. The eleven marker channels are channel 10 and every subsequent tenth channel. The marker voltage is a nominal -5.0 volts, which is generated from a voltage divider tied to the -24.5-volt regulated bus.

Since the operation and circuitry of the two redundant commutators are identical, only one will be described. A simplified block diagram of one commutator is shown on Figure 2-VII-8.

TABLE 2-VII-3. EXTERNAL AND INTERNAL TELEMETRY SIGNALS

Channel	Signal	Channel	Signal	Channel	Signal	Channel	Signal
1	A	31	E	61	E	91	E
2	B	32	E	62	E	92	E
3	C	33	E	63	E	93	E
4	D	34	E	64	E	94	I
5	E	35	E	65	E	95	I
6	E	36	E	66	E	96	I
7	F	37	E	67	E	97	I
8	F	38	E	68	E	98	E
9	G	39	E	69	E	99	E
10	H	40	H	70	H	100	H
11	E	41	E	71	E	101	E
12	E	42	E	72	E	102	E
13	E	43	E	73	E	103	E
14	E	44	G	74	E	104	I
15	E	45	E	75	E	105	G
16	E	46	E	76	E	106	K
17	E	47	E	77	E	107	E
18	E	48	E	78	I	108	G
19	E	49	E	79	E	109	E
20	H	50	H	80	H	110	H
21	E	51	E	81	E	111	E
22	E	52	E	82	I	112	E
23	E	53	G	83	E	113	E
24	E	54	E	84	E	114	E
25	E	55	G	85	E	115	E
26	E	56	E	86	E	116	E
27	E	57	E	87	E	117	E
28	E	58	E	88	E	118	E
29	E	59	E	89	E	119	E
30	H	60	H	90	H	120	E

NOTES:

- A. Internally generated calibration voltage: -0.5 volt.
- B. Internally generated calibration voltage: -1.5 volts for commutator I and -3.5 volts for commutator II.
- C. Internally generated calibration voltage: -3.5 volts for commutator I and -1.5 volts for commutator II.
- D. Internally generated calibration voltage: -4.5 volts.
- E. External signal not conditioned.
- F. External signal from the dual command receiver AGC; conditioned internally.
- G. Two external two-level signals; combined internally into one four-level signal.
- H. Internally generated marker voltage: -5.0 volts.
- I. Two external signals on separate input lines only one of which exists at any time; combined internally by diode OR circuit.
- K. Two external signals on separate input lines only one of which exists at any time; combined internally by resistive circuit.

TABLE 2-VII-4. HOUSEKEEPING TELEMETRY DATA POINT CHARACTERISTICS

Ch. No. (Frame Word)	Function	Type	Nominal Value or Typical Function (volts, unless marked otherwise)	Tolerance On Calibration Book Data	Notes															
1	Calibration	Analog	-0.500	(Negligible) ±0.001																
2 3	Calibration	Analog	-1.500	(Negligible) ±0.002	Commutator 1 contains -1.5 volts in channel 2 and -3.5 volts in channel 3; commutator 2 containing -3.5 volts in channel 2 and -1.5 volts in channel 3.															
3 2	Calibration	Analog	-3.500	(Negligible) ±0.002																
4	Calibration	Analog	-4.500	(Negligible) ±0.002																
5	Satellite Identification	Fixed, digital	See note.	±4 percent	The following sequence will be assigned to the ITOS spacecraft: S/C: <table border="1" style="display: inline-table; vertical-align: middle;"> <tr> <td>M</td> <td>A</td> <td>B</td> <td>C</td> <td>D</td> </tr> <tr> <td>-0.9</td> <td>-1.8</td> <td>-2.7</td> <td>-3.6</td> <td>-4.5</td> </tr> </table> V: <table border="1" style="display: inline-table; vertical-align: middle;"> <tr> <td>-0.9</td> <td>-1.8</td> <td>-2.7</td> <td>-3.6</td> <td>-4.5</td> </tr> </table>	M	A	B	C	D	-0.9	-1.8	-2.7	-3.6	-4.5	-0.9	-1.8	-2.7	-3.6	-4.5
M	A	B	C	D																
-0.9	-1.8	-2.7	-3.6	-4.5																
-0.9	-1.8	-2.7	-3.6	-4.5																
6	DFC Track 3 Data (Eng'g Evaluation Test Point)	Multi- level; digital	Data 1: 0 Bias: -1.5 Data 0: -3.0	+0, -0.5 ±0.5 ±0.5	This channel, when used in the "Manual TLM" mode, monitors the DFC output to track 3 of the ITR (FPR, time code and digital telemetry). In the "Automatic TLM" mode, both the bias and the "1" or "0" levels appear during one channel sample.															
7	Command Receiver No. 1 AGC	Analog		See note.	This point serves as a coarse check on signal input to the receiver. It should be treated as a go/no-go indication.															
8	Command Receiver No. 2 AGC	Analog		See note for channel 7.																
9	Decoder Selection	Multi- level; digital	0 -0.9 -2.7	+0, -0.1 ±0.1 ±0.2	Neither decoder selected. Decoder 2 selected. Decoder 1 selected.															

TABLE 2-VII-4. HOUSEKEEPING TELEMETRY DATA POINT CHARACTERISTICS (Continued)

Ch. No. (Frame Word)	Function	Type	Nominal Value or Typical Function (volts, unless marked otherwise)	Tolerance On Calibration Book Data	Notes
10	Marker	Fixed, digital	-4.9	±0.1	
11	Solar Panel No. 1 Current	Analog	$I = \frac{(V_{TLM} + 0.27)}{0.76}$	±3 percent	V_{TLM} is the measured negative telemetry voltage, yielding a negative current reading, valid for: $-4.45 \leq V_{TLM} \leq -0.4$.
12	Solar Panel No. 2 Current	Analog	See channel 11.		
13	Solar Panel No. 3 Current	Analog	See channel 11.		
14	Solar Array Voltage	Analog	$V_{ARRAY} = \frac{(V_{TLM} - 4.21)}{0.22}$	±2 percent	V_{TLM} is the measured negative telemetry voltage, yielding a negative current reading, valid for: $-4.58 \leq V_{TLM} \leq -0.6$.
15	Unregulated Bus Voltage	Analog	See note.		The same type of circuit is used for this point as for channel 14.
16	Regulated Bus Voltage	Analog	$B_{BUS} = \frac{(V_{TLM} - 2.47)}{0.198}$	±2 percent	V_{TLM} is the measured negative telemetry voltage, yielding a negative voltage reading, valid for: $-4.45 \leq V_{TLM} \leq -0.5$.
17	Shunt Dissipator Current	Analog	$I = \frac{(V_{TLM} + 0.47)}{0.28}$	±15 percent	V_{TLM} is the measured negative telemetry voltage, yielding a negative current reading, valid for: $-4.5 \leq V_{TLM} \leq -0.5$.
18	Shunt Limiter Control Amplifier and Mode Selection	Multi- level; digital	-1.8 -2.7 -3.7 -4.5	±0.1 ±0.2 ±0.2 ±0.2	Control amplifier No. 1 and mode 1 Control amplifier No. 2 and mode 1 Control amplifier No. 1 and mode 2 Control amplifier No. 2 and mode 2
19	-24.5 V Regulator Selection and Charging Mode	Multi- level; digital	-1.8 -2.8 -3.7 -4.4	±0.1 ±0.2 ±0.2 ±0.2	"Regulator No. 1 and Trickle Charge" mode* "Regulator No. 1 and Normal Charge" mode* "Regulator No. 2 and Trickle Charge" mode* "Regulator No. 2 and Normal Charge" mode*

*The indications of charge mode on channel 19 are valid only if the solar array bus voltage (channel 14) is more negative than -26 Vdc. Indications of regulator selection are, however, always valid.

TABLE 2-VII-4. HOUSEKEEPING TELEMETRY DATA POINT CHARACTERISTICS (Continued)

Ch. No. (Frame Word)	Function	Type	Nominal Value or Typical Function (volts, unless marked otherwise)	Tolerance On Calibration Book Data	Notes
20	Marker	Fixed digital	-4.9	±0.1	
21	Shunt Limiter No. 1 Dissipator Tempera- ture	Analog	$T = -2.841 (V_{TLM})^3$ $-19.10 (V_{TLM})^2$ $-66.05 V_{TLM} - 70.88$	±5°C	V_{TLM} is the measured negative telemetry voltage, yielding a reading in degrees Centigrade, valid for: $-4.5 \leq V_{TLM} \leq -0.1$.
22	Shunt Limiter No. 2 Dissipator Tempera- ture	Analog	See channel 21.		
23	Shunt Limiter No. 3 Dissipator Tempera- ture	Analog	See channel 21		
24	Battery No. 1 Voltage	Analog	$V_{BATT} = \frac{(V_{TLM} - 4.13)}{0.218}$	±2 percent	V_{TLM} is the measured negative telemetry voltage, yielding a negative voltage reading in volts, valid for: $-4.65 \leq V_{TLM} \leq -0.6$.
25	Battery No. 1 Charge Current	Analog	$I_{CHG} = \frac{(V_{TLM} + 3.395)}{0.406}$	±2 percent	V_{TLM} is measured negative telemetry voltage, yielding a negative current in amperes, valid for: $-4.35 \leq V_{TLM} \leq -0.5$.
26	Battery No. 1 Temperature	Analog	$T = 1.481 (V_{TLM})^2 - 25.19 V_{TLM}$ -36.29	±2°C	V_{TLM} is the measured negative telemetry voltage, yielding a reading in degrees Centigrade, valid for: $-5.0 \leq V_{TLM} \leq 1.0$.
27	Battery No. 2 Voltage	Analog	See channel 24.		
28	Battery No. 2 Charge Current	Analog	See channel 25.		
29	Battery No. 2 Temperature	Analog	See channel 26.		
30	Marker	Fixed digital	-4.9	±0.1	

TABLE 2-VII-4. HOUSEKEEPING TELEMETRY DATA POINT CHARACTERISTICS (Continued)

Ch. No. (Frame Word)	Function	Type	Nominal Value or Typical Function (volts, unless marked otherwise)	Tolerance On Calibration Book Data	Notes
31	Solar Panel No. 1 Temperature	Analog	$T = -3.501 (V_{TLM})^3 - 23.7 (V_{TLM})^2 - 71.29 V_{TLM} - 102.6$	$\pm 5^\circ C$	V_{TLM} is the measured negative telemetry voltage, yielding a reading in degrees Centigrade, valid for: $-4.7 \leq V_{TLM} \leq 0$.
32	Solar Panel No. 2 Temperature	Analog	See channel 31.		
33	Solar Panel No. 3 Temperature	Analog	See channel 31.		
34	Programmer No. 1 Picture Status	Multi- level; digital	0 -0.9 -1.8 -2.7 -3.6	+0, -0.3 ± 0.3 ± 0.3 ± 0.3 ± 0.3	Off. Standby. Counting T_0 delay. Counting "day" portion of orbit. Counting "night" portion of orbit.
35	Programmer No. 2 Picture Status	Multi- level; digital	See channel 34.		
36	QOMAC; Programmer No. 1 or No. 2 Status	Multi- level; digital	-0.9 -1.8 -2.7 -3.6 -4.5	± 0.2 ± 0.3 ± 0.3 ± 0.3 ± 0.3	Standby (normal or unipolar QOMAC). Counting T_0 (normal QOMAC). Counting quarter orbit (normal QOMAC). Counting T_0 (unipolar QOMAC). Counting quarter orbit (unipolar QOMAC). The selection of the programmer in use is indicated by the power status of channels 34 and 35.

TABLE 2-VII-4. HOUSEKEEPING TELEMETRY DATA POINT CHARACTERISTICS (Continued)

Ch. No. (Frame Word)	Function	Type	Nominal Value or Typical Function (volts, unless marked otherwise)	Tolerance On Calibration Book Data	Notes
37	SR Control; Pro- grammer No. 1 or Status	Multi- level; digital	-1.5	± 0.3	Record and enable real-time SR during night only.
			-2.4	± 0.3	Record and enable real-time SR during night and record SR during day.
			-3.3	± 0.3	Record and enable real-time SR during night and enable real-time SR during day.
			-4.1	± 0.3	Record and enable real-time SR during night and day. The selection of the programmer in use is indicated by the status of channels 34 and 35.
38	QOMAC; Power and Mode Status	Multi- level; digital	0	+0, -0.1	QOMAC power OFF, "Low Torque" mode.
			-0.9	± 0.1	QOMAC power OFF, "High Torque" mode.
			-1.8	± 0.2	QOMAC power ON, "Low Torque" mode.
			-2.7	± 0.2	QOMAC power ON, "High Torque" mode.
39	Mag Bias Power and Polarity	Multi- level; digital	0	+0, -0.1	Mag bias power OFF, positive.
			-0.9	± 0.1	Mag bias power OFF, negative.
			-1.8	± 0.2	Mag bias power ON, positive.
			-2.7	± 0.2	Mag bias power ON, negative.
40	Marker	Fixed digital	-4.9	± 0.1	
41	Mag Bias Switch Position	Multi- level; digital	-0.6	± 0.1	Position 1.
			-1.0	± 0.1	Position 2.
			-1.4	± 0.1	Position 3.
			-1.8	± 0.1	Position 4.
			-2.2	± 0.1	Position 5.
			-2.6	± 0.1	Position 6.
			-3.0	± 0.1	Position 7.
-3.4	± 0.1	Position 8.			

TABLE 2-VII-4. HOUSEKEEPING TELEMETRY DATA POINT CHARACTERISTICS (Continued)

Ch. No. (Frame Word)	Function	Type	Nominal Value or Typical Function (volts, unless marked otherwise)	Tolerance On Calibration Book Data	Notes
41 (cont)			-3.8 -4.2 -4.6 -5.0	± 0.1 ± 0.1 ± 0.1 ± 0.1	Position 9. Position 10. Position 11 (high torque enable). Position 12 (home).
42	Momentum Coil No. 1 Status	Multi- level; digital	0 -2.8 -3.4 -4.7	+0, -0.1 ± 0.2 ± 0.2 ± 0.2	Coil No. 1 ON, positive. Coil No. 1 OFF, positive. Coil No. 1 OFF, negative. Coil No. 1 ON, negative.
43	Momentum Coil No. 2 Status	Multi- level; digital	See Channel 42.		
44	Time Base Unit and Beacon Xmtr Selec- tion	Multi- level; digital	0 -0.9 -2.7 -3.6	+0, -0.1 ± 0.1 ± 0.2 ± 0.2	Time base unit No. 1 and beacon xmtr No. 1. Time base unit No. 2 and beacon xmtr No. 1. Time base unit No. 1 and beacon xmtr No. 2. Time base unit No. 2 and beacon xmtr No. 2.
45	DFC Status	Multi- level; digital	0 -1.8 -3.7 -4.8	+0, -0.1 ± 0.2 ± 0.2 ± 0.2	DFC OFF. Operation in "Record Data" mode. Operation in "Playback Data" mode. Standby.
46	ITR Status	Multi- level; digital	0 -1.8 -2.7 -3.6 -4.5	+0, -0.1 ± 0.2 ± 0.2 ± 0.2 ± 0.2	ITR OFF. Operating in "Record" mode.* Standby.* Operating in "Playback" mode. Playback enabled.
*When ITR is in "Record" mode, both -1.8 and -2.7 volts appear during sample time of one houskeeping channel.					

TABLE 2-VII-4. HOUSEKEEPING TELEMETRY DATA POINT CHARACTERISTICS (Continued)

Ch. No. (Frame Word)	Function	Type	Nominal Value or Typical Function (volts, unless marked otherwise)	Tolerance On Calibration Book Data	Notes
47	IIR Pressure	Analog	$P = \frac{V_{TLM}}{(-0.2)}$	±2 percent	V_{TLM} is the measured negative telemetry voltage, yielding the pressure in psia, valid for: $-5.0 \leq V_{TLM} \leq 0$.
48	SPM Output Power	Analog	0.15 -4.5	±0.3 ±0.3	SPM OFF. SPM ON.
49	FPR Status	Multi- level; digital	0 -2.5 -3.5	+0, -0.1 ±0.2 ±0.3	FPR OFF. FPR ON in "Data" mode. FPR ON in "Calibrate" mode.
50	Marker	Fixed; digital	-4.9	±0.1	
51	Real-Time Xmtr SR Day Data Selection	Multi- level; digital	0 -2.7	+0, -0.1 ±0.2	Visible SR data selected for day. IR SR data selected for day.
52	"Real-Time Xmtr Operation" Mode Selection	Multi- level; digital	0 -2.7	+0, -0.1 ±0.2	Real-time transmission in day only. Real-time transmission in day and night.
53	SR Processor Status	Multi- level; digital	0 -0.9 -2.7	+0, -0.1 ±0.1 ±0.2	Neither SR processor ON. SR processor No. 2 ON. SR processor No. 1 ON.
54	SR Selection	Multi- level; digital	0 -0.9 -1.8	+0, -0.1 ±0.1 ±0.2	Neither SR selected. SR No. 1 selected. SR No. 2 selected.
55	MWA Motor Brush Reserve	Analog	$W = -10.0 (V_{TLM}) + 5.0$	±1.5 mils	V_{TLM} is the measured negative voltage representing the amount of brush wear in mils from the initial dimension established during spacecraft integration. When commutator 1 is used, the indication is for MWA motor 1; when commutator 2 is used, the indication is for MWA motor 2.
56	SR No. 1 Scan Detector	Analog	0 -3.4 -4.0	+0, -0.1 ±0.4 ±0.5	Mirror not rotating. Mirror rotating from backup power only. Normal motor power applied, mirror rotating.

TABLE 2-VII-4. HOUSEKEEPING TELEMETRY DATA POINT CHARACTERISTICS (Continued)

Ch. No. (Frame Word)	Function	Type	Nominal Value or Typical Function (volts, unless marked otherwise)	Tolerance On Calibration Book Data	Notes
57	SR No. 2 Scan Detector	Analog	See Channel 56.		
58	SR No. 1 Housing Temperature "A"	Analog	$T = -0.98 (V_{TLM})^3 - 6.68 (V_{TLM})^2 - 31.22 V_{TLM} - 34.41$	$\pm 2^\circ C$	V_{TLM} is the measured negative telemetry voltage, yielding a temperature reading in degrees Centigrade, valid for: $-3.9 \leq V_{TLM} \leq -1.2$.
59	SR No. 2 Housing Temperature "A"	Analog	See channel 58.		
60	Marker	Fixed, digital	-4.9	± 0.1	
61	SRR Selection	Multi- level; digital	0 -0.9 -1.8 -2.7	+0, -0.1 ± 0.1 ± 0.2 ± 0.2	Neither SRR selected. SRR No. 1 selected, No. 2 not selected. SRR No. 2 selected, No. 1 not selected. Both SRR No. 1 and No. 2 selected.
62	SRR No. 1 Status	Multi- level; digital	0 -0.9 -1.8 -2.7 -3.6	+0, -0.1 ± 0.1 ± 0.2 ± 0.2 ± 0.2	OFF. Standby. Operating, in record mode. Operating, in playback mode. Operating, in playback mode while also being commanded to record.
63	SRR No. 1 Motor Current	Analog	$I = \frac{V_{TLM} + 0.5}{6.2}$	± 10 percent	V_{TLM} is the measured negative telemetry voltage, yielding a negative motor current in amperes, valid for: $-5.0 \leq V_{TLM} \leq -0.5$. Nominal record current = 25 ma. Nominal playback current = 150 ma.
64	SRR No. 1 Pressure	Analog	See channel 47.		

TABLE 2-VII-4. HOUSEKEEPING TELEMETRY DATA POINT CHARACTERISTICS (Continued)

Ch. No. (Frame Word)	Function	Type	Nominal Value or Typical Function (volts, unless marked otherwise)	Tolerance On Calibration Book Data	Notes
65	SRR No. 1 Temperature	Analog	$T = -0.799 (V_{TLM})^3 - 7.46 (V_{TLM})^2 - 34.03 V_{TLM} - 28.82$	$\pm 2^\circ\text{C}$	V_{TLM} is the measured negative telemetry voltage, yielding the temperature reading in degrees Centigrade, valid for: $-5.0 \leq V_{TLM} \leq 0$.
66	SRR No. 2 Status	Multi-level; digital	See channel 62.		
67	SRR No. 2 Motor Current	Analog	See channel 63.		
68	SRR No. 2 Pressure	Analog	See channel 47.		
69	SRR No. 2 Temperature	Analog	See channel 65.		
70	Marker	Fixed, digital	-4.9	± 0.1	
71	AVCS Recorder Selection	Multi-level; digital	0 -0.9 -1.8	+0, -0.1 ± 0.1 ± 0.2	Neither AVCS recorder selected. AVCS recorder No. 1 selected. AVCS recorder No. 2 selected.
72	AVCS Recorder No. 1 Status	Multi-level; digital	0 -0.9 -1.8 -2.7	+0, -0.1 ± 0.1 ± 0.2 ± 0.2	Off. AVCS recorder No. 1 ON, standby. AVCS recorder No. 1 in "Record" mode. AVCS recorder No. 1 in "Playback" mode.
73	AVCS Recorder No. 2 Status	Multi-level; digital	See channel 72.		

TABLE 2-VII-4. HOUSEKEEPING TELEMETRY DATA POINT CHARACTERISTICS (Continued)

Ch. No. (Frame Word)	Function	Type	Nominal Value or Typical Function (volts, unless marked otherwise)	Tolerance On Calibration Book Data	Notes
74	AVCS Recorder No. 1 Pressure	Analog	See channel 47.		
75	AVCS Recorder No. 1 Temperature	Analog	See channel 65.		
76	AVCS Recorder No. 2 Pressure	Analog	See channel 47.		
77	AVCS Recorder No. 2 Temperature	Analog	See channel 65.		
78	AVCS Recorder No. 1 or No. 2 Motor, Phase 1 Current	Analog	-4.0 -2.5 0	± 0.2 ± 0.2 +0 -0.2	AVCS recorder running in either "Record" or "Playback" mode. AVCS recorder starting in either "Record" or "Playback" mode. Recorder motor not running.
79	Multiplexer Selection	Multi- level; digital	-0.9 -1.8	± 0.1 ± 0.2	Multiplexer No. 1 selected. Multiplexer No. 2 selected.
80	Marker	Fixed, Digital	-4.9	± 0.1	
81	S-Band Xmtr Selection	Multi- level; digital	-1.2 -2.4	± 0.4 ± 0.4	S-band transmitter No. 1 selected. S-band transmitter No. 2 selected.
82	S-Band Xmtr No. 1 or No. 2 Output Power	Analog	-1.0	± 0.1	This should be interpreted as a go/no-go check point. The transmitter in operation is indicated on channel 81.

TABLE 2-VII-4. HOUSEKEEPING TELEMETRY DATA POINT CHARACTERISTICS (Continued)

Ch. No. (Frame Word)	Function	Type	Nominal Value or Typical Function (volts, unless marked otherwise)	Tolerance On Calibration Book Data	Notes
83	S-Band Xmtr No. 1 Temperature	Analog	$T = \frac{V_{TLM} + 2.77}{0.0317}$	$\pm 3^{\circ}\text{C}$	V_{TLM} is the measured negative telemetry voltage, yielding the temperature reading in degrees Centigrade, valid for: $-3.1 \leq V_{TLM} \leq -1.0$.
84	S-Band Xmtr No. 2 Temperature	Analog	See channel 83.		
85	Real-Time Xmtr Selection	Multi- level; digital	0 -0.9 -1.8	+0. -0.1 ± 0.1 ± 0.2	Neither transmitter selected. Transmitter No. 1 selected. Transmitter No. 2 selected.
86	Real-Time Xmtr No. 1 Temperature	Analog	$T = -(V_{TLM})^3 - 8.39(V_{TLM})^2 - 37.79 V_{TLM} - 31.23$	$\pm 3^{\circ}\text{C}$	V_{TLM} is the measured negative telemetry voltage, yielding the temperature reading in degrees Centigrade, valid for: $-4.3 \leq V_{TLM} \leq -0.6$.
87	Real-Time Xmtr No. 2 Temperature	Analog	See channel 86.		
88	Real-Time Xmtr No. 1 Power Output	Analog	See note.	See note.	This sensor is quite sensitive to slight VSWR changes. The initial calibration data will be a voltage between -1 and -4 volts. Over the life of the spacecraft this level should not change by more than ± 0.5 volt from the initial value. This telemetry point should, therefore, be treated as a go/no-go point rather than as an analog of the xmtr output power.
89	Real-Time Xmtr No. 2 Power Output	Analog	See channel 88.		
90	Marker	Fixed, digital	-4.9	± 0.1	

TABLE 2-VII-4. HOUSEKEEPING TELEMETRY DATA POINT CHARACTERISTICS (Continued)

Ch. No. (Frame Word)	Function	Type	Nominal Value or Typical Function (volts, unless marked otherwise)	Tolerance On Calibration Book Data	Notes
91	APT Camera Selection	Multi-level; digital	0 -0.9 -1.8	+0, -0.1 ±0.1 ±0.2	Neither camera selected. Camera No. 1 selected. Camera No. 2 selected.
92	APT Vidicon No. 1 Temperature	Analog	$T = 2.34(V_{TLM})^3 + 17.44(V_{TLM})^2 + 64.15V_{TLM} + 110$		V_{TLM} is the measured negative telemetry voltage, yielding the temperature reading in degrees Centigrade, valid for: $-4.1 \leq V_{TLM} \leq 0.4$.
93	APT Vidicon No. 2 Temperature	Analog	See channel 92.		
94	APT Camera No. 1 or No. 2 Grid 1 Regulator Voltage	Analog	$V_{G1} = 45.6V_{TLM} + 65$	±3 volts	V_{TLM} is the measured negative telemetry voltage, yielding the G-1 voltage in negative volts. The nominal value is -50 volts, valid for: $-5.0 \leq V_{TLM} \leq 0$.
95	APT Camera No. 1 or No. 2 Vidicon Fila- ment Current	Analog	$I_{FIL} = -28.4(V_{TLM})^3 - 242.3(V_{TLM})^2 - 699.2V_{TLM} - 652.3$	±3 ma	V_{TLM} is the measured negative telemetry voltage, yielding the filament current in milliamperes. The nominal value is 50 ma, valid for: $-4.5 \leq V_{TLM} \leq -1.9$.
96	APT Camera No. 1 or No. 2 Horizontal and Vertical Deflection	Analog			The analog for this point is time varying, and should be used for troubleshooting in the manual commutator mode.
97	APT Camera No. 1 or No. 2 -6.3 Volt Regulator	Analog	$V_{REG} = 2.05V_{TLM} + 2.48$	±0.3 volt	V_{TLM} is the measured negative telemetry voltage, yielding the regulator voltage in negative volts. The nominal value is -6.3 volts, valid for: $-5.0 \leq V_{TLM} \leq 0$.
98	ATC Flap No. 1 Position	Analog	Angle = $22.9V_{TLM} + 103$	±2 degrees	V_{TLM} is the measured negative telemetry voltage, yielding the flap position in degrees. 0 degree = closed; 90 degrees = open, valid for: $-4.5 \leq V_{TLM} \leq -0.2$.
99	ATC Flap No. 3 Position	Analog	See channel 98.		

TABLE 2-VII-4. HOUSEKEEPING TELEMETRY DATA POINT CHARACTERISTICS (Continued)

Ch. No. (Frame Word)	Function	Type	Nominal Value or Typical Function (volts, unless marked otherwise)	Tolerance On Calibration Book Data	Notes
100	Marker	Fixed digital	-4.9	±0.1	
101	AVCS Camera Selection	Multi- level; digital	0 -0.9 -1.8	+0, -0.1 ±0.1 ±0.2	Neither AVCS camera selected. AVCS camera No. 1 selected. AVCS camera No. 2 selected.
102	AVCS Camera No. 1 Head Temperature	Analog	See channel 65.		
103	AVCS Camera No. 2 Head Temperature	Analog	See channel 65.		
104	AVCS Camera No. 1 or No. 2 Filament Current	Multi- level; digital	-1.7 -3.8 0	±0.3 ±0.4 +0, -0.1	Nominal filament current. Filament open. Filament power OFF.
105	AVCS Camera No. 1 or No. 2 Standby Power	Multi- level; digital	0 -0.9 -2.7	+0, -0.1 ±0.3 ±0.4	No power applied to either camera. Power applied to camera No. 2. Power applied to camera No. 1.
106	AVCS Camera No. 1 or No. 2 Power and +18V Regulator	Multi- level; digital	0 -1.3 -3.6	+0, -0.1 ±0.2 ±0.3	Both -24.5V and +18V OFF. Both -24.5V and +18V ON. -24.5V on, +18V OFF.
107	Pitch Loop and Pitch Sensor Selection	Multi- level; digital	-1.7 -2.7 -3.4 -4.5	±0.2 ±0.2 ±0.3 ±0.3	Pitch loop No. 1 selected, sensors normal. Pitch loop No. 2 selected, sensors normal. Pitch loop No. 1 selected, sensors crossed. Pitch loop No. 2 selected, sensors crossed.
108	"Pitch Loop" Mode and Gain Selection	Multi- level; digital	0 -1.8 -2.7 -3.3	+0, -0.1 ±0.3 ±0.3 ±0.3	"Open Loop" mode, gain relay coarse. "Open Loop" mode, gain relay normal. "Closed Loop" mode, gain relay coarse. "Closed Loop" mode, gain relay normal.

TABLE 2-VII-4. HOUSEKEEPING TELEMETRY DATA POINT CHARACTERISTICS (Continued)

Ch. No. (Frame Word)	Function	Type	Nominal Value or Typical Function (volts, unless marked otherwise)	Tolerance On Calibration Book Data	Notes
109	Pitch Loop Dual Motor Mode Status	Multi- level; digital	0 -1.8 -4.0	+0, -0.1 ±0.5 ±0.5	"Dual Motor " mode enabled. "Dual Motor " mode ON. "Dual Motor " mode disabled.
110	Marker	Fixed, digital	4.9	±0.1	
111	Pitch Loop No. 1 Motor Voltage	Analog	$V_{MTR} = 7.03V_{TLM}$	±0.2	V_{TLM} is the measured negative telemetry voltage, yielding the motor voltage in negative volts, valid for: $-5.0 \leq V_{TLM} \leq -1.4$. *
112	Pitch Loop No. 2 Motor Voltage	Analog	See channel 111.		
113	PCE DC-to-DC Converter Voltage	Analog	-2.2	±0.2	This is a go/no-go indication.
114	SPM Bracket Temperature	Analog	$T = 3.24(V_{TLM})^3 + 26.2 (V_{TLM})^2$ $+ 84.27 V_{TLM} + 102.7$	±5°C	V_{TLM} is the measured negative telemetry volt- age, yielding the temperature in degrees Centigrade, valid for: $-4.9 \leq V_{TLM} \leq -0.2$.
115	Flywheel Bearing Temperature	Analog	$T = 5.39 (V_{TLM})^2 + 43.2 V_{TLM}$ $+ 67.46$	±2°C	V_{TLM} is the measured negative telemetry voltage, yielding the temperature in degrees Centigrade, valid for: $-4.8 \leq V_{TLM} \leq -0.6$.
116	Base Plate Temperature	Analog	See channel 65.		
117	APT Wall Temperature	Analog	See channel 65.		
118	AVCS Wall Temperature	Analog	See channel 65.		
119	Thermal Fence Temperature (Fin)	Analog	$T = 4.55 (V_{TLM})^3 + 24.5 (V_{TLM})^2$ $+ 74.66 V_{TLM} + 114.6$	±2°C	V_{TLM} is the measured negative telemetry voltage, yielding the fence temperature in degrees Centigrade, valid for: $-3.0 \leq V_{TLM} \leq 0$.
120	ATC Reservoir, APT Wall Temperature	Analog	See channel 65.		

* The motor not in use will also indicate some value of voltage due to the back EMF of the motor.

The commutator logic circuits consist of an external clock interface circuit which conditions external clock signals and, in turn, drives a 7-stage binary divider.

The binary outputs of the first 4 stages (binary 1 through 4) are applied to a conventional diode matrix, from which 16X logic functions are derived. The last 3 stages (binary 5, 6, and 7) are applied to another conventional diode matrix from which 8 Y logic functions are derived.

A reset circuit provides a reset function to all binaries initially and at the end of the 121 time slot (See Figure 2-VII-9). An initial delay circuit provides control logic to the initial gate and holds the X-Y logic binaries in the reset mode during the initial delay period.

A DC-to-DC power converter, possessing reverse input voltage protection, converts the 24.5-volt input power for use in the telemetry commutator. Positive and negative voltage regulator circuits accept the rectified inverter output and provide internal operating voltages for the commutator as well as the required external supply outputs.

Operation of the commutator is described below.

(a) Initial Delay and Initial Gate

Upon application of external power, the commutator power supply reaches a point of equilibrium in approximately 50 milliseconds. At this point, the initial delay circuits provide a turn-on logic function to the initial gate; concurrently, the initial delay circuit provides a reset command which resets all binaries. Both of these functions are generated for the duration of the delay period which is approximately 1.2 seconds. Since in the reset condition X1 and Y1 functions would normally be enabled, an inhibiting circuit derived from the reset function is employed to inhibit the X1 logic, thus ensuring that signal input channel 1 is not enabled during the initial gate period. The logic will not respond to external clock pulses during the initial delay period.

(b) Sequential Operational Gates

Upon completion of the initial delay period, the signal input gates of all channels in the group are switched sequentially in response to the positive going edge of the external clock pulses. This is accomplished by AND-gating the Y1 logic function and the individual 16 count X logic functions. The output of this group of gates as well as the initial gate are fed to a common input buffer. The input buffer provides a high input impedance to the signal sources. The Y1 logic function is employed to gate the input buffer in a manner similar to the input gates. The input buffer circuit also contains a constant current source to the collectors of the input gates.

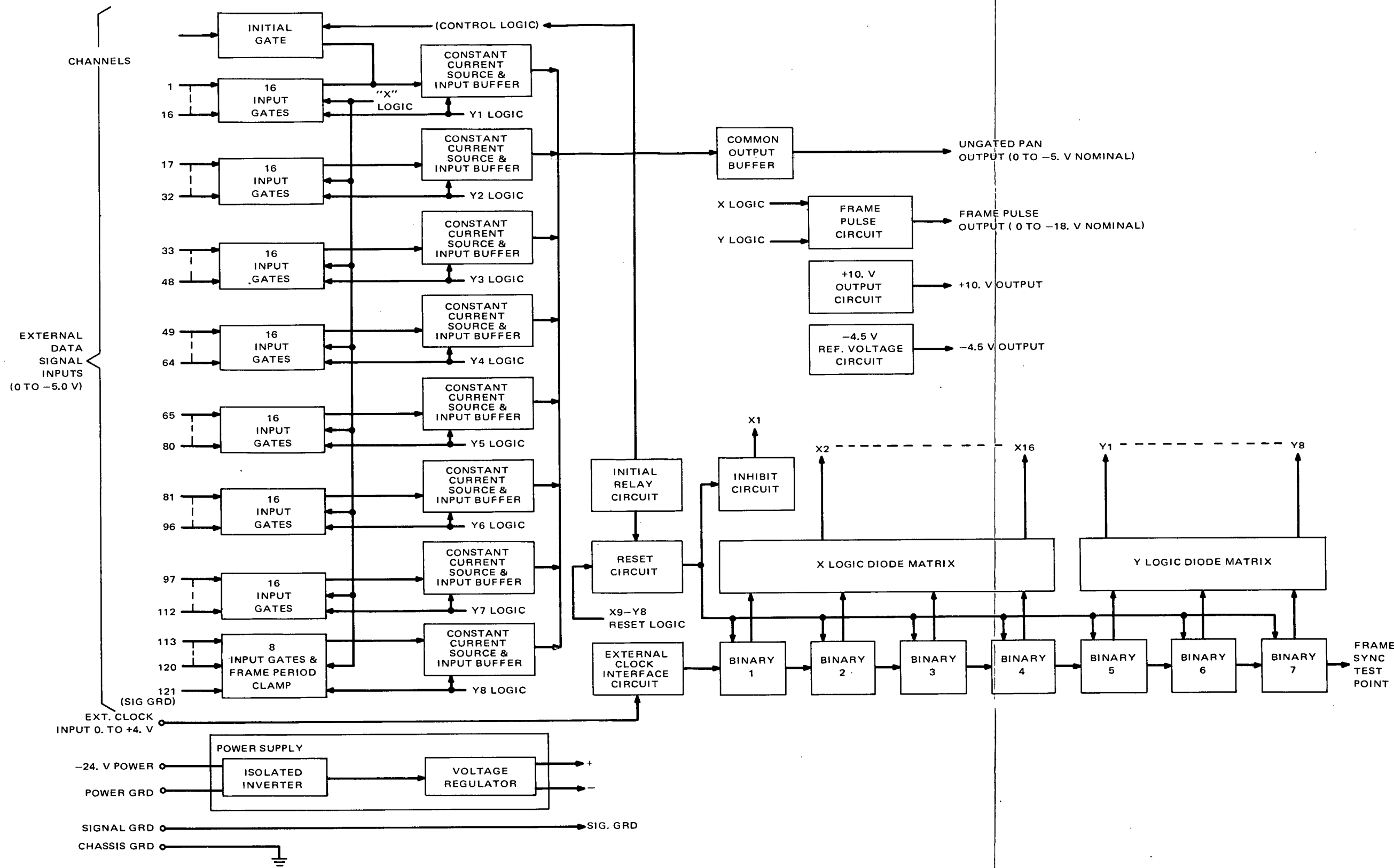
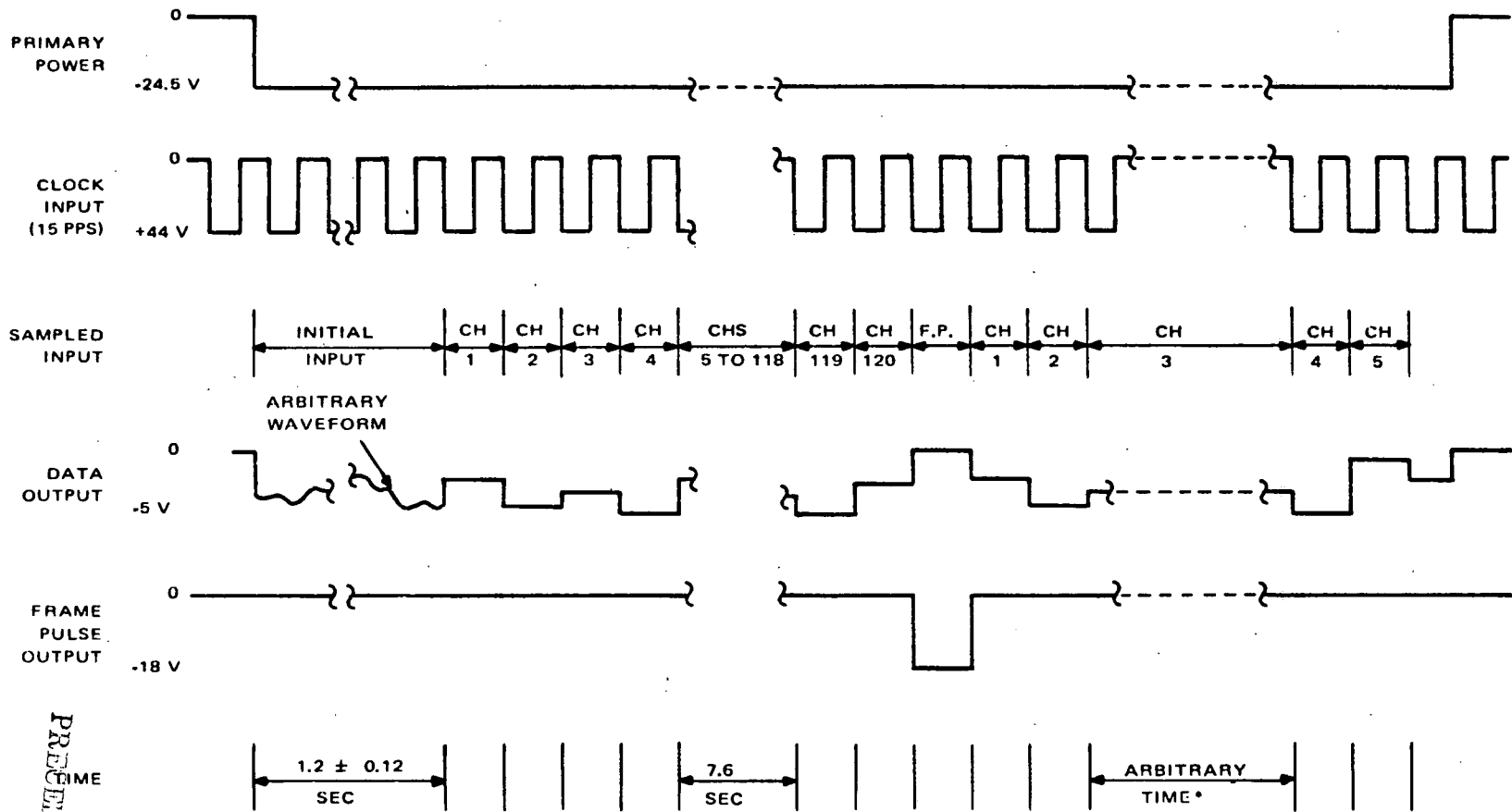


Figure 2-VII-8. 120 Channel Commutator, Block Diagram

FOURTH FRAME 2

FOURTH FRAME 1



NOTE: UNLESS OTHERWISE SPECIFIED, ALL TIME SLOTS SHALL BE 66-2/3 MILLISECONDS NOMINAL.

* ASYNCHRONOUS MODE

Figure 2-VII-9. Telemetry Commutator, Timing Diagram

PRECEDING PAGE BLANK NOT FILMED

(c) *Sequential Operation of Gate Groups*

Upon completion of the switching sequence of the first gate group, the Y2 logic function enables the second group which is sequentially advanced by the 16 count X logic function. In a similar manner each of the gate groups is enabled sequentially in response to Y logic changes. The last gate group consisting of 8 data input gates and a frame period clamp is enabled by the Y8 logic function. The frame period clamp functions in a manner similar to the data signal input gates except that its input is returned to signal ground. This gate provides the required zero level PAM output during channel 121 time slot.

(d) *Common Output Buffer*

The output of each input buffer is connected sequentially to a common output buffer which provides a low impedance PAM output.

(e) *Frame Pulse Output*

Concurrent with the enabling of the frame period clamp during channel 121 time slot, an X9 and Y8 logic functions enable the frame pulse output circuit which generates an output pulse of approximately -18 volts.

d. DUAL SCO

(1) *GENERAL DESCRIPTION*

Two redundant subcarrier oscillators (SCO's) and a mount are contained in a dual SCO assembly. There are two SCO's with a center frequency of 2.3 kHz (SCO 1-1, SCO 2-1) and two with a center frequency of 3.9 kHz (SCO 1-2, SCO 2-2). The design of the SCO assembly is similar to that used in TOS, but only two SCO's are used per side, compared to three per side used on TOS. The dual SCO assembly was supplied by the Dynaplex Division of Teledyne Telemetry Company.

The 2.3-kHz SCO was selected (instead of a higher frequency) due to the requirement that it be suitable for voice channel use. The high baseband bandwidth (160 Hz) required adoption of a ± 20 -percent bandwidth which is not an IRIG standard.

The 3.9-kHz SCO has a ± 7.5 -percent deviation (IRIG channel 9), with a baseband bandwidth of 59 Hz.

The dual SCO assembly was designed to facilitate combined mounting with the dual beacon transmitter assembly, as done in the TOS program. The SCO assembly has a 4- by 4-inch footprint and is 2-25/32 inches high. There are four 0.188-inch diameter mounting holes, one at each corner of the assembly. The maximum weight is 1.6 pounds.

(2) *FUNCTIONAL DESCRIPTION*

The telemetry signals from the command distribution unit in the spacecraft comprise the signal inputs to the SCO's. Inputs used to modulate the 2.3-kHz SCO include:

- Roll sensor 1,
- Roll sensor 2,
- Time code,
- Roll and pitch sensor index,
- Pitch sensor 1, and
- Pitch sensor 2.
- Accelerometer data (beacon No. 1 only).

Inputs used to modulate the 3.9-kHz SCO include:

- Commutator 1,
- Commutator 2,
- Decoder data verification 1,
- Decoder data verification 2,
- Digital solar aspect sensor,
- Solar proton monitor, and
- Accelerometer data (beacon No. 1 only).

Outputs of SCO 1-1 and SCO 1-2 are resistively combined, and the composite signal modulates beacon transmitter 1. Similarly, the outputs of SCO 2-1 and SCO 2-2 are resistively combined to form a modulating signal for the input of beacon transmitter 2. Selection of one of these systems is accomplished by applying power to only one beacon transmitter at a given time.

Amplitudes of the SCO outputs are set so that the nominal deviation indexes of the beacon transmitters are 0.7 radian for the 2.3-kHz SCO and 0.5 radian for the 3.9-kHz SCO. Adjustments are made after the units are assembled into the dual beacon transmitter and SCO assembly configuration.

In addition to the output amplitude control each SCO contains independent potentiometer adjustments for center frequency and deviation sensitivity.

Figure 2-VII-10 is a block diagram showing the two redundant pairs of SCO's in the dual SCO assembly. Only one SCO (1-1) is shown in detail since SCO 1-2 utilizes the same basic circuitry, but with different component values (three capacitors, one resistor, and one potentiometer) for providing the different frequency and sensitivity requirements.

Power from the -24.5-volt bus is converted by an internal voltage regulator to operating levels required for the oscillator circuits.

Input telemetry signals are in the range of 0 to -5 volts. At 0 volt, the SCO oscillates at the lower edge of its band, and at -5 volts, it oscillates at the upper edge. Linearity requirements are ± 1.0 percent for the 2.3-kHz SCO and ± 0.25 percent for the 3.9-kHz SCO.

The frequency of oscillation of the multivibrator in each SCO is voltage controlled by incoming telemetry signal. The multivibrator also contains a starting network to ensure turn-on of the oscillator regardless of whether power is applied gradually or instantaneously. The starting network depends on a saturated-mode transistor switch to provide a delay of 2 to 5 milliseconds depending on the method of power application.

The center frequency and sensitivity of the oscillator are set and maintained over temperature extremes by the frequency control and compensation circuits.

The buffer-shaper stages provide isolation between the multivibrator and the passive filter network. The signal shaping circuits of the buffer-shaper plus the transmission characteristic of the filter provide the necessary output signal characteristics: a sine wave signal containing low harmonic distortion and a flat response across its pass band.

From the filter, the output signal enters a resistive summing network where the outputs of the two SCO's are added into the composite signal to be used in modulating the beacon transmitter.

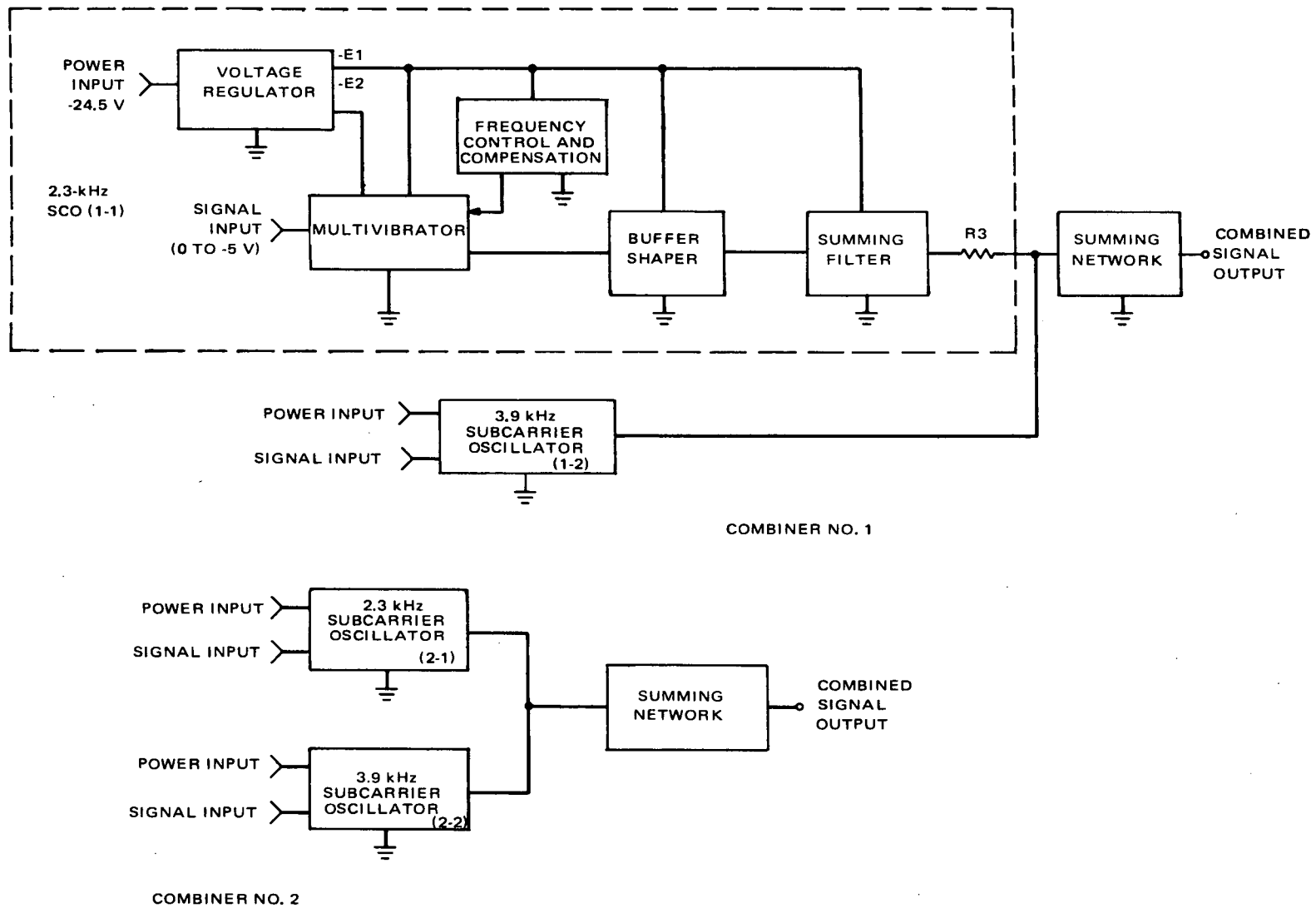


Figure 2-VII-10. Dual SCO, Block Diagram

e. BEACON TRANSMITTER

The TIROS M beacon transmitter is identical with the TOS beacon transmitter. The two redundant beacon transmitters have the same carrier frequency of 136.770 MHz, but only one is operated at a given time (by command selection). The "on" beacon transmitter is continuously modulated by the two frequency-modulated subcarriers with center frequencies of 2.3 and 3.9 kHz; the nominal carrier phase modulation indices for these two signals are 0.7 and 0.5 radian, respectively.

As shown in Figure 2-VII-11, transistor Q1 (with quartz crystal Y1) provides a stable carrier frequency at 34.1925 MHz. The oscillator output feeds the phase modulator CR1 and CR2, two variable-capacitance diodes. These two "vari-cap" diodes, connected back-to-back, give greater dynamic range and less distortion than a single unit. The phase modulator is followed by buffer amplifier Q2, amplifier Q3, varactor multiplier CR3, and power amplifier Q4. A bandpass filter between the power amplifier and the antenna reduces all spurious and harmonic outputs to 60 dB, or more, below the carrier level; the minimum power output is 250 mW.

Voltage regulator Q5 and zener diode VR1 regulate the -24.5-volt supply input to -20 volts and protect the unit against voltages up to -36 volts.

Each beacon transmitter is housed in a milled aluminum case, 4 by 4 by 1.25 inches, with flush top and bottom covers. Mounting holes in the four corners allow the two transmitters to be stacked with the dual SCO.

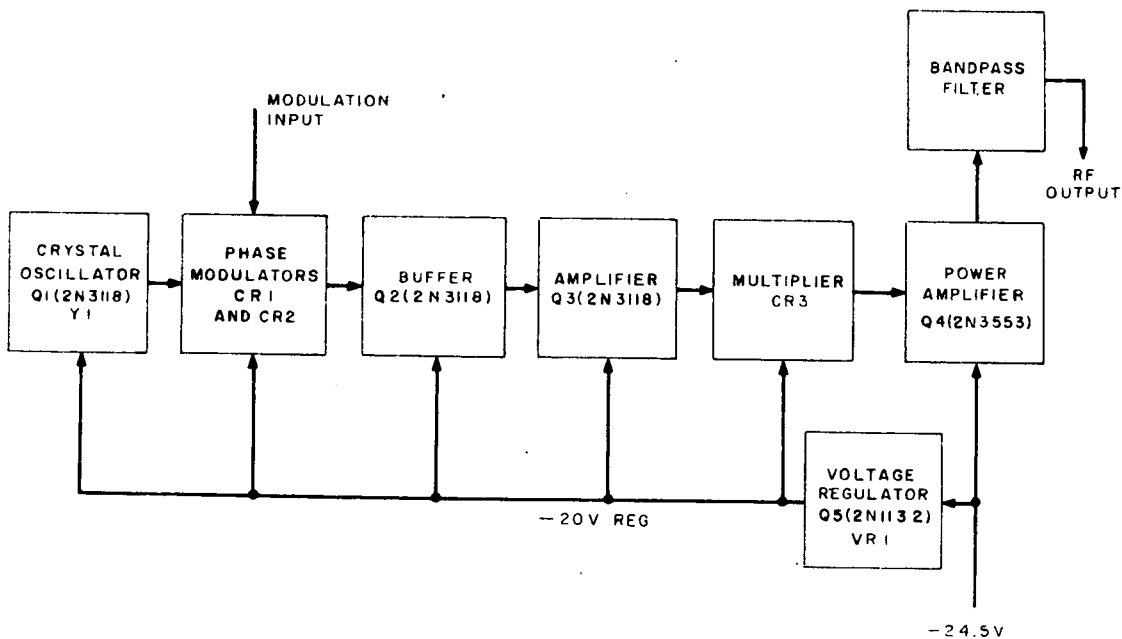


Figure 2-VII-11. Beacon Transmitter, Block Diagram

f. BEACON AND COMMAND ANTENNA GROUP

(1) INTRODUCTION

A single quarter wave stub serves as both the transmitting antenna for the beacon and telemetry signals and as the receiving antenna for the command receiver. The rest of the group comprises a 148-MHz bandpass filter, two 136-MHz notch filters, a "command" hybrid coupler, a 148-MHz notch filter, an RF switch, cables, and terminations. A simplified block diagram of this antenna group is shown in Figure 2-VII-12.

The antenna radiates a linearly polarized pattern at the beacon frequency and receives a similar pattern at the command frequency. The 148-MHz and 136-MHz notch filters perform a diplexing function permitting a single antenna to be used for the beacon transmission and command reception. The 136-MHz notch filter was proven on Relay, TIROS, and TOS spacecraft; it provides isolation

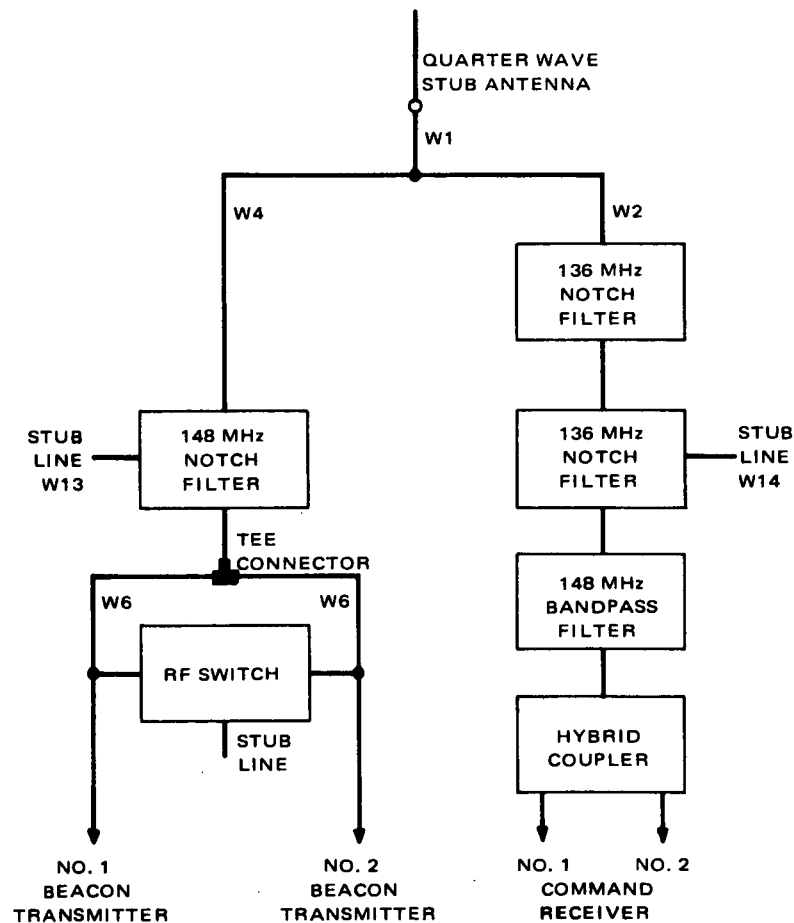


Figure 2-VII-12. Beacon and Command Antenna Group, Simplified Block Diagram

between the beacon transmitter and the command receiver at the beacon frequency. The 148-MHz bandpass filter was flown on TOS spacecraft; it provides the required selectivity for receiving the command carrier frequency and for rejecting out-of-band signals. The hybrid coupler is a new component; it was qualification- and acceptance-tested by Merrimac Research and Development Company, the supplier. The coupler matches the antenna to each command receiver and divides the power equally to each. It also isolates the receivers from each other.

The 148-MHz notch filter suppresses any spurious signal from the beacon transmitters at the command frequency. It also was flown on TOS and TIROS spacecraft.

(2) DESIGN CONSIDERATIONS

At the inception of the ITOS program, the existing TOS APT antenna system was considered for use on the spacecraft. This antenna consists of four quarter-wave elements, all fed in phase for linear polarization at the command frequency, and fed in phase quadrature for circular polarization at the beacon frequency. The coupling network for the four elements is printed stripline consisting of hybrids, balun and stubs. A feasibility study was performed to determine whether the TOS APT system could be directly transplanted onto the larger spacecraft. Extensive pattern and impedance measurements showed serious problems in quadrature feeding of four elements. As a result, measurements were made on a single quarter wave stub at both the command and the beacon frequencies in the interest of finding a more satisfactory solution to the antenna design problem. Patterns at both frequencies were nearly identical to the command pattern obtained by in-phase feeding of the four-element antenna.

The impedance problem of feeding the four elements in phase quadrature is severe, raising serious design problems in the coupling system. The dual frequency impedance matching is greatly simplified with a single element; other advantages are shown in Table 2-VII-5. A quasi-isotropic radiation pattern was achieved by the four-element design of TOS. Due to the form-factor of the ITOS spacecraft, especially with solar panels deployed, a quasi-isotropic pattern no longer can be achieved. From the viewpoint of tradeoffs and overall design, the four-element approach was less feasible and, therefore, abandoned in favor of a single quarter wave stub for both beacon and command functions.

(3) DIPLEXING, ISOLATION, AND INSERTION LOSS

Proper diplexing and isolation characteristics are vital to this subsystem. Diplexing and impedance matching of the antenna at the beacon and receiver frequencies is achieved by the proper length of cable segments

TABLE 2-VII-5. COMPARISON OF SINGLE-ELEMENT AND FOUR-ELEMENT BEACON AND COMMAND ANTENNA DESIGNS

Parameter	Four Quarter Wave Elements	Single Quarter Wave Element
Dipole VSWR	5:1 to 7:1	1.3:1 to 1.8:1
Coupler Insertion Loss	2 dB	0.75 dB
Pattern Effectiveness	Equal	Equal
Received Power		At least 1.25 dB more than four-element design
Design Complexity	Highly complex	Straightforward
Total Weight (with subsystem components and 12 feet of cable)	5.3 pounds	3.3 pounds
Thermal Interface	Thermal fence on panel 5 needs notches to clear elements	No notches necessary
Primary Power	Slight effect of solar cell shadowing	No shadowing
Previous Experience	TOS APT coupling board experience predicts difficulty in matching increased VSWR	Similar to existing space-flown design
Need for Hybrid or Switch	Requires TOS printed hybrid coupler for phasing and connection for two beacons; no switch needed	Printed TOS hybrid coupler not required; however, a simple beacon hybrid or switch is needed

plus the 136-MHz and 148-MHz notch filters. Cable W1 transforms the antenna impedance to approximately 50 ohms at the tee. The 136-MHz helical notch filter essentially places a short at the beacon frequency (f_t) in the receiver line. Cable W2 transforms this short to a high impedance to f_t at the tee. At the command frequency (f_r), the input to W2 looks like approximately 50 ohms. The 148-MHz helical notch filter and cable W4 perform a similar function, except that the input to W4 at the tee looks like a high impedance at f_r and approximately 50 ohms at f_t . Final matching of the antenna system is provided by short-circuited stubs W13 and W14. W13 assures that the input at the tee to W2 looks like 50 ohms at f_r ; W14 performs a similar function at f_t , canceling the reflected antenna susceptance and the residual susceptance of the 148-MHz notch filter.

Transmitter-receiver isolation is important over a broad frequency band in order to prevent desensitization of the command receiver. The 148-MHz band-pass filter provides most of the isolation required. The notch filters provide additional isolation at selected frequencies. Specifically, the 148-MHz notch filter in the beacon side provides rejection of broadband noise and/or low level spurious signals generated by the beacon transmitter, while the 136-MHz notch filters provide additional rejection of both the beacon and real-time transmitter signals. The minimum values of isolation are given in Table 2-VII-6. Values measured on the Electrical Test Model are given in Paragraph 2.VII.C.3.f.(9). The insertion losses for various components of this antenna group are listed in Table 2-VII-7, based on worst-case values of component losses.

(4) 136-MHz NOTCH FILTER

This component is a quarter-wave helical line filter which effectively rejects the notched frequency and produces a low insertion loss at the pass (command signal) frequency; it can be tuned to reject either the beacon or real-time frequency. It is fabricated with two parallel open-ended inductive lines consisting of 28 turns each on a teflon rod. An 18-pF lumped mica capacitor is used for matching purposes at the pass frequency. At the 136-MHz rejection frequency of the open-circuited quarter-wave lines project a short circuit across the main line irrespective of the value of the mica capacitor. At the 148-MHz command frequency, the open-circuited helical lines no longer project a short circuit across the main line since each helical line is 7 degrees longer. The shunting impedance on the main line consists of a high resistance and small inductance. The mica capacitor is utilized to cancel the inductive component and maintain a matched main line from the antenna at f_r , shunted only by the high resistance. In the current design, this filter is tuned to reject the real-time frequency. Isolation at the reject frequency is at least 20 dB. Insertion loss at the command frequency is no more than 0.5 dB.

TABLE 2-VII-6. ISOLATION OF BEACON AND COMMAND ANTENNA GROUP COMPONENTS

	Isolation (dB)				
	Beacon to Receiver			Antenna to Receiver	Beacon to Beacon
	(136 MHz) f_t	(148 MHz) f_r	(108 MHz) f_l	(137 MHz) f_{rt}	(136 MHz) f_t
136-MHz Notch Filters (2)	40 min	0.4		32 min	
148-MHz Notch Filter	0.2	24			
148-MHz Band-pass Filter	33 min	1.5 min	50 min	33 min	
Hybrid Coupler	3.2	3.2	3 min	3.2	
RF Switch					25 min
Cable Losses	0.7	0.7		0.3	
Stub & Reflection Losses	0.6	0.6		0.3	
Total (dB, minimum)	77.7	30.4	53	58.8	25

(5) 148-MHz NOTCH FILTER

This filter is similar in construction to the 136-MHz notch filter, with two differences. The number of turns is reduced to 24-1/4, and the lumped capacitor matching element is replaced with a distributed inductor in the form of a short-circuited stub. This makes the rejection at 148 MHz instead of 136 MHz. Inductive matching is required for the transmitted 136-MHz signal and is provided by a short-circuited stub. Isolation at the reject frequency is at least 24 dB. Insertion loss at the pass frequency is no more than 0.4 dB.

TABLE 2-VII-7. INSERTION LOSSES OF COMPONENTS OF BEACON AND COMMAND ANTENNA GROUP

	Insertion Loss (dB)	
	Beacon to Antenna at 136 MHz	Antenna to Receiver at 148 MHz
136-MHz Notch Filters (2)		1.0
148-MHz Notch Filter	0.4	
148-MHz Bandpass Filter		2.5
Hybrid Coupler Split		3.0
Hybrid Loss		0.5
RF Switch	0.6	
Cable Losses	0.4	0.3
Stub & Reflection Losses	<u>0.6</u>	<u>0.7</u>
Total (dB, maximum)	2.0	8.0

(6) 148-MHz BANDPASS FILTER AND HYBRID COUPLER

The bandpass filter and command hybrid coupler are essentially off-the-shelf vendor components. The filter has a 3-dB bandwidth of 5.2 MHz centered at the command frequency. It has a minimum insertion loss of 1.7 dB at the command frequency. The command signal is split equally by the hybrid coupler to two receivers with a maximum insertion loss of 0.5 dB above the theoretical 3-dB coupling loss.

(7) RF SWITCH

The RF switch is used in conjunction with the RF cable network to place the output of the selected beacon transmitter electrically at the beacon and command antenna port; this is accomplished by shorting the OFF transmitter to ground through relay contacts and an associated series resonant L-C circuit. The active transmitter is then isolated by a 1/4 wave length of cable (W6) which

reflects the short as an open circuit at the tee connector through which the ON transmitter feeds the remainder of the beacon and command subsystem. The interconnecting cables and connectors have been selected for proper match between components.

(8) *ANTENNA ASSEMBLY*

The radiator for this group consists of a shaft and housing assembly; this assembly utilizes a qualified design. It is mounted on panel 5 (see Figure 2-VII-13) but is slightly offset toward the earthward panel for mechanical reasons.

Since the antenna operates at two frequencies and under stowed and deployed modes, the length of the antenna shaft (hence impedance) is a compromise choice.

(9) *PERFORMANCE OF THE ELECTRICAL TEST MODEL (ETM)*

Isolation, insertion loss, and VSWR measurements were made using a full-scale mockup and available TOS and vendor components. Results of ETM tests are tabulated in Table 2-VII-8. This shows that the design meets the requirements of the cognizant specification (RCA PS 1975135) adequately.

(a) *Measurement and Presentation*

Antenna radiation patterns were measured for the beacon and command operations, in both the stowed and deployed positions of the solar panels using a 2/5 scale model. The pattern data was recorded originally in digital form on a radiation distribution plot (RDP), in which the ordinate is the θ variable and the abscissa is the ϕ variable. Contour plots for the beacon and command antenna group, derived from original RDP's, are shown in Figures 2-VII-14, 15, 16 and 17. The radiated power has also been integrated over 4π steradians to determine the power level at the pattern maximum relative to the isotropic level. The contours show directivity which expresses the radiated power relative to the isotropic level in decibels (dBi). Significant regions (I, II, III, and IV) are defined by the figures in the performance specification (RCA PS 1975135). All measurements are made on a 2.5 scale model having six fully conductive sides.

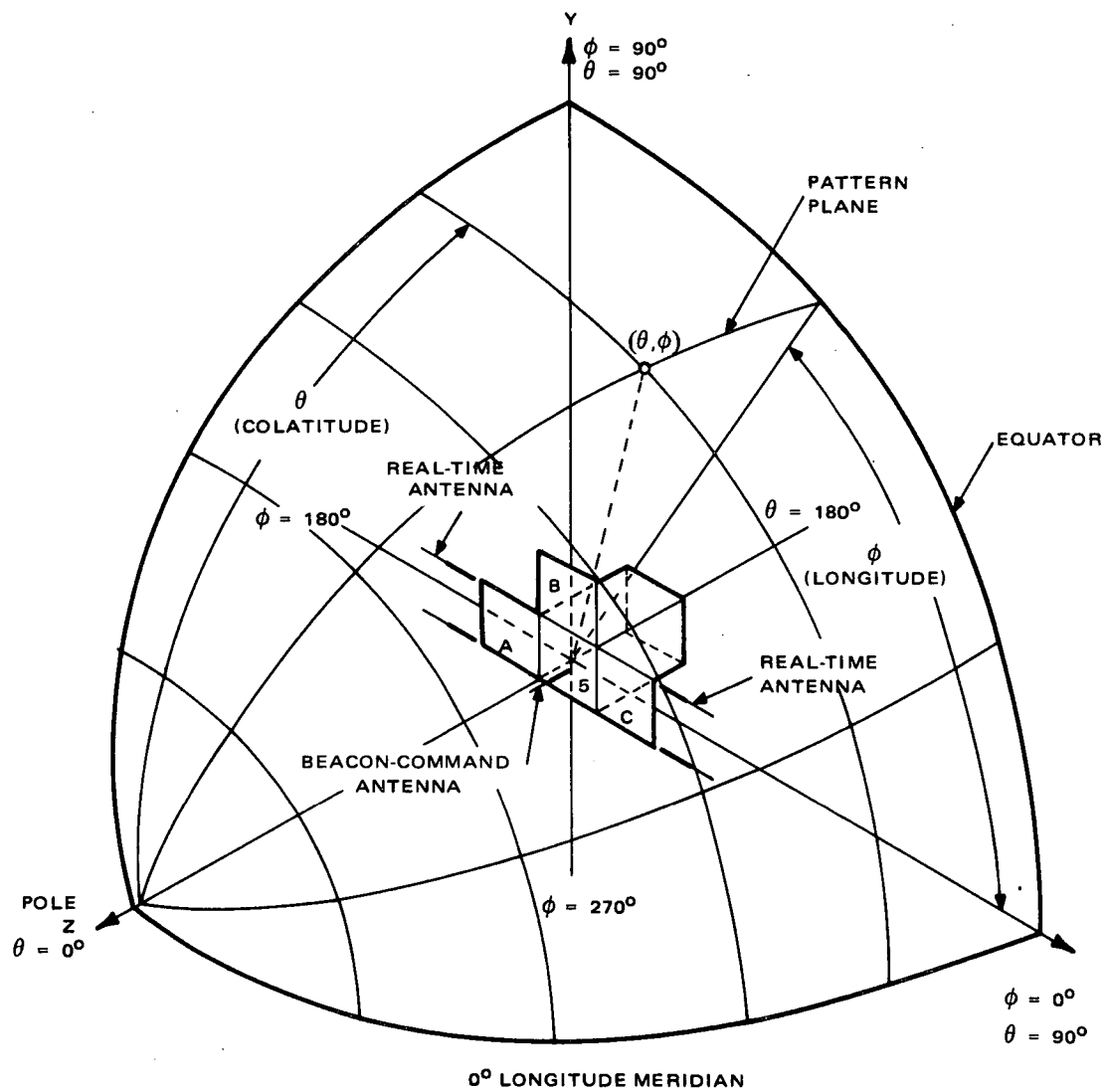


Figure 2-VII-13. Spherical Coordinate System Used For Beacon and Command and Real-Time Antenna Group Measurements

TABLE 2-VII-8. CIRCUIT CHARACTERISTICS OF BEACON AND COMMAND ANTENNA GROUP

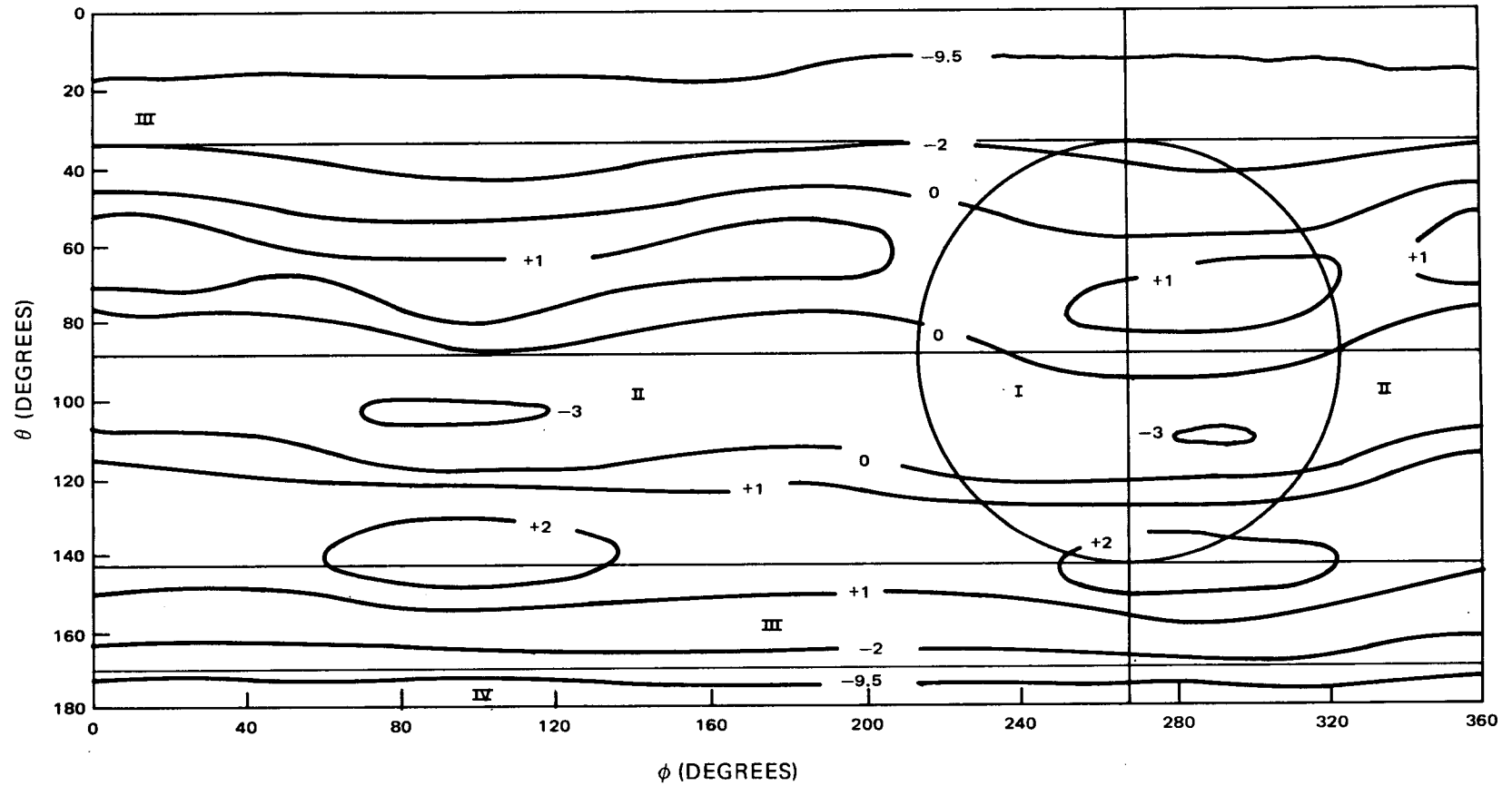
			Solar Panel Mode	
Parameter	Ports	Frequency	Deployed	Stowed
VSWR	Beacon	f_t	1.13	1.48
	Command	f_r	1.16	1.22
Isolation (dB)	Beacon to beacon	f_t	32	30
	Beacon to receiver	f_t	70+	76+
	Beacon to receiver	f_r	37	37
	Beacon to receiver	f_i	57	55
	Antenna to receiver	f_{rt}	80+	80+
Insertion Loss (dB)	Beacon to antenna	f_t		1.3*
	Antenna to receiver	f_r		6.7*

*Not a function of panel mode

(b) *Solar Panels Stowed*

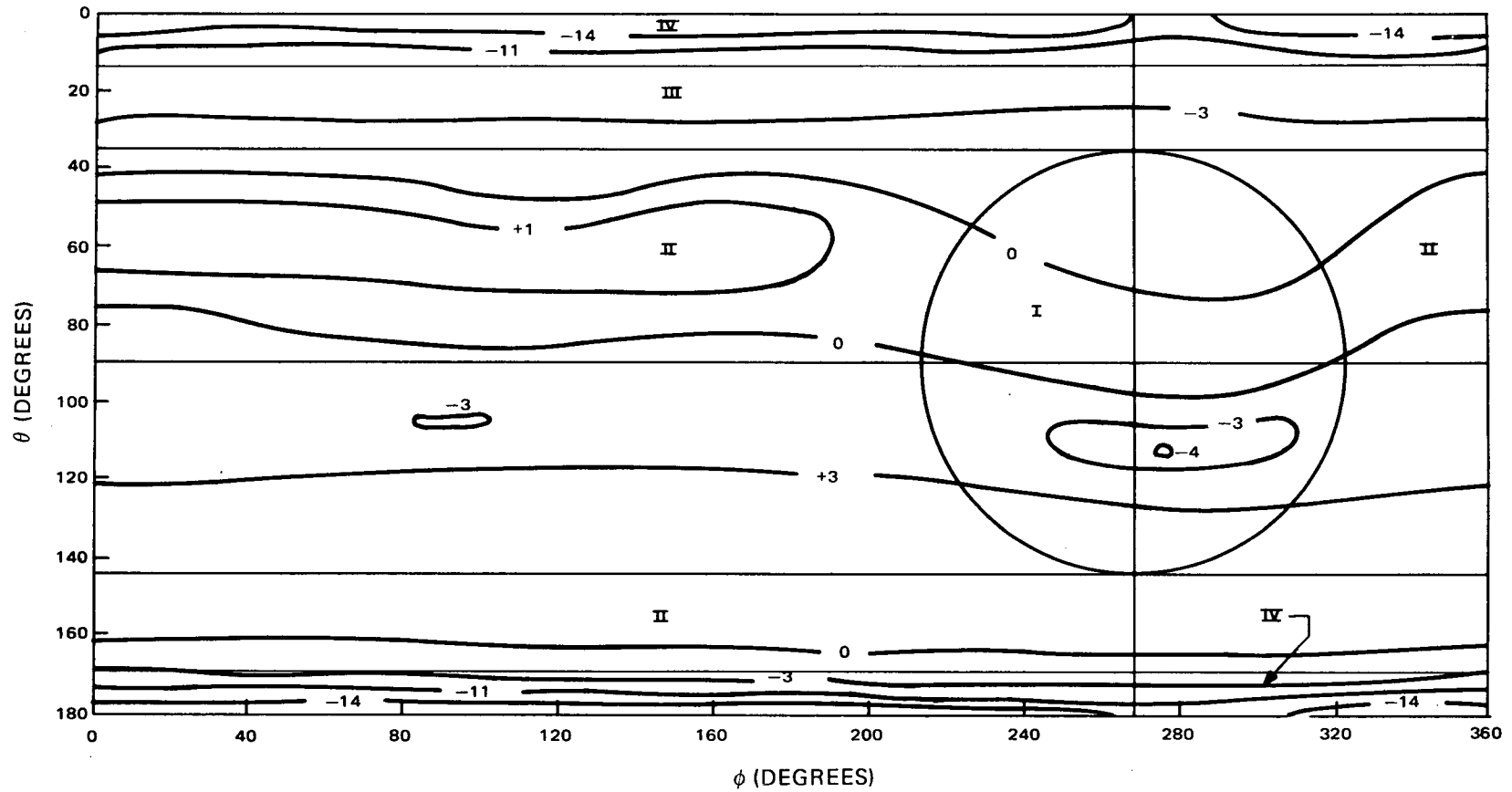
The specification requires a minimum beacon antenna gain of -11.5 dB with respect to linear isotropic in Regions I, II and III with the solar panels stowed. The gain may be less than this in Region IV. Required directivity is as follows:

Minimum required gain	-11.5 dBi
Insertion loss (maximum)	2.0 dB
Net antenna directivity required	- 9.5 dBi



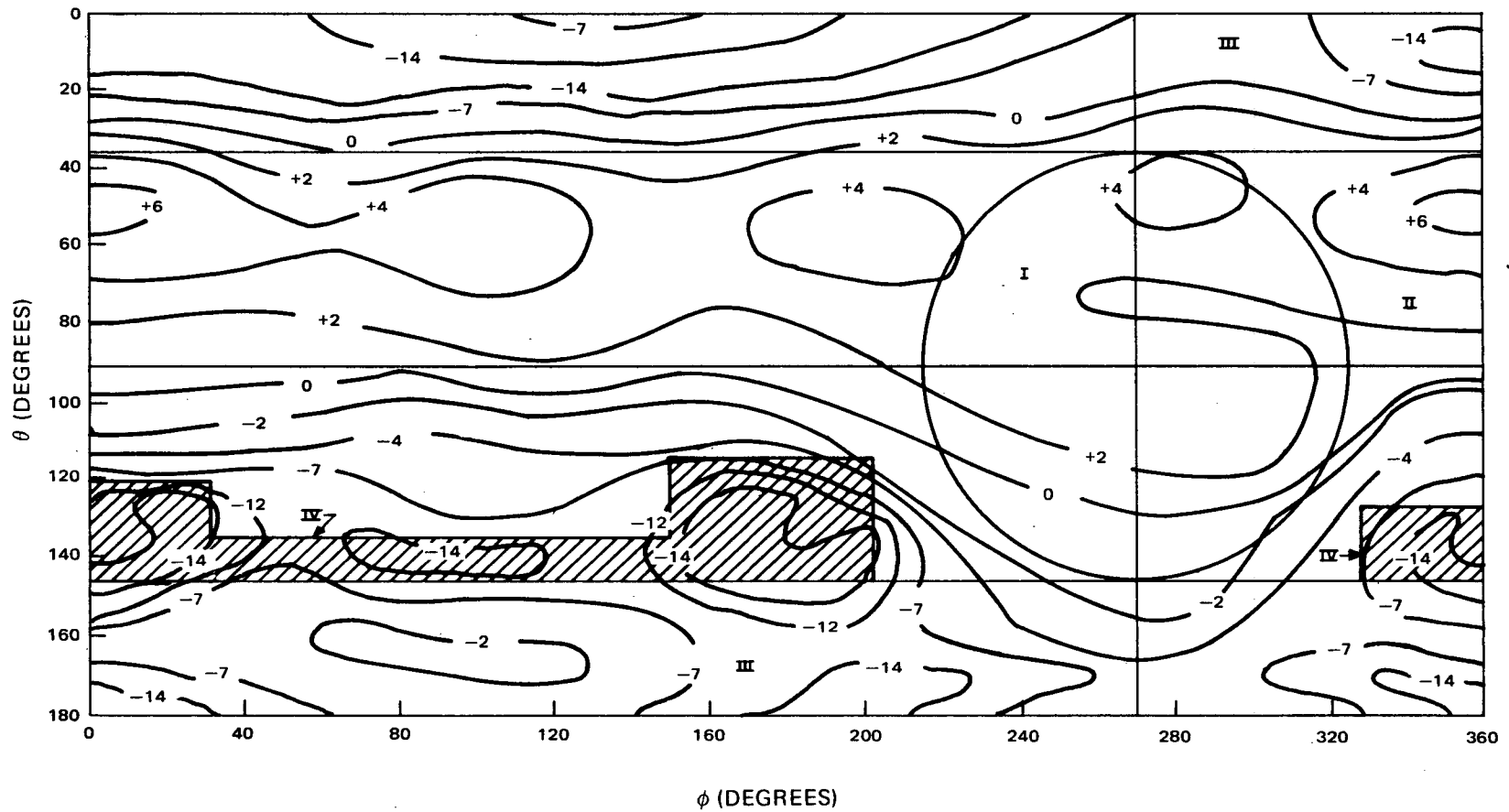
- NOTES: 1. DIRECTIVITY CONTOURS RELATIVE TO LINEAR POLARIZED ISOTROPIC.
 2. FOR GAIN, ADD 2-DB LOSS.
 3. DIRECTIVITY SPECIFICATION: -9.5 DBI
 $\theta = 18$ TO 168 DEGREES

Figure 2-VII-14. Beacon and Command Antenna Contour Plots for Stowed Mode at Beacon Transmitter Frequency



- NOTES: 1. DIRECTIVITY CONTOURS RELATIVE TO LINEAR ISOTROPIC ANTENNA
 2. FOR GAIN, ADD 8-DB LOSS, 3-DB POLARIZATION LOSS; TOTAL: 11 DB
 3. DIRECTIVITY SPECIFICATION: -14 DBI, $\theta = 10$ TO 174 DEGREES

Figure 2-VII-16. Beacon and Command Antenna Contour Plots for Stowed Mode at Command Receiver Frequency



- NOTES: 1. DIRECTIVITY CONTOURS RELATIVE TO LINEAR ISOTROPIC ANTENNA
 2. FOR GAIN, ADD 8-DB LOSS, 3-DB POLARIZATION LOSS: TOTAL 11 DB
 3. DIRECTIVITY SPEC: -7 DBI IN REGION I, -14 DBI IN REGION II

Figure 2-VII-17. Beacon and Command Antenna Contour Plots for Deployed Mode at Command Receiver Frequency

Contours of Figure 2-VII-14 show that minimum directivity is:

	<u>Minimum directivity contour (dBi)</u>	<u>Excess over required directivity (dB)</u>
Region I	-3	6.5
Region II	-3	6.5

Region III encompasses the areas bounded by $\theta = 18$ to 35 degrees and $\theta = 145$ to 168 degrees wherein the specification is satisfied.

It is seen that no pattern contour falls below the gain requirement in these areas. In the polar areas of Region IV, the pattern null region, no specification requirement exists. The beacon antenna radiation pattern distribution adequately meets the specification requirements in the stowed solar panel condition.

(c) *Beacon Pattern, Solar Panels Deployed*

The specification requires a minimum beacon antenna gain of -11.5 dBi in Region I, and -16.5 dBi in Region II with the solar panels deployed. Less gain is required in Region IV and no gain requirement exists in Region III. Required directivity is as follows:

	<u>Region I</u>	<u>Region II</u>
Minimum required gain	-11.5 dBi	-16.5 dBi
Insertion loss	<u>2.0 dB</u>	<u>2.0 dB</u>
Net antenna directivity required	- 9.5 dBi	-14.5 dBi

Contours of Figure 2-VII-15 show that minimum directivity is:

	<u>Minimum directivity contour (dBi)</u>	<u>Excess over required directivity (dB)</u>
Region I	- 3.5	6
Region II	-12.5	2

Regions III and IV have no gain requirement.

The beacon antenna radiation pattern distribution adequately meets the specification requirements in the deployed solar panel condition.

(d) *Command Pattern, Solar Panels Stowed*

The specification requires a minimum command antenna gain of -25 dBi in Regions I, II and III with the solar panels stowed. No gain requirement exists in Region IV. Required directivity is as follows:

Minimum required gain	
Relative to circular isotropic	-25.0 dBi
Relative to linear isotropic	-22.0 dBi
Insertion loss (maximum)	5.0 dB
3-dB hybrid power division	<u>3.0 dB</u>
Net antenna directivity required	-14.0 dBi

Contours of Figure 2-VII-16 show that minimum directivity is:

	<u>Minimum directivity contour (dBi)</u>	<u>Excess over required directivity (dB)</u>
Region I	-4	10
Region II	-3	11

Region III encompasses the areas bounded by $\theta = 10$ to 35 degrees and $\theta = 174$ to 180 degrees wherein the specification is exceeded by 3 dB.

The command antenna radiation pattern distribution adequately meets the specification requirements in the stowed solar panel condition.

(e) *Command Pattern, Solar Panels Deployed*

The specification requires a minimum command antenna gain of -18 dB relative to circular isotropic in Region I, -25 dBi in Region II, and no requirement in Regions III and IV with the solar panels deployed. Required directivity is as follows:

	<u>Region I</u>	<u>Region II</u>
Minimum required gain		
Relative to circular isotropic	-18.0 dBi	-25.0 dBi
Relative to linear isotropic	-15.0 dBi	-22.0 dBi
Insertion loss	5.0 dB	5.0 dB
3-dB hybrid power division	<u>3.0 dB</u>	<u>3.0 dB</u>
Net antenna directivity required	- 7.0 dBi	-14.0 dBi

Contours of Figure 2-VII-17 show that minimum directivity is:

	<u>Minimum directivity contour (dBi)</u>	<u>Excess over required directivity (dB)</u>
Region I	- 2	5
Region II	-12	2

The command antenna radiation pattern distribution adequately meets the specification requirements in the deployed solar panel condition.

D. REAL-TIME VIDEO LINK

1. General Description

The sensor input for the real-time video link is obtained from either one of the two redundant APT cameras or from one of the two redundant scanning radiometers. Under normal operating conditions, the input is obtained from one APT camera during the daylight and from one of the scanning radiometers during the nighttime portion of the orbit. A backup mode permits an input to be obtained from a radiometer during the daytime portion of the orbit.

The signal output of the selected sensor amplitude-modulates a 2.4-kHz sub-carrier; this modulated subcarrier in turn frequency-modulates one of the 137.5-MHz real-time transmitters. The output of the selected transmitter is coupled through a notch filter to a pair of half-wavelength dipoles mounted on the extremity of one of the solar panels. Figure 2-VII-18 shows a simplified block diagram of the real-time data video link.

2. Video Signal Characteristics

a. APT SIGNALS

The APT data is divided into frames, normally 11 frames being transmitted during each orbit. The total coverage of each frame at the nominal orbit altitude is 1700 to 1275 nautical miles, and the resolution at the center of each picture is 2 nautical miles. Each frame contains 600 lines, and is preceded by a 300-Hz "start" tone which is transmitted for 3 seconds, followed by a phasing signal consisting of 12.5-millisecond phasing pulses transmitted every 250 milliseconds for a period of 5 seconds. The duration of each video line is also 250 milliseconds. Each line commences with a 12.5-millisecond blanking period.

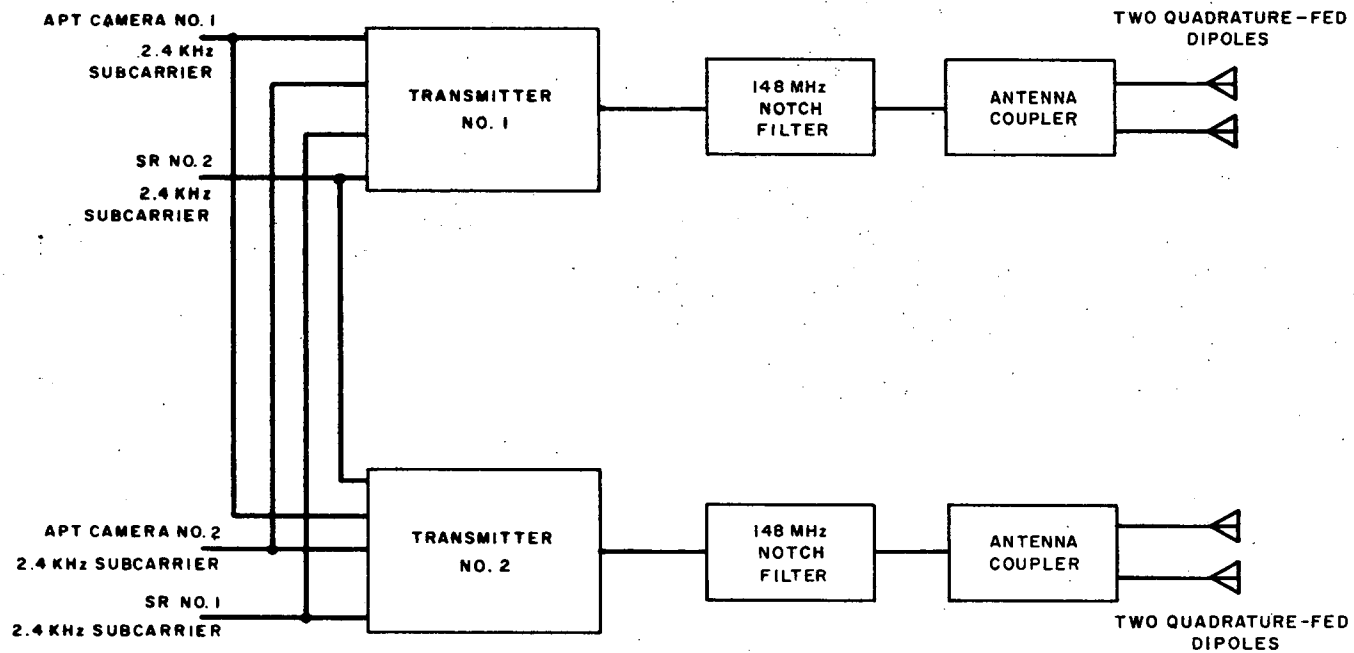


Figure 2-VII-18. Real-Time Transmission Link, Block Diagram

The video signal has a baseband of 1600 Hz, frequencies above 1600 Hz being attenuated at a rate of 24 dB per octave. The modulator stage combines the video signal with a 2400-Hz sine wave to produce the 2400-Hz amplitude-modulated video subcarrier used for modulating the TV transmitter. A white level corresponds to 100-percent subcarrier amplitude, and a black level corresponds to 2.5-percent subcarrier amplitude. During the phasing cycle, the subcarrier is held at the white level except during the phasing pulses which are at black level. During the 600 video lines, the blanking pulse is held at the white level. The modulated subcarrier is applied to the FM modulator in the 137.5-MHz TV transmitter.

b. SR SIGNALS

The scanning radiometer scans at a rate of 48 lines per minute and has an aperture of 5.3 milliradians in the IR channel and 2.8 milliradians in the visible channel. The earth scan occupies 110 degrees of the 360-degree rotation, and the IR sensor resolution is 4.0 nautical miles at the center of the scan; the visible sensor resolution is 2.0 nautical miles. The dynamic range of the IR detector is such that the sensor responds to radiation in the temperature range from 185° to 330°K in the spectral region from 10.5 to 12.5 microns. The visible channel detector responds to a scene brightness of 20 to 8500 foot-lamberts in the spectral region from 0.52 to 0.73 microns.

A marker pulse sequence is generated commencing at a point 75 degrees following the nadir. It consists of one pulse of 60-millisecond duration with a back and front porch of 20 milliseconds. The sync pulse is at -8.0 volts DC while the 330°K/8500-foot-lambert video level is -5.75 volts DC. The porches are at -0.025 volt DC while the 185°K/500-foot-lambert video level is 0.25 volt DC. The spectrum of the IR video signal is from DC to 450 Hz; the spectrum of the visible video signal is from DC to 900 Hz. The spectrum of the SR sync signal is from DC to 1250 Hz.

The SR processor selects either the IR or visible channel for pretransmission processing. The input signals which are from 0 to -8 volts DC are limited to -6 volts DC; this reduces the sync amplitude to approximately the maximum level of the video signal. The IR channel is then inverted so that upon detection at the ground station bright clouds will appear as maximum amplitude signals in both the visible and IR channels. The selected video signal then amplitude-modulates a 2.4-kHz sine wave subcarrier. Figure 2-VII-19 shows typical 2.4-kHz modulating signals for both the visible and IR channels. The modulated subcarrier is then applied to the FM modulator in the 137.5-MHz real-time transmitter.

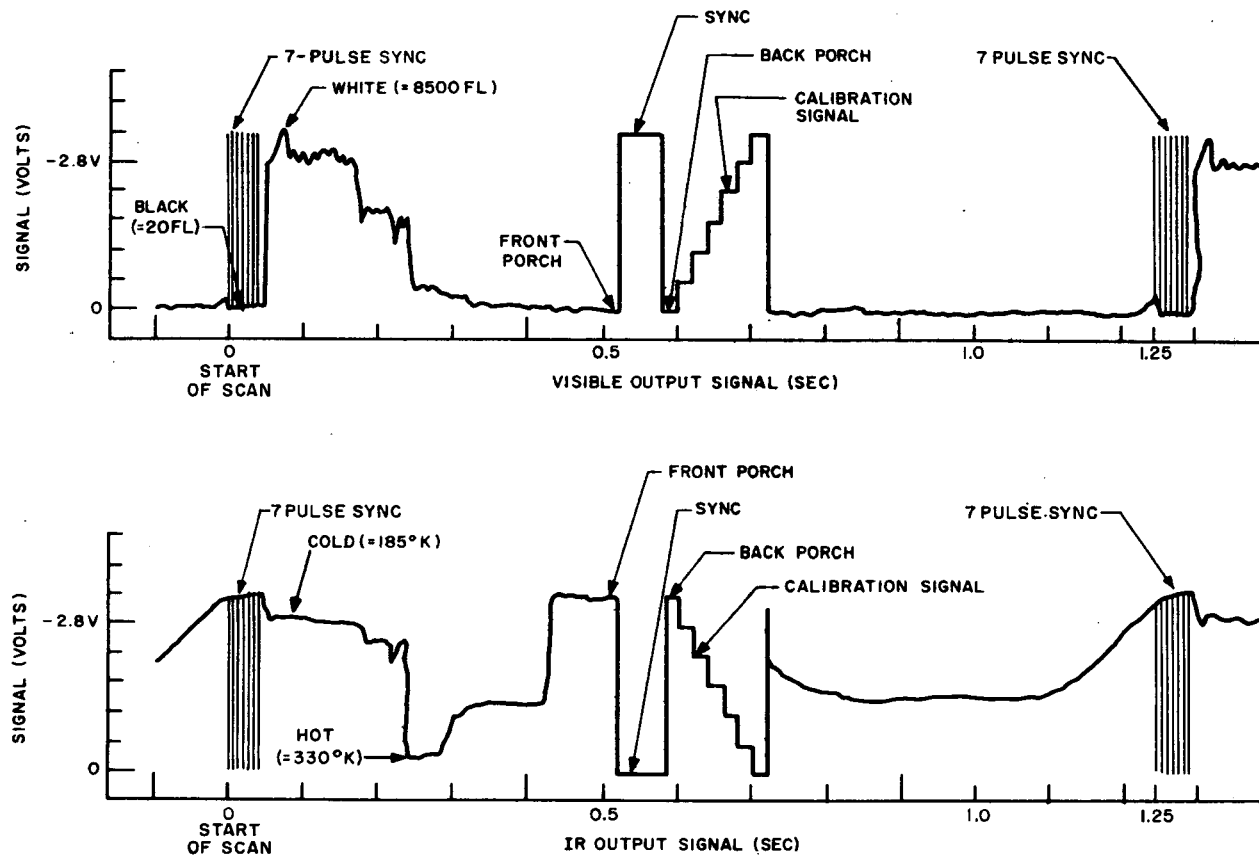


Figure 2-VII-19. Real-Time IR and Visible Channel Subcarrier Modulating Signals in the SR Processor

3. Component Description

a. REAL-TIME TRANSMITTER

(1) GENERAL DESCRIPTION

The real-time transmitter is used to transmit APT video or scanning radiometer signals in real time to the local users. The input signal is an amplitude-modulated 2.4-kHz subcarrier with sidebands from 0.600 to 4.200 kHz; it is used to frequency-modulate the 5-watt RF carrier. Each spacecraft has redundant transmitters with a nominal frequency of 137.5 MHz.

The basic design is similar to that of the TOS F and H APT transmitter. The voltage-controlled crystal oscillator operates at one-eighth of the carrier frequency and is followed by three frequency doublers, a driver, and a power output stage. Frequency modulation is accomplished through driving a varactor diode in series with the crystal. The ITOS transmitter has four video inputs whereas the earlier transmitter has only two. A zener diode with a high power dissipation rating is included in the voltage regulator because of the overvoltage requirement in the ITOS units.

The transmitter is contained in a multicavity gold-plated machined aluminum housing designed to provide good RF shielding for each of the six circuit boards in the box. The modulation amplifier and voltage regulator (A1 board) are on a printed circuit board. The remaining five circuit boards are of gold-plated aluminum with point-to-point wiring between insulated terminals; this short, direct wiring reduces stray reactances.

The five gold-plated aluminum boards are mounted component side down in the housing to provide RF shielding and to permit circuit tuning with the cover removed. In addition, each of the boards rests on continuous internal ledges, which extend to the cover, forming shields about each circuit board.

The transmitter has a 1.5- by 5-inch footprint and is 7.105 inches high. Two transmitters are stacked side-by-side. Each transmitter weighs 2.2 pounds maximum.

(2) FUNCTIONAL DESCRIPTION

A block diagram of the real-time transmitter is shown in Figure 2-VII-20.

Video signal frequencies modulate the voltage-controlled crystal oscillator (VCXO) which has been incorporated into the design to provide the required frequency stability. The frequency of the VCXO is 17.1875 MHz. Multiplication is performed by three transistor doublers which provide a high degree of

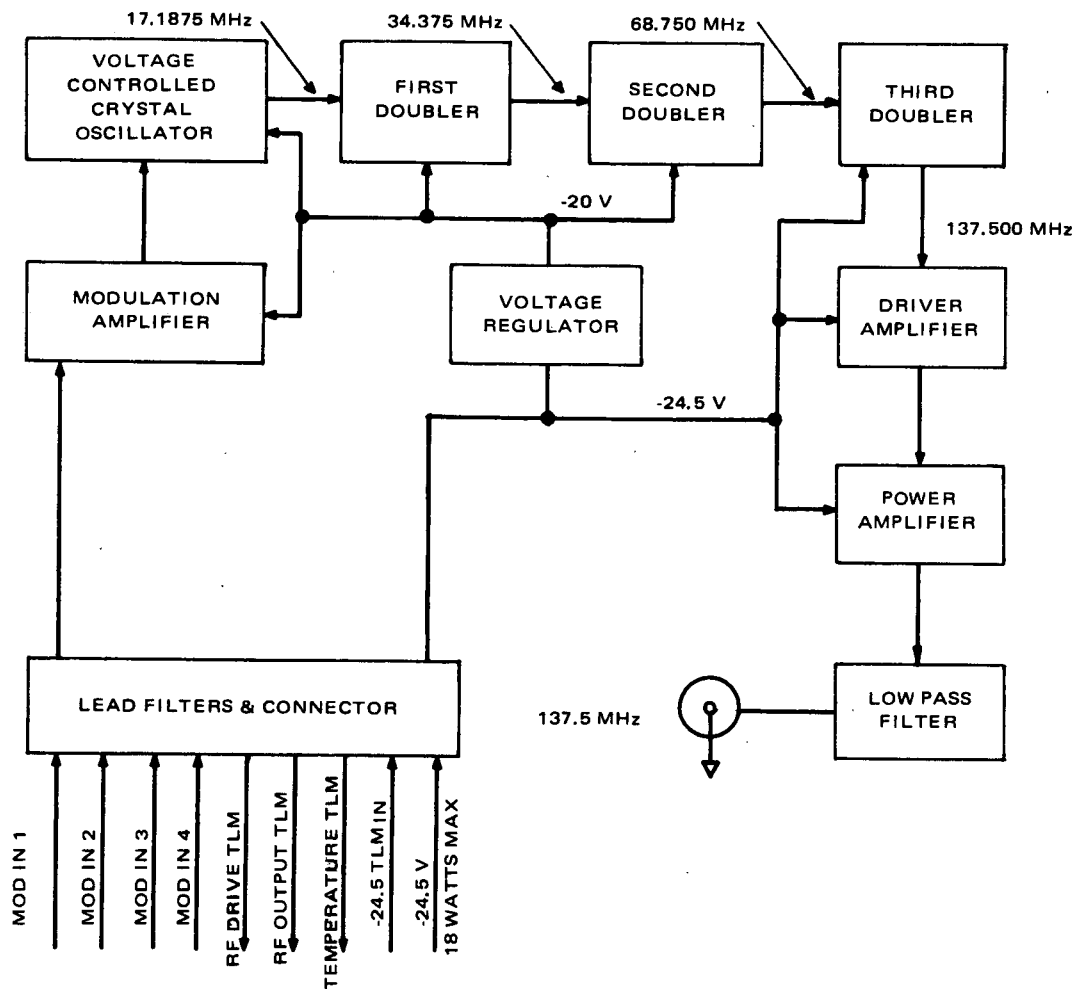


Figure 2-VII-20. Real-Time Transmitter, Block Diagram

stability. Following the doubler chain, the signal passes through driver and power amplifiers and a low pass filter. The final power output is 5 watts or more.

(a) *Modulation Amplifier and Voltage Regulator*

In the modulation amplifier, the input from one of the four sources is amplified to a level sufficient for the prescribed deviation of the VCXO. The amplifier consists of three cascaded stages with separate resistive inputs for the four video signals. The first two stages are AC-coupled, common emitter stages. The signal from the second stage collector is DC-coupled to the base of the third stage. From the third stage, an emitter follower, the signal is returned to the emitter of the first stage through a resistor providing negative voltage feedback. The output of the third stage emitter is AC-coupled to the VCXO through a resistor divider network. An adjustable resistor in series

with a fixed resistor provides control of the output voltage over a range of 50 percent to compensate for VCXO sensitivity variations and amplifier gain variations from unit to unit.

A single series transistor is used as a voltage regulator to provide -20 volts for the modulation amplifier, VCXO, and the first two doubler stages.

(b) Voltage Controlled Crystal Oscillator

The oscillator is a common base, transformer-coupled circuit with a crystal, operating in its series resonant mode, in the collector-to-emitter feedback loop. The stability of the crystal is ± 0.001 percent over the temperature range of -15° to $+60^{\circ}\text{C}$. The overall VCXO frequency stability is ± 0.005 percent over the same temperature range. The oscillator is deviated by applying a voltage to a varactor diode in series with the crystal. The peak deviation at the VCXO output is one-eighth of the 9-kHz deviation at the transmitter output, or approximately 1200 Hz. The 1200-Hz peak deviation is accomplished with a 1-volt rms video input to the modulation amplifier. An adjustable inductor, in series with the varactor, is used to set the initial oscillator frequency; this setting is made with no signal input. A zener diode provides the bias voltage for the varactor diode.

(c) Frequency Doublers

All of the doublers use essentially the same circuit, except for the frequency of operation and minor differences in biasing. Each doubler is biased slightly into forward conduction with no RF drive applied in order to overcome the base emitter drop, V_{BE} . When biased in this manner, the transistor base emitter junction acts as a rectifier on the positive AC input swing without a fixed offset voltage. Part or all of the emitter resistance is capacitively bypassed, thus causing the base emitter junction to act as a peak rectifier. The peak AC current and average DC current are functions of the driving source resistance, the base emitter diode resistance, the transistor, and the size of the emitter resistor. Since the transistor is acting as a peak detector, it conducts only over a portion of the positive input half cycle with a conduction angle α . The amount of second harmonic current flowing is a function of the peak current and the conduction angle. By computing the average-to-peak current ratio from the peak rectifier characteristics, it is possible to establish the conduction angle, and hence the second harmonic current and output power.

(d) *Driver and Power Amplifier*

The driver and power amplifiers are both class C common emitter stages. Both transistors are stud-mounted to dissipate heat generated in the device. Although both the driver and power amplifiers are on the same circuit board, each stage becomes independent for tuneup and debugging purposes when driven from a 50-ohm source and terminated by 50 ohms. The configuration of the input and output matching circuits is identical in both stages. High impedance points, which are contributors to corona during critical pressure, are eliminated by proper design of the impedance matching networks.

Stability of the driver and power amplifiers was a prime consideration in the layout of the board, and short component leads and proper component placement were major objectives. Stability of the power amplifier under a wide range of load VSWR's and phase angles was achieved by the low-Q output circuit. The low pass filter provides additional isolation.

(e) *Telemetry Circuits*

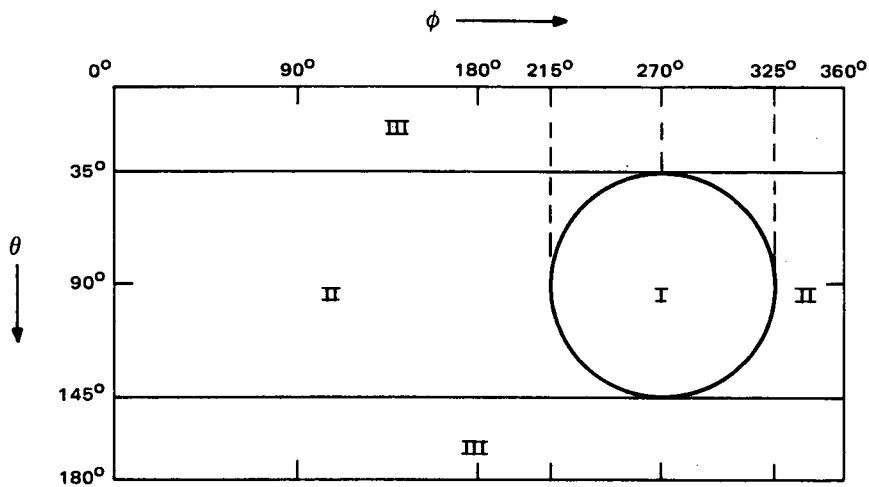
There are three telemetry circuits associated with the transmitter. One measures the temperature of the power amplifier transistor stud, and the other two monitor the driver and power amplifier RF voltages appearing at the transistor collectors. The temperature is monitored by using a simple resistor divider network with a thermistor which is bonded to the circuit board in close proximity to the power amplifier transistor stud. The driver and power telemetry circuits are peak detectors providing DC output voltages.

b. ANTENNA GROUP

(1) *INTRODUCTION*

The earlier TIROS spacecraft had a monopole element mounted on the top surface for reception of the command signals. TOS (ESSA) spacecraft had a different configuration using the same monopole but coupling the real-time (APT) transmitter to it. (Command reception was shifted to the four-dipole array mounted on the TOS baseplate). However, for ITOS spacecraft, new approaches to the real-time antenna were considered.

Because the real-time link operates only during the earth-lock mode of the spacecraft, a directional radiation pattern became desirable. This directionality provides a higher gain over the cone of interest, Region I (Figure 2-VII-21). The simplest approach, a two dipole array, was evaluated on a spacecraft mockup in several antenna configurations.



I = REGION WHICH SUBTENDS EARTH IN EARTH-LOCKED MODE.

II = REGION WHICH ILLUMINATES EARTH IF THE SPACECRAFT SPINS ON ITS Z AXIS BUT EXCLUDING REGION I.

III = REMAINING PATTERN CHARACTERISTIC WHICH EXCLUDES I AND II.

For ϕ and θ see Figure 2-VII-13 (S-band antenna).

Figure 2-VII-21. Gain Requirements, Deployed Panels

(a) Configuration Tests

To assess the most favorable of various alternatives, measurements were made of four different configurations as follows:

- Two half-wave sleeve dipoles in an endfire array mounted at the end of solar panel A and fed in quadrature;
- Two half-wave sleeve dipoles in an endfire array mounted at the end of solar panel C and fed in quadrature;
- Two quarter-wave dipoles in an endfire array mounted similarly to the preceding configuration;
- Two quarter-wave dipoles in a broadside array mounted on panel 5 at the corners nearest earth; and
- Two quarter-wave dipoles in an endfire array centrally located on panel 5.

The half-wave sleeve dipole used in the evaluation tests was constructed by RCA. It consisted of a 21.5-inch long rod less than 0.1 inch in diameter and attached to an assembly consisting of coaxial cable inside a 21.5-inch aluminum tube with a 5/8-inch diameter. The aluminum tube was an

open-circuited section used to prevent RF energy from traveling down the outside of the coaxial feed line. Overall antenna length was 43 inches or a half-wave at 137.5 MHz. Each quarter-wave antenna used in tests was the rod portion of the half-wave antenna described above with a short to the spacecraft being placed at the junction of the 5/8-inch aluminum tube.

With two half-wave dipoles on solar panel A and/or C, the measured linear pattern in the two principal planes ($\theta = 90$ degrees, $\phi = 270$ degrees) compares favorably with the theoretical pattern of two half-wave dipoles in free space. The θ - plane at $\phi = 215$ and 325 degrees was approximately 2 dB below the pattern maximum ($\phi = 270$ degrees). This means that the gain at the edge of the cone of interest for the θ - plane is about +3 dBi (dB with respect to isotropic). Lowest gain of the ϕ - plane at the edge of the cone is about 6.5 dB below the pattern maximum or -1.5 dBi. This pattern produced the highest gain of the four alternatives studied. An array on solar panel A or C consisting of quarter-wave elements had lower gain than the half-wave case. This occurred due to the large amount of energy distributed outside the cone of interest. The quarter-wave broadside array on panel 5 produces undesirable large back lobes which lowers gain in the cone of interest. A quarter-wave endfire array on panel 5 produces a pattern which is the least desirable of the four configurations. A large back lobe is present which is higher than the desired earth-directed beam.

The configuration which produced the best pattern in terms of gain and conical symmetry over the cone of interest was the half-wave endfire array on the end of a solar panel. This configuration also yields the best isolation (25 dB) from the real-time antenna to the beacon and command antenna at the real-time frequency and provides adequate isolation (22 dB) at the command frequency. Decoupling is an important asset since the real-time transmitter has the highest output power of all the spacecraft transmitters. The development of the real-time antenna was based on the conclusion that deployable half-wave dipoles on solar panels are the most feasible approach for ITOS.

(2) DESIGN CONSIDERATIONS

(a) Reliability Enhancement

The original concept for subsystem configuration was that one of the two transmitters would be selected by a coaxial relay and be fed to a single endfire array on the end of solar panel C. Although the coaxial relay circuit had been flown on TOS (ESSA) spacecraft, considerations for improving real-time subsystem reliability generated a design change and two completely redundant circuits were designed (Figure 2-VII-22). This final configuration avoids transmitter switching by connecting each real-time transmitter to its own endfire array. In addition to deleting the relay circuit, this change added a second array, notch filter, hybrid coupler, termination and cable set. Improved

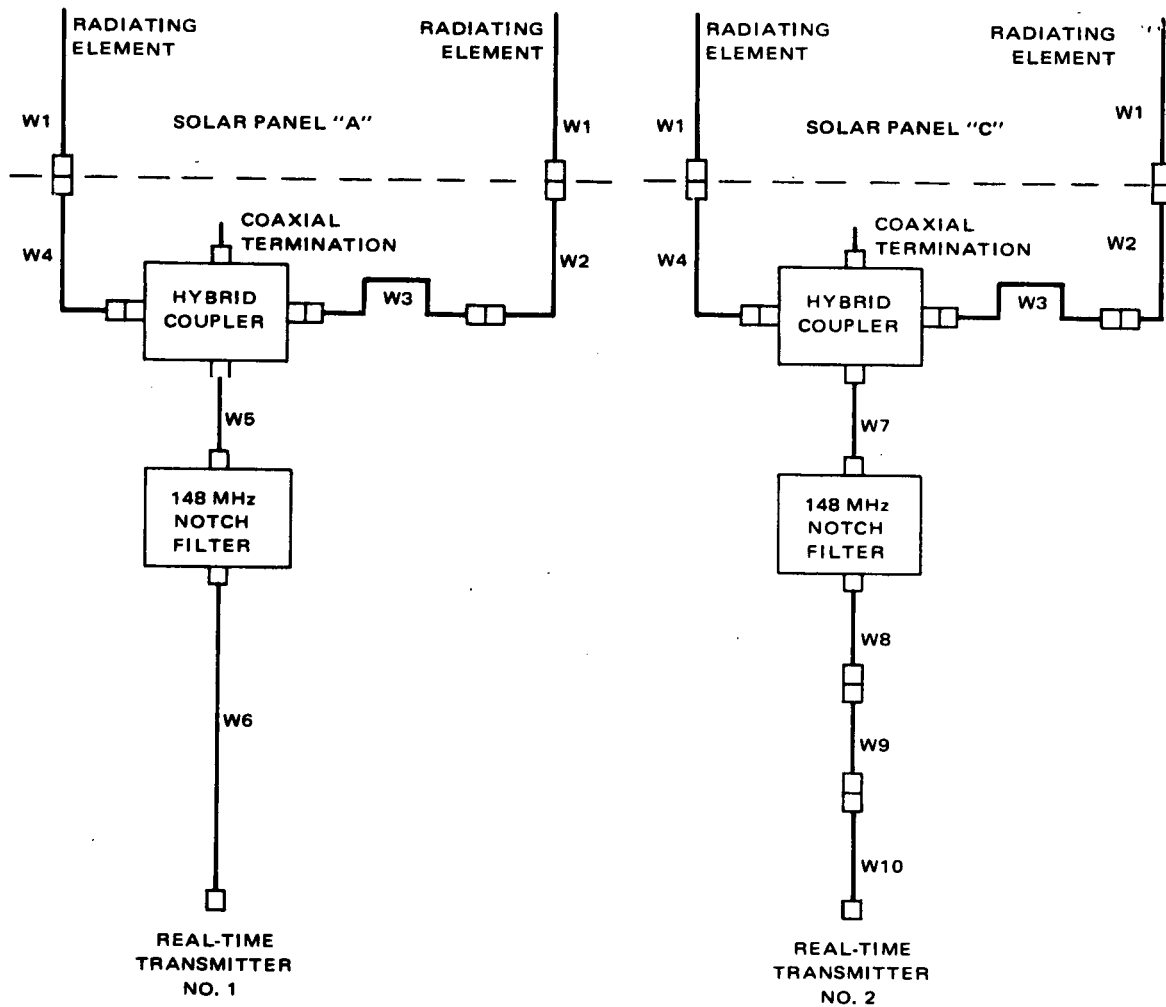


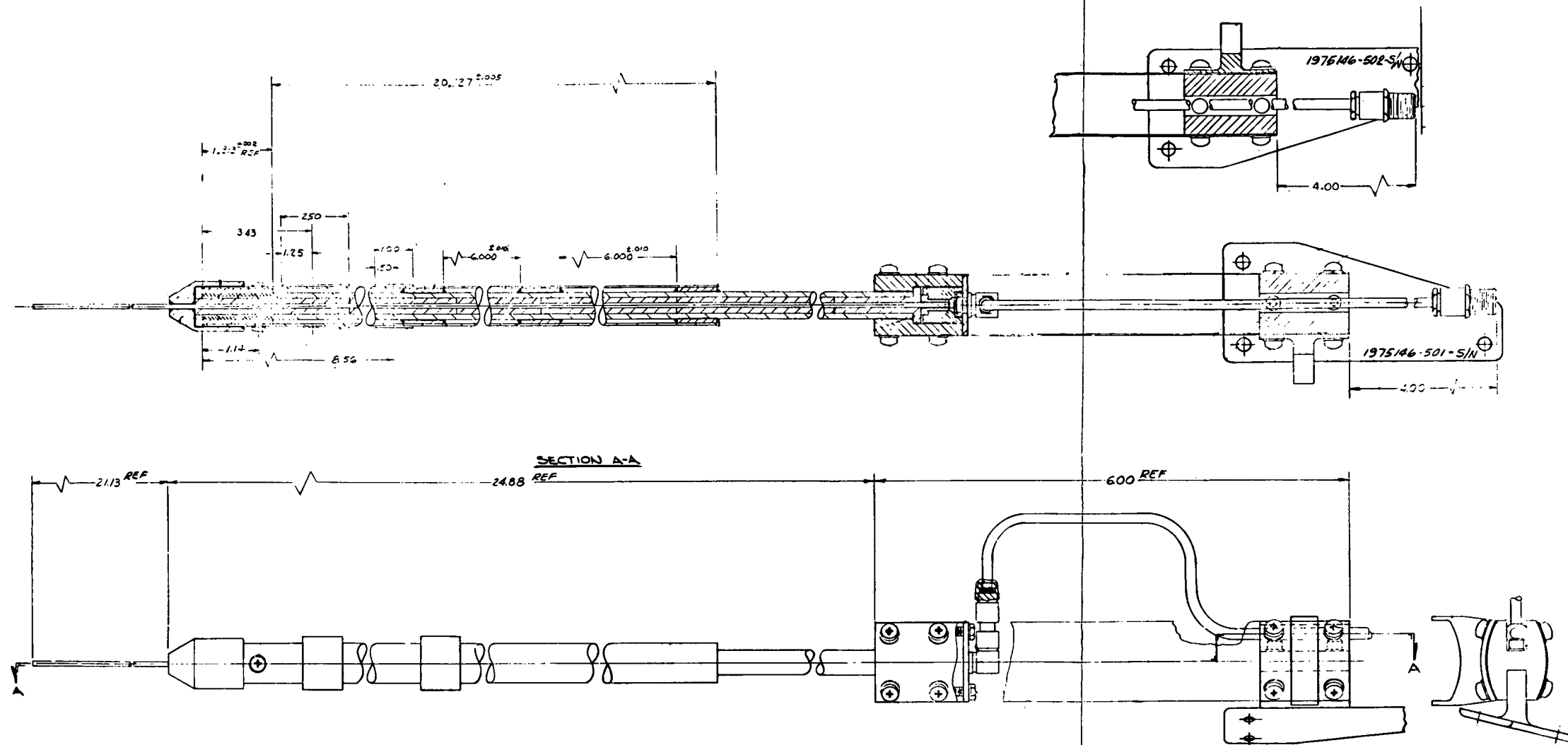
Figure 2-VII-22. Real-Time Antenna Group, Simplified Block Diagram

reliability afforded by a completely redundant configuration is deemed a favorable design tradeoff against the added weight involved.

(b) Deployment Design (Figures 2-VII-23 and 2-VII-24)

Due to the size of the half-wave array and the spacecraft envelope constraints dictated by the booster, the dipoles had to be deployable. The simplest approach is the use of cylindrical springs (Figure 2-VII-24). Each dipole is stowed along the edge of a solar panel when the panels are in a launch configuration; spacecraft body and solar panel brackets constrain the dipoles until panels have opened about 10 degrees from the spacecraft. At this point, no constraint applies and the springs deploy freely in the plane of the solar panel. When each dipole has deployed 180 degrees, its cylindrical spring locks solidly in place.

3



FOLDOUT FRAME 1

Figure 2-VII-23. Antenna Deployment

FOLDOUT FRAME 2

Initial deployment design for each dipole incorporated two springs. This design is adequate for deployment in a 0-G field and has been demonstrated. Two springs lack the energy required to deploy a dipole through 180 degrees against its own weight. Consequently, it became desirable to design the dipole to be deployable in a 1-G field at sea level. A three-spring deployment system was incorporated (2 inside leaves, 1 outside leaf). Deployment tests showed that considerable overshoot occurred when the element deployed in a horizontal plane. A fourth spring, called a stop spring, is included in the final deployment design to prevent overshoot.

(3) *ANTENNA DRIVE AND MATCHING INSERTION LOSS*

RF power from transmitter No. 1 feeds the dipole array on solar panel A; transmitter No. 2 feeds the array on panel C. The hybrid coupler splits power equally and in-phase to each dipole. To generate the directional pattern, the drive to the dipole nearest earth must lag the anti-earth dipole by 90 degrees; this 90-degree delay is achieved by cable W3, which is a quarter-wave transformer section.

The driving point impedance of each dipole is approximately $73 + j0$ ohms when each quarter-wave section is 21.5 inches long. When two such dipoles are fed as an endfire array with 0.41λ spacing and 90-degree differential phase, the calculated impedance of the dipole with leading current goes to about $50 + j0$ ohms; the impedance of the dipole with lagging current goes to about $110 + j0$ ohms. This means that the leading dipole almost perfectly matches the 50-ohm feed line while the lagging dipole has a mismatch yielding a VSWR on its line of about 2.2:1. Transformer matching by cable W3 is used on the feed line of the lagging dipole to improve the match. This quarter-wave transformer (W3) is fabricated with 75-ohm coax and provides the required 90-degree phase differential as well as an impedance match.

In case of a reasonably similar mismatch at the dipoles (which can be experienced when the dipoles are in the stowed mode), the 90-degree differential phase, in combination with the hybrid, results in only a slight degradation in the impedance match seen by each transmitter. This occurs because the reflected power from antenna mismatch is primarily dissipated in the coax termination (item 4) and does not appear on cables W7 or W5.

The total insertion loss to each dipole of the real-time array consists of several contributions, which are listed in Table 2-VII-9 using maximum specified values.

PRECEDING PAGE BLANK NOT FILMED

TABLE 2-VII-9. INSERTION LOSS

	Insertion Loss (dB) Transmitter to Each Dipole
Cable Attenuation	0.6
148-MHz Notch Filter (max)	0.4
Reflection and Interconnection Losses	0.3
Hybrid Split	3.0
Hybrid Loss	0.5
Total (max)	4.8

(4) *148-MHz NOTCH FILTER*

This component was described in Paragraph 2. VII. C. 3. f(5) and is utilized in this subsystem to provide adequate rejection at the command frequency of spurious signals generated by the real-time transmitter.

(5) *HYBRID COUPLER AND TERMINATION*

These components are vendor parts which are used to split the transmitter power equally to each dipole of the endfire array. In contrast to the hybrid in the beacon and command subsystem, which has an internal termination, this hybrid is a four-part device due to its higher input power. Any reflected power from dipoles due to inherent or stowed mismatch is dissipated in a separate termination. This coaxial termination has been flown previously on TOS spacecraft.

(6) *ANTENNA ASSEMBLY*

Each endfire array consists of two half-wave dipoles spaced 0.41λ and driven with their respective currents in 90-degree phase differential. Each dipole is center-fed from a 50-ohm coax, with the coax dressed colinearly with the dipole. The coax feed line dress is achieved by the use of a quarter-wave choke-sleeve isolator, in which the external portion of the sleeve is one quarter-wave length element of the dipole radiator while the inner portion of the sleeve forms an isolating balun. Unbalanced antenna currents are thus eliminated from the coax feed line as it extends colinearly away from the sleeve end of

the dipole. The mechanical design of each antenna assembly (dipole) is entirely new for ITOS, in particular the spring deployment techniques discussed in Paragraph 2. VII.C.3. See Figure 2-VII-23.

(7) *PERFORMANCE OF THE ELECTRICAL TEST MODEL (ETM)*

(a) *Nonradiation Tests*

Input VSWR and insertion loss measurements were made using a full-scale mockup and available TOS and vendor components. Results are discussed below.

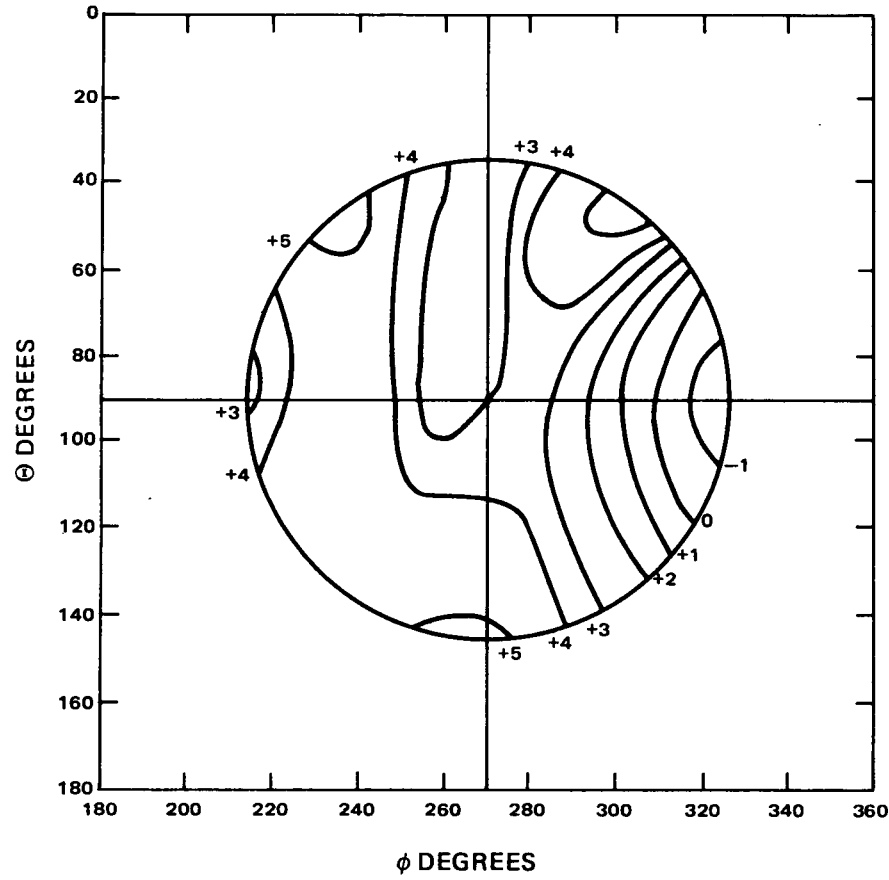
In the operational array mode (deployed dipoles), the dipole having the leading current exhibited a measured impedance of 58 to 60 ohms. The lagging dipole exhibited a measured impedance of 100 to 105 ohms. When the lagging dipole is matched to the hybrid, the VSWR at either transmitter port was no greater than 1.3:1.

In the stowed mode, the measurements were made on a simulated solar panel, fabricated of aluminum screen and frame with dimensions of the actual panel. Stowing the dipoles upsets the match quality at the dipole terminals, but, due to stowing symmetry, the stowed impedances of both dipoles should be similar. The hybrid, under this stowed impedance condition, can isolate the transmitter from the mismatch with slight degradation of input VSWR at the transmitter port. In the presence of the thermal blanket, the stowed impedances of the dipoles will be dissimilar. Under this condition, the input VSWR can be as high as 3:1 depending on the dress of the dipole rods relative to the spacecraft thermal blankets.

The measured insertion loss feeding the transmitter input port and measuring the output at the end of cable W1 was no greater than 4.3 dB. This measurement was made with a 50-ohm termination on the unused antenna port and is 0.5 dB under the specified value. It includes the 3-dB power split of the hybrid coupler. The rejection of spurious signals at the command frequency from the real-time transmitter is dependent on the rejection capability of the 148-MHz notch filter. Minimum rejection measured was 29 dB which exceeds the specified requirement by 9 dB.

(b) *Radiation Characteristics*

Radiation patterns of the real-time antenna were measured on an RDP plot as described in Paragraph 2. VII.C.3. A scaled test array was mounted on panel A of the 2:5 model and measured with a right-hand circularly polarized (RHC) antenna. The radiation pattern is shown in Figure 2-VII-25 with directivity contours labeled with respect to an isotropic antenna of linear



NOTES:

1. DIRECTIVITY CONTOURS SHOWN ARE RELATIVE TO LINEAR ISOTROPIC ANTENNA
2. FOR GAIN, RELATIVE TO CIRCULAR:
 - a. REDUCE 1.8 DB FOR MAXIMUM TRANSMISSION LINE LOSS
 - b. REDUCE 3 DB FOR POLARIZATION LOSS
3. RIGHT-SIDE PANEL ANTENNA WILL BE MIRROR IMAGE, ABOUT $\phi = 270^\circ$ AXIS
4. SPECIFICATION REQUIREMENT: -8.3 DB RELATIVE TO CIRCULAR ISOTROPIC OVER REGION.

Figure 2-VII-25. Real-Time Antenna, Left Panel

polarization. The pattern is asymmetrical because a free space condition does not exist for the array. Currents induced in the edges of the solar panel by the array cause a small degree of radiation yielding a slightly elliptical pattern. This ellipticity generates an asymmetrical RHC pattern. A minimum gain of -8.3 dB is required relative to isotropic when measured with a RHC antenna. This gain requirement is applicable in Region I only; there is no gain requirement in Regions II and III.

In the case of interest (Figure 2-VII-25), the minimum directivity is -1.0 dBi at the point $\theta = 90$ degrees, $\phi = 317$ degrees. Table 2-VII-10 lists the pertinent relationships.

TABLE 2-VII-10. MARGIN CALCULATION FOR REAL-TIME ANTENNA

Parameter	Gain or Loss
Minimum directivity relative to isotropic	-1.0 dBi
Maximum specified insertion loss	1.8 dB
Minimum gain relative to isotropic	-2.8 dBi
Polarization loss in RHC receiving antenna	3.0 dB
Minimum net antenna gain*	-5.8 dB
Minimum gain specified*	-8.3 dB
Excess or margin over spec	2.5 dB
*From transmitter input port to RHC receiving antenna; i. e. , includes all cable losses; insertion loss, and polarization loss.	

It is evident that the real-time antenna successfully meets specified requirements. The RHC pattern generated by the array on panel C will be similar to Figure 2-VII-25 rotated about $\phi = 270$ degrees.

E. S-BAND PLAYBACK FIDEO LINK

1. General

The S-band link is the major means of video data communication from the spacecraft to the CDA stations. Information that has been recorded throughout the satellite orbit is replayed on CDA station command and transmitted as one

multiplexed signal on a 1.6975-GHz carrier. At the CDA stations, this signal is demultiplexed, recorded, and subsequently retransmitted down long lines to NESC* at Suitland, Maryland.

There are three major sources of data for the playback video link: (1) the advanced vidicon camera subsystem (AVCS), (2) the scanning radiometer (SR) subsystem, and (3) the secondary sensors subsystem. The AVCS produces a high-resolution, television-type signal that provides cloud cover data during the daytime portion of the orbit. The SR produces a high-resolution infrared and visible signal that provides cloud cover data during the nighttime portion of the orbit, emitted earth-radiance measurements during day and night, and reflected earth-radiance during the day. The two secondary sensors, the solar proton monitor and the flat plate radiometer, provide digital signals representing proton flux densities and thermal radiation levels, respectively.

The AVCS and SR sensors are fully redundant, and each of the sensors provides inputs to the corresponding tape recorder. The secondary sensors are not redundant, and their outputs are recorded on a single incremental tape recorder. (Telemetry data is also recorded on the incremental tape recorder on a time-shared basis.) The AVCS and SR signals modulate subcarrier oscillators whose output is recorded; the secondary sensor outputs have a digital format that is recorded directly. During playback, each secondary sensor data channel frequency-modulates a subcarrier oscillator. The various subcarriers are combined in one of the redundant multiplexer sections to produce a composite signal having a frequency range from 11 to 480 kHz (see Figure 2-VII-26).

The preceding spectrum frequency-modulates one of the two S-band transmitters. The two transmitters are permanently connected to the antenna coupler, which supplies the S-band array with signals. The radiated wave is right-hand circular (RHC) for either transmitter. The selection of a transmitter is made by application of DC power from the CDU.

At the CDA station, the S-band signal is received by the 85-foot antenna and demodulated by an FM receiver. The subcarriers are then demultiplexed, shifted to the desired output frequency bands, and recorded on a tape recorder. The tape recorder playback is fed into the microwave link for transmission to Suitland, Maryland. There, each of the subcarriers is individually demodulated by a second FM discriminator into a baseband.

2. Signal Characteristics

a. AVCS SIGNALS

The AVCS video signal has a baseband of 60 kHz, and its data is made up of discrete frames. Normally, 11 frames are recorded during each orbit.

*NESC: National Environmental Satellite Center.

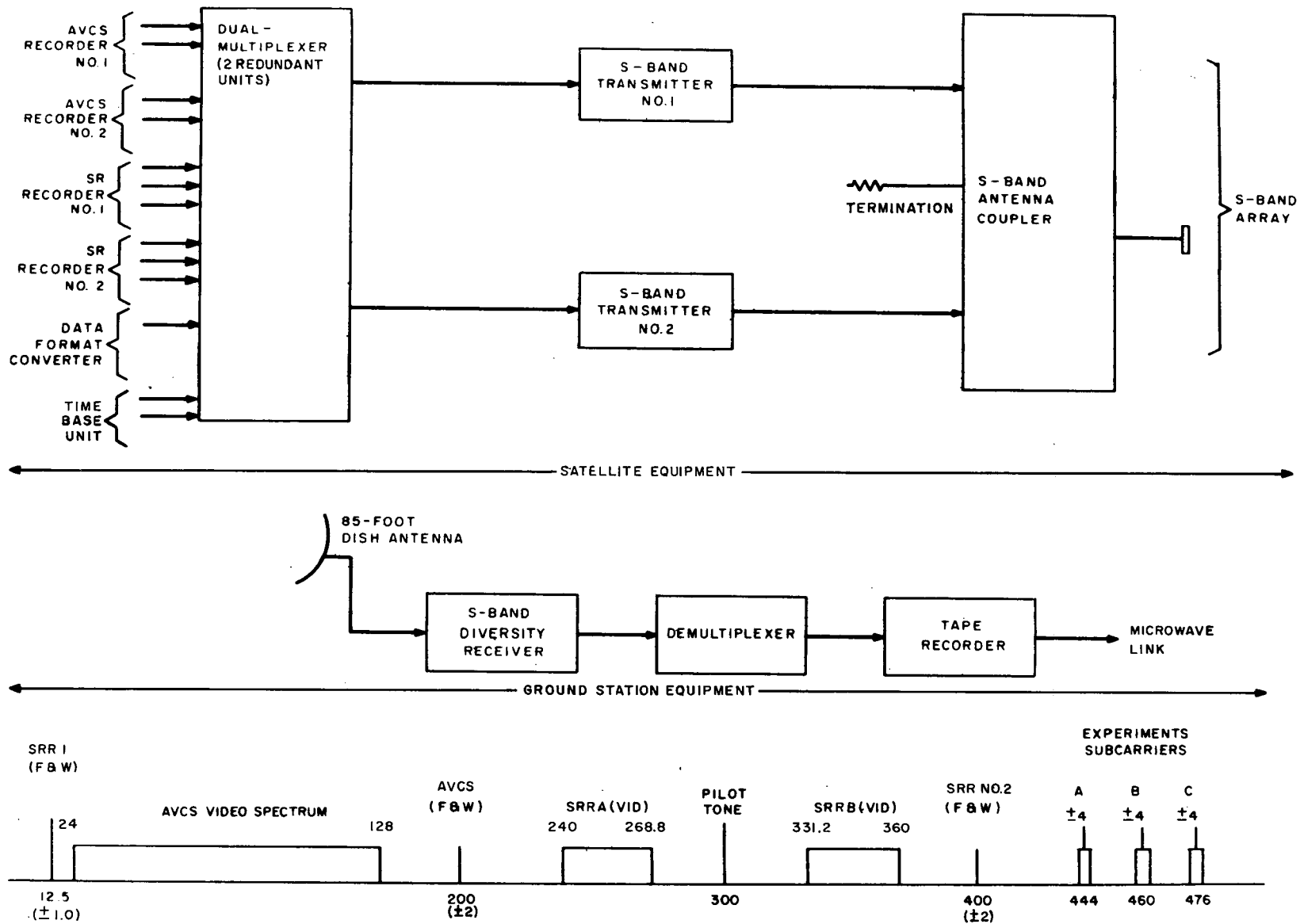


Figure 2-VII-26. Playback Video Link, Block Diagram

Each frame contains 900 lines, of which the first 33.3 and the last 33.3 lines are held at the black level; the remaining 833.3 lines contain video data. Each of the 833.3 lines is preceded by a blacker-than-black sync pulse of 625-microsecond duration; a line and a sync pulse occupy a period of 7.5 milliseconds.

Each frame is followed by a time code signal, which contains 24 RB bits. The first bit of the code is the least significant digit, and the time code resolution is 0.25 second. The code bit rate is 120 bits per second; the duration of each bit is 8.3 milliseconds. The time code is synchronous with the picture timing; four complete time codes follow each frame.

The composite video signal modulates a voltage-controlled oscillator to produce a 72-kHz sync tip, and 84-kHz black level output, and a 120-kHz white level output. These signals are recorded on a selected AVCS tape recorder; a second track of this recorder is fed simultaneously an accurate 50-kHz unmodulated signal. When a command Play Back AVCS Tape Recorder is received, the direction of tape motion is reversed and playback takes place.

b. SCANNING RADIOMETER SIGNALS

The scanning radiometer (SR) scans at a rate of 48 lines per minute and has an aperture of 5.3 milliradians in the IR channel and 2.8 milliradians in the visible channel. The earth portion of the scan occupies 110 degrees of the 360-degree rotation; its IR resolution is 4 nautical miles at the center while the visible resolution is 2.1 nautical miles at the center. The infrared channel is sensitive to the radiation in the spectral region between 10.5 and 12.5 microns; it detects radiation from sources between 185° and 330°K and has a resolution of 4.0°K at 185°K, and 1.0°K at 300°K. The visible channel detector responds to scene brightness of 20 to 8500 foot-lamberts in the spectral region from 0.52 to 0.73 microns.

The baseband spectrum of the IR video signal is from DC to 450 Hz, while the spectrum of the visible signal is from DC to 900 Hz. A sync pulse is inserted in the video data 75 degrees following the nadir. Sync consists of a 60-millisecond pulse with front and back porches of 20 milliseconds duration. The sync pulse is -8 volts DC while the 330°K/20 foot-lambert video level is -5.75 volts DC and the porches are approximately -0.025 volt DC while 185°K/8500 foot lambert video level is -0.25 volt DC. Bright clouds roughly correspond to -0.25 volt in the visible channel and -5.75 volts in the IR channel. The spectrum of the sync signal is from DC to 1250 Hz. The spacecraft tape

recorder, multiplexer, and ground demultiplexer will pass video signals with basebands up to approximately 1 kHz. However, the subcarrier detector on the ground should normally have a 450-Hz output low pass filter in order to improve the detected signal-to-noise ratio. Under strong received signal conditions it may be possible to obtain higher resolution visible data by increasing the ground subcarrier detector low pass filter bandwidth up to 900 Hz and still obtain an adequate signal-to-noise ratio. The period from 90 degrees following one nadir to 90 degrees in advance of the next nadir is time shared between telemetry, time code, and calibration signals.

The composite outputs from the IR processor frequency-modulate a voltage-controlled oscillator in the tape recorder electronics. The oscillator output frequency of 2.4 kHz corresponds to the 0-volt DC level, and that of 3.3 kHz to the sync tip level (-8 volts DC).

The SR tape recorder has three record tracks. The composite IR and visible outputs from the SR processor are recorded on tracks D1 and D3, respectively, while simultaneously, an accurate 3.125-kHz signal is being recorded on track D2. This channel, called the flutter-and-wow channel, will be frequency-modulated by tape speed variations, and thus provide data for later ground correction of time base error on the primary data channels.

During the record mode, the composite infrared and visible channel signals from the SR processor are applied to the respective FM modulators in the SR tape recorder electronics, where they frequency-modulate a 2.85-kHz subcarrier with a maximum frequency deviation from 2.4 to 3.3 kHz. These modulated radiometer signals are then applied to their respective record amplifiers, which apply drive power to tracks of the record head, resulting in the recording of data on tape tracks D1 and D3.

When the playback command is received from the ground station, -24.5-volt DC playback power is applied to the two data playback amplifiers, to the flutter-and-wow playback amplifier, and to the motor driver circuits of the tape recorder, starting the tape playback sequence. Playback tape speed (30 inches per second) is sixteen times record tape speed (1.875 inches per second). Therefore, the instantaneous frequencies are multiplied by 16 during the playback mode. The 3.125-kHz flutter-and-wow carrier is translated to 50 kHz plus or minus the small deviation caused by tape speed variations of the tape recorder. The maximum swing of the modulated radiometer signal frequencies is translated from 2.4 to 3.3 kHz to 38.4 to 52.8 kHz. These signals are applied to the dual multiplexer and used to frequency-modulate the S-band transmitter.

The ITOS system was configured to accommodate a scanning radiometer baseband signal of 450-Hz bandwidth. Subsequent to the finalization of the system and unit performance requirements and design, the visible output of the radiometer was expanded to 900 Hz. For both recorded and real-time channels, the demodulator low pass filters and consequent effects on signal-to-noise ratio represent the dominant constraint on utilization of this signal. The recorded channel capability is constrained principally by the low pass filter in the ESSA/NESC demodulator. Doubling the bandpass from 3.6 kHz to 7.2 kHz will result in a 7-dB reduction of signal-to-noise ratio from 35.7 dB to 28.7 dB. The real-time channel does not constrain the transmission of this data other than by the limitation which would be imposed by a 450-Hz low pass filter for processing SR in an APT ground station. Calculated link worst case signal-to-noise ratio (p-p/rms) for APT (1600-Hz low pass filter) is 34.9 dB, for SR-IR (450-Hz low pass filter) is 40.7 dB, and for SR-Vis (900-Hz low pass filter) is 37.5 dB. Note that if the APT low pass filter is used for all signals, the signal-to-noise ratio for all is 34.9 dB.

c. SECONDARY SENSORS

The secondary sensor data is recorded on three channels of the incremental tape recorder; one channel contains a clock signal, another the solar proton monitor data, and a third contains the flat plate radiometer data, telemetry, and time code. The data input is an NRZ pulse train having a bit rate of 15 bits per second.

The solar proton monitor data is divided into 20 words of 9 bits each. The first word of each frame contains a Barker code, thereby identifying the start of a frame.

The third-track data is divided into 60 words of 8 bits each. The first bit in each word is designated as a "word marker" and is fixed at a logical "0". A special word designated as a "frame marker" consists of 8 bits at logical "1". Each data frame consists of the following words: word 1, frame marker; word 2, frame marker; words 3 through 6, time code; words 7 through 21, flat plate radiometer; and words 22 through 60, telemetry data words.

On a command Play Back Incremental Tape Recorder, the direction of tape motion is reversed and the recorder is replayed continuously at a nominal rate of 2 kilobits per second NRZ (1 kHz). The outputs of the three tracks frequency-shift-key three oscillators centered at 144, 160, and 176 kHz, respectively. The oscillators accept signals up to 2 kHz.

3. Component Description

a. DUAL MULTIPLEXER

The dual multiplexer receives signal inputs from two advanced vidicon camera subsystem (AVCS) tape recorders, two scanning radiometer recorders (SRR), the data format converter (DFC) which processes the secondary experiments data, and the dual time base unit (see Table 2-VII-11). These signal inputs are then combined into a single broadband frequency spectrum capable of modulating either of two S-band transmitters. The dual multiplexer achieves this objective by frequency translation of the input signals (including direct frequency multiplication or division) followed by bandpass filtering and linear summation of the translated signals. The desired output is shown in Figure 2-VII-27.

TABLE 2-VII-11. DUAL MULTIPLEXER SIGNAL INPUTS

Source	Signal
AVCS Tape Recorder No. 1 or No. 2	Video (12 to 180 kHz) Flutter-and-wow (50 kHz)
SR Recorder No. 1	IR video (31.2 to 60 kHz) Visible video (31.2 to 60 kHz) Flutter-and-wow (50 kHz)
SR Recorder No. 2	IR video (31.2 to 60 kHz) Visible video (31.2 to 60 kHz) Flutter-and-wow (50 kHz)
DFC	Composite: sum of three frequency-modulated (± 4 kHz) subcarriers with center frequencies of 144, 160, and 176 kHz
TBU No. 1 or No. 2	300 kHz*
*This signal is used by the dual multiplexer to frequency-translate some of the other input signals.	

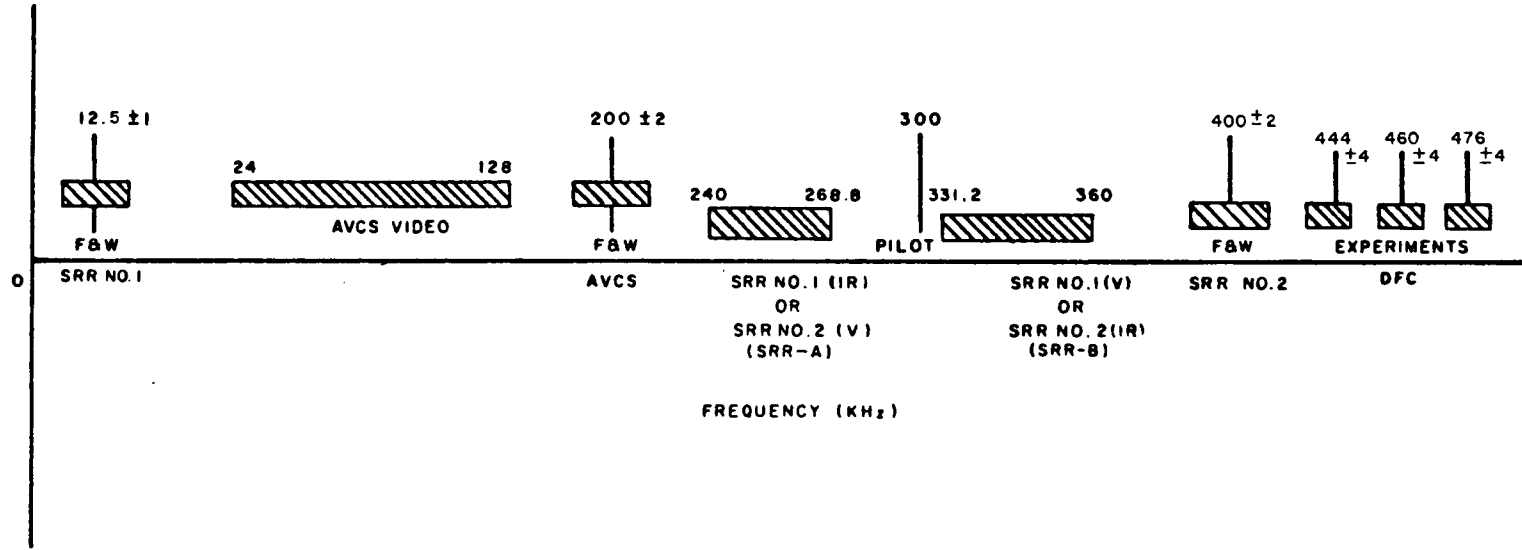


Figure 2-VII-27. Dual Multiplexer Output Spectrum

Two identical multiplexers are included within the dual multiplexer housing. Either multiplexer may be made operable by the application of power from the command distribution unit and can modulate either of two redundant S-band transmitters. The multiplexers are sufficiently buffered from each other so that a failure in one of them will not cause a loss of signal to the other.

The dual multiplexer is packaged in a 13.46- by 5.90- by 7.80-inch rectangular housing. The weight of the box assembly is 10.9 pounds. The output cable assemblies supplied with the multiplexer weigh 0.6 pound, making the total weight 11.5 pounds.

The aluminum housing assembly consists of an extruded base, a sheet metal wrap-around housing and a sheet metal top cover. Structural materials are predominantly aluminum alloy 6061. The dual multiplexer electronics assembly is composed of a total of 17 double-sided printed circuit boards, which plug into a four-layer harness board.

Input connections are provided by means of two 37-pin Cannon "Golden D" type connectors. Output connections are made using the two TM type RF receptacles. All external interface connectors are mounted on the ends of printed circuit boards opposite to the harness board connections and are accessible through the top cover.

Access holes are supplied on the top cover for the output level adjustment controls of all the channels in both multiplexers. These holes also provide a means for outgassing from the interior of the assembly.

All printed circuit board assemblies are conformally coated in accordance with RCA Specification 2021037 and the external finish is the standard AED blue epoxy polyamine coating.

(1) DESIGN HISTORY

Since many similarities existed between the application, design, and functioning of the proposed ITOS multiplexer and the Nimbus-HDRSS* B and D multiplexers, every attempt was made to utilize the Nimbus design techniques and circuitry. However, the completely different signal-processing and redundancy requirements, and differences in mechanical specifications required an almost completely new detailed mechanical and circuit design for the dual multiplexer.

Nimbus-HDRSS designs used for ITOS with relatively minor changes included the double balanced modulators, the frequency doublers, and the summing amplifier. Also adapted from the HDRSS multiplexer was the layout

*HDRSS - High Data Rate Storage System

scheme for the printed circuit boards. This technique utilizes one side of the board as a copper shield and achieves very good isolation of signals between the inputs and outputs of filters and between adjacent boards.

The filter design and evaluation techniques for the HDRSS multiplexers were used extensively, although the actual filter designs were tailored to the differing signal processing requirements.

The original circuit designs developed for the dual multiplexer included the following:

- Input buffering pads,
- Filters,
- Frequency-divider chain,
- Output variable pads,
- Power turn-on transient suppressor,
- Output gating amplifier and cross-coupling arrangement, and
- Harness board.

The major areas of new design were related to the signal-processing and redundancy requirements. A major departure from the Nimbus-HDRSS design was the elimination of local oscillators from the multiplexer, made possible by the frequency allocation scheme used. With this scheme, all frequency translation is accomplished by mixing the signal concerned with a stable 300-kHz input signal from the dual time base unit, or by direct frequency-division or -doubling or a combination of these methods. Using an external local oscillator source reduces the weight, power consumption, and circuit complexity of the dual multiplexer.

New mechanical and thermal designs were required, although the basic mechanical design followed a standardization plan for "blue box" assemblies developed for ITOS; this plan was promoted to establish a similarity between boxes and to reduce costs.

The following paragraphs describe the design history of individual components of the dual multiplexer.

(a) *Input Buffering Pads*

The input signals to the redundant multiplexers are cross-strapped by resistive pads to provide sufficient isolation against faults in the redundant signal inputs or redundant multiplexer sections or both. Resistive isolation was chosen rather than active (i. e. , emitter follower) buffering because of its

greater inherent reliability. A pad loss between 10 and 12 dB was chosen as the best compromise between required isolation and desired output level to the signal processing circuits.

There are two general types of pads required: single input and dual input. Single input pads are required for nonredundant inputs, and dual input pads are used when redundant inputs are available to the dual multiplexer. In either case, an isolated output was provided for each redundant section of the dual multiplexer. The pad configuration is a dual cross-strapped pi network. This general pi configuration has the advantage of permitting any necessary design adjustments by changes in resistor values rather than changes in the pad configuration or printed circuit layout.

To assist in the design and evaluation of these pads, computer programs were developed to permit rapid evaluation of design parameter and component value changes, as well as evaluation of the performance of the system under fault conditions and component-tolerance variations. These programs proved to be valuable time-savers during the course of the design.

The pads were designed and constructed using high stability 1-percent tolerance fixed-film resistors (RN55C type). A total of seven different designs are used in the final multiplexer.

(b) Filters

The dual multiplexer incorporates a total of nine filter designs which were achieved by using tables for normalized filters. In the case of bandpass filters, using these tables results in filters that have geometric symmetry.

In all cases but one, the elliptical function (Cauer) filter configuration was chosen. Filters designed with this configuration provide a constant maximum amplitude ripple and impedance variation within the passband, very sharp cut-off, and a minimum equal ripple attenuation value in the stop band. A Tschebichev-configuration filter was utilized as a bandpass filter following the flutter-and-wow frequency doublers, where the stop band requirements are much less severe. In all cases, the simplest possible filter design compatible with the overall system requirements was chosen in order to minimize the extent of phase equalization required in the system.

A computer program performed the necessary low pass to bandpass transformation and the calculations of the actual filter component values. The filter designs were evaluated with the aid of another computer program to verify the design and to provide a guide to check the actual filter performance. This evaluation was made on the basis of lossless elements; the effects of finite Q values could be determined by comparison with the measured

characteristics. The computer program was set up to provide amplitude response, phase response, and envelope delay over the frequency range selected. The resultant data was used as a basis for the design of the required phase equalizers in the demultiplexer.

The general construction of the filters utilized dipped mica capacitors and adjustable temperature-compensated cup cores to obtain long term and temperature stability. To obtain high-Q coils, particularly in the higher-frequency filters and filters with narrow-percentage bandwidth, Litz wire was used in many cases, as well as a core material most suitable for the desired frequency range.

(c) *Double-Balanced Modulators*

The double-balanced modulators used in the multiplexer are essentially identical with those developed for Nimbus-HDRSS.

Minor modifications to the design replace the local oscillator driver transistor with one having a higher Beta characteristic (Type 2N930) and increase the size of the unbypassed emitter resistor. These changes reduce the loading effect of the transistors on the output of the TBU channel bandpass filter; this reduction was necessary because of the need to drive three buffer amplifiers in parallel from the output of this filter.

Another modification was to reduce the turns ratio of the driver transformer in order to reduce the peak voltage swing in the collector of the driver transistor. Thus, an even more conservative derating was used for this transistor than in the Nimbus circuitry.

(d) *Frequency Doublers*

The flutter-and-wow frequency doublers circuitry is essentially the same as that of Nimbus-HDRSS. A minor change is the addition of a forward-biased diode in the formerly-grounded centertap of the full-wave rectifier doubler-transformer. This diode introduces a DC-level shift to compensate for the DC offset of the rectifier diodes in the doubler circuit, thus improving the efficiency of the doubler at the lower signal levels encountered due to the loss introduced by the input buffering pads.

The buffer transistor was replaced with one having a higher Beta characteristic (Type 2N930) in order to reduce the loading effects of the transistor on the output of the doubler and thereby present a more nearly constant load impedance to the doubler.

(e) *Frequency-Divider Chain*

An output frequency of 12.5 kHz is required from the flutter-and-wow signal of SR recorder No. 1 (initially 50 kHz). To perform the divide by 4 operation, a flip-flop chain using two cascaded low-power DTL integrated circuit JK flip-flops was selected. A simple zener diode regulator provides the required controlled voltage to the integrated circuits. The flip-flop chain is followed by a low pass filter which selects the fundamental frequency component for combination with the other multiplexer signals.

Since the input signal level available from the input buffering pads was too small to operate the flip-flop chain directly, a transistor buffer stage, operated in the switching mode, was used to provide the correct DC levels and switching voltage to the first flip-flop. A clamping diode network is used to reference the input signal to the zener diode voltage, which is the signal ground of the transistor buffer and flip-flop chain.

The clamping network includes a forward biased diode used to cancel the offset voltage of the clamping diode and thus prevent degradation of sensitivity of the transistor buffer stage.

Since the output level from the flip-flops is independent of the input signal level once the triggering level is reached, the input buffering pad loss on this channel was reduced to 6.5 dB nominal to increase the drive level margin to the transistor buffer stage.

A worst-case analysis was performed on the input buffering pads to determine the worst-case drive level margins as a function of component tolerances and faults in the redundant input or redundant multiplexer. The usual worst-case dissipation and output fanout capability analysis was carried out on the dividing chain.

The dividing chain was constructed and tested during Fairchild 9040 series high reliability, low power DTL JK flip-flops.

(f) *Output Variable Pads*

The input signals, after frequency translation and filtering, must be linearly summed to form a composite-spectrum output. This summation is accomplished by resistive attenuators connected together at the very low impedance input of the summing amplifier. The frequency deviation of the S-band transmitter is proportional to the signal levels at the output of the summing amplifier, and, therefore, adjustments are usually provided prior to the summing point to permit compensation for buildup of tolerances in each channel and adjustment of the deviation schedule to the exact desired value.

For Nimbus-HDRSS, the component values within a given range for each of the summing attenuators were selected during testing. For the dual multiplexer, it was decided to eliminate all "select at test" components and, instead, to provide variable adjustment controls for the deviation schedule.

The design goals for these attenuators were as follows:

- ± 40 -percent nominal level-adjustment range, arithmetically centered about the nominal value;
- Minimum input impedance variation about the nominal value; and
- A single variable resistor, of a standard available value, to perform the level adjustment.

The configuration finally chosen was that of a T-pad with a variable resistor forming part of the output (summing) branch. Since it is not possible to calculate exact component values meeting all of the above criteria in closed form, a short program was developed for a time-shared computer to compute the final component values by means of successive iterations. Another program was developed to assist in evaluation of attenuator performance as a function of component tolerances and different settings of the level control.

The pads were designed and constructed using high-stability 1-percent tolerance fixed-film resistors (RN55C type) and high-reliability, wire-wound, miniature potentiometers. Five different designs are included in the multiplexer.

(g) *Summing Amplifier*

The summing amplifier used in each multiplexer uses 6 dB less feedback than in Nimbus-HDRSS B in order to provide additional gain to compensate for the greater overall loss due to the input buffering pads. In addition, as a result of a design-review action item, the dissipation of the output transistor was reduced to conform with the recommended values in the ITOS standard parts list. A DC worst-case tolerance analysis was then performed on the revised circuit. No evidence of any abnormal behavior was encountered.

The calculated input impedance of the summing amplifier is on the order of 5 ohms, thus providing suitable isolation between the summed signal inputs.

A breadboard model of the circuit was constructed and measurements made of distortion and output clipping level; the reduced feedback does not significantly alter the performance of the summing amplifier.

During testing of the Environmental Test Model, an oscillation of the summing amplifier (which had not been present in the breadboard model) was detected. This oscillation was traced to the board grounding layout and corrected by modifying the layout to utilize the entire back side of the printed circuit board as a circuit ground instead of as a remotely connected ground shield, and by rerouting certain signal traces for better output to input isolation.

During further testing, it was discovered that the summing amplifier was sensitive to noise pickup from the regulated power line. This problem was traced to an existing noise flow path from the power line through a biasing resistor to the input of the amplifier. The problem was eliminated by changing the polarity of the transistor from NPN to PNP (i. e. , substitution of Type 2N869A) and reversing the biasing circuit so that the guilty biasing resistor is now returned to ground rather than to the power line. An improvement of 35 dB in noise rejection was obtained in this manner.

(h) Output Gating Amplifier and Cross-Coupling Arrangement

To make the output from either multiplexer available to either of the two S-band transmitters, some form of cross-coupling had to be provided. In addition, it was essential to maintain a high degree of isolation between the two summing amplifier outputs so that a failure in one multiplexer would not affect operation of the other. The cross-coupling arrangement could not significantly degrade the output signal handling capability or introduce distortion, should have a low output impedance to drive the output cables to the transmitters, should be stable under the expected loads, and should have near-unity voltage gain.

The cross-coupling arrangement finally chosen involved two gating amplifiers, each associated with a particular transmitter. Each gating amplifier would have a low input impedance to permit summing of the multiplexer outputs while maintaining a high degree of isolation between the multiplexers.

The configuration chosen for the gating amplifier was that of a shunt feedback pair, similar to the summing amplifier, with the output taken from the emitter of the output transistor to obtain the required low output impedance. PNP (silicon) transistors were utilized to permit the output to be taken directly between emitter and ground, thus isolating noise components introduced by the power line. An additional advantage of the use of PNP transistors was the elimination of any transistor reversed-biased conditions during turn-on.

A simple zener diode regulator was used to provide controlled power to each gating amplifier so that each amplifier could be powered from the same unregulated line that supplies the associated S-band transmitter.

The calculated input impedance of the gating amplifier is on the order of 30 ohms, thus providing adequate isolation between summing amplifier outputs, which are isolated from this point by 5110 ohms. The gain was calculated to be 1.05 with the component values finally chosen.

Computer analyses were made both of the amplifier AC stability and of the shift in DC operating point with worst-case transistor parameter and component tolerances. No evidence of instability or other abnormal behavior was found.

A breadboard model of the circuit was constructed and measurements made of distortion and output clipping level. The clipping level was found to be 8.0 volts p-p, or over 3 times the required output level of 2.5 volts. The total harmonic distortion measured at 3.0 volts p-p output was found to be 0.2 percent.

In addition to the cross-coupled multiplexer inputs, an input test point to the gating amplifiers was provided to permit bypassing of the signal processing circuits of the multiplexer during test or for future applications.

(i) *Power Turn-On Transient Suppressor*

To satisfy the requirements of the performance specification concerning the maximum slope of the leading edge of the turn-on transient current on the regulated voltage supply bus, a 0.5-mH inductor was included in series with the power lead to each multiplexer. This inductor, in conjunction with the multiplexer input filter capacitor-resistor combination, forms a critically damped series RLC circuit which controls the rate of rise of the turn-on transient current.

A diode was placed in parallel with the 0.5-mH inductor to prevent the generation of undesirable voltage transients during turn-off.

(j) *Harness Board*

The harness board is a four-layer printed circuit board; the primary consideration in the layout of this board was the prevention of possible cross-talk of signals between printed circuit traces. This was accomplished by the use of a shield layer, connected to multiplexer ground, between the signal runs and the potentially noisy power runs. In addition, all signal-carrying traces were separated as much as possible from each other.

During the course of ETM testing, some residual crosstalk was noted and traced to (1) signal pickup by the high-gain summing amplifier input and (2) the inherent lack of a provision for grounding the shell of the (Malco) female connectors utilized on the harness board. The first cause was eliminated by

removing the summing amplifier input connections from the harness board altogether and utilizing shielded wire connections for these runs. The second cause was eliminated by modifying the female connectors by attaching a grounding terminal and connecting this terminal to the harness board shield layer.

(k) *Mechanical and Thermal Design*

The multiplexer housing is an example of the "standard" ITOS construction: an extruded base having brazed end plates, a one piece wrap-around body supporting all printed circuit boards in Birtcher slides, and a flanged top cover. Malco connectors on the printed circuit boards mate with a floating four-layer harness board. Two of the printed circuit boards act as connections between the harness board and the Cannon external connectors at the top of the box (these boards contain the input buffering pads and some power supply circuitry).

The concept used in the allocation of electrical circuitry to the printed circuit boards was to divide the overall circuitry in a manner that would reduce crosstalk of signals on harness board runs.

The layout of all circuit boards incorporates a copper shield on the side opposite the components. In addition, MUX 1 and MUX 2 boards are alternated with one another to provide additional shielding. Since only one multiplexer is active at a time, the interleaving of MUX 1 and MUX 2 boards places a dead board between active boards and thereby increases the shielding between circuits.

The copper shields of all circuit boards, as well as the shield layer on the harness board, are connected together and form the internal multiplexer ground reference for both multiplexers. This multiplexer ground is isolated from the housing, which is provided with its own separate ground lead.

A mechanical stress-and-vibration analysis was performed on the multiplexer assembly. As a result of this analysis, two epoxy-glass stiffeners were bonded to each printed circuit board to reduce the maximum deflection levels of the board during vibration. The harness board was similarly modified with four stiffeners.

The harness board and printed circuit board mounting was mechanically decoupled from the structure to decrease the vibration transmissibility levels. This was accomplished by the use of resilient Birtcher slides and permitting lateral excursion of the harness board.

A vibration test, performed on a mechanical demonstration model to evaluate the mechanical design and to provide verification of the theoretical analysis, gave satisfactory results.

A thermal analysis of the dual multiplexer assembly was performed. As a result, thermally conductive epoxy was used to bond selected components to the board to improve heat transfer. To improve the radiation heat transfer, the inside of the housing was painted with a high-emissivity paint ("AED blue").

The total heat dissipation is estimated to be about 1.93 watts.

(2) DETAILED FUNCTIONAL DESCRIPTION

The dual multiplexer consists of two identical multiplexers enclosed in the same housing. Input signals are distributed to the two multiplexers by resistive attenuators, which provide isolation between redundant inputs and also between the two multiplexers. Only one multiplexer is active at any given time.

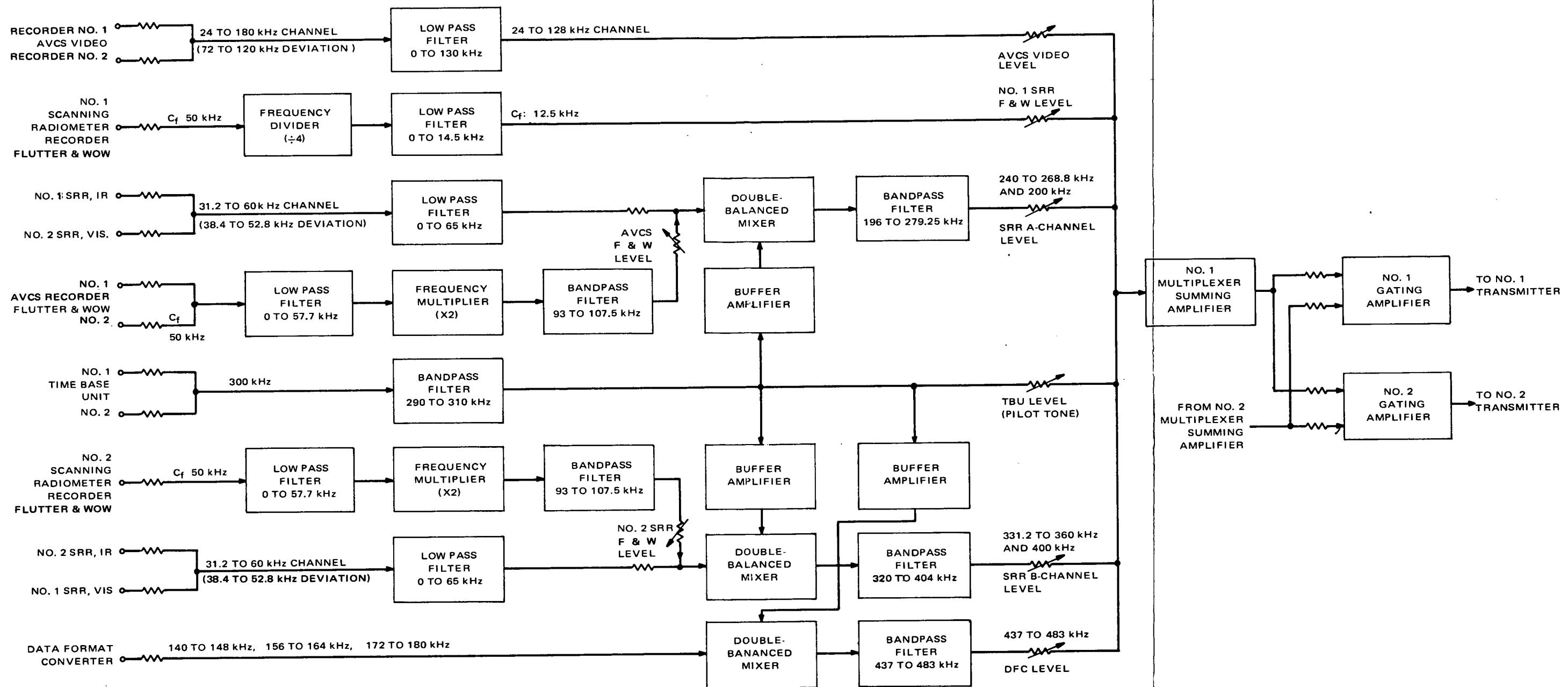
The various input signals are processed within each multiplexer as shown in Figure 2-VII-28. The processing of the individual channel signals is described in detail in the following sections. The processed signals are resistively combined in a linear summing amplifier.

The outputs of the summing amplifiers from both multiplexers are, in turn resistively cross-coupled to the inputs of two linear gating amplifiers as shown in Figure 2-VII-29. Only one gating amplifier is active at any given time. Each gating amplifier feeds one of the S-band transmitters and is powered from the same control relay as the associated S-band transmitter. By this arrangement, the output of the active multiplexer is steered to the active S-band transmitter. Thus, either multiplexer can be used to modulate either S-band transmitter. Resistive isolation is provided by the cross-coupling arrangement, so that a fault in one multiplexer will not affect operation of the other.

(a) AVCS Video Channel

The outputs of the two redundant AVCS recorders are combined in a resistive network which provides a nominal 12.1 dB of isolation from each recorder output to the signal-processing circuits in each multiplexer. However, signals are delivered to this circuit from only one recorder at a time. See RCA 1976095 in the Logic Diagrams Manual previously referenced.

The video signal from the active recorder is a frequency-modulated square wave with a deviation range of 72 to 120 kHz and a maximum modulation frequency of 60 kHz.



EOLDOUT FRAME 1

EOLDOUT FRAME 2

Figure 2-VII-28. Multiplexer Unit, Block Diagram

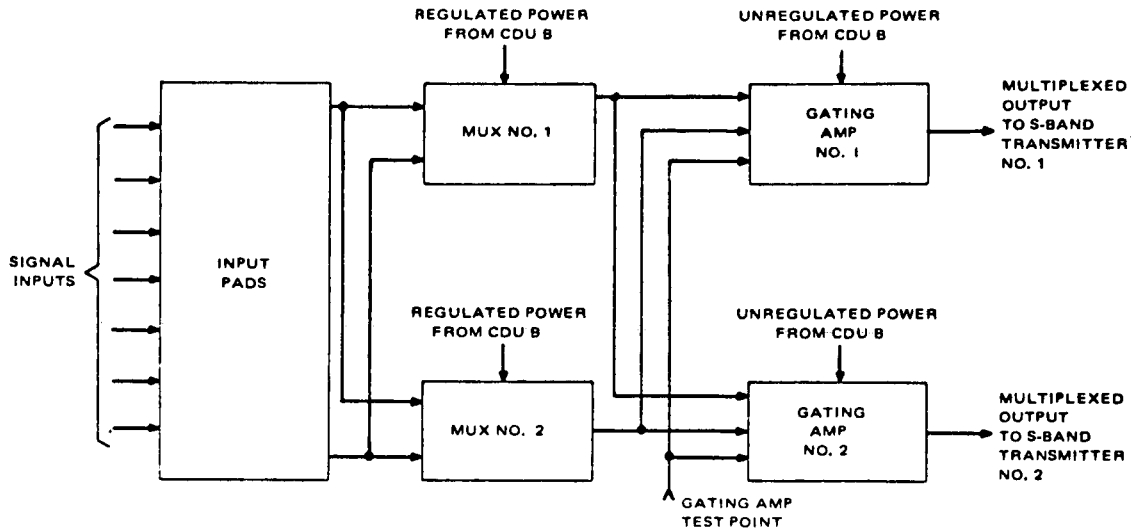


Figure 2-VII-29. Dual Multiplexer, Simplified Block Diagram

For AVCS video, the signal processing circuitry consists merely of a low pass filter and a level adjustment pad. The low pass filter eliminates high frequency components above 130 kHz and the level adjustment pad permits adjustment of the output level to the summing amplifier over a ± 25 -percent nominal range.

(b) *SR Recorder No. 1 Flutter-and-Wow Channel*

The 50-kHz square wave signal from the SRR No. 1 flutter-and-wow output is first passed through a 1:1 transformer to isolate the ground return from the multiplexer ground. The signal is then coupled to the two redundant multiplexers by means of a resistive network. This resistive network provides a nominal 6.4 dB of isolation from the recorder output to the signal processing circuits in each multiplexer.

The signal processing circuitry (see RCA 1976095) consists of a clamping-diode network which references the input signal to a -5.1 -volt regulated voltage obtained from a zener diode. (This voltage is also used as the negative supply for the integrated circuits.) The clamping network includes a forward-biased diode (CR-3), used to cancel the offset voltage of the clamping diode (CR-2). The clamped signal drives a buffer transistor stage which is operated in the switching mode to provide the correct DC levels and switching voltage to the first of two cascaded low power DTL integrated circuit JK flip-flops.

PRECEDING PAGE BLANK NOT TO BE REPRODUCED

The flip-flop divider chain, which lowers the input frequency to 12.5 kHz, is followed by a 0- to 14.5-kHz low pass filter which passes only the fundamental frequency component of the flip-flop chain output. A level adjustment pad permits adjustment of the output level to the summing amplifier over a ± 25 -percent nominal range.

(c) *SRR A Channel*

One output circuit from SRR No. 1 and one from SRR No. 2 are combined by a resistive network (see RCA 1976095). This network provides a nominal 11.7 dB of isolation from each recorder output to the signal processing circuits of each multiplexer. Either the SRR No. 1 infrared output signal or the SRR No. 2 visual output signal is present at any given time.

The active SRR video signal is a frequency-modulated square wave with a deviation range of 38.4 to 52.8 kHz and a maximum IR modulation frequency of 7.2 kHz (14.4 kHz in the visible channel). The signal is processed by first passing it through a low pass filter to eliminate high frequency components above 65 kHz (see RCA 1976095).

The flutter-and-wow outputs from the two redundant AVCS recorders are combined by means of a resistive network. This network provides a nominal 10.5 dB of isolation from each recorder output to the signal-processing circuits of each multiplexer. The 50-kHz square wave signal from only one of the recorders is present at any given time.

The active AVCS flutter-and-wow signal is passed through a 0- to 57.7-kHz low pass filter in order to select the fundamental frequency component. The fundamental signal is then doubled in frequency by passing it through a full-wave rectifier circuit. A forward-biased diode is used to cancel the offset voltage of the rectifier diodes and thus improve the efficiency of the doubler. The doubled signal is amplified by a transistor stage. The fundamental component of the doubled signal (100 kHz) is then selected by means of a narrow bandpass filter (93 to 107.5 kHz).

The frequency-doubled AVCS flutter-and-wow signal is then combined in a resistive network with the filtered SRR video signal. This resistive network provides a means of adjustment of the flutter-and-wow signal level to allow setting the desired video to flutter-and-wow level ratio.

The composite SRR video plus AVCS flutter-and-wow signals, referred to as the SRR A channel signals, are then passed through a double balanced mixer where both lower and upper sidebands are generated by mixing with the 300-kHz signal obtained from the TBU channel (see RCA 1976095).

The lower sideband signal is then selected by a 196- to 279.25-kHz bandpass filter. The output of the filter is fed to a variable output network which provides a means of adjusting the composite SRR A channel level to the summing amplifier over a ± 25 -percent nominal range.

(d) *SRR B Channel*

The SRR B channel is very similar to the SRR A channel previously described.

Processed video signals from either the visual output of SRR No. 1 or the infrared output of SRR No. 2 are combined by means of a resistive network and then split to each multiplexer. This network is identical to the one in the SRR A channel. Only one of these recorder outputs is active at any given time.

The active SRR video signal is processed by first passing it through a low pass filter identical to the one in the SRR A channel.

The 50-kHz square wave signal from SRR No. 2 flutter-and-wow output is coupled to the two multiplexers by means of a resistive network. This network provides a nominal 10.5 dB of isolation from the recorder output to the signal processing circuits in each multiplexer.

The SRR No. 2 flutter-and-wow signal is processed in the same manner as the AVCS flutter-and-wow signal in the SRR A channel. That is, the signal is first passed through a 0- to 57.7-kHz low pass filter, doubled in frequency, amplified, and then passed through a 93- to 107.5-kHz narrow bandpass filter.

The frequency-doubled SRR No. 2 flutter-and-wow signal then combines in a resistive network with the filtered SRR video signal in a similar manner to that in the SRR A channel.

The composite video plus filter-and-wow signals, referred to as the SRR B channel signals, are then passed through a double balanced mixer where both upper and lower sidebands are generated by mixing with the 300-kHz signal obtained from the TBU channel.

The upper sideband is then selected by a 320- to 404-kHz bandpass filter. The output of the filter is fed to a variable output network which provides a means of adjusting the composite SRR B channel level to the summing amplifier over a ± 25 -percent nominal range.

(e) *DFC Channel*

The output signals from the data format converter (DFC) are coupled to the two multiplexers by means of a resistive network. This network provides a nominal 8.8 dB of isolation from the DFC output to the signal processing circuits in each multiplexer. See RCA 1976095.

The output of the DFC is a composite sum of three voltage-controlled-oscillator (VCO) outputs with center frequencies of 144, 160, and 176 kHz. The three VCO's are frequency-modulated by digital data from the secondary experiments (flat plate radiometer and solar proton monitor), telemetry data, and time code information. The VCO outputs have a deviation range of ± 4 kHz. The modulation rate is nominally 2 kilobits per second. Only one nonredundant output is provided from the DFC.

The composite signal from the DFC is passed through a double balanced mixer where both upper and lower sidebands are generated by mixing it with the 300-kHz signal obtained from the TBU channel.

The upper sideband is then selected by a 437- to 483-kHz bandpass filter. The output of the filter is then fed to a variable output network which permits adjustment of the composite DFC channel output level to the summing amplifier over a ± 25 -percent nominal range.

(f) *TBU Channel*

The 300-kHz square wave signals from either of two redundant outputs of the TBU are combined in a resistive network. This network provides a nominal 11.1 dB of attenuation from each TBU output to each multiplexer. Only one TBU output is active at any given time. See RCA 1976095.

The active TBU signal is first passed through a 1:1 turns-ratio transformer to isolate the ground return to the TBU unit. The signal is then passed through a 290- to 310-kHz narrow bandpass filter in order to select the fundamental component. The filtered pilot tone signal is fed to a variable output network which permits adjustment of the output level to the summing amplifier over a ± 25 -percent nominal range.

The filtered 300-kHz signal is also sent to three individual buffer amplifiers which generate the high-level local oscillator signal for the double balanced mixers used in the SRR A, SRR B, and DFC channels previously described. A multiple capacitor arrangement is utilized for coupling the 300-kHz signal to the buffer amplifiers to increase the overall system reliability.

The 300-kHz pilot tone signal is transmitted as part of the modulation of the S-band transmitter for use in the ground station demultiplexer to recover the baseband signals.

(g) *Summing Amplifier*

The processed signals of the various channels in each multiplexer are resistively combined at the input of its summing amplifier. As previously described, the resistive output networks in each channel permit adjustment of the individual output level of each channel over a ± 25 -percent nominal range.

The summing amplifier in each multiplexer consists of a shunt feedback transistor pair. This amplifier features low input impedance, low distortion, high gain and high output-signal handling capability.

The low input impedance of this amplifier provides a high degree of isolation between the signal processing circuits of the various channels. The low distortion and high output signal handling capability prevent the creation of undesirable harmonic or intermodulation distortion products. The high gain compensates for the various losses in the signal processing circuits, notably those of the input resistive networks and double balanced mixers.

(h) *Gating Amplifier*

The composite output signals from the two redundant multiplexers are cross-coupled to the inputs of two linear gating amplifiers. Only one multiplexer is active at any given time.

Each gating amplifier consists of a shunt feedback transistor pair very similar to the multiplexer summing amplifier, but with the output taken from the emitter of the last stage. This amplifier features low input and output impedances, low distortion, and high output signal handling capability. The low input impedance of this amplifier permits a high degree of isolation between the multiplexer outputs so that a fault in one multiplexer will not affect the operation of the other multiplexer. The gating amplifier and isolating network combination is designed to have near unity gain.

The output of each gating amplifier feeds one of the two redundant S-band transmitters. A simple zener regulator is provided so that each gating amplifier can be powered from the same unregulated line that supplies the associated S-band transmitter. Thus, powering a given S-band transmitter automatically powers the associated gating amplifier.

A spare test point summing input to both gating amplifiers is also provided to permit bypassing of the multiplexers during testing or for other future applications.

b. S-BAND TRANSMITTER

The S-band transmitter will be used for transmission of a frequency-division-multiplexed (FDM) spectrum extending from 10 to 480 kHz, consisting of multiple data channels between the spacecraft and ground stations. The transmitter frequency is 1697.5 MHz, and the power requirement at the end of 1 year in orbit is 1 watt, minimum. Each spacecraft contains two such transmitters.

The transmitter, which is a modified Teledyne Model TR-2202I (all solid-state design), is composed of five separate sections:

- Frequency synthesizer,
- Power amplifier,
- Multiplier filter assembly,
- Voltage regulator, and
- Housing.

Figure 2-VII-30 is a block diagram of the S-band transmitter. As shown, the frequency-modulated oscillator (FMO) has a basic frequency of 76.567 MHz, and the crystal oscillator operates at 107.067 MHz. Spurious response is minimized by multiplying the crystal oscillator frequency 6 times ($6 \times 107.067 \text{ MHz} = 642.402 \text{ MHz}$) before mixing with the FMO signal, and then taking the difference frequency from the mixer ($642.402 \text{ MHz} - 76.567 \text{ MHz} = 565.835 \text{ MHz}$).

Carrier modulation is achieved by application of the modulating signal to a modified common base Colpitts oscillator circuit. The modulating signal is applied to a voltage-variable-capacitance diode which is connected across the tank circuit of a common base, modified Colpitts oscillator.

The crystal oscillator is also a common base, modified Colpitts oscillator. A fifth overtone crystal is used in the base to provide a low impedance signal path at the frequency of operation.

The frequency multiplier, Q102, is driven into class C operation by the drive signal from the crystal oscillator. The tripler is followed by doubler transistor Q103, which multiplies the signal frequency to 642.402 MHz.

The mixer is tuned to select only the difference of the FMO and the previously multiplied sixth harmonic of the crystal oscillator. This is followed by a three-stage bandpass filter which will pass the sideband components of the modulating signal while reducing the spurious signals generated by mixing. The amplifier shown in the mixer-amplifier box consists of two stages of amplification, and the output of the mixer-amplifier is 20 milliwatts.

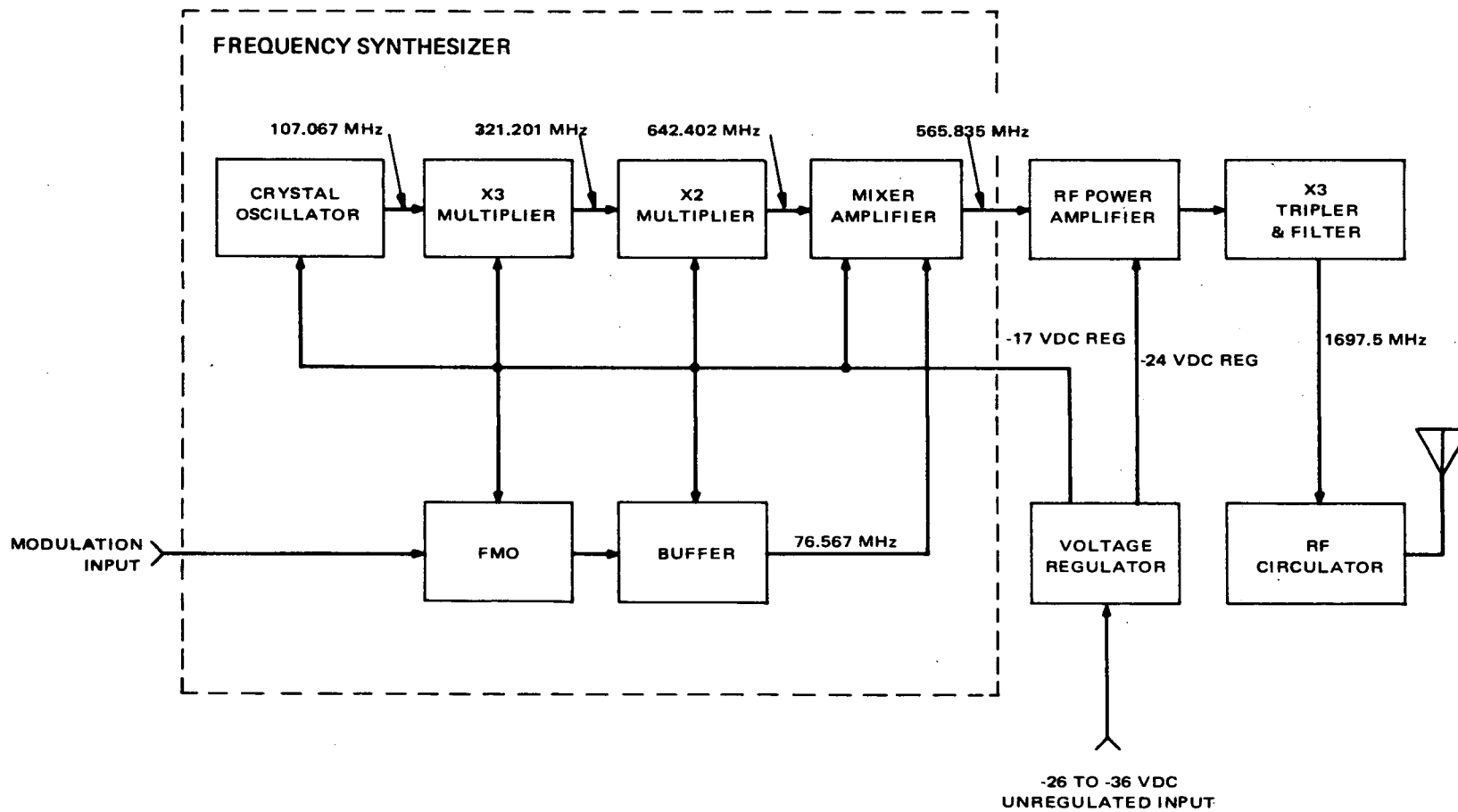


Figure 2-VII-30. S-Band Transmitter, Block Diagram

The power amplifier contains five stages of amplification, and the output level is 12 watts at 565.833 MHz. A bias amplifier transistor provides a stable low impedance source. The first three amplifier stages are operated with the transistors in class A condition in the absence of signal, but each stage is driven into class C operation when the signal is applied. The last two stages are operated with no bias applied and are driven into conduction by the drive signal. The RF amplifier is separated into two chassis to distribute gain and prevent oscillations.

The 2N4959 transistor, which is the epitaxial, passivated, annular process type, was selected because of the relatively high gain (15 dB minimum at 450 MHz) and the small junction area, as evidenced by an emitter-to-base capacitance of 0.8 picofarad maximum. The product of current gain and bandwidth is 1,000 MHz minimum, which indicates that the gain below this frequency will be high.

In the multiplier-filter chassis, lumped constants are used for input matching, and coaxial cavities are used for output matching. A step recovery diode serves as the multiplier.

The purpose of the RF circulator at the output of the multiplier-filter is to provide a constant load, thus assuring desirable bandpass characteristics regardless of load variations. The circulator has an internal load which is capable of continuously dissipating the reflected power if the RF output were open or short-circuited. The RF circulator also includes a telemetering network for monitoring RF power output.

The voltage regulator provides a 17-volt output for the frequency synthesizer and a 24-volt output for the power amplifier. An overcurrent circuit is included in the regulator to limit the current surge during transmitter turn-on.

Frequencies of the crystal oscillator and FMO were chosen to prevent the generation of any fundamental, harmonic, or mixer product that falls within the command receiver frequency band. The transmitter unit is sealed with RFI gaskets to prevent leakage of RF energy, and the regulator is in a separate section of the transmitter, completely RF-sealed. The wires connecting the regulator compartment to the transmitter circuitry pass through RFI filters to prevent RF energy from being conducted to the regulator. The regulator has been bypassed in order to meet the necessary RF and audio susceptibility requirements.

Throughout the entire transmitter, each stage is separated by a compartment that prevents electromagnetic coupling between stages. Each assembly is constructed in a manner to prevent large RF currents from circulating on the outer edges of the chassis, and each chassis is separated into a DC and AC side to prevent the AC from being coupled from one circuit to another. The synthesizer and main power amplifier are separated by the central web in the

housing to prevent the low frequency oscillators from feeding through into the output amplifier and filter. The output filter contains four high-Q cavities. This filter prevents any spurious signal generated by the multiplying process from appearing with the output signal.

Problems which occurred during qualification testing resulted in several design modifications. A power loss, which was attributed to the power amplifier and multiplier, was noticed during thermal-vacuum testing. To overcome this effect, the final three stages of the power amplifier and the input coupling network to the multiplier were encapsulated in Eccof foam FPH. Modifications made to the cavity filters include:

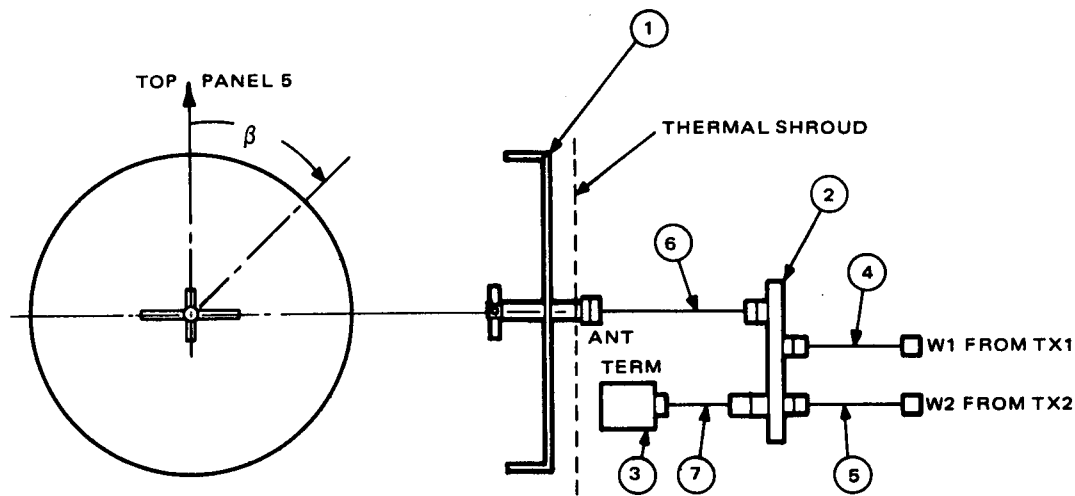
- All sharp edges were removed from the threads on the tuning screws.
- The outer walls of the tuner near the probes were flattened.
- Rexolite bushings were provided in each tuner.
- One probe in the second cavity was replaced with a fixed component.

c. ANTENNA GROUP (Figure 2-VII-31)

(1) INTRODUCTION

In the earth-lock mode of operation, the spacecraft utilizes a shaped-beam, directional, S-band antenna. Two such antennas were developed to provide higher gain at large nadir angles (α in Figure 2-VII-32) and be circularly-polarized. In the first design, the radiator consisted of a four-dipole array configuration over a circular base. This configuration coupled the two transmitters to the antenna via a printed stripline hybrid. Transmitter No. 1 radiated a RHC polarization and transmitter No. 2 radiated LHC polarization, due to the hybrid coupler itself. During the development of the four-element, dual polarized antenna, a system study indicated that the antenna would not be compatible with the CDA stations. While the CDA stations are capable of receiving data from either an RHC or an LHC polarized wave, they are not capable of optimum tracking operation when tracking an LHC polarized signal. The antenna configuration was, therefore, changed to provide RHC polarization of the transmitted wave, regardless of which transmitter is coupled to the antenna.

The second and final antenna configuration employs a single-port, RHC polarized turnstile over a circular base. The radiator is fed by a printed stripline hybrid, which couples both transmitters to the antenna. Radiation from either transmitter is RHC.



ITEM NO.	DESCRIPTION
1	S-BAND ANTENNA
2	S-BAND COUPLER
3	COAXIAL TERMINATION
4	COAXIAL CABLE, W1
5	COAXIAL CABLE, W2
6	COAXIAL CABLE, W3
7	COAXIAL CABLE, W4

Figure 2-VII-31. S-Band Antenna Subsystem

(2) DESIGN CONSIDERATIONS

(a) Reliability

The final design dissipates half of the output power of either transmitter in a termination resistor. This was an accepted system approach that traded off 3 dB of loss in radiated power for the high reliability of the passive hybrid coupler. The approach has a higher apparent reliability associated with state-of-the-art electromechanical, solid-state and ferrite switches. Stripline couplers have been flown on all TOS and ESSA spacecraft with 100-percent reliability.

(b) Spacecraft Effects

The pattern radiated by the S-band antenna consists of radiation from the antenna assembly and from induced spacecraft currents and reflections from protruding sensors.

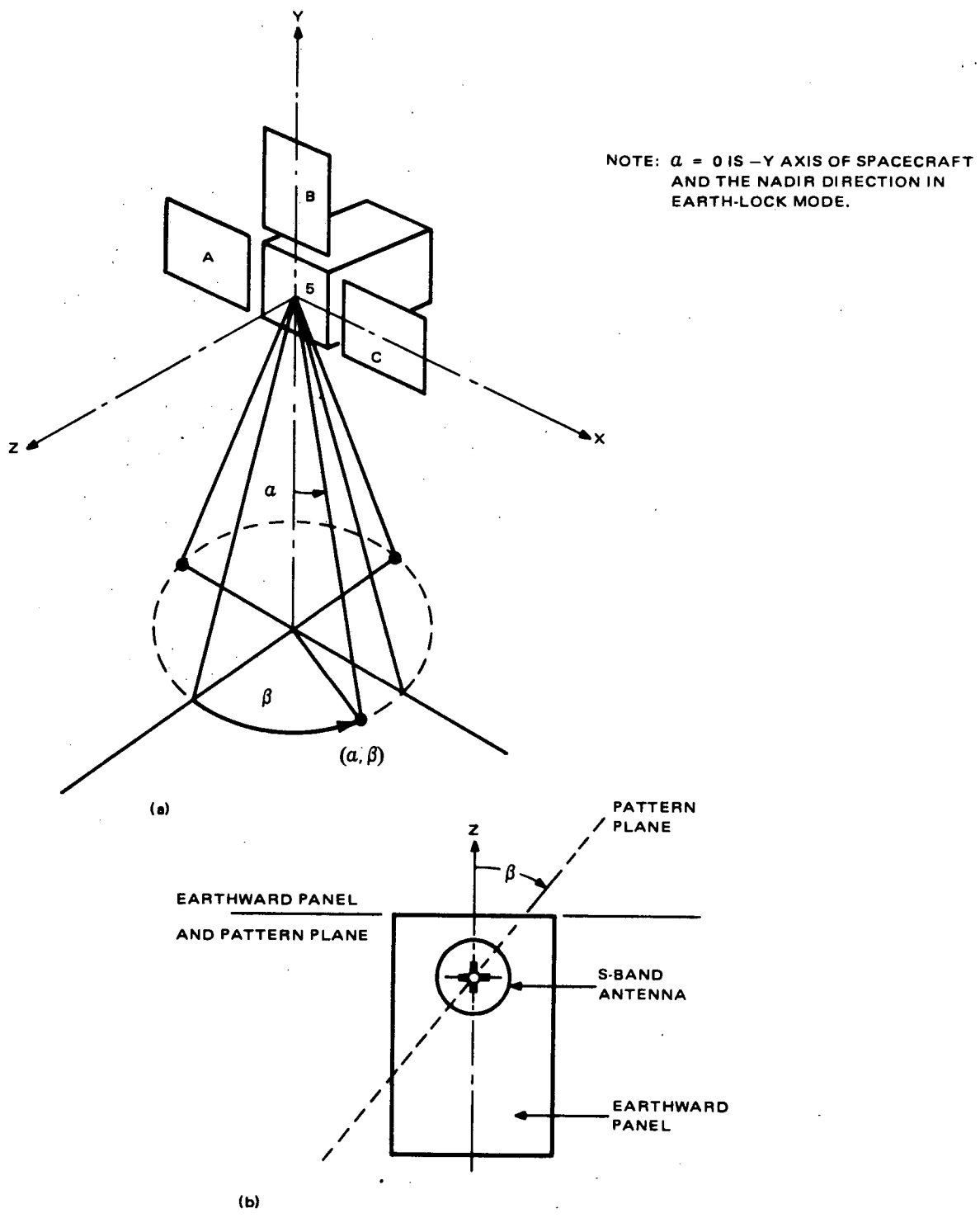


Figure 2-VII-32. Relation of ITOS Spacecraft to the Coordinate System as Used in Pattern Measurements for S-Band Antenna

A circular fence was utilized around the antenna base to minimize effects of the spacecraft on the pattern. Radiation characteristics are almost independent of the spacecraft. The antenna is an integral component that mounts on the earthward panel.

The most critical electrical requirement is the gain at $\alpha = 55$ degrees, which is the nadir angle at the maximum operating slant range. A shaped-beam design approach must be utilized to satisfy the gain requirements. A higher gain is required at larger α angles for the pattern plane which includes the spacecraft axis ($\beta = 0$ degree). Patterns were measured on the spacecraft for two orientations of the turnstile. It was found that the best gain at $\alpha = 55$ degrees, for the $\beta = 0$ degree plane, occurred when the short dipole axis is aligned with the spacecraft axis. This orientation is fixed on the final design by the use of asymmetrical mounting holes for the antenna base and spacecraft.

(3) *INSERTION LOSS, ISOLATION, AND MATCHING*

Total insertion loss from the input end of the transmitter (W1 or W2) to free space is composed of several losses, shown in Table 2-VII-12, based on published data.

Transmitter-to-transmitter isolation is provided by the coupler, which consists of a 70-ohm stripline hybrid. Inherent hybrid isolation is at least 25 dB with matched outputs. Figure 2-VII-33 shows nominal operation when transmitter No. 1 output is 2 watts and inherent hybrid isolation is 25 dB.

TABLE 2-VII-12. INSERTION LOSSES, S-BAND ANTENNA

	Insertion Loss (dB) Transmitter to Antenna
Stripline Loss	0.15
Power Split	3.0
TX and Antenna Cable Losses	0.79
Mismatch Loss	0.18
Antenna Mismatch	0.04
Total (dB, maximum)	4.16

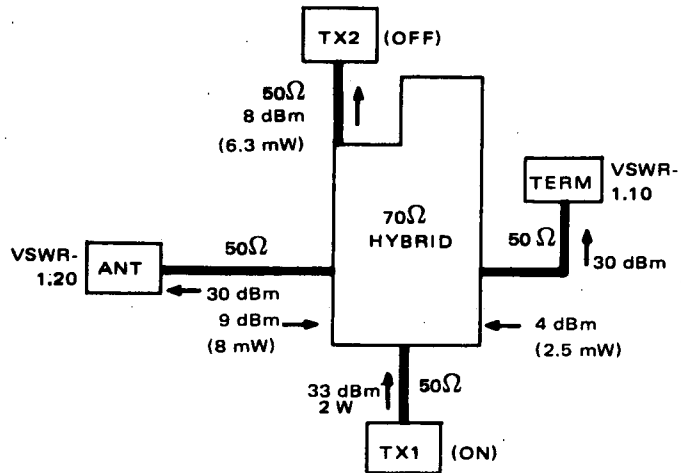
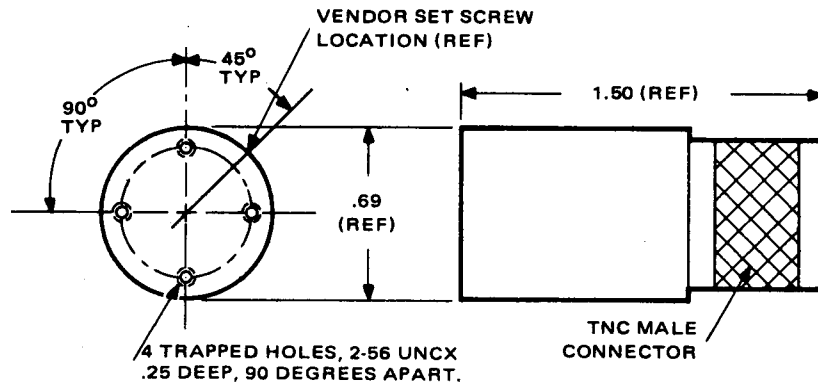


Figure 2-VII-33. Transmitter Isolation



ELECTRICAL CHARACTERISTICS:

VSWR: 1.10 MAX., 130-150 MHz, 1600-1800 MHz
 IMPEDANCE: 50 OHMS NOMINAL
 PWR. RATING: 10 WATTS AVERAGE
 TEMPERATURE RANGE: -55° TO +85°C

Figure 2-VII-34. Coaxial Termination

Reflected power from the antenna and termination are indicated, assuming a maximum VSWR of 1.20, which is a reasonable match for manufactured dipoles. The 1.10 VSWR for the termination is the specified value shown in Figure 2-VII-34.

If all of the reflected power returns to the TX2 port, isolation would be $10 \log 2000/16.8$ or 20.8 dB. Actually some of the reflected power returns to TX1 so that this number is slightly pessimistic. In Figure 2-VII-33, reflected power from the termination is about one quarter of the antenna reflection. It can be shown that 92 percent of the total reflected power can return to the isolation port.

The worst-case isolation is then $10 \log 2000/15.9$ or 21.0 dB. If the termination is a perfect match, only half of the reflected power reaches the isolation port and the isolation is 22.9 dB. It is apparent that these isolation figures are significantly better than the 15-dB isolation.

The total antenna admittance at the dipole (turnstile) consists of the parallel combination of three admittances; the slotted line admittance, the dipole admittance, and the discontinuity capacitive susceptance (see Figure 2-VII-35). This total balanced antenna admittance was measured to be $Y_a = 0.78 + j 0.52$, normalized to a 70-ohm line, at the dipole. The unbalanced impedance that must be matched is $1/4 Y_a$ or $0.22 - j 0.15$, normalized to a 70-ohm line. As shown in Figure 2-VII-35, a quarter-wave section of 27.6 ohms is located at a voltage minimum and transforms the load impedance from 15.3 to 50 ohms. Teflon dielectric converts the input line to a 50-ohm characteristic.

Each input VSWR at the transmitter is not only dependent upon the design of the dipole and coupler, but also on the length of the transmitter and antenna cables. The phasing between reflections at the antenna, each TNC panel connector, and each TNC cable connector directly affects the input VSWR's.

(4) *TERMINATION (ITEM 3, FIGURE 2-VII-33)*

This component is identical with the units employed in the real-time subsystem and loads one port of the printed stripline coupler.

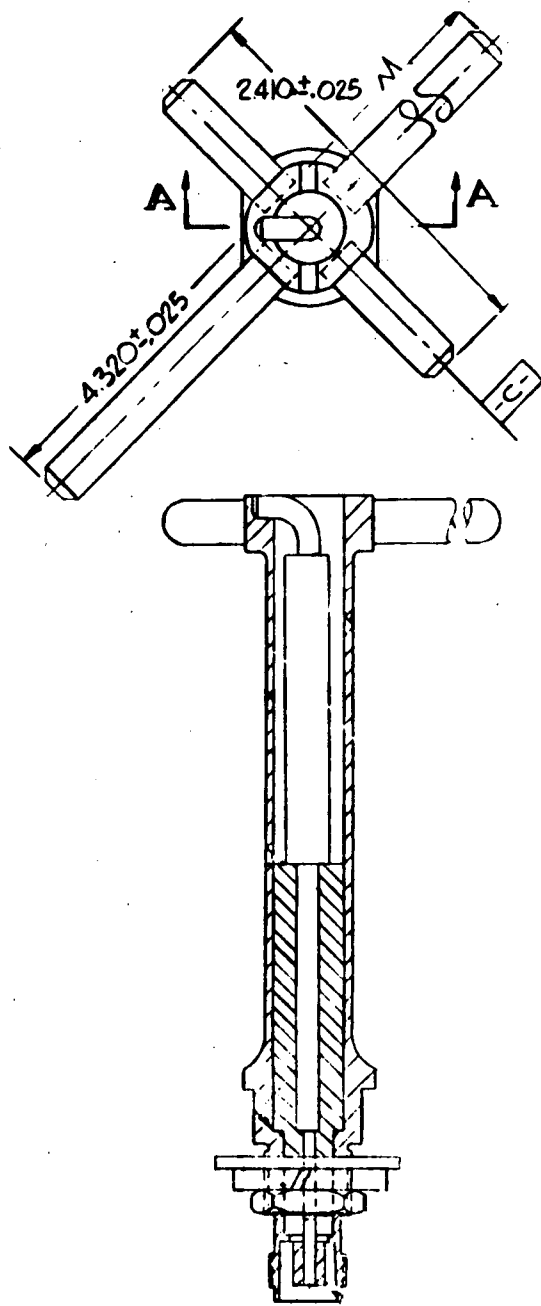
(5) *S-BAND COUPLER (ITEM 2, FIGURE 2-VII-31)*

This component consists of a printed stripline sandwich of Teflon-fiberglass boards. The stripline circuit is a 70-ohm hybrid, which couples both transmitters to the antenna, isolates transmitters, and transfers the crossed-dipole match to the transmitter ports without significant degradation. Reliability of this hybrid coupler is very high as discussed in Paragraph 2. VII. E. 3. c. (2)(a).

(6) *S-BAND ANTENNA ASSEMBLY (ITEM 1, FIGURE 2-VII-31)*

The antenna assembly consists of the crossed-dipole radiator (turnstile) over a circular base. It is designed to give RHC polarization over the required 110-degree beamwidth. Height of the dipoles over the base is chosen to radiate a shaped-beam, which provides higher gain at larger nadir angles.

Electrically, the crossed-dipoles are fed in parallel by a split tube balun. Circular polarization is achieved by exciting two orthogonal dipoles of unequal lengths. Proper excitation occurs when the dipole admittances are essentially



SECTION A-A

Figure 2-VII-35. Dipole Antenna

in quadrature and dipole conductances are equal. Since the critical requirement is the 55-degree gain the excitation need not produce best circularity on the dipole axis ($\alpha = 0$). Final electrical dimensions are listed in the following:

Height of dipoles above base	0.46 λ
Base diameter	1.68 λ
Fence height	0.23 λ
Operating wavelength	6.95 inches
Long dipole length	0.62 λ

(7) PERFORMANCE OF THE ELECTRICAL TEST MODEL (ETM)

VSWR, isolation, and insertion loss measurements were made on the ETM antenna and coupler. Results of these tests are tabulated in Table 2-VII-13 and each parameter meets specified requirements. The ETM isolation and input VSWR are slightly poorer than breadboard results, due to a higher dipole VSWR. Figure 2-VII-36 shows the VSWR frequency characteristic for the ETM antenna. A full-scale ETM model of the antenna was mounted to a test panel, which simulated the earthward panel of the spacecraft.

TABLE 2-VII-13. NONRADIATION CHARACTERISTICS, S-BAND ANTENNA
ETM FREQUENCY = 1697.5 MHz

Temperature/ Termination	VSWR		Isolation (dB)		Insertion Loss (dB)	
	TX1	TX2	TX1 to TX2	TX2 to TX1	TX1 to Ant.	TX2 to Ant.
25°C/50 ohms	1.27	1.36	28	28	4.10	4.10
-15°C/50 ohms	1.29	1.39	32	32	4.05	4.05
+60°C/50 ohms	1.26	1.36	30	30	4.10	4.10
25°C/breadboard dipoles*	1.24	1.28	27	27		
25°C/ETM dipoles	1.31	1.35	25.7	25.7		

*(ETM coupler, breadboard dipoles)

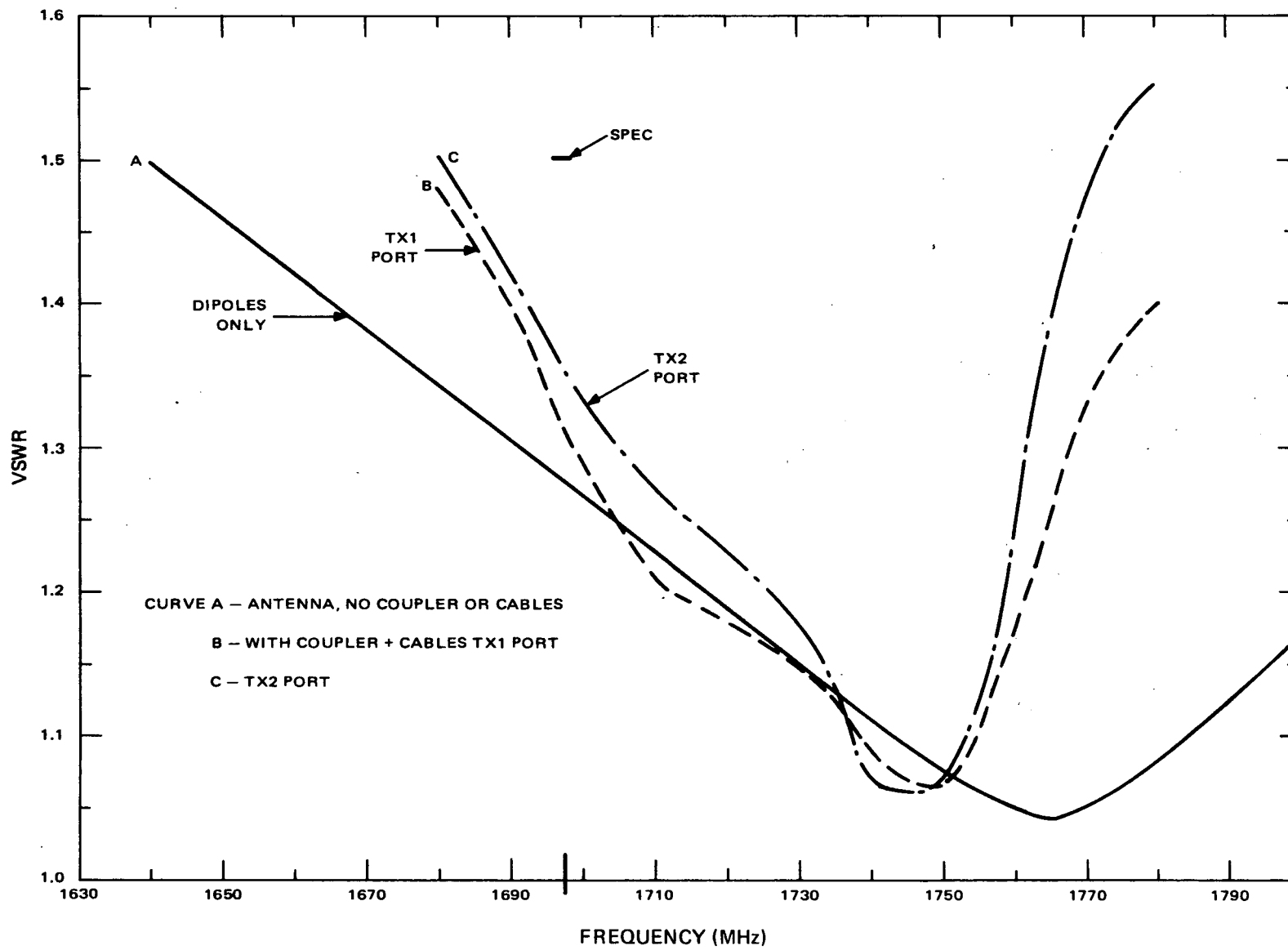


Figure 2-VII-36. S-Band Antenna VSWR, ETM

This test panel included simulation of the radiometric sensors (SR and FPR) and camera lenses (APT and AVCS). The base of the antenna was insulated from the test panel at a spacing of 1 inch.

In performing tests, a small Scientific-Atlanta pedestal was employed in conjunction with its recording equipment. Pen-plots recorded β -plane patterns with α as the variable (Figure 2-VII-32) over 360 degrees. Polarad horn CA-L was utilized as the gain standard (12.2 dBi) and was rotated for making ellipticity tests. A corner reflector with tilted dipole was built and used as the circularly-polarized source antenna. Ellipticity of this source was 1.5 dB.

Figure 2-VII-37 shows the significant patterns measured with the ETM over the coverage beamwidth. The two principal patterns ($\beta = 0$ degree, $\beta = 90$ degrees) are shown relative to the specified gains. Maximum and minimum gain curves are also shown; these are derived from a family of recorded β cuts. For a given nadir angle (α), the gain will be within the cross-hatched region as β is varied. All curves in Figure 2-VII-37 include an insertion loss of 4.1 dB. Table 2-VII-14 compares measured data and specified requirements.

Ellipticity measurements were conducted by replacing the RHC source antenna with the linear Polarad CA-L horn. Ellipticity was measured by rotation of the horn at particular α angles. Figure 2-VII-38 is a maximum ellipticity plot and the poorest measured value was 10 dB. All backlobes beyond $\alpha = 120$ degrees are at least 23 dB below the peak of the pattern, as recorded originally in pen-plots. The S-band antenna subsystem meets all specified requirements.

TABLE 2-VII-14. MEASURED AND SPECIFIED ANTENNA PATTERN DATA

	Spec (dBi)	ETM (dBi)	Excess (dB)
Gain at $\alpha = 55^\circ$ for $\beta = 0^\circ, 180^\circ$	-1.0	+0.7	+1.7
Gain at $\alpha = 55^\circ$ for all other β	-2.5	-1.7	+0.8

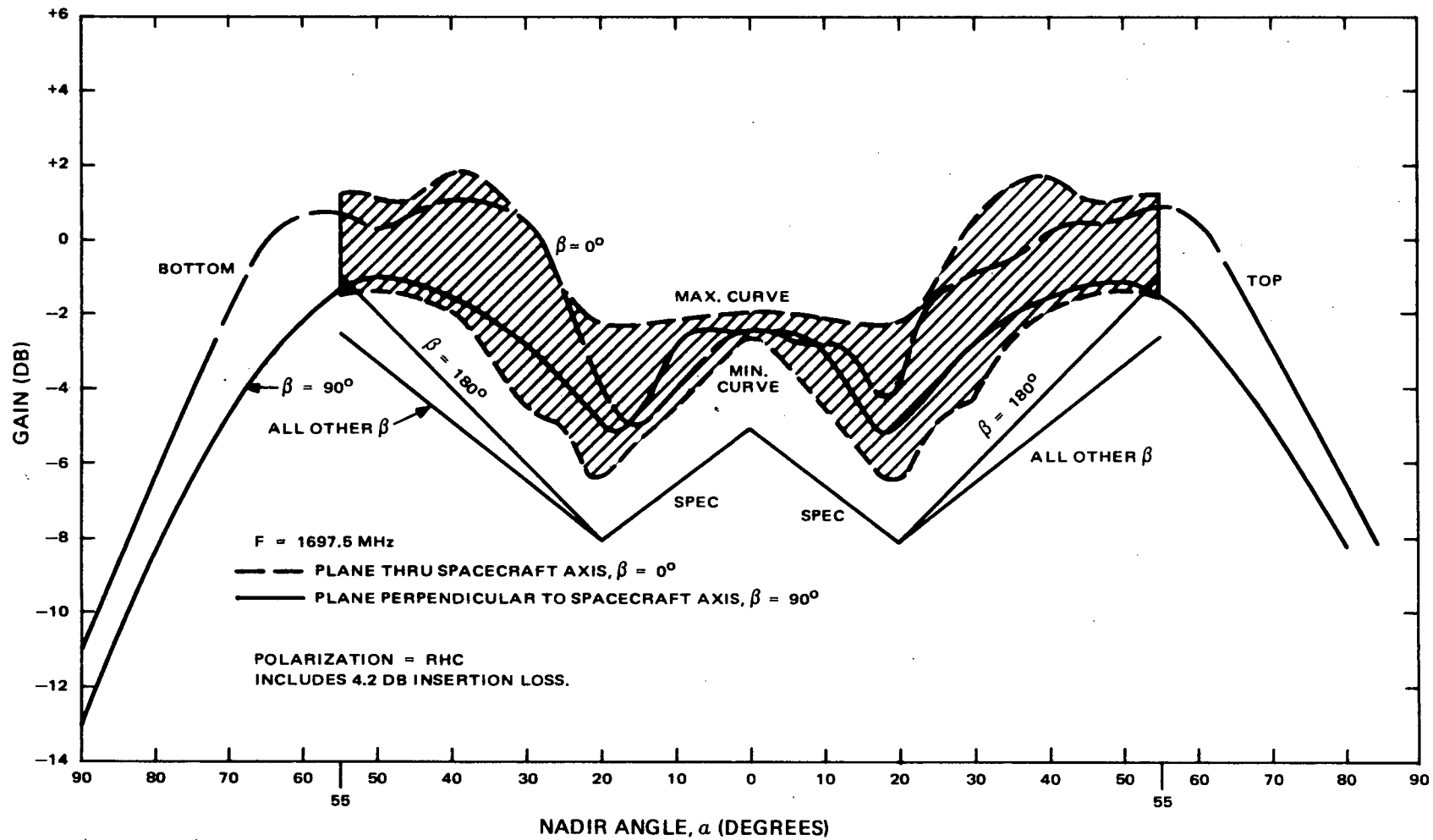


Figure 2-VII-37. S-Band Patterns, ETM

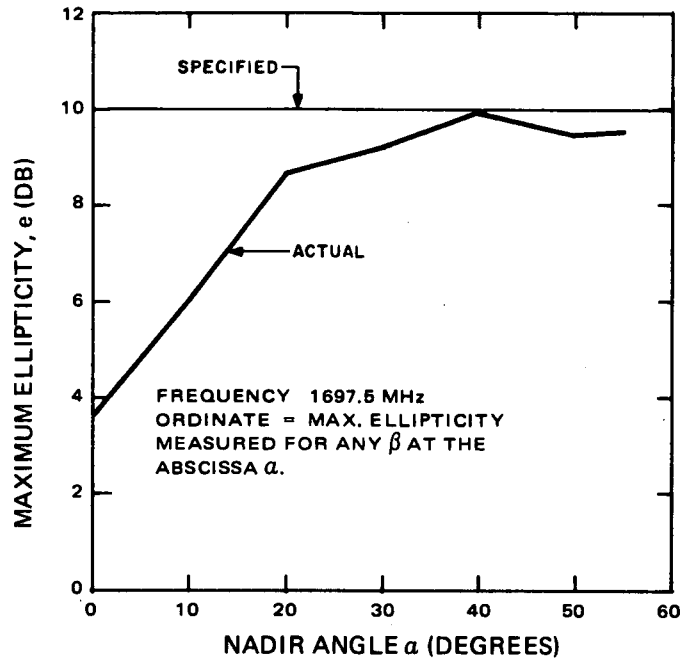


Figure 2-VII-38. S-Band Ellipticity, ETM

SECTION VIII

VEHICLE DYNAMICS SUBSYSTEM

A. SUBSYSTEM DESCRIPTION

The design of the attitude control system is largely dictated by the pointing and stability requirements of the multiple primary sensor system and by the rates of satellite and orbital plane motion. The optimum orientation for the multiple sensor platform is continuous earth orientation. The coupling of a despun platform, through a bearing, to a spinning flywheel is the simplest method of meeting the primary sensor requirements while maintaining all the desirable dynamics of a spin-stabilized spacecraft.

The dynamics subsystem enables the satellite to align and maintain the roll, yaw, and pitch axes with a rotating set of coordinates consisting of the local horizontal, local vertical, and orbit normal. The subsystem will:

- Gyroscopically stabilize the despun platform (equipment module),
- Damp the nutation of the satellite to a half-cone angle of less than 0.3 degree,
- Precess the spacecraft until the momentum vector is nominally aligned with the orbit normal,
- Adjust the total momentum to within ± 1.3 percent of the nominal design value of 212 inch-pound-seconds,
- Align and maintain the attitude about the pitch axis to ± 1 degree about an earth reference, and
- Align and maintain the momentum vector to within ± 1 degree about the orbit normal.

This subsystem is designed to operate continuously in the space environment for at least 1 year. The major functional elements of the subsystem are shown in the block diagram in Figure 2-VIII-1. The subsystem consists of a redundant pitch control loop, functionally redundant magnetic roll and yaw axes control (QOMAC and MBC) including sensors, redundant momentum control coils, redundant nutation dampers, and a digital solar aspect sensor.

In orbit, motion about the pitch axis is controlled by a flywheel and torque motor, utilizing error signals from one of two pitch horizon sensors, and the shaft encoder. The system is redundant, except for the flywheel. The horizon sensors derive their scanning from a mirror mounted on the flywheel. The pitch loop can be commanded to operate in the open-loop or closed-loop mode. The open-loop mode causes the flywheel to rotate at one of two fixed speeds for

dynamic stability, but the equipment module is not earth-oriented. The closed-loop mode causes the wheel to rotate at a speed that will despin the equipment module to 1 revolution per orbit and establish its proper pitch orientation. The pitch control loop is capable of performing this orientation maneuver within a maximum time of 11 minutes after the closed-loop command is received, assuming the spacecraft momentum and roll attitude are within specified design ranges. At nominal conditions, the maximum capture time is about 6 minutes.

If the momentum is not near nominal, redundant magnetic coils can be activated to correct the total spin axis momentum. In addition to pitch axis control, the subsystem provides roll and yaw axis control by ground command. This is accomplished by utilizing the torques developed by the interaction of the earth's magnetic field with controlled dipole moments generated within the spacecraft. The controlled dipole moments are generated by the same type of magnetic coils flown successfully on the TOS spacecraft.

The magnetic bias control (MBC) coil, which is controlled by the magnetic bias switch, provides continuous torquing to offset part of the residual magnetic dipole along the pitch axis (flywheel spin axis) of the spacecraft. The level of current, and thus the dipole magnitude, is adjusted by ground command until the total dipole creates a torque that corrects for attitude changes due to orbital regression. The quarter orbit magnetic attitude control (QOMAC) coil, controlled by the command distribution unit (CDU), provides torquing to precess the spacecraft pitch axis about any desired vector lying in the orbit plane. "Wheel mode" attitude (i. e. , perpendicularity of the pitch axis with respect to the orbit plane) can therefore be maintained. A constant level of current is applied to the QOMAC coil for a period determined by a ground-commanded program, with the direction of current being reversed on a quarter-orbit basis. Three QOMAC modes of operation are provided. The high torque mode uses the combined maximum dipoles of MBC and QOMAC to provide a precession rate of about 10 degrees per orbit at nominal momentum. A lower precession rate (1.2 degrees per orbit) and, therefore, better granularity is obtained with the QOMAC coil operating alone. Finally, in the unipolar mode, the continuous current-on-time is reduced and programmed to generate only unidirectional dipoles at half orbit intervals to achieve precession about the line of nodes.

Spin axis nutation is controlled by liquid dampers similar to those flown on the TOS spacecraft. Nutation may result from the following disturbances: (1) second stage booster nutation, (2) operation of the separation equipment, (3) operation of the magnetic control components, (4) bombardment by micrometeorities, and (5) operation of payload components with uncompensated momentum.

The spacecraft is equipped with IR sensors to provide attitude information during each flywheel revolution. After the spacecraft is oriented in the wheel mode by the second stage booster, roll attitude information can be obtained throughout the orbit, and its availability is only restricted by the location of the ground station. Pitch sensor scanning requires deployment of the solar panels in order to provide

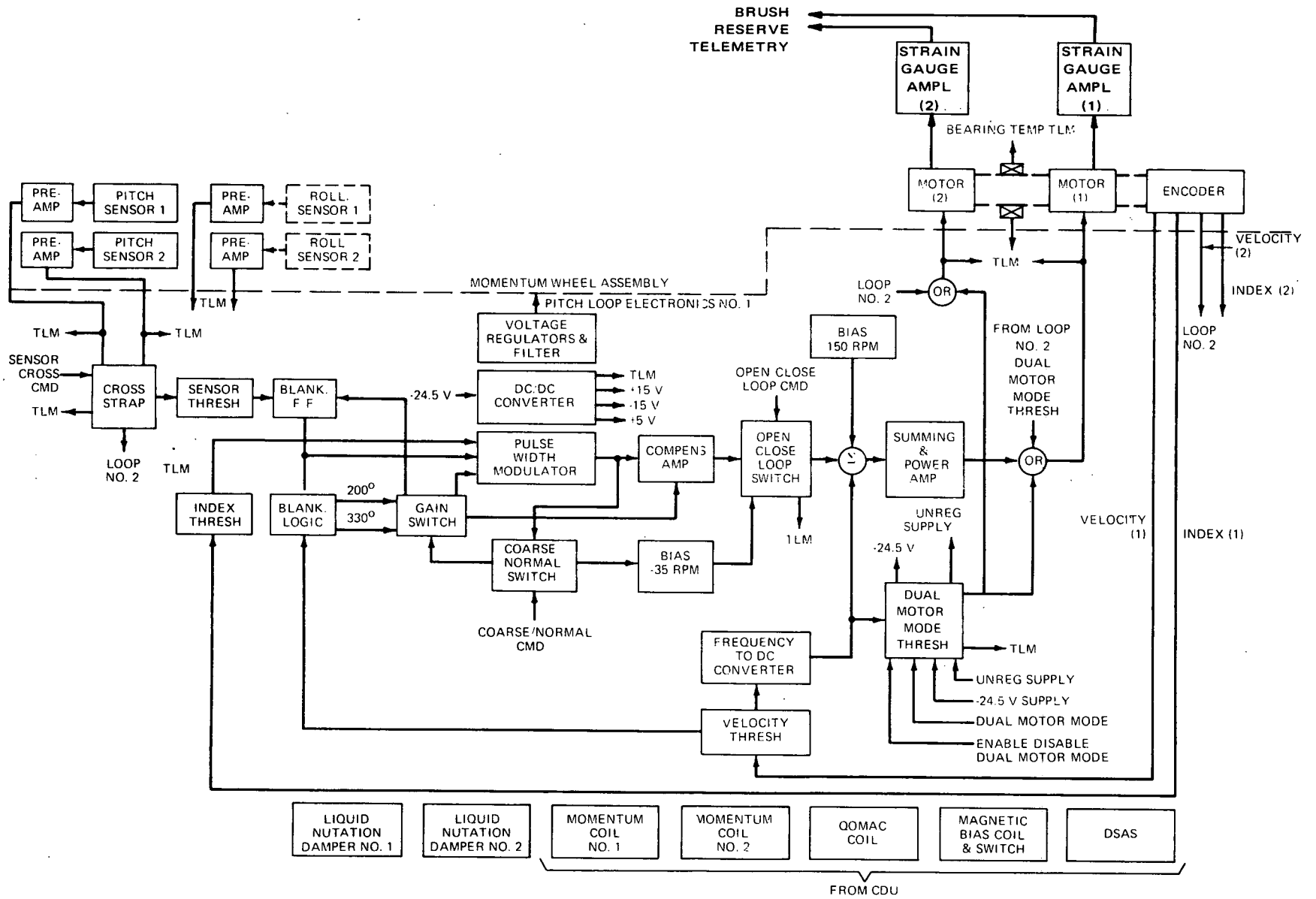


Figure 2-VIII-1. Vehicle Dynamics Subsystem, Block Diagram

an unobstructed field of view. Additional attitude information, of particular value prior to pitch acquisition, can also be obtained from the digital solar aspect sensor (DSAS). The DSAS is similar to those flown on TOS and is mounted on the equipment module.

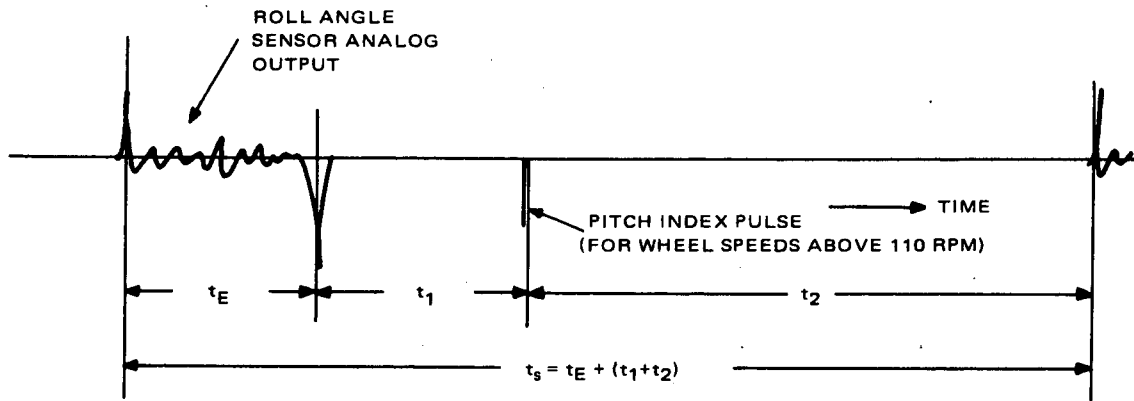
B. INITIAL ORIENTATION MANEUVER

1. Sequence

The initial orientation maneuver consists of the events required to alter the attitude and momentum of the spacecraft from second stage separation to three-axis earth-oriented control.

Subsequent to the reorientation of the second stage and the spacecraft, the pitch axis (rotation axis of flywheel) is nominally perpendicular to the orbit plane. The following sequence of events will then take place:

1. Booster propulsion will spin up the second stage and the spacecraft to 3.3 ± 1.0 , -1.5 rpm.
2. Upon a signal from the second stage, the spacecraft will separate.
3. At the instant of separation, the separation switch will apply unregulated power to the pitch control electronics.
4. The pitch control loop, having been preselected for the open (tachometer)-loop mode and coarse gain setting, will accelerate the momentum wheel assembly to 115 rpm. The acceleration will require 50 seconds, maximum. Simultaneously, the equipment module spin rate will decrease to 1.0 ± 1.0 , -1.5 rpm.
5. The transverse momentum induced by the second stage (including the mismatch of the separation springs) will result in a maximum tipoff and half-cone nutation angle of 15.5 degrees. This figure is based on the maximum transverse spacecraft rate of 3 degrees per second, which was defined by the cognizant NASA agency.
6. The spacecraft nutation will decay with a time constant of about one hour, due to the action of the liquid nutation dampers.
7. Utilizing the roll sensor data telemetered over the 2.3-kHz subcarrier (Figure 2-VIII-2) and the DSAS, the following parameters will be determined during each ground station contact:
 - Roll attitude, based on sensor earth time history, sensor scan period, and spacecraft altitude,
 - Equipment module spin rate, based on DSAS trigger sensor pulses,



- t_E ROLL SENSOR EARTH TIME
- t_s SPIN PERIOD (WHEEL + EQUIPMENT MODULE)
- t_1 TIME FROM ROLL SENSOR EARTH-SKY INTERCEPT TO PITCH INDEX PULSE (CONSTANT AFTER PITCH LOCKON)
- t_2 TIME FROM PITCH INDEX PULSE TO ROLL SENSOR SKY-EARTH PULSE

Figure 2-VIII-2. Typical Signals Telemetered on 2.3-kHz Subcarrier

- Momentum wheel spin rate based on time between successive index pulses,
 - Nutation angle and instantaneous roll angle, based on minimum and maximum sensor earth time in one nutation period (40 seconds maximum).
8. If the maximum roll angle exceeds ± 3 degrees, the QOMAC program will be utilized to bring the attitude within acceptable limits prior to step 11.
 9. If the equipment module spin rate is greater than 1.5 rpm or less than 0.5 rpm, with the momentum wheel rotating at 115 rpm, ground commanded commutation of the momentum coils must be utilized for adjustment prior to step 11.
 10. If the nutation half-cone angle exceeds 2 degrees, additional orbits of damping will be allowed to occur before initiating step 11.
 11. During a ground station pass containing at least 10 minutes of contact time, the tachometer loop will be switched to 150 rpm (normal gain setting). The equipment module spin rate will subsequently be between -0.2 and $+0.8$ rpm. The transient will last no more than 1 minute and can be observed by measurements taken under step 7 above.
 12. At a nominal wheel speed of 150 rpm, the solar panels are deployed by means of a ground command. The solar panel deployment will take a maximum of 170 seconds, and the equipment module spin rate will subsequently be between -0.1 and $+0.5$ rpm.

13. After the completion of the solar panel deployment, the pitch control will be commanded to capture (lock-on earth) by selecting the closed loop mode.

Capture can be verified by observing the magnitude and constant phase relationship between the output of the roll sensor and the pitch index pulse.

Subsequent to capture, the appropriate magnetic torquing coils will be utilized to maintain the pitch axis orthogonal to the orbit plane, and to control the momentum close to the nominal value of 212 inch-pound-seconds.

2. Biased Flywheel Operation

After separation from the second stage, it is necessary to establish a gyroscopically stable spacecraft configuration. Such stability can be achieved if the following equation is satisfied:*

$$\omega_3 (I_3 - I_1) + \omega_f I_f > 0 \quad (2-VIII-1)$$

where

ω_3 is the spacecraft spin rate about the pitch axis,

ω_f is the flywheel spin rate,

I_3 is the spacecraft moment-of-inertia about the spin axis,

I_1 is the spacecraft maximum moment-of-inertia about the transverse axis, and

I_f is the flywheel moment-of-inertia.

This criterion is based on the following assumptions:

(1) Damper on despun body

(2) $H \cos \Theta = I_3 \omega_3 + I_f \omega_f$

(3) $H \sin \Theta = I_1 \omega_1$

*Radio Corporation of America, Astro-Electronics Division, Flywheel Stabilized Magnetically Torqued Attitude Control System for Meteorological Satellites Study Program, Final Report, Contract NAS5-3886, Princeton, N. J., December 4, 1964.

$$(4) \quad 2E = I_3 \omega_3^2 + I_1 \omega_1^2 + I_f \omega_f^2$$

$$(5) \quad \omega_f - \omega_3 = \text{constant}$$

where

H is the total momentum,

Θ is the half-cone nutation angle,

E is the total spacecraft energy, and

ω_1 is the spacecraft spin rate about the transverse axis.

For the unequal transverse moments-of-inertia of ITOS, the maximum value is used to arrive at the conservative stability limits shown in Figures 2-VIII-3 and 2-VIII-4. Assumptions 1 through 4 are definitions applicable to the system. Tachometer loop operation of the flywheel corresponds to assumption 5. Deviations in this constant speed differential can be adjusted with the momentum control by ground command.

Results obtained with a digital computer, which simulated the dynamics in terms of the Euler equations, inertias, and momentum distribution, clearly show that

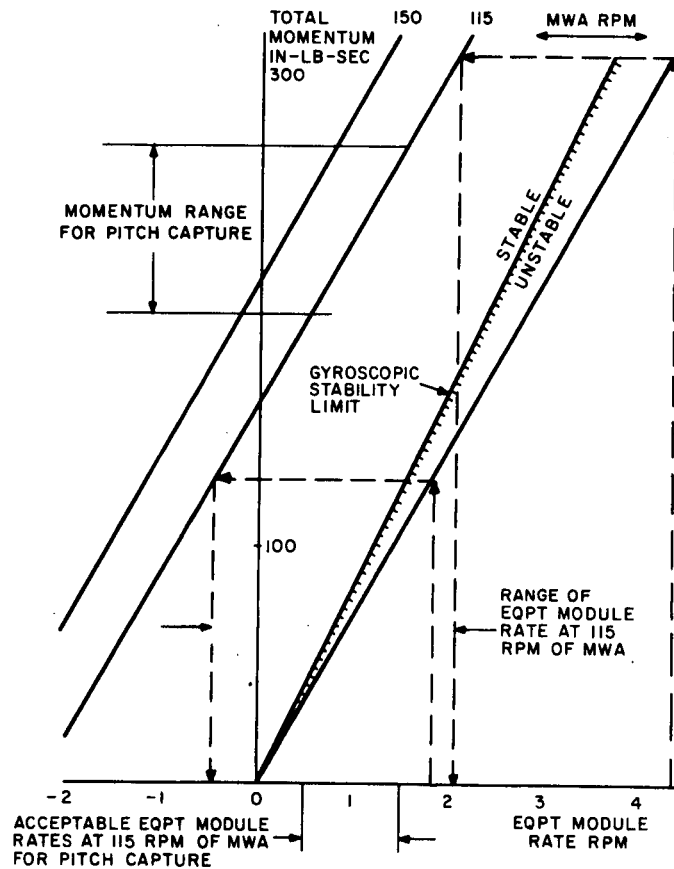


Figure 2-VIII-3. Equipment Module Momentum Versus Spin Rate

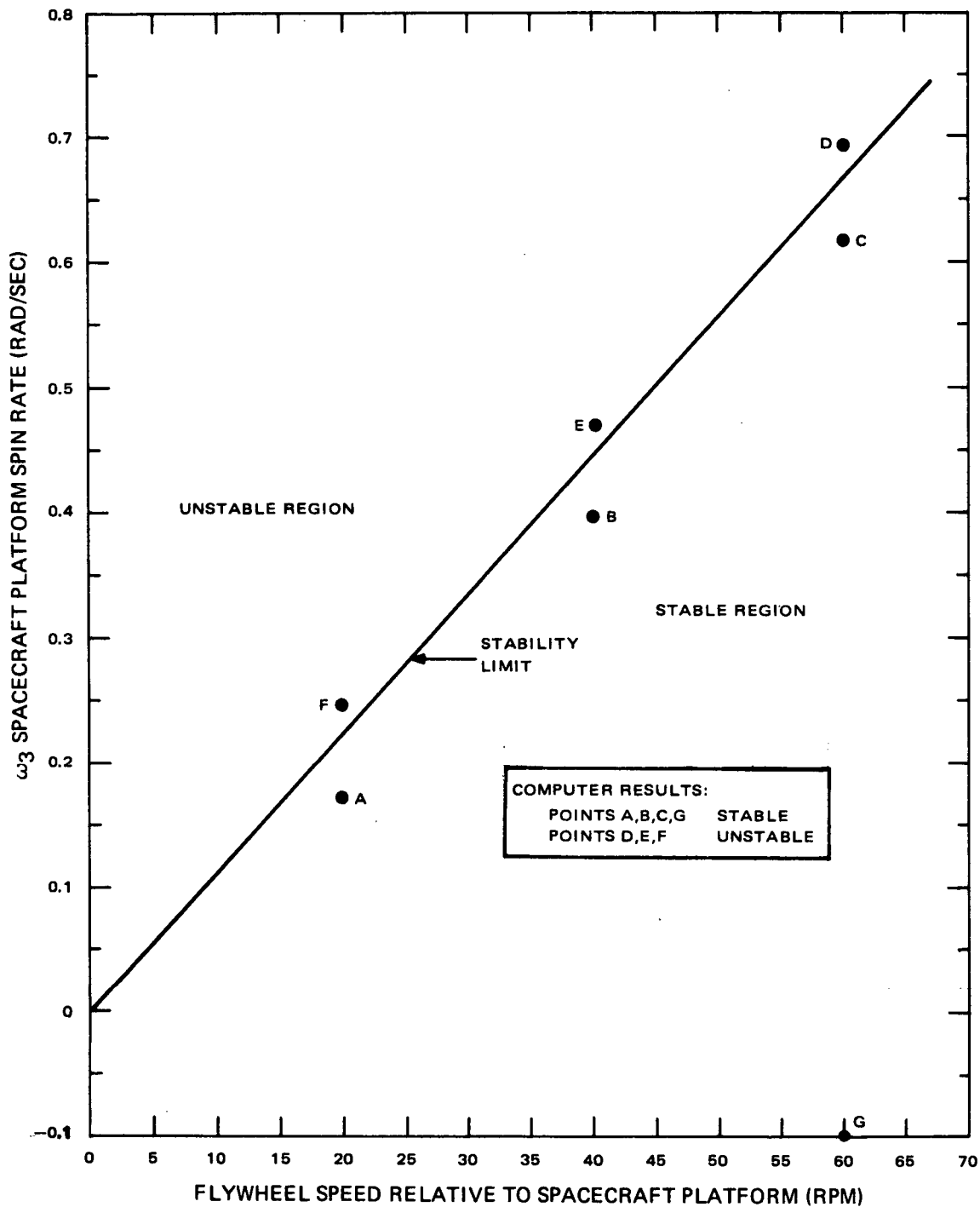


Figure 2-VIII-4. Gyroscopic Stability Prior to Solar Panel Deployment

the stability criteria as given by Equation 2-VIII-1 is correct. Figure 2-VIII-4 shows the correlation between the stability criteria and computer results. Ten computer runs were made at points A through G for relative wheel speeds of 20, 40, and 60 rpm while simulating a nominal nutation angle of 1 degree. As predicted, all points below the line were shown to be gyroscopically stable, while those just above the line were found to be unstable.

C. NUTATION DAMPING

1. General

Nutation occurs when the angular momentum vector and spin vector are not colinear. The spin vector then "cones" about the momentum vector at a rate determined by the inertia characteristics and the spin rates of the spacecraft and the flywheel. This motion must be kept to a minimum since it results in a pointing error of the primary sensors. Redundant dampers in the spacecraft provide an effective and simple method for reducing nutation angles to a small fraction of a degree.*

The optimum liquid damper is a toroid completely filled with silicone oil and mounted with the plane of the toroid parallel to the spin axis. During nutation of the vehicle, transverse angular accelerations excite the oil, causing it to move relative to the damper tube walls. Kinetic energy is transferred to thermal energy through the viscous drag of the fluid. This loss of energy transfers momentum from the transverse axis to the spin axis of the spacecraft, thereby decreasing the nutation. This one-way transfer of energy continues as long as the fluid maintains its Newtonian viscosity characteristics. Thus, for no energy input to the spacecraft, the damper action continues as the nutation cone angle approaches 0 degree.

2. Basic Design

a. MATHEMATICAL ANALYSIS

A mathematical analysis of the dampers is presented in Volume III of Design Study Report for the Improved TOS (ITOS) System, RCA Astro-Electronics Division, Princeton, N.J., June 7, 1968, AED R-3308. (Hereafter, this report will be referred to as the ITOS Design Study Report.) The analysis yields the following equation for computing the damper time constant:

$$\tau = \frac{I_2}{F I_d \cdot \phi} \quad (2-VIII-2)$$

where

- τ is the time constant,
- I_2 is the transverse moment of inertia,
- F is the coupling factor,

*A complete analysis of the dynamic action of these dampers is presented in report referenced in Paragraph B. 2.

- I_d is the damper liquid moment of inertia, and
 $\dot{\phi}$ is the forcing frequency (nutation frequency when earth-locked)

b. MECHANICAL CONFIGURATION

As shown in Figure 2-VIII-5, the nutation damper is not an optimum toroid, as previously defined. The dampers are mounted inside the spacecraft, on opposite sides of the equipment module, with the plane of the dampers parallel to the spin axis. Each damper contains an accumulator-type expansion chamber to act as a void trap for gasses and to allow room for thermal expansion of the fluid. The fluid is a low viscosity silicone oil (Dow Corning type 200). The entire assembly is fabricated from aluminum tubing, with an outside diameter of 1.0 inch and a wall thickness of 0.035 inch. The combined weight of the two nutation dampers is estimated at 11.3 pounds. The nominal damping time constant (subsequent to solar panel deployment and pitch lock-on) is 111 minutes.

c. PRESSURIZATION

The damper performance as predicted by design calculations is based on the absence of vapor bubbles in the tube. These bubbles will form at temperatures below that prevailing during the filling process. In a spinning satellite such as the TOS series or a satellite launched with a rapidly spinning last stage, such bubbles will gather in the radial fill tube and thus have no essential effect on the damping process. However, for the ITOS spacecraft, launched with the two-stage booster, such bubbles could form and remain in the main tube. In this situation the fluid inertia forces would not be able to overcome the surface tension at small angles, thus resulting in a nutation angle threshold. Therefore, the expansion chamber contains an accumulator which permits the fluid volume to vary with temperature, without the resultant formation of bubbles.

3. Time Constant

Table 2-VIII-1 presents a summary of the spacecraft and nutation damper parameters during various dynamic modes.

4. Weight Tradeoff

To determine the optimum angular momentum of the stabilization subsystem, and to minimize the total mass of this subsystem, the concept of

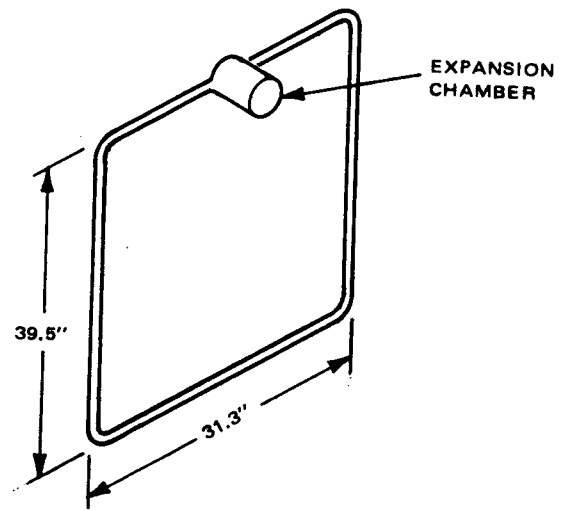
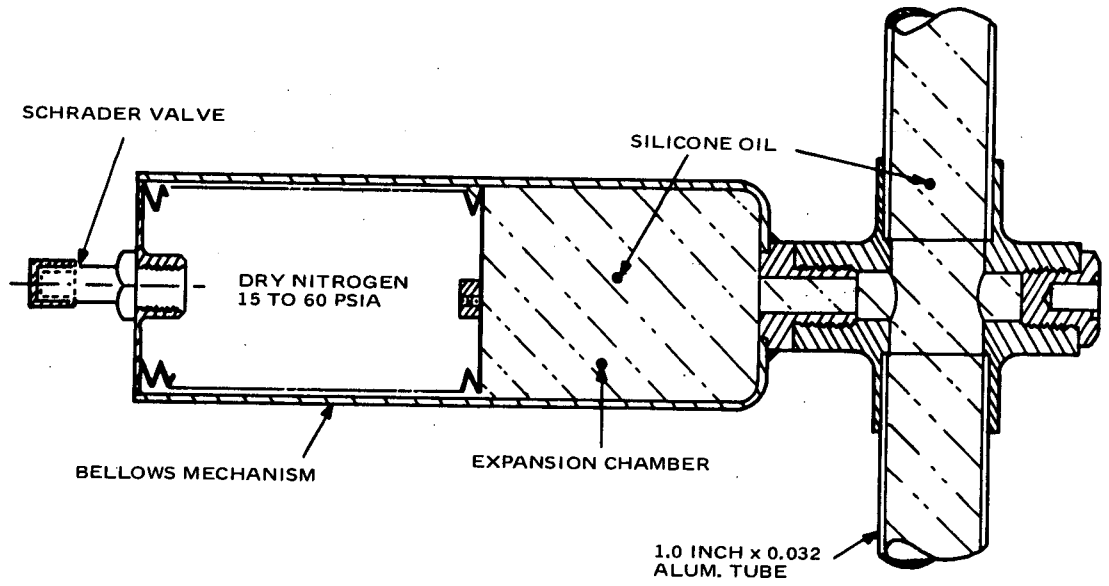


Figure 2-VIII-5. Liquid-Filled Nutation Damper

TABLE 2-VIII-1. DAMPER TIME CONSTANTS DURING VARIOUS MODES

Parameter	Dynamic Mode*	
	1	2
Total Momentum (inch-pound-seconds)	235	212
Nutation Frequency (radians/second)	0.181	0.183
Damper Coupling Factor	0.17	0.17
Time Constant (minutes)	51	111

*Mode:
 1. Flywheel speed at 115 rpm; folded solar panels.
 2. Mission mode (locked pitch loop).

"dynamic mass" was established. The dynamic mass has been defined* as the sum of the mass of the flywheel and the mass of the liquid in the damper assembly, or expressed mathematically:

$$M = \left(\frac{1}{R_f^2 \omega_f} \right) H + \left(\frac{I_2 \sqrt{I_1 I_2}}{F R_d^2 \tau} \right) \frac{1}{H} \quad (2-VIII-3)$$

where

- M is the dynamic mass,
- H is the angular momentum,
- R_f is the flywheel radius of gyration (17.25 inches),
- R_d is the effective radius of gyration of the two nutation dampers (20.4 inches),
- ω_f is the flywheel angular velocity (15.7 radians per second),
- F is the damper coupling factor (0.17),
- I_1 is the maximum transverse moment-of-inertia of satellite (1285 pound-inch-seconds²),

*"Monthly Progress Report No. 2; Flywheel Stabilized Magnetically Torqued Attitude Control System for Meteorological Satellites", dated August 10, 1964 (Contract No. NAS5-3886).

I_2 is the minimum transverse moment-of-inertia of satellite (1010 pound-inch-second²), and

τ is the effective time constant of the two liquid dampers (111 minutes).

The dynamic mass and momentum relationship is shown in Figure 2-VIII-6. Note that a system angular momentum of 150 inch-pound-seconds results in a mass of 18.5 pounds. A system angular momentum of 212 inch-pound-seconds has been chosen (mass equals 21.8 pounds), since a 41-percent increase in the dynamic stiffness can be obtained for a small increase in the dynamic mass.

D. ATTITUDE SENSING

1. General

The following sensors are used for determination of attitude and pitch rate:

- One digital solar aspect sensor (DSAS),
- Two pitch horizon sensors, and
- Two roll horizon sensors.

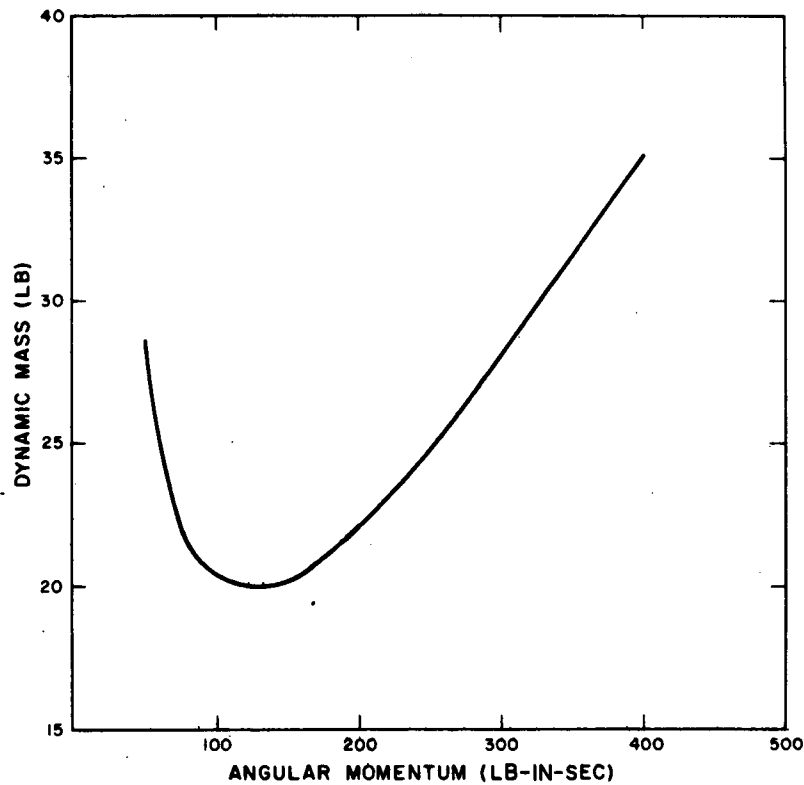


Figure 2-VIII-6. Optimization Curve for Dynamic Mass

The digital solar aspect sensor can be utilized to measure the angle between the spin axis and the earth-sun line and the spin rate of the equipment module. It derives its scanning from the rotation of the equipment module. Prior to pitch lock-on, such a measurement can be accomplished whenever ground station contact is established and the satellite is in daylight. Subsequent to pitch lock-on (i. e., when the equipment module, on which the DSAS is mounted, spins one revolution per orbit), sun angle readout is only possible once or twice a day.

Although the sun angle is of interest, particularly during the acquisition phase, its measurement by means of the DSAS is not essential to the mission.

Pitch and roll measurement is accomplished by means of redundant IR sensors (two for pitch, two for roll). Scanning is accomplished by means of the mirror assembly which is integral with the momentum wheel. The roll sensors can be utilized prior to solar panel deployment.

2. Digital Solar Aspect Sensor

The digital solar aspect sensor DSAS, which has been space-proven on TOS flights, is used to determine the angle between the vehicle-sun line and the flywheel spin axis during the initial orientation maneuver (see Figure 2-VIII-7). It is also useful for measuring equipment module spin rate prior to pitch sensor activation. The indicator has an entrance slit with a field of view of 128 degrees. As the spacecraft rotates, the 128 degree beam generates a solid angle of approximately 3π steradians about the satellite's spin axis. As illustrated in Figure 2-VIII-8, the sunlight that falls upon the entrance slit strikes a reticle that has a 7-bit Gray-coded pattern screen. Seven photocells are positioned behind the Gray-coded pattern, and, depending on the angle of incidence of the sun rays, from 0 to 7 photocells are illuminated. The signal outputs of the 7 cells are amplified, stored, and updated. When a trigger pulse is received from a command photocell, the stored data is read out serially. The DSAS has a resolution of 1.0 degree and an accuracy of ± 0.5 degree.

3. Infrared Sensors

a. GENERAL

The pitch sensor and the roll sensor are identical in construction. They are distinguished by their installation in the momentum wheel and the geometry of their respective scanning mirrors. In the mission mode, the field of view of each sensor intercepts the earth once per flywheel revolution. The bolometers respond to the radiance change between cold space and warm earth, thus producing the horizon-intercept data necessary for determining roll attitude and pitch reference. The scanning geometry is shown in Figure 2-VIII-9.

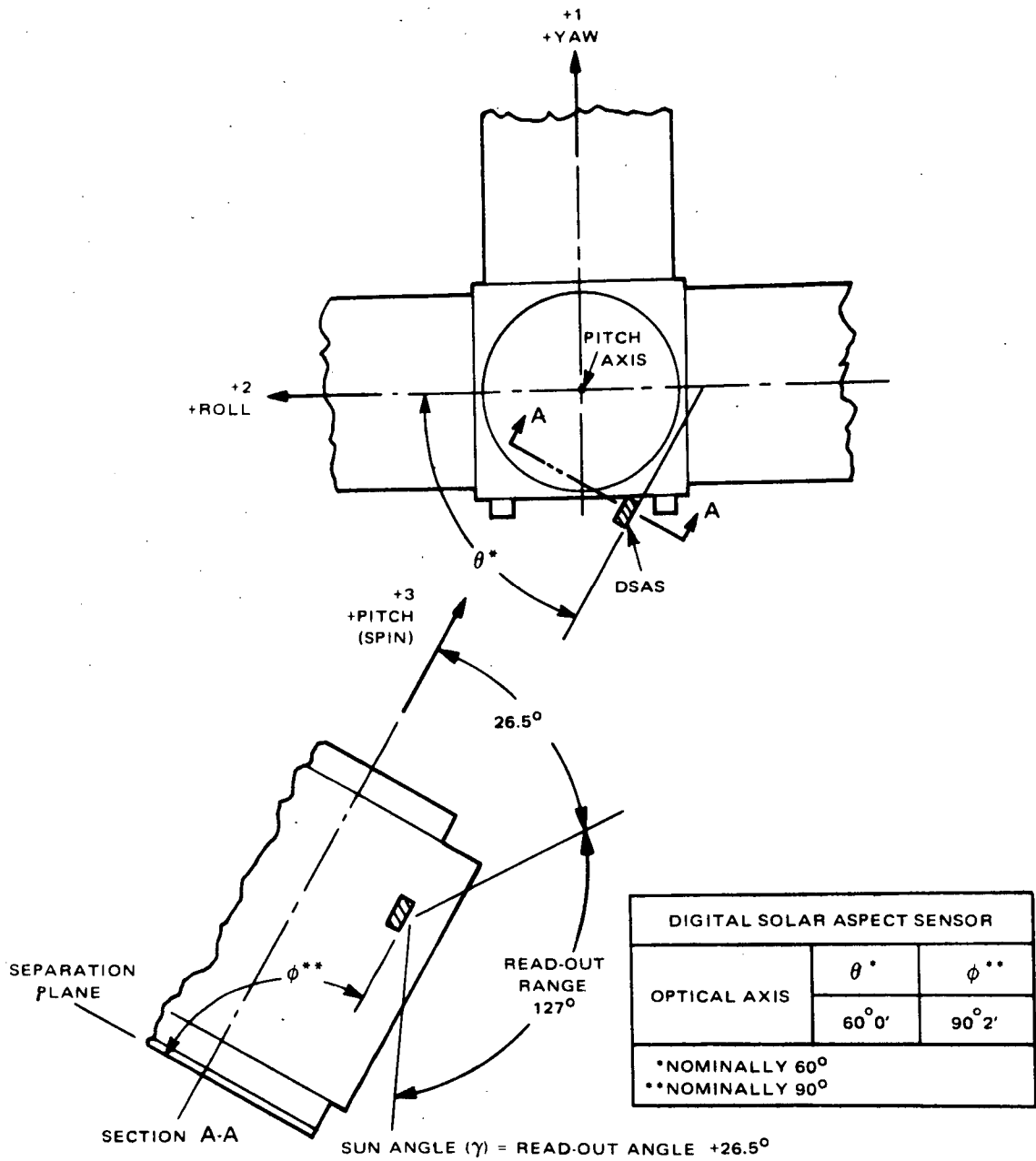


Figure 2-VIII-7. Digital Solar Aspect Sensor Alignment Angles Relative to Spacecraft Reference Axis

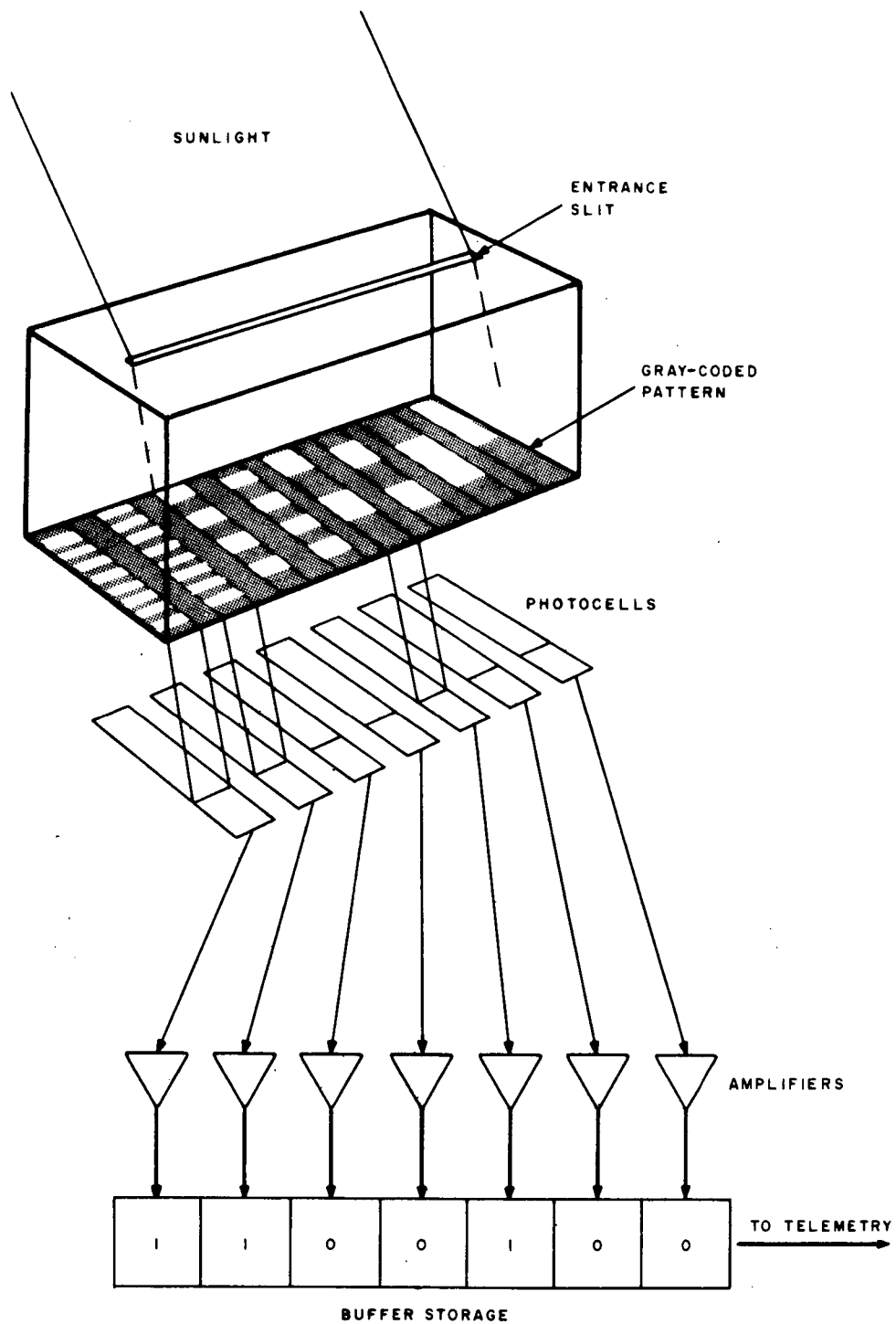


Figure 2-VIII-8. Digital Solar Aspect Sensor, Functional Diagram

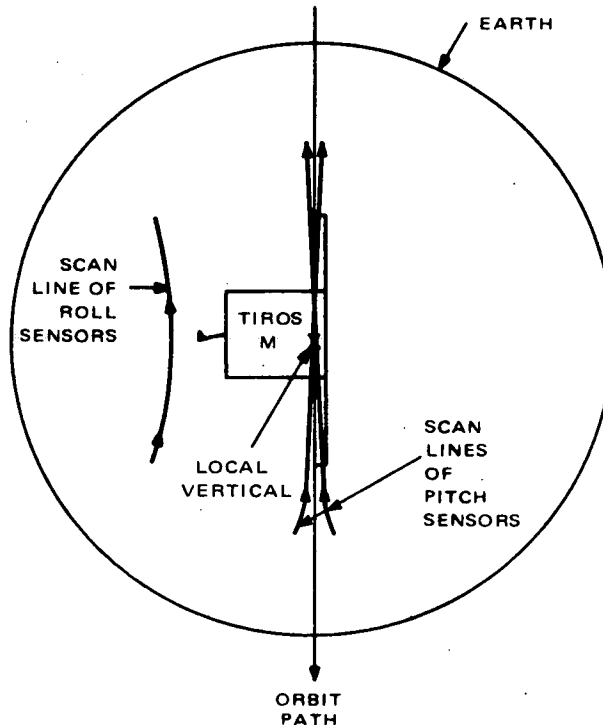


Figure 2-VIII-9. Scan Lines of Attitude Sensors

As shown in Figure 2-VIII-10, each sensor comprises a 1-inch germanium lens system and a germanium-immersed bolometer. The bolometer contains an active thermistor which is exposed to incident radiation, and a compensating thermistor which is shielded from radiation and senses only the ambient temperature changes. The two thermistors form part of a bridge circuit across which a DC bias is applied. When the incident radiation is focused onto the active thermistor, its temperature rises. The change in temperature results in a change of thermistor resistance, which affects the bridge balance and results in a voltage output at the junction of the thermistors. This voltage has two components: (1) a DC component due to the mismatch of the resistance and (2) an AC component due to the change in radiation levels at the earth horizon crossover.

The resistance of each thermistor is approximately 1.40×10^5 ohms at 25°C . The change in resistance that generates a signal equal to the system noise level is less than 0.15 ohm. Since the matching of thermistors is not within 1 percent of their resistance values, at times the DC signal may exceed the AC signal level by a factor of 10^4 . Furthermore, the matching of thermistor resistances is not constant, but shifts with changes in ambient temperature. Since only the AC signal is of interest, the bolometer output is capacitively coupled to the pre-amplifier. This is equivalent to differentiating the AC component while effectively blocking the DC component. During its operation, the scan plane of this sensor intercepts the sun, thereby increasing the sensor recovery time. Since a long

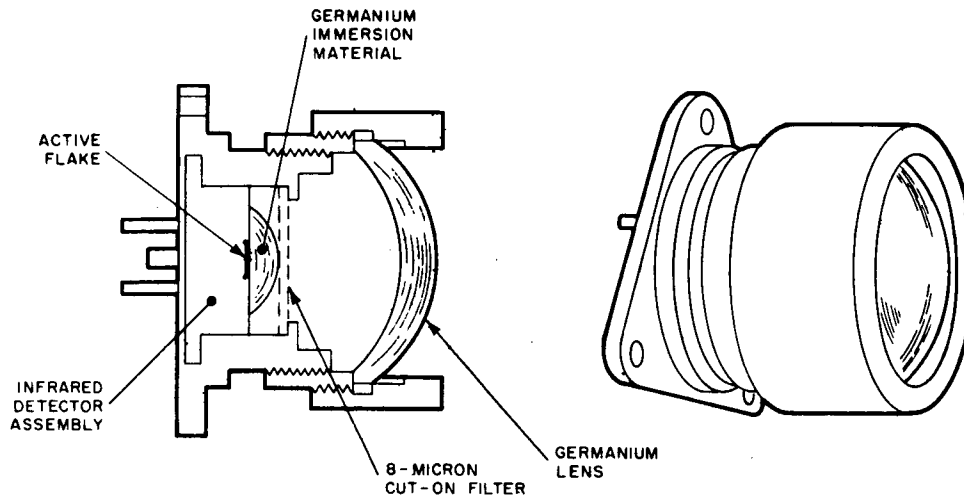


Figure 2-VIII-10. Infrared Bolometer

The effect of off-axis solar radiation inputs upon sensor recovery time is reduced by inclusion of an 8-micron cut-on filter which attenuates the ultraviolet radiation incident upon the bolometer. This filter has previously been used in the TIROS and TOS programs.

b. ELECTRONICS

The sensor electronics associated with the pitch and roll bolometers consist of a preamplifier, filter, regulator, and threshold amplifier (see Figure 2-VIII-11). The electronics are a flight-proven RCA design, modified to provide a bandwidth of approximately 15 to 160 Hz. The preamplifier and filter are located adjacent to the associated bolometers and are mounted on the same plate. The regulator and threshold amplifier are located in the pitch loop electronics package.

The preamplifier includes:

- A capacitor-coupled input and DC-coupled transistor stages throughout,
- A high impedance, low noise field effect transistor input stage,
- A DC bias loop that provides bias point stabilization, and
- Two separate negative feedback loops which maintain stable gain and dynamic characteristics.

The primary function of the regulator is to act as an ultra-low-frequency rejection filter. The circuit is designed to reduce supply line ripple in the frequency range from 0.1 to 15 Hz. An active filter is included in the design to provide additional filtering for the bolometer bias supply in the bandpass of the amplifier.

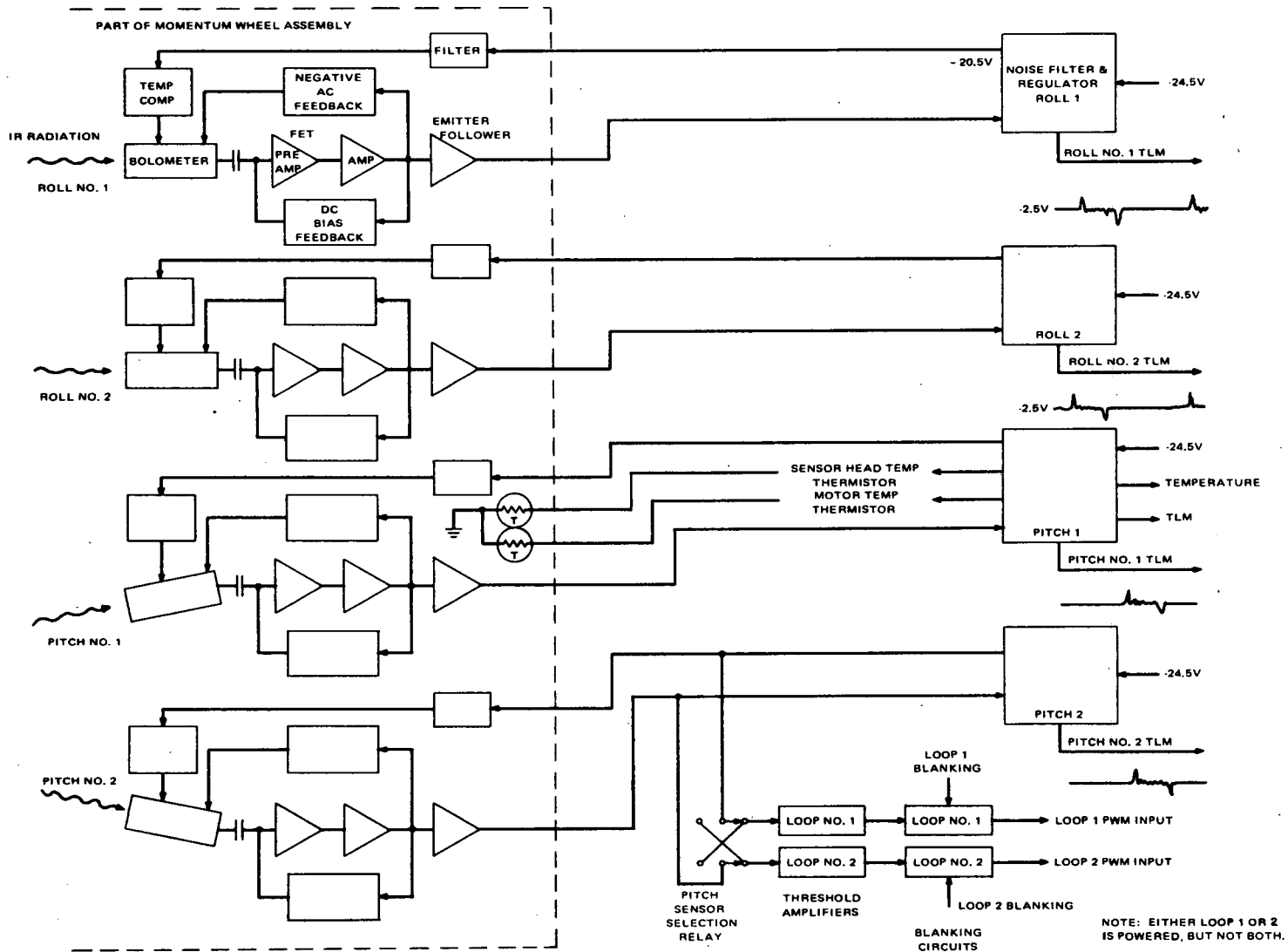


Figure 2-VIII-11. Pitch and Roll Sensor Electronics, Block Diagram

4. Pitch and Roll Sensing

a. GENERAL

The pitch and roll sensors are germanium-immersed bolometers with a 1-inch diameter germanium lens system. As shown in Figure 2-VIII-12, the four bolometers are mounted in a fixed position in the momentum wheel assembly.

A mirror assembly, comprised of reflecting surfaces inclined 25 degrees and 45 degrees, respectively, from the flywheel spin axis, is fixed to the wheel shaft. This assembly reflects the bolometer fields of view. The two mirror surfaces, which are oriented 180 degrees of wheel rotation apart, have an aluminized finish and are protected with a silicon monoxide coating.

Since the roll sensors are mounted parallel to the spin axis, the scan angle between the spin axis and line of sight is 50 degrees. The pitch sensors are tilted towards the spin axis by 3 degrees, so that the scan cone is not symmetrical about the spin axis and describes a sinusoidal variation, as shown in Figure 2-VIII-13. By use of these two differently oriented inclined scans and knowledge of the position of the moon, it is possible to avoid false input signals from the moon. Since the bolometers are heat detectors, they respond equally well to IR inputs from the moon or from the earth. Due to the pitch sensor offset (described above), the limited sensor field of view, and the blanking shown in Figure 2-VIII-13, potentially misleading moon inputs occurring monthly can be avoided.

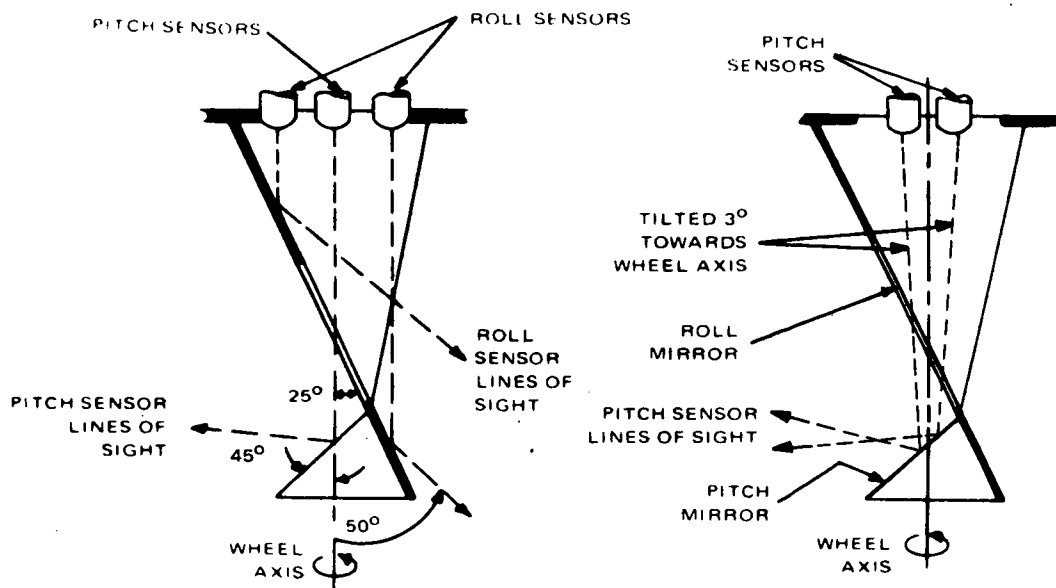


Figure 2-VIII-12. Attitude Sensor Configuration

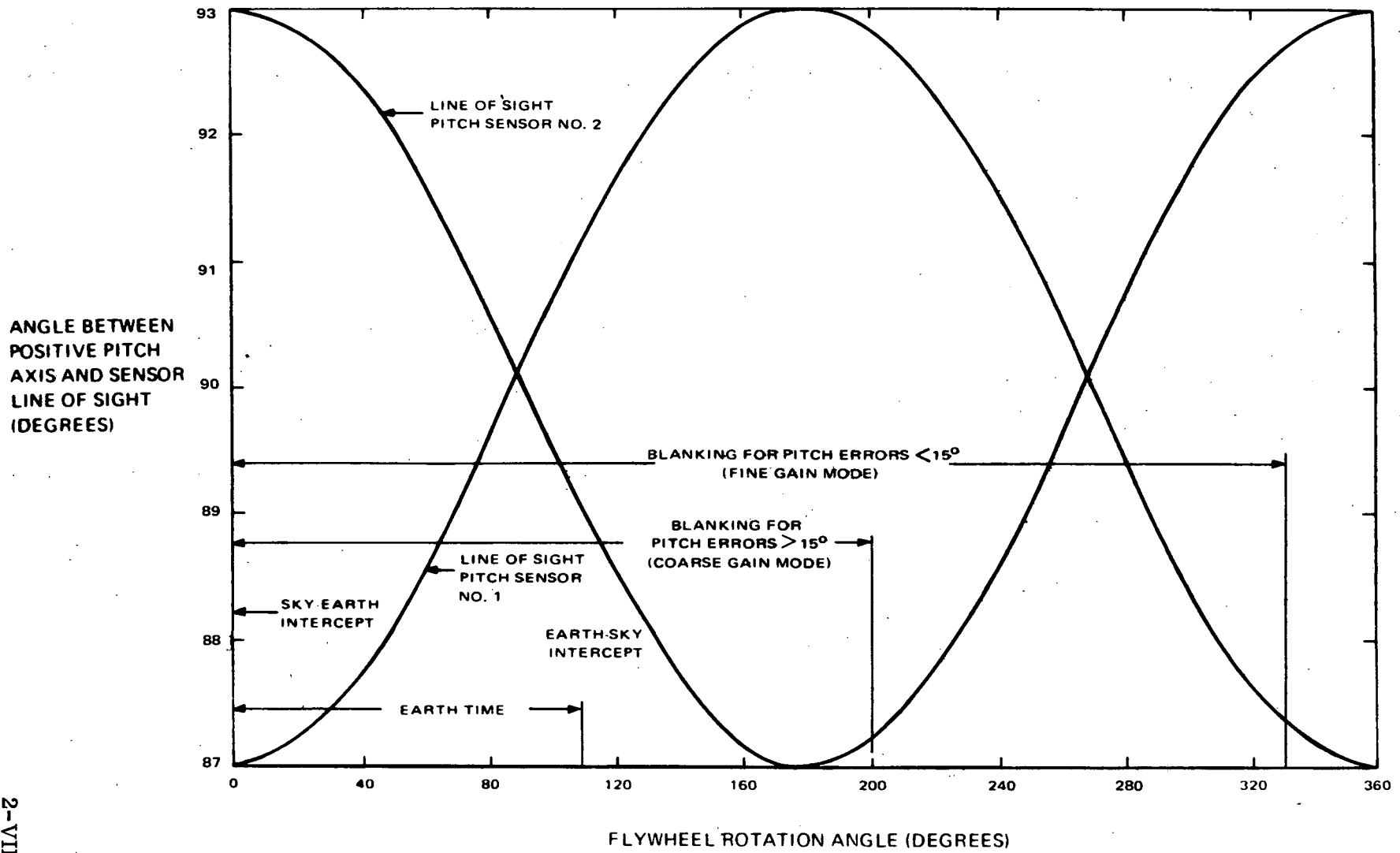


Figure 2-VIII-13. Pitch Sensor Scan Geometry

Either 200 degrees or 330 degrees of pitch rotation of the scan are blanked. The selection is made automatically by the control loop. During conditions where earth lock has taken place, blanking is for 330 degrees, thus minimizing the "window" for the admittance of possible false inputs. When the loop is in the search mode for the sky-earth transition (i. e., prior to pitch lock-on) the blanking is for only 200 degrees of scan, although the 330-degree deblanking pulse is also retained.

b. PITCH SENSING

The pitch control loop utilizes a pulse from one of the pitch sensors, which references the position of the momentum wheel to the earth horizon, and an index pulse, which relates the position of the momentum wheel to the spacecraft structure. Generation of the index pulse is discussed in Paragraph F of this section.

The accuracy of the pitch attitude sensing depends primarily on the uncertainties of locating the infrared horizon. Since the earth-space horizon transition is contaminated by noise from preceding earth and cloud temperature variations, only the space-earth transition is used for pitch determination.

Since a 200°K horizon is caused by high level cloud cover, the actual infrared horizon appears slightly sooner in a sky-earth scan. This causes the 200°K curve to occur slightly earlier in time, when referred to the spacecraft index pulse, and thus causes a compensating time difference between the 280°K and 200°K earth horizons. To avoid false triggering from earth noise subsequent to the space-earth transition, the sensor output is blanked for a portion of the scan (200 degrees while in coarse gain and 330 degrees while in fine gain). Experiments were performed using a 16- to 160-Hz bandpass preamplifier and a bolometer with a 3.0-millisecond basic time constant. Figure 2-VIII-14 shows plots of preamplifier signal level versus time for 200° and 280° horizons.

The above 3.0-millisecond bolometer has been selected in view of the following: (1) satisfactory experimental data when using peaking techniques, (2) previous experience in working with this bolometer, (3) bias source circuitry not available at time of implementation but necessary for a faster time constant bolometer, and (4) possibility of increased noise levels due to the added bias source.

Utilizing the horizon-crossing transition as a reference for the local vertical assumes a circular orbit of known altitude. An elliptical orbit would cause an angular pitch offset from the nominal. In terms of orbit altitude, this offset is plotted in Figure 2-VIII-15.

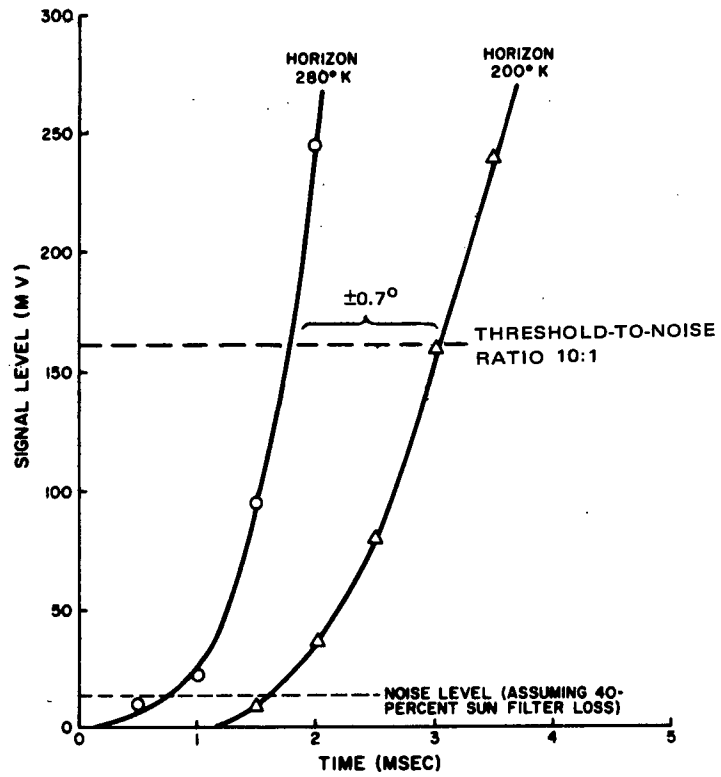


Figure 2-VIII-14. Sensor Electronics Measured Signal Response

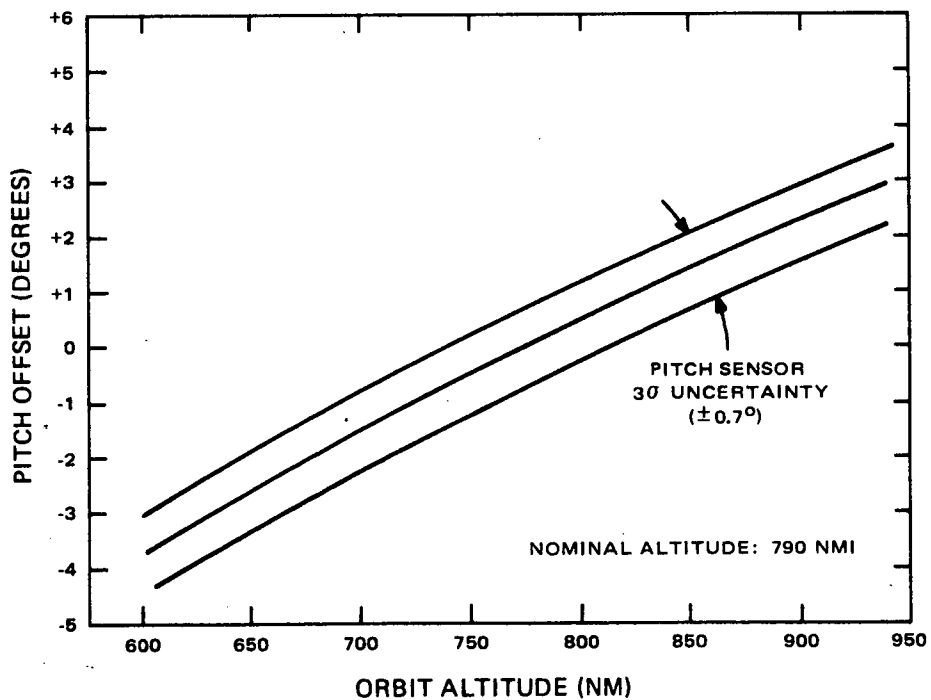


Figure 2-VIII-15. Pitch Offset Versus Orbit Altitude

The effects of temperature changes in the mirror assembly upon the sensor accuracy were considered. The metallic mirror is tied thermally to the fly-wheel and, therefore, can be expected to have a negligible temperature change during one rotation. The bolometers always view the surface of the mirror, and the mirror temperature (and, therefore, the radiant energy from the mirror to the bolometer) will be constant during one spin period. The AC-coupled bolometer electronics will therefore see only changes in the radiant energy due to horizon crossings, with no noticeable signal due to mirror temperature changes.

c. ROLL SENSING

The horizon crossing data generated by either of the two roll sensors is telemetered to a CDA station where it is processed to produce the required error-correction commands.

In normal roll operation, the preamplifier provides an analog signal which produces a telemetry link peak-signal-to-rms-noise level of approximately 37 dB. This value is specified for a spin rate of 150 rpm, a horizon temperature of 280°K, and a grazing angle of 53.6 degrees. The telemetry data is subsequently processed to compute the error corrections required for maintaining proper attitude and spin control.

Since the geometry of the roll sensor scan is essentially a half-Vee scan, satellite ephemeris information is required for attitude determination. If a hybrid technique of combining half-Vee data with pitch data is employed, the ephemeris data is not required. A comparison of these techniques is presented in the ITOS Design Study Report, Volume III. The accuracy of roll determination depends on the method of data reduction at the ground station and the amount of data utilized. Under all circumstances, however, it appears feasible to limit the 3σ scatter in instantaneous roll measurement to about 0.56 degree random plus a bias offset of no more than 0.26 degree.

E. MAGNETIC ATTITUDE CONTROL AND MOMENTUM CONTROL

1. General

The magnetic attitude control and momentum control systems have two basic functions: (1) to keep the spacecraft momentum vector aligned with the orbit normal and (2) to control the total momentum of the satellite so that it is always in the dynamic range of the pitch control loop.

The magnetic attitude control system is similar to that used on the TOS spacecraft; the design is based on the experience acquired during the operation of TOS and earlier TIROS spacecraft. Roll control is maintained by quarter-orbit magnetic attitude control (QOMAC), with similar coils and the same techniques as used on the TOS program. Additional programming flexibility has been added to the basic QOMAC to permit the generation of a unidirectional dipole at half-orbit intervals. This unipolar torquing precesses the satellite about the ascending node, with the primary purpose of counteracting the effects of solar torque. A magnetic bias control (MBC) coil nulls the residual spacecraft magnetic spin axis dipole to a value which produces the required 1-degree-per-day precession rate for orbit regression correction.

The magnetic momentum control system of the spacecraft is similar to the spin control system used on TOS spacecraft. Control coils which are similar to the magnetic spin control (MASC) coils are used in the ITOS spacecraft. The basic change in the operation of the coils is that current commutation is not required after the spacecraft is despun (i. e., when the pitch loop is earth-locked). If momentum adjustments are desired prior to pitch acquisition, coil current must be commutated at half-spin intervals via ground command.

2. Coordinate System

To describe the various controls, orbital geometry, magnetic fields, and related topics covered in this discussion, appropriate coordinate systems must be defined. A set of unit vectors, \hat{l} , \hat{b} , and \hat{n} , is used in describing roll control. A second set, \hat{r} , \hat{t} , and \hat{h} , is required for description of momentum control. As shown in Figure 2-VIII-16, \hat{n} is the orbit normal, \hat{l} is along the ascending node, \hat{b} is perpendicular to \hat{n} and \hat{l} , \hat{r} is along the radius vector from the center of the earth to the spacecraft, and \hat{t} is along the spacecraft velocity vector. The \hat{r} , \hat{t} , and \hat{h} set rotates with respect to the \hat{l} , \hat{b} , and \hat{n} set once per orbit; the rotation angle, β , is the orbit anomaly angle measured from the ascending node.

The spacecraft coordinate system, $\hat{1}$, $\hat{2}$, and $\hat{3}$ and the attitude angles in the \hat{r} , \hat{t} , and \hat{h} system are shown in Figure 2-VIII-17. The momentum vector of the spacecraft is along the $\hat{3}$ axis and should be directed along the orbit normal. Normally, the pitch axis is along the \hat{h} axis, the yaw axis is along the \hat{r} axis, and the roll axis is along the \hat{t} axis. The roll angle, ϕ measured by the horizon sensors, is the angle between the spin vector, $\hat{3}$, and the local horizontal

plane; this angle is cyclic over an orbit due to the gyroscopic stiffness of the spacecraft. Attitude information is obtained from knowledge of the maximum roll angle, ϕ_{\max} , and the point of occurrence in the orbit.

3. Geomagnetic Field Equations

The earth's magnetic field equations have been derived and discussed on many earlier programs, including TOS. The results are the following field equations, in the $\hat{\ell}$, \hat{b} , and \hat{n} coordinate system:

$$B_{\ell} = \frac{K}{R^3} \left[\left(\frac{3}{2} \right) (\cos i \sin i_m \cos \Omega - \sin i \cos i_m) \sin 2\beta \right. \\ \left. + \left(\frac{3}{2} \right) \sin i_m \sin \Omega \cos 2\beta + \left(\frac{1}{2} \right) \sin i_m \sin \Omega \right], \quad (2-VIII-4)$$

$$B_b = \frac{K}{R^3} \left[\left(-\frac{3}{2} \right) (\cos i \sin i_m \cos \Omega - \sin i \cos i_m) \cos 2\beta \right. \\ \left. + \left(\frac{3}{2} \right) \sin i_m \sin \Omega \sin 2\beta + \left(\frac{1}{2} \right) (\cos i \sin i_m \cos \Omega \right. \\ \left. - \sin i \cos i_m) \right], \text{ and} \quad (2-VIII-5)$$

$$B_n = \frac{K}{R^3} (\cos i \cos i_m + \sin i \sin i_m \cos \Omega) \quad (2-VIII-6)$$

This model is sufficiently accurate for ITOS computer prediction purposes.

In the preceding equation

B_{ℓ} , B_b , and B_n are the earth's magnetic field components
in the $\hat{\ell}$, \hat{b} , and \hat{n} coordinate system,

K is the geometric dipole moment constant,

R is the orbit radius,

i is the orbit inclination,

i_m is the earth's magnetic dipole inclination, and

Ω describes the location of the ascending node with respect to the intersection of the geographic and geomagnetic equators.

For a three-axis stabilized spacecraft, the equations are conveniently expressed in the \hat{r} , \hat{t} , and \hat{n} system. This definition is obtained by a rotation around \hat{n} through the angle β . The resulting equations are:

$$B_r = \frac{2K}{R^3} \left[(\cos i \sin i_m \cos \Omega - \sin i \cos i_m) \sin \beta + \sin i_m \sin \Omega \cos \beta \right], \quad (2-VIII-7)$$

$$B_t = \frac{K}{R^3} \left[-(\cos i \sin i_m \cos \Omega - \sin i \cos i_m) \cos \beta + \sin i_m \sin \Omega \sin \beta \right], \text{ and} \quad (2-VIII-8)$$

$$B_n = \frac{K}{R^3} (\cos i \cos i_m + \sin i \sin i_m \cos \Omega). \quad (2-VIII-9)$$

4. Quarter-Orbit Magnetic Attitude Control (QOMAC)

The QOMAC coil is mounted in the spacecraft with its dipole vector aligned parallel to the spin axis. The positive moment, M_Q , of the QOMAC coil is taken in the positive direction of the angular momentum:

$$\overline{M}_Q = \pm M_Q \hat{3}. \quad (2-VIII-10)$$

It has been shown that the precessional motion of the spin axis at any instant will be directed negatively about the direction of the earth's magnetic field at that instant.

Using the uncanted dipole model of the earth's magnetic field, the magnitude of the precession rate* (ω_{PQ}) averaged over one QOMAC torque cycle is:

$$\omega_{PQ} = \frac{3KM_Q}{\pi R^3 H} \sin i, \quad (2-VIII-11)$$

*Radio Corporation of America, Astro-Electronics Division, Design Report for the TIROS Operational Satellite (TOS) System, Contract NAS 5-3173, Princeton, N. J., December 30, 1964.

where H is the total spacecraft momentum. For practical evaluation it is sufficiently accurate to ignore the canted effect of the earth's magnetic dipole.

Table 2-VIII-2 gives the parameters of the ITOS QOMAC coil. For a system momentum of 212 inch-pound-seconds, the low torque precession rate is 0.54 degree per torque cycle or 1.09 degrees per orbit.

TABLE 2-VIII-2. QOMAC COIL PARAMETERS

Parameters	Value
Dipole Moment	4.2 ampere-turn meters ²
Type	Center-tapped
Number of Turns	178 per half
Wire Gage	31 AWG
Wire Resistance	380 ohms
Series Resistor	390 ohms
Current	32 milliamperes (at 24.5 volts)
Power (incl. Series R)	0.78 watts
Weight	0.50 pound

5. Unipolar Torque

The normal QOMAC cycle consists of quarter-orbit reversals of current in the coil, starting at a certain time measured from the ascending node. For the dipole moment of 4.2 ampere-turn meters² (atm²), a precession rate of 0.54 degree per torque cycle is obtained.

As shown in the disturbance analysis, the maximum solar torques along the \hat{b} axis can be as much as 0.6×10^{-4} pound-inches on an orbit averaged basis. This error could be corrected with normal QOMAC and would require a QOMAC cycle every five orbits. However, a unipolar QOMAC programmer has been added which will operate continuously to torque the satellite for approximately 5.6 minutes per half orbit. Then, normal QOMAC will be required only once or twice a week to correct errors due to other disturbances and to correct any possible accumulation of small errors from the unipolar torquing operations. This would also enhance the accuracy of attitude determination. The normal

QOMAC operation will be accomplished with this programmer in the same manner as on TOS.

The unipolar QOMAC programmer will command a positive dipole for a selected duration at two equally spaced intervals per orbit. The pertinent parameters are defined in Figure 2-VIII-18, which is also referenced to the standard QOMAC cycle. This method can precess the satellite up to 3.8 degrees per day, with a resolution of 0.088 degree per day or 0.0035 degree per half orbit. To accomplish this, the programmer requires the following program inputs:

- Delay time (as in normal QOMAC),
- Quarter orbit time (as in normal QOMAC), and
- Unipolar ON time

The negative dipole is always suppressed in this mode. Delay time can be commanded to a maximum of 68.3 minutes with a resolution of 4 seconds. The range for the quarter orbit period is from 25.6 to 34.1 minutes (nominally 28.5 minutes) with a resolution of 4 seconds. Unipolar ON time can be varied from 16 seconds to 17.1 minutes, the latter figure being a function of the orbital period. The resolution of the ON time is 16 seconds.

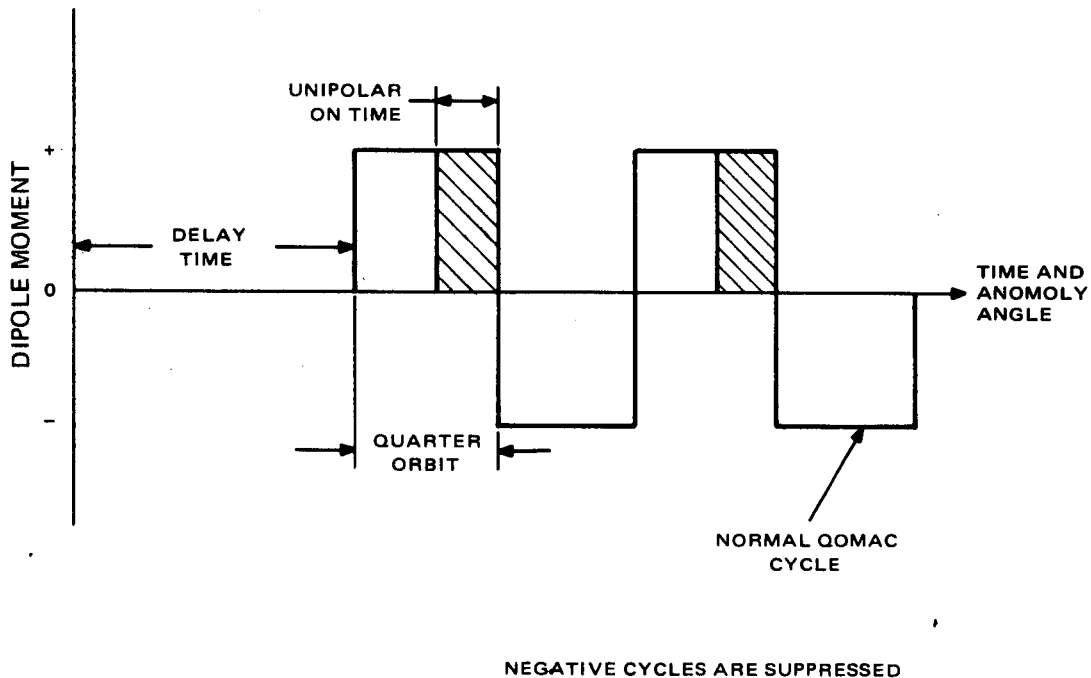


Figure 2-VIII-18. Unipolar Pulse Mode

Figure 2-VIII-19 shows the unipolar pulse superimposed on the significant components of the earth's magnetic field. Generating a dipole pulse which is centered at a latitude of 33 degrees North ascending (and 180 degrees thereafter) will process the spacecraft in the negative \hat{b} direction; the opposite result can be obtained for a dipole centered about 33-degrees North latitude of a descending pass (and 180 degrees thereafter). The average precession rate while torquing under this condition (i.e., for the unipolar pulse centered about the point where the \hat{b} field component is zero) can be expressed as:

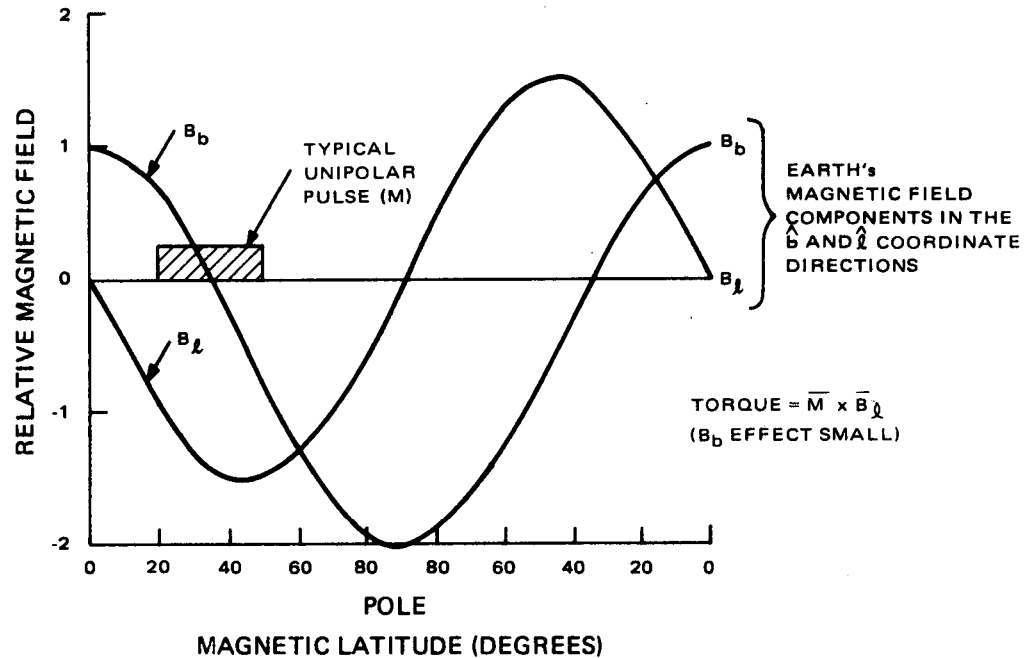


Figure 2-VIII-19. Unipolar Torque Correction for Solar Pressure Disturbance

$$(\bar{\omega}_{pl}) = \frac{3 KM \sin i}{R^3 H a \pi} \cdot \sin 2 \beta_i \sin \frac{a \pi}{2}, \quad (2-VIII-12)$$

where

K is the geomagnetic dipole constant (uncanted dipole model assumed),

R is the orbit radius,

i is the orbit inclination,

M is the coil dipole,

H is the total momentum,

β_i is the angle from the ascending node to the pulse center, and

a is the ratio of ON time to quarter orbit period.

$(\overline{\omega_p})_b = 0$ per unipolar cycle. Once the attitude drift along the \hat{b} axis has been ascertained, both unipolar ON time and delay time can be determined from graphs which are included in the Programming and Control Handbook for TIROS M*.

Calibrations are also supplied to permit some generation of small precessions in the \hat{b} direction by offsetting the unipolar pulse from the nominal position shown in Figure 2-VIII-19. The direction of the orbit-averaged precession axis due to solar torques is approximately along the \hat{l} axis. (See the ITOS Design Study Report.) The precession axis will be somewhat above or below the \hat{l} axis, depending on the time of year.

By selecting the proper delay time (function of β_i) for unipolar torquing, satisfactory solar torque cancellation can be achieved during any season. The shift in the desired position of the dipole with respect to the earth's field varies very slowly over the year and can be plotted against time. Every few weeks a new delay time can be substituted. In this manner, the effects of solar torque can be removed with minimum effort at the ground station.

Two attitude maneuvers were programmed on a digital computer which simulates the torques present. The first simulation was made with no correcting torques. The disturbing torques simulated would in practice include the solar torques, gravity gradient torques, and the effects of the residual dipole along the spin axis. The following data were used as inputs:

Momentum:	200 pound-inch-seconds
Spin moment-of-inertia:	818 pound-inch-seconds ²
Transverse moment-of-inertia:	863 pound-inch-seconds ²
Altitude:	750 nautical miles
Inclination:	101.4 degrees
East longitude of ascending node on first orbit:	0 degrees
Total continuous dipole moment along spin axis:	0.522 atm ²
Solar torque:	6.2×10^{-3} pound-inches
Sun angle:	35 degrees from \hat{n} in the \hat{l}, \hat{n} plane

*RCA Corporation, Astro-Electronics Division, Programming and Control Handbook for TIROS M, AED R-3365F, Contract NAS 5-10306, Princeton, N.J., April 15, 1969.

Figure 2-VIII-20 shows the computer results with nominal drift. The nominal drift of the momentum axis over 75 orbits (6 days) would yield a maximum attitude error of 7.9 degrees. The precession vector would lie approximately along the $+\hat{l}$ axis. Thus, the precession vector produced by unipolar torquing should be along the $-\hat{l}$ axis. The precession needed per orbit would be approximately 0.105 degree or 0.097 percent of that produced by normal QOMAC.

Figure 2-VIII-20 shows the computer results with the unipolar torquing superimposed on the disturbance torques; these results indicate a maximum attitude error of 0.49 degree after 75 orbits. The oscillation shown is due to the effects of the canted dipole. Although this first choice is quite acceptable, a finer choice of parameters based on these results makes the total drift even less.

The unipolar torquing approach for cancellation of attitude drift due to solar pressure torques was selected by RCA because of its inherent design simplicity and demonstrated satisfactory performance.

Additional solutions to this problem, such as canted solar panels or additional compensating vanes on the solar panels, were investigated. The results of these investigations are presented in detail in the ITOS Design Study Report, Volume III.

6. Magnetic Bias Control (MBC)

The MBC coil provides a continuous dipole to offset any undesirable shift in the residual magnetic dipole of the spacecraft along the spin axis (nominal 0.57 atm^2). Coil current is selected by ground command to generate a torque that corrects attitude changes due to orbital regression which proceeds at approximately a 1-degree-per-day precession rate. The MBC coil is wound on the same structure as the QOMAC coil; its dipole moment, M_{MB} , is aligned with the QOMAC coil dipole, as follows:

$$\bar{M}_{MB} = M_{MB} \hat{s} \quad (2\text{-VIII-13})$$

The magnitude of the precession rate, ω_{PMB} , is approximately

$$\omega_{PMB} = \frac{K M_{MB}}{2 R^3 H} \quad (2\text{-VIII-14})$$

Table 2-VIII-3 gives the electromagnetic parameters of the MBC coil for each MBC switch position. The maximum dipole moment of 33.8 atm^2 is used in parallel with the QOMAC coil during the high torque mode of operation. The precession rate is determined from Equation 2-VIII-11.

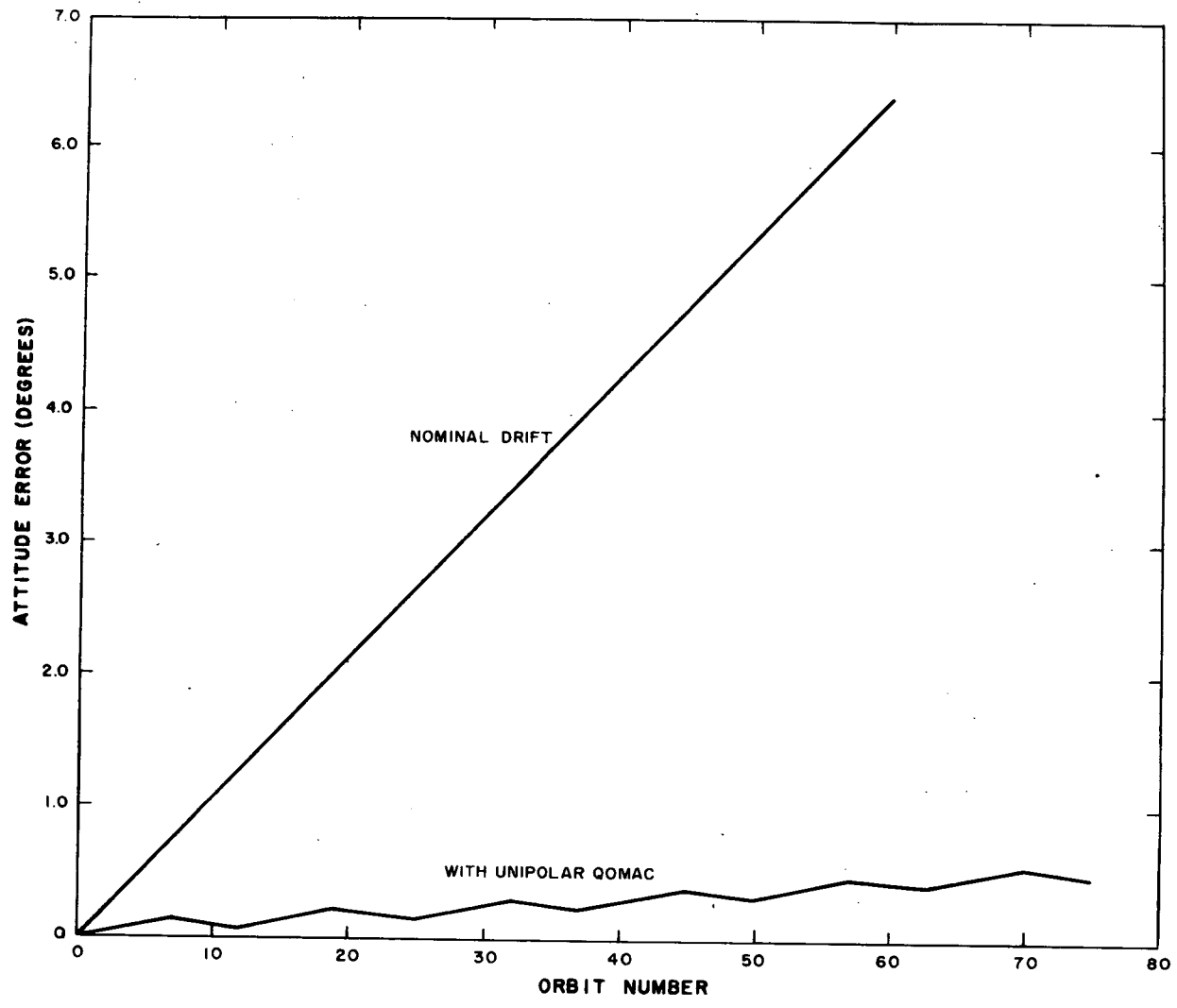


Figure 2-VIII-20. Momentum Vector Attitude Drift

For a system momentum of 212 inch-pound-seconds and a total high torque QOMAC dipole moment of 38.0 atm², the precession rate is 5.0 degrees per torque cycle, or 10.0 degrees per orbit. The dipole moment granularity between switch positions is 0.1 atm². This results in a worst-case drift rate of 0.09 degree per day. The maximum range of dipole moments can produce a controlled attitude change of from -1.7 to +1.7 degrees per day. The physical parameters of the MBC coil in series with MBC switch are presented in Table 2-VIII-4.

TABLE 2-VIII-3. MBC COIL OPERATING PARAMETERS

Switch Position	Current (mA)	Power (watts)	Total Resistance (ohms)	Dipole Moment (atm ²)
1	0.54	0.013	45,430	0.1
2	1.1	0.026	22,730	0.2
3	1.6	0.040	15,130	0.3
4	2.2	0.052	11,130	0.4
5	2.7	0.065	9,220	0.5
6	3.2	0.078	7,630	0.6
7	3.8	0.093	6,470	0.7
8	4.3	0.10	5,750	0.8
9	4.8	0.12	5,120	0.9
10	5.4	0.13	4,450	1.0
11	181	4.4	132	33.8
11	26	0.64	950	4.8
12,0	OFF	-	-	0.0

The switching arrangement for the MBC coil is essentially the same as on the TOS spacecraft, except that the coil polarity is reversed through a DPDT relay rather than with a center-tapped coil; this change was made to reduce the weight of the coil by a factor of two. In the low torque QOMAC mode, the MBC coil polarity is controlled from the CDU, and the power is routed through the

TABLE 2-VIII-4. MBC COIL PHYSICAL PARAMETERS

Parameter	Value
Type	Single Coil
Number of Turns	251
Wire Gage	25 AWG
Wire Resistance	132 ohms
Weight	2.1 pounds

switch resistors. In the high torque QOMAC mode, the MBC polarity is controlled by a set of QOMAC programmer drivers, and the power is applied from the -24.5-volt source on position 11 of the magnetic bias switch. When the QOMAC coil is enabled, the CDU connects the MBC coil directly across the regulated 24.5-volt potential; this results in the maximum coil dipole of 33.8 atm². In this CDU state, the QOMAC and MBC coils are operated in parallel ($4.2 + 33.8 = 38 \text{ atm}^2$). When the QOMAC coil is disabled, the MBC coil remains connected to the QOMAC programmer with an 820-ohm resistor inserted in series; this produces a QOMAC backup mode of 4.8 atm².

7. Magnetic Bias Switch

The magnetic bias switch consists of a rotary solenoid switch mechanism which controls the current levels, and thus the dipole magnitudes, of the MBC coil. The switch, shown schematically in Figure 2-VIII-21, is stepped by ground command. A second wafer on the switch provides means for telemetering the position. The unit weighs 0.8 pound and occupies approximately a 3.5-inch cube.

8. Momentum Control After Pitch Lock

a. MOMENTUM MAGNITUDE

The total momentum of the spacecraft must be controlled between specified limits around the nominal design point to keep within the dynamic range of the pitch control loop. Magnetic pitch axis momentum control produces a torque collinear with the momentum axis. This may be obtained by positioning the plane of each coil parallel to the flywheel axis; two momentum coils are mounted in this way in the ITOS spacecraft. Any momentum change will be transferred directly to a change in spin rate of the flywheel through the pitch control loop.

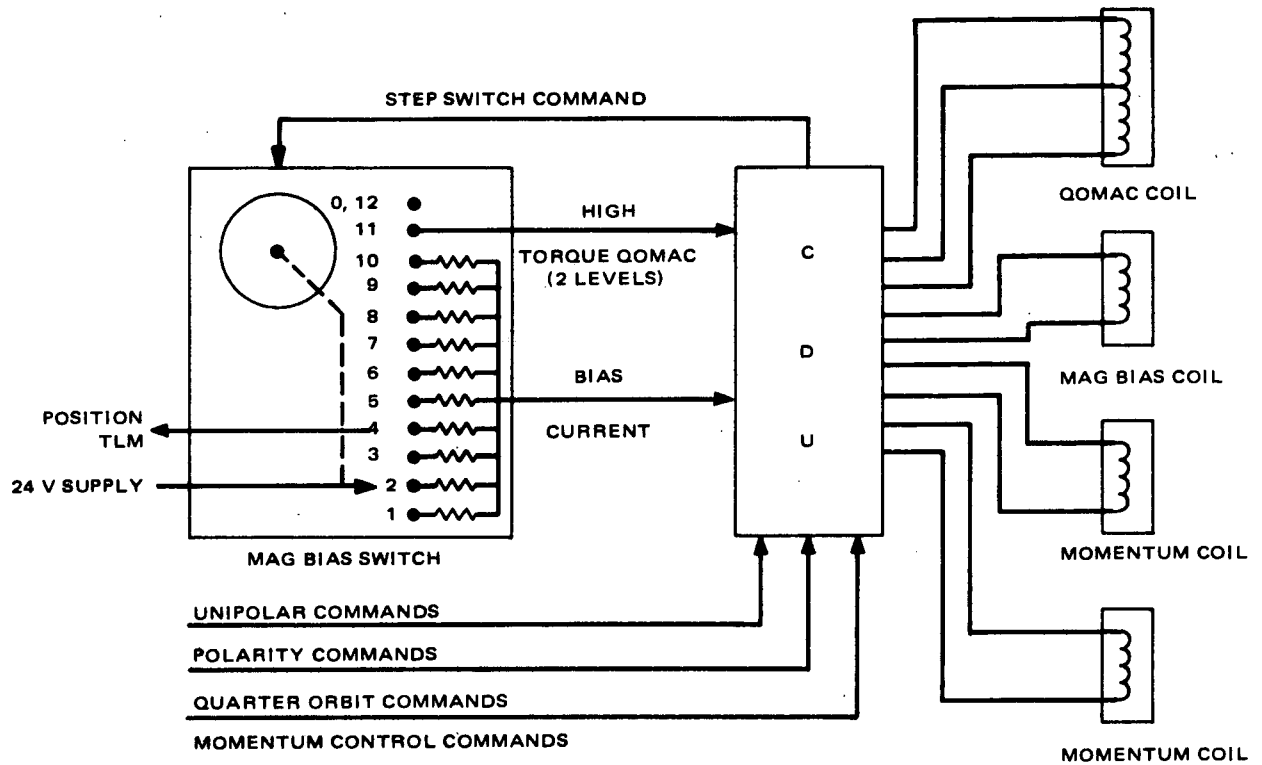


Figure 2-VIII-21. Magnetic Momentum Vector Control, Simplified Block Diagram

Considering a coil with its dipole moment, M_{MM} , in the $\hat{1}$, $\hat{2}$ plane at an angle of γ from the $\hat{1}$ axis, the magnetic dipole moment is as follows:

$$\overline{M}_{MM} = M_{MM} (\cos \gamma \hat{1} + \sin \gamma \hat{2}). \quad (2-VIII-15)$$

The interaction of this moment with the earth's magnetic field produces two torques: one, T_{SPIN} , changes the magnitude of the momentum and the other, T_{PREC} , has the undesirable effect of changing the direction of the momentum vector. These torques are:

$$\overline{T}_{SPIN} = M_{MM} (B_2 \cos \gamma - B_1 \sin \gamma) \hat{3} \text{ and} \quad (2-VIII-16)$$

$$\overline{T}_{PREC} = M_{MM} (B_3 \sin \gamma \hat{1} - B_3 \cos \gamma \hat{2}).$$

The $\hat{1}$, $\hat{2}$ and $\hat{3}$ coordinate axes are nominally aligned with the \hat{r} , \hat{t} , and \hat{n} axes, and thus, for small attitude error angles:

$$B_1 = B_r,$$

$$B_2 = B_t, \text{ and}$$

$$B_3 = B_n$$

where B_1 , B_2 , and B_3 are the earth's magnetic field components in the $\hat{1}$, $\hat{2}$, and $\hat{3}$ coordinate system.

As can be seen from field Equations 2-VIII-7 and 8, over some torquing interval, $\Delta\beta$, the average magnitude of B_r is twice that of B_t . To take advantage of this, the angle between the momentum coil dipole moment and the $\hat{1}$ axis is made 90 degrees (i.e., the positive dipole moment lies along the $\hat{2}$ axis, or nominally along the spacecraft velocity vector \hat{t}). The torque equations are then:

$$\begin{aligned}\bar{T}_{SPIN} &= -M_{MM} B_1 \hat{3} \text{ and} \\ \bar{T}_{PREC} &= M_{MM} B_3 \hat{1}.\end{aligned}\tag{2-VIII-17}$$

b. SPIN MOMENTUM CHANGE (T_{SPIN})

The torque along the momentum axis, T_{SPIN} , is the desired torque which will change the magnitude of the total spacecraft momentum. When Equations 2-VIII-9 and 2-VIII-17 are analyzed ($B_r = B_1$), they yield a zero average torque over an entire orbit. Therefore, the coil momentum should only be applied over a partial orbit, specifically limited to the rela-time acquisition by the ground stations. The average torquer, T_{SPIN} , over some interval β_s to β_f , is as follows:

$$\begin{aligned}\tilde{T}_{SPIN} &= \frac{-2M_{MM}K}{(\beta_f - \beta_s)R^3} \left[-(\cos i \sin i_m \cos \Omega - \sin i \cos i_m) (\cos \beta_f - \cos \beta_s) \right. \\ &\quad \left. + \sin i_m \sin \Omega (\sin \beta_f - \sin \beta_s) \right].\end{aligned}\tag{2-VIII-18}$$

With the pitch control in the closed-loop mode, a momentum change will cause a direct change in the flywheel spin rate as follows:

$$T_{SPIN} = \frac{d}{dt} H = I_f \frac{d}{dt} \omega_f.\tag{2-VIII-19}$$

where I_f is the flywheel moment-of-inertia and ω_f is the flywheel spin rate. Thus, the average spin torque acting over an interval Δt changes the flywheel spin rate as follows:

$$\Delta \omega_f = \frac{\Delta t}{I_f} \tilde{T}_{SPIN}.\tag{2-VIII-20}$$

The parameters of each momentum coil are given in Table 2-VIII-5.

TABLE 2-VIII-5. MOMENTUM COIL PARAMETERS

Parameter	Value
Dipole Moment	10.4 atm ²
Type	Single Coil
Number of Turns	160
Wire Gage	30 AWG
Wire Resistance	314 ohms
Series Resistor	12 ohms
Current	75 milliamperes
Power	1.8 watts
Weight	0.3 pound

Polarity reversals of the momentum coils are made through a DPDT relay as in the MBC coil. The spin rate change for one coil as a function of the torquing period is given in Figure 2-VIII-22. This figure assumes a nominal altitude of 790 nautical miles to the sun-synchronous orbit, and several ascending nodes. A spin rate change is determined by the difference between the final and initial value of $\Delta \omega_f$ corresponding to a given torquing period. The most efficient area of operation is near the north pole ($\beta \approx 90$ degrees). As an example, for a torquing interval of from 60 to 107.05 degrees (corresponding to a 15-minute pass), the spin rate change would be 1.76 rpm for the case of a 200-degree East longitude ascending node. If both momentum coils were used, the change would be twice this amount. From Figure 2-VIII-22, a torquing interval of some predetermined length, starting at some point in the ground station contact circle, can be established to give the required momentum (spin rate) change within specified limits.

c. PRECESSION DUE TO MOMENTUM CORRECTION (T_{PREC})

The torque along the \hat{l} axis, T_{PREC} , is an undesired torque which will change the direction of the momentum vector or precess the spacecraft. The torque equation is

$$\bar{T}_{\text{PREC}} = M_{\text{MM}} B_3 \hat{i} = \frac{M_{\text{MM}} K}{R^3} \left[\cos i \cos i_m + \sin i \sin i_m \cos \Omega \right] \hat{i} \quad (2\text{-VIII-21})$$

The precession torque is a constant (for a given ascending node); hence, the attitude change generated is a function of the period of time that the momentum coil is turned on. The precession rate is a constant along the \hat{l} axis, but this axis is rotating in the orbit fixed \hat{l} , \hat{b} , and \hat{n} coordinate system. The precession torque in the fixed coordinate system is as follows:

$$T_{\text{PREC}} = M_{\text{MM}} B_3 (\cos \beta \hat{l} + \sin \beta \hat{b}_o) \quad (2\text{-VIII-22})$$

Taking the average torque over the torquing interval, β_s to β_f , yields:

$$\tilde{T}_{\text{PREC}} = \frac{M_{\text{MM}} K}{(\beta_f - \beta_s) R^3} (\cos i \cos i_m + \sin i \sin i_m \cos \Omega) \left[(\sin \beta_f - \sin \beta_s) \hat{l} - (\cos \beta_f - \cos \beta_s) \hat{b} \right]. \quad (2\text{-VIII-23})$$

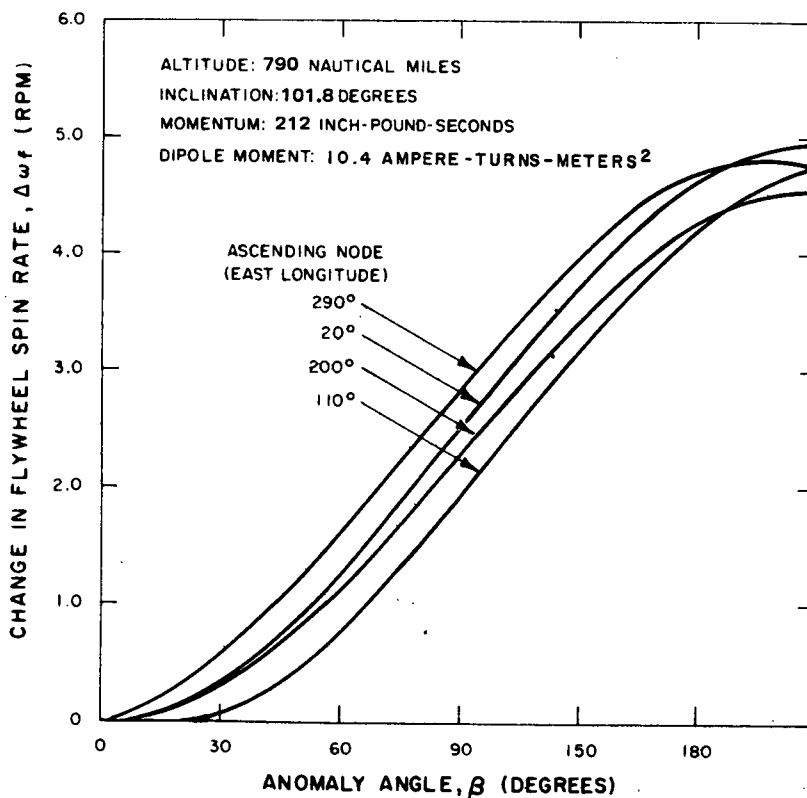


Figure 2-VIII-22. Momentum Change Versus Torquing Period (single coil)

The absolute value of the angular change, $\Delta \phi$, produced during the torquing time, Δt , is:

$$\left| \Delta \phi \right| \approx \left| \tilde{T}_{\text{PREC}} \right| \frac{\Delta t}{H} . \quad (2\text{-VIII-24})$$

A graph of this angular change is shown in Figure 2-VIII-23 as a function of the orbit anomaly angle; curves are plotted for several ascending nodes. The attitude error generated is the difference in value between the final and initial $\Delta \phi$ angles, corresponding to the torquing interval. For the example cited earlier of an ascending node of 200 degrees East longitude and a torquing interval of from 60 to 107.5 degrees (for a 1.76-rpm change in flywheel speed), the error generated in attitude would be 0.11 degree. For an ascending node of 20 degrees East longitude, no attitude change would be produced regardless of the torquing period. Thus, a judicious choice of the orbit for momentum changes will keep the effects of attitude error to a minimum.

If both momentum coils are used for momentum corrections, the attitude change will be twice that shown in Figure 2-VIII-23 for the same torquing interval. For the same momentum change, however, the coils would have to be on for only half the time required for one coil.

9. Momentum Control Prior To Pitch Lock

Since the 3σ tolerances of the Delta spinup range have been defined as +1.0/-1.5 rpm, ground commanded commutation of the momentum coils is required to permit momentum adjustment prior to the initial pitch lock-on. The maximum spinup deviation which can be accommodated if pitch lock is to be achieved without momentum commutation is ± 0.5 rpm. Figure 2-VIII-24 shows the pertinent geometric relationships for this operation. The coil dipole (two momentum coils producing a total of 20.6 atm²) and the stator pitch index position are located on the equipment module; the roll sensor line of sight and the rotor pitch index position are located on the momentum wheel (MWA) as shown in Figure 2-VIII-24. Therefore, the position of the coil dipole is uniquely defined by the relationship between sensor horizon crossing and pitch index pulse occurrence.

As shown in Figure 2-VIII-25, the commutation of the coil has to be phased with respect to the angle θ_i ; i.e., the angle between the sky-earth transition of the roll sensor and the index pulse location. These signals are being telemetered on the 2.3 kHz subcarrier. Although intended for the monitoring of pitch offset in the operational mode, the signals are also suitable as a phasing reference for the initial momentum adjustment.

Ideally, commutation should take place when the coil dipole is coincident with the magnetic field vector in the orbit plane. This field vector is oriented with respect to the ascending node by the angle:

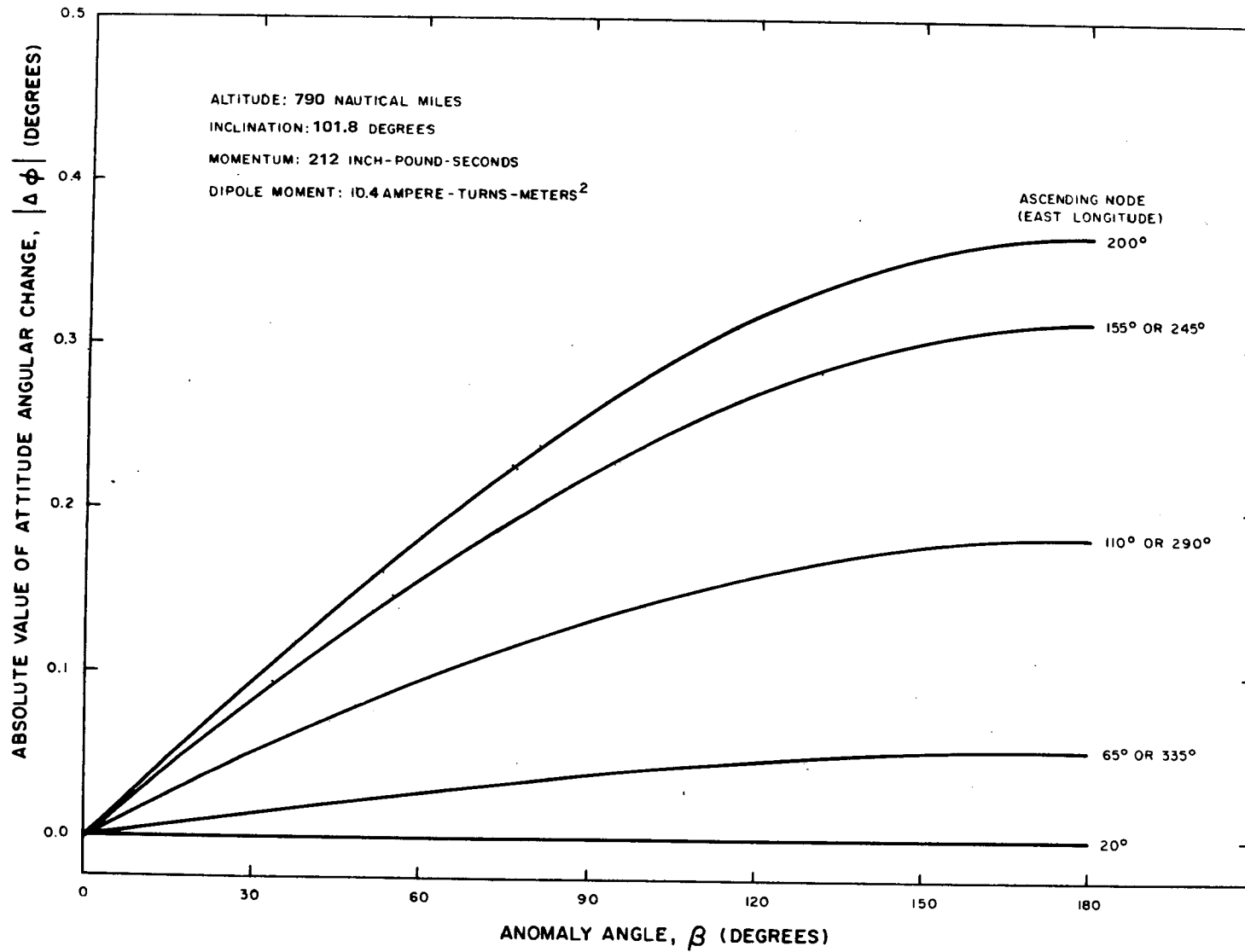


Figure 2-VIII-23. Attitude Change Versus Torquing Period (Single Coil)

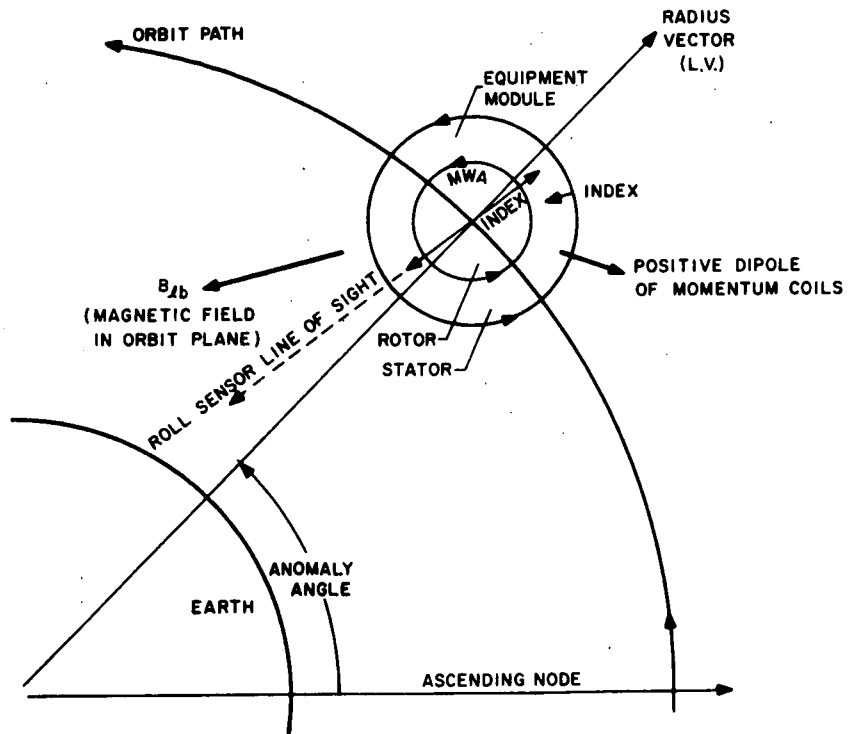


Figure 2-VIII-24. Geometry for Momentum Control Prior to Pitch Lock

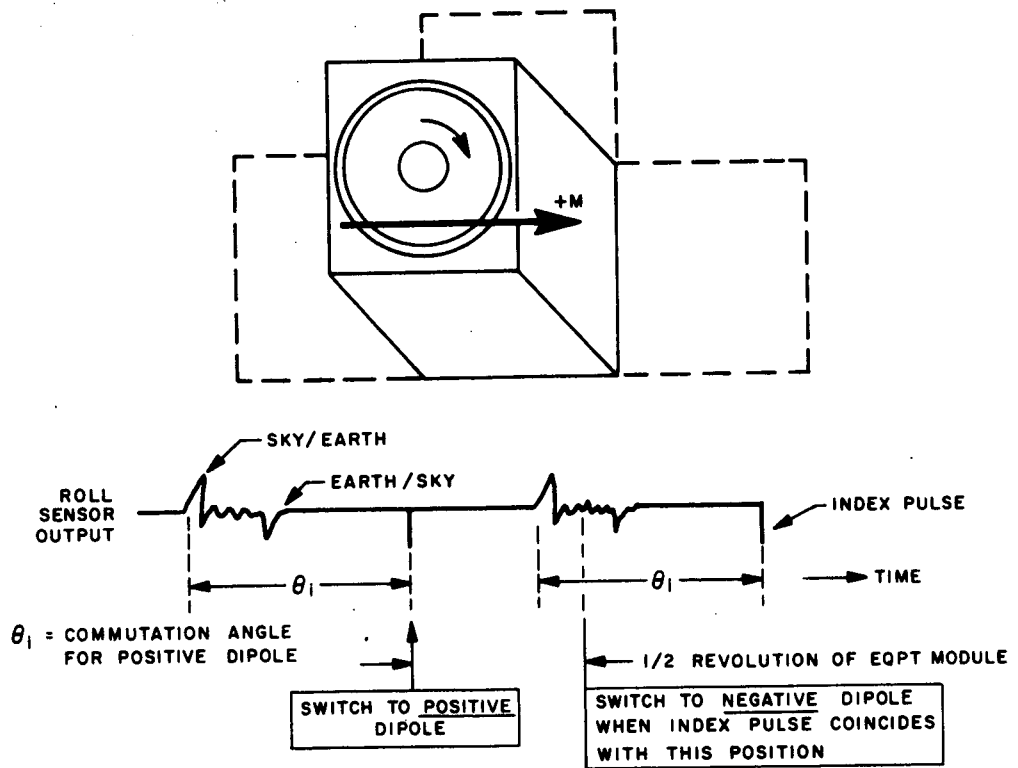


Figure 2-VIII-25. Dipole and Phase Definition for Momentum Control Prior to Pitch Lock

$$\beta \ell b = \tan^{-1} \left\{ \frac{(1/2) \sin i \cos i_m (3 \cos 2\beta - 1) + \sin i_m \left[(1/2) \cos i \cos \Omega \right]}{(-3/2) \sin i \cos i_m \sin 2\beta + \sin i_m \left[(1/2) \sin \Omega + (3/4) (\cos i + 1) \right]} \right\} \left\{ \frac{(-3/4) (\cos i + 1) \cos (2\beta + \Omega) - 3/4 (\cos i) \cos (2\beta - \Omega)}{\sin (2\beta + \Omega) + (3/4) (\cos i - 1) \sin (2\beta - \Omega)} \right\}$$

(2-VIII-25)

where

- i is the orbit inclination,
- i_m is the inclination of earth's magnetic dipole,
- β is the satellite anomaly, and
- Ω is the angle from line of nodes of geographic and magnetic equator to orbit ascending node.

Although Ω introduces some variation in the desired commutation point, the effect is secondary and can be ignored. Therefore, the simple calibration shown in Figure 2-VIII-26, can be used for proper phasing. Here, the angle θ_i (i.e., the point for switching to the positive dipole) is expressed as a percent of the total scan period. With the MWA rate controlled in the tachometer loop mode at 150 rpm, such phasing will decrease momentum in case of excessive spinup and increase momentum for insufficient second stage rate. Triggering the display scope at the ground station from the sky-earth transition facilitates the use of a simple slide-rule-type phasing indicator as a command aid. The frequency of commutating ground commands is a function of the equipment module spin rate, which represents the deviation from the nominal operational momentum. Figure 2-VIII-27 shows that the period between dipole reversals is expected to be no less than 15 seconds; this is compatible with the available command capability.

The efficiency of torquing depends on the accuracy of phasing. Figure 2-VIII-28 illustrates that an error of 1 or 2 seconds results in only minor performance penalties. Similarity, nominal deviations from zero roll attitude are not of primary importance; however, it is recommended that the momentum adjustment be made in the presence of roll angles not in excess of 10 degrees.

Except for the immediate vicinity of the magnetic equator using both coils (20.6 atm²) will change momentum at approximately 0.2 inch-pound-second per minute. For an available total contact time of about 180 minutes per day from Gilmore and

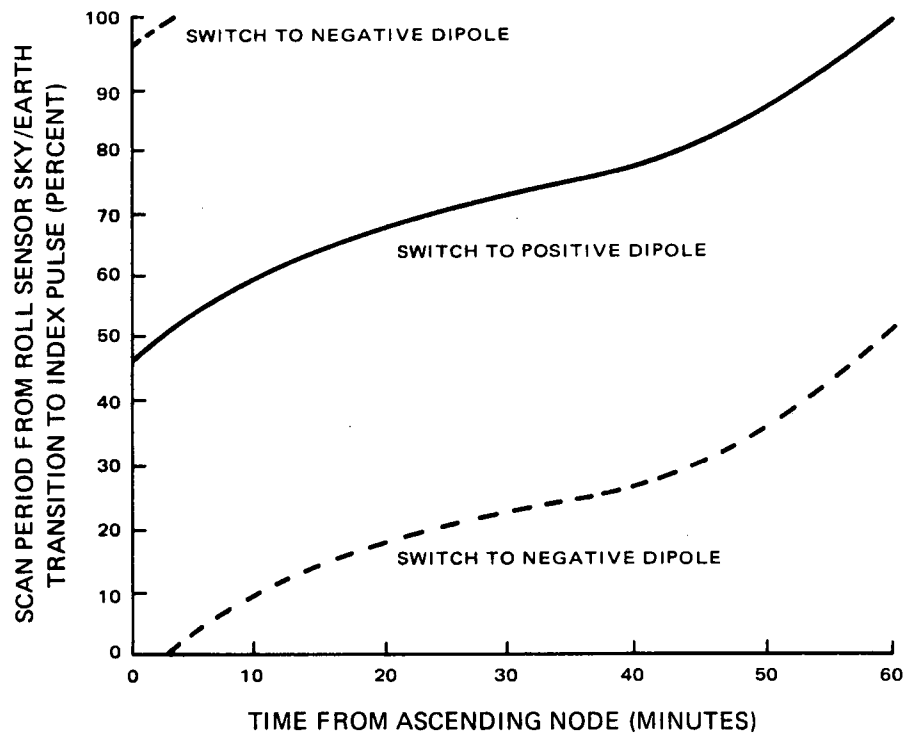
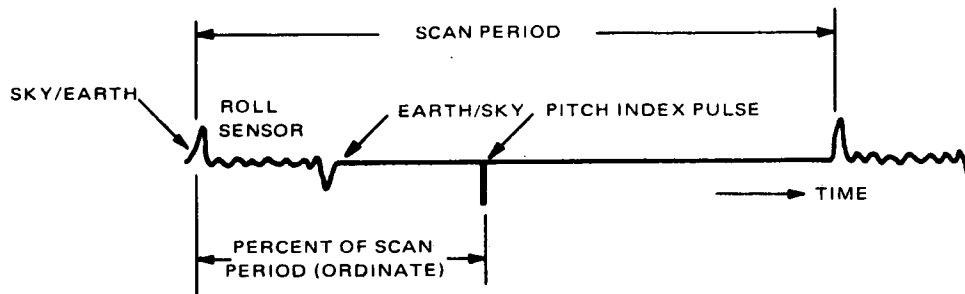


Figure 2-VIII-26. Ground-Commanded Momentum Coil Commutation Utilizing Roll Sensor and Pitch Index (MWA = 150 rpm; Altitude = 790 nmi)

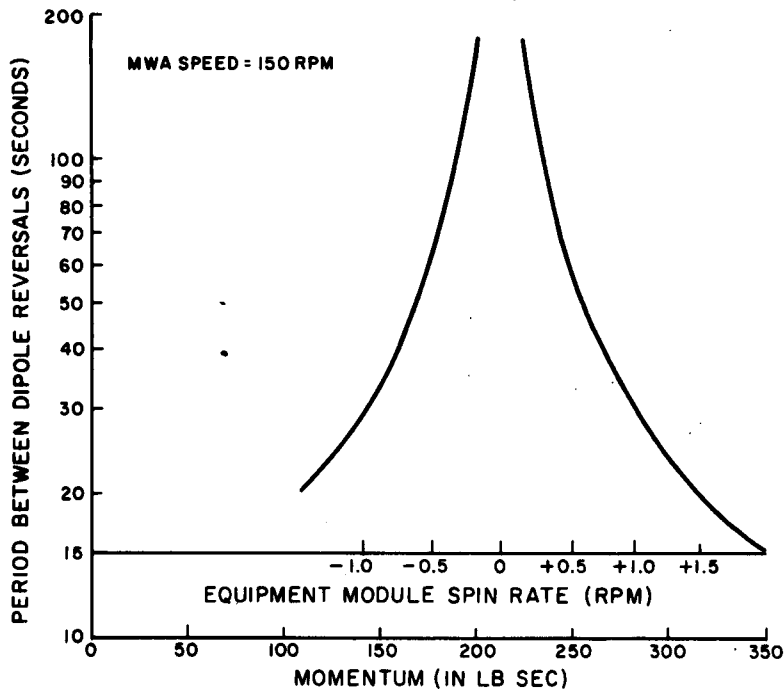


Figure 2-VIII-27. Time Between Required Momentum Coil Dipole Reversals Prior to Pitch Lock

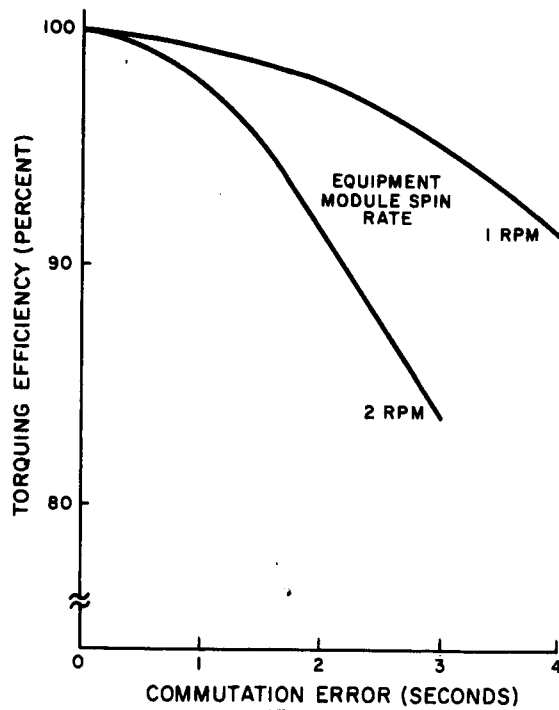


Figure 2-VIII-28. Commutation Error Effect on Torquing Efficiency

and Wallops, a maximum adjustment of 0.4 rpm per day (in terms of the folded panel inertia) can be obtained. This figure is based on an 80-percent commutation efficiency while operating in the nominal orbit. Therefore, a maximum time of 2.5 days would be required prior to pitch lock in order to adjust the 1.0/-1.5 rpm initial spin tolerance about nominal to the required pre pitch lock-in tolerance of ± 0.5 rpm. For the initial spin within ± 0.5 rpm of nominal momentum, adjustment prior to panel deployment and pitch lock is not required.

F. PITCH CONTROL

1. General

The pitch axis control loop maintains the spacecraft body in the desired orientation about the pitch axis with respect to an earth reference. In the absence of roll errors, this consists of aligning the yaw axis with the local vertical throughout the orbit. Pitch axis control is commanded into operation after solar panel deployment.

The satellite is controlled about the pitch axis by means of momentum transfer between the flywheel and the body. Momentum is transferred with a DC torque motor which couples the flywheel to the body. The torque motor is controlled by a reference voltage developed when a sky-earth horizon pulse is compared with a reference index pulse produced by a shaft encoder. Normally the pitch horizon sensor generates a horizon pulse for each rotation of the flywheel during the sky-earth transition. The reference index pulse is produced by a variable reluctance pickoff coil passing a reference point fixed in the body. For the particular orbit altitude, this reference point is geometrically positioned so that the horizon pulse and the index pulse are time coincident when there is a zero pitch error. An operational block diagram of the pitch axis control loop is shown in Figure 2-VIII-29.

Two redundant pitch axis control loops are provided. Either of the torque motors with its corresponding electronic channel will be selected by ground command, and either pitch sensor can be used with each of these channels.

The position error detector, which detects deviation of the body axis from the nominal local vertical, uses pulse width modulation (PWM) to measure the time difference between the horizon pulse and the index pulse. An error signal is produced with constant amplitude, variable pulse width, and either polarity; the width of the error signal is proportional to the magnitude of the angular error and the polarity is a function of its direction. The signal is shaped to an amplitude-modulated voltage by filtering (smoothing circuit). Subsequently, this voltage is compensated by frequency sensitive networks (compensation amplifier) and applied to the speed control loop. The voltages from the fixed-speed bias and the compensated-position error circuits are compared, in a summing amplifier, with a rate signal proportional to the relative rotational speed between flywheel and body. This latter rate signal is generated by a magnetic pulse encoder mounted integrally with the drive motor and generating 360 equally spaced pulses per revolution. The pulses are converted to a DC voltage by means of a frequency-to-DC converter and are smoothed by a simple lag circuit. The sum of the bias, position error, and rate signals is applied through a power amplifier to the armature of the DC torque motor. Finally, motor action transfers momentum between the flywheel and the body, thus reducing the pitch position error toward a value of zero.

During the initial pitch acquisition, the pitch error may be large enough to saturate the amplifiers. Under these conditions, the effective loop gain would be reduced and the tachometer loop time constant would be increased, leading to a possibility of control instability. To eliminate this condition, a two-mode control system is utilized. The compensation amplifier gain is switched to a low value (coarse-gain mode) when the position error exceeds a value that would normally cause the unstable condition. Ensuring stability by loop gain reduction under all expected conditions will also result in larger pointing errors for momentum deviations from the nominal momentum of 212 inch-pound-seconds. When the pitch error is reduced to a nominal value of 15 degrees, the system is automatically switched to the high (fine) gain control mode. For stability reasons, the compensation provided by the frequency sensitive network of the compensation amplifier is not utilized for the coarse-gain mode (i.e., for the larger position errors possible during the initial pitch acquisition). A ground commanded override can be used to place the loop in the coarse gain mode if desired.

2. Pitch Sensing

The pitch control error detector requires input pulses from a pitch horizon sensor and an index associated with the flywheel and the spacecraft body. Any deviation of the two pulses from coincidence generates an error signal which adjusts the speed of the torque motor. To obtain horizon information, one of two sensors shown in the block diagram of Figure 2-VIII-29 and the mechanical layout of Figure 2-VIII-30 will be used.

The sky-earth pulse obtained from the pitch horizon sensor is phase-compared to a magnetically generated index pulse from the encoder. Figure 2-VIII-31 illustrates the applicable geometry for the pitch horizon sensor with an encoder index pulse. The line of sight of the primary sensor axis (camera and SR) is offset from the horizon by the half-earth angle, as defined by the orbit altitude at the instant of index pulse occurrence. Before launching, the encoder stator is positioned such that the required transition sensed by the horizon sensor coincides with the magnetic index pulse, as required for the anticipated altitude; this achieved by properly aligning the entire electromechanical momentum wheel assembly relative to the spacecraft body.

3. Servo Design

The single axis pitch control block diagram in Figure 2-VIII-29 has an open-loop transfer function for the fine gain mode as follows:

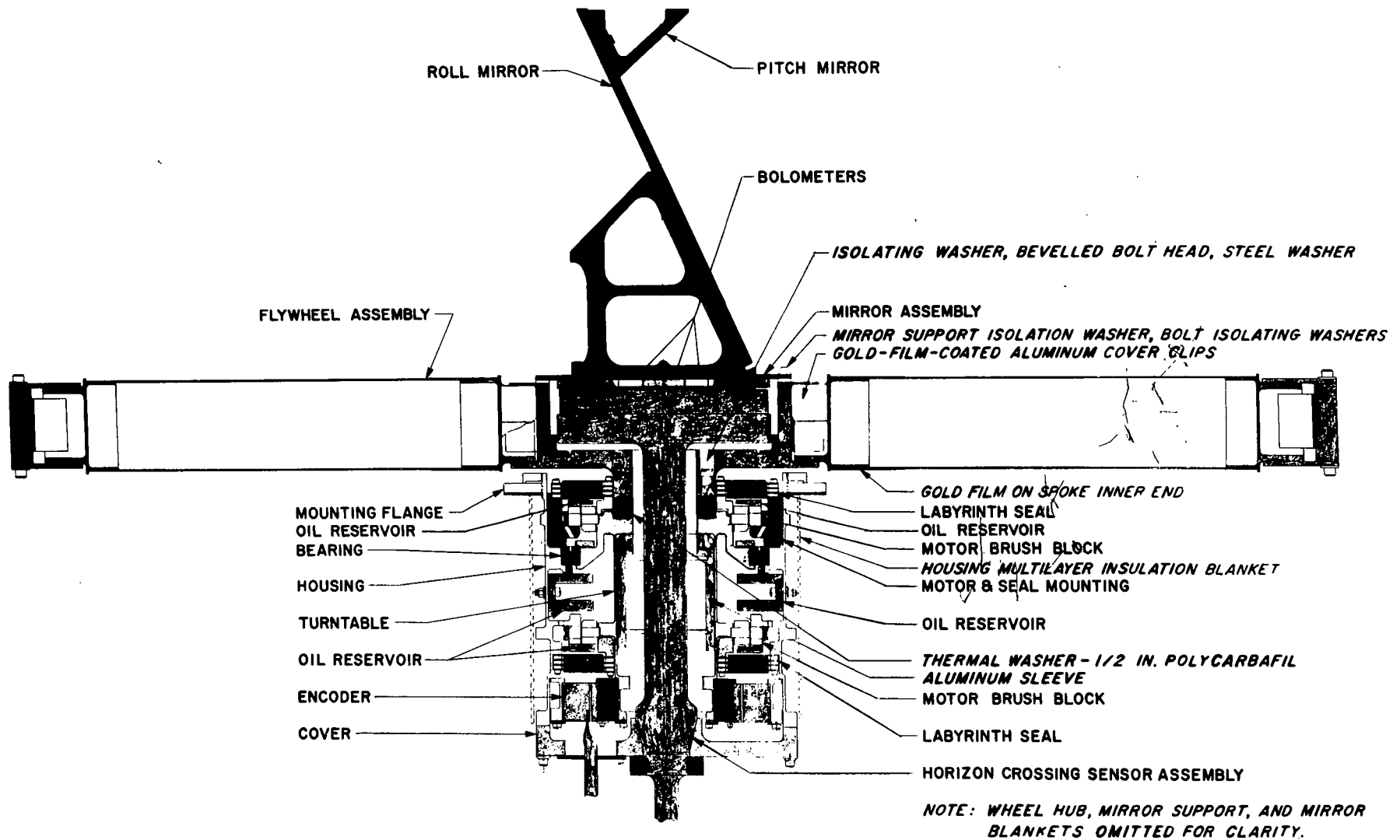


Figure 2-VIII-30. Momentum Wheel Assembly, Cross Section

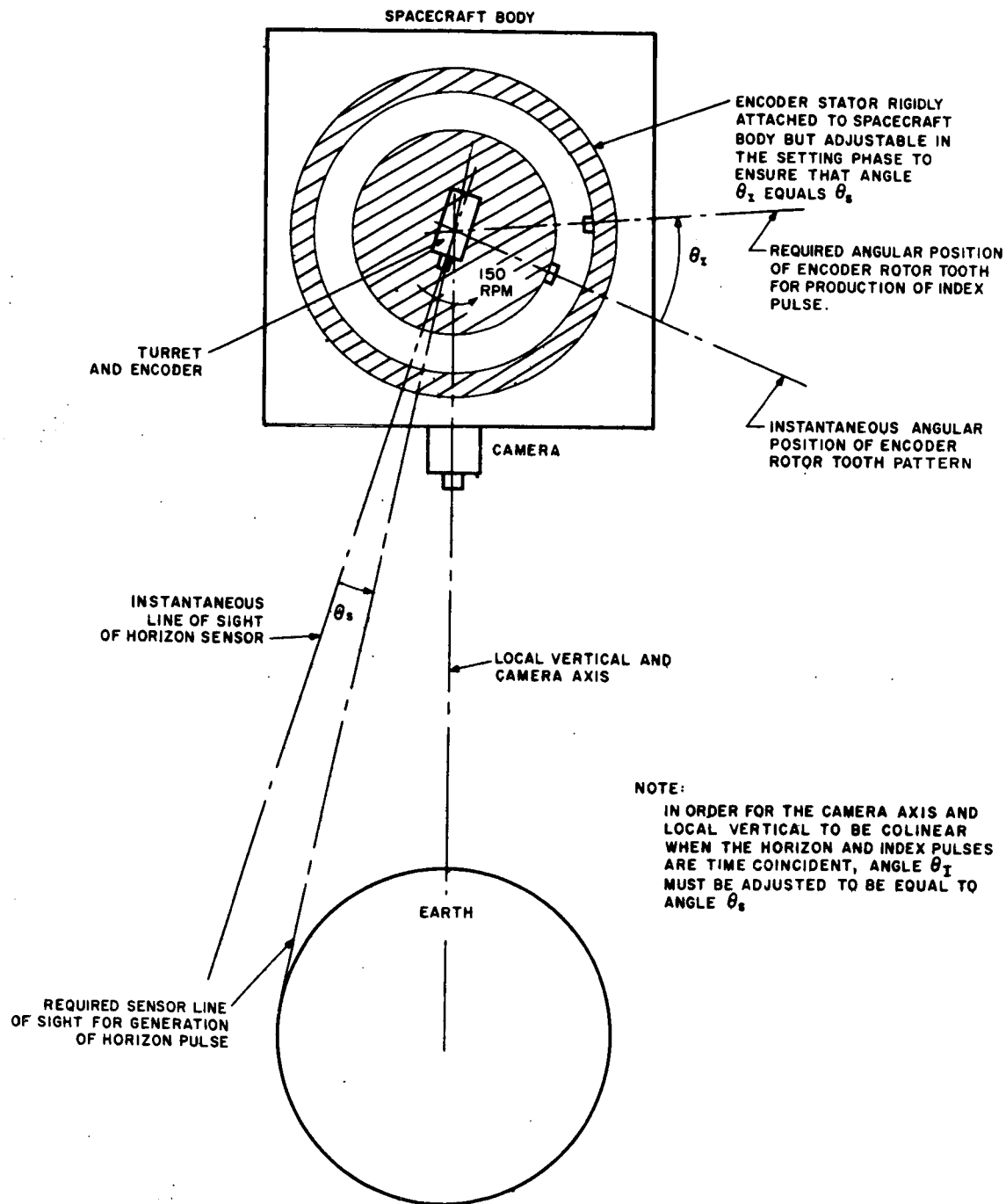


Figure 2-VIII-31. Geometry of Horizon Pulse and Reference Index Pulse

$$G(S) = \frac{\left(\frac{1 - e^{-TS}}{ST(1 + ST_S)} \right) \left(\frac{K_S K_c}{S} \right) \left(\frac{1 + T_1 S}{1 + T_2 S} \right) \left(\frac{I_f}{I_f + I_3} \right) \left(\frac{K_t K_a}{D + K_a K_f K_t} \right)}{\left(1 + \frac{I_e S}{(D + K_c K_t K_f)} \right)}$$

(2-VIII-26)

where:

- S is the Laplacian operator,
- T is the sampling period (nominal 0.4 second),
- K_S is the modulator DC gain (0.98 volt per radian),
- K_c is the compensation amplifier fine gain (45.2 volts per volt),
- K_{cc} is the compensation amplifier coarse gain (2.42 volts per volt),
- T_1 is the small-error compensation amplifier lead (22.3 seconds),
- T_2 is the small error compensation amplifier lag (417 seconds),
- I_f is the flywheel moment-of-inertia (13.5 inch-pound-seconds²),
- I_3 is the body moment-of-inertia about the pitch axis (1144 inch-pound-seconds²),

$$I_e = \frac{I_f I_3}{I_f + I_3} = 13.5 \text{ inch-pound-seconds}^2,$$

- K_t is the motor torque constant (3.3 ounce-inches per volt),
- K_a is the power (and summing) amplifier gain (118 volts per volt),
- K_f is the tachometer feedback gain (0.276 volt per radian per second),
- D is the motor damping, equivalent to back emf (2.42 ounce-inches per radian per second),

H is the nominal momentum (212 inch-pound-seconds), and
 T_S is the PWM smoothing lag (0.8 second).

The PWM error detector transfer function is

$$G(S)_{\text{PWM}} = \frac{1 - e^{-TS}}{ST} \quad (2\text{-VIII-27})$$

The above equation is an approximation derived from sampled data theory. For sinusoidal analysis purposes, this transfer function can be expressed as follows:

$$G(j\omega)_{\text{PWM}} = \frac{\sin \frac{\omega T}{2} e^{\frac{-j\omega T}{2}}}{\frac{\omega T}{2}} \quad (2\text{-VIII-28})$$

And, since the sampling period T will always be small compared with ω .

$$G(j\omega)_{\text{PWM}} = e^{\frac{-j\omega T}{2}} \quad (2\text{-VIII-29})$$

According to the tradeoff in the dynamic mass of the flywheel and the nutation damper the nominal momentum stored within the flywheel is defined as 212 inch-pound-seconds. For the 17.25-inch radius of gyration achievable within the envelope limits of the attach fitting, and the nominal spin rate of 150 rpm, the inertia ratio between vehicle pitch axis and flywheel is about 85. The selected nominal wheel speed is not only conducive to low brush wear and good commutation but also compatible with the attitude sensing scanning requirements and reasonable sampling rates. Within the above constraints, it is desirable to minimize the pitch position offset for this Class I servo loop resulting from momentum deviations. Selecting a velocity gain as:

$$K_V = \frac{K_s K_c K_t K_a}{D + K_c K_t K_f} \frac{I_f}{I_f + I_3} = 1.9 \text{ sec}^{-1} \quad (2\text{-VIII-30})$$

will limit the pitch offset to 0.29 degree for the sizable momentum deviation of 5 percent from the nominal 212 inch-pound-second value.

Figures 2-VIII-32 and 2-VIII-33 are the open-loop Bode plots of the single axis position loop for both fine-gain and coarse-gain cases. The figures indicate the need for the coarse-gain region. Although the system is adequately stable in its linear range, the phase margin of the fine gain curve would suffer severely if the loop gain were to decrease due to amplifier saturation.

It should be observed that the crossover frequency occurs at about 0.1 radian per second for both fine gain and coarse gain cases, or about two orders of magnitude below the nominal sampling frequency of 15.7 radians per second. The PWM can be represented in simplified fashion as indicated above, and a PWM smoothing network with a time constant in the vicinity of the sampling frequency has little effect on the system stability. The open-loop Bode plot of the tachometer loop is shown in Figure 2-VIII-34.

The gain switching circuit reduces the loop gain (compensation amplifier) and removes the lag-lead compensation network in the presence of large pitch errors, which are expected during the initial pitch acquisition and might recur during recovery from unexpectedly large disturbances. Without such switching, amplifier saturations would result in a highly under-damped system.

4. Three-Axis Considerations

The previous discussion concerned the servo design in terms of a single (pitch) axis loop. Since the inertia distribution of the ITOS spacecraft with panels deployed contains a substantial misalignment of the principle axes, sizeable products of inertia are present with respect to the spacecraft axes. These products, in combination with the pitch-roll sensitivity of the pitch sensor, significantly modify the dynamic characteristics of the single axis pitch loop in the vicinity of the nutation frequency. To assure stability over the required momentum and roll angle range, analytical studies by means of a digital computer simulation and a simplified linearized servo technique have been utilized to define acceptable product of inertia ranges. The mechanism of cross-coupling and possible instability in the loop is for the torque motor to induce a small roll error, which produces a pseudo pitch error, which calls again for a corrective torque.

The method by which the system is broken down for digital computer simulation is shown in Figure 2-VIII-35. The dynamics are represented by the relationship of the sensed pitch error θ_E with respect to the servo torque T_D and the pitch control loop (i.e., the relationship of the servo torque with respect to the sensed pitch error).

The most recent dynamic studies show satisfactory performance for the following conditions:

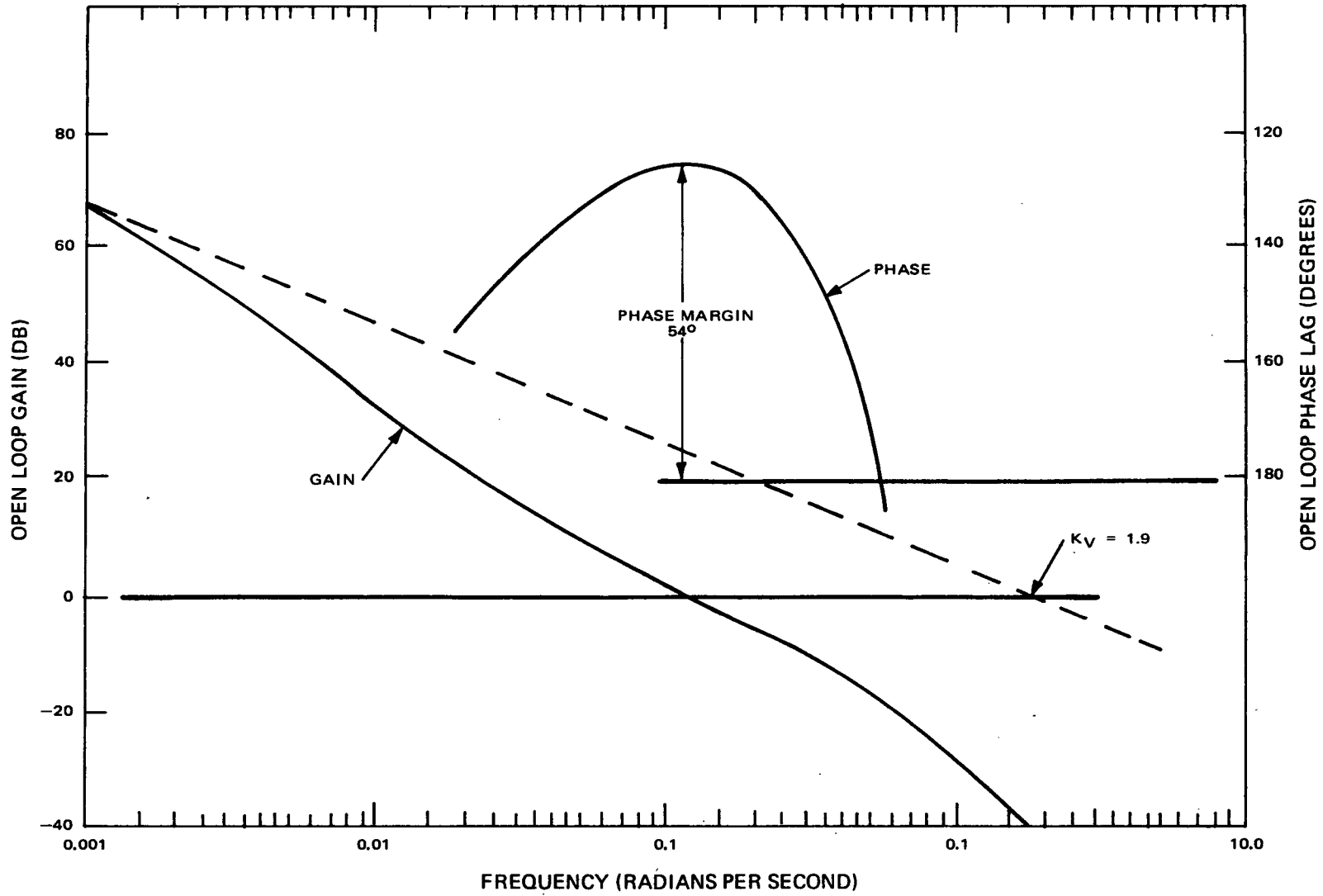


Figure 2-VIII-32. Open Loop Frequency Response of Pitch Control Loop (without Cross-Coupling, Fine Gain)

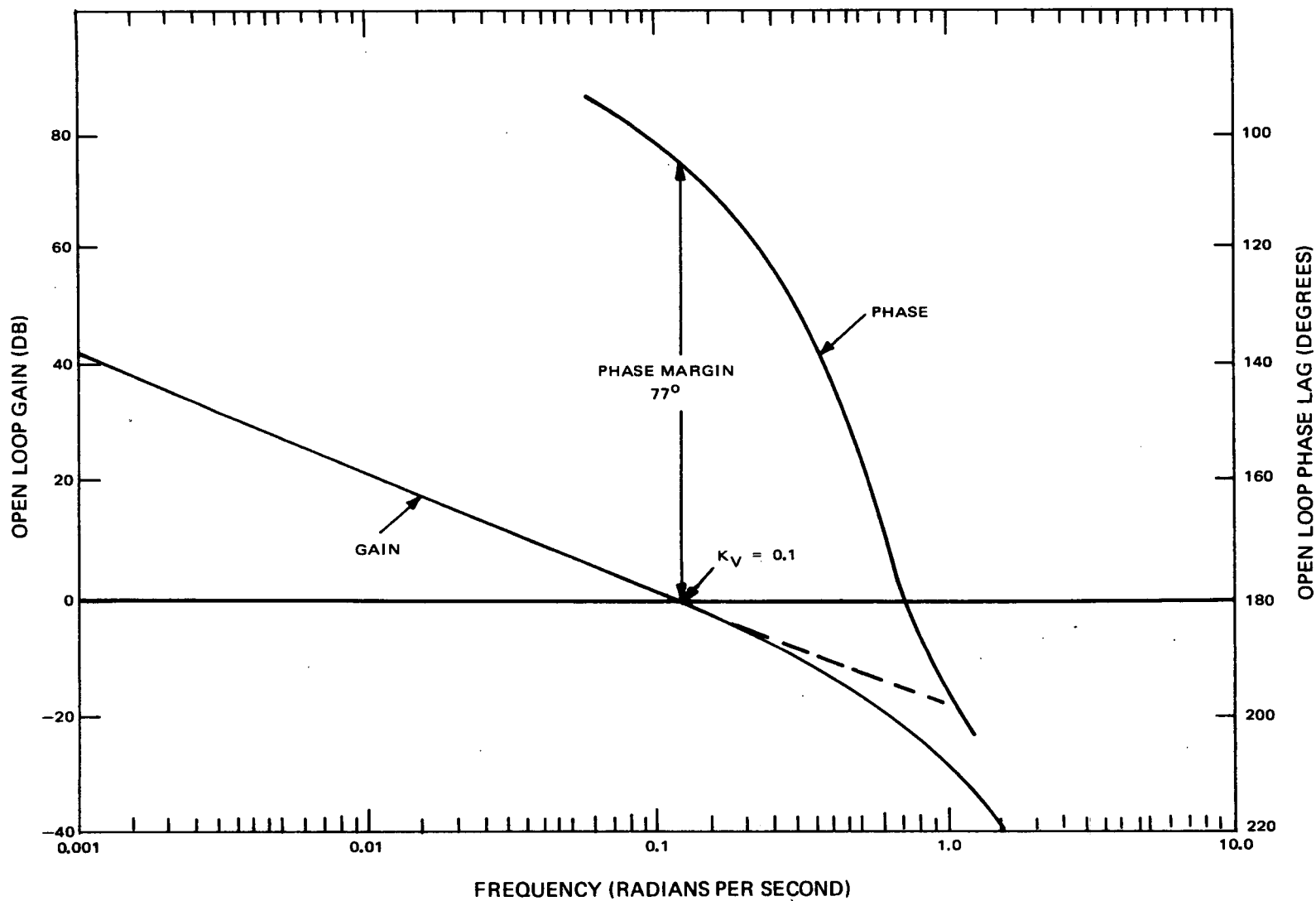


Figure 2-VIII-33. Open Loop Frequency Response of Pitch Control Loop
(Without Cross-Coupling, Coarse Gain)

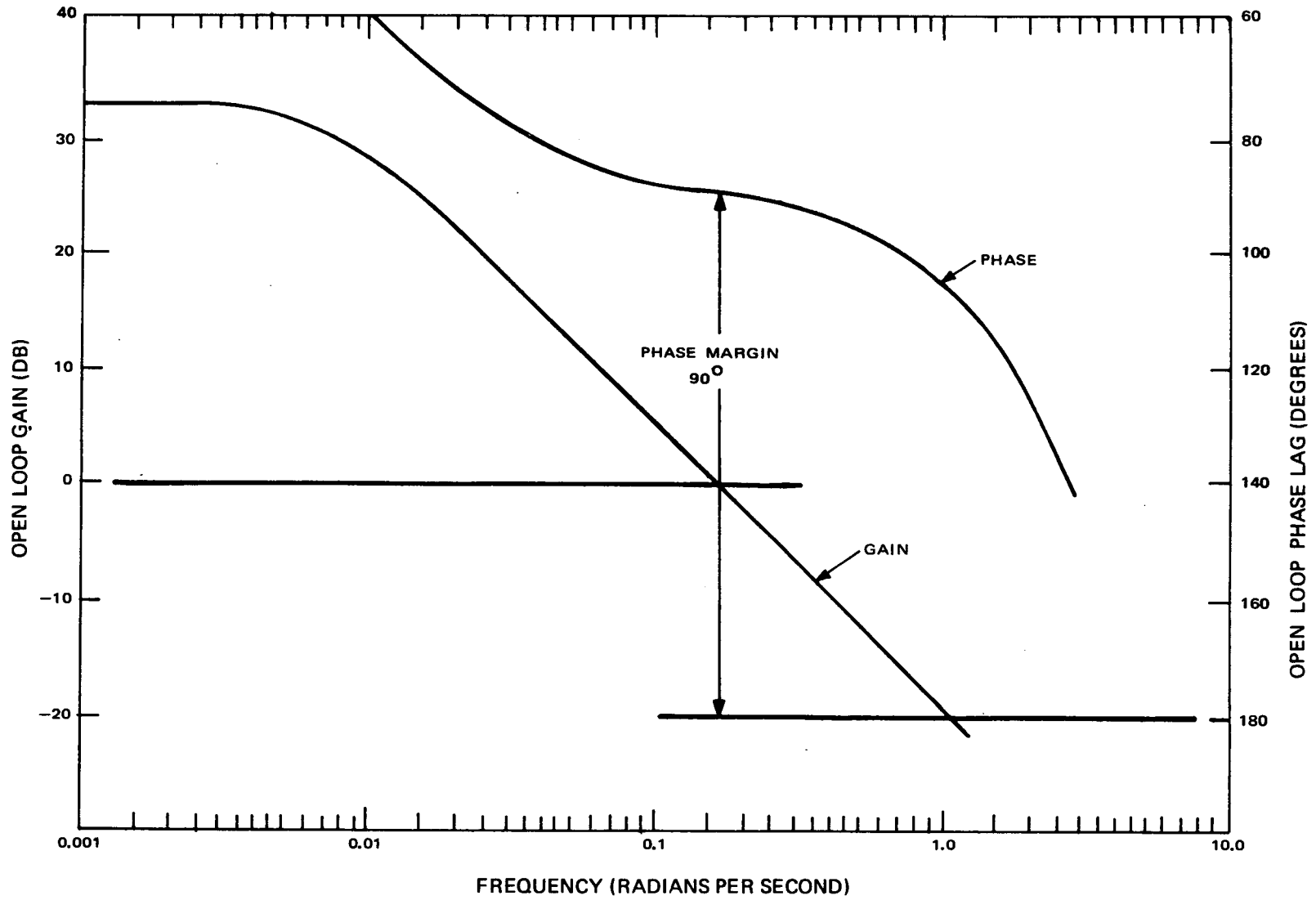
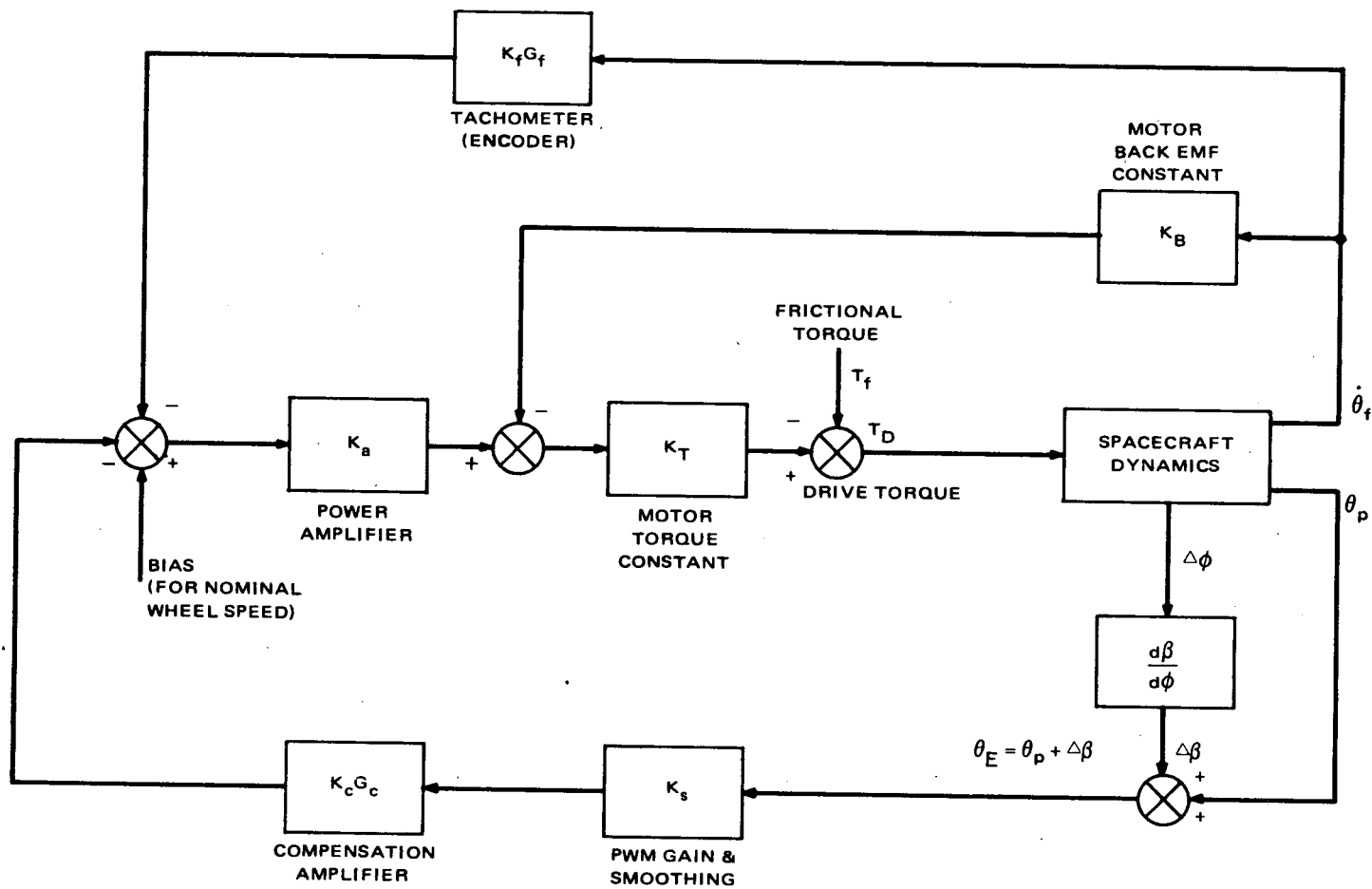


Figure 2-VIII-34. Open Loop Frequency Response of Tachometer Loop



θ_p : ANGLE BETWEEN SATELLITE YAW AXIS AND PLANE FORMED BY THE NOMINAL LOCAL VERTICAL AND THE PITCH AXIS.

$\Delta\beta$: FALSE ERROR CAUSED BY THE ROLL ANGLE DEVIATION AND THE EARTH'S CURVATURE.

Figure 2-VIII-35. Digital Computer Simulation of Pitch Loop System

<u>Momentum Range</u>	<u>Roll Angle Range</u>	<u>Mode</u>
199 to 270 inch-pound-seconds	-3 to +3 degrees	Initial capture
201 to 223 inch-pound-seconds	-3 to +3 degrees	Operational

The corresponding inertia ranges are listed in Table 2-VIII-6.

TABLE 2-VIII-6. COMPUTED INERTIA RANGES FOR PITCH CONTROL LOOP

Inertia Components	Range (pound-inch-second ²)	
	Minimum	Maximum
I ₁₁ (yaw moment)	1260	1308
I ₂₂ (roll moment)	991	1029
I ₃₃ (pitch moment)	1123	1165
I ₁₂ (yaw-roll product)	-2.3	10.5
I ₂₃ (roll-pitch product)	-13.7	-8.1
I ₁₃ (yaw-pitch product)	77	82.6

Examining the pertinent analytical expressions will clarify this important cross-coupling mode. The pitch control subsystem transfer function in terms of the torque output T_D resulting from an apparent pitch error θ_E can be linearized as:

$$\frac{T_D(S)}{\theta_E(S)} = K_a K_t K_s K_c \left(\frac{I_e}{D + K_a K_t K_f} \right) \left(\frac{T_1 S + 1}{T_2 S + 1} \right) \left(\frac{1}{1 + T_S S} \right) \left(\frac{S}{\frac{I_e S}{D + K_a K_t K_f} + 1} \right) \quad (2-VIII-31)$$

This transfer function gives the torque response of the pitch loop to a pitch position error. Similarly, the transfer function of the spacecraft in terms of the apparent pitch error θ_E output resulting from a torque T_D input can be linearized for small angles to:

$$\begin{aligned}
& - \left\{ 1 + \frac{S}{H_3} \left[(I_{13} \cos \theta_p - I_{23} \sin \theta_p) \frac{dB}{d\phi} + (I_{23} \cos \theta_p + I_{13} \sin \theta_p) \tan \phi \right. \right. \\
& \quad \left. \left. + \left(\frac{I_d^2 I_{11} \gamma H_3}{I_{11} I_{22} \gamma^2 + I_d^2 H_3^2} \right) \right] + \frac{S^2}{H_3^2} \left[(I_{11} I_{22} - I_{12}^2) + (I_{11} I_{23} + I_{12} I_{13}) \cos \theta_p \right. \right. \\
& \quad \left. \left. + (I_{13} I_{22} + I_{12} I_{23}) \sin \theta_p \right) \frac{dB}{d\theta} - \left((I_{13} I_{22} + I_{12} I_{23}) \cos \theta_p \right. \right. \\
& \quad \left. \left. - (I_{11} I_{23} + I_{12} I_{13}) \tan \phi \right] \right\} \\
\frac{\theta_E (S)}{T_D (S)} = & \frac{\left\{ 1 + \frac{S}{H_3} \left(\frac{I_d^2 I_{11} \gamma H_3}{I_{11} I_{22} \gamma^2 + I_d^2 H_3^2} \right) + \frac{S^2}{H_3^2} \left[(I_{11} I_{22} - I_{12}^2) \right. \right. \\
& \quad \left. \left. - \frac{(I_{22} I_{13}^2 + I_{11} I_{23}^2 + 2 I_{12} I_{13} I_{23})}{(I_{33} - I_f)} \right] \right\}}{S^2 (I_{33} - I_f)} \quad (2-VIII-32)
\end{aligned}$$

where:

- I_{11} is the yaw moment of inertia,
- I_{22} is the roll moment of inertia
- I_{33} is the pitch moment-of-inertia,
- I_{12} is the yaw-roll product of inertia,
- I_{13} is the yaw-pitch product of inertia,
- I_{23} is the roll-pitch product of inertia,
- I_d is the moment of the inertia of damper fluid about roll axis,
- I_f is the moment of inertia of the wheel about pitch axis,
- T_D is the pitch motor accelerating torque,
- γ is the damper torque constant (torque per radial rate)
- H_3 is the momentum about pitch axis,

- θ_p is the pitch angular offset $(H_3 - 212)/K_v I_{33}$
 dB/d is the coupling factor of apparent pitch error due to roll angle and earth's curvature,
 ϕ is roll angle
 θ_E is the overall error detected by the pitch sensor.

Without product of inertia terms; i. e., without principle axes misalignment; the Equation 2-VIII-32 reduces to

$$\frac{\theta_E (S)}{T_D (S)} = \frac{-1}{S^2 (I_{33} - I_F)} \quad (2-VIII-33)$$

The product of Equations 2-VIII-31 and 2-VIII-33 represent the single axis open loop transfer function treated in the previous section. The cross-coupling expression, Equation 2-VIII-32, shows the double integration relating torque to pitch error to be modified by the ratio of two quadratics. Because of the very low damping inherent in both the numerator and denominator of this ratio, the gain is within 1 dB and the phase within 5 degrees of zero for all frequencies greater or less than +5 percent of the nutation frequency. Within the range of +5 percent of the nutation frequency, large changes of gain and phase can occur in this cross-coupling term. Examination of this narrow frequency range by digital computer techniques permits rapid stability determination of any likely combination of parameters. However, it must be emphasized that these derived transfer functions are based on certain linearized assumptions, such as small pitch errors, small roll angle deviations, and absence of saturation. Therefore, it was necessary to obtain final stability verification by means of the available three-axis computer simulation; this holds true in particular for the examination of capture characteristics.

Table 2-VIII-7 is a summary of the three-axis computer study, which examined the capture characteristics and the stability of the pitch loop. Satisfactory performance was demonstrated for combinations of both pitch sensors, the specification roll angle range, the anticipated momentum range just prior to initial pitch capture, the predicted extremes of unregulated supply voltage, the maximum and minimum friction load, coarse and fine gain modes, servo tolerances, and the likely initial nutation angles. Based on prior studies including the linearized analysis, these computer runs always employed the most conservative combinations of inertias and tolerances in the equation of system stability. (See Table 2-VIII-8.)

Runs 1 to 14 examined system stability with an initial nutation angle of 1 degree. Runs 15 to 38 simulated pitch capture for various initial conditions, including changes in the phase angle of the nutation cycle. Runs 39 to 60 are additional stability verifications, and runs 61 to 63 represent three captures with the summing amplifier clamp set at 105 rpm minimum instead of the 120 rpm

TABLE 2-VIII-7. SUMMARY OF THREE-AXIS PITCH LOOP COMPUTER SIMULATION

Run No.	Pitch Sensor (α^*)	Roll Angle (degrees)	Momentum (in-lb-sec)	Motor Supply Voltage	Friction Load (in-oz)	Gain Mode	Initial Nutation Angle (degrees)	Maximum Nutation Angle After Capture (degrees)	Capture Time (seconds)	Damping Time Constant (minutes)	Damping Time Constant + Nutation Danger Time Constant
1	87	+3	199	35	20	C	1			148.4	1.22
2	87	+3	199	↓	↓	F	↓			99.1	0.82
3	87	+3	199	↓	↓	C	↓			79.1	0.65
4	93	-3	270	↓	↓	F	↓			48.5	0.54
5	93	-3	270	↓	↓	F	↓			88.1	0.97
6	93	-3	270	↓	↓	C	↓			32.8	0.36
7	87	+1.	201	↓	↓	C	↓			74.4	0.61
8	87	+3	201	↓	↓	C	↓			194.5	1.60
9	87	+5	201	↓	↓	C	↓			-313.2	-2.58
10	93	-3	223	↓	↓	F	↓			91.0	0.83
11	93	-5	223	↓	↓	F	↓			84.6	0.78
12	93	-10	223	↓	↓	F	↓			75.7	0.69
13	87	+3	270	↓	↓	C	↓			208.3	2.3
14	93	-3	199	↓	↓	F	↓			46.5	0.38
15	87	+3	199	↓	↓		0	0.34	228	102.9	0.85
16	87	+3	212	↓	↓		0	0.70	180	83.4	0.73
17	93	-3	212	↓	↓		0	0.88	315	52.6	0.46
18	93	-3	270	↓	↓		0	0.58	310	34.8	0.38
19	87	+3	199	26.5	↓		0	0.34	228		
20	87	+3	212	26.5	↓		0	0.70	180		
21	93	-3	212	26.5	↓		0	0.41	288	52.7	0.46
22	93	-3	270	26.5	↓		0	0.07	340		
23	87	+3	199	35	8		0	0.25	254	102.7	0.85
24	87	+3	212	35	8		0	0.81	190	83.4	
25	93	-3	212	35	8		0	0.37	396		
26	93	-3	270	35	8		0	0.57	307	35.1	0.39
27	87	+3	199	26.5	8		0	0.25	254		
28	87	+3	212	26.5	8		0	0.81	190		
29	93	-3	212	26.5	8		0	0.62	422		
30	93	-3	270	26.5	8		0	0.47	490		
31	87	+3	199	35	20		0.25	0.43	227	102.3	0.84

2-VIII-63

* α = angle from scanning axis to sensor line of sight at sky/earth intercept

TABLE 2-VIII-7. SUMMARY OF THREE-AXIS PITCH LOOP COMPUTER SIMULATION (Cont.)

Run No.	Pitch Sensor (α^*)	Roll Angle (degrees)	Momentum (in-lb-sec)	Motor Supply Voltage	Friction Load (in-oz)	Gain Mode	Initial Nutation Angle (degrees)	Maximum Nutation Angle After Capture (degrees)	Capture Time (seconds)	Damping Time Constant (minutes)	Damping Time Constant \div Nutation Danger Time Constant
32	87	+3	199	35	20		0.25	0.56	227	102.7	0.85
33	87	+3	199				0.25	0.39	227	102.9	0.85
34	87	+3	199				0.25	0.11	227		
35	93	-3	270				1	0.95	310	34.8	0.38
36	93	-3	270					0.63	313	34.9	0.39
37	93	-3	270					1.46	311	34.9	0.39
38	93	-3	270					1.58	310	34.4	0.38
39	87	+3	201			C				169.4	1.40
40	87	+3	201			C				173.4	1.43
41	87	+3	201			C				167.8	1.39
42	87	+3	201			C				186.0	1.53
43	87	+3	201			C				185.0	1.52
44	87	+3	201			C				141.4	1.16
45	93	-3	223			F				80.6	0.74
46	93	-3	223			F				89.3	0.82
47	93	-3	223			F				84.7	0.78
48	93	-3	223			F				81.2	0.74
49	93	-3	223			F				89.5	0.82
50	93	-3	223			F				85.8	0.79
51	93	+5	201			C				394.7	3.35
52	93	+12	201			C				37.6	0.31
53	87	+3	270			C				126.2	1.4
54	87	+3	270			C				208.7	2.3
55	87	+3	270			C				137.5	1.52
56	87	+5	270			C				-288.4	-3.2
57	93	-3	199			C				42.7	0.34
58	86.6	+3	201			C				144.2	1.19
59	86.6	+3	270			C				165.3	1.85
60	93.5	-3	223			F				129.6	1.19
61	87	+3	212				0	1.41	149	83.5	0.73
62	93	-3	212				0	1.44	275	52.7	0.46
63	87	+3	199				0.25	1.15	165	103.1	0.85

* α = angle from scanning axis to sensor line of sight at sky/earth intercept

TABLE 2-VIII-8. INERTIA VALUES USED IN COMPUTER STUDY

Inertia (Spacecraft Axis)	Maximum (lb-in-sec ²)	Nominal (lb-in-sec ²)	Minimum (lb-in-sec ²)
Yaw (I ₁₁)	1326	1302	1278
Roll (I ₂₂)	1042	1023	1004
Pitch (I ₃₃)	1168	1147	1126
Yaw-Roll (I ₁₂)	12.2	5.8	-0.6
Yaw-Pitch (I ₁₃)	81.6	78.8	76.0
Roll-Pitch (I ₂₃)	-5.0	-7.8	-10.6

maximum. Runs 39 to 43 checked any possible stability deterioration when altering inertia parameters to opposite tolerance extremes; comparison to the reference run No. 8 shows an improvement in every case. A similar comparison was performed during runs 45 to 49, which are referenced to the worst case inertia combination of run No. 10. The TIROS M flight inertias, instead of the ETM values, were used for runs 58 to 60; these runs correspond to the ETM spacecraft runs 8, 13, and 10.

For all stability runs, and where possible, also for capture transients, the damping time constant is non-dimensionalized with the nutation damper time constant. Thus, ratios less than one indicate improved stability due to cross-coupling, those greater than one show a decrease in performance, whereas negative time constants and ratios indicate unstable conditions.

The capture time for all examined cases is less than the 11-minute specification limit. This limit is based on a single axis phase plane computer analysis, where the initial pitch position error was varied in steps of 0.6 radian from 0.3 to 5.7 radians. Of the approximately 160 captures thus examined, the longest one took 11 minutes. This extreme value was computed for minimum friction load (8 inch-ounces), maximum unregulated motor voltage (35 volts), minimum momentum (199 inch-pound-seconds), and a worst case initial pitch position error. Capture under nominal conditions can be achieved in less than seven minutes.

5. Capture Verification

In order to permit a verification of the ability to capture, a dynamic suspension test rig was designed and built for single axis simulation. This rig permitted the suspension of the spacecraft by means of a torsional pendulum, consisting of a supporting structure, a three-wire suspension element, and a

servo drive. The servo, when in the follow mode, essentially decouples the spacecraft from ground by always seeking to eliminate any torsional displacement about the pitch axis, which is the axis of suspension. The desired momentum is initially stored in the spacecraft by running the MWA and the equipment module at their respectively desired speeds, utilizing the PCE tachometer loop for the former and the suspension rig tachometer loop for the latter. IR targets are viewed by the scanning pitch sensor to obtain earth reference for the phase lock loop.

Both the ETM and flight spacecraft were tested while suspended; capture runs were obtained in both vacuum and air. Good correlation was obtained with computer predictions. The flight spacecraft (without solar panels) successfully completed the seven required single axis captures given in Table 2-VIII-9.

The last capture is of particular interest since it not only falls below the minimum momentum of 199 inch-pound-seconds required in the applicable specification, but also because it utilized the 115-rpm clamping action of the summing amplifier. Figure 2-VIII-36 shows this transient in terms of a phase-plane plot. Just as in the six previous test runs, excellent convergence to pitch capture was achieved.

TABLE 2-VIII-9. SINGLE-AXIS CAPTURE DATA OBTAINED
IN SUSPENSION RIG TESTING

Initial Momentum (in-lb-sec)	Initial Pitch Error (degrees)	Time to Capture (seconds)	Final MWA Speed (rpm)
212	117	120	140
212	262	170	140
263	211	270	170
203	-127	110	134
211	199	160	144
212	304	210	150
181	-112	170	128

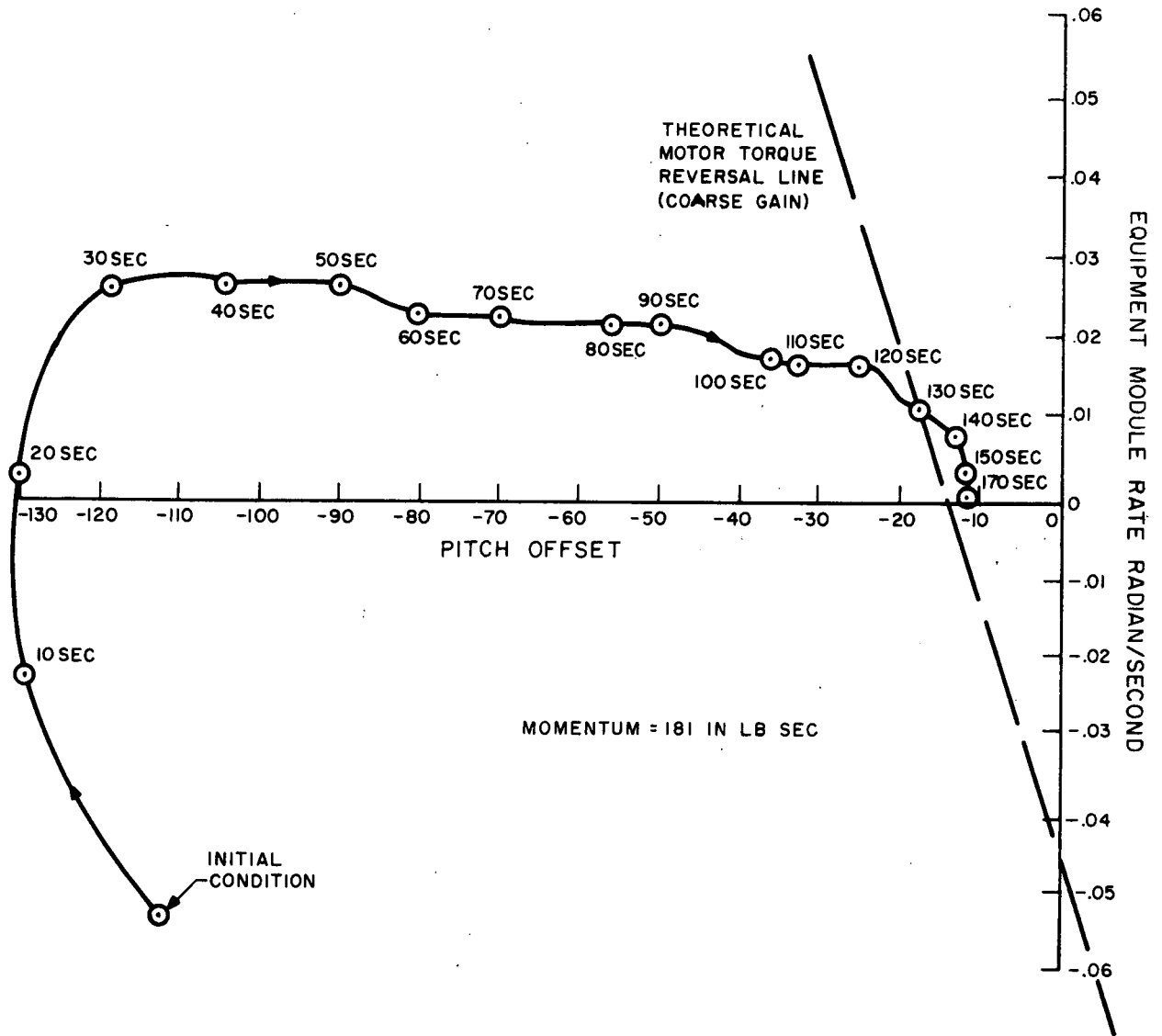


Figure 2-VIII-36. Pitch Capture Phase-Plane Plot (Dynamic Suspension Rig)

6. Component Description

a. GENERAL

The pitch axis control loop consists of the following components:

- Pulse width modulator (PWM) error detector
- Compensation amplifier
- Gain switching circuit
- Summing amplifier
- Power amplifier
- Torque motor
- Encoder
- Encoder electronics
- Frequency-to-DC converter
- DC-to-DC converter
- Roll and pitch sensors
- Sensor threshold amplifiers
- Blanking circuits
- Telemetry
- Wheel speed threshold
- Electronics box

The sensors and sensor amplifiers are discussed in Paragraph 2.VIII.F.5.k. A general functional description of the remaining components follows. The entire pitch axis control loop is shown in Figure 2-VIII-1. Table 2-VIII-10 lists the electronic specifications for these components.

b. PULSE WIDTH MODULATOR (PWM) ERROR DETECTOR

The block diagram of the PWM error detector is shown in Figure 2-VIII-1. The function of the PWM is to generate an error pulse whose width is proportional to the time difference between the horizon sensor pulse and the index pulse from the encoder. The polarity of the error pulse is determined by the order of occurrence of the input pulse, corresponding to a plus or minus pitch error. The error pulse is then filtered through an RC lag network to provide an average DC level.

TABLE 2-VIII-10. PITCH AXIS CONTROL LOOP ELECTRONIC SPECIFICATIONS

Component	Characteristic	Specification
Pulse Width Modulator	Index pulse	30 $\begin{smallmatrix} +1 \\ -5 \end{smallmatrix}$ Volts neg
	Horizon sensor pulse	14 \pm 2 Volts neg
	Input pulse duration	>100 microseconds
	Input impedance (horizon)	10 kilohms \pm 20 percent
	Input impedance (index)	20 kilohms \pm 20 percent
	Output impedance (loop)	12.15 kilohms \pm 5 percent
	Output impedance (gain switch)	9.09 kilohms \pm 5 percent
	Gain	0.98 Volt per radian \pm 5 percent*
	Smoothing time constant	0.8 second \pm 15 percent*
Supply voltages	-24.5, -15, and +15 volts	
Compensation Amplifier	Coarse gain	2.43 volts per volt \pm 4 percent*
	Fine gain	45.2 volts per volt \pm 4 percent*
	Input impedance	42.2 kilohms \pm 1 percent
	Output impedance	\leq 100 ohms
	Supply voltages	+15 and -15 volts
Gain Switching Circuit	Input impedance	>150 kilohms
	Threshold	\pm 0.26-volt \pm 0.04 volt error (15 degrees)
	Supply voltages	-24.5, -15, and +15 volts
Summing Amplifier	Gain	19.6 volts/volt \pm 4 percent*
	Input impedance	51.1 kilohms \pm 1 percent
	Output impedance	< 500 ohms
	Supply voltages	-15 and +15 volts

* End of life (EOL) tolerance

TABLE 2-VIII-10. PITCH AXIS CONTROL LOOP ELECTRONIC SPECIFICATION (Continued)

Component	Characteristic	Specification
Power Amplifier	Gain	6.1 volts per volt +5 percent -20 percent
	Input impedance	≥ 100 kilohms
	Output impedance	≤ 2 ohms
	Supply voltages	-26 to -36 volts
Encoder Index Electronics	Input impedance	> 100 kilohms
	Input signal level	0 to 230 millivolts p-p
	Output impedance	< 1000 ohms
	Output signal level	30 $\frac{+1}{-5}$ volts p-p
	Supply voltages	+15 and -15 volts
Frequency-to-DC Converter	Sensitivity	0.281 volts per radian per second
	Smoothing time constant	0.05 second
	Ripple	≤ 100 millivolts p-p, at 900 Hz
	Input impedance	> 100 kilohms
	Output impedance	10 kilohms ± 0.5 percent
	Supply voltage	-24.5, +15, and -15 volts
	Static offset	≤ ± 20 millivolts
DC-to-DC Converter	Output voltages	+15, +5, and -15 volts
	Efficiency	65 percent at rated load
	Supply voltage	-24.5 volts ± 1 percent
Blanking Circuits	Blanking angles (pitch sensor)	200 degrees (coarse) or 330 degrees (fine)
	Supply voltages	-15, +5, and +15 volts

Operationally, the leading edges of the input pulses set their respective control binaries which feed a difference amplifier. The difference amplifier provides the bipolar output error pulse which is then fed into the RC lag network.

After both binaries are set, the AND gate looks for the next positive tachometer pulse, which initiates reset, and the binaries are ready to accept the next set of input pulses. Should the binaries fail to reset for some reason, a second reset pulse which is derived from the 200-degree blanking pulse is OR'ed into the reset circuit of the PWM and will reset the PWM. However, this will only occur in the fine gain mode. The error measurement characteristics are shown in Figure 2-VIII-37. As the analog error decreases, the pulse width error decreases correspondingly. The equivalent error after smoothing is a satisfactory linearization of the analog error.

c. COMPENSATION AMPLIFIER

The compensation amplifier is a high gain DC operational amplifier used to generate transfer characteristics. The inverting operational amplifier is shown in Figure 2-VIII-38.

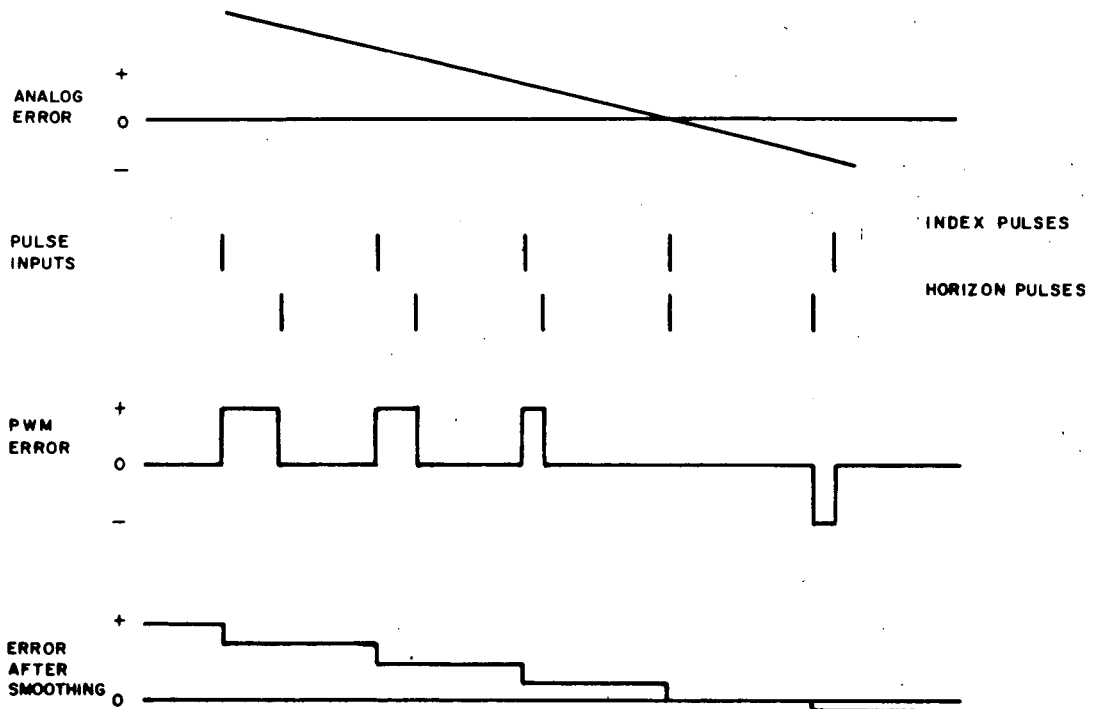


Figure 2-VIII-37. Error Detection

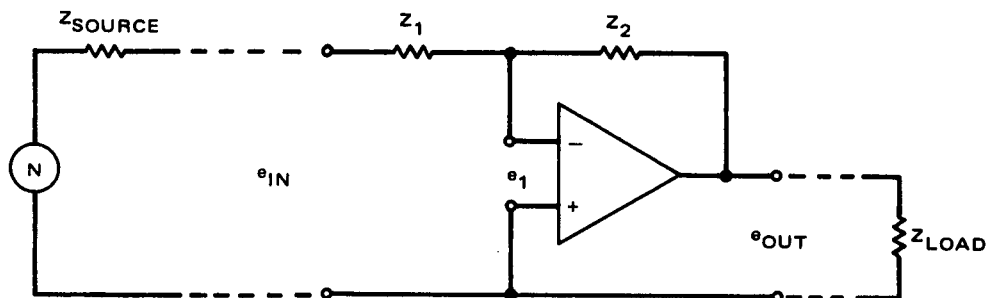


Figure 2-VIII-38. Operational Amplifier, Simplified Schematic Diagram

Assuming zero source impedance, very large load impedance, infinite gain, and infinite input impedance, it can be shown that the transfer characteristic of the compensation amplifier is as follows:

$$\frac{E_{out}}{E_{in}} = \frac{Z_2}{Z_1}, \quad (2-VIII-34)$$

By adjusting Z_2 properly, signal gain and phase compensation are provided.

d. GAIN SWITCHING CIRCUIT

A block diagram of the gain switching circuit is shown in Figure 2-VIII-39. This circuit consists of a differential amplifier that produces the absolute value of the smoothed error signal, a filter, a threshold circuit, and a relay driver. When the error exceeds a preset value, the relay driver is activated, switching the gain and phase characteristics in the compensation amplifier.

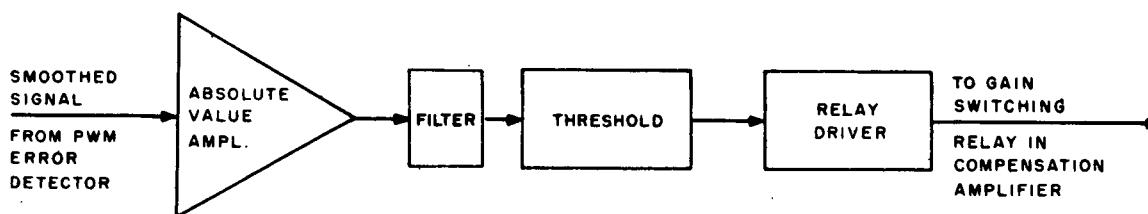


Figure 2-VIII-39. Gain Switching Circuit, Block Diagram

e. SUMMING AMPLIFIER

The summing amplifier, as shown in Figure 2-VIII-40, is a high gain DC operational amplifier which sums the motor bias voltage, the frequency-to-DC converter output, and the compensated position error signal. In the open loop mode the compensated error signal is removed and the motor bias voltage is

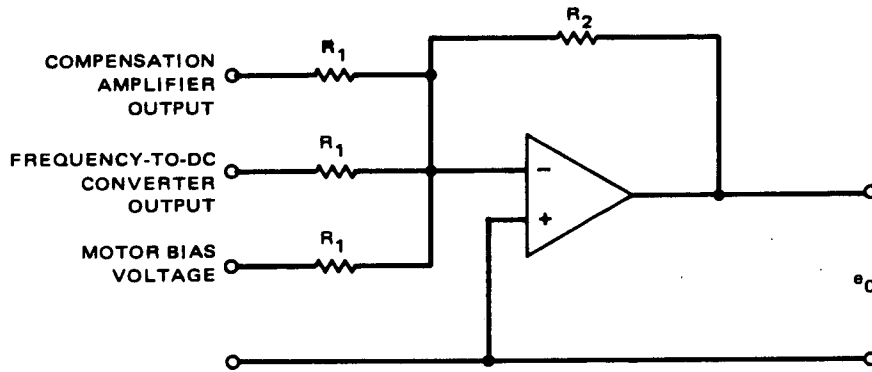


Figure 2-VIII-40. Summing Amplifier, Simplified Schematic Diagram

determined by the position of the COARSE/NORMAL relay. The motor speed is 150 rpm for the normal mode and 115 rpm for the coarse mode. A clamping circuit prohibits the motor speed from falling below 115 rpm by limiting the minimum net input voltage to the summing amplifier.

f. POWER AMPLIFIER

The power amplifier, as shown in Figure 2-VIII-1, extends the dynamic range of the summing amplifier to the full extent of the unregulated power supply, and it serves as an efficient power interface between the summing amplifier and the torque motor.

g. TORQUE MOTOR

The following criteria were applied in the selection of a torque motor for the pitch axis control loop:

1. The inside diameter of the motor has to be large enough to provide proper support and installation of the pitch and roll horizon sensors. This permits the use of mirror-scanned horizon sensors and eliminates the need for sensor slip rings.
2. The motor operates from the -26- to -36-volt unregulated power supply to avoid the inefficiencies associated with DC-to-DC power conversions.
3. The motor must be capable of supplying 20 ounce-inches of steady-state friction torque (due to bearing friction, brush friction, and magnetic drag), and it must have an adequate reserve capability to allow capture for a ± 15 -percent momentum change from the initial value.

4. The motor must be a direct drive pancake-type unit to eliminate any gearing requirements.

The Inland model T-4437A DC torquer or its equivalent was selected for the redundant configuration shown in Figure 2-VIII-30. For the minimum available voltage of 24 volts (allowing 2 volts for power amplifier drop), the torque and speed characteristics shown in Figure 2-VIII-41 satisfy criteria 2 and 3. The sensor layout in Figure 2-VIII-30 satisfies criterion 1; criterion 4 is also apparent from this figure. The motor, exclusive of the power amplifier, requires 3.44 watts at the design point.

Before the brush-type torque motor was selected, special attention was focused on the proper and reliable operation of the armature brushes throughout the life of the mission. Testing conducted by RCA under thermal vacuum conditions with 50/50 silver graphite brushes demonstrated proper and reliable operation. Both bearing and brushes operated in an oil vapor atmosphere of a low vapor pressure synthetic lubricant, stored within the momentum wheel assembly. It is of interest to note that the motor manufacturer experienced significantly higher silver graphite wear rates under standard atmospheric conditions. Therefore, it appeared that, from the standpoint of brush wear, the lubrication provided for the ITOS design in vacuum conditions was superior to that used under standard atmospheric conditions.

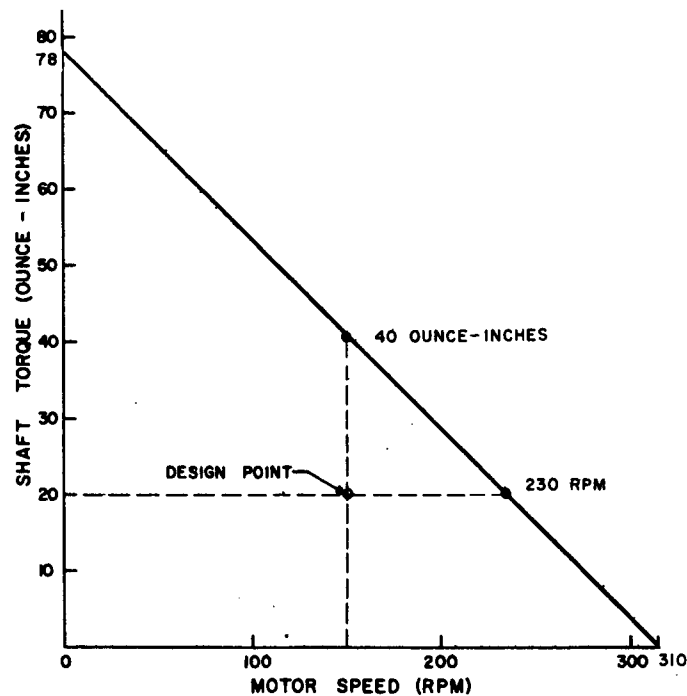
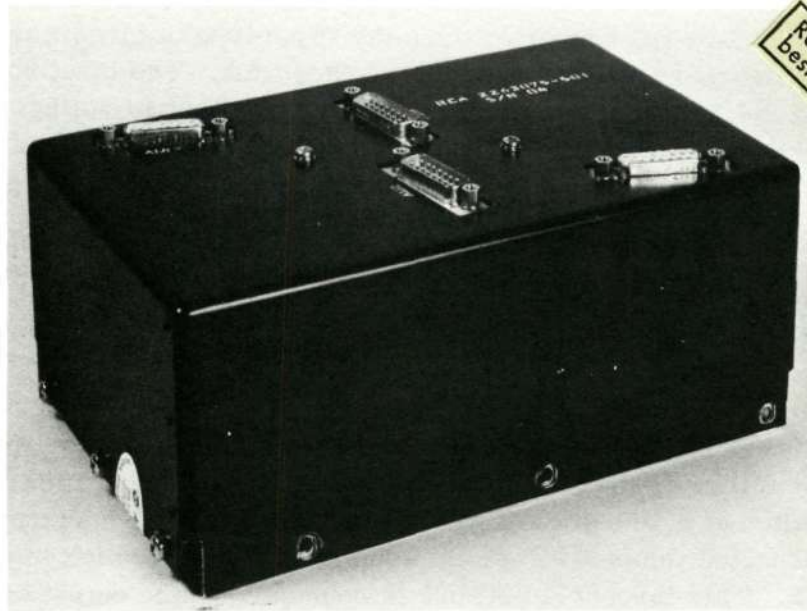


Figure 2-VIII-41. Torque and Speed Characteristics at Power Amplifier Voltage for Inland Torque Motor of -24 Volts

Difficulties encountered during life testing of the motor led to intensive study of motor brush wear and of methods for overcoming brush wear. The test results and study are discussed in paragraph F.8 of this section. The brush wear study led to the use of diethyl hexyl sebacate as a lubricant, replacing the dioctyl adipate originally used. In addition, design changes were made to reduce thermal coupling, making the unit more isothermal. During testing, a strain gage assembly and amplifier were used to monitor brush reserve. These items were incorporated in the ITOS design to provide a continuous telemetered monitoring of brush reserve during operation in orbit. The amplifier assembly is shown in Figure 2-VIII-42.



Reproduced from
best available copy.

Figure 2-VIII-42. Brush Reserve Amplifier Assembly

h. ENCODER

The encoder is a two-track magnetic variable reluctance transducer with redundant windings for each output, one pair of outputs for each loop. The unit has full peripheral sensors that minimize the effects of shaft misalignment and mounting eccentricities. One of the tracks (velocity track) provides 360 pulses per revolution for rate (tachometer) feedback around the motor. The other track (index track) consists of a suitable tooth pattern on the rotor and stator; this track produces the desired pitch index pulse. The outputs from the encoder are low-level signals which require amplification and processing before they can be utilized in the pitch control loop.

i. ENCODER ELECTRONICS

A block diagram of the encoder electronics is shown in Figure 2-VIII-1. There are two output signals for each loop. The two output signals (the line of 360 pulses per revolution, and the pitch index pulse from the encoder) are amplified by threshold amplifiers, one for each signal. The velocity signal essentially thresholds at the zero crossings to produce sharp pulses. The index signal thresholds at a level less than 100 rpm.

j. DC-TO-DC CONVERTER

The DC-to-DC converter uses the same type of circuit as that utilized in the other DC-to-DC converters in the spacecraft. The input voltage to the converter is -24.5 volts DC ± 1 percent; the nominal output voltages are +15, +5, and -15 volts DC. At load current levels from 20 to 100 milliamperes on each output tap, a 3-percent tolerance is maintained on output voltage, with a minimum overall conversion efficiency of 65 percent.

k. PITCH SENSOR THRESHOLD AMPLIFIERS

The threshold level of the sensors will be set 10 to 1 above the zero-to-peak noise. This corresponds to a level of 160 millivolts. The threshold amplifier following the horizon sensor is a biased DC operational amplifier, set to switch at a 160-millivolt input. For a sky-earth horizon crossing at the lowest expected temperatures, the input is sufficiently high to exceed the threshold. This threshold network is connected at the output of each of the pitch horizon sensors by ground-command switches. Cross-coupling of the pitch horizon sensors is possible from the ground.

l. EARTH BLANKING

As the horizon sensors scan the earth, the varying temperatures of the earth can cause fluctuations in the bolometer output. From previous experience, it is reasonable to assume that during the earth time, many pulses will be produced that will trigger the threshold circuit. To keep these earth pulses from interfering with the pitch axis control loop electronics, earth blanking of the sensor outputs is included.

A 9-bit shift register (capacity 511 pulses) is used to count the encoder tachometer pulses. Since there are 360 pulses per revolution, each pulse corresponds to 1 degree of rotation.

The shift register is reset at the end of 360 tachometer pulses or the receipt of a sky-to-earth pitch sensor pulse (whichever occurs first).

Outputs are taken from the register at 200 pulses (or 200 degrees) and 330 pulses (or 330 degrees). These are used in the blanking.

In the final gain mode, all horizon sensor threshold amplifier outputs are blanked out between 0 and 330 degrees. The region from 0 to 200 degrees is used for the coarse gain condition to permit rapid horizon acquisition in the case of a large pitch error, with the 330-degree deblanking pulse being retained for backup purposes.

m. ELECTRONICS BOX

The box basically consists of three parts: top cover, wrapper and base. The top cover houses five connectors: two are test point connectors, one is for command and telemetry, and two are for interface with the momentum wheel assembly. The wrapper encloses the seven circuit boards which are mounted in Birtcher slides and plug into board connectors on the harness board. The harness board provides the electrical tie between circuit boards and the interface with the outside connectors. The base houses the two DC-to-DC converters, the two power resistors used in the wheel speed threshold circuit, and the two power transistors used in the power amplifier. The potted box weight is 7.1 pounds.

7. Pitch Control Mechanical Design

The pitch control electromechanical assembly is a single unit consisting of an outer fixed housing and an inner rotating turntable, each shaped to mount and retain the following essential parts: (1) encoder with redundant coils, (2) labyrinth seals, (3) redundant torque motors, (4) oil reservoirs, (5) flywheel, (6) mirror, and (7) bolometers and bolometer electronics. The turntable assembly is supported by the external housing through a single bearing as shown in Figure 2-VIII-29.

The assembly resorts to a single bearing rather than two spaced bearings for support of a rotating shaft for the following reasons:

- The single bearing has less friction than two bearings.
- The single bearing allows visible assembly control over the concentricity of the motors. If two bearings were used they would require adequate axial spacing to give a reasonable base, requiring motor mounting between bearings. With the necessary assembly tolerances, such an arrangement introduces greater concentricity tolerances.

- The single bearing shortens the assembly, thus saving weight.
- The single bearing can perform all of the system requirements satisfactorily.

The Conrad four-point contact ball bearing is the Kaydon KD45XP with selected diametral clearance between 0.0008 and 0.0012 inch. The angular tilt is held to 0.00045 radians maximum.

The allowable load values on the bearing, based on a standard usable Brinell value, are:

- Radial load: 12,400 pounds,
- Thrust load: 30,800 pounds, and
- Moment: 31,000 pound inches.

Calculations show that an adverse differential temperature (i.e., inner race warmer than outer) of 13° C would just eliminate the minimum diametral clearance of 0.0008 inch. Normally, at this temperature differential, bearing binding would commence. Selecting a temperature safety factor of 2.0 established a maximum desirable race temperature differential of 60° C (i.e., inner race warmer than outer). Analysis shows that even in an emergency power overload case, this differential is unlikely to exceed 1° C in the steady state, giving a wide safety margin.

A thermal investigation of the assembly under all likely conditions shows an absolute maximum gradient, with inner race cooler than outer, of less than 6° C, with a probable maximum of only about 2° C, at a maximum initial diametral clearance of 0.0012 inch, a differential temperature in this sense of 10° C can be tolerated before the encoder gap, the critical gap from geometry, can be closed due to increased shaft wobble from the thermal increase in diametral clearance.

The bearing races and balls are of SAE52100 steel which shows excellent oxidation resistance up to 250° F. This resistance plus an oil film will preclude any corrosion of the bearing during storage.

Each motor consists of three separate parts: a two-segment brush assembly, an armature, and a stator. Radial self-locking screws (see Figure 2-VIII-29) align the stator to the rotational center of the bearing.

The encoder is installed at the top of the assembly. Both the rotating part and the fixed part of this magnetic transducer are shown mounted through adaptors which allow flexibility to accommodate the exact dimensions of the encoder.

Three oil reservoirs composed of Nylasint, store 60 grams of lubricant, or about one third by volume. Lubrication is achieved by low pressure vaporization of the oil in the closed housing. The vapor is able to lubricate the motor brushes and bearings. The synthetic lubricant is diethyl hexyl sebacate, a dibasic-acid ester. Selection of this lubricant is based on its successful performance during thermal vacuum tests.

Associated with the oil vapor pressure is a labyrinth-type sealing system. The leak rate of this labyrinth controls the life of the lubrication. The labyrinth seals are constructed of stacks of magnesium sheets of the proper diameter and thickness so that the rotating sheets have a nominal 0.02-inch clearance and thus no rubbing contact and zero associated friction. Experience has shown this construction to be satisfactory.

The theoretical lubricant loss rate through the two labyrinth seals can be predicted for the applicable free molecular flow regime as follows:*

$$W = \left[0.0583 P \left(\frac{M}{T} \right)^{1/2} A \right] f \quad (2-VIII-35)$$

where

W is the oil loss rate (grams per second),

P is the vapor pressure (mm Hg),

M is the molecular weight of the oil,

T is the oil temperature (°K),

A is the aperture area (cm²), and

f is the transmission probability of molecular flow.

The transmission probability is a function of the length-to-clearance ratio of the seal, and of the number of directional changes from the inner cavity to the outer environment. Each of the two labyrinth seals consists of 14 consecutive L-shaped segments. For diethyl hexyl sebacate (molecular weight, 426), the loss rate is illustrated in Figure 2-VIII-42.

Four bolometers, as shown in Figure 2-VIII-29, are mounted on a support tee which extends through the rotating platform to a fixture point. Electronics for preamplifying the bolometer signals are mounted on the platform adjacent to the bolometers. Optical axes of the bolometers are aligned by a shimming technique.

* W.A. Salmon and C.M. Apt, "A Lubrication System for Space Vehicles", Automotive engineering Congress Paper 632E, January 1963, and D. Stantler, "Vacuum Technology", International Science and Technology, No. 13, January 1963, pp. 46-54.

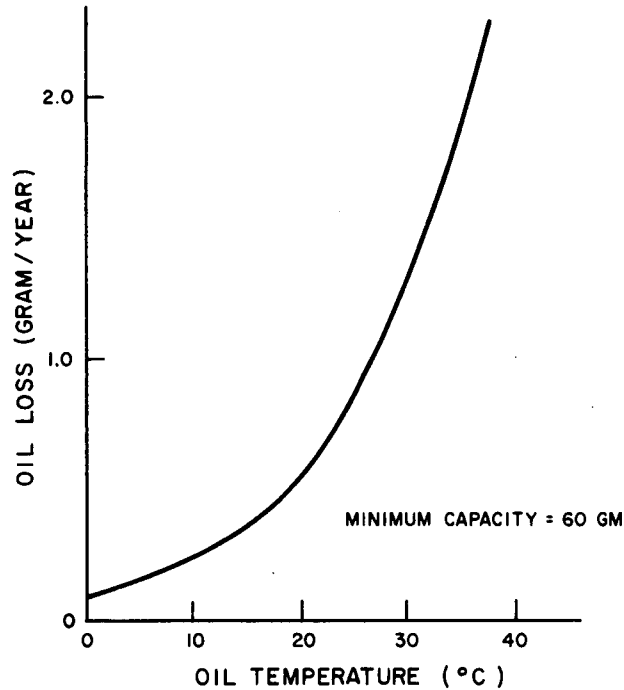


Figure 2-VIII-43. Molecular Flow Loss of MWA Lubricant P-10 (Diethyl-hexyl Sebacate)

A spoked flywheel having a continuous rim is attached to the rotating platform. The outside diameter of the flywheel is selected to just clear the inside of the marman clamp, extending from the baseplate section of the satellite. When the four separation-spring-operated, mushroom-shaped, pushoff pads are removed from the adapter, the pitch axis control assembly, complete with flywheel, is inserted and attached to the baseplate.

Attached to the hub of the flywheel is the sensor mirror assembly, which includes the large roll mirror and the smaller 45-degree pitch mirror. The pitch mirror reflects its signal to the pitch bolometers through a hole in the roll mirror. The roll mirror reflects to signal to either of the roll bolometers. Each mirror uses 6061-T3 aluminum alloy as a structural base on which a pure aluminum surface finish is vacuum deposited and overcoated with silicon monoxide. Prior to the final finish, nickel electroplating and physical surfacing is performed as required.

The lower end of the roll mirror shown in Figure 2-VIII-30 is a flat plate cantilever. Centrifugal force from rotation at 150 rpm will cause deflection of the mirror. Calculations show a local change in the mirror angle, from the installed flat mirror, as approximately 2 minutes of arc at the extreme tip and 1 minute of arc at 0.6 inch from the tip, a position corresponding to the centerline of sight of roll bolometer No. 2. Even though reflections double these angles, such changes are insignificant.

8. Applicable Test Results

a. GENERAL

The basic ITOS design was an outgrowth of a similar type of assembly constructed for preliminary test purposes. The test unit was a single motor assembly using 50/50 silver graphite brushes, with the motor in a labyrinth-sealed housing containing a dioctyl adipate vapor lubrication system. The test unit was tested in thermal vacuum for a period of 6 months with the wheel rotating continuously at 150 rpm over a test temperature of 0° to 25°C. At the conclusion of the test the unit was disassembled and inspected. The brushes had worn less than 0.003 inch out of a possible 0.050 inch, the oil assembly loss was less than 1 gram, and the bearing showed no signs of wear. The above test proved the feasibility of this type of device for the momentum wheel assembly and was used as the basis for design. Due to the redundancy requirements of the program two motors were used in the same assembly for this design.

During early prototype testing it became apparent that the thermal conditions on the redundant motor system could cause brush wear at a rate not consistent with the wearout requirements. Due to the construction of the device, severe thermal gradients existed both axially and radially when the device was tested in a space environment simulation. This was caused by the thermal coupling of the MWA rotor to space, which caused the rotor to be significantly colder than the stator. Computed values indicated the delta temperature between the two motor rotors was on the order of 40°C and the radial gradient from rotor to stator was on the order of 15°C. These thermal gradients had a severe effect on the lubricating oil distribution within the unit. When the motor rotor was very cold compared to the rest of the assembly, the oil tended to build up a heavy film on the commutator. This overfilming manifested itself as an insulating layer between the motor brushes and commutator. Instead of continuous current through the brushes into the commutator, there resulted a "punch through" effect whereby the current was random and of a high density. This caused both an electrically noisy operation and severe local heating, resulting in excessive brush wear rates.

Different thermal conditions existed between the two motors in the assembly. By making certain adjustments during the preliminary test program it was possible to get either of the two motors operating in a satisfactory fashion, but it was obvious that further design changes would be necessary to completely implement the system satisfactorily. It should be noted that during this testing, by adjusting test conditions to increase the temperature of the colder motor, the warmer motor became even warmer. An extension of this would cause the warmer motor to become so hot that insufficient lubrication would be present. This would cause an increase in the "frictional" wear rate as opposed to the electrical wear described.

Based on the above findings it became clear that design changes were necessary to make the MWA more isothermal and to reduce the heat loss through the flywheel and mirror assembly into space. A test of the MWA under locked rotor conditions was made to determine the conductances of the various internal elements and interfaces of the MWA and a computer program was initiated to predict internal temperatures under various operating conditions and the effect of design changes on the unit.

At this time a NASA-RCA decision was made to reduce the test temperature from a range of from -15° to $+60^{\circ}\text{C}$ to a range of from 0° to 30°C to be more realistic with regard to the requirements, and to change the lubricating oil from dioctyl adipate to diethyl hexyl sebacate. This oil has a vapor pressure from 5 to 10 times less than dioctyl adipate over the test temperature range. This tended to reduce the overfilming characteristics possible at the higher temperatures.

Based on the test and computer programs, design changes were made which reduced thermal coupling to space and made the unit more isothermal. (These design changes are shown in *italic* on Figure 2-VIII-30, MWA cross section.)

With the unit in this final flight configuration, several long term tests were made. The test results are described in paragraph 8.c below.

b. TEST DESCRIPTIONS

The initial TIROS M MWA prototype tests were performed in a thermal vacuum chamber under essentially isothermal conditions (i.e., the flywheel and the motor assembly were exposed to the same thermal conditions). During the first subsystem test, the accidental omission of a thermal blanket on one segment of the facility caused the MWA to be exposed to a large thermal gradient. As a result of this gradient the motor brushes wore at an extremely rapid rate. A complete review of the test program and reanalysis of the system were undertaken to ensure that the MWA design was satisfactory for the expected environment. As a result of this analysis the design changes noted previously were made and the test configuration was modified. Early testing was done in a thermal vacuum facility in which the total environment was maintained at the same temperature. Although this is satisfactory for an isothermal design MWA, the review of the ITOS system showed that the flywheel would get much colder than the baseplate mounting point of the MWA and coupling to space was relatively high; therefore, proper simulation of the environment would require a two temperature system. All component testing was then done in a thermal vacuum chamber in which the housing temperature and the flywheel temperature were independently controlled to those temperatures predicted for orbital conditions.

The early test history of the TIROS M MWA prior to design changes was all short-term and clearly pointed out that frictional wear due to under-lubrication and electrical wear due to overfilming could reduce mission capability by at least an order of magnitude in time.

The applicable test history was obtained from three long-term tests in thermal vacuum with the MWA in final flight configuration. These tests proved that the MWA motor had excellent wear characteristics and that the bearing was well suited for its application.

In order to monitor brush wear continuously, a strain gage was mounted to a spring connecting one of the four brushes to the brush blocks. Subsequent measurement of the brushes showed that there was excellent correlation between actual brush wear and the brush wear indicated by strain gage measurement. The use of this continuous monitoring device was instrumental in determining conditions which would increase the brush wear rate. Based on observations during the testing the following can be concluded:

- Over a test range of 0° to +35°C, wear is minimal at the higher temperature.
- Transient temperature conditions are unfavorable. The maximum transient during test was a 25°C change at 3°C per hour.
- After transient, the wear rate decreases with time.
- Minimization of switching drive power to the two motors is favored for projected long life. The switching generally upsets the thermal conditions and is somewhat equivalent to a thermal transient.
- None of the above conditions will exist in orbit and the predicted MWA orbital temperature range of +17° to +25°C is favorable to projected long life.

The three long-term units tested were designated as MWA 05, MWA 01PP, and MWA 02P. Of the three, MWA 05 was in final flight configuration for a full 6-month test period, whereas MWA 01PP and MWA 02P were reconfigured during the test program to determine the effect of addition and omission of oil reservoirs in the vicinity and in line of sight of the motor brushes. In addition, MWA 02P was the subject of a special test whereby it was soaked at -15°C for 24 hours nonrotating and was then turned on.

c. BRUSH WEAR DATA

Test profiles for the three long-term tests are shown in Figure 2-VIII-44. The M1 and M2 reservoirs are those reservoirs in the vicinity of motor 1 (fly-wheel end) and motor 2 (anti-flywheel end), respectively.

The total brush wear for each of the three tests is given in Table 2-VIII-11 for the test profile (Figure 2-VIII-44). The projected life is based on a wear rate of the worst case motor over the full temperature conditions and includes wear due to the severe temperature transients shown. On this basis the projected life is conservative.

Shown in Table 2-VIII-12 is the brush wear summary for the three tests, broken down into two temperature ranges. The +15° to +35°C range covers the orbital temperature prediction and is more indicative of expected life-time. Again this is very conservative since all transient wear is included in the projected figures. It should be noted that, although not rigorously defined, the strain gage and optical readings should not be interpreted to more than 0.002 inch (2 mil) accuracy. At the conclusion of the 6-month test on MWA 05, plus some special testing described later, the unit was disassembled and the brushes were optically measured. The brush toe measurements (the most accurate

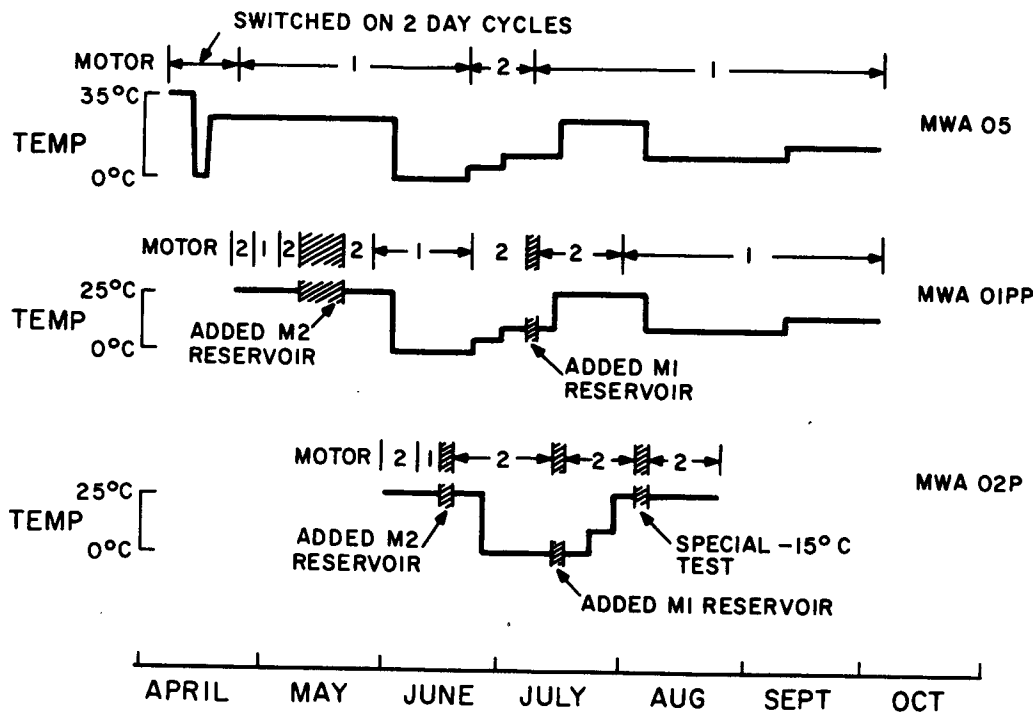


Figure 2-VIII-44. MWA Long-Term Test Profiles

TABLE 2-VIII-11. LIFE TEST BRUSH WEAR SUMMARY

Unit	Total Test Time (hours)	Total Wear (mils)		Projected Life (years)
		M1	M2	
05	4270	3.73	6.95	3.5
01PP	3560	9.11	15.4	1.3
02P	1780	10.1	7.67	1.0

NOTES:

Total wear including transient wear.

Orbital temp. range: +17°C to +25°C.

MWA 05 test range: 0 to 35°C.

MWA 01PP and 02P test range: 0 to 25°C.

Projected life based on 50-mil brush height and motor with maximum wear rate.

TABLE 2-VIII-12. LIFE TEST BRUSH WEAR SUMMARY

Unit	Total Time (hours)	Total Wear (mils)		Projected Life (years)
		M1	M2	
Brush Wear Over +15°C to +35°C Temp.				
05*	2460	1.64	2.24	6.25
01PP*	1810	4.03	5.8	1.8
02P*	1020	5.76	3.6	1.0
Brush Wear Over 0°C to +10°C Temp.				
05	1810	2.08	4.71	2.2
01PP	1750	5.08	9.56	1.05
02P	760	4.34	4.07	1.0

*Individual test temperature ranges were:

05 15° to 35°C

01PP 15° to 25°C

02P 15° to 25°C

place to measure) showed good correspondence with the strain gage measurements, to the accuracy noted. Actual wear of the brushes to which the strain gages attach is compared with the strain gage readings.

	<u>Physical</u>	<u>Strain Gage</u>
M1 wear (mils)	0.0031	0.0037
M2 wear (mils)	0.004	0.007

The measurements of each of the four M1 motor brushes on the MWA 05 showed a range of from 0.0031 to 0.0066 inch and from 0.0038 to 0.0059 inch on M2 motor.

Figure 2-VIII-45 is a photograph of the MWA 05, with motor No. 1 exposed, at the completion of the 6-month life test and a wheel tilt test described below.

d. SPECIAL TESTS

(1) WHEEL TILT TEST

At the conclusion of the 6-month life test on MWA 05, NASA requested a special test to determine the effects of rotor tilt on brush wear since the bearing has a nominal clearance of 0.0015 inch and in a zero gravity field the rotor could possibly be tilted. The test was performed to show the effect of operation in this mode, in a thermal vacuum. A weight was placed on the rim of the flywheel with the flywheel parallel to earth. The forces involved caused the flywheel to take its maximum tilt. The test was run for a period of 17 days and evidenced no change in the brush wear rate. It is concluded that there is negligible brush wear effect due to bearing clearance.

(2) MOTOR SURVIVAL TEST

At the conclusion of the MWA 01PP life test, a special test was conducted on this unit to determine survival of the MWA if brushes on one of the motors were worn down. Although this would be an abnormal condition, the test was performed to show additional margins of performance. The brushes on motor 1 were deliberately worn down (by emery cloth) to the spring clip holding the brushes and the test was started in thermal vacuum with motor 1 powered. The initial motor current was 0.155 ampere, which is about nominal. After 10 days of running at 150 rpm, the motor current increased to 0.485 ampere. At that time the thermal vacuum facility inadvertently went out of pressure specification and the unit was turned off for 6 hours. When operation was started again the

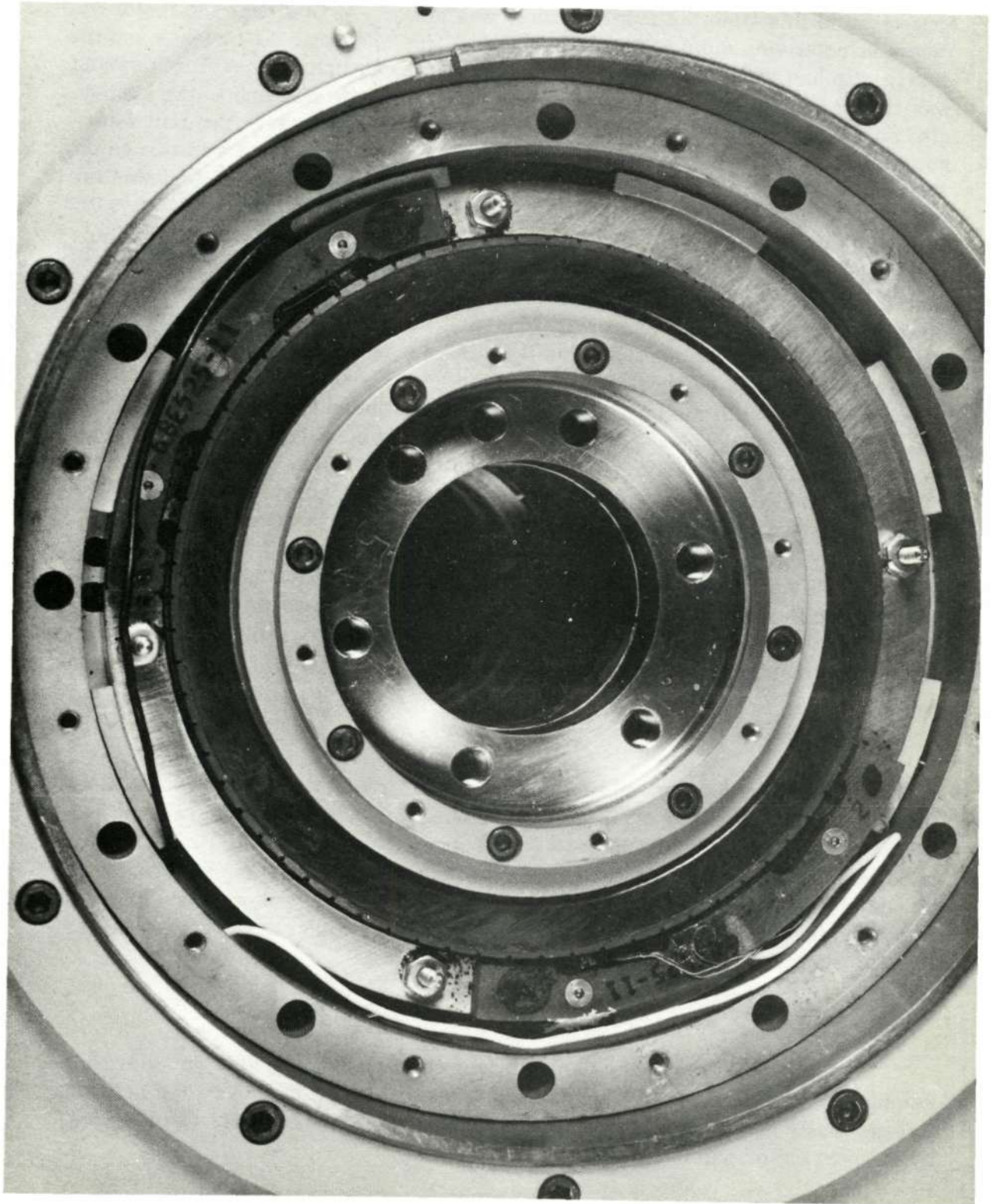


Figure 2-VIII-45. No. 1 Motor Brush Wear at Completion of 6 Month Life Test (MWA 05)

motor current was 0.200 ampere. Seventeen days after start the motor current was up to 1.0 ampere and the unit was stopped for inspection. It should be noted that prior to this time the motor voltage was noisy. At this time the motor voltage was relatively quiet. Upon inspection it was seen that the brushes and the spring clip had worn completely down on motor 1, so that the beryllium spring was riding against the commutator. The fast wear rate was due to the spring clip material imbedding in the brushes and accelerating wear. The unit was not disturbed and was returned to thermal vacuum, and motor 2 was turned on. The unit was then run for 37 additional days on motor 2 before the test was terminated by mutual agreement with NASA. The motor 2 current during this test varied between 0.300 and 0.600 ampere. This was expected, since the magnetic load increased due to embedment of material between the motor 1 commutator slots. A total running time of 55 days after motor 1 brushes were worn down was considered satisfactory evidence of survival, and indications were that the test could have continued until motor 2 brushes wore down at their normal rate. It should be noted that during the last 37 days of running a periodic check was made with motor 1 powered. This continued to show control although the motor current reached 1.3 amperes. It should also be noted that during the last 37 days the motor voltage was electrically clean. The capability to run under these abnormal conditions with characteristically high currents is limited by torque motor saturation corresponding to the available power supply potential.

Figure 2-VIII-46 shows one brush at completion of life test, after deliberately wearing the brush to the spring clip, and with the brush worn down to the spring. Note that the unit was run for 37 days after the last photograph (C) was taken at which time testing was terminated by choice.

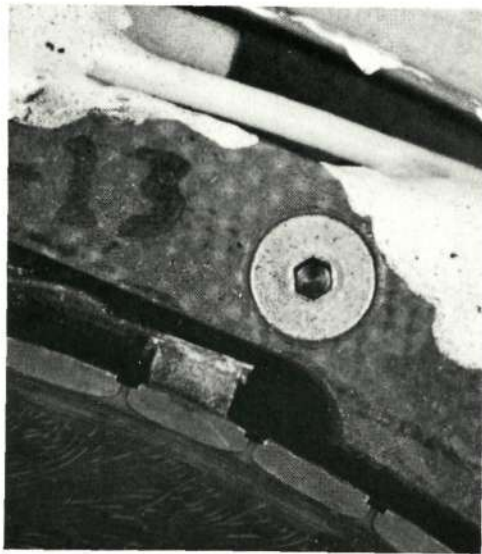
e. OIL LOSS

By weighing the assemblies before and after testing, the oil loss rate was found to be less than 1.0 gram after 4300 hours on MWA 05; 3.0 grams after 4500 hours on MWA 01PP; and 4.6 grams after 2600 on MWA 02P. This variance is dependent upon the test cycle exposure and the moisture absorbed after breaking thermal vacuum. The MWA oil reservoirs store more than 60 grams of oil and projecting the test conditions, even in the worst case, more than a 10-year supply of oil is available.

f. BEARING WEAR

At the completion of the 6-month test on MWA 05, the unit was disassembled and the bearing was inspected. Visual inspection showed the bearing in essentially new condition. This was confirmed by independent examination by the bearing manufacturer.

This bearing underwent two independent 6-month tests and several tests of shorter duration in thermal vacuum and in no case was there been any noticeable wear or signs of deterioration.



(A) START TEST



(B) BRUSH WORN TO CLIP



(C) BRUSH / CLIP WORN TO SPRING

Figure 2-VIII-46. Motor Survival Test (MWA 01PP, Motor No. 1)

G. ACCURACY ANALYSIS

1. General

The attitude of the ITOS spacecraft is defined with respect to the rotating coordinates \hat{n} (orbit normal) and \hat{f} (local vertical), as shown in Figure 2-VIII-47. The discussion on measurement and control accuracy which follows is based on the availability of accurate ephemeris data to define the motion of these coordinates.

The attitude performance specification requires ± 1.0 -degree uncertainty in the body axes position with respect to the orbit normal and local vertical at any instant. Since leading edge triggering of the pitch axis control loop is required, it is clear that orbit variations due to eccentricities cannot be removed without a priori knowledge. The worst-case variation of the earth's included angle for an orbit eccentricity of 0.01 would result in an apparent shift of 0.9 degree in local vertical. Therefore, all reference to the pitch error, Θ , will be to the nominal local vertical as defined by the nominal circular orbit geometry. It is further assumed that no attempt will be made to track the motion of the true local vertical with respect to that defined by the nominal geometry for an elliptical orbit within the specified tolerances. However, a small constant offset, resulting from a fixed altitude error can be removed by changing the nominal system momentum. An offset resulting from orbit parameter deviations is not included in any discussion dealing with attitude errors.

2. Pointing

The attitude deviations to be considered are as follows:

- | | |
|--------------------|--|
| ϕ_{\max} | is the angle between the spacecraft momentum vector, \vec{H} , and the orbit normal, \hat{n} ; also called maximum roll angle. |
| Θ | is the angle between the primary sensor axis and the known local offset, also called pitch error. |
| Θ_1, ϕ_1 | is the misalignment between the optical line of sight of the pitch-axis horizon sensor and the flywheel spin axis. |
| Θ_2, ϕ_2 | is the misalignment between the optical line of sight of the roll-axis horizon sensor and the flywheel spin axis. |
| Θ_3, ϕ_3 | is the misalignment between the pitch mirror normal and the flywheel spin axis. |
| Θ_4, ϕ_4 | is the misalignment between the roll mirror normal and the flywheel spin axis. |
| Θ_5, ϕ_5 | is the misalignment between the mounting surface of primary sensors and the flywheel spin axis. |

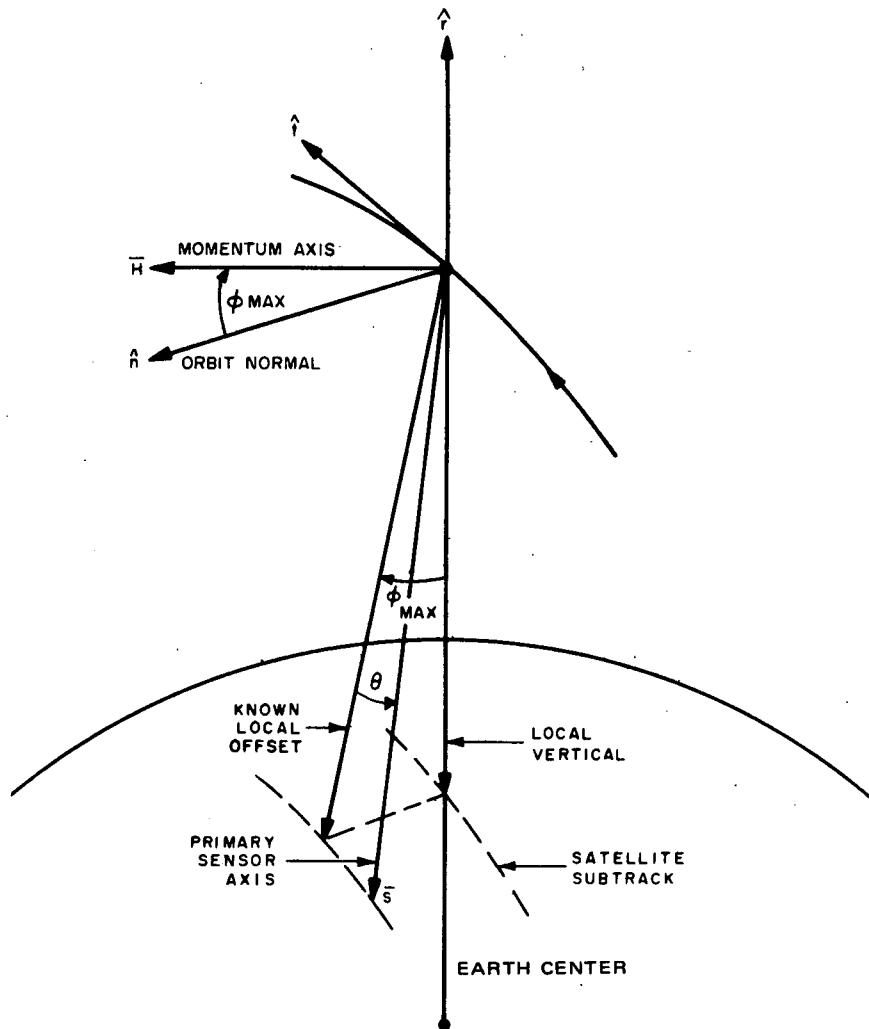


Figure 2-VIII-47. Spacecraft Reference Coordinates

- Θ_6, ϕ_6 is the misalignment between the flywheel spin axis and the angular momentum axis due to tape recorder operation (or other transverse momentum devices).
- Θ_7, ϕ_7 is the misalignment between the flywheel spin axis and the angular momentum axis due to the principal moment of inertia misalignment.
- Θ_8, ϕ_8 is the misalignment between the flywheel spin axis and the angular momentum axis due to flywheel unbalance.
- Θ_9, ϕ_9 is the misalignment between the flywheel spin axis and the nominal pitch axis due to bearing free motion.
- Θ_{10}, ϕ_{10} is the measurement error in determining the alignment of the spin axis with respect to the local horizontal plane due to:

- a. Radiance changes,
- b. Noise,
- c. Horizon gradient variations, or
- d. Ground data processing.

Θ_{11}, ϕ_{11}

is the measurement error in determining the line of sight between the satellite and the sky-earth intercept with respect to:

- a. Radiance changes,
- b. Noise,
- c. Horizon gradient variations,
- d. Threshold level variations,
- e. Sensor gain changes,
- f. Index pulse alignment.

Θ_{12}, ϕ_{12}

is the measurement error introduced by the pitch axis servo loop with respect to:

- a. ~~Disturbances,~~
- b. Torque load changes,
- c. Momentum changes, or
- d. Gain changes.

Θ_{13}, ϕ_{13}

is the cyclic deviation between the orbit normal and the angular momentum vector due to:

- a. Residual magnetic dipole changes,
- b. Solar torques, or
- c. Gravity gradient torques.

The tolerances assigned to the deviations with subscripts 3, 4, and 5 are based on static measurements using a variety of surface plates, theodolites, and shims. The basis for the deviation with subscripts 1 and 2 is the sensor profiles in terms of the half-power points, as referenced to the mechanical horizon sensor alignment; the horizon sensors are adjusted using shims.

Angular deviations designated by subscript 6 relate to the amount of uncompensated momentum of the various tape recorders in combination with the intended duty cycle pertaining to AVCS and SR equipment and to other momentum deviations.

Angular deviations identified by subscript 7 result from the misalignment of the principal moment-of-inertia with respect to the flywheel spin axis.

Angular deviations identified with subscript 8 can be determined from the equation for the angular shift between the flywheel spin axis and the nominal pitch axis due to mass unbalance in the flywheel, as follows:

$$\phi_8 = \frac{m\delta d + P_{xy}}{I_T} \quad (2-VIII-35)$$

where

$m\delta$ is static unbalance (2 inch-ounces),

d is distance from spacecraft center of gravity to flywheel center of gravity (16 inches),

P_{xy} is dynamic unbalance (32 inch²-ounces), and

I_T is transverse moment of inertia of spacecraft (1144 pound-inch-seconds²).

Most of the dynamic unbalance is caused by the scanning mirror. Substituting the above figures results in a half-cone angle of 0.00052 degree.

The torque motor bearing has an angular misalignment of 0.027 degree, resulting in the applicable tolerance angle pertaining to subscript 9.

The tolerances pertaining to subscript 10 are defined by the random and bias roll measurement tolerances of 0.175 degree (10 sample average during 4 seconds) and 0.162 degree, respectively.

The instantaneous pitch measurement capability is related to the ratio of threshold to zero-to-peak noise and is a function of earth horizon radiance changes and other pertinent parameters associated with subscript 11.

Noise effects are not included since the pitch axis servo loop will nullify this effect by inherent filtering action.

Attitude deviations designated by subscript 12 represent the pitch offset due to changes in servo gains and bias drifts primarily induced by thermal and aging effects.

As indicated in the disturbance analysis summary, attitude deviations can be anticipated due to residual dipoles, solar torques, gravity gradient torques, and momentum offsets. These tolerances are represented by subscript 13.

The attitude deviations are summarized in Tables 2-VIII-13 through 2-VIII-16. As indicated in Tables 2-VIII-13 and 2-VIII-14, some of the tolerances cause a random scatter for roll (ϕ) determination, during a nominal 10-minute measurement pass; other deviations have a definite biasing effect on the roll angle.

TABLE 2-VIII-13. RANDOM ROLL ERROR CONTRIBUTIONS*

Attitude Deviations		Roll Error (degrees)	
Category	Description	Single Sample	10 Samples (4-second average)
6	Transverse Momentum (Tape Recorder - Worst Case)	0.042	0.042
8	Flywheel Unbalance	0.00052	0.00016
9	Bearing Free Motion	0.027	0.009
10	Roll Horizon Sensor (noise and ground data processing)	*0.553	0.175
3 σ Tolerance (RSS-value)		0.556	0.180
*High frequency with respect to 10 minutes of roll deter- mination; best slope fit.			

TABLE 2-VIII-14. BIAS ROLL ERROR CONTRIBUTIONS*

Attitude Deviations		Roll Error (degrees)
Category	Description	
2	Roll Sensor Misalignment	0.152
4	Roll Mirror Misalignment	0.152
7	Principal Moment of inertia Misalignment	0.0195
10	Roll Horizon Sensor (horizon variations, radiance changes)	0.162
3 σ Tolerance (RSS-value)		0.280
*During 10 minutes of roll determination; best slope fit		

TABLE 2-VIII-15. MAXIMUM PRINCIPAL-POINT* ROLL-ERROR CONTRIBUTIONS

Item	Attitude Deviation		Maximum Roll Error (degrees)
	Category	Description	
a		Least square fit of 10 minutes of random data with 3σ tolerance of 0.180 degree, maximum error for 10 average samples taken every half minute	0.233
b	5	Primary sensor mounting surface misalignment	0.100
c	6	Transverse Momentum (Tape Recorder-Worst Case)	0.042
d			
e	8	Flywheel unbalance	0.00052
f	13	Solar torque (cyclic)	0.018
g	13	Gravity gradient torque	0.059
h	13	Roll/yaw residual dipole (1 atm^2 along transverse axis)	0.034
i		3σ Tolerance (RSS-value) for Items a through h	0.266
j	13	Residual magnetic dipole (0.05 atm^2 along pitch axis), drift amassed in four orbits	0.03
k	13	Solar torque (twice per orbit unipolar torquing)	0.054
l		Vector addition of Items j and k	0.062
m		Bias roll error	0.280
		Maximum principle point roll error Summation of Items i, l, and m)	0.608
*Exclusive of errors within primary sensor optics.			

TABLE 2-VIII-16. PITCH-ERROR CONTRIBUTIONS

Attitude Deviation		
Category	Description	Pitch Error (Degrees)
1, 3	Alignment (RSS-value)	±0.1
11	Horizon Index Pulse Phasing	±0.1
11	Horizon Sensing Variation	±0.7
12	Servo Loop Tolerances	±0.28
12	Momentum Variation (±1.3 momentum offset)	± .075
	3σ Error (RSS-value)	±0.77

The largest contribution to the random uncertainty in nominal roll measurement results from the horizon sensor tolerances; averaging 10 samples (4 seconds of data) for each measurement point will naturally reduce this random scatter. The 3σ random roll tolerance due to all causes listed in Table 2-VIII-13 results in a maximum roll attitude uncertainty by least-square fit as stipulated in the ITOS Design Study Report, Volume III. The principal point maximum roll error is a function of this least-square fit uncertainty and a number of other factors as shown in Table 2-VIII-15. Random factors due to various coning motions, primary sensor mounting uncertainties, and a maximum roll least-square scatter are combined by the root-sum-square (rss) method.

Unless precessional motion due to the residual spin axis, uncompensated magnetic dipole, and solar torque is rectified by calibration, this motion must be included in the attitude uncertainty. Precession motion that causes roll errors due to solar torque is primarily about the line of nodes (i.e., the $\pm \hat{\ell}$ axis) and precession due to residual magnetism and, at times, solar torque is about a line in the orbit plane perpendicular to the nodes (i.e., the $\pm \hat{b}$). Table 2-VIII-15 combines these two drifts vectorially.

Adding the rss scatter, the precessional drifts, and the biasing effect on the roll angle will result in the maximum principal point roll deviation, as shown in Table 2-VIII-15.

The principal point tolerance due to pitch attitude uncertainties is shown in Table 2-VIII-16.

Noise has no influence on the accuracy of pitch control because the servo bandwidth shows a closed loop crossover of any 0.15 radian per second.

Sensor pointing offsets due to elliptical orbits are analyzed in the ITOS Design Study Report, Volume III, which also covers the effects of elliptical orbits on attitude and momentum performance.

In summary, the tabulations show that the principal point uncertainty about the roll or yaw axis is ± 0.64 degree with unipolar torquing and 10-sample averaging, whereas the tolerance about the pitch axis is ± 0.76 degree. This is compatible with the specification requirements.

3. Jitter

Jitter about the pitch axis is estimated to be no more than 0.005 degree per second. The sources from which this value was computed are described in the following paragraphs.

Motor commutator ripple (W_{P1}):

$$W_{P1} = \frac{T_{d1}}{I_3 \omega_{d1}} = 0.28 \times 10^{-5} \text{ degree per second} \quad (2\text{-VIII-36})$$

where

T_{d1} is the disturbance torque (1 ounce-inch),

I_3 is the body moment-of-inertia about the pitch axis (1144 pound-inch-second²), and

ω_{d1} is the ripple disturbance torque frequency (1115 radians per second at 150-rpm motor speed).

Motor "once around" torque (W_{p2}):

$$W_{p2} = \frac{T_{d2}}{I_3 \omega_{d2}} = 0.20 \times 10^{-3} \text{ degree per second} \quad (2\text{-VIII-37})$$

where

T_{d2} is the disturbance torque (1 inch-ounce) and

ω_{d2} is the disturbance torque frequency (15.7 radians per second at 150-rpm motor speed).

Tachometer ripple (W_{pt}):

$$W_{pt} = \frac{E_f K_a K_t}{I_3 \omega_{dt} \left[\left(\frac{L_a}{R_a} \omega_{dt} \right)^2 + 1 \right]^{1/2}} = 0.72 \times 10^{-5} \text{ degree per second} \quad (2\text{-VIII-38})$$

where

- E_f is the tachometer ripple voltage (± 0.12 volt),
 K_a is the power amplifier gain (118 volts per volt),
 K_t is the motor torque constant (3.3 inch-ounces per volt),
 L_a is the motor inductance (19.6×10^{-3} henry),
 R_a is the motor winding resistance (32.1 ohms), and
 ω_{dt} is the disturbance torque frequency (5652 radians per second at 150 rpm)

PWM error detector ripple (W_{pD}):

$$W_{pD} = \frac{2\pi K_v T_1 t_o^2}{T_s T_m T_2} = 2.8 \times 10^{-5} \text{ degree per second} \quad (2\text{-VIII-39})$$

where

- K_v is the system velocity gain (1.9 sec^{-1}),
 T_1 is the compensation lead time constant (22.3 seconds),
 T_2 is the compensation lag time constant (417 seconds),
 T_s is the smoothing time constant (0.8 second),
 T_m is the motor loop time constant (2 seconds), and
 t_o is the pulse width (1.1×10^{-3} second for a one degree position error at 150 rpm).

Orbit ellipticity (W_{pc}):

$$W_{pc} = \frac{\epsilon R_e}{\sqrt{R_o^2 - R_e^2}} \omega_o = 1.1 \times 10^{-3} \text{ degree per second} \quad (2\text{-VIII-40})$$

where

- R_e is the earth's radius (3444 nautical miles),
 R_o is the nominal circular orbit radius (4234 nautical miles),
 ω_o is the nominal orbital rate (9.1×10^{-4} radian per second), and
 ϵ is the orbit eccentricity (0.0147; 3σ limit for ESSA).

Deadband oscillations (W_{pd}):

Jitter due to deadband oscillations produces a system resolution of 0.002 degree with state-of-the-art components as follows:

$$W_{pd} = A\omega_n = 0.30 \times 10^{-3} \text{ degree per second} \quad (2\text{-VIII-41})$$

where

A is the system resolution (2×10^{-3} degree) and

ω_n is the system natural frequency (0.15 radian per second).

Radiance variations (W_{pr}):

Jitter due to radiance variations will be associated with the sensor error on any three successive sky-earth pulses with a tolerance of +0.2 to -0.2 degree in the worst-case. This can be expressed as:

$$W_{pr} = \Delta\theta \frac{2\pi}{2TG\left(\frac{1}{2T}\right)} = 0.506 \times 10^{-3} \text{ degree per second} \quad (2\text{-VIII-42})$$

where

T is the sampling period (0.4 second),

$\Delta\theta$ is the angular error (0.2 degree), and

$G\left(\frac{1}{2T}\right)$ is the pitch servo attenuation at the half-sampling frequency (3100:1).

Bias speed variation (W_{ps}):

The bias speed will change due to varying temperature effects on the reference voltage. For a 1°C change in temperature, a 0.1-percent change in bias voltage is anticipated as a tolerance. For a maximum linear temperature change of 5°C per quarter orbit, the speed change for this period will be 0.5 percent. In terms of change in body rate, this results in

$$\Delta W_3 \approx \frac{\Delta W_f}{I_3/I_f} = 0.053 \text{ degree per second} \quad (2\text{-VIII-43})$$

where

ΔW_3 is the equivalent change in body rate,

I_f is the flywheel moment of inertia (13.5 pound-inch-seconds²), and

ΔW_f is the equivalent change in flywheel spin rate.

To reduce this change in body rate to zero, the pitch position error will be

$$\Delta \Theta = \frac{\Delta W_3}{K_V} = 0.028 \text{ degree.} \quad (2\text{-VIII-44})$$

For 1725 seconds per quarter orbit, the resulting jitter is

$$W_{ps} = \frac{0.028 \text{ degree}}{1725 \text{ seconds}} = 1.62 \times 10^{-5} \text{ degree per second.} \quad (2\text{-VIII-45})$$

Cloud Cover Variation (W_{pc}):

A cloud layer obscuring the horizon will produce an error in the measurement of location of the horizon as well as a rate input to the system. This rate can be expressed as

$$W_{pc} = \frac{\omega_o \left[\sin^{-1} \left(\frac{R_e + \Delta h}{R_o} \right) - \sin^{-1} \left(\frac{R_e}{R_o} \right) \right]}{90^\circ + \sin^{-1} \left(\frac{R_e + \Delta h}{R_o} \right) - \sin^{-1} \left(\frac{R_e}{R_o} \right) - \sin^{-1} \left(\frac{R_e}{R_e + \Delta h} \right)} \quad (2\text{-VIII-46})$$

where

- ω_o is the orbital rate,
- R_E is the earth's radius,
- R is the orbit radius, and
- Δh is the cloud height.

For a cloud height of 10 nautical miles,

$$W_{pc} = 1.7 \times 10^{-3} \text{ degree per second}$$

Seasonal Variation (W_{ps}):

At twice orbital rate, the variation in earth temperature introduces a jitter, which is a function of the infrared detector. This maximum jitter rate is

$$W_{ps} = 2 \Delta \Theta \omega_o = 1.3 \times 10^{-3} \text{ degree per second}$$

where

- $\Delta \Theta$ is the maximum pitch offset due to earth's temperature, and
- ω_o is the orbital rate.

Jitter about the roll axis of the spacecraft under a moment free condition can be assumed to be zero under the action of the liquid-filled nutation damper. However, there are two sources of internal disturbances that produce undesired motion about the spacecraft roll and yaw axes, namely, the tape recorders and the flywheel.

As shown in the discussion on disturbances in the ITOS Design Study Report, Volume III, maximum coning due to tape recorder operation can reach a maximum half angle of 0.042 degree. The jitter is

$$W_{T_t} = 0.042 \dot{\psi} = 0.008 \text{ degree per second,} \quad (2\text{-VIII-47})$$

where $\dot{\psi}$ is the nutation frequency (0.183 radian per second).

Similarly, flywheel unbalance results in a half-cone angle of 5.2×10^{-4} degree. Jitter due to this can be expressed as:

$$W_{T_f} = 5.2 \times 10^{-4} \omega_f = 8.2 \times 10^{-3} \text{ degree per second,} \quad (2\text{-VIII-48})$$

where ω_f is the flywheel spin rate (150 rpm).

The 3σ roll jitter is 0.012 degree per second which is an rss value for the above two jitter rates as uncorrelated values.

H. SYSTEM INTERFACES

1. Power

The power for this subsystem will be supplied at -26 to -36 volts unregulated and at -24.5 volts regulated from the spacecraft power supply. Other voltages used in the pitch axis control loop will be derived in a dc-to-dc converter operating from the -24.5-volt supply. Table 2-VIII-17 gives the power requirements for the operational mode.

2. Command and Control

All required switching will be routed through the command distribution unit (CDU).

3. Telemetry

All telemetry data will be routed to the signal conditioner. All points in the pitch axis control loop will be conditioned to assure compatibility with voltage and impedance requirements of the spacecraft telemetry subsystem.

TABLE 2-VIII-17. OPERATIONAL POWER REQUIREMENTS

Item	Power at -24.5 Volts (watts)	Operation Time	Equivalent Continuous Drain (watts)
Pitch Axis Control Loop*	8.4	Continuous	8.6
Magnetic Bias Coil	0.013 to 0.13	Continuous	0.013 to 0.13
Momentum Coil	1.8 per coil	**	**
QOMAC Coil	0.78	1/5 orbit/orbit (23 minutes)	0.16
Total (Continuous maximum)			8.89
*Power from both regulated (-24.5 volts) and unregulated (-26 volts) supplies. **As required for adjustment.			

I. DISTURBANCE ANALYSIS

A summary of all significant disturbances with a brief description of dynamic effect on the spacecraft is given in Table 2-VIII-18. The following constitutes an outline of the material which led to the tabulated predictions.

1. Residual Magnetic Dipoles

The magnetic bias coil nulls the dipole along the spacecraft pitch axis (3)* to the value required for sun synchronous precession. On a spinning spacecraft such as TOS, the effects of residual dipoles along the transverse axes (1 and 2) cancel over each spin. For the three-axis stabilized TIROS M, transverse residual dipoles cause both an attitude precession and a momentum change. These effects will cancel over a complete orbit, but the instantaneous values will add to the roll/yaw and pitch attitude errors.

For the earth oriented spacecraft, dipoles along the three axes result in the following disturbance torque.

$$\vec{T} = \vec{M} \times \vec{B} = \hat{1} (M_2 B_n - M_3 B_t) + \hat{2} (M_3 B_r - M_1 B_n) + \hat{3} (M_1 B_t - M_2 B_r)$$

(2-VIII-49)

*All notations and coordinate systems are based on the material presented in Section VIII.E.

TABLE 2-VIII-18. SUMMARY OF DISTURBANCES AND EFFECTS

Source of Disturbance	Axis of Torque	Effect of Disturbance on Spacecraft
1. Residual Magnetic Dipole	(1) Pitch	(1) Sinusoidal modulation of momentum, ± 0.15 percent peak change in momentum, ± 0.009 degree peak pitch error, zero average over an orbit
a. 1 atm^2 Along Yaw Axis	(2) Roll	(2) Slow precession of pitch axis around a cone, one complete cycle per orbit, maximum excursion of 0.034 degree
b. 1 atm^2 Along Roll Axis	(1) Pitch	(1) Sinusoidal modulation of momentum, ± 0.3 percent peak change in momentum, ± 0.017 degree peak pitch error, zero average over an orbit
c. 0.05 atm^2 Along Pitch Axis (resolution of mag bias coil)	(2) Yaw	(2) Slow precession of pitch axis around a cone, one complete cycle per orbit, maximum excursion of 0.034 degree
	$\pm \hat{e}$	Net drift of ± 0.086 degree per day about the \hat{b} axis.
2. Solar Pressure	(1) $\hat{l} \hat{b}$ plane	(1) Slow precession of momentum vector in response to torque, which is normal to a plane defined by the spacecraft pitch (spin) axis and the sun line; magnitude and direction is function of sun angle and season

TABLE 2-VIII-18. SUMMARY OF DISTURBANCES AND EFFECTS (Continued)

Source of Disturbance	Axis of Torque	Effect of Disturbance on Spacecraft			
2. Solar Pressure (Con't)		Disturbance Torque in 10^{-4} inch-pounds			
		Time of Year	Sun Angle (degrees)		
			30	45	60
		Summer Solstice	+0.4 \hat{l} - 0.49 \hat{b}	+0.32 \hat{l} -0.38 \hat{b}	+0.23 \hat{l} -0.27 \hat{b}
		Winter Solstice	-0.25 \hat{l} -0.58 \hat{b}	-0.20 \hat{l} -0.46 \hat{b}	-0.15 \hat{l} -0.33 \hat{b}
		Maximum potential \hat{l} precession of 1.35 degrees per day is corrected by unipolar torquing. Maximum potential \hat{b} precession of +.93 degree per day is corrected by mag bias torquing.			
		(2)	\hat{l} \hat{b} plane	(2) Sinusoidal modulation of attitude angles, magnitude is function of sun angle.	
			Sun Angle (degrees)	Peak-to-Peak Variations (degrees)	
			30	0.027	
			45	0.018	
	60	0.009			
(3)	Pitch	(3) Sinusoidal modulation of momentum, zero average per orbit, peak change is function of sun angle			

TABLE 2-VIII-18. SUMMARY OF DISTURBANCES AND EFFECTS (Continued)

Source of Disturbance	Axis of Torque	Effect of Disturbance on Spacecraft	
2. Solar Pressure (cont'd)		Sun Angle (degrees)	Momentum Change (max percent)
		30	0.037
		45	0.020
3. Magnetic Hysteresis and Eddy-Current Losses	Pitch	Slow decay of momentum; 1 percent per week maximum.	
4. Gravity Gradient	Roll	Sinusoidal precession at orbital frequency, zero average per orbit; peak change in attitude is 0.059 degree.	
	Pitch	Slow decay of momentum; 2.8 percent per week nominal. Occasional momentum control required.	
5. Internal Rotating Components (un- compensated transverse momentum)	-	Residual offset due to continuously running components is 0.04 degree. Maximum half cone nutation angle with anticipated payload duty cycles is 0.042 degrees.	

because of the interaction with the earth's magnetic field (components B_r , B_t , B_n).

A torque acting on a body with stored momentum, \bar{H} , is given by

$$\bar{T} = \frac{d}{dt} |\bar{H}| \hat{3} + |\bar{H}| \frac{d}{dt} \hat{3} \quad (2-VIII-50)$$

where w is the angular velocity of the rotating axis system with respect to an inertially fixed set. The change in $\hat{3}$ is a change in direction only and implies a rotation about an axis normal to $\hat{3}$:

$$\frac{d}{dt} \hat{3} = \bar{w}_p \times \hat{3} \quad (2-VIII-51)$$

where w_p is the precessional rate of the spacecraft. The disturbance torque due to residual dipoles, therefore, results in the following:

$$\bar{T} = \bar{M} \times \bar{B} = \frac{d}{dt} |\bar{H}| \hat{3} + |\bar{H}| (\bar{w}_p \times \hat{3}) \quad (2-VIII-52)$$

Ignoring the small residual along the pitch ($\hat{3}$) axis due to the resolution of the mag bias coil, the transverse disturbance can be stated as:

$$\bar{H} (\bar{w}_p \times \hat{3}) = \hat{1} (M_2 B_n) - \hat{2} (M_1 B_n) \quad (2-VIII-53)$$

$$|\bar{w}_p| = \frac{MB_n}{H}$$

The maximum deviation due to this precession occurs after half orbit:

$$\theta_p = \frac{M B_n \tau_{orbit}}{H \pi} \quad (2-VIII-54)$$

returning to zero at the completion of an entire orbital period. For the nominal momentum (212 inch-pound-seconds), nominal orbital period (115 minutes), nominal altitude of 790 nautical miles (and therefore nominal normal field B_n for the mission mode), the maximum θ_p excursion per one atm² of transverse residual is 0.034 degree.

Similarly, the pitch axis disturbance can be expressed as follows:

$$\frac{d}{dt} |\bar{H}| \hat{3} = \hat{3} (M_1 B_t - M_2 B_r) \quad (2-VIII-55)$$

For a transverse dipole along the roll axis of one atm², this results in a maximum momentum deviation of about 0.3 percent per half orbit, and a zero net momentum change for an entire orbit. Utilizing a velocity gain of 1.9 sec⁻¹ and a pitch to wheel inertia ratio of 85 shows this momentum modulation to result in a maximum pitch offset of 0.017 degree. The effect of a one atm² dipole along the yaw axis on the momentum modulation is trivial.

2. Solar Torques

In the ITOS design, the solar array is deployed so that it lies in the orbital plane during the operational mode. This arrangement results in a large offset between the center-of-pressure and the center-of-gravity, thus giving rise to a solar torque having both cyclical and secular components. The resulting solar torque changes both the magnitude and direction of the spacecraft momentum vector.

Radiation forces are produced by absorbed photons, specularly reflected photons, and diffusely reflected photons. The sum of these fractions (α for absorbed, ρ_s for specularly reflected, ρ_d for diffusely reflected) is equal to the total incident energy on a surface.

$$\alpha + \rho_s + \rho_d = 1 \quad (2\text{-VIII-56})$$

It can be shown that the elementary force on the area dA can be expressed as

$$\overline{d^2F} = P_o dA \left[\hat{s} \alpha (\hat{s} \cdot \hat{N}) + 2\hat{N} \rho_s (\hat{s} \cdot \hat{N})^2 + \rho_d \left(\hat{s} + \frac{2}{3} \hat{N} \right) (\hat{s} \cdot \hat{N}) \right] \quad (2\text{-VIII-57})$$

where

\hat{s} is a unit vector in the direction of the sun,

\hat{N} is the unit vector, normal to the surface dA and positive toward the surface, and

P_o is the solar radiation pressure.

The torque on the spacecraft due to illumination of area dA is

$$\overline{d^2T} = (\bar{r} - \bar{r}_e) \times \overline{d^2F} \quad (2\text{-VIII-58})$$

where

\bar{r} is the vector from any convenient origin to dA and

\bar{r}_e is the vector from same origin to center of rotation about which torques are to be taken.

Integrating this expression over the illuminated portion of the spacecraft surface produces the total solar disturbance torque acting on the three solar panels, the top, and the side facing the earth and results in the following secular disturbance torque, which acts about an axis perpendicular to the plane defined by the spacecraft spin axis and the sun vector.

$$\begin{aligned}
 T = & \left\{ +3 (L - r_e) A_B (\alpha_B + \rho_{dB}) \cos \sigma + (L - R_e) A_t (\alpha_t + \rho_{dt}) \cos \sigma \right. \\
 & + \frac{1}{2\pi} \left(\frac{\pi + 2}{4} \right) A_s (\alpha_s + \rho_{ds}) a \cos \sigma \\
 & + \frac{1}{\pi\sqrt{2}} A_s (\alpha_s + \rho_{ds}) \left(\frac{L}{2} - r_e \right) \sin \sigma \\
 & + \frac{5}{3\pi\sqrt{2}} A_s \left(\frac{L}{2} - r_e \right) \rho_{ss} \sin \sigma \\
 & \left. + \frac{1}{3\pi} \left(\frac{\pi + 2}{4} \right) A_s \rho_{ds} \left(\frac{L}{2} - r_e \right) \right\} P_o \sin \sigma \left[\sin \lambda' \hat{l} - \cos \lambda' \hat{b} \right]
 \end{aligned}$$

(2-VIII-59)

where

- L is the length of spacecraft measured along the pitch axis,
- r_e is the displacement from origin of the spacecraft coordinate system to center of rotation about which torques are taken,
- A_B is the area of one panel

α_B , ρ_d , and ρ_d are the photon fractions defined above,

- σ is the angle from sun line to \hat{n} axis (sun angle),
- A_s is the area of earth facing side,
- A_t is the area of top of spacecraft containing the solar fence,
- λ' is the anomaly of the projection of the sun line in the orbit plane,
- a is the radial distance from the pitch axis to a side, and
- P_o is the solar radiation pressure.

Subscript s is the side,

B is the solar panel, and

t is the top (solar fence area).

For a 3 pm ascending node orbit, the angle λ' varies from +38.9 degrees to -23.4 degrees in the course of one year. The resulting solar torques, averaged over one orbit, are tabulated below in pound-inches:

Time of Year	Sun Angle (degrees)		
	30	45	60
Summer solstice	$+ .40 \times 10^{-4} \hat{l}$	$+ .32 \times 10^{-4} \hat{l}$	$+ .23 \times 10^{-4} \hat{l}$
	$- .49 \times 10^{-4} \hat{b}$	$- .38 \times 10^{-4} \hat{b}$	$- .27 \times 10^{-4} \hat{b}$
Winter solstice	$- .25 \times 10^{-4} \hat{l}$	$- .20 \times 10^{-4} \hat{l}$	$- .15 \times 10^{-4} \hat{l}$
	$- .58 \times 10^{-4} \hat{b}$	$- .46 \times 10^{-4} \hat{b}$	$- .33 \times 10^{-4} \hat{b}$
Percent sun time	100	80.5	74

The torques at 45- and 60-degree sun angles are considerably reduced due to the partially eclipsed orbit. The torque along the negative \hat{b} axis results in a precession vector along the ascending node (positive \hat{l} axis). This disturbance is counteracted by utilizing unipolar torquing for a few minutes per half orbit in a programmed mode. The torque along the $\pm \hat{l}$ axis is corrected by the dipole of the mag bias coil. The orbit average torque value of $+3.2 \times 10^{-5}$ pound-inch, occurring at summer solstice and a 45-degree sun angle, requires a dipole of -0.43 atm^2 as compensation from the mag bias coil. At the time of the winter solstice, a 30 degree sun angle will result in a disturbance torque of -2.5×10^{-5} pound-inch, thus necessitating a mag bias dipole of $+0.34 \text{ atm}^2$ for compensation. The range of the mag bias dipole is $\pm 1.0 \text{ atm}^2$ about the 0.57 atm^2 value, provided by a permanent magnet for sun synchronous precession of the spacecraft.

The torque contribution due to the force component normal to the anti-earth solar panel results in a cyclical disturbance when the spacecraft is in sunlight for the entire orbit (0.027 degree maximum variation occurring at 30-degree sun angle.) However, for partially eclipsed orbit this force produces a compensating torque which reduces the secular disturbance in the $\hat{l} \hat{b}$ plane by about 15 percent.

3. Magnetic Losses

a. HYSTERESIS

The momentum losses due to hysteresis are sensitive to the presence and distribution of magnetic material in the spacecraft. Based on previous experience in the TOS/ESSA series and the emphasis on minimizing the μ metal usage in the ITOS spacecraft, a maximum momentum decay of 1 percent per week is predicted due to hysteresis effects.

b. EDDY CURRENT

The eddy current losses are very small since the major portion of the spacecraft makes only one revolution per orbit. Even the spinning MWA rim should not result in any significant losses, because the interconnecting spokes are nonconducting.

4. Gravity Gradient

The disturbing torque due to gravity gradients arises from the fact that the principal moment-of-inertia axis does not coincide with the earth oriented spacecraft axis. The lack of symmetry is primarily due to the deployed solar panels, and manifests itself in the presence of inertia products. The general torque due to gravity gradient, acting about the mass center of a vehicle of arbitrary configuration, can be expressed as

$$T_{gg} = -3 w_o^2 (\hat{\rho} \times \bar{\phi} \cdot \hat{\rho}) \quad (2-VIII-60)$$

where w_o is the orbital rate,

$\hat{\rho}$ is a unit vector from orbit focus toward the spacecraft mass center, and

$\bar{\phi}$ is a dyadic formed of the outer product $\sum_n m_n (\bar{r}_n \bar{r}_n)$ with m_n the mass of the n^{th} particle and \bar{r}_n its directed displacement relative to the vehicle mass center.

For ITOS, the spacecraft axes 1, 2, 3 are respectively aligned with the local vertical, the velocity vector, and the orbit normal. Therefore, the gravity gradient torque reduces to the simple expression

$$T_{gg} = -3w_o^2 (-I_{13} \hat{2} + I_{12} \hat{3}) \quad (2-VIII-61)$$

where I_{13} and I_{12} are the yaw-pitch and yaw-roll inertia products of inertia respectively.

The roll torque is sinusoidal over one orbit and will average to zero; the maximum roll/yaw attitude deviation due to the torque about the 2 axis occurs after half an orbit and equals 0.059 degrees. The torque along the 3 or pitch axis results in a nominal momentum decay of 0.85 inch-pound-second per day (1.5 inch-pound-second per day maximum). This is equivalent to a nominal 2.8-percent decay per week of the MWA rate. Occasional momentum control torquing can correct for this loss.

5. Internal Rotating Components

All rotating components are mounted in the spacecraft such that their momentum vectors lie along the roll axis. When a component such as a tape recorder is on, the total momentum of the spacecraft no longer lies along the spin axis of the flywheel. The spin axis will trace out a cone about the total momentum vector, the half-cone angle being a function of the magnitude of the transverse momentum components and the time they are turned on.

Figure 2-VIII-48 shows the curves traced out by the tip of the spin axis. The angle γ_0 is the initial nutation half-cone angle. When transverse momentum is added to the spacecraft, the total momentum vector tip effectively shifts from point O to point P by the angles β_1 and β_2 . The spin axis now traces a curve bounded by the angles $\theta_{1\max}$ and $\theta_{2\max}$. These angles are functions of the location of the spin axis at the exact time the transverse momentum is added. θ_1 and θ_2 will be maximums if the spin axis were at the maximum distance from point P as is shown in the figure. When the rotating component is turned off, the momentum vector returns to point O, and the spin axis cones about that point. Again, the cone angle will depend on where the spin axis is located when the component is turned off. The worst case would occur if the spin axis were at point Q. For different phasing, the nutation angle could actually decrease.

The expressions for the maximum possible θ_1 and θ_2 are:

$$\theta_{1\max} = \sqrt{\frac{\lambda_B}{\lambda_A}} \gamma_0 + \beta_1 + \sqrt{\frac{\lambda_B}{\lambda_A}} \sqrt{\beta_2^2 + \frac{\lambda_A}{\lambda_B} \beta_1^2}, \quad (2\text{-VIII-62})$$

$$\theta_{2\max} = \gamma_0 + \beta_2 + \sqrt{\beta_2^2 + \frac{\lambda_A}{\lambda_B} \beta_1^2},$$

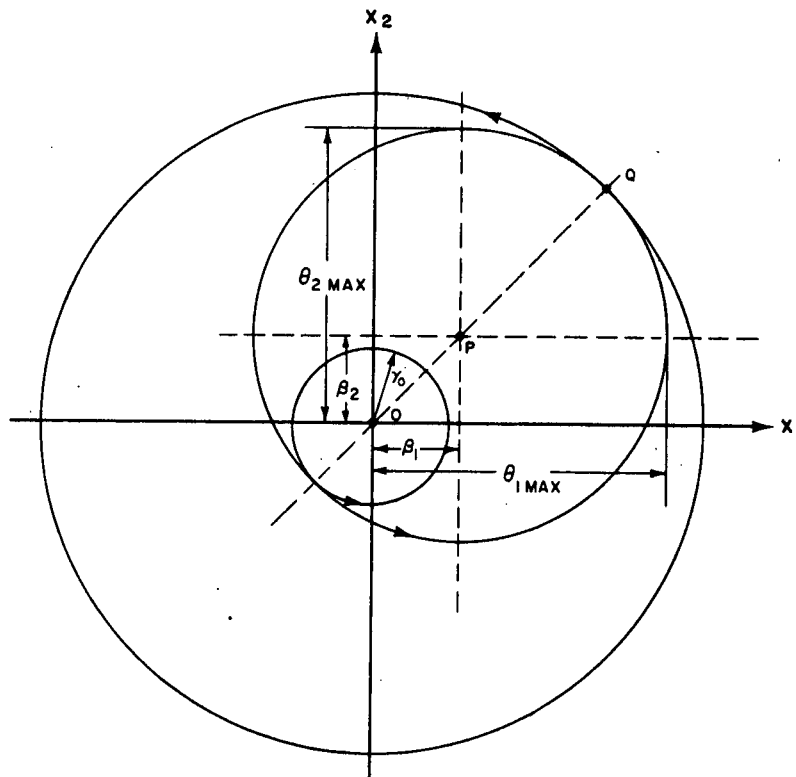


Figure 2-VIII-48. Nutation Cone Angles Due To Transverse Momentum

where

$$\lambda_A = \left(\frac{I_z - I_y}{I_y} \right) \omega_o + \frac{h_z}{I_z},$$

$$\lambda_B = \left(\frac{I_z - I_x}{I_x} \right) \omega_o + \frac{h_z}{I_z},$$

$$\beta_1 = \frac{h_y}{I_y \lambda_A},$$

$$\beta_2 = \frac{h_x}{I_x \lambda_B},$$

- I_x is the inertia about the yaw axis (1285 pound-inch-seconds²),
 I_y is the inertia about the roll axis (1010 pound-inch-seconds²),
 I_z is the inertia about the pitch axis (1144 pound-inch-seconds²),
 h_z is the flywheel momentum (212 pound-inch-seconds),
 γ_o is the initial nutation angle, and
 ω_o is the orbital rate.

All rotating components are located with their axes of rotation parallel to the roll axis. Thus $h_x = \beta_2 = 0$. Also, $\lambda_A \approx \lambda_B = 0.183$ since h_z is large. This reduces Equation 2-VIII-61 to:

$$\theta_1 \text{ max} = \gamma_o + 2 \beta_1, \tag{2-VIII-63}$$

$$\theta_2 \text{ max} = \gamma_o + \beta_1.$$

The four rotating components and their momentums are listed in Table 2-VIII-19. The normal sequence of operation, which covers a half-orbit period and occurs every orbit, is as follows:

- (1) Two radiometers run continuously.
- (2) One SR recorder records continuously for a half orbit.
- (3) The SR recorder is turned off.
- (4) One AVCS recorder is put in the record mode and takes 11 pictures.

TABLE 2-VIII-19. TRANSVERSE MOMENTUM DISTURBANCES

Component	Momentum (in-lb-sec)	Operation
Radiometers (2)	0.14	Continuous (2 simultaneously)
SR Recorders (2)	Record: 0.0025 Playback: 0.04	One records continuously for 1/2 orbit or for full orbit; both playback simultaneously every third orbit.
Incremental Tape Recorder (1)	0.002	Playback for 1 minute once per orbit
AVCS Recorder*	0.02	Records for 10.25 second every 260 seconds, 11 times per orbit Playback every third orbit
*Normally, one of the two AVCS recorders is operated, the redundant unit being reserved as backup.		

- (5) The SR recorder is played back.
- (6) During this time the AVCS recorder is played back.
- (7) The AVCS recorder is put in the record mode and takes one picture.
- (8) The SR recorder playback is stopped.
- (9) The SR recorder is put in the record mode.

During operations (1) and (2) of the sequence, the spacecraft is offset by an angle of less than 0.04 degree. Since these components are running continuously, and the spacecraft is earth locked, this offset is constant with respect to the yaw-pitch plane. Each step from operation (3) to (9) will change the nutation angle as will each turn-on and turn-off of the AVCS recorder during the picture-taking sequence. Since the phasing of the disturbance with respect to the nutation cycle changes continuously, the operation of the various components will cause both increases and decreases in the nutation angle.

A computer simulation of three orbits, the results of which are depicted in Table 2-VIII-20, indicates a final half cone nutation angle of 0.018 degree for an initial value of 0.056 degree. The assumption was made that the accumulated SR and AVCS data of three orbits was played back at the end of the third orbit. The maximum nutation angle of 0.042 degree is equivalent to a jitter rate 0.008 degree per second.

TABLE 2-VIII-20. THREE ORBIT COMPUTER SIMULATION OF UNCOMPENSATED MOMENTUM EFFECTS*

Orbit	Disturbance	Max. Nutation Angle (Deg)	Jitter (Deg/Sec)
1	AVCS Recorder, 2×10^{-2} in-lb-sec 10.25 sec on, 249.75 sec off, 11 cycles	0.056	0.010
2	AVCS Recorder, 2×10^{-2} in-lb-sec 10.25 sec on, 249.75 sec off, 11 cycles	0.028	0.005
3	AVCS Recorder, 2×10^{-2} in-lb-sec 10.25 sec on, 249.75 sec off, 11 cycles SR Recorder playback 4×10^{-2} in-lb-sec for 9 minutes AVCS Recorder playback 2×10^{-2} in-lb-sec for 6 minutes (during SR playback)	0.042	0.008
Completion of Orbit 3		0.018	0.003

*Initial Nutation Angle = 0.056 degree

SECTION IX

POWER SUPPLY SUBSYSTEM

A. GENERAL

The ITOS power supply subsystem consists of a solar cell array, redundant series voltage regulators, a shunt dissipator with redundant control amplifiers, two nickel-cadmium batteries, each with its own charge controller, and associated telemetry circuits. The subsystem supplies a regulated output of -24.5 volts and an unregulated output of -26.0 to -36.2 volts to spacecraft loads.

The spacecraft loads for one orbit are listed in Table 2-IX-1. Command loads are not included as part of the design load, since they do not occur regularly during each orbit and since they have a negligible effect over a long-term period. The values given in Table 2-IX-1 include the upper specification limits for the loads and the measured values obtained during box tests. The loading shown for each orbit represents the following spacecraft operation:

- Scanning radiometer data recorded and transmitted in real time during remote earth night,
- Eleven AVCS pictures taken and recorded during subpoint day,
- Eleven APT pictures taken and transmitted during subpoint day, and
- An 8-minute CDA station contact including readout, via the S-band transmission link, of AVCS and radiometer picture information and secondary sensor data.

Worst-case energy balance analyses have been performed for the specification load values in Table 2-IX-1, based upon the spacecraft operation described above. Table 2-IX-2 shows that a small energy deficit exists under these conditions. An additional analysis was performed for nominal or expected conditions.* The test values from Table 2-IX-1 for load currents were used in this analysis, and SR operation (real time and recorded) during daytime is added to the load profile. The power system is in energy balance under these conditions, as Table 2-IX-2 shows.

* Nominal case uses measured solar cell I-V curves, 1968 expected radiation flux, nominal solar constant, and nominal battery charge rate conditions, as well as other factors which produce an expected, rather than a worst-case, condition.

TABLE 2-IX-1. ITOS LOAD REQUIREMENTS*

Equipment	Continuous		Programmed	Commanded	Comments
	Spec (mA)	Test (mA)	Spec (mA)	Test (mA)	
Mag Bias Switch	3 ^{1, 2}	—	NA	NA	Continuous except during ITR playback
Pitch Control Electronics	131	140	NA	NA	
Roll Sensors (2 ON)	4 ³	—	NA	NA	
Pitch Control Electronics ⁴	196	186	NA	NA	
Pitch Sensor (2 ON)	4 ³	—	NA	NA	
Dual SCO	24	20	NA	NA	
Beacon Transmitter	85	73	NA	NA	
Real-Time Transmitter	735	710	NA	NA	
Dual Programmer	125	98	NA	NA	
Dual Time Base Unit	150	126	NA	NA	
Solar Proton Monitor	82	85	NA	NA	
Flat Plate Radiometer	40	40	NA	NA	
Digital TLM Power	100	—	NA	NA	
CDU Power	8 ⁵	—	NA	NA	
Data Format Converter	NA	NA	97 ⁶	87 ⁶	

* All loads at -24.5 volts unless indicated otherwise.

1 Based on midrange setting of MBS

2 In position No. 11, spec load is 186 mA

3 For each sensor

4 Supplied from unregulated bus

5 Estimated

6 Includes 5.35-volt power for ITR

TABLE 2-IX-1. ITOS LOAD REQUIREMENTS* (Continued)

Equipment	Continuous		Programmed	Commanded	Comments
	Spec (mA)	Test (mA)	Spec (mA)	Test (mA)	
Data Format Converter (Continued)	NA	NA	186	120	Approx 1 min for ITR playback
Attitude Control Coil	NA	NA	32	—	Unipolar or normal QOMAC modes
Momentum Control Coil	NA	NA	75	—	As required during CDA contact
Digital Solar Aspect Sensor	NA	NA	20	12	Only during CDA contact
Commutated TLM Signal Conditioner	NA	NA	180	146	9.25 for each TLM frame
Dual Decoder ¹ and	110	96	NA	NA	Operates in standby except for CDA contact
Dual Command Receiver	(standby) NA (decoding)	NA	225	203	During CDA contact
Incremental Tape Recorder (ITR)	NA	NA	191/2:50% duty cycle = 97 ²	82 ²	Records continuously, except for playback
S-Band Transmitter ¹	NA	NA	201	90	Playback for approx 1 min
Multiplexer ¹	NA	NA	1700	1555	During playback
			45	33	During playback

* All loads at -24.5 unless indicated otherwise.
¹ Supplied from unregulated bus
² Average value during recording

TABLE 2-IX-1. ITOS LOAD REQUIREMENTS* (Continued)

Equipment	Continuous		Programmed	Commanded	Comments
	Spec (mA)	Test (mA)	Spec (mA)	Test (mA)	
Multiplexer APT			50 Quies: 20 Ped: 940 ¹ Read: 735 ² Hold: 695 ³	29 10 830 615	During playback Programmer night During pix sequence
AVCS Camera	NA	NA	Quies: 12 Main pwr: 410 ⁴ Stdby oper: 120 Pk shut: 7.0A	10 380 72 4.5A	Programmer night During pix sequence
AVCS Recorder	NA	NA	<u>Motor</u> Stdby: 27 Start: 2300 Run: 600 <u>Electronics</u> 150 350 10	25 2000-2300 500-600 110 35 10	Programmer night and between pix 1.5 sec for each pix and playback 8.75 sec for each pix and playback 10.25 sec each pix Playback current Standby: prog night and between pix
<p>* All loads at -24.5 volts unless indicated otherwise.</p> <p>1 8 seconds duration each pix</p> <p>2 150 seconds duration each pix</p> <p>3 102 seconds duration each pix</p> <p>4 54.25 seconds duration each pix</p>					

TABLE 2-IX-1. ITOS LOAD REQUIREMENTS* (Continued)

Equipment	Continuous		Programmed	Commanded	Comments
	Spec (mA)	Test (mA)	Spec (mA)	Test (mA)	
Scanning Radiometer Sub-system SR Processor	NA	NA	50	38	On with SR electronics
Scanning Radiometer:					
Electronics	NA	NA	150	²	Record and playback current
Motor 2 ON	140 ea	²	NA	NA	Not to be commanded off
Electronics ¹	10 ea	4	NA	NA	On with SR motor
SR Recorder:					
Standby	NA	NA	25	25	
Recording	NA	NA	305	180	
Playback	NA	NA	410	245	

* All loads at -24.5 volts unless indicated otherwise.
¹ Supplied from unregulated bus.
² Test data - A single SR motor and electronics unit requires 252 mA compared to 150 + 140 = 290 mA specified. An individual SR motor draws 81 mA.

TABLE 2-IX-2. ENERGY BALANCE ANALYSIS RESULTS

Case	Months After Launch	Sun Angle (degrees)	Radiation Environment (flux year)	Spacecraft Load Profile	Source of Load Values	Energy Balance Status
Worst	6	60	1965	SR recorded day and night; 11 AVCS and 11 APT pix; 8-minute read-out each orbit	Equipment Specs	Deficit - Equivalent to excess load current of 110mA
	6	60	1965		Test data	In balance - Negligible deficit equivalent to 4mA
Expected	6	60	1968	Same as worst-case plus SR subsystem recorded day and night.	Test data	Energy balance achieved
	12	60	1968		Test data	Energy balance achieved.
Note: Beacon and digital telemetry off.						

For design purposes, the definition of the operational load, as it applies to establishing the criteria for end-of-life conditions, is based upon the specification limits for the loads and excludes the beacon and dual subcarrier oscillator loads and digital telemetry power. The beacons and the digital telemetry system may be turned off during the operational life of the satellite if telemetry indicates that the array output is not sufficient to permit recharging of the batteries.

Figure 2-IX-1 shows the load profile, constructed from the data in Table 2-IX-1. The upper curve represents the regulated load; the lower curve represents the load on the unregulated bus. The load profile is periodically updated to reflect the latest load requirements.

The subsystem power drain is not included in the operational load profile since it is a function of solar array output and satellite eclipse conditions. However, it is included in the total load on the solar array and/or batteries. The subsystem losses are listed in Table 2-IX-3. The figures presented are worst-case values.

Analog telemetry will be interrogated as required, and the average load due to commutator operation will be considered zero. The digital telemetry will be assumed to be off for the design case (worst-case analysis) as described above.

The subsystem loads during the preoperational mode (launch through establishment of earth lock, which occurs at the end of the initial orientation maneuver) are listed in Table 2-IX-4. This phase of the mission is expected to last less than 24 hours. Until the panels are deployed, the batteries (and the solar array at reduced power levels) support the preoperational loads.

Since the power supply subsystem is designed on a worst-case basis, it will be able to support a greater load than anticipated under expected or nominal conditions.

B. FUNCTIONAL DESCRIPTION

1. General

A block diagram of the power supply subsystem is shown in Figure 2-IX-2. The detailed logic diagram for the TIROS M/ITOS power system is RCA 1976097, which may be found in a separate manual.* The power supply subsystem consists

* RCA Corporation, Astro-Electronics Division, TIROS M/ITOS Spacecraft Logic Diagrams, AED M-2175, Contract NAS5-10306, Princeton, N.J., June 15, 1969, Revised September 26, 1969.

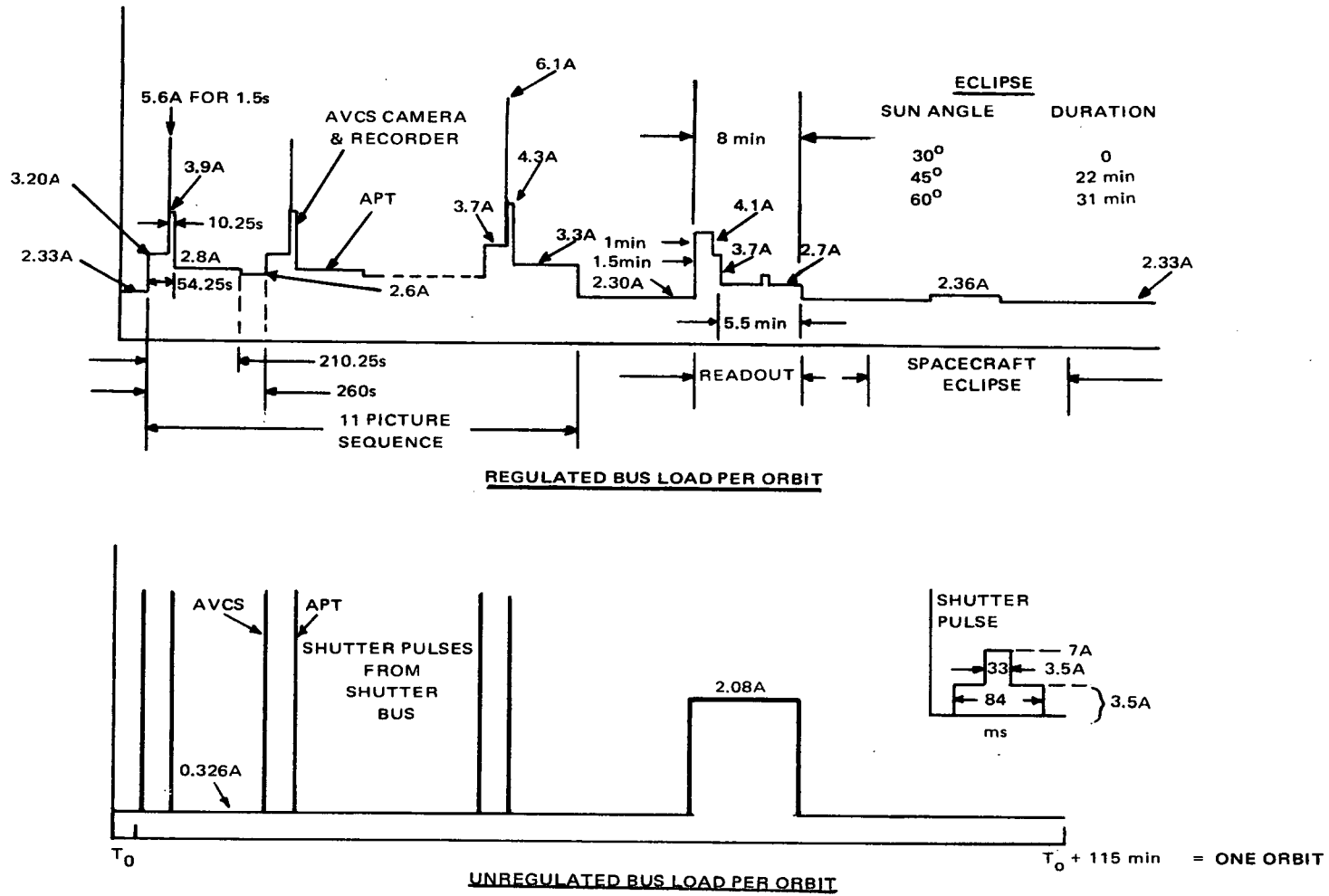


Figure 2-IX-1. Orbit Load Profile

TABLE 2-IX-3. POWER SUPPLY SUBSYSTEM LOSSES
(ORBIT AVERAGE VALUES)

Description	During Satellite Eclipse (mA)	During Satellite Day (mA)
Series Voltage Regulator	180	180
Charge Controllers	20	70
Shunt Limiter Control Amplifiers	20	60
Totals	220	310

TABLE 2-IX-4. POWER SUPPLY SUBSYSTEM LOADS DURING
PREOPERATIONAL MODE

Equipment	Load-Spec Values (mA)
MBS	(186)
QOMAC	32
Momentum Coil	(75)
PCE (Regulated)	131
PCE Motor (Unregulated)	196
Roll and Pitch Sensors	16
Dual SCO and Beacon	109
DSAS	20
Dual Time Base Unit	150
Dual Decoder and Command Receiver	110
Scanning Radiometer (Unregulated)	20
Scanning Radiometer Motors (2 ON)	280
Programmer	125
Totals	1,189 (without MBS and momentum coil); or 1,375 (with MBS and no momentum coil)

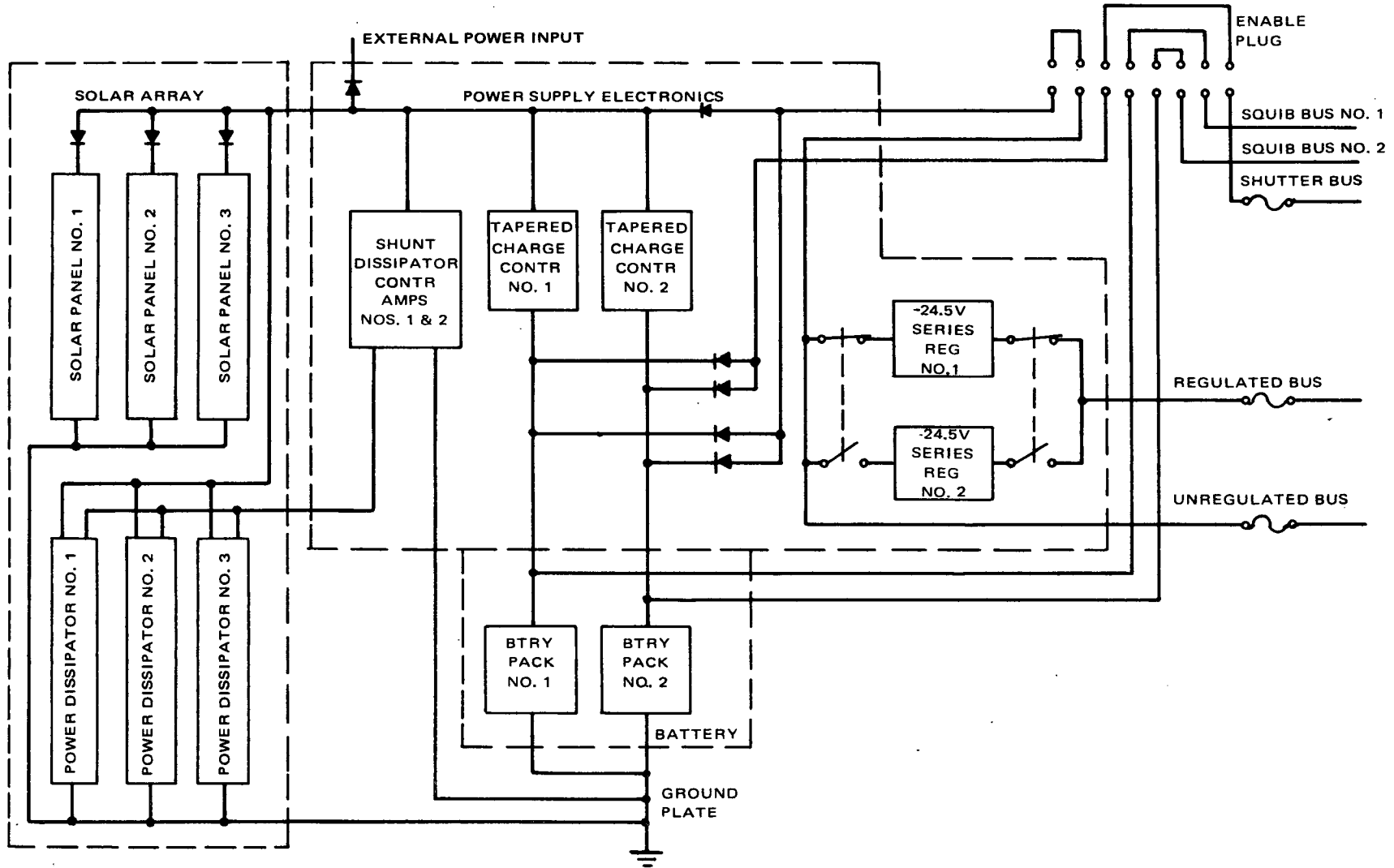


Figure 2-IX-2. Power Supply Subsystem, Block Diagram

of a solar array, a shunt limiter, batteries, charge controllers, and series voltage regulators. The solar array converts incident energy from the sun to electrical energy. The shunt limiter prevents the array bus voltage from exceeding prescribed limits by shunting array current which is not needed to recharge the batteries and supply the spacecraft load. The shunt limiter consists of three shunt dissipator load sections, mounted on each of the three solar panels, and two control amplifiers, located in the power supply electronics. The batteries supply power to the spacecraft during eclipse periods and also supply peak loads during satellite day. The charge controllers provide protection for the batteries by limiting charge currents to proper levels during charge and overcharge periods. The redundant series voltage regulators maintain the regulated bus within limits during variations in load current and input voltage. Only one regulator at a time can be connected into the system; the regulators are selected by ground command.

Certain loads are powered from the unregulated bus, as noted in Table 2-IX-1. The shutter busses and the two squib load buses (one from each battery) are powered directly from the batteries. An enable plug is provided to enable external battery charging through the external power input with all loads disconnected. When the plug is removed, all load power is interrupted.

A ground plate next to the power supply electronics unit is the main spacecraft grounding point. Subsidiary ground plates are provided, on the APT and the AVCS equipment panels, and are connected to the main ground plate by cables.

The operation of the ITOS power supply subsystem is similar to the TOS subsystem, except that the ITOS solar panels are deployed and the voltage in the battery charge controllers is limited. Table 2-IX-5 presents a summary of the design features of this subsystem.

2. Solar Array

The solar array consists of three curved panels, each hinged to a side of the spacecraft at the edge near the thermal fence. Prior to deployment, the panels are held against the sides of the spacecraft. After the initial orientation, the panels are deployed so that they are perpendicular to the spacecraft sides. Each panel is approximately 37 inches wide, measured along the hinge line, and 65 inches long. The cells are bonded directly to an aluminum honeycomb structure.

TABLE 2-IX-5. SUMMARY OF ITOS POWER SUPPLY
SUBSYSTEM PARAMETERS

Parameter	Value
POWER SUPPLY ELECTRONICS	
Units per spacecraft	1
Minimum input voltage to battery	-26.5 volts
Maximum array current capability (with external shunt dissipators connected, 1-ampere regulated load, and two batteries connected)	12.5 amperes
Regulated bus output with maximum steady-state 6-ampere load	-24.5 volts \pm 1 percent
Unregulated output voltage	-26 to -36.2 volts
Regulated bus output with a 10-ampere transient load, less than 1 millisecond in duration, and rise and fall time to less than 200 microseconds, in addition to steady-state load	-24.5 volts -1 percent, +2 percent
Charge current limit to each battery	0.95 \pm 0.08 ampere
Maximum battery voltage limit at battery temperature:	
10°C	34.42 volts
25°C	33.25 volts
Battery trickle charge by ground command	0.15 \pm 0.05 ampere per battery
Weight	11.2 pounds (max)
SOLAR ARRAY	
Panels per spacecraft	3
Dimensions, each of three identical panels	65.15 by 36.38 inches along the chord
Panel shape	Curved (75.6-inch radius)
Solar cell area	2 by 2 cm each

TABLE 2-IX-5. SUMMARY OF ITOS POWER SUPPLY SUBSYSTEM PARAMETERS (Continued)

Parameter	Value
SOLAR ARRAY (Continued)	
Base resistivity	1 to 2 ohm/cm
Cover glass thickness (microsheet)	0.006 inch
Air-mass-zero efficiency (with cover glass)	10.3 to 11.6 percent
Solar cell (with cover glass)	
Short-circuit current (I_{SC})	121.1 mA at 28°C (10.3 percent efficiency)
Open-circuit voltage (V_{OC})	0.586 volt at 28°C
Maximum-power-point current (I_{MP})	102.0 mA at 28°C (10.3 percent efficiency)
Maximum-power-point voltage (V_{MP})	0.475 (10.3 percent efficiency)
Circuits per panel	5
Strings per circuit	9 (equal to 9 parallel cells)
Strings per panel	45
Strings per array	135
Series cells per string	76
Array diode type	JAN IN1206
Radiation degradation factors (6 months, 1965 flux):	
Voltage	0.920
Current	0.821
Panel weight (with shunt dissipator)	20.5 pounds (max)*
Array weight	61.5 pounds (max)*
* Does not include weight of: deployment mechanism, locking mechanism, hinges, bumpers, or snubbers.	

TABLE 2-IX-5. SUMMARY OF ITOS POWER SUPPLY SUBSYSTEM PARAMETERS (Continued)

Parameter	Value
BATTERY (NICKEL CADMIUM)	
Batteries per spacecraft	2
Cells per battery	23 in series
Storage capacity	4 ampere-hours per cell (min)
Weight	16.0 pounds each (max)
Charge control method	Taper charging with voltage and temperature control
Operating temperature	10° to 35°C
Charge rate	0.95 ±0.08 ampere per battery (normal maximum), taper charge rate determined by battery voltage and temperature
Maximum depth of discharge	18.8 percent (readout during day at 60-degree sun angle)

3. Batteries

The batteries employ rectangular 4-ampere-hour capacity nickel-cadmium cells. The cells are arranged in two batteries of 23 cells each. The cells of each battery are arranged in two rows, one row of 12 and the other row of 11; the 23 cells are wired in series. The two batteries discharge in parallel into the system loads through diodes. The batteries are mounted on the baseplate of the spacecraft.

4. Series Voltage Regulators

The series voltage regulators are a part of the power supply electronics. The voltage regulators are electrically similar to the TOS regulators, but are capable of supplying a higher load current. The regulators are redundant units and are selected by the ground command.

5. Charge Controllers

Battery charging is controlled by two taper charge circuits, one for each battery. Both of these circuits are in the power supply electronics. The charge current to the battery is limited to a maximum value when the battery voltage is below the limit prescribed for the battery temperature. When the battery voltage reaches the voltage limit, the charge controller reduces the charge current to hold the battery voltage at the prescribed limit. The voltage limit corresponds closely to the point where the battery has been returned to a fully charged state. The battery will continue to overcharge at reduced rates after the voltage limit is reduced.

The voltage limit thus ensures that the charge current will be reduced to a safe overcharge rate for the battery. Some overcharging of the battery is required in order to sustain satisfactory charge-discharge cycling performance during the entire mission. Use of a voltage limit allows initial charge rates as high as C/4, as compared to C/10 for TOS for a similar battery temperature range.*

The overcharge characteristic is a result of several iterative design cycles. A higher overcharge voltage limit results in greater overcharge rates and higher thermal dissipation. The final voltage-temperature characteristics have been modified at high temperatures to limit thermal dissipation as well as to allow adequate overcharge to meet the cycling demands of the mission.

The charge current can be reduced to the trickle charge rate (150 ±50 milliamperes per battery) upon command from a ground station. Although the voltage limit ensures that a fully charged battery will be charged at a reduced rate, the trickle charge feature further reduces the heat dissipation in the battery, during 100-percent sunlight operation, by further reducing the charge current. This

*C represents the nominal battery capacity in ampere-hours.

mode of operation should be used when telemetry indicates that the battery temperature exceeds 35°C.

6. Shunt Limiter

Shunt limiting is essential to ITOS because of the wide variation of solar energy input to the array, a consequence of operating over the 30- to 60-degree sun angle range. Since an increase in solar energy input increases the voltage level of the array output, the array voltage is limited to prevent the overstressing of components.

The shunt limiter is similar in concept to the TOS shunt limiter, but due to a higher power-handling requirement, the unit has nine rather than four parallel power dissipating sections. Eight power sections can handle the maximum output from the array.

The power handling components of the dissipator are mounted on the back of the solar array panels. Two redundant control amplifiers to drive the nine power sections are contained in the power supply electronics.

The control amplifier compares the solar array bus voltage to a reference, and, if the array voltage exceeds the reference voltage, it provides drive current to the dissipators. The dissipators then load the solar array to limit the array voltage to the desired maximum value.

7. System Protection

All system loads are fused with the Littelfuse high reliability subminiature Picofuse. This fuse type requires no encapsulation and is available in ratings from 0.125 to 5.0 amperes. A 3-to-1 safety margin was used in selecting fuse ratings. The largest fuse rating used on the regulated bus is 5 amperes.

An evaluation of the operating characteristics of the regulator and the current versus blow time characteristics of the fuses has indicated that no damage can be done to the -24.5-volt regulators if they are required to blow any of the fuses on the bus. The evaluation considered the available power to the regulator, and then described the excursions of the regulator operating point when the regulator is required to supply the additional current to blow the fuse. The limiting characteristic in all conditions is the maximum junction temperature reached in the

three parallel pass transistors of the regulator. Under no conditions can this temperature reach the maximum allowable operating temperature, even under worst-case circuit degradation characteristics and worst-case thermal environment for the power supply electronics.

C. COMPONENTS

1. Solar Cell Array

a. DESIGN HISTORY

The primary purpose of the solar cell array is to provide power for the spacecraft loads and for recharging the storage batteries by converting the incident solar energy into electrical energy.

The ITOS solar cell array, with its three solar panels, was designed to provide sufficient power to operate the ITOS spacecraft in a full electronic load capacity for at least 6 months and to last mechanically for at least 1 year. To help achieve this, parametric analyses of materials and/or processes were performed on the following:

- Solar Cell Cover Glass (Microsheet Versus Fused Silica).

Tests based on the most accurate space environmental radiation data showed an insignificant difference in the percent of transmission loss between Microsheet, Corning Glass 0211, and Fused Silica, Corning Glass 7940, for the orbit involved. Microsheet was selected for the cover glass.

- Solar Cell Base Resistivity (1 ohm/cm versus 10 ohm/cm).

A radiation damage resistance analysis indicated that both the 1- and the 10-ohm/cm solar cells were acceptable. However, an analysis of the voltage and current temperature characteristics indicated that the 1-ohm/cm solar cells offered less temperature degradation and, therefore, they were selected. The temperature coefficient for the 1-ohm/cm cells is 2.2 mV/°C while that for the 10-ohm/cm cells is 2.5 mV/°C.

- Solar Panel Insulation (SMP-Fiber Glass Versus Solar Ply).

Solar Ply, a polyvinyl-fluoride material, was selected over the formerly used SMP-fiber glass and scrim cloth combination for the following reasons:

- (1) Solar Ply is applied from a roll in a thin uniform solid sheet onto the aluminum skin of the solar panel substrate; therefore, there is no formation of bubbles or voids which require subsequent touchup. (With the SMP-fiber glass and porous woven cloth coatings, bubbles and voids do appear and touchup is necessary.);
- (2) Solar Ply is superior to the SMP combination in breakdown voltage (1000 volts/mil as compared to 560 volts/mil);
- (3) Solar Ply requires a material thickness of 2.25 mils as compared to 3 to 3.5 mils for the SMP combination; and
- (4) Solar Ply is capable of withstanding temperatures up to +150°C.

Solar Ply is laminated to the aluminum skin prior to mating of the skin and honeycomb structure.

- Electrically Connecting the Solar Cells Along the Solar Panel Curvature Versus Connecting Across the Solar Panel Curvature.

The solar cells are electrically connected in series along the solar panel curvature because an analysis indicated that there would be an end-of-life loss of 46.6 percent short-circuit current if the same solar cells in series were electrically connected across the solar panel curvature.

b. CHARACTERISTICS

Each of the three ITOS solar panels is 65.15 inches long by 36.38 inches wide. The width of the panel, as measured along the curved surface, is 36.64 inches. Each panel has a nominal radius of curvature of 75.61 inches and is 0.515 inch thick when the honeycomb, aluminum skins, Solar Ply insulation, and skin adhesives are all bonded together into a lightweight substrate. Three ribs provide support to the substrate and also act as a thermal mass for the three shunt dissipator sections located on each panel. The panels weigh a maximum of 20.5 pounds each, excluding antenna snubbers, etc.

Five solar cell modules, electrically connected in parallel, are bonded to each solar panel. The three ITOS solar panels are connected in parallel for a total of 15 modules. Electrical feedback protection is maintained by redundant diodes which isolate each module.

Each of the 5 solar cell modules is made up of 9 strings of solar cells, with the 9 strings connected in parallel and each string consisting of 76 cells connected in series. For ground testing purposes, the series circuit is divided into two separate sections of 38 series cells. All solar cells are electrically connected in series and parallel using 2-mil thick silver mesh. RTV 560/580 is used to bond the solar cells to the solar panel. Radiation protection for each solar cell is provided by 6-mil microsheet cover glass with Sylgard 182 as the cover glass adhesive. Each cover glass is optically coated on top with an antireflective coating and on the bottom with a blue reflective coating to reject ultraviolet.

c. FUNCTIONAL DESCRIPTION

The ITOS solar cell array, comprising three solar panels, has two major functions: (1) to supply electrical power to the spacecraft and (2) to provide mechanical support for the shunt dissipator elements, with sufficient thermal paths and mass to ensure that the maximum and minimum temperature extremes of the components are not exceeded.

The solar cell array meets the mission end-of-life spacecraft electrical requirements after allowances have been made for the following parameters:

- (1) Angle to the sun vector,
- (2) Curved panel surface,
- (3) Blocking diode drop,
- (4) Telemetry resistor drop,
- (5) Variation of temperature over the curved panel surface versus time in orbit,
- (6) Variation of solar illumination incidence angle on the curved panel surface versus time in orbit,
- (7) The product of the following assumed current degradations:
 - Solar constant 0.967
 - Power prediction 0.97

- UV damage 1.00
- Curved panel model 0.995, and

(8) The product of the following assumed voltage degradation:

- Wiring loss 0.98

In addition, the initial power output must not exceed the limits set by the shunt dissipator limitations.

The maximum and minimum current voltage (I-V) solar cell characteristics are shown in Figure 2-IX-3. The lower curve in Figure 2-IX-3 represents the minimum solar cell characteristics with 6 months radiation degradation per the 1965 flux data. Expected total output is then degraded by the aforementioned parameters.

In addition to the general environmental conditions of launch thrust and vibration loads, space vacuum, charged particulate irradiation (1965 data) and orbital sun angles of 30 to 60 degrees, the solar panel assemblies are designed to withstand general flight temperature extremes of +42°C to -88°C with local warm spots ranging up to +87°C if launched on a 30-degree sun angle orbit. These warm spots would occur directly over the shunt dissipator components. When array output limiting occurs through localized heating, the affected cell voltages will adjust by decreasing the total string current and, thus, the shunt drive current, thereby reducing the local heating effect. The end result is a stabilized self-leveling situation among the spacecraft loads, the solar panel output, and the panel temperature. This array limiting situation can only occur when there is excess energy available for diversion to the shunt dissipators.

Since the solar array is a constant current source (i.e., high impedance source), the array bus voltage will increase as the spacecraft loads are removed. Therefore, current must be shunted through the shunt dissipator sections to maintain the solar array bus voltage below an upper limit of -36.8 volts.

Each of the nine shunt dissipator sections is designed to dissipate one-eighth of the total 490-watt shunt dissipator requirement. This means that only eight sections are required to handle worst-case condition. Figure 2-IX-4 shows the amount of power each component per shunt section may dissipate. At the maximum power levels, the solar panel provides sufficient thermal paths to limit the upper temperature extremes of the components within their design limits.

Mechanical packaging of the nine shunt dissipator sections is accomplished by locating one section on each of the panel support ribs. At each point where the shunt transistors are attached to the panel ribs, an additional amount of thermal mass is attached to limit the lower temperature extreme of the transistors.

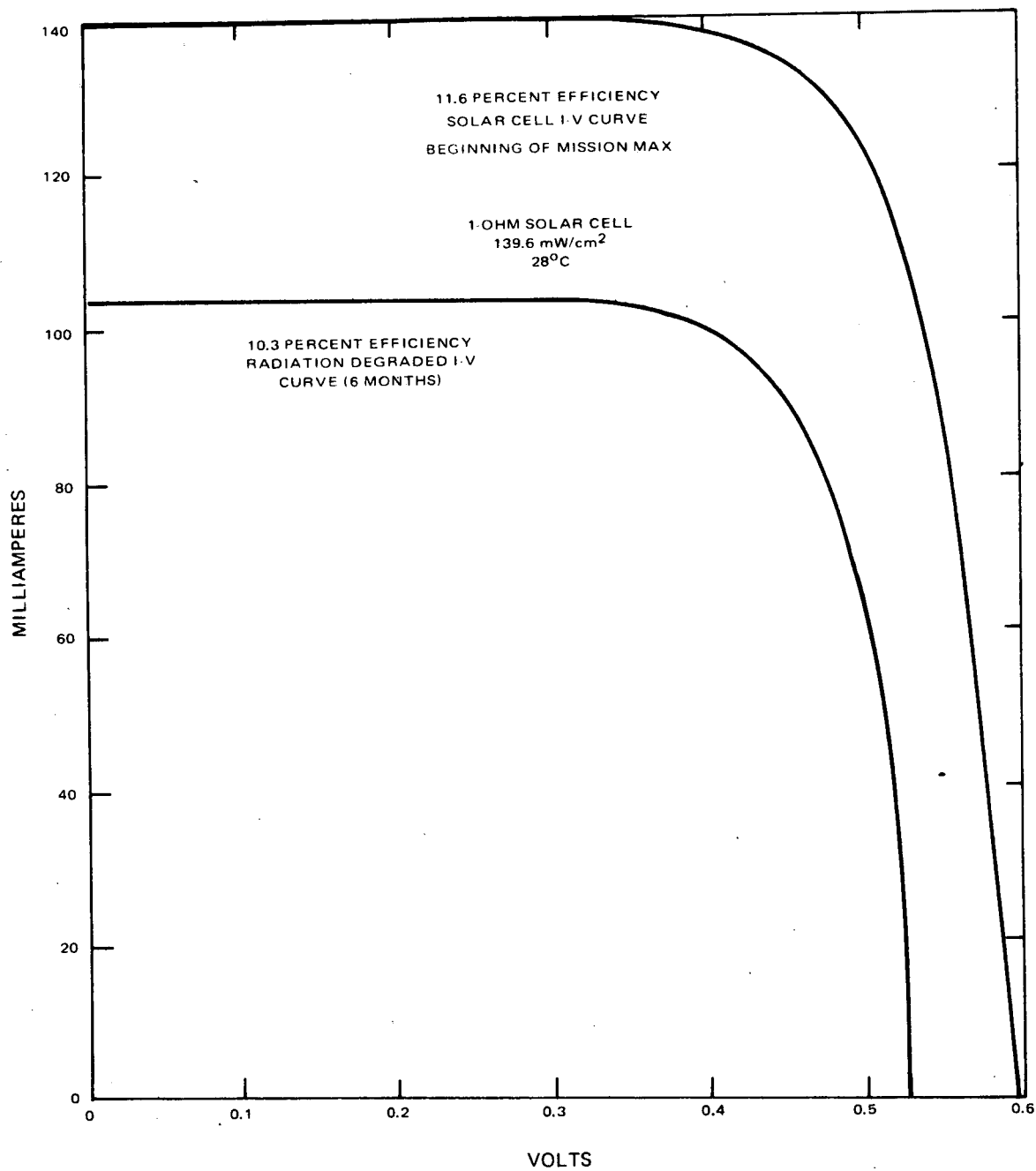


Figure 2-IX-3. Maximum and Minimum Current Array Solar Cell Characteristics

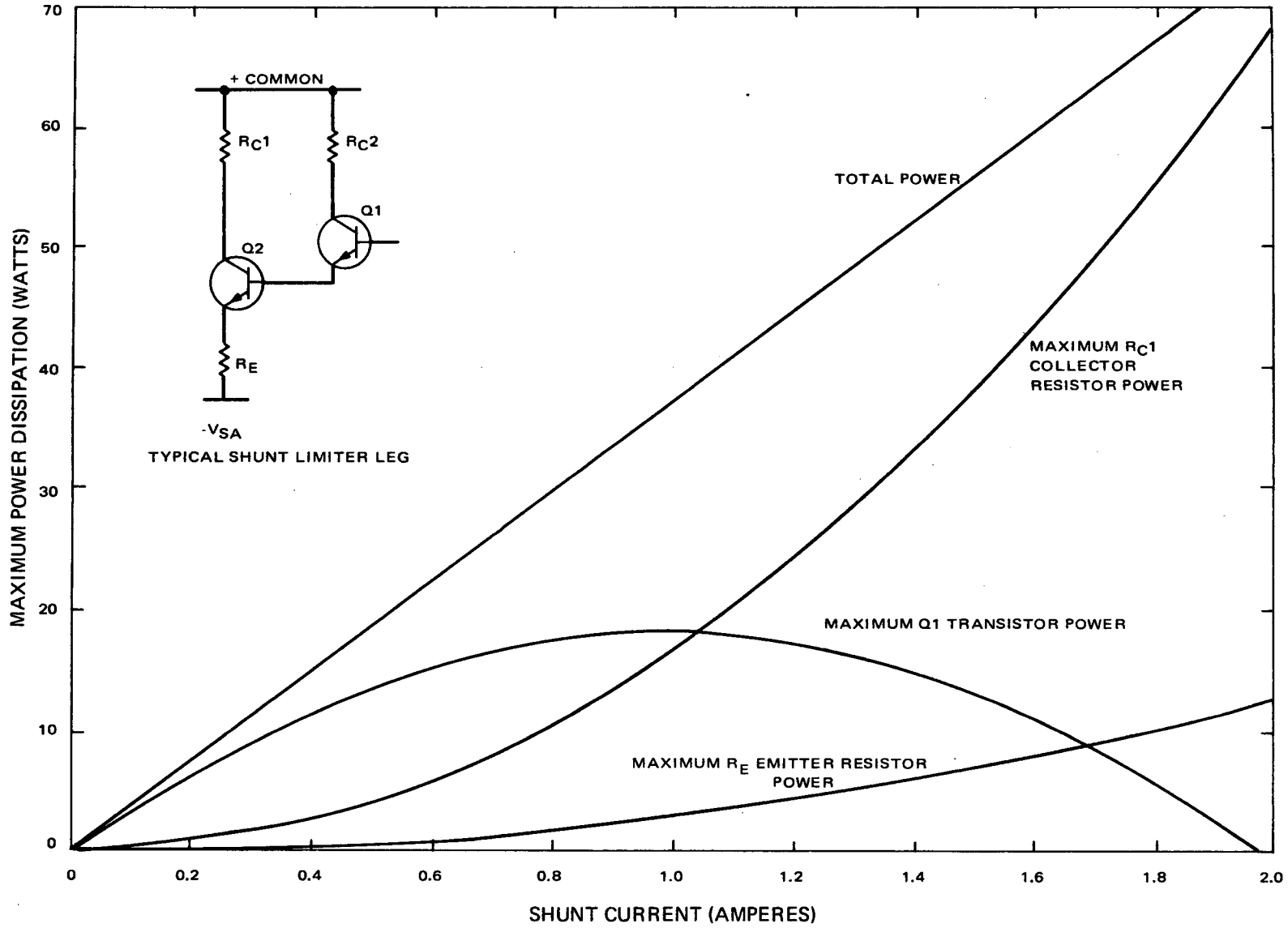


Figure 2-IX-4. Power Dissipation Versus Shunt Current (per Shunt Dissipator)

Temperature extremes approaching -55°C are expected on the dissipator components as the spacecraft emerges from the earth eclipse in a 60-degree sun angle orbit at end-of-life (EOL). Analysis has indicated that in a 75-degree sun angle orbit the transistors can be expected to cool to a temperature below the recommended lower limit of -55°C .

2. Batteries

a. GENERAL DESCRIPTION

The power supply subsystem of the ITOS spacecraft contains two nickel cadmium batteries. These batteries store part of the electrical energy generated by the solar array during periods of sunlight and supply electrical energy to the spacecraft during periods of eclipse or during periods when the spacecraft power requirements exceed the solar array capability. The two batteries are not redundant; both are necessary to fulfill the design requirements of the power subsystem.

Each battery is an assembly of 23 series-connected, sealed, nickel-cadmium cells having a minimum 4.0-ampere-hour rating. The design is an evolution of the 21-cell batteries used on the TOS and FOTOS spacecraft. Basic differences, in addition to the number of cells per battery, are:

- A drawn stainless steel case was used for fabrication, in place of the welded steel case (see Figure 2-IX-5).
- The nickel-cadmium cell terminals are perforated, tinned copper discs, to facilitate soldering, in place of stainless steel or iron.
- The thermal path for heat dissipation from the nickel-cadmium cells is through the bottom of each individual cell, instead of the side-walls of certain selected cells.
- Each individual cell is mechanically clamped into the battery module, as shown in Figure 2-IX-6; instead of relying solely upon friction to keep the cell in place.
- A clear plastic cover is installed over the top of the battery pack.

Maximum battery weight is 16.0 pounds which is packaged in an assembly approximately 5.8 by 5.0 by 11.8 inches. In addition to 23 nickel-cadmium cells, each



Reproduced from
best available copy.

Figure 2-IX-5. Drawn-Case, 4-Ampere-Hour, Battery Cell

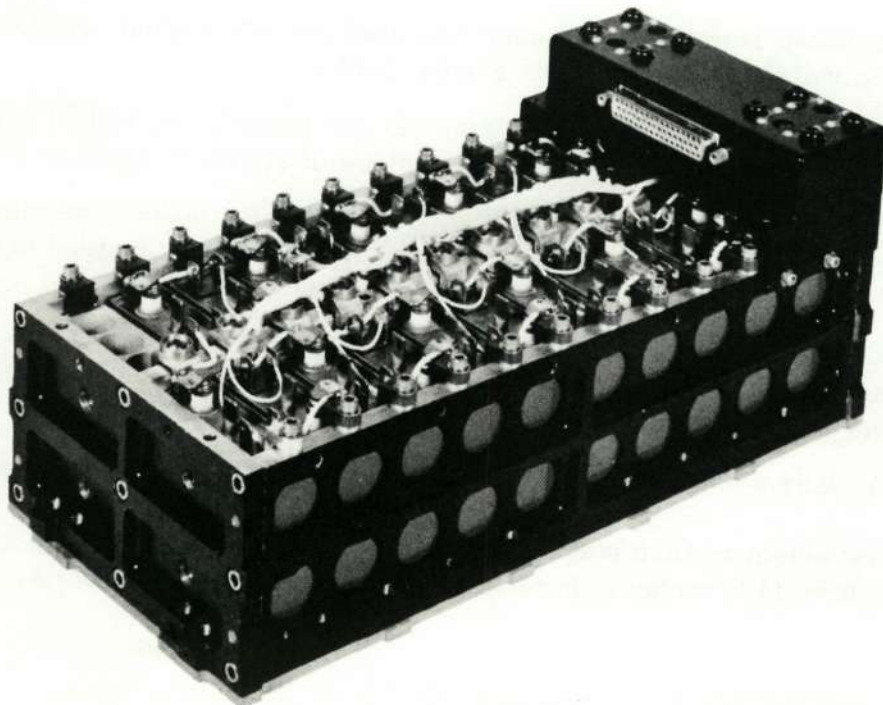


Figure 2-IX-6. Battery, Top Cover Removed

battery assembly contains two thermistors which provide temperature signals for charge control and telemetry circuits. A 50-pin cannon connector provides the electrical interface between each battery and the other units of power subsystem. A baseplate approximately 5.5 by 11.6 inches is the mechanical interface between each battery and the spacecraft.

b. DESIGN HISTORY

Two batteries of 4-ampere-hour cells were chosen rather than one battery of 8-ampere-hour cells since 4-ampere-hour cells had been previously used in FOTOS spacecraft and in other RCA power subsystems. The number of cells per battery was originally proposed to be 22 but as the worst-case requirements became more rigidly defined, the design was changed to 23 cells to meet the minimum voltage requirements after 6 months of operation.

c. DETAILED FUNCTIONAL DESCRIPTION

The batteries are capable of accepting a charge current of up to 1.03 amperes, provided the voltage is limited to a maximum value dependent on temperature, as defined in Figure 2-IX-7. In the ITOS power subsystem, the charge controller provides this limit. During overcharge, the batteries may continue to be charged at a rate which maintains this voltage limit, but at no time exceeds it. The maximum battery overcharge of 35.21 volts occurs at 0°C.

The batteries have a minimum capacity of 4 ampere-hours each, or a total of 8 ampere-hours for the power subsystem. This can be more specifically defined by stating that under a 2.00-ampere load, each battery will maintain a terminal voltage above 26.45 volts for a minimum of 2.00 hours when the battery temperature is 25°C. When the battery temperature is either increased or decreased, the available ampere-hour capacity will decrease.

When the batteries are repetitively charged and discharged (cycled), the end-of-discharge battery voltage will decrease as a function of the number of cycles. The ITOS batteries are capable of maintaining a minimum terminal voltage of 26.5 volts for a minimum 2280 cycles (6 months) when the temperature and load requirements vary as predicted in the overall system analysis. The battery temperature is expected to remain in the range of 14° to 35°C over the life of the spacecraft with the discharge per orbit ranging from 0.01 to 0.76 ampere-hour.

The battery electrical connections are shown in Figure 2-IX-8. All interconnections between cells are redundant, using two 18 gauge wires; the connections between the end cell terminals and the positive and negative bus bars use three

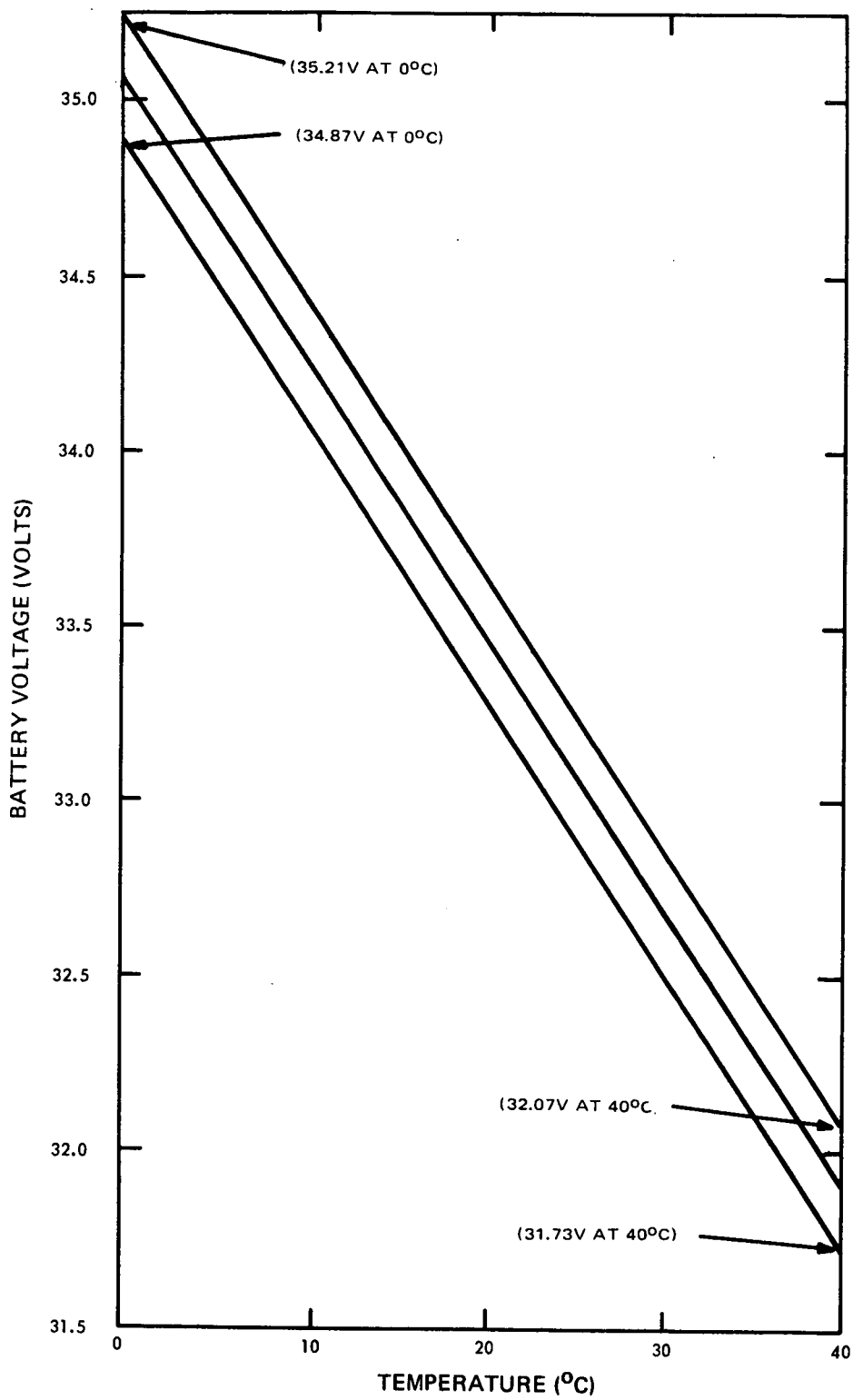


Figure 2-IX-7. Battery Charging Voltage Limit Versus Temperature

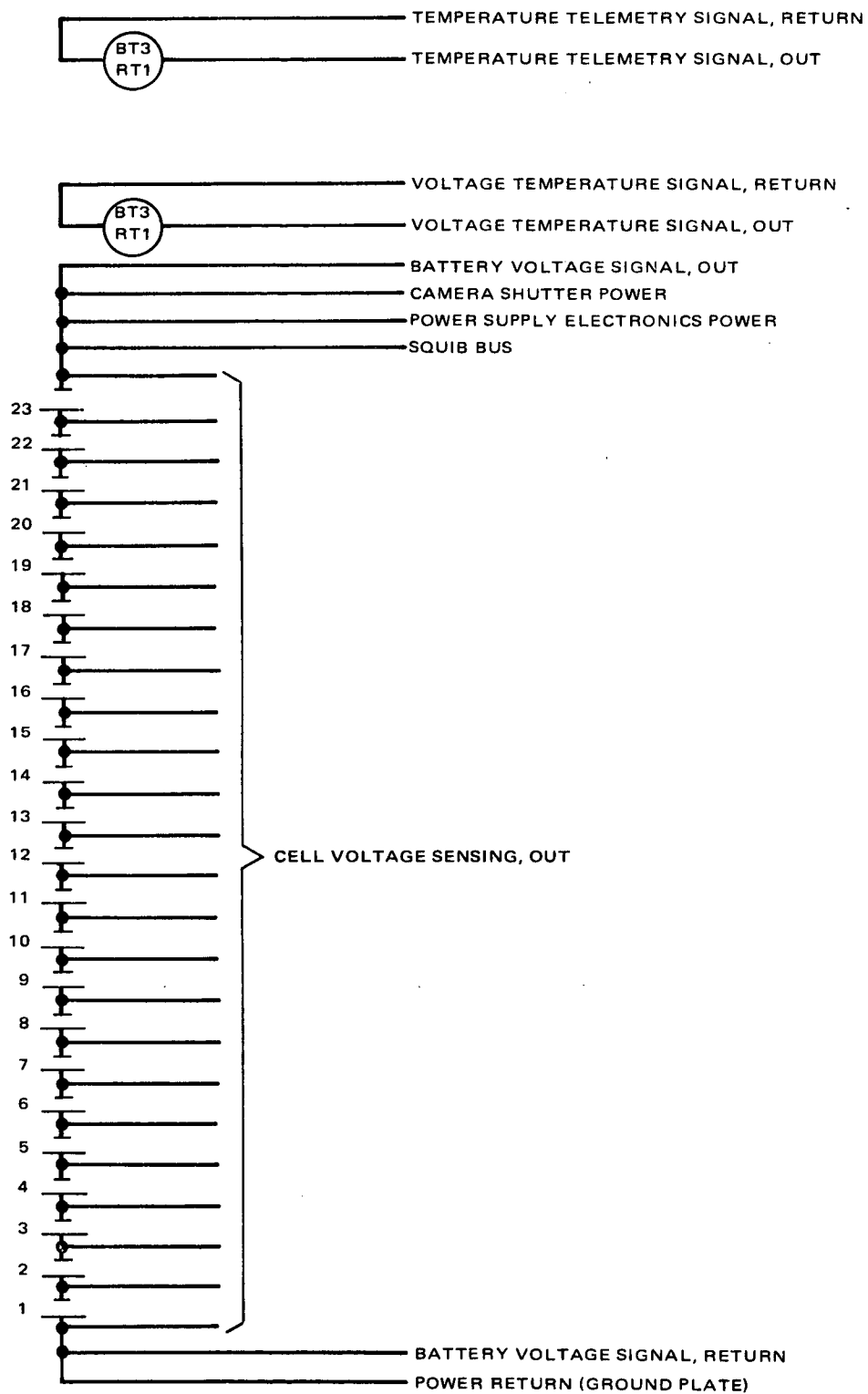


Figure 2-IX-8. Battery Electrical Diagram

18 gauge wires. All of the cell voltage-sensing wires and the thermistor wiring are 26 gauge. All connections between the bus bars and the 50-pin connector are of 20 gauge wire and, in all cases, there is a minimum of two wires in each power output path for redundancy.

3. Power Supply Electronics

a. GENERAL DESCRIPTION

The power supply electronics (PSE) is a major unit of the ITOS spacecraft electrical power subsystem. The required circuitry is contained within a 10.50- by 5.75- by 7.93-inch rectangular unit (Figure 2-IX-9). The assembled unit weighs 12.5 pounds.

Operating in a spacecraft environment, the PSE performs four major functions:

- Power distribution and voltage regulation.

During satellite day, this unit accepts solar array and/or battery power at voltage levels varying between -26.5 and -36.8 volts and distributes conditioned power to spacecraft loads. During the satellite night, the PSE accepts battery power at voltage levels varying between approximately -26.5 and -31.5 volts and distributes conditioned power to spacecraft loads. One of two redundant voltage regulators provides a voltage of -24.5 volts to loads requiring total steady-state currents up to 6 amperes and short-term transient currents of 10 amperes. An unregulated voltage in the range of -26.0 to -36.2 volts is available for unregulated loads.

- Battery charge control.

When solar power is available, circuits within the PSE control the recharging of the power subsystem battery modules at a maximum rate of approximately 1 ampere by sensing battery voltage and temperature. Separate control circuits are provided for each battery module.

- Ground control commands and analog telemetry signals.

The PSE provides a means for switching voltage regulators and shunt limiter amplifiers and reducing the battery charge current when signaled by ground command signals. Telemetry circuits are included to provide output analog signals of key power subsystem performance parameters.

- Shunt limiter control.

The PSE contains two redundant shunt limiter control amplifiers to sense the solar array bus voltage and provide a signal to control nine remote shunt dissipator sections. The shunt dissipator sections, located on the solar array panels, act as a shunt load on the solar array to maintain the solar array bus voltage below an upper limit of -36.8 volts.

There are two automatic switching circuits, one for each control amplifier, which act to remove a shorted control amplifier.

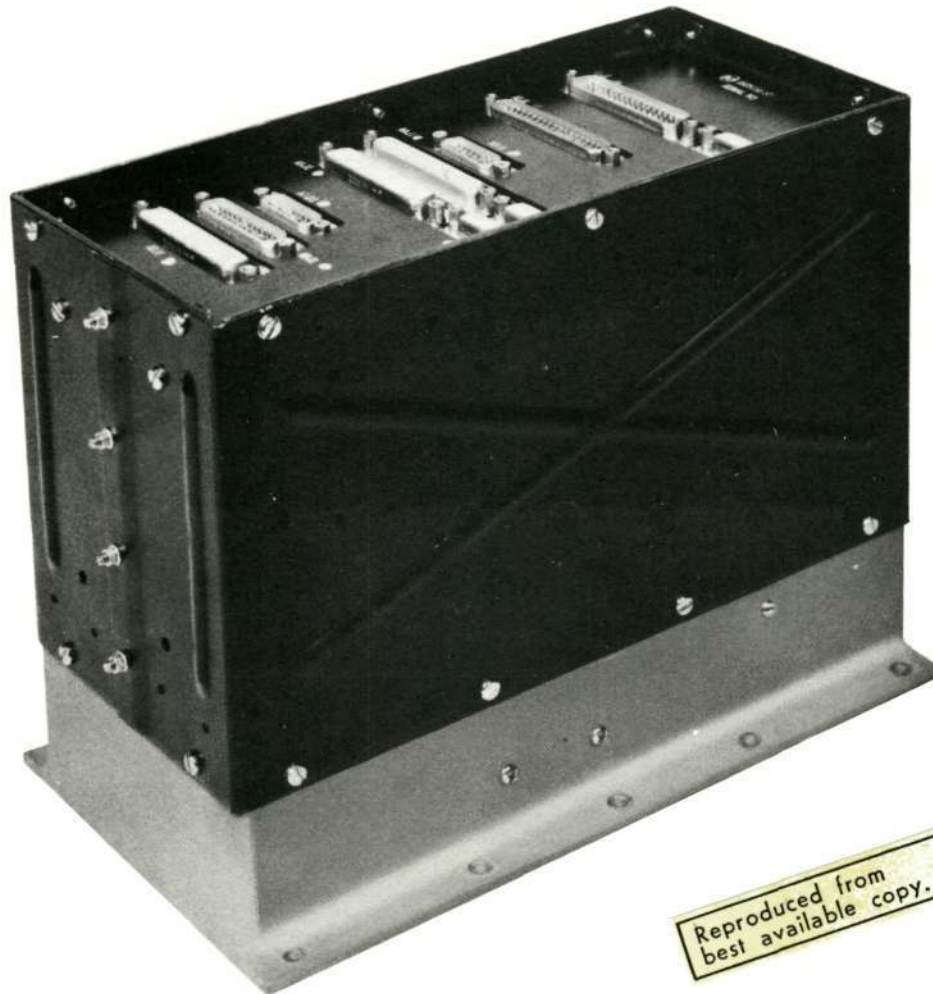


Figure 2-IX-9. Power Supply Electronics

b. FUNCTIONAL OPERATION

(1) VOLTAGE REGULATOR

(a) General Description

Two identical voltage regulators are incorporated in the ITOS spacecraft. Each regulator is capable of providing a -24.5 ± 0.25 -volt regulated bus to the spacecraft systems over a load current range of 0.40 to 6 amperes. One regulator supplies the total -24.5 -volt bus load and the second is in a power off mode, ready to be switched on line via ground command in the event of failure of the on line regulator. Only one regulator can be commanded on line at any time.

The -24.5 -volt regulator is shown in block diagram form in Figure 2-IX-10. A differential amplifier compares voltage variations across the load with a voltage reference zener diode. The output of the differential amplifier is directly coupled to a second differential amplifier connected in complementary symmetry. A stage of current gain provides the necessary drive to the series-pass transistors to support the required load current.

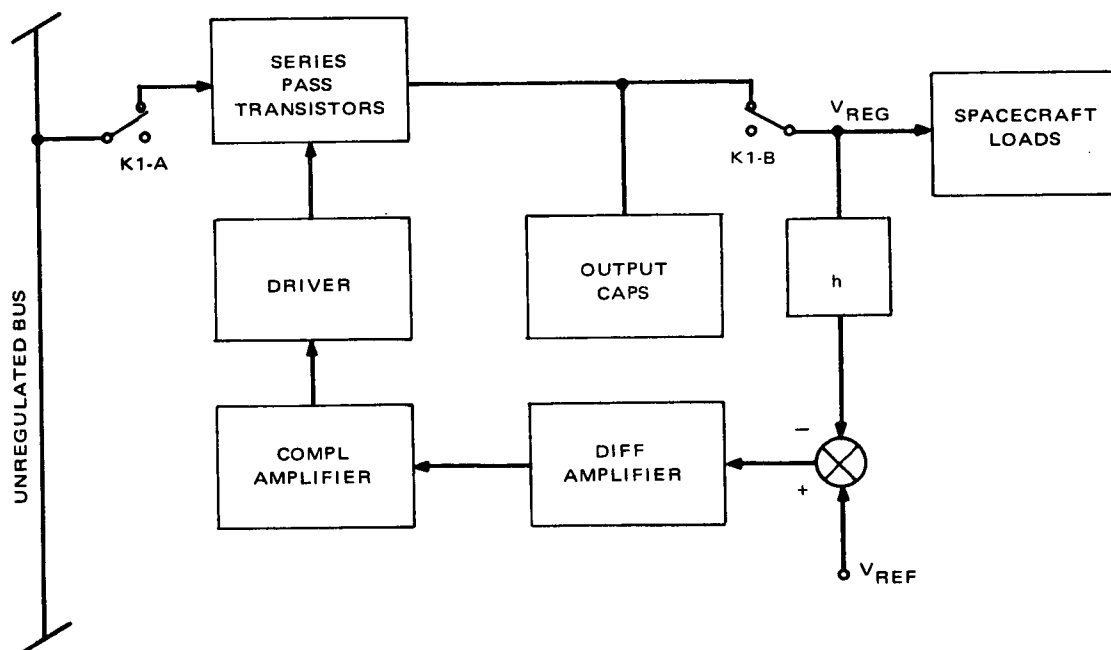


Figure 2-IX-10. -24.5 Volt Regulator, Block Diagram

(b) *Functional Operation*

A change in load voltage, due either to load resistance or input voltage fluctuations, when applied to the base of Q7-A (see Figure 2-IX-11) by the voltage divider network (R10 to R14) is compared to the temperature compensated reference, VR1, and appears as an amplified error voltage at the collectors of Q7-A and Q7-B. If the load voltage decreases, the collector voltages of Q7-A and Q7-B will decrease and increase, respectively, and the complementary differential amplifier Q5 and Q6 will deliver additional base current to the drive transistor, Q4.

The small current increase to the base of Q4 results in a sufficiently large increase in current to the load, due to the Beta multiplication of the driver Q4 and the parallel configuration of pass transistors Q1, Q2, and Q3. The increase in load current restores the load voltage to its predisturbance level. The phase of the error signal is such that negative feedback is introduced in a closed loop and any deviation is inherently self-correcting.

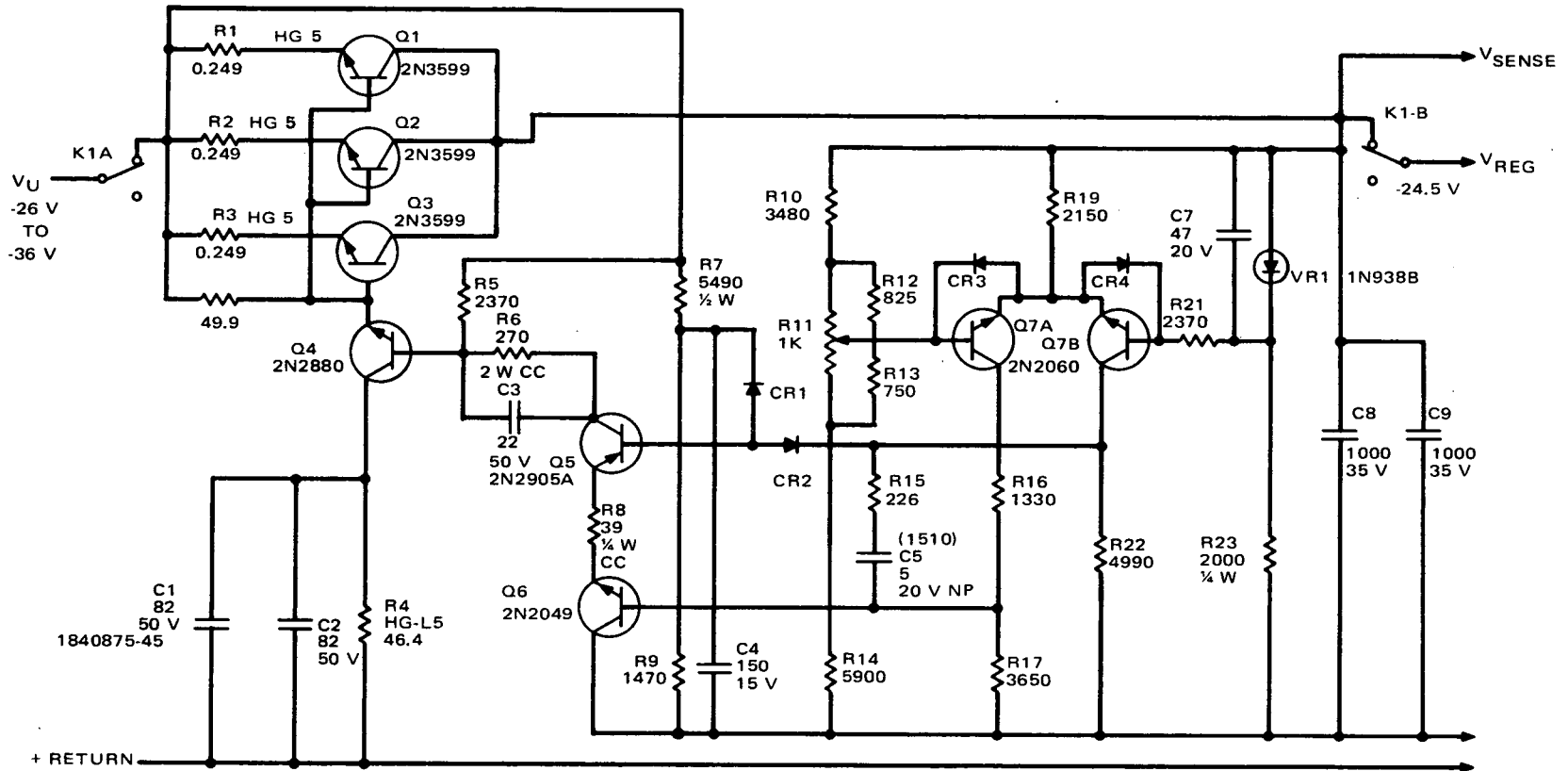
The R15-C5 network provides internal gain/phase compensation, starting the gain roll-off at a low frequency and with a controlled rate of decrease. The output capacitors (C8 and C9) provide a low output impedance at frequencies beyond the point where the normal regulator impedance increases because of loop gain reduction.

The regulator starting power is applied to the base of Q5 through R7 and CR1. When the output voltage rises sufficiently to turn on Q7-B, CR1 becomes reverse biased, the transistor Q7-B supplies the necessary base drive to Q5 and the output voltage continues to rise. At the -24.5-volt level, Q7-A starts to conduct and negative feedback prevents further increase of the output voltage. CR2 prevents current flow through R22 and the collector to base junction of Q7-B upon the initial application of power to the input terminals. Capacitors C4 and C7 slow down the starting circuit and the feedback loop, respectively, during regulator turn-on to maintain gradual charging of the output capacitors and to prevent heavy surge currents through the series transistors Q1, Q2, and Q3.

(2) *SHUNT LIMITER*

(a) *General Description*

The ITOS shunt limiter was designed to limit the voltage on the solar array bus to a safe upper limit.



UNLESS OTHERWISE NOTED:

ALL RESISTANCE VALUES ARE IN OHMS

ALL CAPACITANCE VALUES ARE IN MICROFARADS

ALL DIODES ARE TYPE 1N645

Figure 2-IX-11. Voltage Regulator, TIROS M

High reliability is assured by use of basic circuitry similar to that used on flight-proven shunt regulators on the TOS spacecraft. However, additional redundancy and more substantial derating factors were applied to achieve the 1-year minimum life requirement.

As shown on Figure 2-IX-12, power to ITOS spacecraft loads is furnished by the solar array. Since the solar array is a constant current source, the solar array bus voltage tends to increase as the spacecraft loads are removed. Control of the maximum solar array bus voltage is achieved by shunting current through the shunt dissipator sections when the control amplifier(s) sense an increase in solar array voltage above a cut-in level. The shunt limiter consists of nine shunt dissipator power sections on the solar array panels and two control amplifiers in the power supply electronics unit.

Sensing of the solar array bus voltage is done by both control amplifiers. Each control amplifier compares the solar bus voltage to a voltage reference and provides an output current which is proportional to the difference (error signal). The control amplifier output current is fed through isolation diodes to a common bus and then through isolation networks to each of the shunt dissipators.

The shunt dissipator amplifies the control current, causing some of the solar array current to become shunt limiter current, which, in turn, decreases the solar bus voltage to a level where the control amplifier error signal is minimized. The net effect is a closed-loop, negative-feedback, control system which provides voltage limiting.

Either, or both, of the control amplifier outputs are connected or disconnected by two relays which may be actuated by either ground command or by an automatic failure (short circuit) detection control. Both amplifiers cannot be simultaneously disconnected.

The threshold, or cut-in, voltage of each of the two control amplifiers is 36.25 volts, when the total shunt dissipator current is 0.1 ampere. Temperature and aging effects may cause the threshold voltage to vary by no more than ± 0.25 volt at the end of 1 year including all environmental effects. The solar array bus voltage may increase by 0.3 volt, maximum, when the shunt dissipator current increases from 0.1 to 15.3 amperes. (The 15.3-ampere current figure is the 9 leg dissipator capacity as compared to a beginning-of-life array current, at $\gamma = 30^\circ$, of 13.8 amperes.)

Below the shunt limiter threshold voltage, the solar array bus impedance is reduced by two filter capacitors which are connected between the solar array bus and positive return.

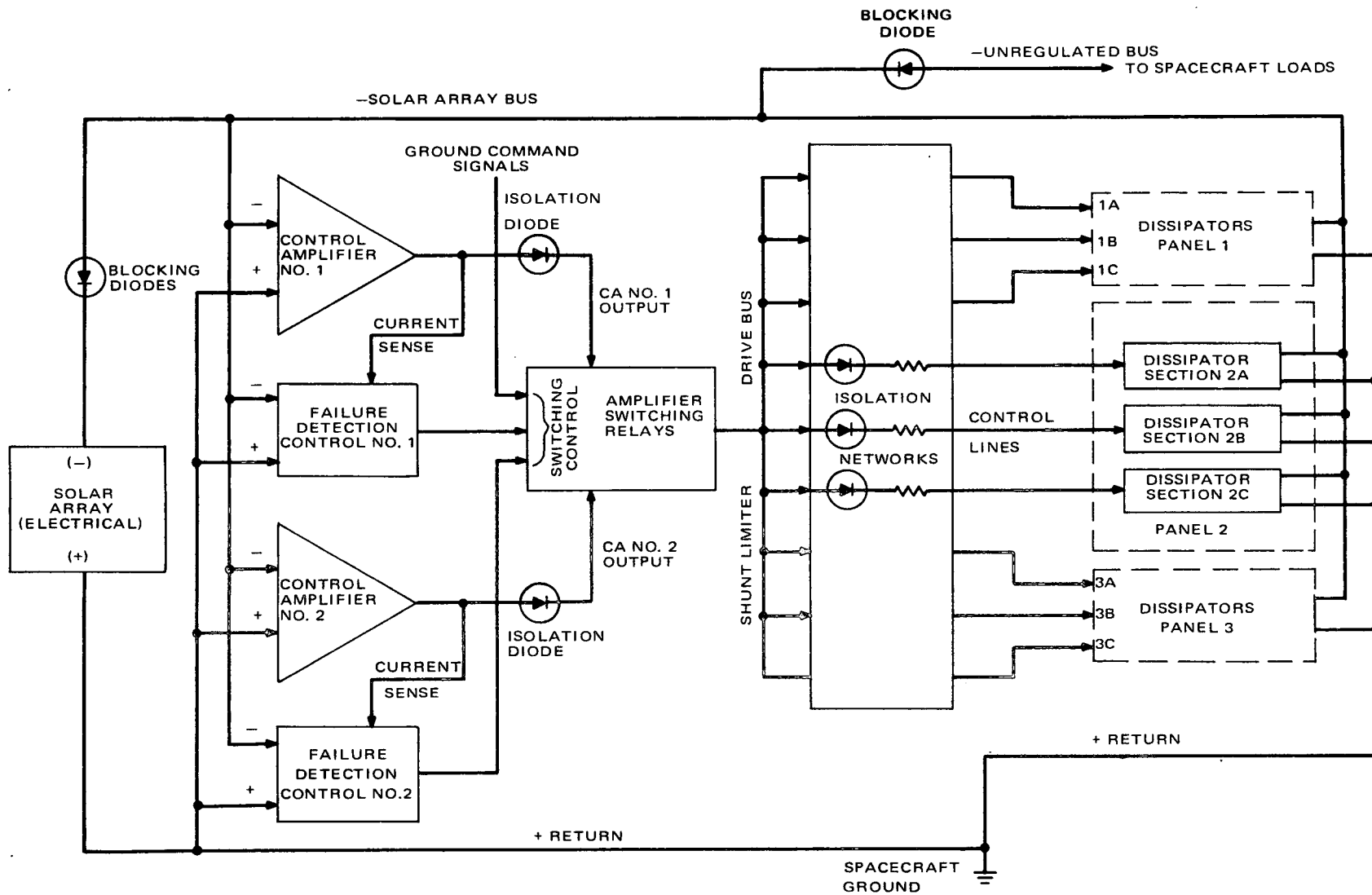


Figure 2-IX-12. Shunt Limiter, Functional Block Diagram

The control amplifier failure detection control protects the spacecraft against any failure in a control amplifier which causes the shunt dissipators to be turned on in error. This is done by detecting a simultaneous condition of solar array voltage less than -29 volts and the presence of control amplifier output current. Each of the two redundant control amplifiers is provided with an independent failure detection control. The functional diagram of this control is shown in Figure 2-IX-13.

(b) *Functional Operation*

1. Control Amplifier

Figure 2-IX-14 shows that portion of the shunt limiter which is located on boards A14, A15, and the heat sink (A11) of the PSE. The control amplifier is shown in the top half of the figure.

Transistor Q401, a dual NPN transistor, is a differential amplifier which compares the voltage sensed by the voltage divider (resistors R401 through R405) against the reference voltage provided by zener diode VR401. Resistor R408 provides bias current to VR401. Adjustable resistor R404 compensates for the initial tolerances of the voltage divider resistors and reference zener VR401.

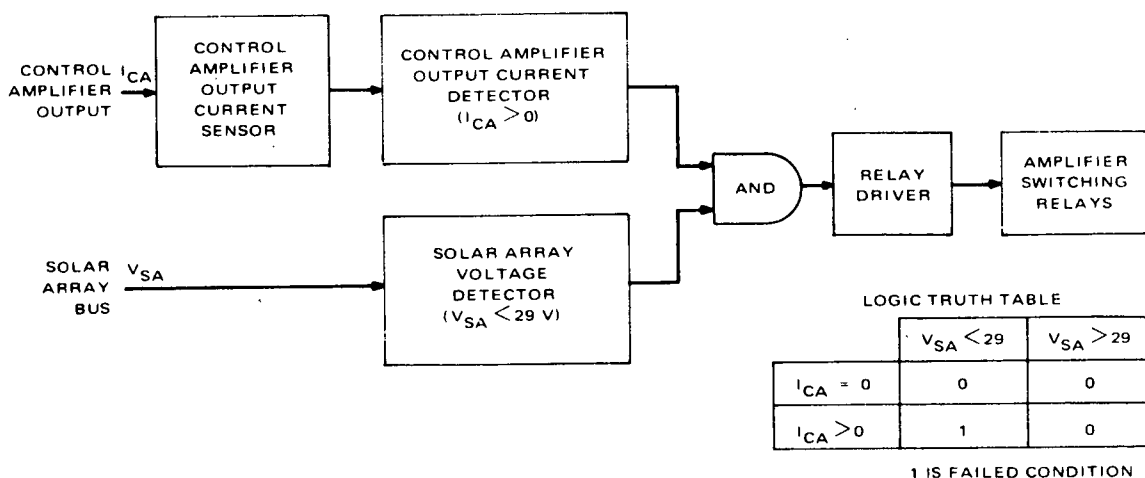


Figure 2-IX-13. Control Amplifier Detection Control, Block Diagram

Diodes CR401 and CR402 provide reverse voltage breakdown protection for the base-to-emitter junctions of Q401 and Q402.

The differential amplifier output is a voltage, developed across collector resistors R409 and R410, which drives Q402. Resistor R409 also provides degenerative feedback for the driver stage, Q402, to minimize variations in the open-loop gain characteristic of the amplifier.

Capacitor C401 compensates for the open loop frequency response characteristic of the amplifier, to assure adequate stabilization against circuit oscillation while allowing adequate load transient response and output impedance.

The second control amplifier (A15 board), not shown, is identical to the first control amplifier (A14 board).

Transistor Q409 and resistor R429 (located on the PSE heat sink) provide the additional current gain required to drive the total shunt current of 15.3 amperes in the nine shunt dissipator sections.

Capacitors C405 and C406 provide the specified solar bus impedance characteristic when the solar bus voltage is less than the shunt limiter threshold level (i.e., shunt limiter is OFF). They also serve to reduce the effects of load transients on the solar bus voltage.

2. Signal Distribution Board

Signal distribution from the two control amplifiers to the nine shunt dissipators is accomplished by the components shown in Figure 2-IX-15. These components are mounted on board A2 in the PSE.

Diodes CR427 and CR428 provide the isolation of the control amplifiers required to permit proper operation of the failure protection circuits to be described below.

The outputs of the two control amplifiers are fed to the shunt limiter drive bus (connecting the anodes of diodes CR406 through CR414) through contacts of magnetic-latching relays K1 and K2. These relays provide capability to operate with either one or both control amplifiers connected. The relays can be actuated by ground command or by the control amplifier automatic failure detection controls. The second sets of contacts are used to provide relay-position telemetry. Diodes CR415 through CR418, and CR423 through CR426, serve to clamp the fly-back voltage generated when the relay coils are driven.

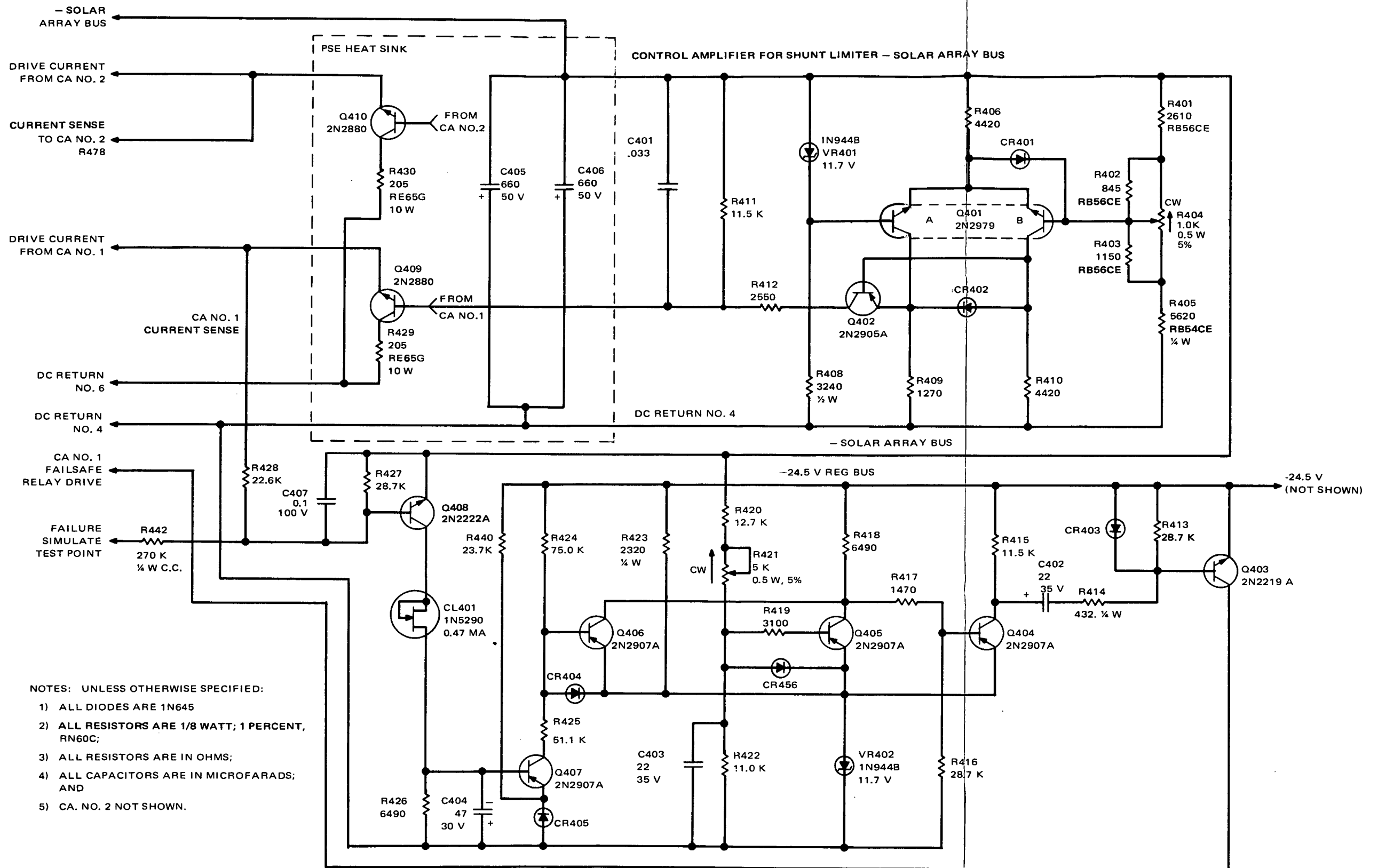
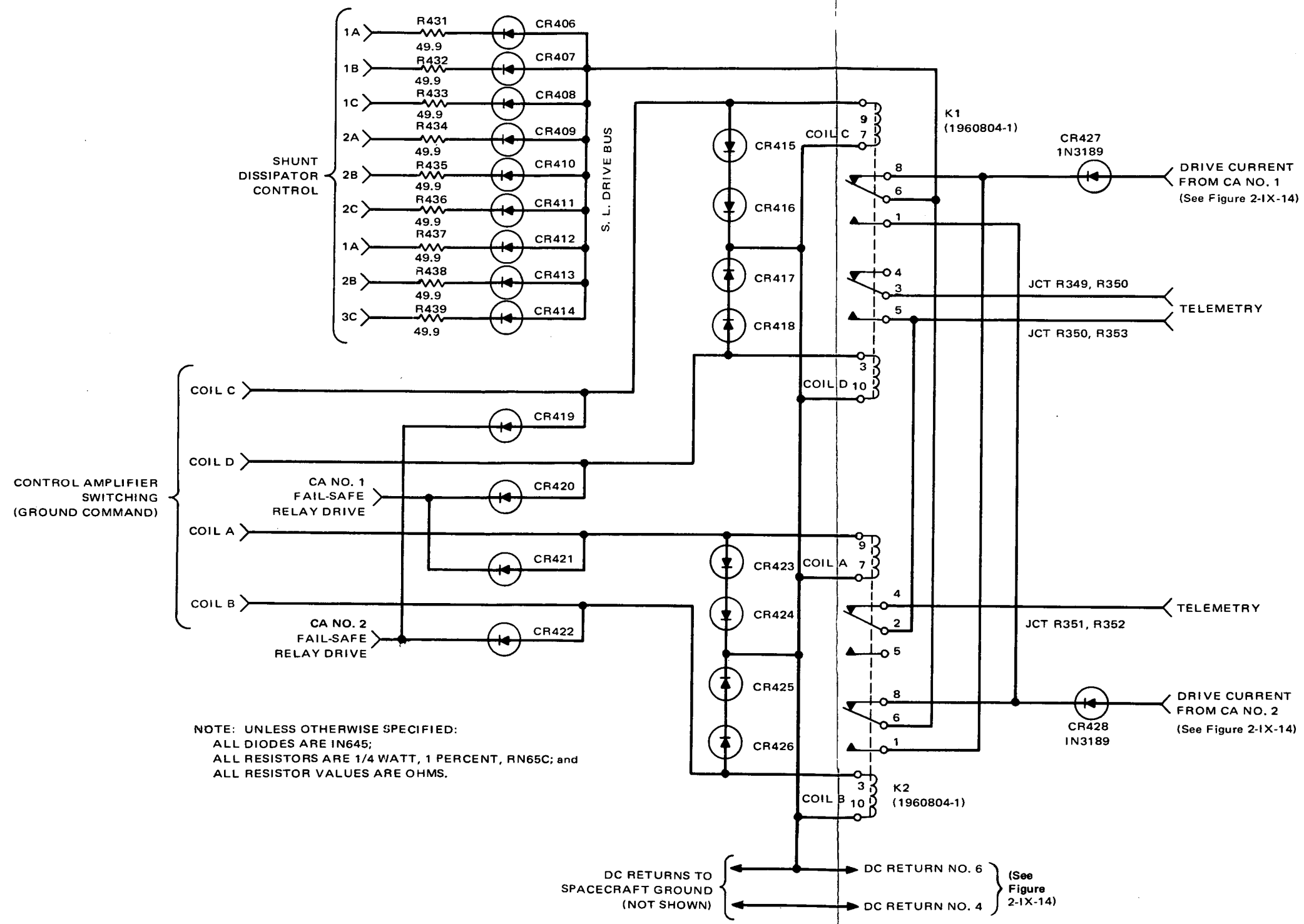


Figure 2-IX-14. Control Amplifier, Schematic Diagram



FOLDOUT FRAME 1

Figure 2-IX-15. Signal Distribution Board, Schematic Diagram

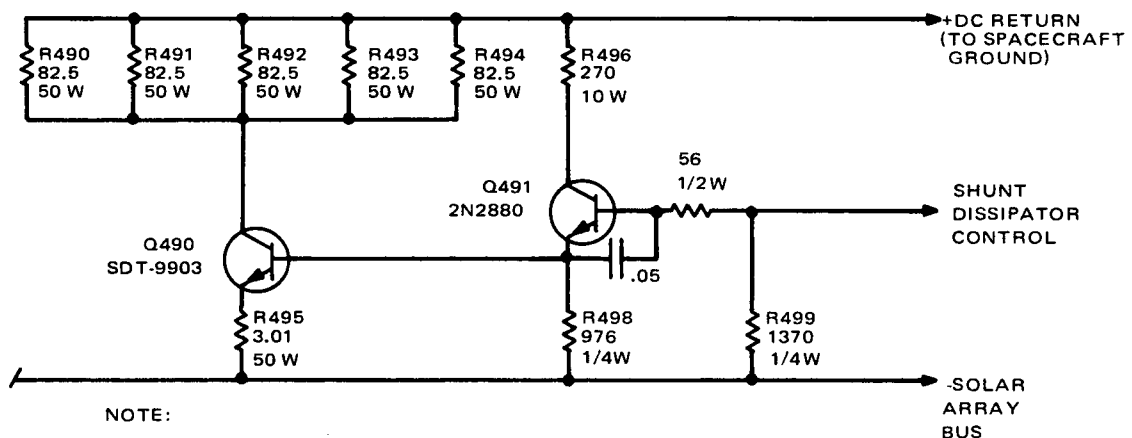
Diodes CR406 through CR414 and resistors R431 through R439 provide isolation of each shunt dissipator section from the others, thus preventing a failure in one section from disabling or interfering with the operation of the other sections.

Diodes CR419 through CR422 form two OR gates which allow one driver in the failure detection circuits to drive both relays simultaneously. If the diodes in the ground command switching lines (not located in PSE) are considered, independent control by both ground command and failure circuits is achieved.

3. Shunt Dissipator

Each of the nine shunt dissipator sections are identical electrically. Three sections are placed on each of the three solar array panels. The circuit operation of one section is described below.

As shown on Figure 2-IX-16, control current, from one of the control amplifier outputs, drives the base of Q491. A path for the leakage current of Q491 is provided by R499, which prevents thermal runaway at elevated temperatures. Drive current for Q490 is obtained from the emitter of Q491. A leakage current path for Q490 is provided by R498. Equalization of current between the power transistor of all the sections is primarily controlled by R495. Collector resistors R490 through R496, minimize the power dissipation in the power transistor Q490 and the power driver transistor Q491.



NOTE:
 ALL RESISTORS ARE IN OHMS
 THREE OF ABOVE SECTIONS REQUIRED
 PER SOLAR ARRAY PANEL; NINE (9)
 PER SPACECRAFT.

Figure 2-IX-16. Shunt Dissipator Leg (Part of Shunt Dissipator), Schematic Diagram

An isolation resistor (not shown) connects the collector of Q490 to a test connector to provide a test point. This resistor provides protection in the event that the test point is shorted at the connector.

4. Failure Detection Control

The failure detection control, shown in the lower half of Figure 2-IX-14, eliminates the effects of certain control amplifier failures by disconnecting the faulty control amplifier.

Control amplifier output current is sensed as a voltage level at the emitter of Q409 when the current flows. This current is detected by Q408 which turns on, causing Q407 to also turn on and which, in turn, drives Q406 off by shunting its base current through R425 to ground. Capacitors C404 and C407 provide noise immunity and timing delays for the current detector. Current limiting diode CL401 is used to decrease the sensitivity of the timing of variations in the solar bus voltage with minimum shunt current loss. Diode CR405 (biased by R440) and the base emitter voltage threshold of Q407 provide a long latching delay while allowing a shorter unlatching time.

Resistor R423 biases zener diode VR402 to establish a fixed voltage level at the emitter tie point of transistors Q404, Q405, and Q406.

The solar array bus voltage is detected by voltage divider resistors R420, R421 and R422 and transistor Q405. The detection level is -29 ± 1 volts. Trimpot R421 is used to compensate for the initial tolerances of the divider and VR402. If the solar bus voltage is greater than -29 volts, then Q405 is on; Q405 is off for bus voltages less than -29 volts. Capacitor C403 provides noise immunity. The AND gating function occurs when both Q405 and Q406 are off simultaneously, which provides drive current through R417 to the base of Q404. This causes Schmitt trigger action which "snaps" Q404, on, providing a step voltage across R415. This voltage is AC-coupled through C402 and R414 to Q403, which drives the appropriate relay (K1 and K2) coils (see Figure 2-IX-15) with a pulse.

Diodes CR403, CR404, and CR456 provide base-emitter reverse-voltage protection for their associated transistors.

(3) BATTERY CHARGE CONTROLLER

(a) General Description

The charge controller consists of circuitry within the PSE unit, and its function is to control recharging of the spacecraft nickel-cadmium batteries.

Two identical controllers are provided, one for each of the two battery packs. Each circuit, with its associated battery, is independent of the other and both operate at the same time. The functional block diagram of a single TIROS M charge controller is shown in Figure 2-IX-17.

The purpose of the charge controller is to protect the battery from overcurrent, overvoltage, and overtemperature conditions while it is being charged. The circuit performs this function by monitoring and operating upon the following parameters:

- Battery charge current,
- Battery temperature, and
- Battery terminal voltage.

The control circuitry was designed to accept signal inputs corresponding to each of the above parameters and to compare these inputs with built-in references. Deviations or error signals are amplified and ultimately adjust battery charging current in such a manner as to decrease the error.

There are three normal modes in which the charge controller might operate. These modes or regions of operation are indicated in Figure 2-IX-18.

In Region I, charging current should be as close as possible to the maximum allowable current to maintain energy balance. The tolerance requirements on the charge current have dictated a closed-loop or feedback type of current regulating circuit.

In Figure 2-IX-19, V_{R1} represents a reference voltage derived from a temperature compensating zener diode and a voltage divider; G_1 represents the forward gain or transconductance of the transistor circuitry; and h represents the feedback element which senses battery current, I_B , and transforms the current level to a voltage level which is compared with V_{R1} . The difference between V_{R1} and the converted current level is the error, E , which activates the forward gain to control the charge current.

In Region II, the voltage to which the battery may charge must be limited. It is desirable to adjust this limiting voltage with battery temperature in the manner suggested in Figure 2-IX-7.

Normally, at the beginning of charge, the battery will cause the charge controller to operate in Region I, the current limited mode. As the battery is charged, its terminal voltage and/or temperature will increase. Should the voltage/temperature combination enter Region II, the charge controller will sense this condition and

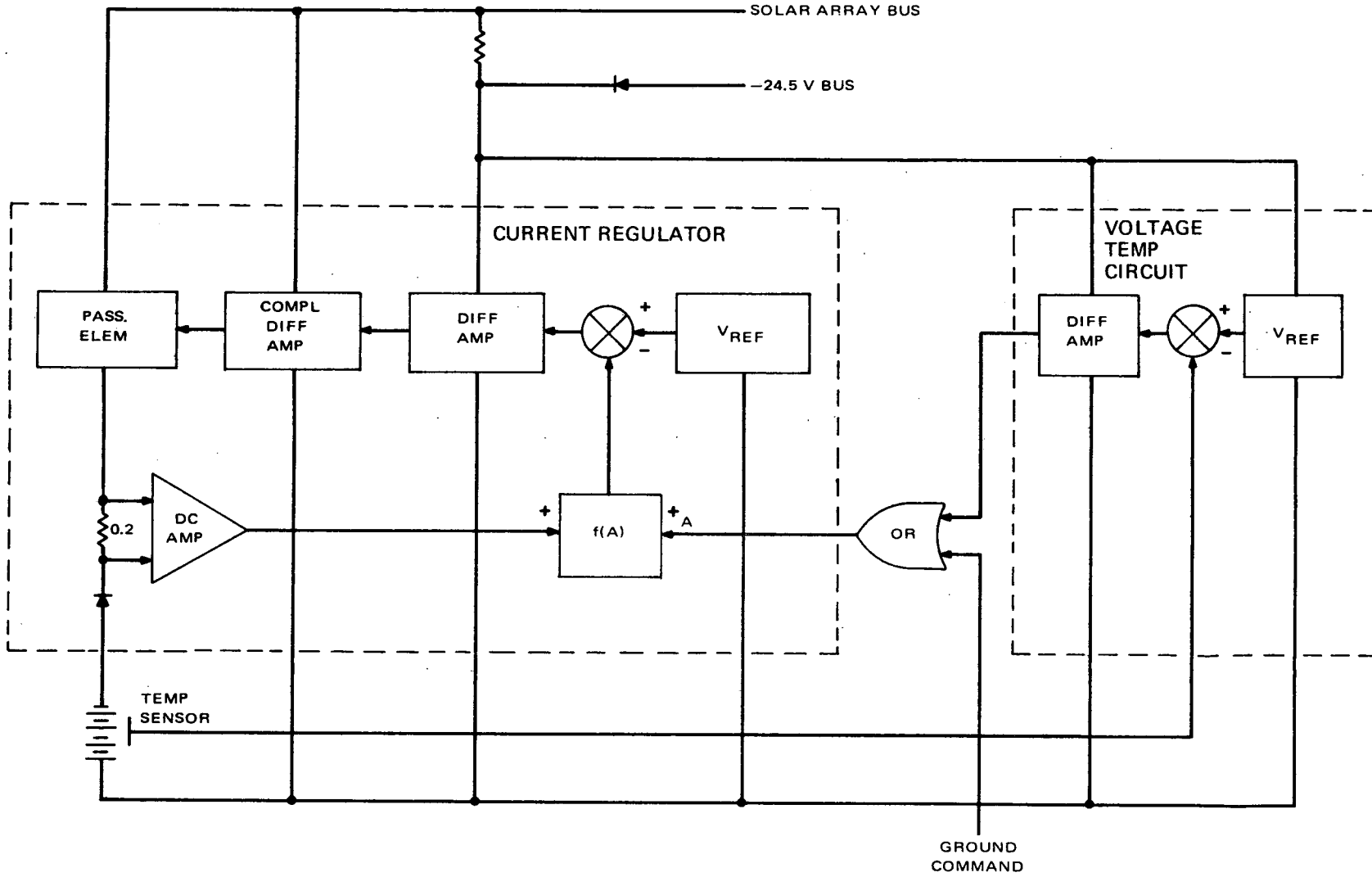


Figure 2-IX-17. Battery Charge Controller, Functional Block Diagram

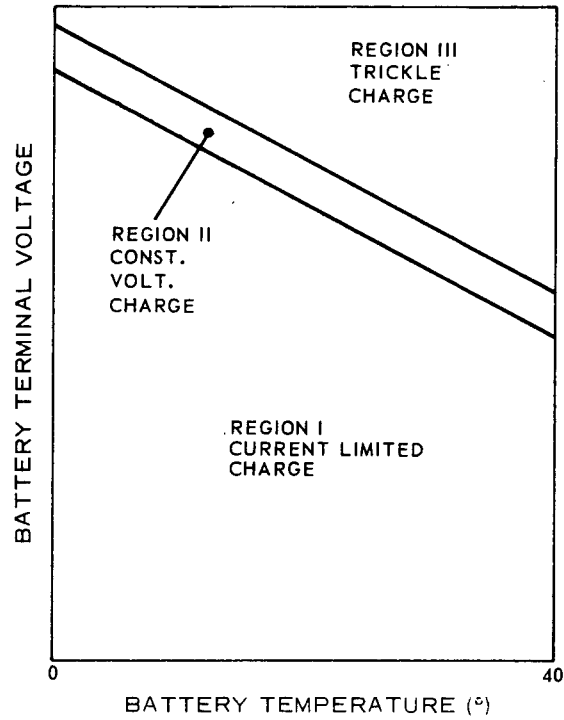


Figure 2-IX-18. Regions of Charge Controller Operation

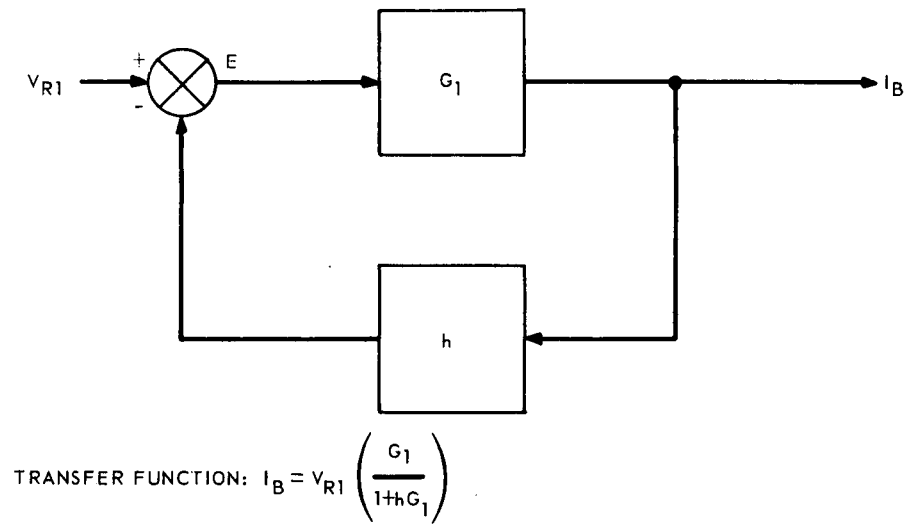


Figure 2-IX-19. Current Regulator, Block Diagram

will function to maintain the operating condition of the battery within this region. Since the charge controller may operate directly on charge current and on other parameters only as a function of charge current, the circuitry was designed to vary the current in order to maintain operation in Region II.

Within Region II, the charge controller becomes essentially a voltage regulator with an output voltage related to temperature. Figure 2-IX-21 illustrates this mode of operation.

If the gain, G_L , is high, then it may be shown that

$$V_B = V_{R2} \left(1 + \frac{R_T}{R_d} \right)$$

where

G_L is effective transconductance of transistor circuitry in Region II,

V_B is battery voltage,

V_{R2} is reference voltage for voltage-temperature circuit,

R_d is constant resistance, and

R_T is temperature sensitive resistor with a negative temperature coefficient.

As the battery temperature increases, R_T decreases, thereby reducing the value of V_B at which the circuit will regulate.

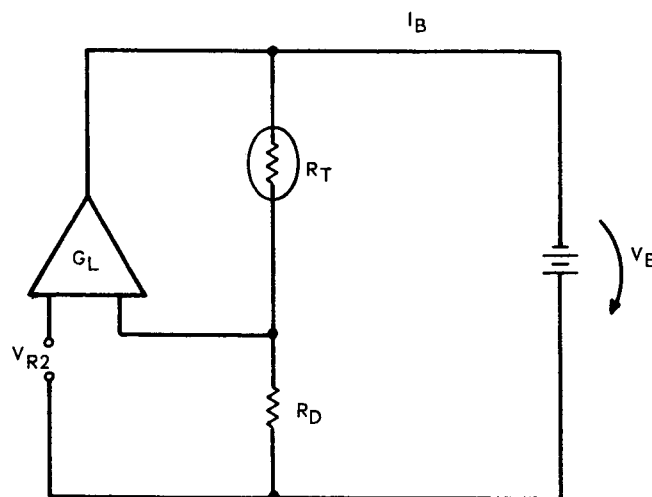


Figure 2-IX-20. Charge Controller Operation in Region II, Simplified Schematic

In Region III, the charge controller operates as a constant current regulator in essentially the same manner as in Region I, with the exception that the regulated current is the trickle charge current. This condition would occur in Region II operation if battery voltage and temperature conditions forced the voltage/temperature circuit to reduce charging current to the trickle charge limit.

As has been established in the foregoing discussion, the transition from one operating region to another is made when there are changes in the operating mode of the charge controller system. The basic operating mode is regulation of charge current. All transitions are accomplished by causing a reduction in the level of regulated current as a function of signal inputs to the current regulator from a ground command trickle charge circuit and/or the voltage/temperature sensing circuits. The nature of these signals is a voltage level shift from a high impedance point which is OR-gated into the appropriate current regulator input. Figure 2-IX-17 presents an operational diagram showing these signals. As indicated, the sensing signal inputs modify the feedback ratio of the current regulator in order to effect a change in the battery current.

For protection against various possible failure modes and for flexibility of load programming, a ground command is included. On a single command, both charge controllers are placed in the trickle charge mode regardless of which region the charge controllers may be operating. This circuit is shown in the charge controller schematic, Figure 2-IX-21. Here, the trickle charge control, derived from the circuitry, provides a trickle charge signal to each charge controller voltage sensing circuit at its point of connection to the current regulator loop. This signal will be in effect so long as the ground commanded relay is maintained at the trickle charge position.

Storage cell temperatures are sensed for the battery voltage/temperature charge control. A temperature sensor is used for this function. The normal failure mode for the temperature sensor is an open circuit. However, the circuit configuration is such that if the sensor opens, the battery will remain subjected to normal charge rate.

(b) *Functional Operation*

Figure 2-IX-21 includes a schematic diagram of the current regulator. Transistor Q11, a dual PNP transistor, forms a differential amplifier which compares the reference voltage developed from zener diode CR12 with the voltage output from a current-to-voltage transducer. The current-to-voltage transducer (Q5, Q6, Q7, and associated components) can be divided into three major sections:

- Current sensing resistors R55 and R56,
- DC single-ended amplifier (Q6, Q7, and associated components), and
- Bias source (Q5 and associated components).

The use of R55 and R56 in parallel reduces the probability of losing the ability to charge the batteries. Transistor Q6B amplifies the voltage drop developed across R55 and R56 to produce 5.0 volts at Q11A base (corresponding to 0.95-ampere charge current). Resistors R45 and R48 stabilize the voltage gain through de-generation. Resistors R47 and R49 are used to reduce changes in output voltage caused by battery voltage variations. As can be seen from the collector characteristics of Q6 (2N2060), the collector current is not entirely independent of collector voltage but tends to increase slightly with an increase in applied voltage. This effect is compensated for by modifying the bias in Q6 in a manner that reduces the collector current as collector voltage increases. Resistor R39 aids in developing a constant voltage source at the base of Q6B. The temperature characteristic of Q6B (V_{BE}) is virtually identical to that of Q6A (V_{BE}), resulting in the bias voltage at Q6A tracking variations in Q6B with changes in ambient temperature. (This is due to Q6B being connected as a diode and used as a compensating element for the base of Q6A.)

Transistor Q9 serves to modify the current-to-voltage transducer ratio when signal inputs are present from either the voltage/temperature circuit or trickle charge command circuit; Q9 is operated in saturation when no inputs are present. Injection of a signal current into the base circuit of Q9 modifies the effective load resistance of the current-to-voltage transducer, thereby directly changing its transformation ratio. Diode CR14 prevents excessive reverse biasing of the base emitter junction of Q9.

Also shown in Figure 2-IX-21 is a schematic diagram of the battery voltage/temperature circuit. The circuit consists of a differential amplifier whose inputs are a reference voltage, provided by a temperature compensated zener diode CR27, and a voltage proportional to battery voltage and temperature derived from the R71, R72, R73, and R(T) voltage divider.

The output of the amplifier is a current proportional to the difference in the two input voltages.

Minimum drift is achieved by the use of the temperature compensated zener (CR27), dual-packaged transistors Q15, Q16, and Q17, high stability resistors in the sensing arms, and the symmetrical arrangement used throughout, up to and including the output stage. Resistor R87 also aids in drift stabilization by matching the source impedances of the reference and the signal.

An adjustment is provided by R80 to compensate for initial circuit inaccuracies due to zener diode and resistor tolerances.

Transistors Q15A, Q16A, and Q17A are protected against excessive reverse bias of the IR base emitter junctions by diodes CR25, CR22, and CR21, respectively.

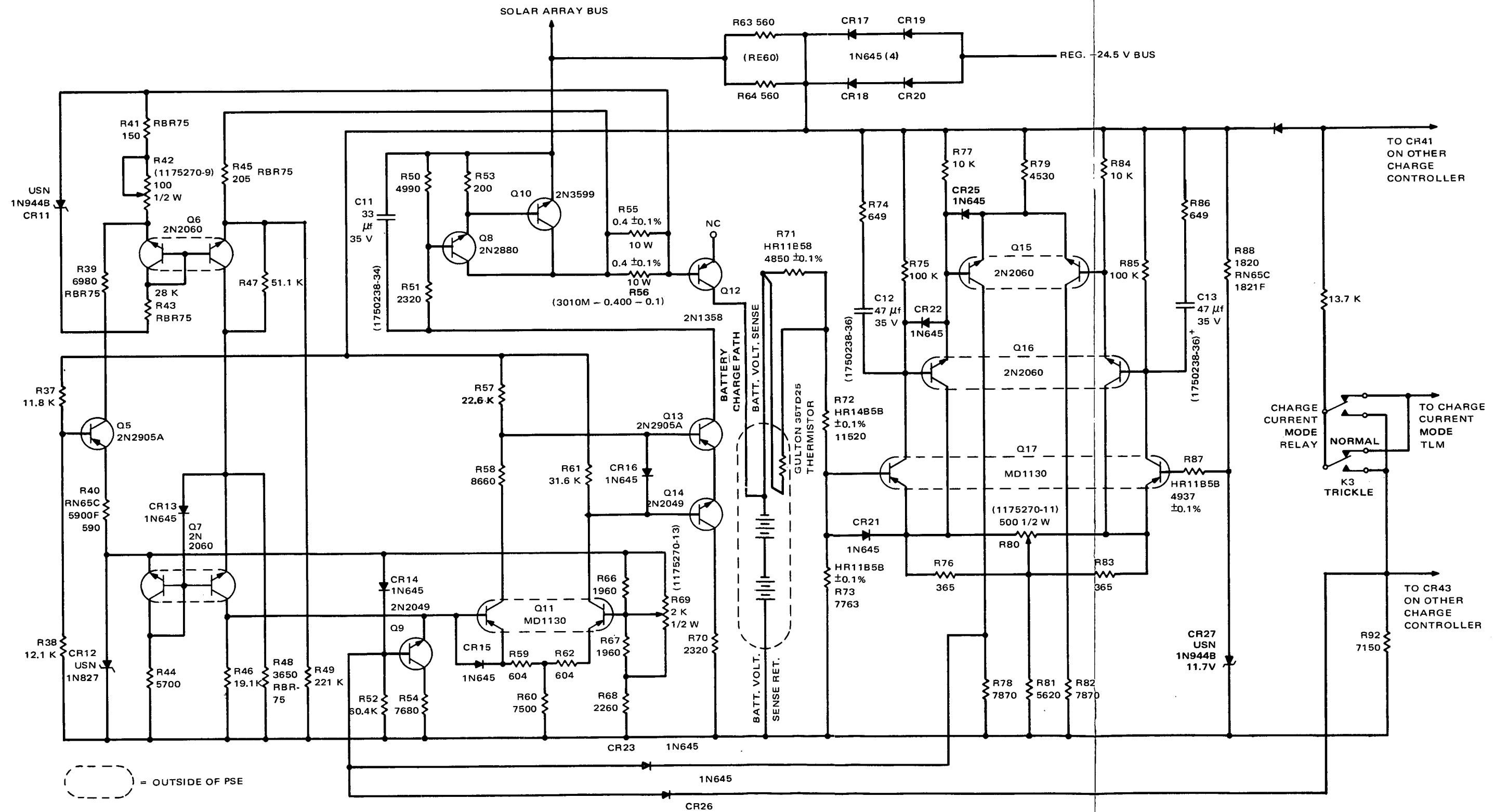


Figure 2-IX-21. Charge Controller, Schematic Diagram

FOLDOUT FRAME 1

FOLDOUT FRAME 2

Also shown in Figure 2-IX-21 is a schematic diagram of the ground command trickle charge circuit. At relay K3 closure, the circuit delivers a step-current to the current regulator which causes the battery current, I_B , to be reduced to the trickle charge level. The circuit operates on both charge controllers. The charge controllers will remain in the trickle mode until a ground command signal opens the relay.

(4) *TELEMETRY*

(a) *General Description*

The ITOS power supply subsystem consists of a solar cell energy conversion array, redundant series regulators, a shunt limiter with redundant control amplifiers, two nickel-cadmium batteries each with their own charge controller, and associated telemetry circuits. Various subsystem functions are telemetered to provide a means of analyzing the performance of the subsystem in meeting the spacecraft power requirements and to provide information in the event of power subsystem or spacecraft failure. These telemetry functions are useful during the spacecraft test phases as well as during orbital flight. To provide a more detailed insight into the functional significance of the telemetered parameters, they are discussed at length either individually or in related groups. A summary of the characteristics of the telemetry circuits is shown in Table 2-IX-6. The majority of these circuits were previously used on the Nimbus B program.

(b) *Voltage Telemetry*

Simple resistor dividers heretofore employed to measure voltages throughout the power subsystem have been replaced by expanded scale voltage sensing circuits for improved resolution. These circuits also provide isolated signal output returns which may be connected to the encoder signal ground at any point without interference from power ground currents.

There are two voltage sensing circuits, as shown in Figures 2-IX-22 and 2-IX-23, but they are functionally identical. The main difference between the two circuits is in the voltage ranges telemetered.

Circuit operation is as follows. No output appears across R4 until the voltage to be telemetered exceeds the reference voltage of the base of Q1B. The voltage developed across R3, as the telemetered voltage increases, establishes an emitter current in Q1B which for large values of current gain equals the collector current. Since the collector current is essentially independent of collector voltage, the output appearing across R4 will be independent of voltages between the

TABLE 2-IX-6. SUMMARY OF TELEMETRY CHARACTERISTICS

Symbol	Telemetry Type	Nominal Input Range	Nominal Output Range (volts)	Open Circuit Accuracy ¹	Source Impedance ⁷ (in kilohms)	Max Shunt Loss (mA)	
						ON	OFF
V ₁	Solar Array Voltage	-22 to -40V	-0.5 to -4.5	1% ²	5.3 ±5%	2.6	1.2
V ₂ V ₃	Battery Voltage	-22 to -40V	-0.5 to -4.5	1% ²	5.3 ±5%	2.6	1.2 (ca)
V ₄	Unreg Bus Voltage	-22 to -40V	-0.5 to -4.5	1% ²	5.3 ±5%	2.6	1.2
V ₅	Reg Bus Voltage	-15 to 35V	-0.5 to -4.5	1% ³	5.3 ±5%	3.0	0.97
T ₁ T ₂	Battery Temperature	-10° to +50°C	-1.0 to -4.5	2°C ⁴	2.65 ±12%	1.6	0 (ca)
T ₃ T ₄ T ₅	Shunt Lim Temperature	-65° to +100°C	-0.1 to -4.5	8.8°C ⁴	2.70 ±12%	1.6	0 (ea)
T ₆	PSE Temperature	-10° to +85°C	-1.0 to -4.5	4.5°C ⁴	2.70 ±12%	1.6	0
T ₇ T ₈ T ₉	Solar Array Temperature	-100° to +60°C	-0.1 to -4.5	8.7°C ⁴	2.75 ±12%	1.6	0
I _{1a} I _{1b} I _{1c}	Solar Array Current	0 to 5.2 A	-0.5 to -4.5	3% ⁵	4.35 ±3%	6.3	0.72 (ca)
I ₂	Shunt Lim Current	0 to 15.3 A	-0.5 to -4.5	6% ²	2.48 ±2%	0.2	0
I ₃ I ₄	Battery Charge Current	0 to 1.0 A	-0.5 to -4.5	3% ⁵	4.35 ±3%	6.6	0.73
		Condition					
V ₆	Shunt Lim Control Ampl Selector	Control Ampl 1 ON Only	-1.8	5% ⁶	2.70 ±7%	1.5	1.5
		Control Ampl 2 ON Only	-4.49				
		Both Control Ampl ON	{ -2.7 -3.73				
V ₇	Regulator and Charge ⁸ Current Mode Selector	Reg 1 ON-Trickle Chrg ON	-2.85	8% ⁶	2.475 ±18%	3.27	3.27
		Reg 1 ON-Chrg Cur Norm	-1.80				
		Reg 2 ON-Trickle Chrg ON	-4.40				
		Reg 2 ON-Chrg Cur Norm	-3.70				

¹Calibrated, worst-case, full scale accuracy. This represents the maximum, full scale deviation from a calibration curve for an end-of-life period of 1 year.

²Calibration at 25°C and V_R midrange.

⁵Calibration at three temperatures and regulated and unregulated voltage midrange.

³Calibration at 25°C and V_u midrange.

⁶Without calibration curve.

⁴Calibration at V_R midrange.

⁷< 30 kilohms (specification).

⁸Value only when solar array is illuminated.

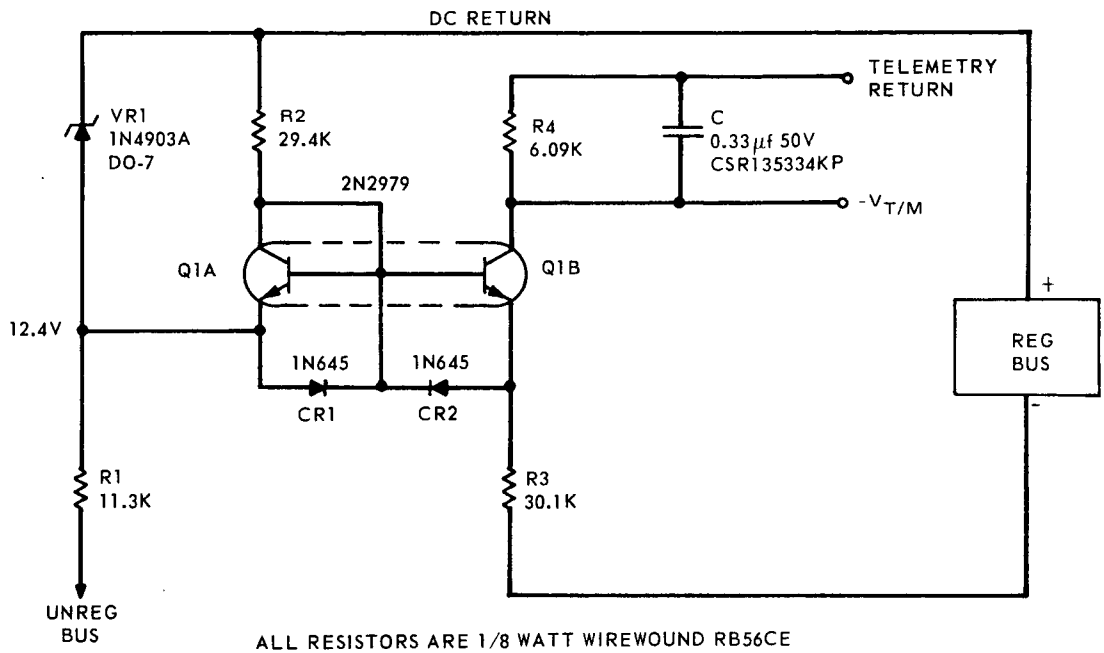


Figure 2-IX-22. Regulated Bus Voltage Telemetry, Schematic Diagram

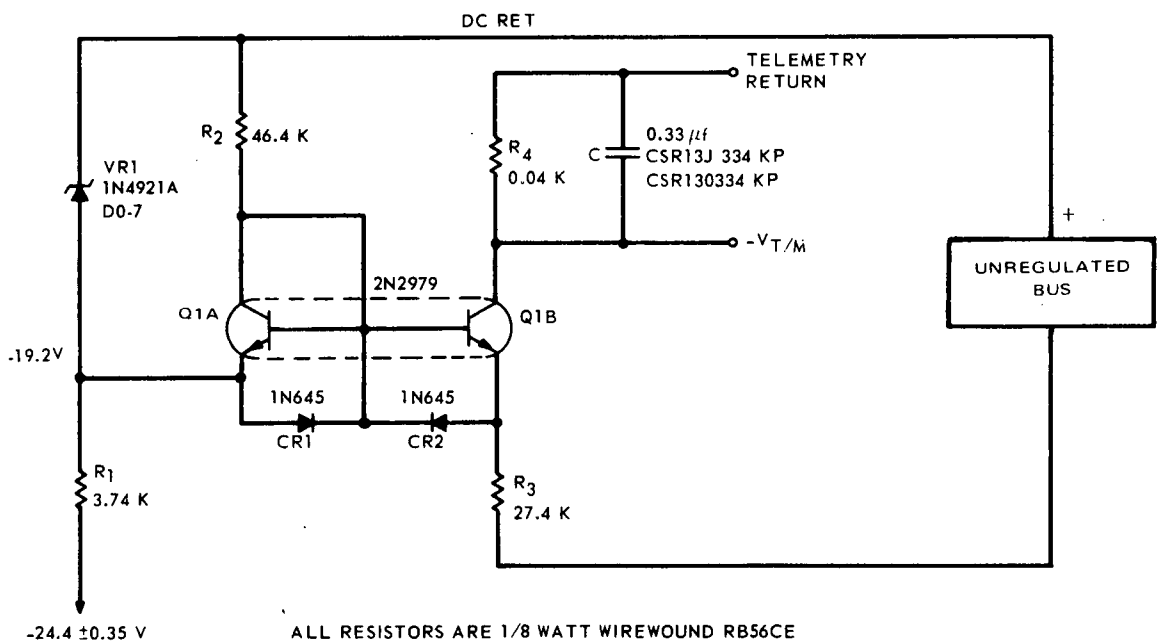


Figure 2-IX-23. Solar Array, Battery, and Unregulated Bus Voltage Telemetry, Schematic Diagram

power ground and the telemetry encoder grounds. Q1A is connected in such a manner as to cancel temperature variations in V_{BE} of Q1B. The capacitor across R4 reduces any high frequency noise which might appear in the output.

(c) *On-Off Telemetry Functional Operation*

The shunt limiter control amplifier selector telemetry provides four distinct voltage levels, depending on the states of the control amplifiers switching relay. The four levels are required so that each of the four relay state combinations is known. As shown in Figure 2-IX-24, the circuit operates as a simple resistor voltage divider with selected resistors shorted out to produce the desired voltage levels.

The combination regulator selector and charge current mode selector on-off telemetry circuit also provides four distinct voltage levels to define the various states of the two circuits simultaneously. The circuit configuration is shown in Figure 2-IX-25.

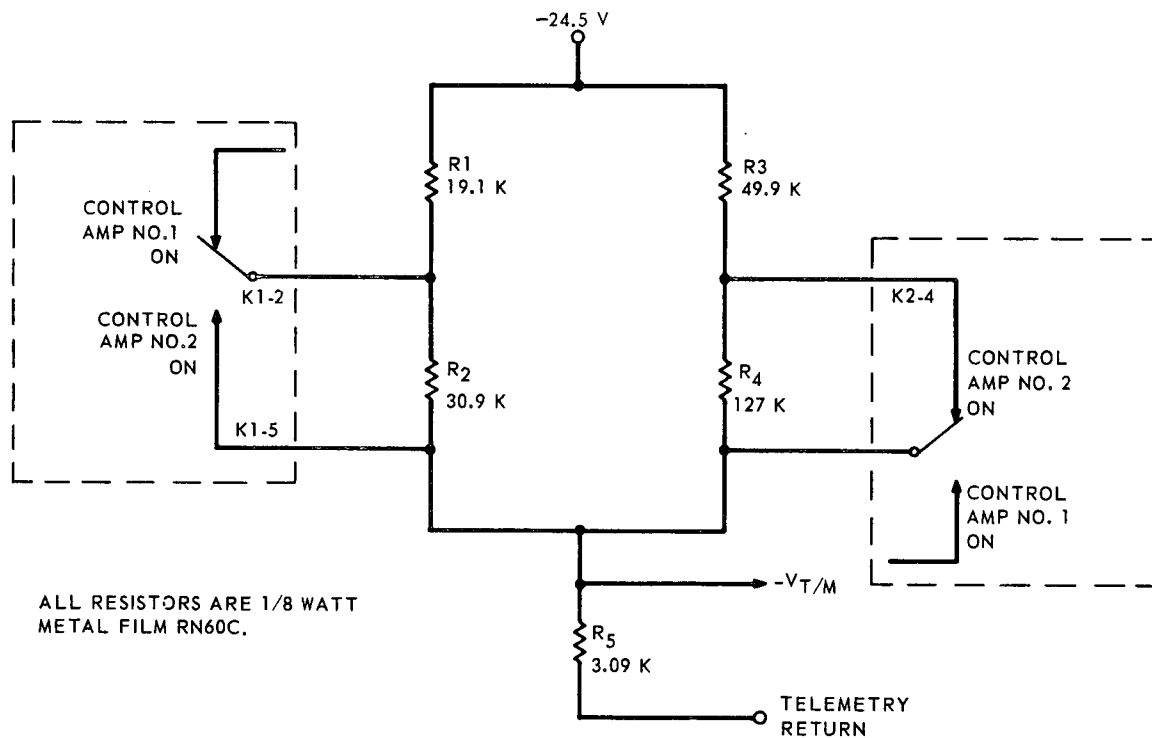
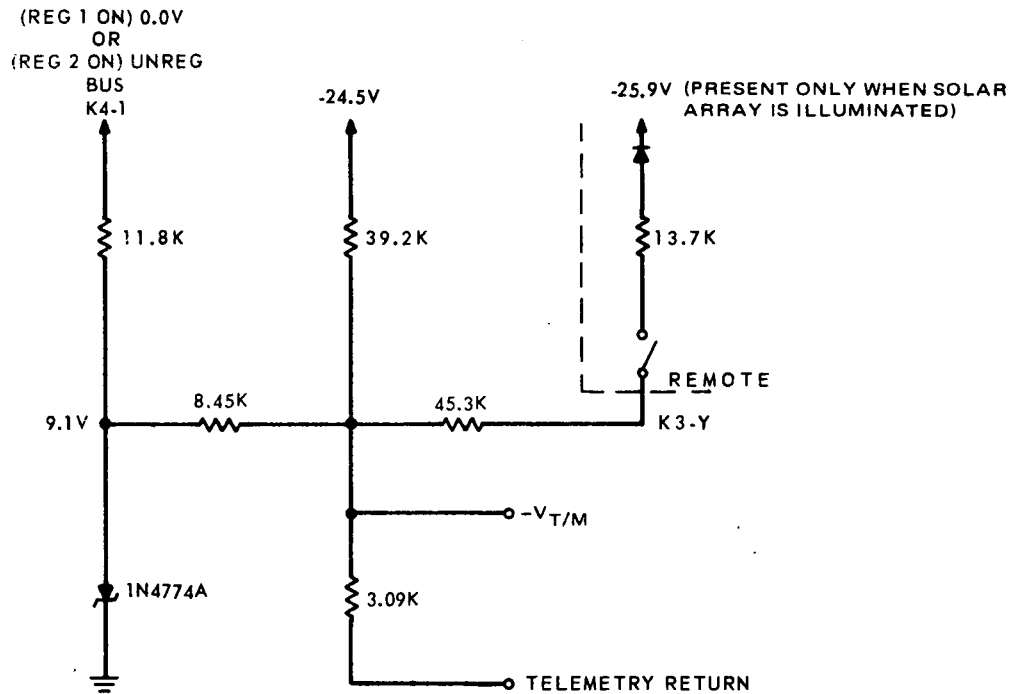


Figure 2-IX-24. Shunt Limiter Control Amplifier Selector Telemetry, Schematic Diagram



ALL RESISTORS ARE 1/8 WATT METAL FILM RN60C.

Figure 2-IX-25. Regulator and Charge Current Mode Selector Telemetry, Schematic Diagram

A zener diode is used to establish a relatively constant voltage for the regulator selector section represented by the unregulated bus. The remainder of the circuit operates as a simple resistor voltage divider with resistance values selected to produce the desired voltage levels for each of the combined on-off conditions.

(d) *Temperature Telemetry Functional Operation*

All temperature telemetry circuits consist of resistor-thermistor voltage dividers designed to produce the most linear telemetry characteristics over the temperature ranges desired. Thermistors are located on the batteries, the PSE baseplate, the solar array, and near the warmest transistor of the shunt limiter. Any change in temperature causes a change in thermistor resistance, and, in turn, a change in the current flowing through the output resistor. A capacitor across each output reduces any high frequency noise which might appear. The different temperature telemetry circuits are shown in Figures 2-IX-26 through 2-IX-29.

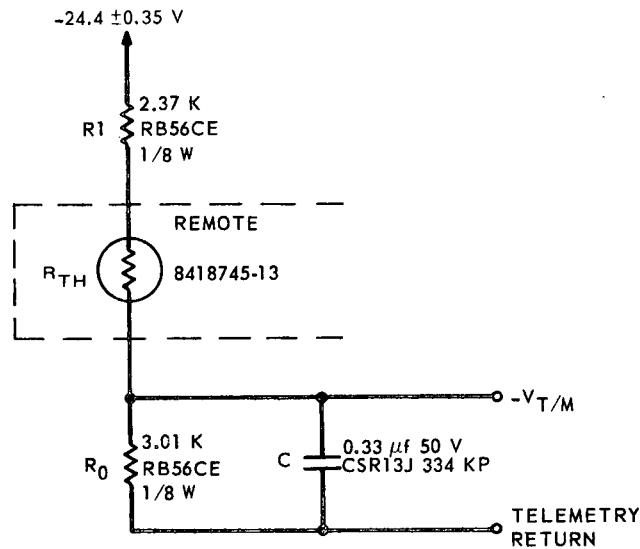


Figure 2-IX-26. Battery Temperature Telemetry, Schematic Diagram

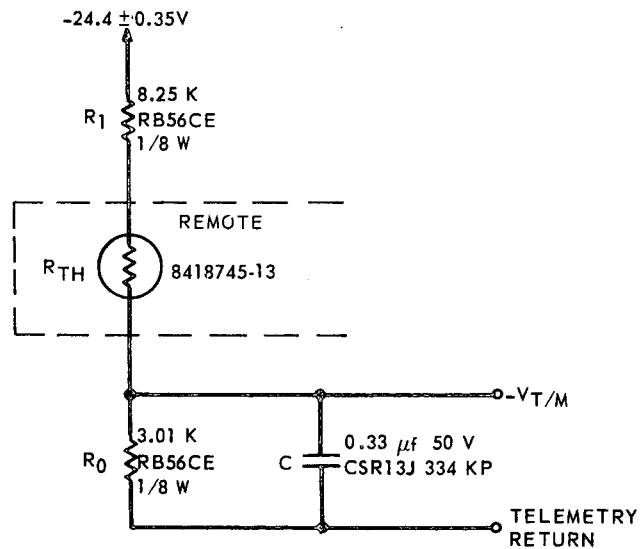


Figure 2-IX-27. PSE Temperature Telemetry, Schematic Diagram

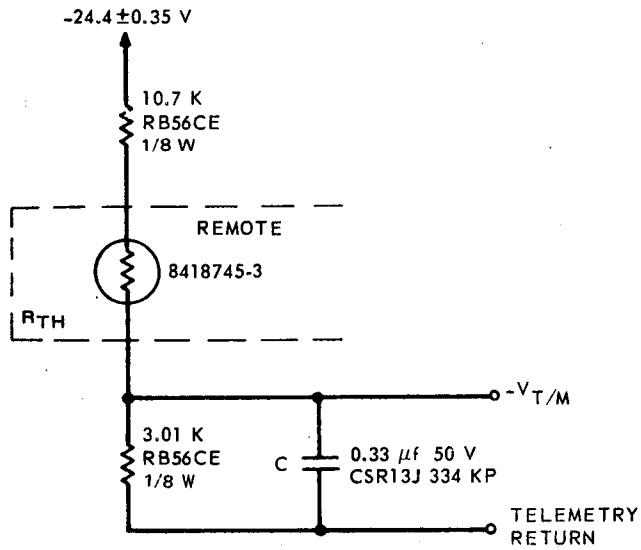


Figure 2-IX-28. Shunt Limiter Temperature Telemetry, Schematic Diagram

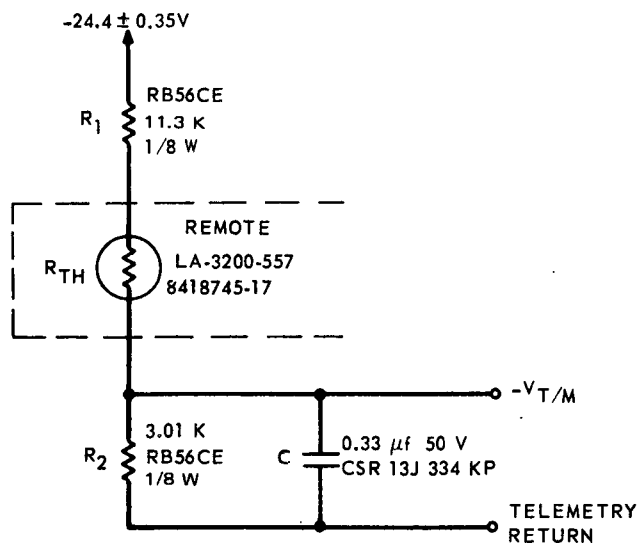


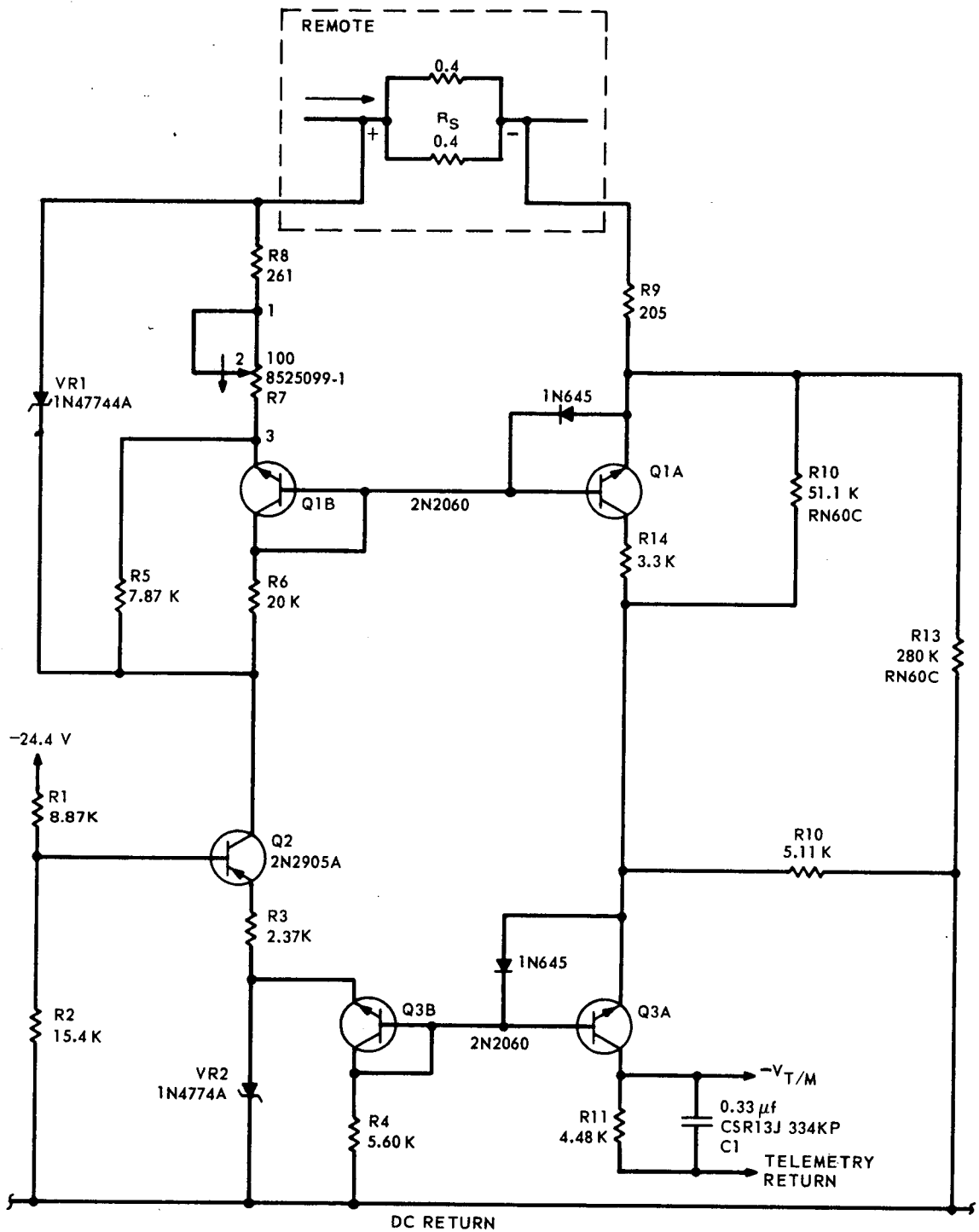
Figure 2-IX-29. Solar Array Temperature Telemetry, Schematic Diagram

(e) *Current Telemetry*

The battery charge current and the solar panel current telemetry circuits are shown in Figures 2-IX-30 and 2-IX-31. Both circuits are functionally identical. A voltage drop is created across the sensing resistors by the current telemetered. This drop is then converted to a usable analog telemetry signal.

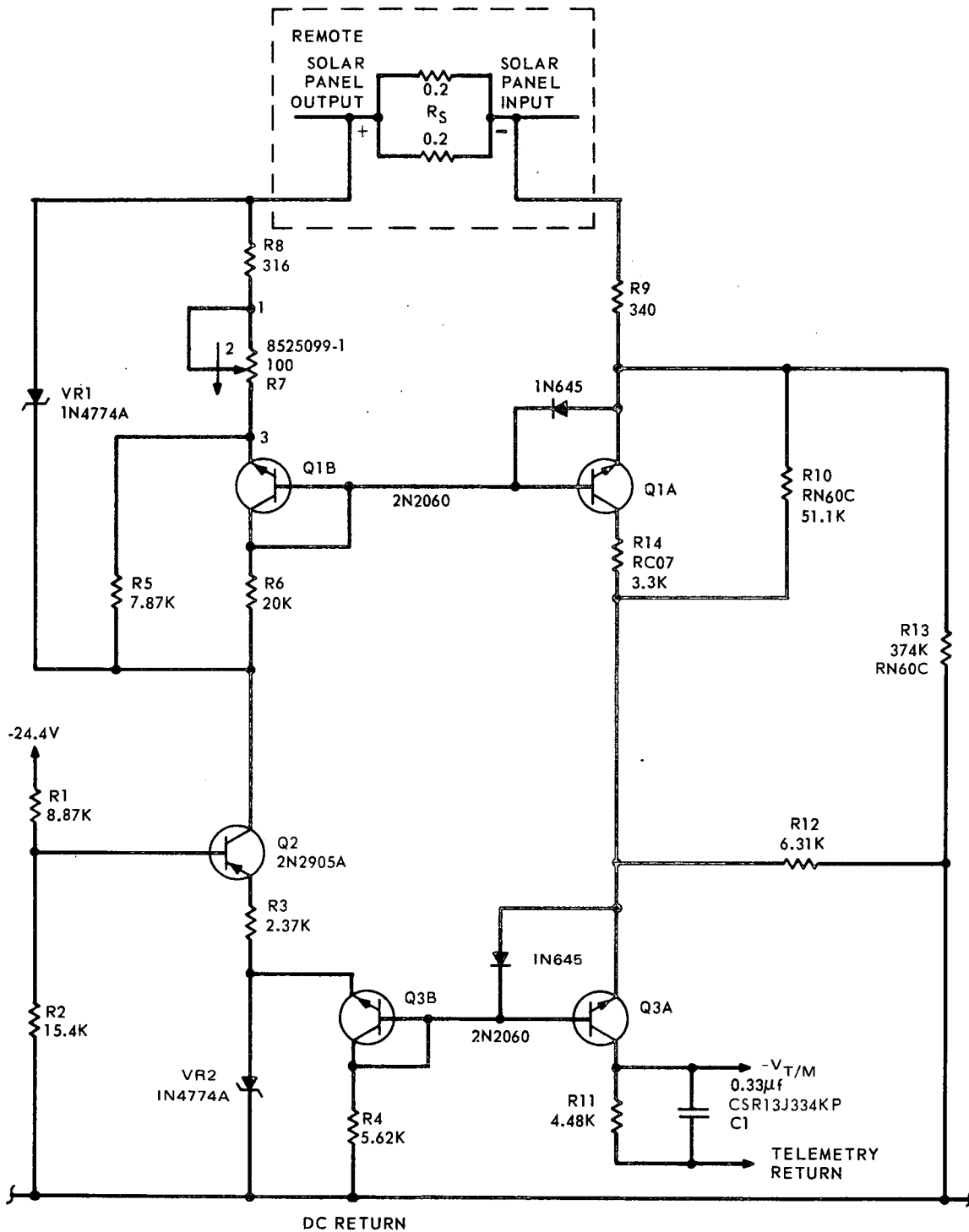
Circuit operation is as follows: two common-base transistor amplifiers (Q1 and Q3) are used to produce voltage gain by virtue of the input to output impedance transformation. Fixed bias is applied to the base of Q1B by a voltage divider connected across a zener diode, VR1. The temperature dependence of both Q1 base emitter junctions are virtually identical; therefore, the bias voltage divider tends to track variations in $Q1-V_{BE}$ due to changes in ambient temperature. The bias circuit of Q3 is similar to that of Q1 with zener diode VR2 acting as a fixed bias voltage source. Zener diode VR2 also maintains a maximum voltage limit on the telemetry output to prevent excessive voltages from being applied to the telemetry encoder. Transistor Q2 serves as a constant current source for the bias network. Resistors R1 and R2 form a voltage divider which determines bias voltage at the base of Q2. The resistance R3 determines the collector current flowing in Q2. Trimpot R7 sets the bias for the first stage and thus controls the offset level of the telemetry characteristic. However, this adjustment does not affect the circuit gain or slope of the telemetry characteristic.

Current sensing resistors R_S are connected in parallel and inserted in series with the current to be measured. The use of two resistors in parallel reduces the risk of losing a battery or an array panel in the event a resistor fails by opening. As the current varies through its range, a voltage is developed across the sensing resistors. Transistors Q1A and Q3A amplify this voltage drop to produce the telemetry signal. Resistor R9 aids in stabilizing the voltage gain through degeneration. In order to achieve linear amplification, the transistors are operated in the central portion of the collector load lines. Operation in the collector current cutoff region is prevented in Q1A and Q3A by the voltage offset. Therefore, when signal current is zero, collector currents will be minimum and the telemetry signal will be a nominal 0.5 volt. Resistors R10 and R13 are used to reduce the error in telemetry output voltage caused by the unregulated bus voltage variations. The collector current flowing in a transistor is not entirely independent of collector voltage and tends to increase slightly with an increase in applied voltage. This effect is compensated for by modifying the bias on the transistor with R13, in a manner that reduces base current as voltage increases. R10 is used to swamp out the effects of collector resistance. Capacitor C1 across the telemetry output reduces any high frequency noise which might appear.



ALL RESISTORS ARE 1/8 WATT WIREWOUND
RB56CE TYPE EXCEPT WHERE SPECIFIED.

Figure 2-IX-30. Battery Charge Current Telemetry, Schematic Diagram



ALL RESISTORS ARE 1/8 WATT WIREWOUND RB56CE TYPE EXCEPT WHERE SPECIFIED.

Figure 2-IX-31. Solar Panel Current Telemetry, Schematic Diagram

The shunt dissipator current telemetry, as shown in Figure 2-IX-32, consists of a simple resistor voltage divider connected across the collector resistor of the shunt dissipator through which the main portion of the shunt dissipator current flows.

Resistor R1 provides a 0.5-volt offset voltage when that current is zero. There is also an output capacitor for noise suppression.

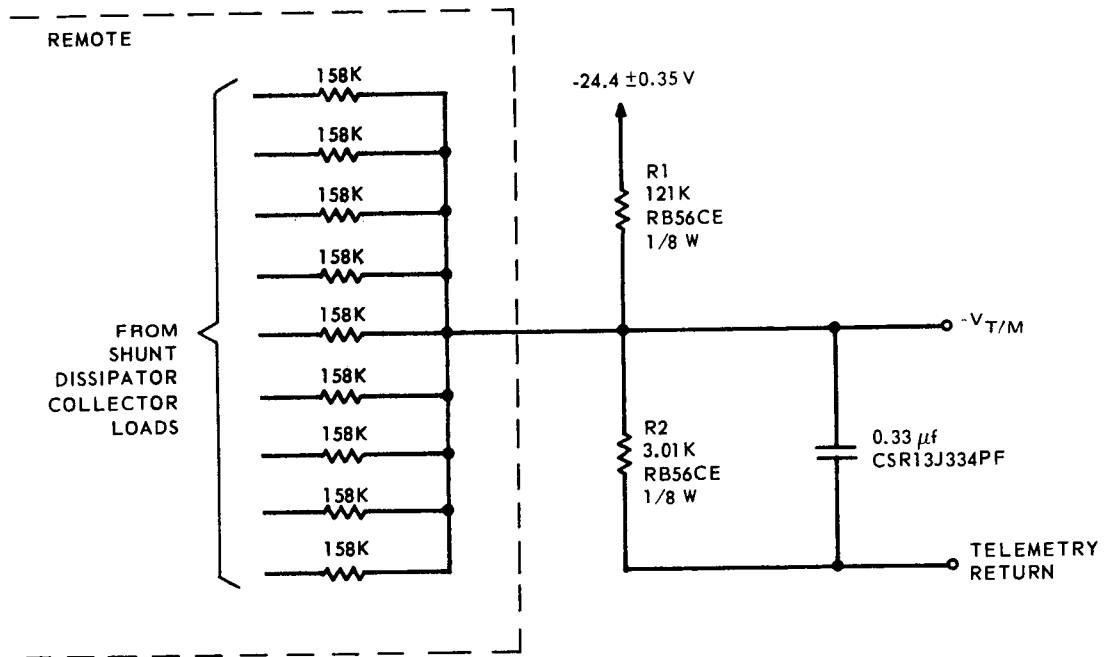


Figure 2-IX-32. Shunt Dissipator Current Telemetry, Schematic Diagram